HYDROXYAPATITE-BASED MATERIALS FOR SMART ANTITUMOR DRUG DELIVERY SYSTEMS, ENDOCYTIC PATHWAYS AND ENDOSOMAL TRAFFICKING

Manuel Rivas Cañas

Ph.D Thesis

UNIVERSITAT POLITÈCNICA DE CATALUNYA
BARCELONATECH
Escola d'Enginyeria de Barcelona Est

HYDROXYAPATITE-BASED MATERIALS FOR SMART ANTITUMOR DRUG DELIVERY SYSTEMS, ENDOCYTIC PATHWAYS AND ENDOSOMAL TRAFFICKING

Polymers and Biopolymers

Manuel Rivas Cañas

Advisors: Jordi Puiggalí Bellalta and Luís Javier del Valle Mendoza

Departament d'Enginyeria Química
Escola d'Enginyeria de Barcelona Est
Universitat Politècnica de Catalunya

Barcelona, 2019

"Supongamos que la mente sea un papel en blanco, vacío de todo carácter impreso, sin ninguna idea, ¿Cómo llegar a obtener todo el conocimiento de los fenómenos?"

"A esto respondo con una sola palabra: Experiencia".

John Locke. (Ensayo: II.2.)

ABSTRACT

Development of new drug molecule is expensive and time consuming. Improving safety efficacy ratio of “old” drugs has been attempted using different methods such as individualizing drug therapy, dose titration, and therapeutic drug monitoring. Delivering drug at controlled rate, slow delivery, targeted delivery are other very attractive methods and have been pursued vigorously. Now a new class of bioceramics based on calcium phosphate (CaP) salts is on the verge of being widely applied in the clinic. Among various types of CaP, hydroxyapatite (HAp) have attracted more attention in biomedical fields due to its exceptional features such as biocompatibility, bioactivity, osteoconductivity and osteoinductivity.

Its "chemical similarity" with the mineralized phase of biologic bone makes it unique. HAp as an excellent carrier of osteoinductive growth factors and osteogenic cell populations. HAp can incorporate the drug molecules either physically or chemically so that the drug retains intact until it reaches to the target site. It could also gradually degrade and then deliver the drug in a controlled manner over time. So therefore, this bioceramic is an excellent candidate for targeted drug delivery regardless of its density. Careful selection of reaction conditions, reagent concentrations and adsorption agents often provides a degree of size and shape control in nanoparticles dissolution, and a considerable amount of recent research has been devoted to developing such methods.

Biomineralization processes provide astonishingly complex and functional solid structures that are composed of very different materials with remarkable properties. Mg^{2+}, $CO_3^{2-}$and F^- are among the most relevant ions that may be incorporated into HAp, these minor species affecting the morphology, stability and properties of the mineral. In order to prepare synthetic HAp for biomedical applications, knowledge about the formation and stability of HAp in general is a prerequisite. Researchers outside the field of biomineralization have determined that mitochondria can produce inorganic phosphates, like orthophosphates, polyphosphates and phosphonates, as well as store calcium in a calcium-polyphosphate complex. This association between polyphosphate/ phosphonate biochemistry and apatite biomineralization is new. The study of polyphosphate and phosphonate chemistry remains on the fringe of chemistry and biochemistry. This thesis is intended to convey knowledge about these aspects of HAp.

Delivery of drug carriers to the target cells can be only a part of the whole story of successful drug targeting. Some drug carriers may have to gain access to and get inside the cytoplasm of a target cell in order to release the drug at the optimum rate for the pharmacological effectiveness. In that sense, intracellular targeting is an important systemic targeting. On the other hand, in some pathologies, especially in cancer, cell defends itself actively by using molecular ‘pumps’ in cell membrane that actively expel drugs form the interior -multidrug resistance (MDR)- and therefore their impairment is likely to have a significant therapeutic benefit. Thus, understanding mechanism of intracellular localization is critical in developing some drug delivery systems. This release is strongly influenced by resistances to mass transfer, intracrystalline diffusion and adsorpted species. The main goal of this thesis is to design an effective MDR reversing nanoparticulate drug delivery system consists of a HAp polymeric matrix from which the drug is released intracellularly.

Finally, we study injectable hydrogels utilizing polymer-nanoparticle (NP) interactions between peptides and hydroxyapatite NPs. Transient and reversible hydrophobic forces between the NPs and peptide chains govern the self-assembly of hydrogels. Owing to the hierarchical structure of the gel, molecular delivery is controlled both by Fickian diffusion and erosion-based release affording differential release of multiple compounds from a single material.

ACKNOWLEDGEMENTS

Cuando hablamos de la gratitud, como de los conjuntos infinitos, ¿es el todo mayor que la parte?. Aún así, no puedo comenzar este discurso sin agradecer en carne, huesos y alma a mi mujer Ana, a mis hijos Marina y Joan, a mis padres y a mi hermano. A ellos he debido siempre todo o incluso más. Atención, desvelos y absoluta dedicación. Agradecer al bienaventurado Dr. Luis Javier del Valle, que me rescató de una delicadísima situación personal y me regaló el tiempo, los libros, la escuela y los compañeros que hicieron posible este proyecto. Al Prof. Dr. Jordi Puiggalí, que no sólo administró a manos llenas su generosidad conmigo sino que añadió el don de su tiempo y conocimientos en esta aventura. Al Prof. Dr. Carlos Alemán, y su proverbial enseñanza de que en muchas ocasiones lo fundamental no es la visión de conjunto, sino la relevancia de los detalles significativos. A la Dra. Lourdes Franco, quien me enseñó que hay una fuerza motriz más poderosa que la electricidad y la energía atómica: la voluntad.

Quiero expresar mi enorme gratitud a la compañía B. Braun Surgical S.A., por la financiación y la contribución al desarrollo del proyecto. En especial al Dr. Pau Turon por las discusiones mantenidas. Gracias por confiar en el grupo y en el proyecto.

A todos los compañeros del grupo y del departamento, que llevaron hasta lo extraordinario su amabilidad y atenciones. Y a todos los grandes maestros que me han instruido, ya fuera en persona o en efigie de letras.

A todas estas personas y a mis amigos se debe esta tesis por completo. En especial a Alex, mi mejor amigo y a la Dra. Montse Sedó, la mejor terapeuta. Sin todos vosotros no se habría compuesto ni una sola palabra del tratado que sigue. Espero no haberos defraudado, en cualquier caso la responsabilidad de cualquier error cometido o problema causado durante este periodo es enteramente mía.

SCIENTIFIC PUBLICATIONS

Scientific publications derived from this thesis:

- del Valle, L.J., Bertran, O., Chaves, G., Revilla-López, G., Rivas, M., Casas, M.T., Casanovas, J., Turon, P., Puiggalí, J. & Alemán, C. DNA adsorbed on hydroxyapatite surfaces. *J. Mater. Chem. B*, 2, 6953-6966 (2014).

- Bertran, O., del Valle, L.J., Revilla-López, G., Rivas, M., Chaves, G., Casas, M.T., Casanovas, J., Turon, P., Puiggalí, J. & Alemán, C. Synergistic approach to elucidate the incorporation of magnesium ions into hydroxyapatite. *Chem. Eur. J*., 21, 2537 – 2546 (2015).

- Rivas, M., Casanovas, J., del Valle, L.J., Bertran, O., Revilla-López, G., Turon, P., Puiggalí, J. & Alemán, C. An experimental-computer modeling study of inorganic phosphates surface adsorption on hydroxyapatite particles. *Dalton Trans*., 44, 9980-9991 (2015).

- Rivas, M., del Valle, L.J., Rodriguez-Rivero, A.M., Turon, P., Puiggalí, J. & Alemán, C. Loading of an antibiotic into biocoated hydroxyapatite nanoparticles: smart antitumor platforms with regulated release. *ACS Biomater. Sci. Eng*., 26 , 3234-3245 (2018).

- Rivas, M., del Valle, L.J., Turon, P., Puiggalí, J. & Alemán, C. Influence of the atmosphere conditions in the structure, properties and solubility of fluorine-substituted hydroxyapatites. *Mater Chem Phys*., 226, 279-289 (2019).

- Rivas, M., del Valle, L.J., Alemán, C. & Puiggalí, J. Peptide self-assembly into hydrogels for biomedical Applications related to hydroxyapatite. *Gels*, 5, 14 (2019).

- Rivas, M., Pelechà, M., Franco, L., del Valle, L.J., Turon, P., Alemán, C. & Puiggalí, J. Incorporation of chloramphenicol loaded hydroxyapatite nanoparticles into polylactide. *Submitted. Revision process* (2019).

- Rivas, M., Turon, P., Alemán, C., Puiggalí, J. & del Valle, L.J. Intracellular calcium deregulation mediated by hydroxyapatite nanoparticles. *Submitted. Revision process* (2019).

- Rivas, M., Turon, P., Alemán, C., Puiggalí, J. & del Valle, L.J. Role of the intracellular calcium in the tumor aggressiveness. An interplay of diferent cell types: epithelial, endothelial and fibroblast cells. *Submitted. Revision process* (2019).

CONFERENCE PROCEEDINGS

- Rivas, M., Pelechà, M., Franco, L., del Valle, L.J., Turon, P., Alemán, C. & Puiggalí, J. Delayed chloramphenicol release through encapsulation of hydroxyapatite nanoparticles containing the drug into polylactide nanofibers. Poster at *Fifth International Conference on Multifunctional, Hybrid and Nanomaterials*, 6th-10th March 2017, Lisboa, Portugal.

- Rivas, M., Pelechà, M., Franco, L., del Valle, L.J., Turon, P., Alemán, C. & Puiggalí, J. Delayed chloramphenicol release through encapsulation of hydroxyapatite nanoparticles containing the drug into polylactide nanofibers. Poster at *Polymers: Design, Function and Application,* 21th-23th April 2018, Barcelona, Spain.

GLOSSARY OF ACRONYMS

ABC	(ATP)-binding cassette transporter
ACP	Amorphous calcium phosphate
APP	Alkylpolyphosphonate
ATM	Atmospheric (conditions)
ATMP	Amino-tris(methylenephosphonic acid)
ATP	Adenosine triphosphate
ATR	Attenuated Total Reflection
B-DNA	DNA which double helix is right handed with about 10−10.5 nucleotides per turn
BE	Binding Energy
bFGF	Basic fibroblast growth factor
BMPBP	Morphogenetic protein-2 biomimetic peptide
BMP-2	Bone morphogenetic protein-2
BMSC	Bone mesenchymal stem cells
BP	Bisphosphonate
BSE	Biomaterial Science and Engineering
BSSE	Basis Set Superposition Error
BTE	Bone tissue engineering
CA	Contact Angle
CAC	Citric acid cycle
CaP	Calcium phosphate particles
Ca/P	Calcium/Phosphorus ratio
CAP	Co-assembled peptide
CaP-DNA	DNA complexed with calcium phosphate particles
cHAp	Crystalline hydroxyapatite
CFU	Colony Forming Units
COS-1	Green monkey kidney fibroblast cells
CP	Counterpoise
CSC	Cancer stem cells
CV	Cyclic Voltammetry
$\boldsymbol{d}$	Distance from surface
$\boldsymbol{D_{cc}}$	Inter-strand distance
DCP	Dicalcium phosphate

DCPA	Dicalcium phosphate anhydrous
DCPD	Dicalcium phosphate dehydrate
DDS	Drug delivery system
d_{ee}	End-to end distance
D_{eff}	Effective Diameter
DFT	Density Functional Theory
DGTA	Differential Gravimetric Thermal Analysis
DHAp	Calcium-deficient carbonate hydroxyapatite
DLS	Dynamic Light Scattering
DMEM	Dulbecco's Modified Eagle Medium
DMSO	Dimethylsulfoxide
DNA	Deoxyribonucleic Acid
DNA-HAp	DNA complexed with hydroxyapatite
DNaseI	Deoxyribonuclease I restriction enzyme
DPSC	Dental pulp stem cell
DTPMP	Diethylenetriamine penta(methylene phosphonic acid)
ECM	Extracellular matrix
EPR	Enhanced permeation and retention
ε	Interaction potential energy
E_a	Activation energy
E_{bind}	Binding energy
E. coli	Escherichia coli
E_{des}	Desorption energy
EDTA	Ethylenediaminetetraacetic acid
EDTMP	Ethylenediamine tetra(methylene phosphonic acid)
EDX	Energy Dispersive X-ray spectroscopy
EE	Encapsulation Efficiency
E_{ele}	Electrostatic energy
EGTA	Ethylene glycol-bis(2-aminoethylether)-N,N,N′,N′-tetraacetic acid
EIS	Electrochemical Impedance Spectroscopy
EtOH	Ethanol
E_{vdW}	van der Waals energy
FAp	Fluorapatite
FBS	Fetal Bovine Serum

FDA	Food and Drug Administration
F-HAp	Fluorine-substituded hydroxyapatite
Fmoc	9-fluorenylmethyloxycarbonil
FTIR	Fourier Transform Infrared Spectroscopy
GEPI	Genetically engineered peptides that selectively bind to inorganic compound
$g_{x-y}(r)$	Radial distribution function of $x-y$ pairs (where x and y refers to X and Y atoms)
HAp	Hydroxyapatite
HEDP	1-hydroxyethylene disphosphonic acid
HF	Hartree-Fock
hMSCs	Human mesenchymal stem cells
HT	Hydrothermal
HUVEC	Human Umbilical Vein Endothelial Cells
ISO	International Organization for Standardization
IC_{50}	Half maximal inhibitory concentration
k_{ad}	Adsorption rate
k_{de}	Desorption rate
K_L	Langmuir constant
L	Crystallite size
LB	Luria-Bertani (bacteria medium)
L_{Eff}	Loading efficiency
LMWD	Low molecular weight drug
MCF-7	Epithelial cells from breast adenocarcinoma
MD	Molecular Dynamics
MDR	Multidrug resistance
MIA PaCa-2	Epithelial cells from human pancreas carcinoma
mRNA	Messenger RNA
MRP	Multidrug resistance-associated protein
mtDNA	Mitochondrial DNA
mTPT	Mitochondrial permeability transition pore
MTT	3-(4, 5-dimethylthiazol-2-yl)-2, 5-diphenyltetrazolium bromide
NOS	Nitric oxide synthase
NP	Nanoparticle
OCP	Octacalcium phosphate

PA	Peptide amphiphile
PBS	Phosphate-Buffered Saline
PCP	Phosphonate
PE	Potential energy
PMMA	Polymethyl methacrylate
PNP	Polymer–nanoparticle
PNS	Peptide nanosheet
pen/strep	Penicillin/streptomicin
p-FAp	Polarized fluorapatite
p-F-HAp	Polarized fluorine-substituded hydroxyapatite
P-gp	P-glycoprotein
p-HAp	Polarized hydroxyapatite
PLA	Poly(lactic acid) or polylactic acid or polylactide
PME	Particle- Mesh Ewald (method)
pMT4	Docichyl-phosphate-mannose-protein mannosyl transferase plasmid
polyP	Polyphosphate
QM	Quantum-Mechanics
RDF	Radial Distribution Function
R_g	Radius of gyration
RNA	Ribonucleic Acid
ROS	Reactive oxygen species
S	Binding sites per unit area
SAP	Self-assembly peptide
Sal1	Streptomyces albus G restriction enzyme
SEM	Scanning Electron Microscopy
s-HAp	Sintered hydroxyapatite
siRNA	Silencing Ribonucleic Acid
TAC	Tricarboxylic acid
TBE	Tris-borate-EDTA
TCP	Tricalcium phosphate
TCPS	Tissue Culture Polystyrene
TEM	Transmission Electron Microscopy
T_g	Glass transition temperature
TGA	Thermal Gravimetric Analysis
tRNA	Transfer Ribonucleic Acid

TSP	Thermal Stimulated Polarization
UV	Ultraviolet (spectroscopy)
UV-Vis	Ultraviolet-Visible (spectroscopy)
VEGF	Vascular endothelial growth factor
WA	Water Absorption
WAXD	Wide-Angle X-ray Diffraction
WAXS	Wide-Angle X-ray Scattering
WH	Whitlocktite
X_c	Crystallinity
XPS	X-ray Photoelectron Spectroscopy
XRD	X-ray Diffraction
Z-DNA	DNA which double helix is left handed with about 12 nucleotides per turn
ZP	Zeta Potential

TABLE OF CONTENTS

STRUCTURE OF THE THESIS

The thesis consists of eleven chapters followed by a summary of the conclusions drawn from the whole work.

Chapter 1 is a general introduction of the thesis which includes a brief review of calcium phosphate materials used as drug delivery systems. Polymer therapeutic is a term used to describe an increasingly important area of biopharmaceutics in which a linear or branched polymer chains behaves either as the bioactive (a polymer drug) or, more commonly, as the inert carrier to which a therapeutic is covalently linked, as in the case of polymer-drug conjugates, polymer-protein conjugates and multicomponent polyplexes. Hierarchical progression modern drug delivery begins with the use of polymer carriers to elicit spatio-temporal release of therapeutics in both pulsative dose delivery products and implanted reservoir systems. Application of hydroxyapatite (HAp) nanoparticles as an intelligent delivery system can solve the need for specific targeting, intracellular transport, biocompatibility while integrating elements of responsive behaviour to physiological environments and recognitive feedback control. In this context, it is of fundamental importance to discover the effect of biomolecules on kinetics of nucleation and crystal growth of calcium phosphate crystals, which shed light on the understanding of the mechanism of biomineralization. Here, we introduce some general detection methods, including analyses of chemical composition, X-ray diffraction techniques, spectrophotometry and molecular dynamics simulations; to study the crystallization kinetics of calcium phosphate in solution.

Chapter 2 includes the general and specific objectives of this thesis.

Chapter 3 presents kinetics studies of the mineralization process of DNA adsorbed on HAp surfaces. The key factors that contribute to a well-controlled process of mineralization as seen in biology include solubility, supersaturation, and energetics. Mineralized tissues have remarkable hierarchical structures that have evolved over time to achieve great functions in a large variety of organisms. Organic phases play a key role in templating the structure of mineralized tissues; therefore, their matrices are often hybrid in composition, varying widely in the relative content of organic and inorganic substances. Understanding the complex integration of hard and soft phases that biology achieves in mineralized matrices across scales and its link to properties is knowledge of great value to materials chemistry. Mammographic mammary microcalcifications are

routinely used for the early detection of breast cancer, however the mechanisms by which they form remain unclear. A more global comprehension of bone qualities will need further works designed to characterize what are the consequences on whole bone strength of changes at nano- or microstructure levels relative to each other.

Chapter 4 describes the influence of magnesium content in HAp mineralization properties. Magnesium has been hypothesized to prevent the upregulation of osteoblastic genes that potentially drives calcification. However, extracellular effects of magnesium on HAp formation are largely neglected. Although it has been reported previously that Mg^{2+} inhibits calcification, most study set-ups do not allow to discriminate between extracellular reduction of crystal formation and intracellular inhibition of osteogenic conversion. Our findings demonstrate a role for Mg^{2+} in preventing mineralization involving direct extracellular Ca-apatite crystal inhibition. The driving force of calcification in our model is not osteoblastic transdifferentiation but mainly HAp formation and deposition. Therefore, any intracellular effects of Mg^{2+} involving modification of osteogenic genes cannot be excluded.

Chapter 5 presents the morphology of the particles, containing ACP and HAp with different concentrations of various polyP, pyrophosphate and phosphonate concentrations, as well as their effects in HAp and ACP crystallization. Natural HAp, a bio-ceramic material which is crystalline to different scale, has been used as a biomaterial to fabricate scaffolds for *in situ* bone regeneration and other tissue engineering purposes. In contrast to natural HAp, synthetic apatite is much less effective. In general, while HAp is bioactive, its interaction and biocompatibility with existing bone tissue is low. These properties have been attributed to a minimal degradability in the physiological environment. There is increasing evidence that inorganic calcium-polyphosphates (polyP), and biophophonates are involved in human bone HAp formation. This process of basic calcium phosphate biocrystallization with polyP, pyrophosphate and phosphonate solutions occurs in a medium of complex composition. Important information concerning the formation of low-soluble phases in multicomponent biological systems could be obtained on the basis of thermodynamic calculations and computational simulations thereby conditions for precipitating the compounds would be determined. In this case there is a number of the difficulties connected, first of all, with a complicated structure of the system under simulation as well as with a variety of simultaneous processes. In this connection, studies concerning the features of phase formation processes in biological liquids is of currently central importance.

Chapter 6 describes the influence of synthetic conditions in composition of precipitated HAp, fluorine-substituded HAp (xF-HAp) and fluorapatite (FAp), considering different atmospheres, temperatures and pressures. Fluoride (F^-) is a trace element that is incorporated into bone mineral during bone formation. Fluoride substitutes for the hydroxyl group in HAp, forming fluorapatite (FAp). Previous studies have suggested that FAp has a similar biocompatibility with HAp in terms of its fixation to bone and bone in-growth. These studies used discs doped with various amounts of fluoride ion F^- to investigate the effect of F^- content on osteoblastic cell behaviour. They concluded that FAp is biocompatible and that the amount of F^- affects cell attachment, proliferation, morphology and differentiation of osteoblastic cells, proposing this to be related directly to the release of the fluoride ions. Since hygiene products like toothpastes and prophylactic gels contain fluoride ions, the present work evaluate the effect of fluoride ions on xF-HAp dental alloys used, for example, as dental implants and superstructures. The dose-dependent effects on mechanical properties are well-known, but the underlying mechanisms are still not fully understood. Furthermore, dose level alone is not the only factor affecting bone quality; the role of atmospheric factors has been emphasized in some clinical studies. FAp has also gained much interest as pure form; FAp is known to have a greater chemical stability and hence lower bioresorption rate than HAp. There is potential that as HAp forms xF-HAp, by selective substitution of OH^- with F^- it may be possible to alter the dissolution properties and biological properties of the material.

Chapter 7 evaluates the HAp toxicity impact in living cells. Although liposomal systems have made the most headway in the clinic, they are under further optimization to be safer to normal tissues and long-circulating in blood, yet able to efficiently accumulate and transfer drug in a sustained manner to targeted sites. For biodegradable polymer-based drug delivery systems, there are concerns that polymer acidic byproducts or degrading polymer fragments can adversely affect the drug they are delivering or the tissues they interact with. Often an undesirable late stage, uncontrolled and massive drug release is observed with polymer-based drug delivery systems. Bioceramics, such as calcium phosphates (ACP), represent another class of materials suitable for use as a carrier for drugs, non-viral gene delivery, antigens, enzymes, and proteins. ACP can be produced at a low cost and is simple to manufacture. HAp is a type of calcium phosphate that has a similar chemical structure to bone mineral, and hence has excellent biocompatibility, bioactivity, and high affinity to proteins, DNA, chemotherapy drugs, and antigens.

Localized pharmaceutical treatments utilizing ACP as a drug carrier have been achieved by injections or surgical placement of disks, pellets or particulates. The localized drug release from these ACP-based controlled release systems minimized the high concentration of drugs typically required in the bloodstream and other organs to achieve therapeutic outcomes. The ACP also provided a means to minimize unnecessary systemic toxicity and reduce the need for repeated dosing often required of most drugs. Due to the low solubility of the HAp in physiological conditions, HAp remains for long periods after *in vivo* subcutaneous placement. The large sintered disks and large particle sizes of HAp utilized in the previously researched formulations would remain *in vivo* long after drug release. This led to our interest in investigating nano-sized HAp particles that could speed carrier resorption, allow greater tumor or tissue perfusion, and perhaps overcome drug resistance through intracellular drug/particle uptake observed with particulate drug delivery formulations. Particle enhanced endocytosis may endow the particulate drug delivery systems with an ability to bypass p-glycoprotein efflux pump and lead to sequestration of anticancer drugs in acidic intracellular compartments, yielding high cytotoxicity. In order to use HAp nanoparticles as an efficient drug carrier for localized chemotherapy treatment, it is important to investigate the *in vitro* toxicity profile. Our study confirms the favorable properties of HAp nanoparticles for intratumoral anti-cancer drug delivery applications.

Chapter 8 presents the metabolic regulation of intracellular calcium in relation to the intracellular uptake of HAp. Calcifications are not only one of the most important early diagnostic markers of breast cancer, but are also increasingly believed to aggravate the proliferation of cancer cells and invasion of surrounding tissue. Moreover, this influence appears to vary with calcification composition. Despite this, remarkably little is known about the composition and crystal structure of the most common type of breast calcifications, and how this differs between benign and malignant lesions. There is evidence that calcifications in breast cancer are not simply passive products of the disease process, but may have an active role in mitogenesis, upregulation of gene expression and enhanced migration of tumor cells. In particular, calcifications associated with breast cancer consist predominantly of HAp, and there is evidence that nanoscale properties of HAp may have an important role in regulating breast cancer cell behavior. Understanding the nature of calcifications, and how and why they form, is important in developing a complete picture of the factors affecting tumor development and progression.

Autophagy is an evolutionarily conserved lysosomal catabolic process used as an internal engine in response to nutrient starvation or metabolic stress. A number of protein complexes and an intricate network of stress signaling cascades impinge on the regulation of autophagy. Ca^{2+} , as a major intracellular second messenger, regulates multiple physiological and pathological functions. Although significant information is already well-established about the role of Ca^{2+} in apoptosis, its role in autophagy has been recently determined and is poorly understood. Intracellular Ca^{2+} positively and negatively affects autophagy. Recent studies, evidence for both views and the interplay of Ca^{2+} between autophagy and apoptosis induction are discussed. The available data revealed the bidirectional role of Ca^{2+} in the regulation of autophagy. Moreover, the data also indicated that this role probably depends on the context of time, space, Ca^{2+} source, and cell state, thus either preventing or enhancing autophagy. Although in some contexts autophagy suppresses tumorigenesis, in most contexts autophagy facilitates tumorigenesis. Cancers can upregulate autophagy to survive microenvironmental stress and to increase growth and aggressiveness. Mechanisms by which autophagy promotes cancer include suppressing induction of the p53 tumor suppressor protein and maintaining metabolic function of mitochondria. Efforts to inhibit autophagy to improve cancer therapy have thereby attracted great interest.

Chapter 9 describes the preparation and characterization of antibiotic-loaded HAp nanoparticles coated with polyphosphate as a smart antitumor drug delivery system. The majority of polymer conjugates are designed as anticancer therapeutics, although other diseases have also been targeted, including rheumatoid arthritis, diabetes, hepatitis B and C, and ischemia. The popularity of conjugates for anticancer agents is a result of a passive tumor targeting phenomenon named as the enhanced permeation and retention (EPR) effect. It has been shown that the tumor concentration of anticancer therapeutics can increase up to 70-fold as a part of circulating macromolecular systems such as polymer conjugates. However, recent studies have shown that tumor targeting may not be able to be achieved exclusively by the EPR effect owing to difficulties in reaching cancer cells deep inside malignant tissues, which underscores the need for synergistic passive and active targeting strategies. Since the advent of controlled release polymer drug delivery systems, the polymer therapeutics field has exploded as the focus has shifted toward strategies that facilitate targeted release, especially for anticancer drugs, which often have severe negative side effects. For a polymer-drug conjugate to be both practical and effective, several features are desired: (a) nontoxic and non-immunogenic polymer carrier, (b) molecular weight high enough to ensure long circulation times,

(c) adequate loading/carrying capacity in relation to the potency of the drug, (d) linker must be stable during transport but easily cleaved for optimum delivery upon arrival at target and (e) the ability to target desired tissue by active and/or passive means. On the other hand, the “Endo-symbiotic Theory of Mitochondrial Evolution” states that mitochondria originally evolved from aerobic bacteria that were incorporated into eukaryotic cells, during millions of years of adaptation. Consistent with this theory, several studies have recently shown that certain classes of well-known antibiotics that inhibit bacterial protein synthesis, can also be used to successfully target mitochondrial protein translation, especially in cancer stem-like cells (CSCs). In this work, we have exploited this premise to design chloramphenicol-loaded HAp nanoparticles coated with polyphosphate in order to obtain an effective antitumor platform.

Chapter 10 presents release, antimicrobial tests, cell adhesion and proliferation studies of the incorporation of CAM loaded hydroxyapatite nanoparticles into polylactide nanofibers. The required release rates of the therapeutic agents depend on the medicinal application; for example, the optimal release time of hormones is in the range of months, while peroral administration requires that the drug is released as fast as possible. Due to the internal architecture, nanofibers are well suited for various medicinal applications, such as carriers for cell culture tissue engineering scaffolds or wound dressings. The incorporation of biologically or pharmacologically active compounds into the nanofibers may be very useful for these applications. Recent studies have evaluated the release kinetics of hydrophobic and hydrophilic molecules of various molecular weights from nanofibers prepared from polycaprolactone, polylactide and polyvinyl alcohol. The release rate and the total released amount positively correlated with molecular weight of the incorporated molecules. This trend was observed for all of the prepared nanofibrous carriers. However, the influence of the chemical composition of nanofibers was even more distinct -the highest amount of hydrophobic molecules released from polyvinyl alcohol nanofibers, the lowest amount from polylactide nanofibers. These findings can be applied to develop nanofibrous drug carriers systems for the local delivery of pharmacologically active compounds, because the auxiliary molecules encapsulating the drug can effectively control the drug release kinetics. Generally, nanofibers that carry drugs follow several basic designs - nanofibers with homogenous structures in which the drug is dispersed throughout the polymer matrix, core-shell nanofibers for which the matrix carrying the drug is covered by pure polymer and nanofibers with the pharmacologically active compounds immobilized on their surface. For homogenous nanofibers, the rate of release decreases with time, because the drug must travel progressively longer distances to diffuse to the fiber periphery, which requires more time.

Contrary, the core–shell design provides the delivery system with the diffusion rate of the therapeutic agent stable throughout the life. In this work, we designed a polylactide nanofiber incorporating CAM encapsulated HAp nanoparticles which enables an stable and low diffusion rate.

Chapter 11 provides an overview of structure/function relationships within biological scaffolds materials compose of extracellular matrix and self-assembling peptides, and to extend these relationships to other synthetic scaffold materials when possible. In the context on this overview, the term “function” is used in the broadest sense including biochemical and physiological effect. The extracellular matrix (ECM) is a highly complex cell-secreted biomaterial that gives rise to all tissues and organs of the human body. It is three-dimensionally arranged and is composed of various origin-specific molecules that can be structural and instructional proteins. Although most of the ECM proteins are well-described and characterized, their origin or tissue-specific spatio-temporal distribution remains the focus of intense research. Peptide self-assembly nanostructures could construct well-defined structures through the noncovalent forces including electrostatic interaction, hydrophobic reaction, hydrogen bonding, and $\pi - \pi$ stacking. The morphology and function of the peptide self-assembly nanostructures can be manipulated from the molecular level by tuning the types and structure of peptides, or external triggers such as temperature, pH value, and electric fields. We develop a physical description of self-assembly hydrogels utilizing polymer-HAp-nanoparticles, owing to their hierarchical structure, these new formulated systems are able to mimic the characteristics of the ECM; and hold great promise for the fields of drug delivery, tissue engineering and regenerative medicine.

1.

INTRODUCTION

1.1 Hydroxyapatite as a calcium phosphate specie

1.1.1 INTRODUCTION

The discovery more than a century ago, by medical researchers, of calcium phosphate salts as the mineral phase of bone and teeth, was the starting point of interest in these salts as a material to enhance healing of bone fractures. Nevertheless, only at the end of the 1960s the preparation of bioceramic compounds from calcium phosphate powders was achieved. This new class of materials is currently being widely applied in the biomedical field, although some aspects like rate of biodegradation and resorption cannot be quantitatively predicted yet. Factors affecting the rate of resorption of the implant include those related to the physical features of the material (*e.g*., surface area, crystallite size), chemical (*e.g*., factors such as atomic and ionic substitutions in the lattice) and biological factors (*e.g*., types of cells surrounding the implant, specific location of the implant, age, species, sex, and hormone levels).[1]

Polycrystalline calcium orthophosphates can be obtained as a loose powder by precipitation from aqueous solution. These precipitates can contain different amounts of H^+ and OH^- ions as well as water molecules, depending on the experimental conditions. Through hydrothermal techniques, the temperature can be raised above 100 ^{0}C and in practice up to 1000 ^{0}C.[2] Other experimental preparations can also contain "foreign ions" when the precipitations are carried out in their presence in the aqueous solution.

Polycrystalline calcium phosphates can also be prepared in the form of more or less dense bodies. In this way, the porosity can be lowered either by "hot pressing" or by "liquid phase sintering". In addition, calcium phosphates can be doped with "foreign ions". Both ways of synthesis, hydrothermal and ceramic, are relevant for the production of calcium phosphates able to be employed as implants or drug delivery systems.

Finally apatite is a group of phosphate minerals, usually referred as hydroxyapatite, fluorapatite and chlorapatite, with high concentrations of OH^-, F^- and Cl^- ions in the crystal, respectively. The formula of the admixture of the three most common endmembers is written as $Ca_{10}(PO_4)_6(R)_2$, where $R = OH, F$ or Cl.

1.1.2 FORMATION OF CALCIUM ORTHOPHOSPHATES BY PRECIPITATION FROM AQUEOUS SOLUTIONS

Early studies used the addition of Ca^{2+} aqueous solution to phosphate aqueous solution or the reverse to obtain precipitates of calcium phosphates. In 1904, Cameron and Hurst[3] have mentioned the existence of dicalcium phosphate (DCP), dicalcium phosphate dihydrate (DCPD), tricalcium phosphate (TCP), and apatite, of which all but not the latter were characterized by their chemical composition at that time, whereas apatite was known as a mineral. In 1917, Basset[4] specified that $CaHPO_4$ (DCP) and $CaHPO_4 \cdot 2H_2O$ (DCPD) could exist as solid phases, the latter forming preferentially under 36 ºC.[5]

The preparation of pure octocalcium phosphate (OCP) was first carried out by Newesely in 1961.[6] The exact number of water molecules in its formula $Ca_8(HPO_4)_2(PO_4)_4 \cdot 5H_2O$ was elucidated by the determination of its crystal structure.[7] OCP was formed in a pure form, when $CaHPO_4$ was hydrolyzed in a solution buffered between pH 5.8 and 7.1. The temperature had to be kept below 65 ^{0}C at pH 5.8 and below 38 ^{0}C at pH 7.1. Direct precipitation was also possible at pH 6.5 from acetate-phosphate buffers by the addition of calcium nitrate solution.

In 1933, Sanfourche[8] found that under certain conditions, the first precipitate was none of the above-mentioned crystalline compounds. It was a “gelatinous” amorphous calcium phosphate (ACP), which was then characterized by several methods.[9] ACP could take days before to be transformed into one of these above indicated crystalline compounds. ACP contains HPO_4^{2+} ions and its Ca/P ratio was found to be 1.36 $\pm$ 0.02, initially and changed to 1.47 $\pm$ 0.03 upon washing.[10]

1.1.3 METASTABLE STATES OF CALCIUM PHOSPHATES IN AQUEOUS SYSTEMS

A compilation of the calcium phosphates pertinent to aqueous systems is given in **Table 1.1**, together with the space group of their crystal structures and the most reliable value of their solubility product constant ($pK_{sp} = -\log_{10}(K_{sp})$).

Table 1.1. Calcium phosphates relevant to aqueous systems: dicalcium phosphate (DCP), dicalcium phosphate dihydrate (DCPD), octocalcium phosphate (OCP), whitlocktite (WH), hydroxyapatite (HAp) and calcium-deficient carbonate hydroxyapatite (DHAp).

Ca/P	Notation	Formula	Space group	pK_{sp}	Mineral name
1	DCP	$CaHPO_4$	P1	6.90	Monetite
1	DCPD	$CaHPO_4 \cdot 2H_2O$	C2/c	6.59	Brushite
1.33	OCP	$Ca_8(HPO_4)_2(PO_4)_4 \cdot 5\,H_2O$	P1	68.6	-
1.43	WH	$Ca_{10}(HPO_4)\,(PO_4)_6$	R3c	81.7	Whitlocktite
1.67	HAp	$Ca_{10}(PO_4)_6\,(OH)_2$	$P6_3/m$	112.2	Hydroxyapatite
1.50	DHAp	$Ca_9(HPO_4)\,(PO_4)_5\,(OH)$	$P6_3/m$	85.1	Calcium-deficient carbonate hydroxyapatite

The occurrence of metastable states during the precipitation and formation of calcium phosphates has extensively been reported. There is not much agreement about the nature of the first precipitate and the consecutive transitions into other calcium phosphates, although physical methods like monitoring of pH[11] and X-ray diffraction analysis[12] have been applied in this field since their development. In 1967, Berry[12] postulated the formation of defective hydroxyapatites, which can vary in composition from $Ca_9(PO_4)_6 \cdot 2H_2O$ to $Ca_{10}(PO_4)_6\,(OH)_2$.

In 1937, Fouretier[13] found that the first precipitate was a mixture of DCPD and ACP, which hydrolyzed to a “hydrated” apatite. In 1950, Arnold[14] proposed that OCP and HAp could form a continuous series of solids so that no preparations with composition lying between them would be likely to be identical. In 1957, Strates *et al.*[15] found that DCPD was the first precipitate which hydrolyzes into a defective hydroxyapatite. In 1962. Brown *et al.*[16] postulated that OCP and HAp did not form solids, but formed epitactical and topotactical mixtures with a sandwich structure. In 1965, Eanes *et al.*[17] found an amorphous calcium phosphate which hydrolyzed into a defective apatite in about 5 h.

The type of precipitate depended largely on the degree of supersaturation.[18] At low supersaturation DCPD was formed which, above pH 6.3, hydrolyzed into OCP and at high supersaturation an amorphous product was formed directly from aqueous solution.

Combining this information, a scheme indicating the equilibrium species at different pHs in (**Figure 1.1**) was postulated. Most experiments mentioned here were carried out in the range 5 < pH < 8, the transformations are pH-sensitive.[18] This characteristic together with the varying degrees of supersaturation, can explain the apparent differences found between the various authors.

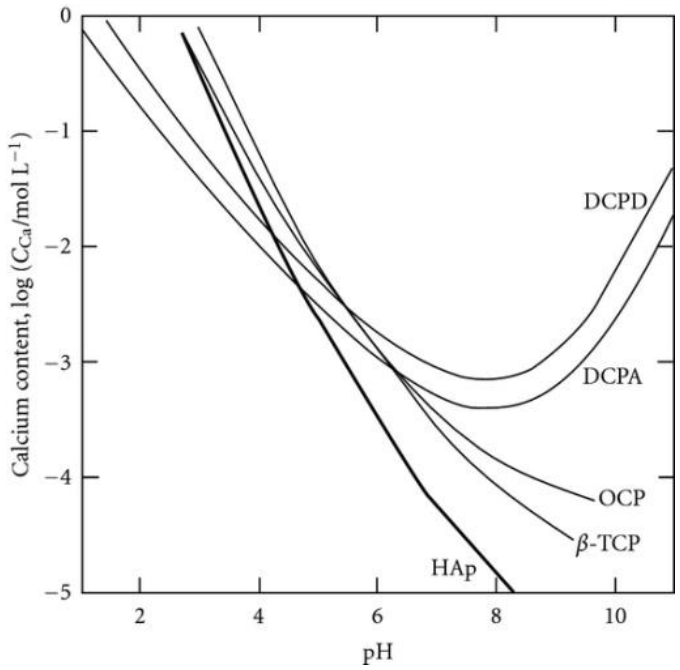

Figure 1.1. Solubility curves of calcium orthophosphoric compounds at 37°C, depending on pH in aqueous solution. HAp: hydroxyapatite $Ca_{10}(PO_4)_6\,(OH)_2$, TCP: calcium phosphate $Ca_3(PO_4)_2$, OCP: octacalcium phosphate $Ca_8(HPO_4)_2(PO_4)_4 \cdot 5\,H_2O$, DCPA: dicalcium phosphate anhydrous $CaHPO_4$, DCPD: dicalcium phosphate dihydrate $CaHPO_4 \cdot 2H_2O$, adapted from *Driessens, F.C.M., Bull. Soc. Chim. Bel. 89, 663 (1980)*.

1.1.4 PREPARATION OF SYNTHETIC HAp BY PRECIPITATION FROM AQUEOUS SOLUTIONS AND BY SOLID-STATE REACTION

The commercial routes to produce synthetic hydroxyapatite are based on aqueous precipitation or conversion from a solid-state reaction. Aqueous precipitation is most

often performed following two possible routes: a reaction between a calcium salt and an alkalinephosphate[19] or a reaction between calcium hydroxide or calcium carbonate and phosphoric acid.[20] Other routes are those including solid-state processing,[21] hydrolysis[22] and hydrothermal synthesis.[23]

The first author to present the right formula for hydroxyapatite $Ca_{10}(PO_4)_6\,(OH)_2$ probably was Forster[24] in 1932 being Scheleede *et al.*[25] who prepared a pure chemical hydroxyapatite by precipitation from aqueous solutions. They subjected either an unstable precipitate of defective hydroxyapatite $Ca_9(HPO_4)\,(PO_4)_5(OH)$ or a high-temperature product of tetracalcium phosphate $Ca_4(PO_4)_2O$ to hydrolysis at temperatures up to 90 º C:

$$3Ca_4(PO_4)_2O + 3H_2O \rightarrow Ca_{10}(PO_4)_6\,(OH)_2 + 2Ca(OH)_2 \qquad (1.1)$$

1.1.5 HAp CRYSTAL STRUCTURE

The hydroxyapatite lattice contains two kinds of calcium positions; columnar and hexagonal. There is a net constituted by four “columnar calcium” ions that occupy the $\left[\frac{1}{3}, \frac{2}{3}, 0\right]$ and $\left[\frac{1}{3}, \frac{2}{3}, \frac{1}{2}\right]$ lattice points. The “hexagonal calcium” ions are located on planes parallel to the basal plane at $c = \frac{1}{4}$ and $c = \frac{3}{4}$ witch also contains the six ${PO_4}^{3-}$ groups. The OH^- groups are located in columns parallel to the *c* axis, at the corners of the unit cell, which may be viewed as passing through the centers of the triangle formed by the “hexagonal calcium” ions. Successive hexagonal calcium triangles are rotated through 60 º (**Figure 1.2**).[26]

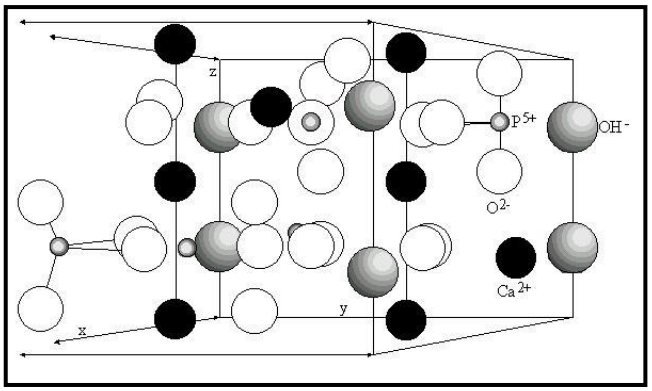

Figure 1.2. Crystal structure of hydroxyapatite (hexagonal, $P6_3/m$, $a = 9.4125$, $c = 6.8765$ Å).

1.1.6 INCORPORATION OF "FOREIGN" IONS INTO HAp CRYSTAL STRUCTURE

The route and conditions under which synthetic HAp is produced will greatly influence its physical and chemical characteristics. Defects and impurities on hydroxyapatite may be identified as substitutional or as discrete, extraneous crystalline phases (as discussed below). Ions that may be incorporated into the HAp structure, either intentionally or unintentionally include carbonate ions (substituting for hydroxyl or phosphate groups), fluoride ions (substituting hydroxyl groups), silicon, or silicate ions (substituting phosphorus or phosphate groups) and magnesium ions (substituting calcium ions).[27]

1.1.6.1 Incorporation of carbonate "foreign" ions into the HAp crystal structure in the precipitation process from aqueous solutions

Hydroxyapatite phase in bone contains 4–8 % in weight of carbonate, properly described as dahllite. Mineral composition varies with age and it is always calcium deficient, with phosphate and carbonate ions in the crystal lattice. The formula $\mathrm{Ca}_{8.3}(\mathrm{PO}_4)_{4.3}\ (\mathrm{CO})_{3\mathrm{x}}(\mathrm{HPO}_4)_{\mathrm{y}}(\mathrm{OH})_{0.3}$ represents the average composition of bone, where *y* decreases and x increases with age, while the sum x and y remains constant and equal to 1.7.[28] Mineral crystals grow under a specific orientation, with the c axes of the crystals approximately parallel to the long axes of the collagen fibers where they are deposited. Electron microscopy techniques enabled this information to be obtained.[29] The hexagonal structures of the apatite group are so stable that they support many kinds of defects, even excess ions stuffed in intermediate positions of the lattice. So there exist many cation and anion-defective apatites. The lattice parameters of such preparations were not well established and apparently depended on the way of precipitation.[30]

The bones are characterized by their composition, crystalline structure, morphology, particle size and orientation. The apatite structure hosts carbonate in two positions: the OH^- sub-lattice producing the so-called type A carbonate apatites or the $(\mathrm{PO}_4)^{3-}$ sub-lattice, named type B apatites (**Figure 1.3**).

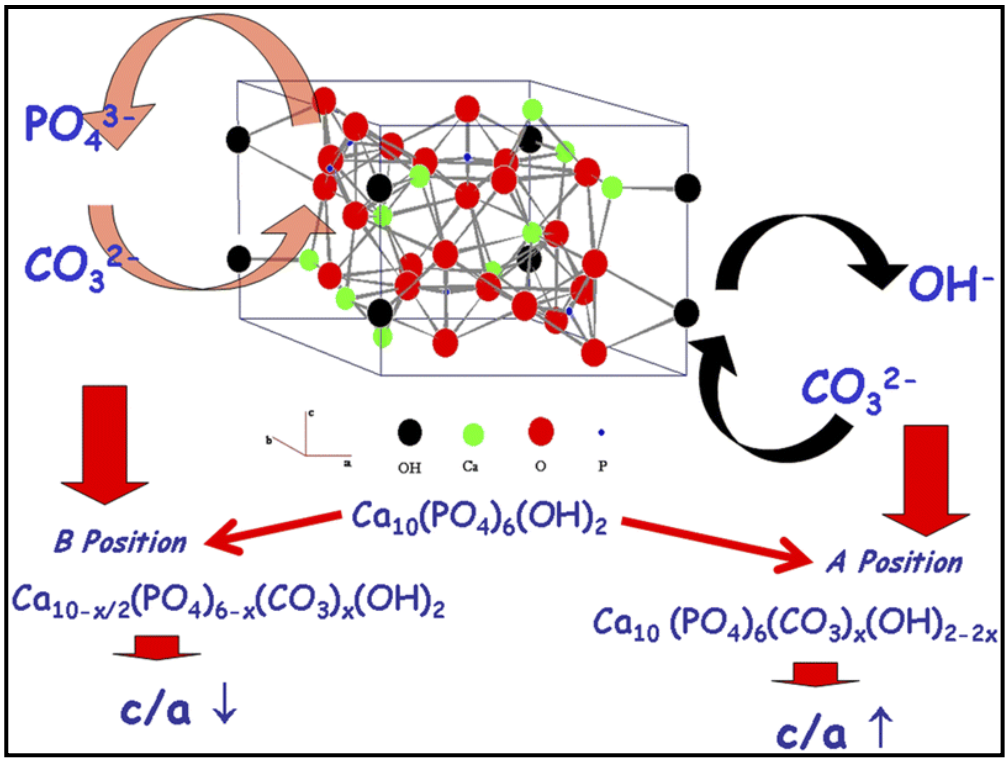

Figure 1.3. Crystalline structure and likely ionic substitutions in carbonate apatites.

In 1971 Labarthe *et al*.[31] succeeded obtaining carbonated hydroxyapatites by co-precipitation of calcium carbonate and phosphates. X-ray analysis of the products revealed their structure related to apatite, whereas chemical analysis revealed the following formula:

$$\mathrm{Ca_{10-x+u}(PO_4)_{6-u}(CO_3)_x(OH)_{2-x+2u}} \quad (1.2)$$

with $0 \leq x \leq 2$ and $0 \leq u \leq \frac{1}{2}$.[30] Nevertheless, an alternative formula for the same compounds was proposed by Bacquet G. *et al*.[32] in 1981

$$\mathrm{Ca_{10-x+u}(PO_4)_{6-u}(CO_3)_x(H_2O)_z(OH)_{2-x+2u}} \quad (1.3)$$

Through the equilibrium, which was proven to play a role in calcium-deficient carbonate apatites:[33]

$$\mathrm{H_2O + PO_4^{3-} \rightleftharpoons OH^- + HPO_4^{2-}} \quad (1.4)$$

The lattice parameters of such preparations were not well established and apparently depended on the way of preparation.[30]

In 1967, LeGeros *et al*.[34] studied the stability of ACP in CO_3^{2-} containing aqueous solutions and found that the crystallization was retarded. Although it was not clear in which parts of the pathways of **Figure 1** this happens, it might well be in the first crystallization to OCP, as Newesely[6] had suggested that carbonate reacts with OCP in 1961.

1.1.6.2 Incorporation of magnesium "foreign" ions into the HAp crystal structure in the precipitation process from aqueous solutions

The presence of Mg^{2+} ions in the aqueous solution stabilizes the structure of whitlocktite and causes its preferential formation respect to other calcium phosphates that could be formed under such conditions of precipitation.[35] In 1962, Boulet *et al*.[36] get evidences from precipitation studies that Mg^{2+} ions were incorporated in the "gelatinous" precipitate of ACP. In 1965, Bachra *et al*.[37] determined a so-called precipitation diagram for the system "calcium-carbonate-phosphate" and found that in the presence of Mg^{2+} ions, the ACP phase grew up at the expenses of the HAp phase. In another paper they reported that the Mg^{2+} ion stabilized the ACP precipitate and disturbed the crystallization of the HAp phase.[38]

The presence of Mg^{2+} ions can retard the transformation of ACP (finely dispersed whitlockite) into other calcium phosphates. In 1970, Termine *et al.*[39] determined the time that elapsed during the solution-mediated transformation of ACP into HAp and found that addition of small amounts of Mg^{2+}ions increased that period. In 1962, Brown *et al*.[16] reported that Mg^{2+} ions in a concentration as low as 0.001 $mol \cdot l^{-1}$ completely blocked the hydrolysis of OCP into HAp. On the other hand it was found that Mg^{2+} ions had no effect on the formation of DCPD in precipitation studies carried out from slightly acidic solutions.[36]

1.1.6.3 Incorporation of fluoride "foreign" ions into the HAp crystal structure in the precipitation process from aqueous solutions

The interaction of fluoride with HAp produces a fluorohydroxyapatite (FHAp), by substitution of OH^- by F^- (see **Figure 1.4**). This result gave rise to an increase of hydrogen bonding, decreased the size of the crystal lattice, and decreased the overall solubility.

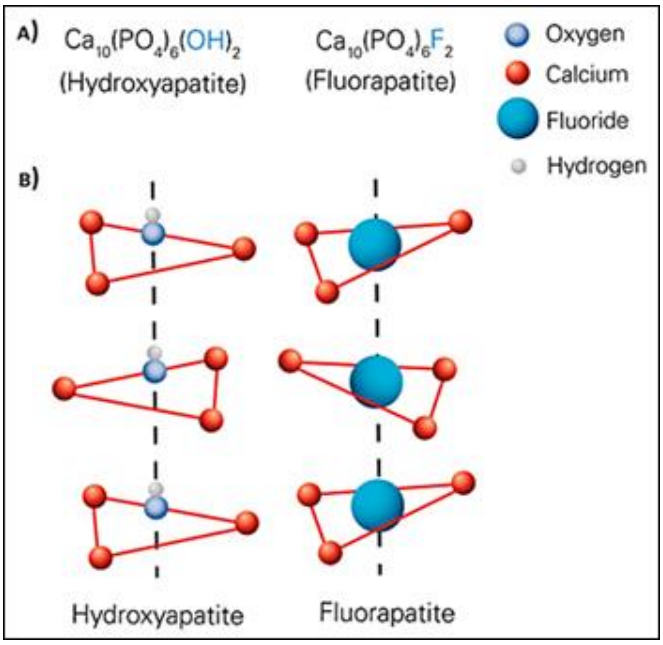

Figure 1.4. A). Fluoride ions (F^-) replace hydroxyl ions (OH^-) in HAp to form FHAp. (B). A portion of the HAp crystal lattice is depicted showing the replacement of hydroxide for fluoride, adapted from: *Posner A.S. The mineral of bone. Clin Orthop Relat Res. 200, 87-99 (1985).*

Solid suspensions of HAp and fluorhydroxyapatite (FHAp) could be prepared by mixing an ammonium phosphate and ammonium fluoride containing solution with a calcium nitrate solution at a certain rate at boiling temperature. CO_2 was excluded from the reaction vessel.[40] Care must be taken with this procedure to avoid the formation of CaF_2 as an impurity phase due to its limited solubility.

Hydrolysis of acidic calcium phosphates such as DCPD and OCP into HAp is accelerated by the presence of F^- ions in the aqueous solution.[41] It appears that these ions promotes the formation of the HAp phase, and decreases the ACP phase.[42] Basically, this process curtails the metastable states.

1.2 Solute adsorption on hydroxyapatite particles

Adsorption is one of the ways used for the modification of the hydroxyapatite surface by means of the accumulation of a foreign substance at the interface. Regarding the complexity of considered systems one can state that the adsorption of solutes on HAp may occur by various mechanisms that are very difficult to analyze. Adsorption of compounds on HAp is controlled by both physical factors and chemical interactions, which depend on the characteristics of the adsorbent (surface area, pore size

distribution, and surface chemistry), the nature of the adsorbate (molecular weight and size, functional groups, polarity, solubility), and the condition of the background solution (pH, temperature, presence of competitive solutes, ionic strength). Since there are several mechanisms that can affect the adsorption, it is important to understand the role of each individual factor that could be responsible of the adsorption for a given adsorbate/adsorbent combination and under certain background conditions.

1.2.1 PHYSICAL AND CHEMICAL ADSORPTION

It is useful to distinguish two broad classes of adsorption (physisorption and chemisorption) depending on the nature of the surface forces. The forces of physical adsorption consist of the ubiquitous dispersion-repulsion forces (van der Waals, which are a fundamental property of all matter, supplemented by various electrostatic contributions/polarization, field-dipole and field-gradient-quadrupole interactions).[43] The forces involved in chemisorption are much stronger and involves a substantial degree of electron transfer or electron sharing, as in the formation of a chemical bond. As a result, chemisorption is highly specific and the adsorption energies are generally substantially greater than those for physical adsorption.[44] Chemisorption is limited by its nature to monolayer coverage of the surface whereas, in physical adsorption, multilayer adsorption is common.

In the case of pure physisorption (*e.g.* Ar /metals), the only attraction between the adsorbing species and the surface arises from weak van der Waals forces. As illustrated in **Figure 1.5**, these forces give rise to a shallow minimum in the potential energy (PE) curve at a relatively large distance from the surface (typically $d > 0.3$ nm) before the strong repulsive forces arising from electron density overlap cause a rapid increase in the total energy. There is no barrier to prevent the atom or molecule which is approaching the surface from entering this physisorption well, *i.e*. the process is not activated and the kinetics of physisorption is invariably fast.

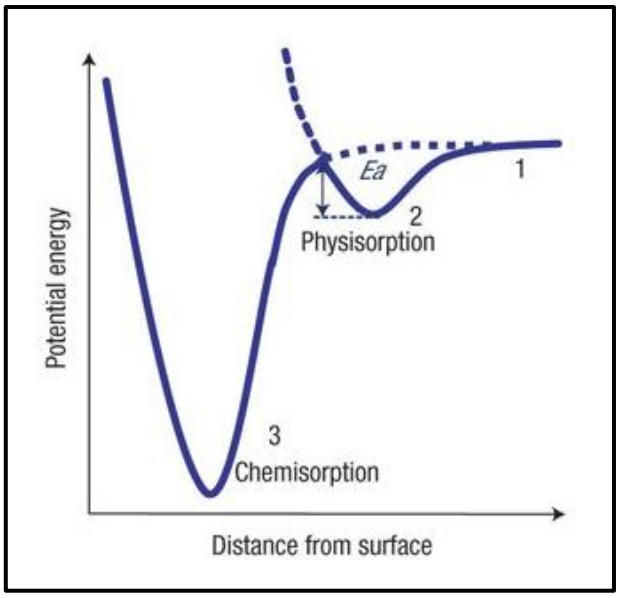

Figure 1.5. Potential energy profile versus distance for physisorption and molecular chemisorption.

Chemisorption is usually connected with a chemical reaction **Figure 1.5**. Therefore, it is not surprising that the molecules must overcome an activation energy E_A. Often the molecules are firstly physisorpbed to the surface and in a second, much slower, step the bond is established. For desorption both the adsorption energy Q and the activation energy must be overcome. The desorption energy E_{des} is thus larger than the adsorption energy. **Figure 1.5** shows the PE curves due to physisorption and chemisorption separately - in practice, the PE curve for any real molecule capable of undergoing chemisorption is best described by a combination of the two curves, with a curve crossing at the point at which chemisorption forces begin to dominate over those arising from physisorption alone. However, in cases where chemical bond formation between the adsorbate and substrate can also occur, the PE curve is dominated by a much deeper chemisorption minimum at shorter values of d.

A simple model to describe adsorption was presented by Langmuir[45] in 1918, assuming that on the surface there are a certain number of binding sites per unit area S. Of these binding sites, S_1 are occupied with adsorbate and $S_0 = S - S_1$ are vacant. The adsorption rate Ad_r in moles per second and per unit area is proportional to the number of vacant binding sites S_0 and the concentration of the substance in the liquid phase *c* (*i.e.* $Ad_r = k_{ad} c S_0$). The desorption rate is proportional to the number of adsorbed molecules S_1 and equal to $k_{de} S_1$; where k_{ad} and k_{de} are constants. In equilibrium, the

adsorption rate must be equal to the desorption rate, where $K_L = \frac{k_{ad}}{k_{de}}$ is the so-called Langmuir constant.

The surfaces of adsorbents such as activated carbons, highly-silicon zeolites and hydroxyapatites are essentially nonpolar. Most substances bind to HAp through London dispersion forces. This should mean that it preferentially adsorbs larger molecules and non-polar molecules since they would have larger dispersion forces. With non-polar adsorbents van der Waals forces are dominant, and relative affinity is determined largely by the size and polarizability of the sorbate molecules.[46]

1.2.2 ADSORPTION AND CATALYSIS

When Berzelius in 1836 coined the word catalysis[47] and used it to describe a number of observations that had already been recorded in the literature, he clearly recognized that the reacting components in catalytic reactions were held to the surface or adsorbed during the period in which they were reacting. Since then, many authors have been studied the relationship between adsorption and catalysis. With homogeneous catalysts the catalyst and all the reactants are in a single phase usually either liquid or an aqueous solution. Invariably the catalyst is taken up into the chemical reaction before being returned unaltered at the end of the reaction[48] (**Figure 1.6**). Most industrial catalyzed reactions are of the heterogeneous type, where the reactants and the catalyst are in different phases. Usually the catalyst is in the solid phase whilst the reactants are either liquid or gaseous. In industrial applications the catalyst is often supported on a substrate that allows the effective surface to be increased and the catalyst to be fixed in place.[49] The route by which a heterogeneous catalyst works is shown in **Figure 1.7**.

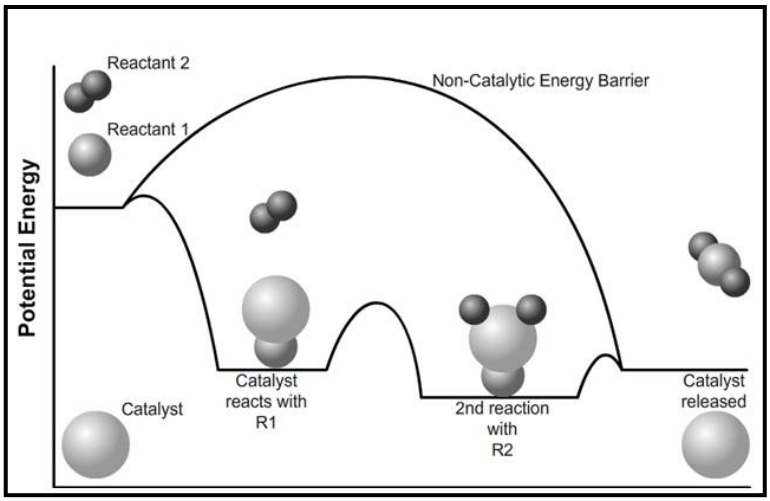

Figure 1.6. Scheme of a homogeneous catalysis. The catalysts are present in the same phase as the substances which are going into the reaction phase.

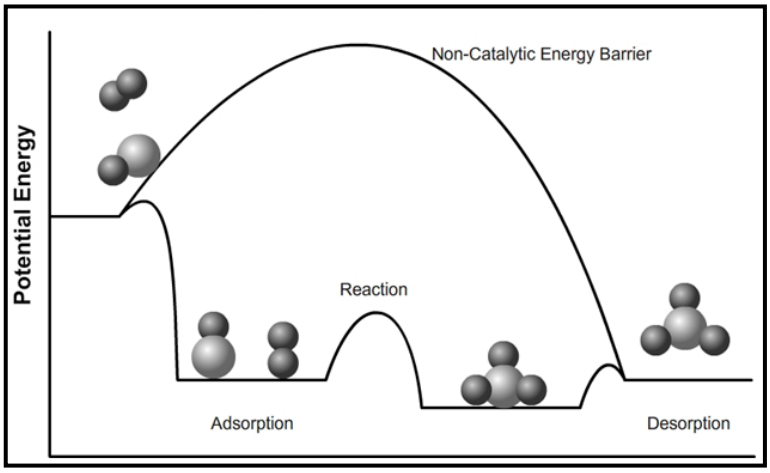

Figure 1.7. Scheme of a heterogeneous catalysis. The reactants diffuse to the catalyst surface and adsorb onto it, via the formation of chemical bonds.

1.2.3 STABILITY OF CALCIUM PHOSPHATES IN CONTACT WITH AQUEOUS SOLUTIONS

Solid calcium phosphates in contact with aqueous solutions can exchange ions giving rise to an equilibrium between the ions in the aqueous phase and those placed on the surface of the solid phase. The bulk of the solid is not involved as solid-state diffusion is excluded at ordinary temperatures, which are low in comparison with the melting point of the solids. It should be mentioned that the ions which can be exchanged at the surface of a solid calcium phosphate are involved in several secondary reactions occurring in the aqueous phase.

Another fact that should be remarked is that some calcium phosphates are not stable when they are in contact with certain aqueous solutions. Initial dissolution of the solid phase may then result in the re-precipitation of another solid calcium phosphate phase. The latter may be formed as separate particles so that the transformation of the first solid into the second can be complete. Re-precipitation can also lead a very thin impervious layer on the particles of the first solid, so the partial transition into the second solid may be barely detectable.

Contrary to expectations, and related with the statement described above, HAp was found to dissolve much more slowly than the other calcium phosphates not naturally occurring in bone and having similar ceramic structures and degrees of purity.[50]

1.2.4 ROLE OF SOLUTION pH ON SOLUTE ADSORPTION AT THE HAp SURFACE

Solute interactions with the HAp structure depend on the type and dissociation of the solute. In turn, degree of dissociation depends on the pH of the solutions. Charges are acquired by the dissolution of cations, Ca^{+2} ions are dissolved in the liquid leaving a negatively charged mineral behind. Other cations that are initially dissolved in the liquid might partially replace the original cations. The total charge is determined by the ion exchange properties of the HAp. Final charge of the solid is only partially due to processes at its surface since depletion of positive charge in the bulk may be a more significant factor. In water this phenomenon leads to a relatively constant charge, which is not very sensitive to pH.[51]

1.2.5 ROLE OF PORE SIZE DISTRIBUTION ON SOLUTE ADSORPTION ON HAp SURFACE

Two major groups of pores can be distinguished in HAp ceramics: macropores with diameters ranging in the order of 100 to 500 μm (**Figure 1.8**) and micropores of less than few microns that can be distinguished in the walls that surrounded the large open pores (**Figure 1.8 inset**).

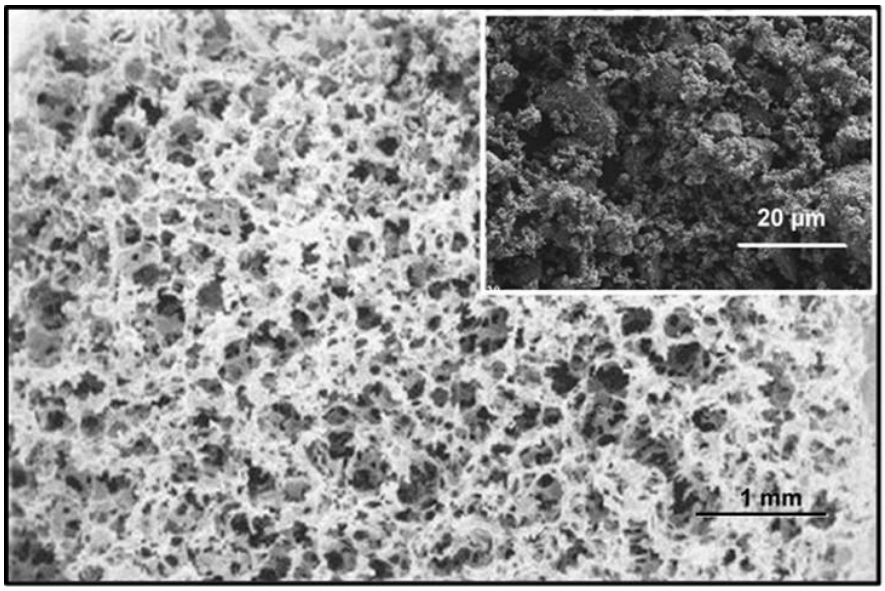

Figure 1.8. HAp ceramic with macropores of about 150 to 200 µm surrounded by walls containing micropores (inset).

In order to calculate the distribution of pore sizes, it is necessary to develop a model to relate the pore width with the condensation pressure.[52] Pore filling is the main physical adsorption mechanism in small micropores because the overlapping of pore wall potentials results in stronger binding of the adsorbate. In the case of some organic molecules of a large size, molecular sieve effects may also occur because the pore width is narrower than the dimensions of the adsorbate molecules or because the shape of the pores does not allow the molecules of the adsorbate to penetrate into the micropores. In the case of protein adsorption on HAp, there are multiple contact points between adsorbate and adsorbent, being the adsorption phenomenon enhanced.[53] It seems that differences in porosity are not only necessary, but also sufficient to explain differences in the degradation and adsorption rates.[54]

1.2.6 ROLE OF BULK CRYSTALLOGRAPHIC PROPERTIES ON SOLUTE ADSORPTION ON HAp

It is not clear if the surface area is the only factor that controls the physical adsorption on HAp particles. In 1979, when injecting HAp powders in rat synovial joints, Denko and Petricevic[55] found a decrease in inflammation when powders were heated to about 200 ºC, the usual sterilization temperature. In addition, it has already been mentioned that in 1980, Klein and de Groot[56] investigated protein adsorption on HAp, heated at various temperatures, and found indications that adsorption depended strongly on

sintering temperature. It is obvious that the sintering temperature of HAp ceramics significantly affects their adsorption responses *in vitro* or *in vivo*. In a typical adsorption process, a large number of parameters should be taken into account and their values should be adjusted during the adsorption optimization. The most important parameter is the crystalline structure of the initial hydroxyapatite.[57]

The HAp ceramics sintered at different temperatures exhibit a wide variation of structural parameters. In 2003, Guo *et al*.[58] studied the crystalline structure of HAp powders sintered at different temperatures (*i.e*. 600, 800, 1000, 1200 ^{0}C). A series of structural parameters, such as, cell lattice parameters (a and c), distances between characteristic atoms, internal energy and density, were calculated to characterize the crystalline structure of HAp at an atomic level. The broadening effect observed for X-ray diffraction (XRD) reflections was also evaluated to determine micro-strain and crystalline size. Results demonstrated that the increase of the sintered temperature to a decrease of the internal energy and micro-strain and an increase of the crystalline size. Hence, we must conclude that although porosity plays an important role in biodegradation and adsorption on HAp, crystallographic factors may be also important.

In 2007, Deutsch *et al*.[59] made a computational approach based on density functional theory to study the electrostatic properties of adsorbed polar molecules on different non-polar surfaces. They found that this adsorption had a strong dependence on monolayer coverage, and established the crucial role of long-range bulk crystallographic properties and cooperative behavior, in addition to local chemical properties.

1.2.7 ADSORPTION OF POLYPHOSPHATES AND PHOSPHONATES ON HAp

Polyphosphates (polyPs) are synthesized by the condensation of phosphate species through dehydratation processes (**Figure 1.9.a**), such as heating, or enzymatic condensation. In this context, condensation means the merging of two ortophosphates, one orthophosphate and one polyP, or two polyP molecules to yield one longer polyP molecule and water. The condensed phosphate ions are linked together as polymers through phosphoanhydride ($P-O-P$) bonds.

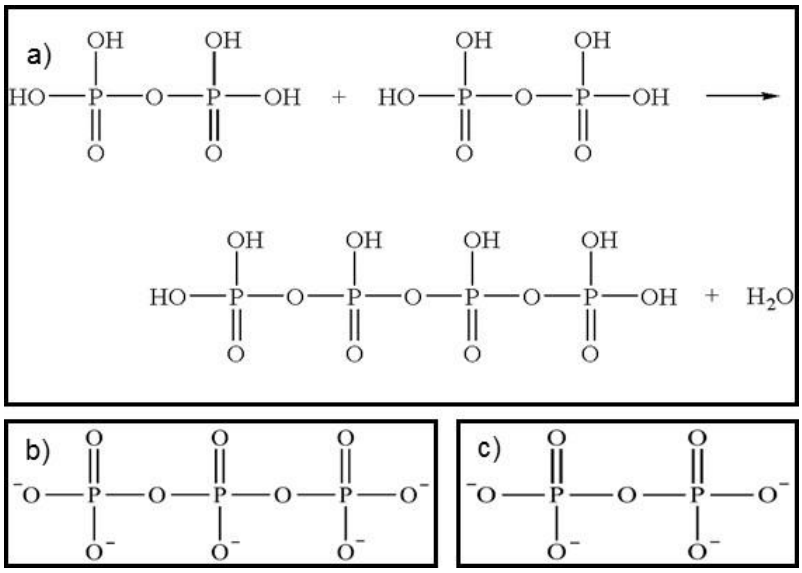

Figure 1.9. a) Scheme of polyphosphate condensation reaction, b) linear structure of tripolyphosphate and c) linear structure of pyrophosphate.

PolyP has a strong affinity for the HAp surface, providing high resistance against successive acid attacks and capacity to decrease enamel dissolution. In recent years, a number of growth factors or therapeutics agents, such as bone morphogenetic protein-2 (BMP-2),[60] basic fibroblast growth factor (bFGF),[61] platelet-derived growth factor (PDGF),[62] polyP,[63] have been introduced with tissue engineering techniques to enhance bone regeneration.

Phosphonates (PCPc) are organophosphorus compounds containing $C-PO(OH)_2$ or $C-PO(OR)_2$ groups (where $R = \text{alkyl, aryl groups}$). Numerous experiments on PCP compounds, which possess $P-C-P$ bonds in place of the $P-O-P$ bond of polyP, have provided further support for the role of phosphonates in calcium metabolism. PCPs have effects very similar to those of polyP on the behavior of calcium phosphate *in vivo* and prevent the dissolution of hydroxyapatite. PCPs are more resistant to chemical and enzymatic hydrolysis than polyP.[64] PCPs can be considered as nonhydrolyzable analogues of polyP. Some of the most used PCPs are alkylpolyphosphonates (APPs), such as aminotris(methylenephosphonic acid) (ATMP), 1-hydroxyethylidene disphosphonic acid (HEDP), ethylenediamine tetra(methylene phosphonic acid) (EDTMP), and diethylenetriamine penta(methylene phosphonic acid) (DTPMP).[65,66]

The adsorption of polyPs and PCPs onto HAp can be explained by a simple Langmuir adsorption model in a single-polyP system and by a competitive Langmuir adsorption model in a binary-polyP system. In single solute systems, tripolyphosphate (**Figure 1.9.b**) (a polyP with three condensed phosphates) exhibited the stronger adsorption process, followed by pyrophosphate (**Figure 1.9.c**) (the simplest member of group of polyPs with two condensed phosphates) and phosphonates.[67] The adsorption effects were two orders of magnitude greater than the adsorption effect for a simple orthophosphate.

1.2.8 DNA ADSORPTION ON HAp SURFACES

The adsorption kinetics of DNA on various solid substrates has been a popular research topic in previous decades due to their numerous applications, particularly in the development of DNA-based devices, such as biosensors[68-70] micro arrays[71,72] and transistors.[73,74] Experimentally, the DNA has a strong adsorption onto the HAp surface simply by immersing HAp into a beaker containing the aqueous DNA solution. HAp-bound DNA is more resistant to decay and less susceptible to degradation by serum and nucleases, which may account for the long-term persistence of DNA in bone and tooth.[75] Due to this reason, HAp has been used in the chromatographic separation of proteins and DNA.[76]

The chemical interaction between DNA macromolecules and hard tissues in vertebrate is of foremost importance in paleogenetics, as bones and teeth represent a major substrate for the genetic material after cell death. Recently, the empirical hypothesis of DNA protection over time thanks to its adsorption on hard tissues was revisited from a physico-chemical viewpoint.[77] In particular, the existence of a strong interaction between phosphate groups of DNA backbone and the surface of apatite nanocrystals (mimicking bone/dentin mineral) was confirmed on an experimental basis.[78] By extrapolation, this hypothesis may also appear informative for researchers interested in the origins of life on Earth, where the occurrence and preservation of primitive biomolecules such as nucleotides is of prime relevance. Indeed, as in the case of DNA, the adsorption of nucleotides onto mineral substrates constitutive of the Earth's geochemistry such as apatites[79] (*e.g.* present in metamorphic rocks of pelitic, carbonate, basaltic, and ultramafic composition) may provide protection against premature degradation by environmental factors.

The atomically smooth surface and stable chemical properties of HAp make it an ideal substrate for DNA adsorption. Thus, it has been commonly used in experimental research, such as studies of DNA conformation and DNA interactions with solid substrates. A DNA molecule is typically negatively charged due to its sugar phosphate backbone, which results in a loose bind with negatively charged ceramics surfaces in most aqueous environments thanks to electrostatic repulsion. To explain tight adsorption of DNA on a HAp surface, we must consider the presence of calcium cations.[80]

In addition to cation species, the DNA adsorption and the corresponding conformation is also significantly influenced by pH[81,82] ionic strength,[83] DNA conformation in solutions[84] and competition between monovalent and divalent cations.[85] Despite the breadth of prior research, the ion-mediated binding mechanism and its influence on DNA adsorption kinetics have not yet been clearly understood.

DNA is used by the cells to store and transmit information. DNA has a covalently linked backbone made of nucleotides (nitrogen bases bind to alternating pentoses and highly negatively charged phosphates) (**Figure 1.10**). Thus, it acts as a polyanion in a layer-by-layer deposition process. Whether DNA conserves its double helix structure or not is of importance for potential applications like the express diagnostic of virus.[86]

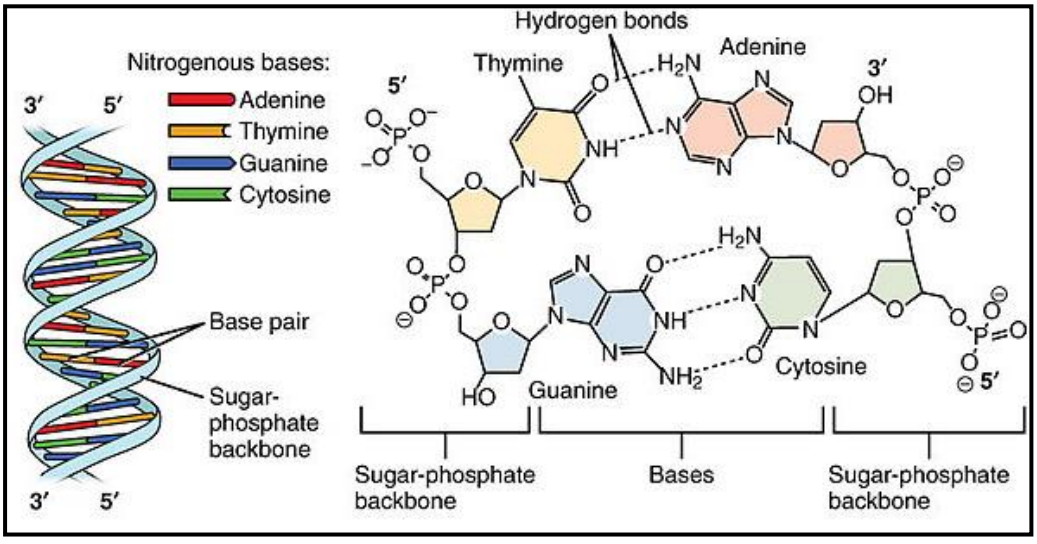

Figure 1.10. The chemical assembly of the three parts of the nucleotide, the phosphate, the nitrogenous base and the pentose sugar. Adapted from *Russell, Peter iGenetics. New York: Benjamin Cummings (2001)*.

The atoms of a molecule are not strictly fixed in their equilibrium positions. They may be pushed away from, and oscillate around, their positions due to various external effects,

such as thermal collisions between a given macromolecule and molecules of the solvent.[87] In a real system, these oscillations hardly alter the lengths of covalent bonds. Partial charges in some atom positions occur, first at all, because the bond angles (*i.e.*, the angles between adjacent chemical bonds) can be deformed.[88] In addition, parts of the molecule can rotate with respect to each other, around the axes of single covalent bonds (but not around double ones). This rotation is sometimes expressed in terms of a molecule having a few different 'rotational-isomeric forms'.[89]

A classic example of a polymer with a different flexibility mechanism is a DNA double helix. Since it consists of two chains, rotations in one of them are prevented by the other,[90] so the only remaining way in which the chain can flex is by deformation of the angles between the bonds.[91] Thus, the DNA molecules dominantly alter configuration by expanding and contracting, conserving its functionality in most of the *in vivo* processes or in experimental situations resembling *in vivo* conditions. A conformational transition inside the multilayers may arise from temperature[92] or pH changes.[93] A biopolymer is designed in order to keep its structure unchanged, from the moment it is synthesized until it is destroyed. The Russian physical Lifshitz suggested this analogy in 1968, in describing the linear memory of biopolymers as if they always remember the linear structure they were given when synthesized.[94]

1.3 Electrical dipole and space charge thermopolarization in hydroxyapatite

Most surfaces in water are charged, because water is a good solvent for ions due to its high dielectric constant. Alternatively, a surface can be charged as a consequence of the adsorption of ions adsorb or their dissociation. A protein might, for instance, expose their amino groups and become protonated $(-\mathrm{NH_2} + \mathrm{H^+} \rightarrow \mathrm{NH_3^+})$ or alternatively become negatively charged if dissociation of protons from their carboxylic groups is prevalent $(-\mathrm{COOH} \rightarrow -\mathrm{COO^-} + \mathrm{H^+})$.

Another way of charging a conducting surface is by the application of an external electric potential between this surface and a counter-electrode. This is typically done in an electrochemical cell. Surface charges cause an electric field which attracts counter ions. When a polarizable charge distribution is placed in an external potential field, the induced multipole moments are completely determined by the polarizabilities of the charge

distributions.[95] These polarizabilities depend solely on the internal structure of the charge distribution.

The internal structure of the charge distribution of ionic crystals like hydroxyapatite is a result of the Coulomb attraction between the positive and the negative ions. This Coulombic energy is usually calculated on the basis of a point-ion model of the crystal.[96] In a similar fashion, in the theory of macroscopic polarization of matter by an external electric field, the atoms are always considered as point dipoles. Actually, the ions and atoms are charge distributions of finite extend which are deformable (polarizable) in the crystalline electric field.[97]

It should be remarked that the considerations given above only apply to crystals whose charge distributions have net charges, *i.e*. crystals whose binding energy is (at least partly) of ionic character.[98] The net charges of the ions give rise to the initial crystalline electric field which is the main cause of the induction of all the higher multipole moments.[99]

The fact that the polarization energy is relatively small, does not imply that its calculation is only of minor interest. As has already been suggested by Landau and Lifshitz in 1984,[100] the polarization energy could play an important role in considerations about the relative stability of the various lattice types. On these grounds it must be concluded that stability considerations in which the polarization energy is neglected are not reliable.[101]

1.3.1 STERN THEORY OF THE DIFFUSE DOUBLE LAYER

An electric double layer is constituted by a charged surface and the layer of the directly binded counter ions (**Figure 1.11**). In fact, this double layer is similar to a plate capacitor, being in honour of the work of Ludwig Helmholtz on electric capacitors called the Helmhotz layer.[102]

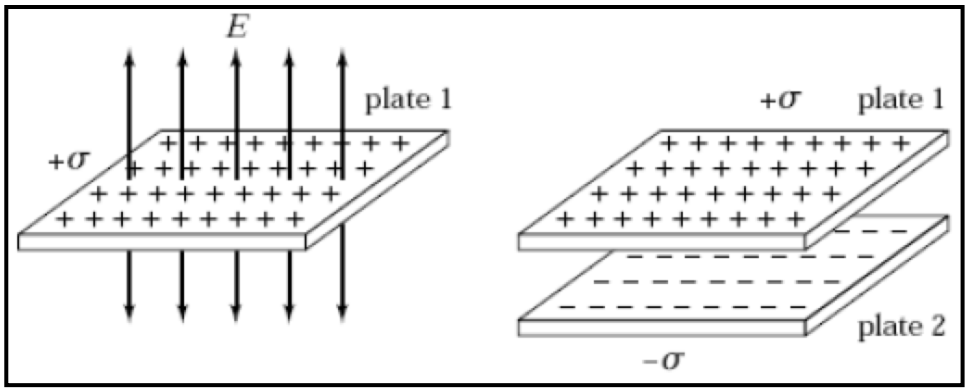

Figure 1.11. The surface charge density for plates in a capacitor (*right*) and the electric field strength associated with either side of plate 1 and the electric field lines for this plate (*left*).

In the years 1910-1917 Gouy and Chapman went a step further[103,104] taking into account a thermal motion of the ions. Thermal fluctuations tend to drive the counter ions away from the surface leading to the formation of a diffuse layer, which is more extended than a molecular layer. In 1924, Stern combined the ideas of Helmholtz and that of a diffuse layer.[105] In Stern theory we take a pragmatic, though somewhat artificial, approach and divide the double layer into two parts: an inner part, the Stern layer, and an outer part, the Gouy-Chapman or diffuse layer. Essentially the Stern layer is a layer of ions which is directly adsorbed to the surface and which is immobile. In contrast, the Gouy-Chapman layer consists of mobile ions, which obey Poisson-Boltzmann statistics (**Figure 1.12**). The potential at the point where the bound Stern layer ends and the mobile diffuse layer begins is the zeta potential (ζ potential).[106]

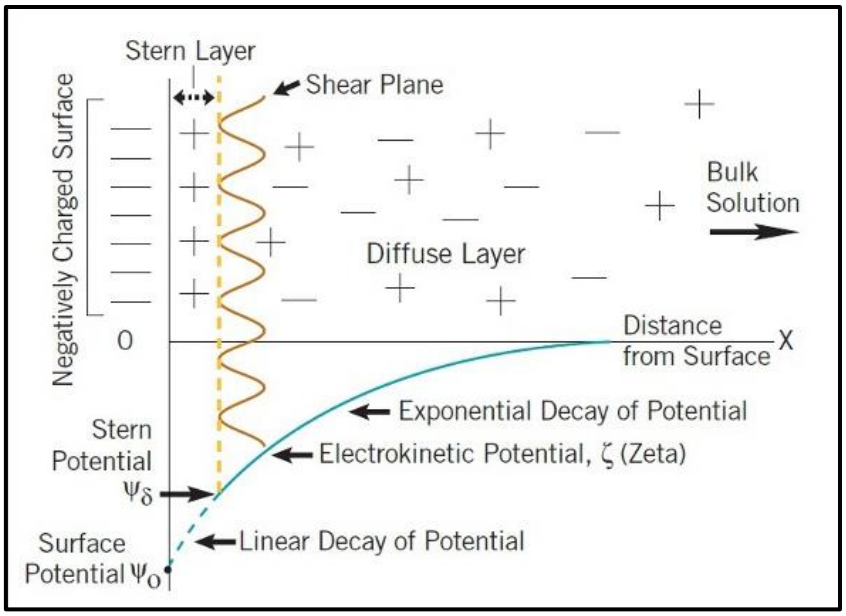

Figure 1.12. Simplified model of the electric double-layer at a charged interface in aqueous solution.

1.3.2 CORRELATION BETWEEN HIGH-TEMPERATURE ELECTRIC RESPONSE AND MICROSTRUCTURAL PROPERTIES OF HAp

It has been reported that the temperature increase has much higher impact on the conductivity of HAp compared with geometric factors such as the grain size.[107] Dense materials exhibit the highest conductivity at elevated temperatures (> 700 °C) since behavior is dominated by bulk ionic conductivity.[108] HAp is not only a calcium phosphate but also a hydroxide. The lattice OH^- ions are aligned along the *c*-axis of HAp. The crystal structure of stoichiometric HAp without OH^- defects is monoclinic phase (space group $P2_1/c$) at room temperature.[109,110] The monoclinic HAp shows an antiferroelectric property, and changes to hexagonal (space group $P6_3/m$) phase at about 210° C .[109,110] Extensive dehydroxylation during sintering of HAp starts above 700° C.[111] Surface HAp charge density can be enhanced by a sintering process and exposure to DC electric fields of few kV/cm.[112,113]

1.4 Toxicity impact of hydroxyapatiye nanoparticles

The paths of released calcium and phosphate ions from resorbable and nearly non-degradable implanted HAp materials have been traced with different methods such as serum and urine calcium and phosphate levels, and in different animal models without any abnormal results. In addition, no particular or pathological reactions were found in detailed histological studies on the major organs including very detailed kidney histology.[114,115] These results lead to the conclusion that the calcium and phosphate ions dissolved from these materials are reintegrated into the usual regulatory systems of the body and are normally handled (deposited or removed) (**Figure 1.13**). The liver, skin, brain, heart, kidney, lung and intestine did not show any abnormal content of the labeled calcium.[116]

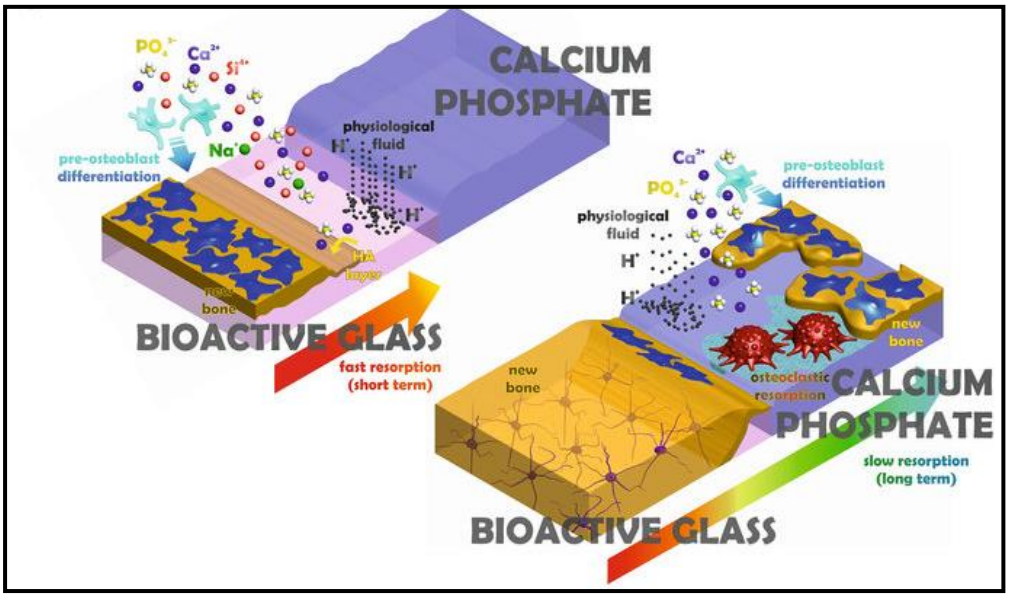

Figure 1.13. The outer bioactive layer of the implant is resorbed within an initial stage by the physiological fluid, favoring the precipitation of an osteoconductive HAp layer and the differentiation of osteoblast precursors required for intensive bone formation. Subsequently, the inner multiphasic CaP is slowly resorbed by mediation of osteoclasts and physiological fluid, releasing chemical species that promote bone ingrowth and providing stability at long term. Adapted from *Comesaña R., Lusquiños F. et al. Toward Smart Implant Synthesis: Bonding Bioceramics of Different Resorbability to Match Bone Growth Rates. Scientific Reports 5, Article number: 10677 (2015).*

A nanomaterial is roughly defined as a material with a base constituent between 1×10^{-9} and 100×10^{-9} meters in length that exhibits at least one property that deviates from the value for the equivalent bulk material.[117] Cell-specific targeting can be achieved by attaching drugs to individually designed carriers. Recent developments in nanotechnology have shown that nanoparticles have a great potential as drug carriers. Due to their small sizes, the nanostructures exhibit unique physicochemical and biological properties (*e.g.,* an enhanced reactive area as well as an ability to cross cell and tissue barriers) that make them a favorable material for biomedical applications.

Schematic drawing of the cytosolic delivery and organelle-specific targeting of drug loaded nanoparticles via receptor-mediated endocytosis is shown in **Figure 1.14**. After receptor mediated cell association with nanoparticles, the nanoparticles are engulfed in a vesicle known as an early endosome. On the other hand, if nanoparticles are captured in early endosomes, they may make their way to lysosomes as late endosomes where their degradation takes place. Only fraction of non-degraded drug released in the cytoplasm interacts with cellular organelles in a random fashion. However, cytosolic delivery of a fraction of organelle-targeted nanoparticles via endosomal escape or from lysosomes travel to the targeting organelles to deliver their therapeutic cargo.[118]

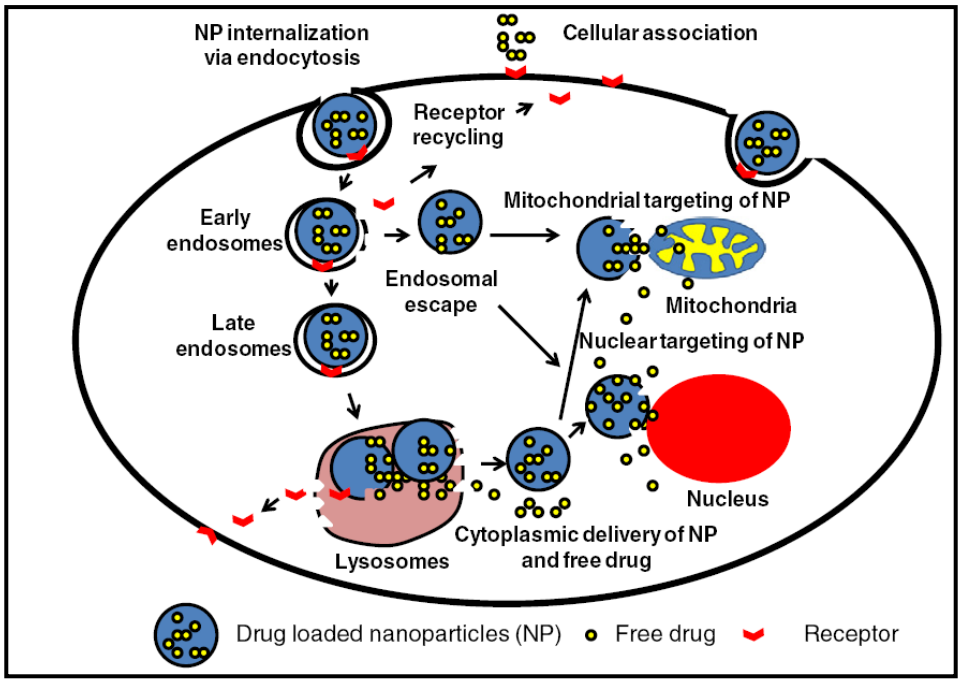

Figure 1.14. Schematic drawing of cytosolic delivery and organelle-specific targeting of drug loaded nanoparticles via receptor-mediated endocytosis. Adapted from *Sorkin A., A. Gabi, Eds. Springer New York. pp. 1–31 (2013)*.

Properties that can be different between bulk materials and their nanosized counterparts include electrical and thermal conductivity, mechanical properties, optical behavior, and surface reactivity. The unique physicochemical properties of engineered nanomaterials are unquestionably valuable in many technologies. However, these properties are also cause of concern about their potential toxicological effects on biological systems.

These nanoparticles (NPs) are likely to increase an unnecessary infinite toxicological effect on animals and environment, although their toxicological effects associated with human exposure are still unknown. In order to understand the effects of these exposures, this chapter seeks to examine the various toxicological portal routes associated with NPs exposures. Due to their small size, individual nanomaterials and small agglomerates may be deposited deep within the lungs when inhaled, reaching areas that are not as easily accessed by larger materials. Also, their size may permit them to pass directly through tissues and cell membranes, allowing them to translocate from their initial site of exposure to other organs in the body.

In addition to their small size, the increased surface area per unit mass of nanomaterials increases their potential for interaction with biological components. A high specific surface area may lead to increased adsorption of physiological surfactants and macromolecules, which may alter the surface chemistry of the nanomaterial. The combination of nanomaterial size, surface area, and surface energy characteristics are likely to initiate effects in biological systems that are not possible with the bulk form of the same materials. Therefore, it is of outstanding importance to investigate the potential hazards of nanomaterial exposure.[119,120]

1.4.1 EFFECT OF CALCIUM ON THE GENERATION OF REACTIVE OXYGEN SPECIES

Unlike the ionic calcium cell entry, the internalization process of HAp precipitates is a very complex process. There are mixed reports on the effect of primary particle size on HAp intracellular entry.[121,122] The key question is that effective internalization of HAp particles is provided not only by optimal calcium and phosphate concentrations but also by the size of the non-agglomerated precipitate. The mechanism by which nanosized particles are usually taken up is endocytosis which is limited to the size range of approximately 20−200 nm in diameter, above this size phagocytosis is thought to predominate.[123]

To accomplish a successful cytoplasmic internalization HAp particles must penetrate the cell membrane either at the cell surface or after endocytosis and undergo subsequent cytoplasm targeting.[124] HAp particles of different size are dissolved in the acidic lysosomes, leading to sudden rises of ionic calcium levels, which are slowly pumped into intracellular calcium stores, such as mitochondria, endoplasmatic reticulum or out of the cell.[125,126]

Calcium is a key regulator of mitochondrial function and acts at several levels within the organelle to stimulate adenosine triphosphate (ATP) synthesis. However, the dysregulation of mitochondrial $[\mathrm{Ca}]^{2+}$ homeostasis is now recognized to play a key role in several pathologies.[127] For example, mitochondrial matrix $[\mathrm{Ca}]^{2+}$ overload can lead to enhanced generation of reactive oxygen species (ROS),[128] triggering of the permeability transition pore and cytochrome c release, ultimately leading to apoptosis and necrosis.[129] The interplay between the conventional and novel roles of mitochondria has received little consideration, and an examination of recent mitochondrial science reveals several incompatibilities with classic bioenergetic viewpoints. An example is the role of Ca^{2+} in regulating organelle function and dysfunction. The question about how can Ca^{2+}, a physiological stimulus for ATP synthesis,[130, 131] become a pathological stimulus for ROS generation, cytochrome c release, and apoptosis is an open question. This apparent mitochondrial Ca^{2+} paradox revolves around a two-hit hypothesis (see **Figure 1.15**) in which a concurrent pathological stimulus can turn Ca^{2+} from a physiological to a pathological effector.

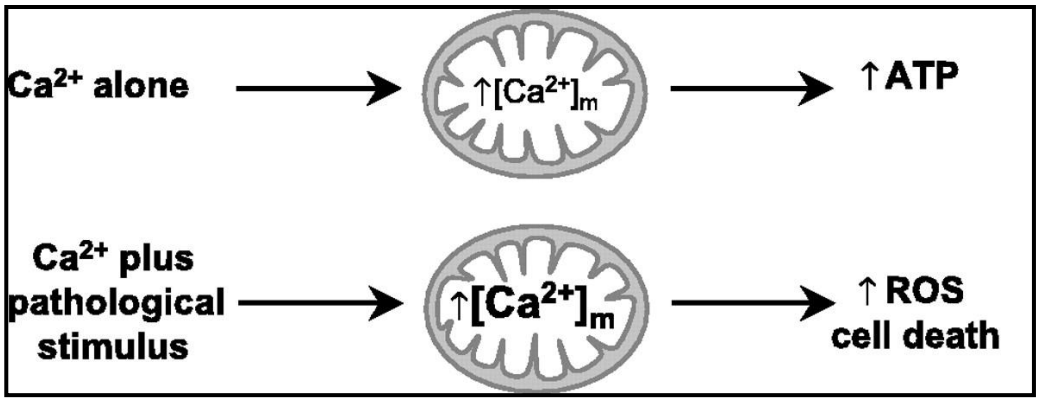

Figure 1.15. Two-hit hypothesis for mitochondrial Ca^{2+} in physiology and pathology. Under physiological conditions, Ca^{2+} is beneficial for mitochondrial function. However, in the presence of an overriding pathological stimulus, Ca^{2+} is detrimental. Similarly, Ca^{2+} can potentiate a subthreshold pathological stimulus, resulting in pathogenic consequences. Adapted from *Brookes P.S. et al. ATP, and ROS: a mitochondrial love-hate triangle. Am J Physiol Cell Physiol. 287 (4), 817-33 (2004).*

At the heart of understanding how Ca^{2+} can be both a physiological and a pathological effector of mitochondrial function is the issue of how Ca^{2+} modulates mitochondrial ROS generation. **Figure 1.16** shows the theoretical mechanisms by which Ca^{2+} can enhance ROS generation. The citric acid cycle (CAC) -also known as the tricarboxylic acid (TCA) cycle or the Krebs cycle[132,133] - is a series of chemical reactions used by all aerobic organisms to release stored energy through the oxidation of acetyl-CoA derived from carbohydrates, fats, and proteins into carbon dioxide and chemical energy in the form of adenosine triphosphate (ATP). Stimulation of the TCA cycle and mitochondrial oxidative phosphorylation (ox-phos) by Ca^{2+} would enhance ROS output by making the whole mitochondrion work faster and consume more O_2. Indeed, mitochondrial ROS generation correlates well with metabolic rate,[134,135] suggesting that a faster metabolism simply results in more respiratory chain electron leakage.

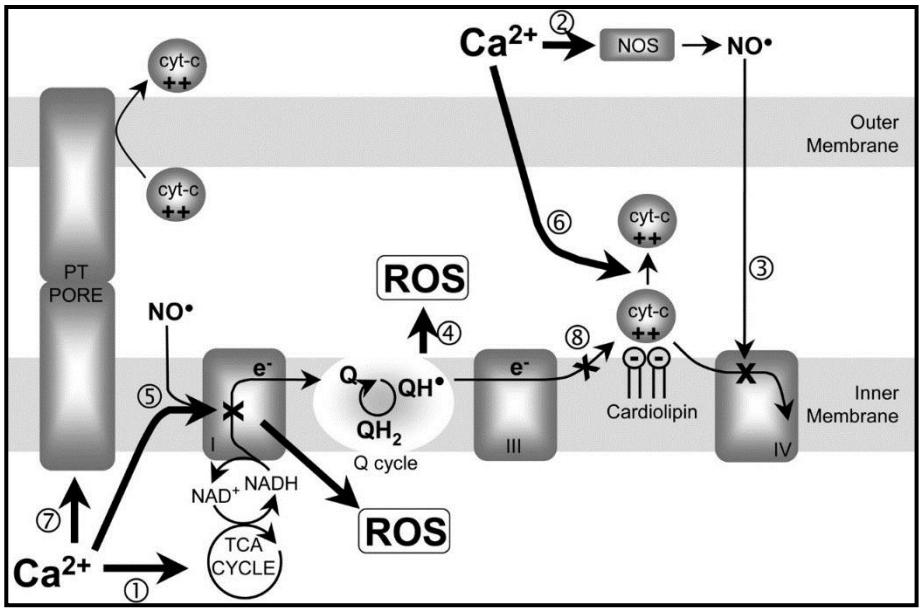

Figure 1.16. Mechanisms for Ca^{2+} stimulation of mitochondrial ROS generation. Ca^{2+} stimulation of the TCA cycle (1) will enhance electron flow into the respiratory chain, and Ca^{2+} stimulation of nitric oxide synthase (NOS). The subsequent nitric oxide (NO·) generation (2) would inhibit respiration at complex IV (3). These events would enhance ROS generation from the Q cycle (4). In addition, NO· and Ca^{2+} can inhibit complex I, possibly enhancing ROS generation from this complex (5). Ca^{2+} also dissociates cytochrome c (cyt-c) from the inner membrane cardiolipin (6) and at high concentrations triggers cytochrome c release across the outer membrane (7). The subsequent inhibition at complex III (8) would enhance ROS generation at the Q cycle (4). Complex II is omitted from this diagram for clarity. Adapted from *Brookes P.S., Yisang Yoon Y., James L. Robotham J.L., M. W. Anders M.W., Shey-Shing Sheu S-S. Calcium, ATP, and ROS: a mitochondrial love-hate triangle. American Journal of Physiology - Cell Physiology. 287, 817-833 (2004)*.

These results continue to expand and refine the above working hypothesis that deregulation of $[Ca]^{2+}$ results in a number of phenomena from activation of signaling mechanism and alterations in cellular structure to alterations in gene expression, all of which contribute to or play a critical role in cellular toxicity, including carcinogenesis and cell death.[136,137,138]

1.5 Hydroxyapatite nanoparticles as a drug delivery system

The main focus of this chapter is the understanding of the transport and release of molecules in HAp with adsorbed substances, and the kinetics of the release. Multiple

approaches have been formulated to achieve these objectives, including polymer coating and the use of drug carriers. Most carriers are artificially assembled supramolecular structures composed of biocompatible elements, with sizes ranging from tens of nanometers to a few microns (**Figure 1.17**).

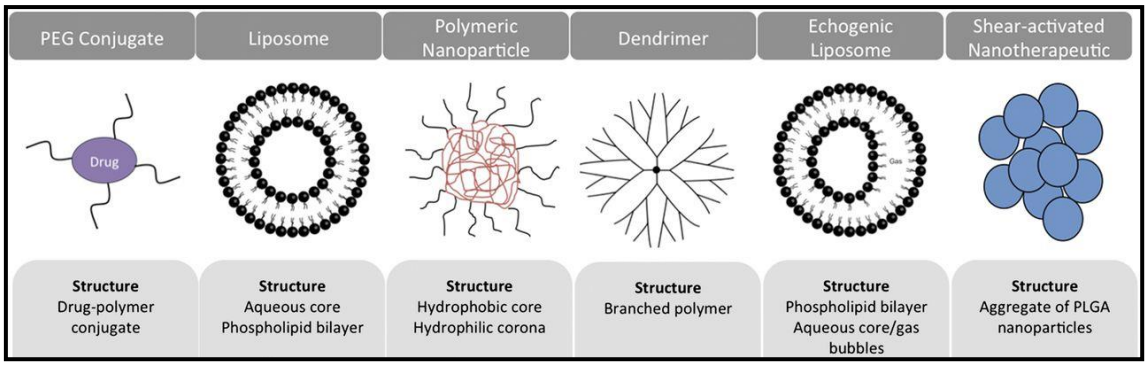

Figure 1.17. Examples of classes of carriers tested for delivery of drugs and their principal structure. Synthetic carriers vary in size from few nanometers to several microns, shape, stability, and principle of drug loading and release. Adapted from *Greineder C.F., Howard M.D., Carnemolla R., Cines D.B. and Muzykantov V. Advanced drug delivery systems for antithrombotic agents. Blood. 122, 1565-1575 (2013)*.

Design of materials for drug delivery systems requires an accurate selection considering different levels of magnification. On the molecular level, it is important to choose either a material that is indifferent under physiological conditions or a material that resembles a body human tissue.[139] HAp belongs to the second category.[140] As a result of extensive experimentation with biomaterials, several key factors have emerged to deliver drugs to their targets in a controlled manner (**Figure 1.18**). Specifically, varying the hydrophilicity, crystallinity and molecular weight of the matrix allows researchers to adjust the matrix degradation and, subsequently, control the rate of drug delivery.[141]

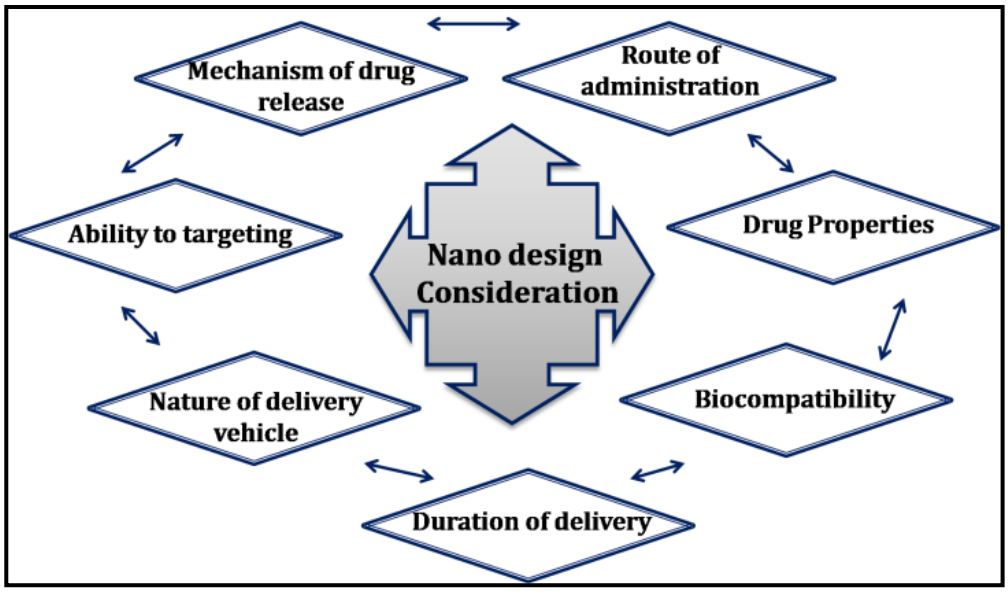

Figure 1.18. Requirements for the design of polymeric nanoparticles to be used as smart drug delivery system. Adapted from *Application of Nanotechnology in Drug Delivery, edited by Ali Demir Sezer, ISBN 978-953-51-1628-8, published: July 25 (2014)*.

Solid suspensions are further classified into substitutional crystalline solid, interstitial solid and amorphous solid solutions. In substitutional crystalline solid solutions, a molecule of carrier/solvent is replaced by a solute molecule whereas an interstitial/solid solution consists of dissolved solute molecules occupying interstices within the carrier matrix. Amorphous solid solutions consist of the drug molecularly, but irregularly, dispersed within the amorphous carrier. Microfine crystalline dispersions consist of a molecular dispersion of a crystalline drug in a carrier.[142,143,144]

The crystalline form of a drug delivery system offers advantages in terms of high purity and physical/chemical stability compared to amorphous solid dispersions. However, constraints associated to lattice energy must be overcome to allow solute molecules to dissolve. The amorphous state exhibits a disordered structure in comparison to the crystalline state and possesses higher free energy. Thus it offers enhanced apparent solubility, dissolution rate and oral bioavailability.[145] The use of high throughput methods in drug discovery has led to compounds with more lipophilic properties and hence poor solubility,[146,147] and dissolution-limited bioavailability. In the case of poorly soluble but well-permeable drug delivery systems, high free energy states such as the amorphous form can significantly improve 'apparent' solubility,[148] often leading to a large increase in dissolution rate in the gastro-intestinal tract and consequently an increased bioavailability.

For biodegradable polymer based drug delivery systems, there are concerns about the possibility that polymer acidic byproducts or degraded polymer fragments can adversely affect drug and tissues. Often an undesirable late stage, uncontrolled and massive drug release is observed with polymer based drug delivery systems.[149] Bioceramics, such as HAp, represent another class of materials suitable for use as a carrier for drugs, non-viral gene delivery, antigens, enzymes, and proteins. HAp can be produced at a low cost and is simple to manufacture. While there is low cumulative release in neutral phosphate saline buffer, the nanoconjugates of HAp are significantly more soluble in acidic solutions. This property may make the nanoHAp/ drug delivery system particularly suited for *in vivo* intratumoral drug delivery applications in which the acidic pH of tumor tissue will lead eventually to a complete drug release.

As far as the physicochemistry of the phases in HAp is considered, the processes of local dissolution and local reprecipitation of HAp can be comprehended only by assuming that the rate of its breakdown may depend very much on the type of additives used for its fabrication and on its pure structure.[150] Much work has still to be done to develop the optimum composition for each field in which the use of HAp delivery systems should be clinically indicated.

1.5.1 ELEMENTS OF THE BIOLOGICAL ENVIRONMENT

The central idea developed in the previous chapter of toxicity is that biological performance should be defined in terms of the interaction between materials and their biological environment. This is not different from the normal consideration given during an engineering design process to the material aspects of performance and durability. However, there are two relative quantitative aspects that set biological performance apart and create the need for an independent study of material and host responses.

1. *High demand*. The biological environment, especially internal to living systems, is a remarkably aggressive one. It is a milieu of high chemical activity combined with a highly variable spectrum of combined mechanical processes.

2. *Invariant conditions*. Despite its aggressive aspects, the biological environment displays an extraordinary quality of constancy in both physical conditions and composition. Complex control systems exist to maintain that constancy; thus,

deviations from established conditions due to the presence of materials may be expected to incite restoring responses (see **Figure 1.19**).

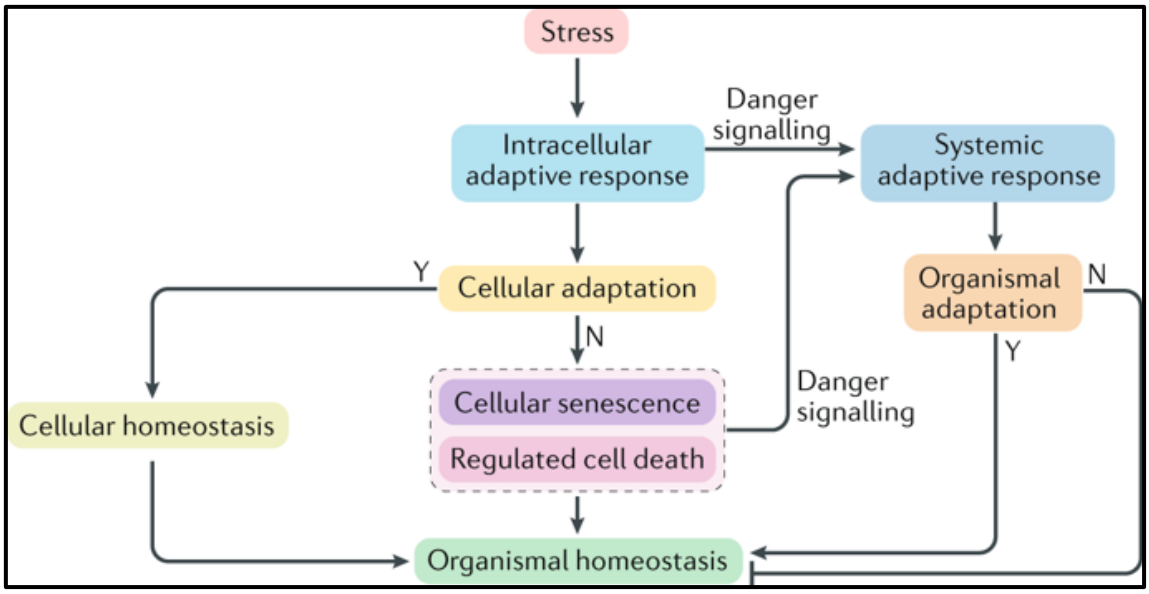

Figure 1.19. Mammalian cells respond to stress by activating mechanisms that support cellular functions and hence maintain microenvironmental and organismal homeostasis. *Adapted from Made S., Windelspecht M., and Cox D. Human Biology. 13th Ed. New York: McGraw-Hill (2014).*

The advent of the unit cell concept in materials science had a revolutionary effect on our understanding of materials properties and their dependence on structure. Therefore, it is natural, as we move forward in biological research, to look for a similar unifying paradigm for physical scientists and engineers. This new point of view strongly supports a novel approach to ensure the efficacy and safety of drug delivery systems (DDS) in cell therapy. In early biomaterials science and engineering (BSE) studies, tissues were regarded as continuous, largely homogenous materials, possessing some anisotropy of structure and properties. Since most experimental studies were performed on dead tissues, cells were viewed as imperfections in structure, rather like defects in crystalline materials, and largely overlooked. It was understood that cellular function defined the living state, but that was not a concern for engineers. There was a general, usually unspoken, assumption that living and dead materials had the same physical properties.

1.5.2 USE OF CALCIUM PHOSPHATE PRECIPITATES AS A TRANSFECTION AGENT

Transfection denotes the introduction of functional foreign DNA into the cell nucleus with the aim of repairing missing cell function and to provide means to enhance or silence gene expression. Entry of nucleic acids into cells cannot be performed without help as a transfection reagent. This process comprises three main steps: complexation of nucleic acids, interaction with the cellular membrane and entry into the cell. Subsequent step correspond to the intracellular transport into the nucleus (**Figure 1.20**).

Of the inorganic vectors investigated, calcium phosphate is by far the most widely used and studied biomaterial because it can transfect a wide variety of mammalian cells i*n vitro*[125] and avoid issues such as immune responses[151] and high toxicity associated with other techniques.[152] Despite its widespread use as an *in vitro* transfection agent, little attention has been given to the composition and physical properties of calcium phosphate particles and their possible use as a drug delivery system. The vectors are often referred as ACP-DNA complexes and little or no physico-chemical analysis of such particles has been performed. This makes elucidation of the critical physico-chemical parameters for drug delivery system extremely challenging. Although the standard calcium phosphate transfection method was established over 40 years ago, only a few investigations of uses of calcium phosphates as a drug delivery system have been reported until now.[153,154]

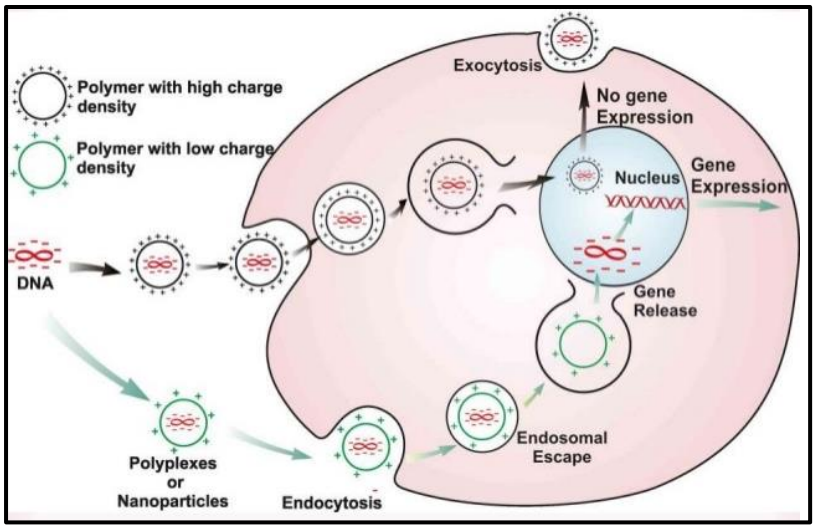

Figure 1.20. Calcium phosphate transfection mechanism. Adapted from *Welzel, Radtke, Meyer-Zaika, Heumannb and Epple Transfection of cells with custom-made phosphate nanoparticles coated with DNA. Journal of Materials Chemistry. 14, 33-49 (2004)*.

1.6 Delivery of antibiotics by hydroxyapatite drug delivery systems to target cancer cells

Two review articles published in 2000 and 2011 by Hanahan and Weinberg have lately dominated the discourse about carcinogenesis among researchers.[155,156] They stated a belief that "the complexities of the disease, described in the laboratory and the clinic, will become understandable in terms of a small number of underlying principles". The six original hallmarks of cancer that they proposed, as well as two new ones that has become evident in the following years; and that they included in their last revision, are the followings: 1) Sustaining proliferative signaling, 2) Evading growth suppressors, 3) Enabling replicative immortality, 4) Resisting cell death, 5) Inducing angiogenesis, 6) Activating invasion and metastasis, 7) Avoiding immune destruction and 8) Deregulating cellular energetic (**Figures 1.21**).

The chronic and often uncontrolled cell proliferation that represents the essence of neoplastic disease involves not only deregulated control of cell proliferation but also corresponding adjustments of energy metabolism in order to fuel cell grown and division.[155,156] Under aerobic conditions, normal cells process glucose, first to pyruvate via glycolysis in the cytosol and thereafter via oxidative phosphorylation to carbon dioxide in the mitochondria. Under anaerobic conditions, glycolysis is favoured and relatively scarce pyruvate is dispatched to the oxygen-consuming mitochondria. Otto Warburg first

observed in 1956 an anomalous characteristic of cancer cell energy metabolism.[157] However, the first significant insight into the cause of aerobic glycolysis came from Wallace in 1992.[158,159] Even in the presence of oxygen, cancer cells can reprogram their glucose metabolism, and thus their energy production, leading to a state that has been termed aerobic glycolysis (**Figure 1.22**).

The mitochondria produce most of the cellular energy, generate much of the endogenous oxygen species (ROS), and regulate programmed cell death (apoptosis) via the mitochondrial permeability transition pore (mTPT). Now, mitochondrial defects have been accepted to play an important role in the development and progression of cancer. Warburg's observation stimulated many investigators to analyze mitochondrial function in tumor cells. This revealed that mitochondrial number of oxphos activities were frequently downregulated in many cancers[160] and that mRNA levels for certain mitochondrial DNA (mtDNA) encoded genes were upregulated.[161,162]

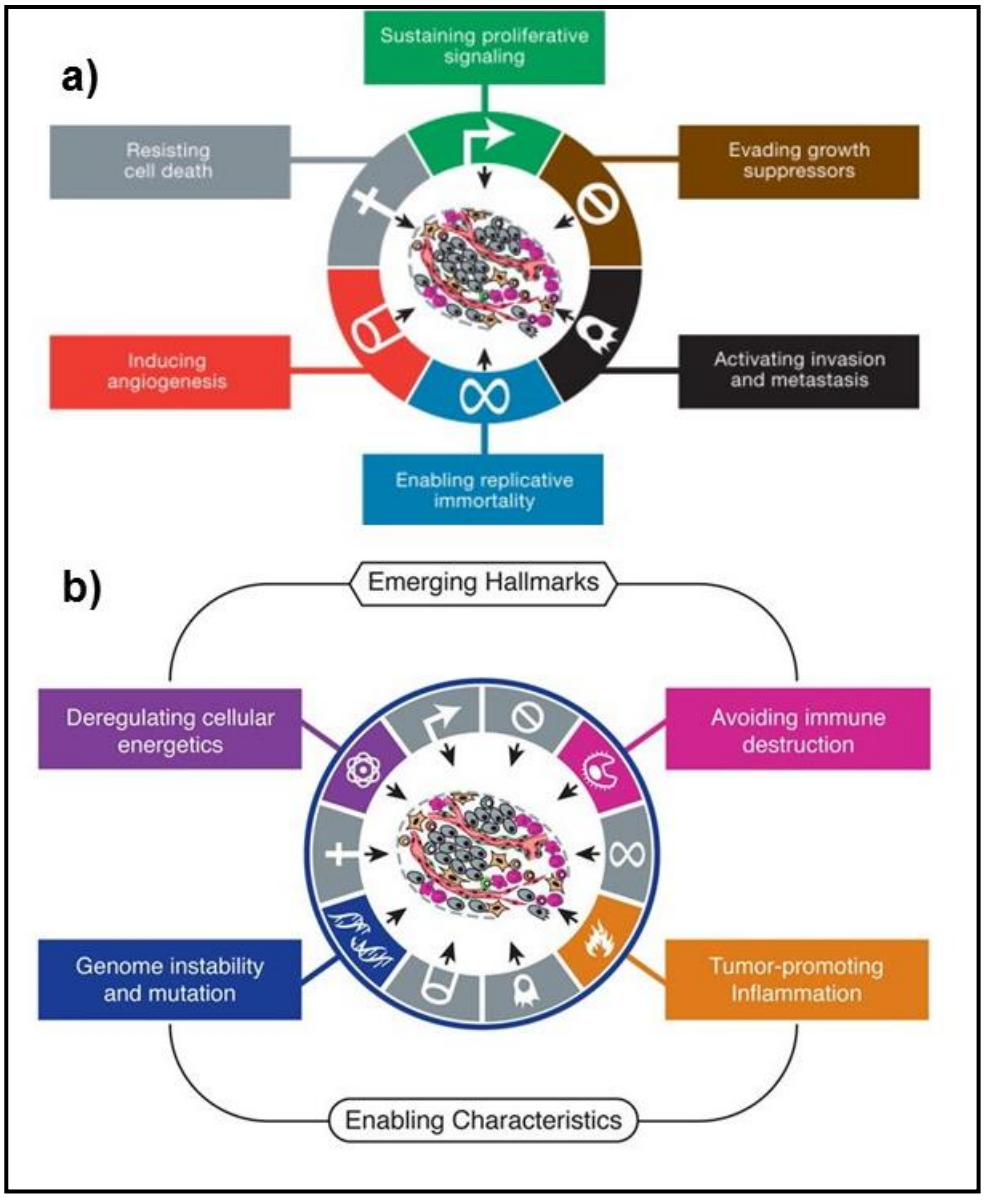

Figure 1.21. The hallmarks of cancer, this illustration encompasses the six hallmark capabilities originally proposed by Douglas Hanahan and Robert Weinberg in their 2000 perspective (a), and then two emerging hallmarks and the two enabling characteristics proposed in their 2011 perspective (b). Adapted from *Hanahan and Weinberg. Hallmarks of cancer: the next generation. Cell, 144, 646-674 (2011).*

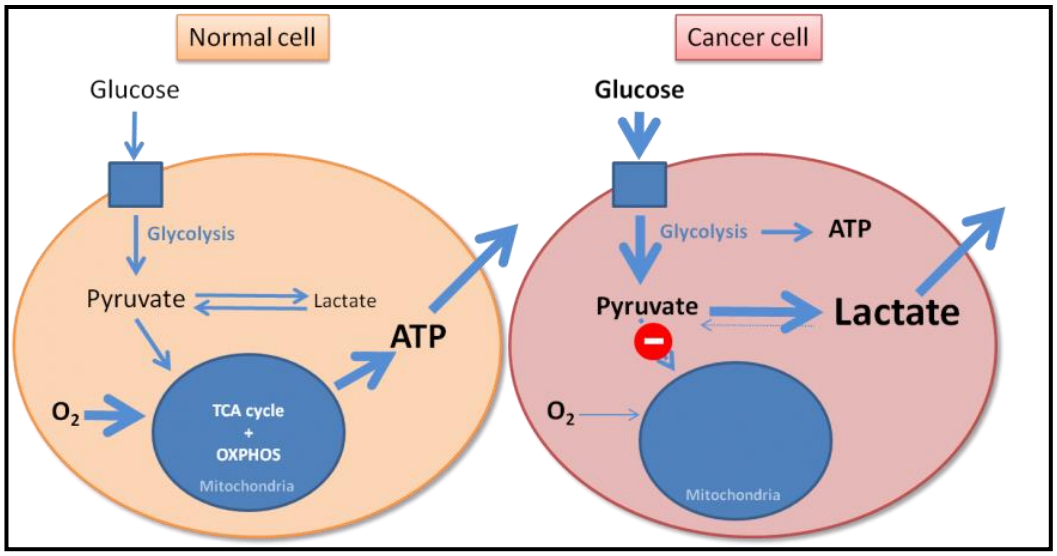

Figure 1.22. Otto Warburg's theory on the origins of cancer postulates that tumor cells have defects in mitochondrial oxidative phosphorylation and therefore rely on high levels of aerobic glycolysis (the Warburg effect) as the major source for ATP to fuel cellular proliferation. This was in contrast to normal cells which primarily utilize oxidative phosphorylation for growth and survival. Adapted from *Hsu and Sabatini Cancer Cell Metabolism: Warburg and Beyond. Cell. 134(5): 703–707 (2008)*.

1.6.1 EFFECT OF ANTIBIOTICS ON CANCER STEM CELLS

The effects of antibiotics on mitochondrial biogenesis can be explained by the endosymbiotic theory of mitochondrial evolution. In 1967, Lynn Margulis gathered diverse microbiological observations to support what is now known as the endosymbiotic theory.[163] Her publication is considered now as a landmark paper on the origin of eukaryotic cells (cells with a nucleus, like those of plants and animals). According to the endosymbiotic theory proposed by Margulis, mitochondria evolved from ancient symbiotic prokaryotes (organisms without nuclei, such as bacteria) (**Figure 1.23**).

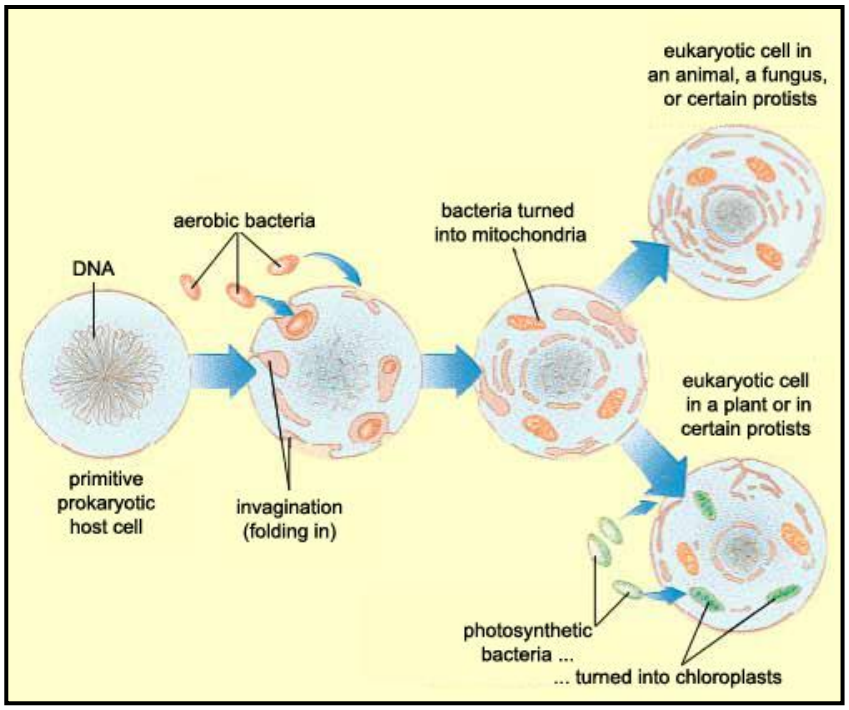

Figure 1.23. Endosymbiosis theory: Mitochondria originated following endocytosis of a proteobacteria by another prokaryotic cell. Adapted from *Martin W. and Mentel M. The Origin of Mitochondria. Nature Education. 3(9), 47-58 (2010).*

Tumour metabolism is recognized as a key therapeutic target in oncology. Mitochondria provide energy through their ability to convert glucose into ATP, which is the main energy source for cellular functions. Due to their similarities to bacteria, mitochondria can actually trigger severe illness in humans. This is why drugs that target prokaryotic protein synthesis can also target mitochondrial biogenesis in several cancer eukaryotic cells. In infectious disease, antibiotics have well-known metabolic side effects on human cells, due to mitochondrial disruption. In 2015, Lisanti *et al*.[164] envisaged that repurposing of antibiotics could be a novel strategy for the treatment of cancer. In 2014, in contrast with the reduction in mitochondrial mass in normal stem cells, Lisanti and colleagues demonstrated an increase in mitochondrial protein abundance in breast cancer stem cells (CSC), defined by growth as mammospheres.[165]

The stem cell theory of cancer proposes that among all cancerous cells, a few act as stem cells that reproduce themselves and sustain the cancer, much like normal stem cells renew and sustain our organs and tissues. In this view cancer cells that are not stem cells can cause problems, but they cannot sustain an attack on our bodies over the long term.[166] The idea that cancer is primarily driven by a smaller population of stem-cells has important implications. For instance, many new anti-cancer therapies are

evaluated based on their ability to shrink tumors, but if therapies are not sufficient to kill the cancer stem cells, the tumor will soon grow back (often with a resistance to the previously used therapy).[167]

To test their hypothesis, Lisanti *et al*. examined the effects of four different classes of antibiotics on tumor-sphere formation, which provides a functional assay to quantitavely measure CSC proliferative expansion and survival. The researchers found that common antibiotics, including erythromycins (azithromycin) and tetracyclines (doxycycline), prevented tumour-sphere formation in 12 cell lines, across eight cancer types. Their global phenotypic approach to target cancer as a single disease of stemness may also help to avoid drug resistance. They speculate that genetic changes (oncogenic mutations, amplifications/deletions, and tumor-initiating CSCs (**Figure 1.24**), favoured tumor recurrence, metastasis and drug resistance. Thus, it would be advantageous to phenotypically target stemness directly, instead of targeting individual genetic changes, in different cancer types. This would allow the treatment of cancer in a mutation-independent fashion.

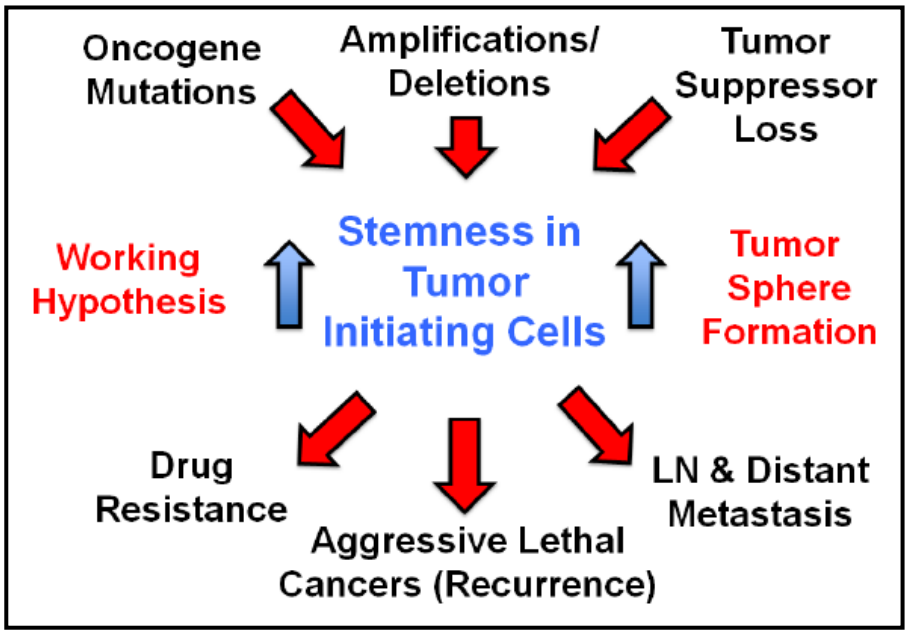

Figure 1.24. A mutation-independent approach to cancer therapy. Adapted from *Lamb, Ozsvari, Lisanti. Antibiotics that target mitochondria effectively eradicate cancer stem cells, across multiple tumor types: treating cancer like an infectious disease. Oncotarget, 5, 56-78 (2015).*

1.6.2 MULTIDRUG RESISTANCE (MDR) MECHANISMS IN CANCER THERAPY

Resistance to therapy has been correlated to the presence of at least two molecular pumps in tumour-cells membranes that expel drugs form the interior. This allows tumor cells to avoid the toxic effects of the drug or molecular processes within the nucleous or the cytoplasm. The two pumps commonly found to confer chemoresistance in cancer are P-glycoprotein (P-gp) and the so-called multidrug resistance-associated protein (MRP).[168]

To be multidrug-resistant, cells are thought to have one or both of the following features: (i) Lower intracellular drug concentration,[169] possibly in conjunction with compartmentation of the drug away from the site of drug action (the nucleus),[170] and/or (ii) Altered susceptibility to the drug and increased repair mechanisms.[171,172] A lower intracellular concentration of drug may be obtained by a decreased rate of uptake of drug or an enhanced efflux of drug from the cell. In the most widely accepted hypothesis for MDR, P-gp acts as a plasmalemmal ATP-dependent drug pump to extrude drug molecules from the cell.[173] P-gp-mediated drug transport is saturable[174] and capable of acting against a concentration gradient of its substrate.[175]

The development of multidrug resistance (MDR) is a major obstacle to effective cancer chemotherapy. After a long period of chemotherapy, many patients suffer from MDR, which can reduce therapy efficiency and lead to treatment failure.[176] The high level of resistance is usually caused by complex MDR mechanisms (**Figure 1.25**). Among them, overexpression of the adenosine triphosphate (ATP)-binding cassette transporters (ABC), such as P-gp, is one of the most prevalent mechanisms.[177] Tumor cells possess highly ordered internal resistance. This P-gp encoded by the MDR-1 gene acts as drug efflux pump that exports a wide range of chemotherapeutic drugs and will reduce the accumulation of functional drugs in MDR cancer cells, resulting in low cancer chemotherapeutic efficacy.[178] Currently, only a few tissue-derived advanced cancers can be cured by chemotherapeutic drugs. Furthermore, these tumors may also recur and become drug resistant.[179] Therefore, overcoming the drug resistance of tumors is a serious challenge for successful chemotherapy.

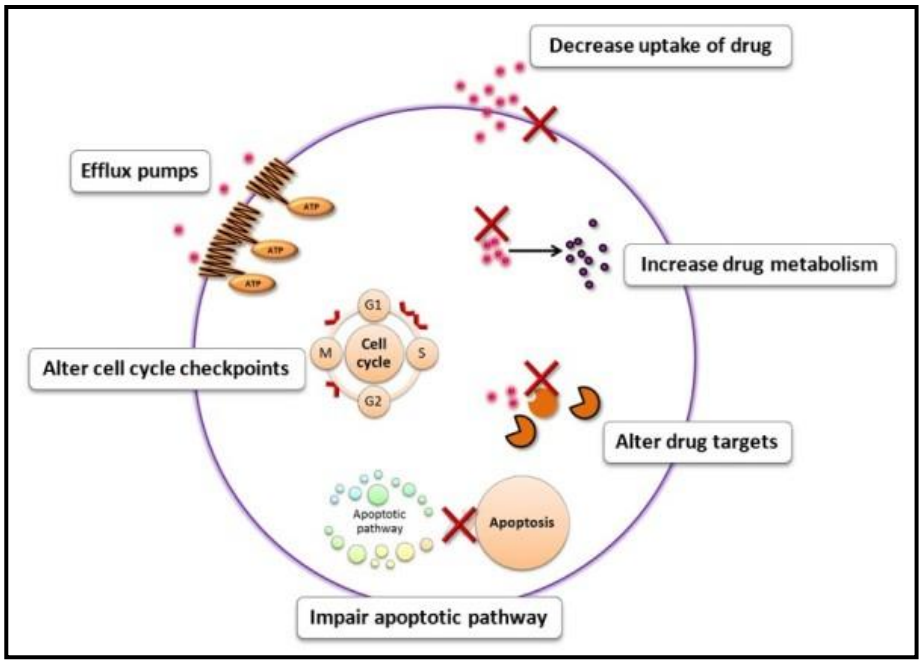

Figure 1.25. Mechanisms of MDR towards cancer chemotherapeutic drugs. Cancer cells can develop resistance to multiple drugs by various mechanisms as depicted. Mechanisms include: (a) Decreased uptake of drug, (b) Reduced intracellular drug concentration by efflux pumps, (c) Altered cell cycle checkpoints, (d) Altered drug targets, (e) Increased metabolism of drug and (f) Induced emergency response genes to impair apoptotic pathway. Adapted from *Baguley. Multiple drug resistance mechanisms in cancer. Mol Biotechnol. 46 (3), 308-16 (2010)*.

1.6.3 OVERCOMING MULTIDRUG-RESISTANT CANCER WITH SMART HAp NANOPARTICLES

Previous studies have shown that nano-sized particles, such as lipids, micelles, and inorganic hybrid particles, can bypass the P-gp efflux pumps and alter the intracellular accumulation of chemotherapeutic drugs.[180,181] In a recent study, biodegradable polymer capsules offered a promising means to circumvent P-gp-mediated MDR.[182] The capsules were internalized by MDR cells via endocytosis and were designed for the subsequent intracellular release of the drugs by enzymatic degradation in lysosomes. Some of these synthetic nanoparticles are able to escape the endosomal/liposomal compartment and change intracellular trafficking to increase the drug concentration in MDR cancer cell.

MDR significantly decreases the efficacy of anticancer drugs and causes tumor recurrence. The advancements in nanotechnology have let the use of nanoformulations to overcome drug resistance. P-gp and other drug efflux transporters are considered to

be critical in pumping anticancer drugs out of cells and causing chemotherapy failure.[182] Nanoparticles have been investigated to address P-gp and have been shown to improve anticancer efficacy, providing a new strategy to overcome MDR.

In this thesis, it is proposed that the failure to apply the approach of Lisanti *et al.* in the elimination of adult tumor cells by the use of antibiotics, falls in the fact that such cells have an overexpression of the mechanism of expulsion of the drug, whereas tumor stem cells do not present such mechanism.

Because drug delivery nanosystems transport pharmaceutical compounds in the body, it is important to understand their physiochemical properties to safely achieve a desired therapeutic effect. Particularly, more efforts have been made to explore the potential of HAp nanoparticles for the encapsulation of anticancer drugs. In this line, HAp nanoparticles with a diameter < 200 nm encapsulating chloramphenicol (CAM) have been used in order to increase the intracellular accumulation of CAM.

Nanoparticles are always designed to inhibit or bypass efflux pumps on the membrane or to enhance endocytosis when recognizing MDR tumor. In order to separate endocytosis from an endocytosis-phagocytosis mixed mechanism as processes able to facilitate the incorporation of particles, the effect of filtration has been examined for removing aggregates > 200 nm in diameter. This is an important feature, because phagocytosis mechanism is the predominant one with particles with a diameter higher than 200 nm. The calcium phosphate particles that enter by phagocytosis mechanisms are too thick to dissolve in the intracellular medium and are all carried out outside of cells, without being degraded. If calcium phosphate particles are incorporated via endocytosis, degradation of CAM could occur due to the acidic medium. Also, if the rate is not the appropiate the P-gp transporter can be activated. These types of issues have already been addressed when DNA was introduced into the interior of the cell using calcium phosphate particles.[121]

In order to achieve a good HAp + CAM system, hydroxyapatites with different crystalinities and coated with several particles as polyphosphates, or phosphonates have been tested. The aim is to obtain a type of nanoparticles that: (i) are introduced through the endocytic route into the adult tumor cell, (ii) are not degraded within the lysosomal, (iii) release CAM in the cytoplasm and (iv) release CAM at a rate that does not activate the drug-gradient activation mechanisms of the P-gp type ejection pumps.

1.7 Self-assembly hydrogels

Low molecular weight drugs (LMWD) are very efficient cytocidal agents in the closed space of a monolayer culture dish. Unlike the situation in culture, following the administration of LMWD to patients, these drugs are cleared quickly in the body. In addition, the drugs are distributed throughout the body, resulting in serious side effects.[183] Consequently, the delivery system becomes a barrier preventing drug attacking targeting cells.

In the past, most research into disease initiation and development, as well as into the progression from local to systemic disease, has focused on the tissue *per se*. However, it is becoming increasingly evident that the configuration of the local microenvironment and the nature of dynamic interactions occurring between cellular and structural elements of the stroma can play significant roles (**Figure 1.26**).[184] An understanding of these interactions will thus facilitate the development of strategies to manipulate the microenvironment, which are likely to represent the next important set of additions of the therapeutic armamentarium. Here, we describe the novel stroma related drug delivery system, using self-assembled peptide-HAp nanoparticles as a model system.

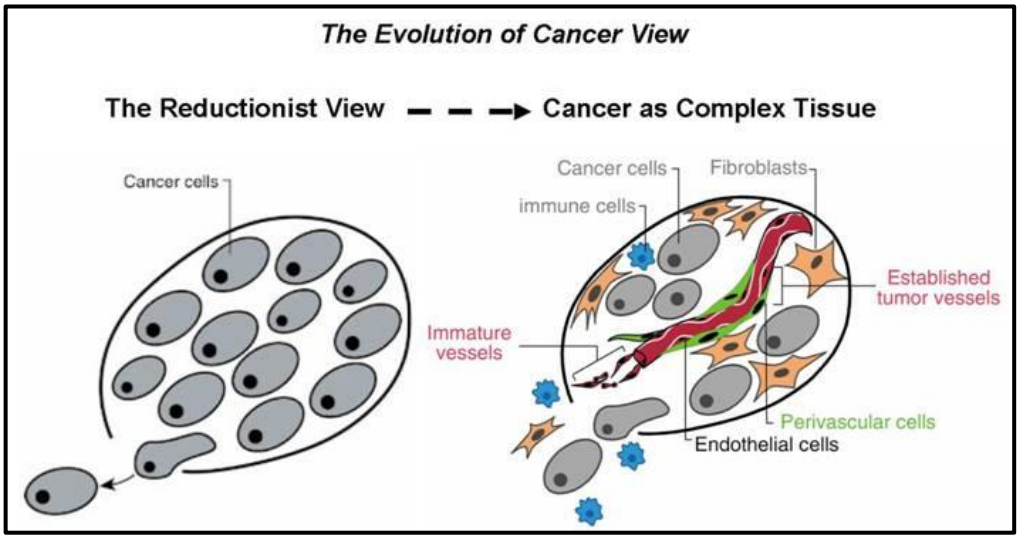

Figure 1.26. The evolution of cancer view. The field of cancer research has largely been guided by a reductionist focus on cancer cells and the genes within them (left picture). A remarkable evolution in thinking about cancer has taken place over the past several years. Right picture: the conceptual notion of tumors as aberrant organs composed of both cancer cells and conscripted normal cell types, all making functional contributions to tumor phenotypes. Adapted from *Hanahan, D. & Weinberg R.A. The hallmarks of cancer. Cell. 7, 100 (1), 57-70 (2000).*

1.7.1 NEW DISEASE STROMA-TARGETING THERAPY

Like in modern Physics, the interesting thing is that the dynamical nature of space-time explicitly suggests a functional understanding of certain crucial space-time features. Thereby motivating the functional emergence framework.[185]

It is increasingly apparent that normal and malignant tissues require complex local and systemic stromal interactions for development and progression. It has been repeatedly demonstrated that disease development and progression is highly dependent on specialized stroma, as disease rarely develop in the absence of this microenvironment. The critical function of the stroma during disease transformation and progression, suggests that targeting it in conjunction with the pathological cells may be a synergistic strategy for therapeutic intervention (**Figure 1.27**).

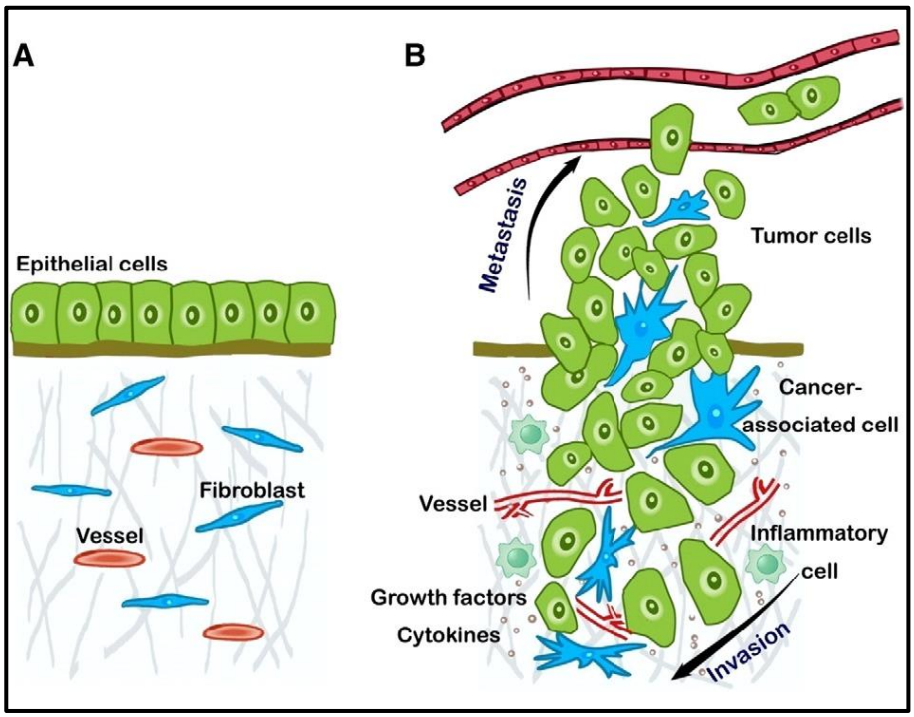

Figure 1.27. Differences between normal stroma and malignant tumor microenvironment. (A) Normal tissue is composed of orderly arranged epithelial cells and supportive stromal cells including quiescent fibroblasts and blood vessels that collectively inhibit inappropriate epithelial proliferation. (B) In malignant tumor tissue, activated cancer-associated fibroblasts and inflammatory cells have close crosstalk to tumor cells via plentiful growth factors and cytokines; newly formed vasculature carries nutritional support to tumor cells. Adapted from *Chauhan, V.P.& Jain, R.K. Strategies for advancing cancer nanomedicine. Nat Mater. 12, 958-962 (2013).*

This new disease stroma-targeting therapy may result in an increased duration of drug exposure and be a highly effective new therapy particularly for refractory, stroma rich diseases. The kinetics of drug distribution within living tissues are considered to be a function of interstitial conductivity, which is determined by the quantity and density of the extracellular matrix (*e.g.* proteoglycan, fibronectin) and fibrosis (*e.g.* fibrin, collagen fibers) in the stroma.[187] This led us to design a novel alternative drug delivery strategy that turned this apparent handicap into an asset.

1.7.2 SELF-ASSEMBLY HYDROGELS UTILIZING PEPTIDE-NANOPARTICLE INTERACTION

Hydrogels comprise an important class of material well-suited for a range of applications on account of their high water content and highly tunable mechanical properties.[188] Many hydrogel systems utilize covalent crosslinking approaches,[189] including radical processes initiated by light, temperature and pH.[190] These covalently crosslinked hydrogels form robust, tough and elastic materials; however, they can be limited by the irreversibility of their crosslinks.

Self-assembly via non-covalent crosslinks provides a route to fabricate mouldable and injectable hydrogels with shear-thinning and self-healing properties arising strong, yet transient and reversible crosslinks.[191] However, the shear-thinning and self-healing hydrogels presented to date are limited by poor mechanics and slow self-healing to require challenging, costly and poorly scalable synthesis of macromolecular components through protein engineering or complex, multi-step chemical functionalization.

Solving the structure of hydrogel is pivotal to achieving success in rational drug delivery design and other biotechnological endeavours (**Figure 1.28**). Within the field of self-assembly, polymer-NP interactions have arisen as a simple route to assemble tunable and self-healing polymeric materials without the need for complex synthetic approaches or specialized small-molecule binding partners.[192] Peptides with their variable side chains are ideal candidates for synthesizing biodegradable functional hydrogels. Following these approaches, we study shear-thinning and self-healing hydrogels in a mild, modular and scalable manner based solely on interactions between peptide derivatives and HAp NPs for biomedical applications.

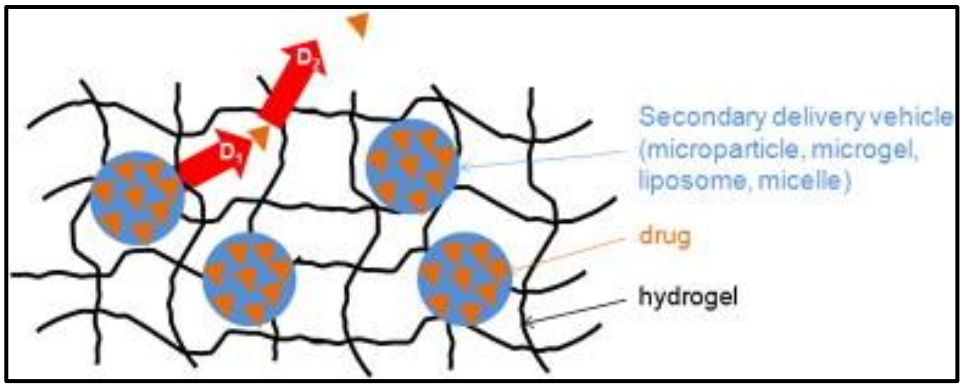

Figure 1.28. "Plum pudding", composite hydrogels containing drug encapsulated in a secondary controlled release vehicle (*e.g*. microparticles, nanoparticles, microgels, liposomes, micelles). D_1 and D_2 represent the diffusion coefficients of drug out of the hydrogel (D_1= release from secondary release vehicle; D_2= diffusion through hydrogel). Adapted from *Hoare, T.R. & Kohane D.S. Hydrogels in drug delivery: progress and challenges. Polymer. 49, 1993-2007 (2008).*

1.8 Computational and numerical methods

Various computational techniques have been established to describe and predict the mechanical and physical properties of materials on many different size and time scales (**Figure 1.29**). These vary from atomistic methods such as molecular statics and dynamics to continuum mechanics and the finite element method. Unfortunately, many recent technologies fall into a gap between length scales, where none of the aforementioned methods is applicable alone. Such cases include nanoporous and nanocrystalline polymers. Microstructural features of such systems are on the order of a few nanometers, thus requiring atomistic resolution, but representative volumes are too large to be modelled by molecular dynamics.

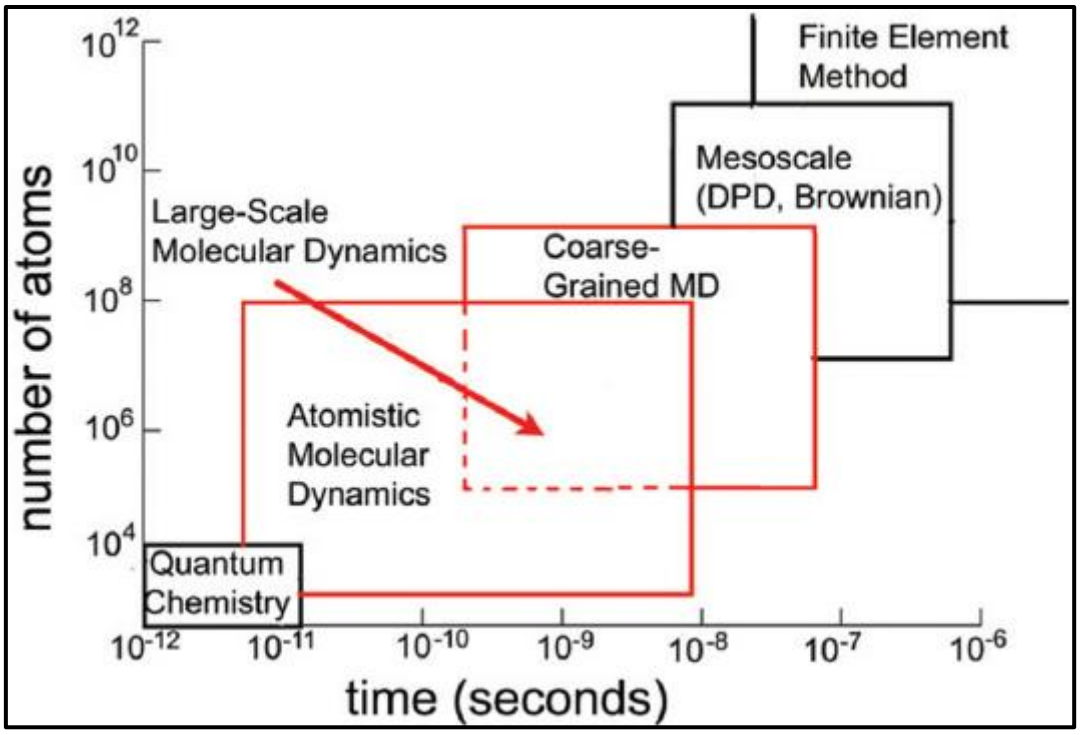

Figure 1.29. Modeling and simulation methods and corresponding system sizes and times.

A major advance in the physics of polymers occurred in 1949 when Flory[193] provided a simple but consistent argument for the swelling (compared to the ideal chain size) of flexible polymer chains, which is based on excluded volume interactions. In essence, the Flory result for the dependence of the radius of gyration R_g on the degree of polymerization *N* is obtained by minimizing the elastic energy (due to chain connectivity) and the repulsive energy arising from the volume excluded by the different monomers. The resulting prediction for the exponent ν that defines the gyration radius ($R_g \approx aN^{\nu}$) is remarkably accurate for all space dimensions, *d*. For all practical purposes the Flory result[194] ($\nu = 3 \cdot (d+2)$) may be considered exact.[195]

The fundamental understanding of the reasons for the success of the Flory theory is still lacking. In an attempt to derive the Flory exponent Edwards proposed a model for polymers that bears his name in 1965.[196] This paper brought to provide, for the first time, methods of functional integrals and theory to bear polymer physics problems. Edwards proposed a very simple form for the short range repulsive potential describing the interactions between monomers.

Several studies utilizing the Edwards model for polymers followed.[197] In addition, new results concerning polymer statistics were obtained using lattice models,[198]

enumerations of self-avoiding walks, and relationships from Ising models.[199] This is a mathematical model of ferromagnetism based on statistical mechanics. The model consists of discrete variables that represent magnetic dipole moments of atomic spins that can be in one of two states $(+1 \text{ or } -1)$. The spins are arranged in a graph, usually a lattice, allowing each spin to interact with its neighbours. The model allows the identification of phase transitions, as a simplified model of reality. The two-dimensional square-lattice Ising model is was one of the simplest statistical models to show a phase transition. However, an understanding of the varied universal behavior of polymer solutions was lacking. This state of affairs in polymer physics was changed dramatically after the work of de Gennes who showed a connection between polymer statistics and phase transitions.[200]

The general approach of polymers is rooted in statistical mechanics, and particularly in critical phenomena. The motivation for studying these models comes from the chemistry and physics of macromolecules, being models attempts to represent, in a simple manner, the entropic contribution to the free energy made by the conformational degrees of freedom of macromolecules.[201] The thermodynamic properties of a given model should logically reflect the behavior of a polymer.[202]

The statistical approach for polymer physics is based on an analogy between a polymer chain and either a Brownian motion, or other type of a random walk, the self-avoiding walk. The simplest possible polymer model is presented by the ideal chain, corresponding to a simple random walk.[203]

The ideal chain model assumes that polymer segments can overlap with each other as if the chain was a phantom chain. In reality, two segments cannot occupy the same space at the same time. This interaction between segments is called the excluded volume interaction. The simplest formulation of excluded volume is the self-avoiding random walk, a random walk that cannot repeat its previous path.[204] A path of a walk of *N* steps in three dimensions represents a conformation of a polymer with excluded volume interaction. Because of the self-avoiding nature of this model, the number of possible conformations is significantly reduced. The radius of gyration is generally larger than that of the ideal chain.[205]

Because the modelled atoms can represent a variety of different real systems, the absolute values of the atom's sizes lack any meaning. Similarly, absolute values of any time intervals are meaningless. The only relevant figures are those representing ratios

of different length and time scales. The situation is a little different for the lengths. A computer cannot simulate an infinite system. Therefore, one length scale is involved in all simulations: it is the size of the box in which all modelled atoms and molecules are confined -the model universe-. We shall define all the distances, radii, etc., using an artificial unitary length.

The modelled atoms obey to standard laws of classical mechanics, *i.e*. Newton's laws. As long as an atom is far enough form all others, neglected forces act on it, and inertia makes it move in a straight line with constant velocity. Of course, velocities of atoms change upon their collisions: when two atoms come close enough that each one enters the region of attraction surrounding the other. Then, both atoms go faster according to energy and momentum conservation.

In the modelled world, just as in the real one, the energy of any system is conserved. In particular, the total energy of the entire modelled universe, *i.e.* the entire box, is conserved -unless we choose to stop the program and charge energy.

It must be noticed also that the only meaningful units for energy and temperature in the modelled world are related to the interaction potential energies ε.[206] Just as in the cases of length and time, we do not specify any relation of those energies to any specific number of joules or degrees of the real world.

In these configurations, the system consists of $i \times j \times k$ identical cells organized in perfect rows, columns and layers, each cell containing equal numbers of different atoms and molecules. Thus, instead of locating the hundreds of atoms of the entire system, one can define only several atoms in one cell.[207] The other cells will be the perfect copies of this particular cell, but the entire configuration world look like an artificial cubic crystal.[208]

1.8.1 MOLECULAR DYNAMICS SIMULATION

To obtain relevant microscopic information, atomistic molecular dynamics (MD) simulations have been carried out. We call molecular dynamics (MD) a computer simulation technique where the time evolution of a set of interacting atoms is followed by integrating their equations of motion.[209] Molecular dynamics is a statistical mechanical method like Monte Carlo, it is a way to obtain a set of configurations distributed according

to some statistical function, or statistical ensemble. In molecular dynamics we follow the laws of classical mechanics, the Newton's 2nd law the most notable:

$$F_i = m_i \cdot a_i \quad (Eq\ 1.1)$$

where i defines each atom in a system constituted by *N* atoms, m_i is the atom mass, $a_i = \frac{d^2 r_i}{dt^2}$ its acceleration, and F_i the force acting upon it, due to the interactions with other atoms. Therefore, molecular dynamics is a deterministic technique: given an initial set of positions and velocities, the subsequent time evolution is in principle completely determined. The computer calculates a trajectory in a 6-*N* dimensional phase space (3*N* positions and 3*N* moments). However, such trajectory is not usually relevant by itself. According to statistical physics, physical quantities are represented by averaged values over configurations distributed according to a certain statistical ensemble. A trajectory obtained by molecular dynamics provides such a set of configurations.[210] Therefore, a physical quantity determined by simulation is an arithmetic average of the various instantaneous values assumed by that quantity during the simulation. Statistical physics is the link between the microscopic behavior and thermodynamics. In **Figure 1.30**, it is show the summary of the computational method used in MD.

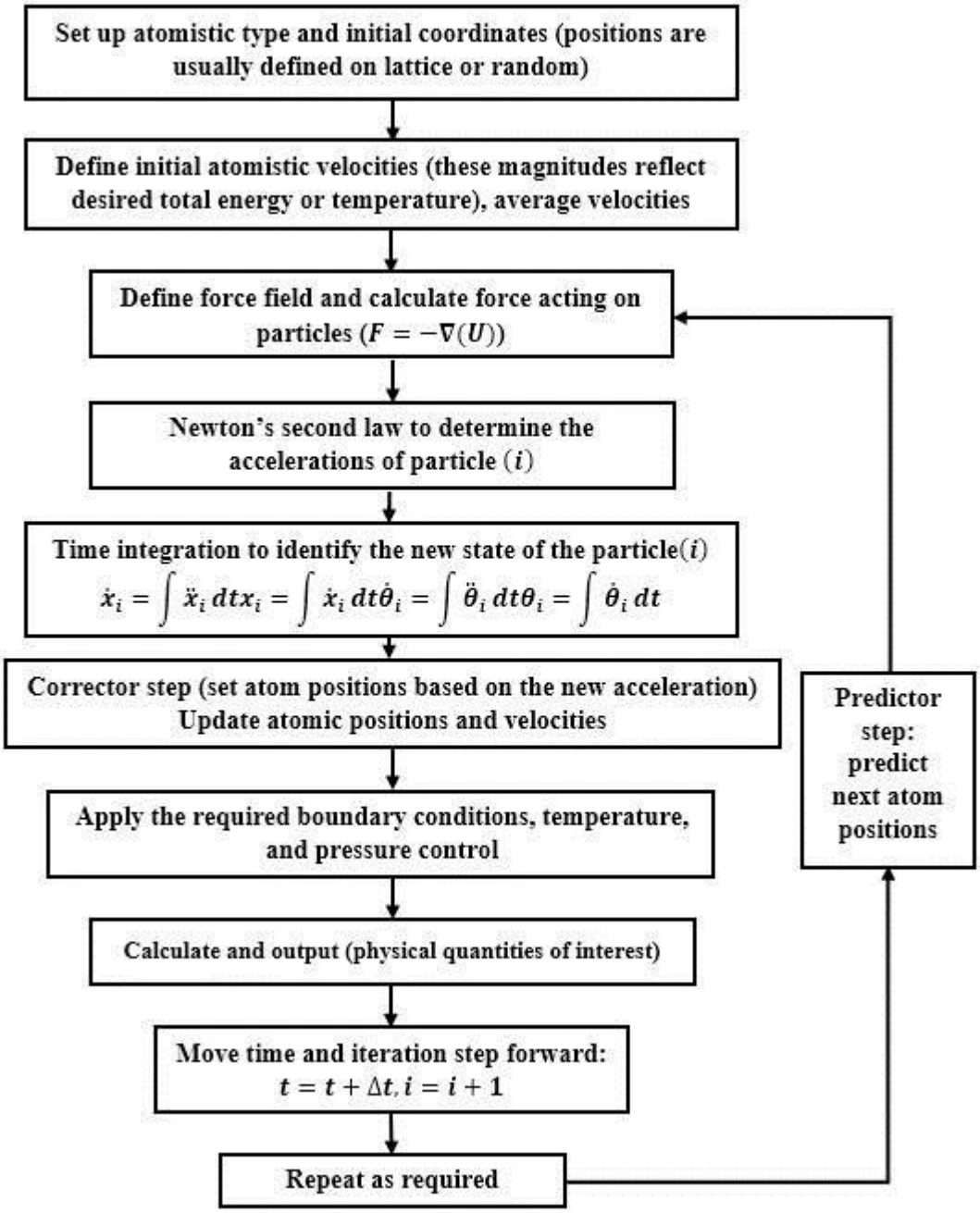

Figure 1.30. Simplified schematic of the molecular dynamics algorithm.

1.8.2 MOLECULAR DYNAMICS WITH LENNARD-JONES POTENTIAL

Molecular dynamics is centered in the study of the interactions between atoms, and specifically in the way as the atoms move under the action of interacting forces. This process is dynamic since the atoms move, their relative positions change as well as the interacting forces.[211]

A simulation becomes realistic (*i.e.* it is able to mimics the behavior of real system) only when the calculated interatomic forces are similar to those that real atoms would experience when arranged in the same configuration.[212]

Forces are usually obtained as the gradient of a potential energy function depending on the positions of the particles. The realism of the simulation therefore depends on the ability of the potential chosen to reproduce the behavior of the material under the conditions at which the simulation is run.[213] The problem of selecting, or constructing, potentials (called force-field problem) is still under study by the scientific community. In this thesis, however, we will take into account only the most commonly used pairwise interaction mode of Lennard-Jones pair potential.[214] The Lennard-Jones potential is given by the expression:[215]

$$V(r) = 4\varepsilon\left[\left(\frac{\sigma}{r}\right)^{12} - \left(\frac{\sigma}{r}\right)^{6}\right] \quad (Eq\ 1.2)$$

Where ε is the depth of the potential well, σ is the finite distance at which the inter-particle potential is zero, r is the distance between the particles. This Eq 1.2 describes a potential that has an attractive tail (*i.e*. a negative value since we put the arbitrary zero of the energy at the value of the potential when the two particles are at an infinite distance apart) at large r, it reaches a minimum around 1.122 σ, and it is strongly repulsive at shorter distance, passing through 0 at $r = \sigma$ and increasing steeply as r is decreased further (**Figure 1.31**).[216]

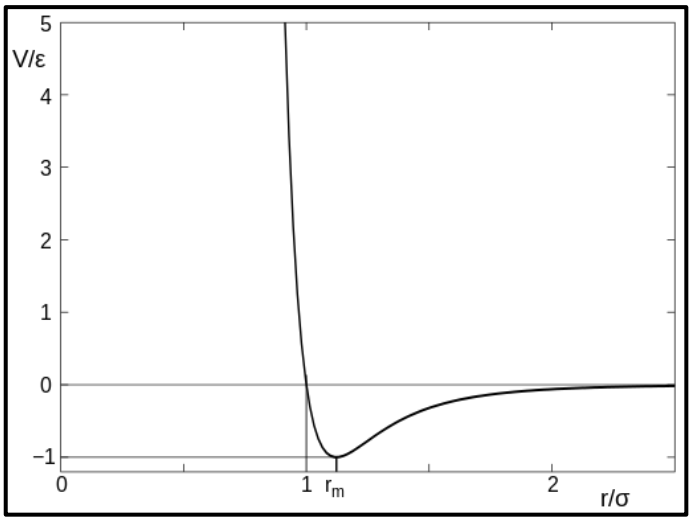

Figure 1.31. A graph of strength versus distance for the Lennard-Jones potential.

The term $\sim 1/r^{12}$ is predominant at short distances and consequently models the repulsion between atoms when they are brought very close to each other. Its physical origin is related to the Pauli principle when the electronic clouds surrounding the atoms starts to overlap, the energy of the system increases abruptly.[217]

The term $\sim 1/r^{6}$ dominating at large distance, constitute the attractive part. This is the term that gives cohesion to the system. A $\sim 1/r^{6}$ attraction is originated by van der Waals dispersion forces, originated by dipole-dipole interactions in turn due to fluctuating dipoles.[214] The parameters ε and σ are chosen to fit the physical properties of the materials.

One of the most important static properties that can be used to characterize liquids in general and Lennard-Jones liquids in particular is the radial distribution function $g(r)$ so defined.[218]

$$g(r) = \frac{1}{\rho 4\pi r^2 dr} \sum_{ij} \langle \delta\left(r - \left|r_i - r_j\right|\right) \rangle \quad (Eq\ 1.3)$$

where $\delta(x)$ is the function defined by values of 1 and 0 for $x = 0$ and $x \neq 0$, respectively.

In statistical mechanics, the radial distribution function (or pair correlation function) $g(r)$ of a system of particles (atoms, molecules, colloids, etc,) describes how density varies as a function of the distance from a reference particle.[219] In simpler terms it is a measure of the possibility of finding a particle at a distance r away from a given reference particle. For an additive potential as the Lennard-Jones, the knowledge of $g(r)$ provides enough information to calculate thermodynamical properties, particularly energy and pressure.[216]

1.8.3 QUANTUM MECHANICS AND MOLECULAR DYNAMICS

Generally speaking, quantum-mechanical (QM) models do not fall under the category of molecular dynamics force fields. There are several QM-based-MD methods, which can be used in a similar wat to classical force models by invoking the Hellmann-Feynman theorem. The most rigorous way to study an atomic/molecular system is to solve the Schrödinger (or Dirac) equation for the nuclei and electrons in question. However, the

computational load for an accurate solution is very high. In addition, solving the time-dependent Schrödinger equation for dynamic systems is even more demanding. So, in practice, one needs to make one sort of approximation with the QM approach (**Figure 1.32**).

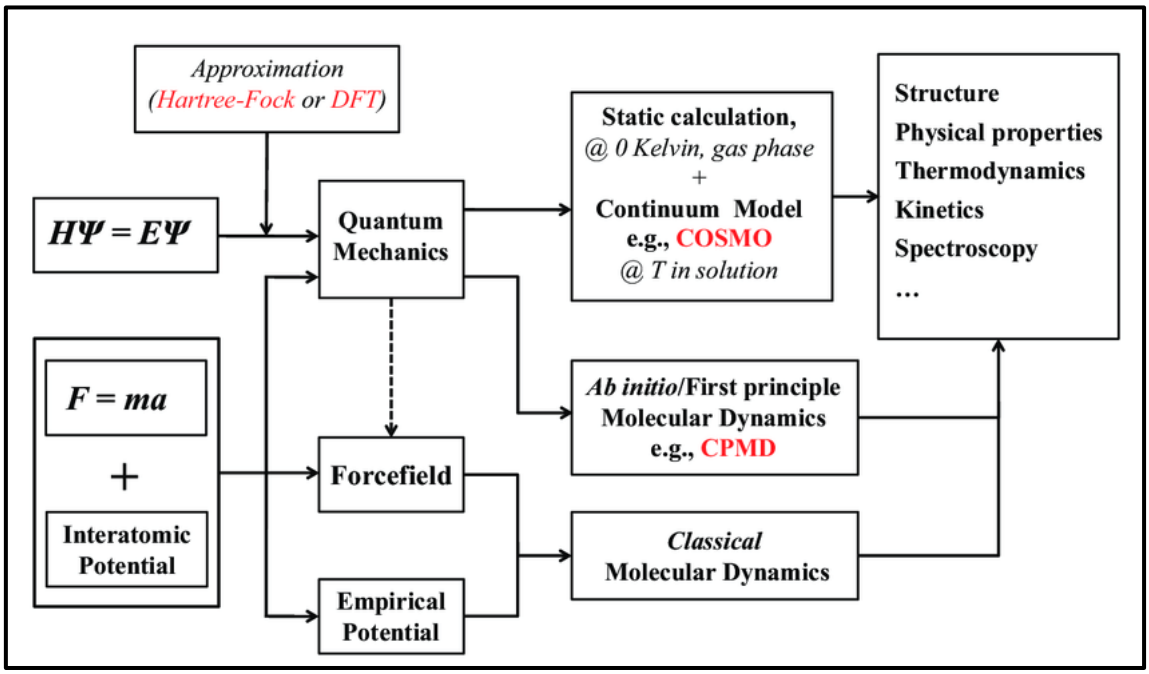

Figure 1.32. Theories and approaches of molecular simulation methods.

Ab initio quantum chemistry methods are computational methods based on quantum chemistry first principles without fitting the experimental data.[220] *Ab initio* electronic structure methods have the advantage that they can be made to converge to the exact solution, when all approximations are sufficiently small in magnitude and when the finite set of basic functions tends toward the limit of a complete set. The most popular classes of *ab initio* electronic structure methods are: (i) Hartree–Fock (HF) and (ii) density functional theory.

1.8.4 MOLECULAR DYNAMICS SIMULATIONS OF DNA AND PROTEINS

There are important limitations when MD method (using Leonard-Jones potential) is applied to study the motion of biological macromolecules such as proteins and nucleic acids.

1.8.4.1 Problems related to the functional form

The basic functional form of potential energy in molecular mechanics includes bonded terms for interactions of atoms that are linked by covalent bonds, and non-bonded (also called “noncovalent”) terms that describe the long-range electrostatic and van der Waals forces. The specific decomposition of these terms depends on the force field, but a general form for the total energy in an additive force field can be written as $E_{total} = E_{bonded} + E_{nonbonded}$ where the components of the covalent and non-covalent contibutions are given by the following equations:

$$E_{bonded} = E_{bond} + E_{angle} + E_{dihedral} \quad (Eq\ 1.4)$$

$$E_{nonbonded} = E_{electrostatic} + E_{van\ der\ Waals} \quad (Eq\ 1.5)$$

The bond and angle terms are usually modelled by quadratic energy functions that do not allow bond breaking. The functional form for dihedral angles is highly variable. Additional, “improper torsional” terms may be added to enforce the planarity of aromatic rings and other conjugated systems, and “cross-terms” that describe coupling of different internal variables, such as angles and bond lengths.[221]

The nonbonded terms are most computationally intensive. In our model we have limited interactions to pair-wise energies. The van der Waals term has been computed with a Lennard-Jones potential and the electrostatic term with Coulomb’s law, and both have been buffered or scaled by a constant factor to account for electronic polarizability.[222]

1.8.4.2 Problems with parameterization

In addition to the functional form of the potentials, force fields define a set of parameters for different types of atoms, chemical bonds, dihedral angles and so on. The parameter sets are usually empirical. A force field would include distinct parameters for an oxygen atom in a carbonyl functional group and in a hydroxyl group. The typical parameter set includes values for atomic mass, van der Waals radius, and partial charge for individual atoms; equilibrium values of bond lengths, bond angles, and dihedral angles for pairs, triplets, and quadruplets of bonded atoms, and values corresponding to the effective spring constant for each potential.[223] The selected Lennard-Jones force field parameters use a “fixed-charge” model by which each atom is assigned to a single value for the atomic charge that is not affected by the local electrostatic environment. Proposed development for protein and DNA force fields should incorporate models for

polarizability, in which a particle's charge is influenced by electrostatic interactions with its neighbors. However the introduction of polarizability into classic force fields has been inhibited by the high computational cost associated with calculation of the local electrostatic field.[224]

All interaction potentials have an empirical nature since are based on numerous approximations and derived from a large set of experimental data. The Lennard-Jonnes energy functions do not account for electronic polarization of the environment, an effect that can significantly reduce electrostatic interactions of partial atomic charge. This problem was addressed by developing "polarizable fields".[225-227] However, application of a single value of dielectric constant is questionable in the highly heterogeneous environments of proteins and DNA, and the nature of the dielectric depends on the model used.[87,228]

1.8.4.3 Problems with the use of classic potential fields

Limitations of MD with Leonard-Jones force potential are related not only to the selected parameter sets, but also to the underlying molecular mechanic force fields. A single run of an MD simulation optimizes the potential energy, rather than the free energy of DNA, meaning that all entropic contributions to thermodynamic stability of DNA structure are neglected. The neglected contributions include the conformational entropy of the nucleotide chain (which is the main factor that destabilizes DNA structure) and hydrophobic interactions that are known as main driving force of DNA folding.[229] Another important factor is associated to the intramolecular hydrogen bonds[230] which are not explicitly included in the selected force field, but can be described as Coulombic interactions of atomic point charges. This is a crude approximation because hydrogen bonds have a partially quantum mechanical nature. Furthermore, electrostatic interactions are usually calculated using the dielectric constant of vacuum, although the surrounding aqueous solution has a much higher dielectric constant. The use of a macroscopic dielectric constant at short interatomic distances is questionable since all types of van der Waals forces are ultimately of electrostatic origin and therefore depend on dielectric properties of the environment.[231]

Theoretical methods can help to achieve a more detailed understanding of DNA structure and function, but their practical use is hampered by the multiscale nature of this molecule. In this regard, the study of DNA covers a broad range of different topics, from sub-Angstrom details of the electronic distributions of nucleobases, to the mechanical

properties of millimeter-long chromatin fibers. It is very unlikely that quantum-mechanical MD will replace its classical counterpart in the near future. The time scales and system sizes that can be tackled with QM methods are still too small. The constant development of better classical force modes is crucial for the advancement of the field: (i) reactive force fields, and (ii) coarse-grained force models.

1.9 References

1. Bourne, G.H. The biochemistry and physiology of bone. Vol 2, 2nd ed., Academic Press, New York (1972).
2. Seuter, A.M.J.H. Existence region of calcium hydroxyapatite and the equilibrium with coexisting phases at elevated temperatures. In Anderson J.S., Robert M.W., Stone F.S. (ed): Reactivity of solids. London, Chapman and Hall, 806-812 (1972).
3. Cameron H.U., MacNab I., Pilliar R.M. Evaluation of a biodegradable ceramic. *J. Biomed. Mater. Res*. **11**, 179 (1977).
4. Basset, H. The phosphates of calcium. IV. The basic phosphates. *J. Chem. Soc.* **111**, 620-629 (1917).
5. Basset, H. The phosphates of calcium. V. Revision of the earlier space diagram. *J. Chem. Soc*. **2949**, 643-662 (1958).
6. Newesely, H. Changes in crystal types of low solubility calcium phosphates in the presence of accompanying ions. *Arch. Oral Biol*. **6**, 174-188 (1961).
7. Brown, W.E. Crystal structure of octacalcium phosphate. *Nature*. **196**, 48 -56 (1962).
8. Sanfouche, M.A. Recherches sur l'acide phosphorique et les phosphates. I. La formation des phosphates alcalino-terreux basique. *Bull. Soc. Chim. Fr.* **53**, 951-970 (1933).
9. Termine, J.D. & Posner, A.S. Calcium phosphate formation in vitro. I. Factors affecting initial phase separation. *Arch. Biochem. Biophys*. **140**, 307-318 (1970).
10. Limin, S., Laurence, C. & Chow, S.A. Preparation and properties of nanoparticles of calcium phosphates with various Ca/P ratios. *J Res Natl Inst Stand Technol*. **115(4)**, 243–255 (2010).
11. Flora, N. J., Yoder, C. H. & Jenkins H. D. B. Lattice energies of apatites and the estimation of Hf°(PO_4^{3-}g). *Inorg. Chem*. **43**, 2340-2345 (2004).
12. Berry, E. E. The structure and composition of some calcium-deficient apatites. *Journal of Nuclear Chemistry*. **29**, 317-327 (1967).
13. Fouretier, G. La precipitation du phosphate tricalcique et l'hydroxyapatite. *C.R. Acad. Sci*. **205**, 413-421 (1937).
14. Arnold, P.W. The nature of precipitated calcium phosphates. *Transactions of the Faraday Society*. **46**, 45-57 (1950).
15. Strates, B.S., Neuman, W.F., Levinskas, G.J. The solubility of bone mineral II. Precipitation of near-neutral solutions of calcium and phosphorus. *J. Phys. Chem*. **61**, 279-292 (1957).
16. Brown, W.E., Smith J.R., Lehr, J.R. & Frazier A.W. Crystallographic and chemical relations between octacalcium phosphate and hydroxyapatite. *Nature*. **196**, 1050-1055 (1962).
17. Eanes, E.D., Gillesen, P.H. & Posner, A.S. Intermediate states in the precipitation of hydroxyapatites. *Nature*. **208**, 365-372 (1965).

18. Newesely, H. Umwandlungsvorgänge bei calciumphosphaten. Calcified Tissues, Fleisch H., Blackwood H.J.J., Owen M. Eds., Springer Verlag, Basel, 136 (1965).

19. Kijima, T. & Tsutsumi, M. Preparation and thermal properties of dense polycrystalline oxyhydroxyapatite. *Journal of the American Ceramic Society*. **45**, 123-156 (1979).

20. Mcdowell, M., Gregory, T.M. & Brown, W.E. Solubility of $Ca_5(PO_4)_3OH$ in the system system $Ca(OH)_2 - H_3PO_4 - H_2O$ at 5, 15 qnd 37 º C. *J Res Natl Bur Stand*. **81A**, 273-281 (1974).

21. Fowler, B.O. Infrared studies of apatite. Preparation of normal and isotopically substituted calcium, strontium and barium hydroxyapatite and spectra-structure correlations. *Inorg. Chem*. **13**, 207-218 (1974).

22. Perloff, A. & Posner, A.S. Preparation of pure hydroxyapatite crystals. *Science*. **124(3222)**, 583-584 (1956).

23. Young, R.A. & Holcomb, D.W. Variability of hydroxyapatite preparations. *Calcif Tissue Int.* **34**, 217-232 (1982).

24. Foster, O. Z. *Anorg. Allg. Chem*. **13**, (1892), cited by Schleede, A., Schmidt, W., & Kindt, H. *Z. Electrochem*. **38**. 633-645 (1932).

25. Schleede, A., Schmidt, W. & Kindt, M. Zu kenntnisder calciumphosphate und apatite. *Z. Elektrochem*. **38**, 633-650 (1932).

26. Uskokovic,V. & Uskokovic, D.P. Review nanosized hydroxyapatite and other calcium phosphates: chemistry of formation and application as drug and gene delivery agents. *Journal of biomedical materials research B: applied biomaterials*. **96**, 345-365 (2011).

27. Tsuber, V.K. & Lesnikovich, L.A. Synthesis, identification and determination of impurities in bioactive hydroxyapatite. *Pharm. Chem. Journal*. **40**, 445-458 (2006).

28. LeGeros, R. Z. Calcium Phosphates in Oral Biology and Medicine. *Monographs in Oral Science*. Vol. 15: ed. H. M. Myers and S. Karger, Basel (1991).

29. Park, J. B. & Lakes, R. S. Composites as Biomaterials, in Biomaterials. An Introduction. ed. Plenum Press, New York and London, 2nd edn, 169–18 (1992).

30. Labarthe, J.C., Therasse, M., Bonel, G. & Montel, G. Sur la structure des apatites phosphocalcique. *CR Acad. Sci. Ser. C.* **276**, 1175-1191 (1973).

31. Labarthe, J.C., Bonel, G. & Montel, G. Sur la localization des ions carbonate dans le reseau des apatites calcique. *CR Acad. Sci. Ser. C*. **273**, 349-365 (1971).

32. Bacquet, G., Quang, V.O, Vignoles, M. & Bonel G. ESR of the F^+ Centre in B-Type Carbonated Hydroxyapatite. *Phys. Stat. Sol*. **68**, 56-67 (1981).

33. Bonel, G., Labarthe, J.C. & Vignoles, C. Contribution à l'étude structural des apatites carbonates de type B. *Physco-Chimie et Cristallographie des Apatites d'Intèret Biologique*. **230**, 117-128 (1975).

34. LeGeros, R.Z., Trautz, O.R., LeGeros, J.P. & Klein, E. Apatite crystallites: effects of carbonate on morphology. *Science*. **155**, 1409-1420 (1967).

35. Lagier, R. & Baud, C.A. Magnesium Whitlockite, a Calcium Phosphate Crystal of Special Interest in Pathology. *Pathology - Research and Practice* . **199(5)**, 329-335 (2003).

36. Boulet, M., Marier, J.R. & Rose, D. Effect of magnesium on formation of calcium phosphate precipitates. *Arch. Biochem. Biophys*. **96**, 629-637 (1962).

37. Bachra, B.N., Trautz, O.R. & Simon, S.L. A precipitation diagram for the system calcium-carbonate-phosphate and the heterogenous nucleation of solids in the metastability region. *Advances in Fluoride Research and Dental Caries Prevention*. **3**, 101-108 (1965).

38. Featherstone, J.D.B., Mayer, I., Driessens, F.C.M., Verbeeck, R.M.H. & Heijligers, H.J.M. Synthetic apatites containing Na, Mg, and CO_3 and their comparison with tooth enamel mineral. *Calcif Tissue Int*. **35**,169- 171 (1983).

39. Termine, J.D., Peckauskas, R.A. & Posner, A.S. Calcium phosphate formation in vitro. II. Effects of environment on amorphous-crystalline transformation. *Arch Biochem Biophys*. **140(2)**, 18–325 (1970).

40. Moreno, E.C. & Hay, D. J. Adsorption of amino acids onto hydroxyapatite. *J Colloid Interface Sci*. **59**, 283-292 (1977).

41. Duff, E.J. Orthophosphate-I formation of apatites from calcium phosphates in potassium fluoride solutions. *J Inorg Nucl Chem*. **32**, 3103-3106 (1970).

42. Tafu, M. & Chohji, T. Reaction of calcium hydrogenphosphate dihydrate (DCPD) with a solution containing a small amount of fluoride. *J Ceram Soc Jpn.* **113**, 363-367 (2005).

43. Tao, J. & Rappe, A.M. Physical adsorption theory of van der Waals interactions between particles and clean surfaces. *Phys. Rev. Lett.* **112**, 56-69 (2014).

44. Oura, K., Lifshits, V.G., Saranin, A.A., Zotov, A.V. & Katayana, M. Surface science, an introduction. Berlin: Springer (2003).

45. Langmuir, I. The Adsorption of Gases on Plane Surface of Glass, Mica and Platinum. *The Research Laboratory of The General Electric Company*. **40**, 1361–1402 (1918).

46. Misra, D.N. Adsorption from solutions on synthetic hydroxyapatite: nonaqueous vs. aqueous solvents. *J. Biomed. Mater. Res*. **48(6)**, 848-55 (1999).

47. Berzelius, J.J. Quelques Idées sur une Nouvelle Force Agissant Dans les Combinaisons des Corps Organiques. *Ann. Chim*. **61**, 146-151 (1836).

48. van Leeuwen, W. N. M. & Chadwick, J. C. Homogeneous Catalysts. Wiley-VCH, Weinheim (2011).

49. Swathi, R.S. & Sebastian, K.L. Molecular mechanism of heterogeneous catalysis. *Resonance*. **13 (6)**, 548-560, (2008).

50. Junqueira, L. C. & Carneiro, J. Inorganic matter represents about 50 % of the dry weight of bone crystals show imperfections and are not identical to the hydroxylapatite found in the rock minerals. McGraw-Hill Companies. p. 144 (2003).

51. Nishimura, S., Tateyama, K. & Jinnai, K. Zeta potential measurement of muscovite mica basal plane-aqueous solution interface by means of plane interface technique. *Colloid Interface Sci*. **152**, 359-379 (1992)

52. Lastoskie, C., Gubbins, K.E. & Quirke, N. Pore size distribution analysis of microporous carbons: a density functional theory approach. *J. Phys. Chem***. 97 (18)**, 4786-4796 (1993).

53. Pelekani, C. & SnoeyinnK, V.L. A kinetic study of competitive adsorption between atrazine and Congo red dye on activated carbon, the importance of pore size distribution. *Carbon*. **39(1)**, 25-37 (2001).

54. Bodhak, S., Bose, S. & Bandyopadhyay, A. Role of Surface Charge and Wettability on Early Stage Mineralization and Bone Cell (Materials Interactions of Polarized Hydroxyapatite*). Acta Biomater*. **5 (6)**, 2178–2188 (2009).

55. Denko, C.W. & Petricevic, M. Hydroxyapatite crystal- induced inflammation and prostaglandin. *J Rheuma*. **6**, 117-123 (1979).

56. Klein, C. P. A. T. & de Groot, K. Interaction of some serum proteins with hydroxylapatite and other materials. *Journal of Biomedical Materials Research*. **14**, 705-712 (1980).

57. Skwarek, E., Janusz, W. & Sternik, D. The influence of the hydroxyapatite synthesis method on the electrochemical, surface and adsorption properties of hydroxyapatite. *Adsorption Science & Technology*. **35(5–6)**, 507–518 (2017).

58. Guo, L., Huang, M. & Zhang, X. Effects of sintering temperature on structure of hydroxyapatite studied with Rietveld method. *J Mater Sci Mater Med.* **14(9)**, 817-822 (2003).

59. Deutsch, D., Natan, A., Shapira, Y. & Kronik, L. Electrostatic Properties of Adsorbed Polar Molecules: Opposite Behavior of a Single Molecule and a Molecular Monolayer. *J. Am. Chem. Soc*. **129**, 2989-2997 (2007).

60. Jeon, O., Song, S.J., Kang, S.W., Putnam, A.J. & Kim, B.S. Enhancement of ectopic bone formation by bone morphogenetic protein-2 released from a heparin-conjugated poly (L-lactic-co-glycolic acid) scaffold. *Biomaterials*. **28(17)**, 2763-2771 (2007).

61. Mabilleau, G. Effects of FGF-2 release form a hydrogel polymer on bone mass and microarchitecture. *Biomaterials*. **29**, 1593-600 (2008).

62. Arm, D.M. Effect of controlled release of platelet-derived growth factor form a porous hydroxyapatite implant on bone ingrowth. *Biomaterials*. **17**, 703-709 (1996).

63. Shiba, T. Modulation of mitogenic activity of fibroblast growth factors by inorganic polyphosphate. *J Biol Chem*. **278**, 26788-26792 (2003).

64. Agarwal, V. Structural and mechanistic insights into C-P bond hydrolysis by phosphonoacetate hydrolase. *Chemistry & Biology*. **18**, 1230-1240 (2011).

65. Freedman, L.D. & Doak, G.O. The preparation and properties of phosphonic acids. *Chemical Reviews*. **57 (3)**, 479-525 (1957).

66. Engel, R.L. & Cohen, I. Synthesis of carbon-phosphorus bond. 2nd CRC Press: New York (2004).

67. Doi, K., Kubo, T. & Takeshita R. Inorganic polyphosphate adsorbed onto hydroxyapatite for guided bone regeneration: an animal study. *Dental materials Journal*. **33(2)**, 179-186 (2014).

68. Takenaka, S., Yamashita, K., Takagi, M., Uto, Y. & Kondo, H. DNA sensing on a DNA probe-modified electrode using ferrocenylnaphthalene diimide as the electrochemically active ligand. *Anal. Chem.* **72**, 1334–1341 (2000).

69. Azek, F., Grossiord, C., Joannes, M., Limoges, B. & Brossier, P. Hybridization Assay at a Disposable Electrochemical Biosensor for the Attomole Detection of Amplified Human Cytomegalovirus DNA. *Analytical Biochemistry*. **284**, 107–113 (2000).

70. Drummond, T. G., Hill, M. G. & Barton J. K. Electrochemical DNA sensors. *Nat Biotechnol*. **21**, 1192–1199 (2003).

71. Pease, A. C. Light-generated oligonucleotide arrays for rapid DNA sequence analysis. *Proceedings of the National Academy of Sciences*. **91**, 5022–5026 (1994).

72. Schena, M., Shalon, D., Davis, R. W. & Brown, P. O. Quantitative monitoring of gene expression patterns with a complementary DNA microarray. *Science*. **270**, 467–470 (1995).

73. Yoo, K. H. Electrical Conduction through Poly(dA)-Poly(dT) and Poly(dG)-Poly(dC) DNA Molecules. *Phys. Rev. Lett*. **87**, 198102 (2001).

74. Keren, K., Berman, R. S., Buchstab, E., Sivan, U. & Braun, E. DNA-templated carbon nanotube field-effect Transistor. *Science*. **302**, 1380–1382 (2003).

75. Brundin, M. & Figdor, D. DNA binding to hydroxyapatite: a potential mechanism for preservation of microbial DNA. *Journal of Endodontics.* **39**, 112-116 (2013).

76. Tiselius, A., Hjerten, S. & Levin, O. Protein chromatography on calcium phosphate columns. *Arch. Biochem. Biophys*. **65**, 132-155 (1956).

77. Lindahl, T. Instability and decay of the primary structure of DNA. *Nature*. **362**, 709 - 715 (1993).

78. Welzel,T., Radtke, I., Meyer-Zaika, W., Heumann, R. & Epple, M. Transfection of cells with custom-made calcium phosphate nanoparticles coated with DNA. *J. Mater. Chem B.* **14**, 2213–2217 (2004).

79. Spear, F.S. & Pyle, J.M. Apatite, monazite, and xenotime in metamorphic rocks. *Reviews in Mineralogy and Geochemistry, Mineralogical Society of America.* **48**, 293–335 (2002).

80. Benzanilla, M., Manne, S., Laney, D. E. & Lyubchenko, Y. L. Adsorption of DNA to mica, silylated mica, and minerals: characterization by atomic force microscopy. *Langmuir*. **11**, 655–659 (1995).

81. Romanowski, G., Lorenz, M. G. & Wackernagel, W. Adsorption of plasmid DNA to mineral surfaces and protection against DNase. *Applied and Environmental Microbiology.* **57**, 1057–1061 (1991).

82. Vanderbilt, D. & King-Smith, R.D. Electric polarization as a bulk quantity and its relation to surface charge. *Phys.Rev.* **48**, 4442-4458 (1993).

83. Pastré, D. Anionic polyelectrolyte adsorption on mica mediated by multivalent cations: a solution to DNA imaging by atomic force microscopy under high ionic strengths. *Langmuir*. 22(15), 6651–6660 (2006).

84. Song. Y. A novel strategy to construct a flat-lying DNA monolayer on a mica surface. *J. Phys. Chem. B*. **110**, 10792–10798 (2006).

85. Nguyen, T. H. & Elimelech, M. Plasmid DNA adsorption on silica: kinetics and conformational changes in monovalent and divalent Salts. *Biomacromolecules.* **8**, 24–32 (2007).

86. Bustin, S. A., & Mueller, R. Real-time reverse transcription PCR (qRT-PCR) and its potential use in clinical diagnosis. *Clin. Sci*. **109**, 365-379 (2005).

87. Schutz, C.N. & Warshel, A. What are the dielectric "constants" of proteins and how to validate electrostatic models? *Proteins.* **44**, 400-417, (2001).

88. Torgerson, J.R., Branning, D., Monken, C. H. & Mandel, L. Violations of locality in polarization-correlation measurements with phase shifters. *Phys. Rev*. **51**, 4400-4416 (1995).

89. Barton, D. The principles of conformational analysis. Nobel Media AB. Elsevier Publishing Co. Retrieved 10 November (2013).

90. Luscombe, N.M., Austin, S.E., Berman, H.M. & Thornton, J.M. An overview of the structures of protein-DNA complexes. *Genome Biol.; 1(1), Reviews 001*. **43**, 67-98 (2000).

91. Luisi, B.F. DNA-protein interaction at high resolution. In DNA-Protein Structural Interactions Edited by Lilley DMJ New York: Oxford University Press, 1–48 (1995).

92. Zhou, J., Gregurick, S. K., Krueger, S. & Schwarz, F. P. Conformational changes in single-strand DNA as a function of temperature by SANS. *Biophys J.* **90(2)**, 544–551 (2006).

93. Wu, S., Wang, X., Ye, X. & Zhang, G. pH-Induced conformational change and dimerization of DNA chains investigated by analytical ultracentrifugation. *J Phys Chem B.* **117(39)**, 11541-11547 (2013).

94. Lifshitz, I.M. Some problems of the statistical theory of biopolymers. *Zh. Eksp. Teor. Fiz.* **5**, 2408-2420 (1968).

95. Kittel, C. Introduction to Solid State Physics. 7th. edition, Wiley, New York (1996).

96. Stalke, D. Meaningful Structural Descriptors from Charge Density. *Chem. Eur J.* **17**, 9264–9278 (2011).

97. Macchi, P. Modern charge density studies: The entanglement of experiment and theory. *Cryst. Cryst. Rev.* **19**, 58–101 (2013).

98. Resta, R. Macroscopic polarization in crystalline dielectrics: the geometric phase approach. *Rev Mod. Phys.* **66**, 899-912 (1994).

99. Vanderbilt, D. & King-Smith, R.D. Electric polarization as a bulk quantity and its relation to surface charge. *Phys.Rev.* **48**, 4442-4458 (1993).

100. Landau, L.D. & Lifshitz, E.M. Electrodynamics of Continuous Media. Pergamon Press, pp. 7 and 192 (1984).

101. King-Smith R.D. & Vanderbilt, D. Theory of polarization of crystalline solids. *Phys. Rev*. **47**, 1651-1667 (1993).

102. Helmholtz, H. Ueber einige Gesetze der Vertheilung elektrischer Ströme in körperlichen Leitern mit Anwendung auf die thierisch-elektrischen Versuche. *Annalen der Physik und Chemie*. **165 (6)**, 211–233 (1853).
103. Guo, L., Huang, M. & Zhang, X. Effects of sintering temperature on structure of hydroxyapatite studied with Rietveld method. *J Mater Sci Mater Med.* **14(9)**, 817-822 (2003).
104. Chapman, D.L. A contribution to the theory of electrocapillarity. *Philosophical Magazine*. **25**, 148-160 (1913).
105. Stern O. *Zeitschrift für Elektrochemie*. **30**, 508-523 (1924).
106. Hunter, R.J. Foundations of Colloid Science. Oxford University Press (1989).
107. Lukic, M.J., Jovalekic, C., Markovic, S. & Uskolovic, D. Enhanced high-temperature electrical response of hydroxyapatite upon grain size refinement. *Materials Research Bulletin*. **61**, 534-538 (2014).
108. Nagai, M. & Nishino, T. Surface conduction of porous hydroxyapatite ceramics at elevated temperatures. *Solid State Ionics*. **28-30**, 1456-61 (1988).
109. Yashima, M., Kubo, N., Omoto, K., Fujimori, H., Fujii, K. & Ohoyama K. Diffusion path and conduction mechanism of protons in hydroxyapatite. *The Journal of Physical Chemistry C*. **118 (10)**, 5180-5187 (2014).
110. Ma, G. & Liu, X.Y. Hydroxyapatite: Hexagonal or Monoclinic? *Cryst. Growth Des.* **9**, 2991-2304 (2009).
111. Fujimori, H., Toya, H., Ioku, K. & Yoshimura, M. In situ observation of defects in hydroxyapatite up to 1200 ° C by ultraviolet Raman Spectroscopy. *Chem. Phys. Lett*. **325**, 383-390 (2000).
112. Yamashita, K., Kitagaki, K. & Umegaki, T. Thermal-instability and proton conductivity of ceramic hydroxyapatite at high-temperatures. *J Am Ceram Soc*. **78**, 1191-1197 (1995).
113. Horiuchi, N., Nakamura, M. & Yamashita, K. Proton conduction related electrical dipole and space charge polarization in hydroxyapatite. *J of applied physics*. **112**, 134-156 (2012).
114. Cameron F.K. & Hurst, L.A. The action of water and saline solutions upon certain slightly soluble phosphates. *J. Am. Chem. Soc*. **26**, 885 (1904).
115. Ferraro, J.W. Experimental evaluation of ceramic calcium phosphate as a substitute for bone grafts. Plast. *Reconstruct. Surg*. **63**, 634-646 (1979).
116. Hassler, C.R., McCoy, L.G. & Clarke, L.C. Studies on the degradability of large tricalcium phosphate segments. *Proc. 2nd Ann. Meet. Soc. Biomater*. **88**, 145-167 (1976).
117. Banfield, J. F. & Navrotsky, A. Eds. Nanoparticles and the Environment. Washington, DC: Mineralogical Society of America (2001).
118. Biswas, S. & Torchilin, V. P. Nanopreparations for Organelle-specific Delivery in Cancer. *Advanced Drug Delivery Reviews*. **66 C**, 26-41 (2013).
119. Nel, A., Xia, T., Mädler, L. & Li, N. Toxic potential of materials at the nanolevel. *Science*. **331 (5761)**, 622-627 (2006).
120. Gogotsi, Y. How safe are nanotubes and other nanofilaments*? Mat Res Innovat.* **7**, 192-194 (2003).
121. Luo, D. Synthetic DNA delivery systems. *Nature Biotechnology*. **18(1)**, 33-37 (2000).

122. Chowdhury, EH. High-efficiency gene delivery for expression in mammalian cells by nanoprecipitates of Ca-Mg phosphate. *Gene*. **341**, 77-82 (2004).

123. Xiang, SD. Pathogen recognition and development of particulate vaccines: does size matter? *Methods*. **40(1)**, 1-9 (2006).

124. Nakanishi, M. Nuclear targeting of DNA. *Eur J Pharm Sci*. **13**, 17-24 (2001).

125. Jordan, M. Transfecting mammalian cells: optimization of critical parameters affecting calcium-phosphate precipitate formation. *Nucleic Acids Research.* **24(4)**, 596-601 (1996).

126. Orrantia, E. Intracellular distribution of DNA internalized through calcium phosphate precipitation. *Exp Cell Res.* **190**, 170-1744 (1990).

127. Nicholls, D.G., Budd, S.L. & Castilho, R.F. Excitotoxicity and mitochondria. *Biochem Soc Symp*. **66**, 55-67 (1999).

128. Alirol, E. Mitochondria and cancer: is there a morphological connection? *Oncogene*. **25**, 4706-4716 (2006).

129. Brookes, P. S., Yoon, Y. & Sheu, S.S. Calcium, ATP, and ROS: a mitochondrial love-hate triangle. *Am J Physiol Cell Physiol*. **287**, 817-833 (2004).

130. Balaban, R.S. Cardiac energy metabolism homeostasis: role of cytosolic calcium. *J Mol Cell Cardiol*. **34**, 1259–1271 (2002).

131. Hansford, R.G. & Zorov, D. Role of mitochondrial calcium transport in the control of substrate oxidation. *Mol Cell Biochem*. **184**, 359–369 (1998).

132. Krebs, H.A. & Weitzman, P.D. Krebs' citric acid cycle: half a century and still turning. *London: Biochemical Society*. **54**, 25-34 (1987).

133. Lowenstein, J.M. Methods in Enzymology. Volume 13: Citric Acid Cycle. Boston: Academic Press (1969).

134. Perez-Campo, R.**,** Lopez-Torres, M., Cadenas, S., Rojas, C., & Barja, G**.** The rate of free radical production as a determinant of the rate of aging: evidence from the comparative approach. *J Comp Physiol*. **168**, 149–158 (1998).

135. Sohal, R.S. & Allen, R.G. Relationship between metabolic rate, free radicals, differentiation and aging: a unified theory. *Basic Life Sci*. **35**, 75–*104*, (1995).

136. Contreras, L. Mitochondria: the calcium connection. *Biochim Biophys Acta*. **1797**, 607-18 (2010).

137. Munaron, L. Endothelial calcium machinery and angiogenesis: understanding physiology to interfere with pathology. *Curr Med Chem*. **16**, 4691-703 (2009).

138. Saidak, Z. The role of the calcium-sensing receptor in the development and progression of cancer. *Endocrinol Rev*. **30**, 1787-95 (2009).

139. Vallet-Regi, M. Revisiting ceramics for medical applications. *Dalton Trans*. **28**, 5211–5220 (2006).

140. Parikh, S. Bone graft substitutes in modern orthopedics. *Orthopedics*. **25**, 1301–1310 (2002).

141. Yokoyama, M., Kwon, G.S., Okano, T., Sakurai, Y., Seto, T. & Kataoka, K. Preparation of micelle-forming polymer-drug conjugates. *Bioconjugate Chemistry.* **3(4)**, 295–301 (1992).

142. Porter, C.J., Trevaskis, N.L. Lipids and lipid-based formulations: optimizing the oral delivery of lipophilic drugs. *Nature Rev Drug Discovery*. **6(3)**, 231-248 (2007).

143. Chiou, W.L. & Riegelman, S. Pharmaceutical applications of solid dispersion systems. *J Pharm Sci*. **60(9)**, 1281-1302 (1971).

144. Qiu, Y. & Chen, Y. Developing solid oral dosage forms. Pharmaceutical theory and practice. Academic Press (2009).

145. Zhang, M. & Li, H. Formulation and delivery of improved amorphous fenobibrate solid dispersions prepared by thin film freezing. *Eur J Pharm Biopharm*. **67**, 234-245 (2012).

146. Keseru, G.M. & Makara, G.M. The influence of lead discovery strategies on the properties of drug candidates. *Nature Reviews, drug Discovery*. **8**, 203-221 (2009).

147. Lipinski, C.A. Drug-like properties and the causes of poor solubility and poor permeability. *Journal of Pharmaceutical and Toxicological Methods*. **44**, 235-250 (2000).

148. Hancock, B.C. & Parks, M. What is the true solubility advantage for amorphous pharmaceuticals? *Pharm Res.* **17**, 397-412 (2000).

149. Spenlehauer, G., Vert, M. & Benoit, J.P. In vitro and In vivo degradation of poly (D, L lactide/glycolide) type microspheres made by solvent evaporation method. *Biomaterials*. **10**, 557–563 (1989).

150. Osborn, J.F. & Newesely, H. The material science of calcium phosphate ceramics. *Biomaterials*. **1**, 108-119 (1980).

151. Crystal, R.G. Transfer of genes to humans-early lessons and obstacles to success. *Science*. **270 (5235)**, 404-410 (1995).

152. Kim, YH. Polyethylenimine with acid-labile linkages as a biodegradable gene carrier. *Journal of Controlled Release.* **103(1)**, 209-19 (2005).

153. Fogueri, L.R. & Singh, S. Smart polymers for controlled delivery of proteins and peptides: a review of patents. *Recent Pat. Drug Deliv. Formul*. **3**, 40–48 (2009).

154. Ginebra, M.P. Calcium phosphate cements as bone drug delivery systems: a review. *J. Control. Release*. **113**, 102–110 (2006).

155. Hanahan, D. & Weinberg, R.A. The hallmarks of cancer. *Cell*. **100**, 57-70 (2000).

156. Hanahan, D. & Weinberg, R.A. Hallmarks of cancer: the next generation. *Cell*. **144**, 646-674 (2011).

157. Warburg, O. On the origin of cancer cells. *Science*. **123**, 309-314 (1956).

158. Wallace, D.C. Mitochondrial genetics: a paradigm for aging and degenerative diseases? *Science*. **256**, 628–632 (1992).

159. Wallace, D.C. A mitochondrial paradigm of metabolic and degenerative diseases, aging, and cancer: a dawn for evolutionary medicine. *Annu. Rev. Genet*. **39**, 359-407 (2005).

160. Pedersen, P.L. Tumor mitochondria and the bioenergetics of cancer cells. *Prog Exp Tumor Res.* **22**, 190-274 (1978).

161. Labiche, R.A. Gene expression and tumor cell escape from host effect mechanisms in murine large cell lymphoma. *J Cell Biochem*. **36 (4)**, 393-403 (1988).

162. Labiche, R.A. Transcripts of the mitocondrial gene NDS are overexpressed in highly metastatic murine large cell lymphoma. *In Vivo*. **6(4)**, 317-324 (1992).

163. Sagan, L. On the Origin of Mitosing Cells. *Journal of Theoretical Biology*. **14**, 225–274 (1967).

164. Lamb, R., Ozsvari, B., Lisanti, C.L. & Lisanti, M.P. Antibiotics that target mitochondria effectively eradicate cancer stem cells, across multiple tumor types: treating cancer like an infectious disease. *Oncotarget*. **5**, 34-67 (2015).

165. Lamb, R., Harrison, H., Hulit, J., Smith, D.L., Lisanti, M.P. & Sotgia, F. Mitochondria as new therapeutic targets for eradicating cancer stem cells: Quantitative proteomics and functional validation via MCT1/2 inhibition. *Oncotarget*. **5(22)**: 11029-11037 (2014).

166. Rattan, R., Fehmi, A. & Munkarah A. Metformin: an emerging new therapeutic option for targeting cancer stem cells and metastasis. *J Oncol.* **56**, 234-256 (2012).

167. Hirsch, H.A., Iliopoulos, D., Tsichlis, P.N. & Struhl K. Metformin selectively targets cancer stem cells, and acts together with chemotherapy to block tumor growth and prolong remission. *Cancer Res*. **69(19)**, 7507-7511 (2009).

168. Fojo, A.T. & Ueda, K. Expression of a multidrug-resistance gene in human tumors and tissue. *Proc Natl Acad Sci USA*. **84(1)**, 265-269 (1987).

169. Nielsen, D. & Skovsgaard, T. P-glycoprotein as multidrug transporter: A critical review of current multidrug resistant cell lines. *Biochim Biophys Acta*. **1139**, 169–183 (1992).

170. Schuurhuis, G.J., Broxterman, H.J., de Lange, J.H.M., Pinedo, H.M., van Heijningen, T.M.H., Kuiper, C.M., Scheffer, G.L., Scheper, R.J., van Kalken, C.K., Baak, J.P.A. & Lankelma, J. Early multidrug resistance, defined by changes in intracellular doxorubicin distribution, independent of P-glycoprotein. *Br J Cancer*. **64**, 857–861 (1991).

171. De Isabella, P., Capranico, G. & Zunino F. The role of topoisomerase II in drug resistance. *Life Sci*. **48**, 2195–2205 (1991).

172. Klohs, W.D., Steinkampf, R.W., Leopold, W.R. & Fry, D.W. Potentiation of adriamycin, trimetrexate and an AMSA analog (CI-921) cytotoxicities by amiodarone and reserpine in multidrug resistant P388 cells. *Proc Am Assoc Cancer Res*. **28**, 298–302 (1987).

173. Gottesman, M.M. & Pastan, I. Biochemistry of multidrug resistance mediated by the multidrug transporter. *Annu Rev Biochem*. **62**, 385–427 (1993).

174. Spoelstra, E.C., Dekker, H., Schuurhuis, G.J., Broxterman, H.J. & Lankelma, J. P-glycoprotein drug efflux pump involved in the mechanisms of intrinsic drug resistance in various colon cancer cell lines. *Biochem Pharmacol*. **41**: 349–359 (1991).

175. Ruetz, S. & Gros, P. A mechanism for P-glycoprotein action in multidrug resistance: Are we there yet. *Trends Pharmacol Sci*. **15**, 260–263 (1994).

176. Szakacs, G. & Paterson, J.K. Targeting multidrug resistance in cancer. *Nat Rev Drug Discov*. **5(3)**, 219-234 (2006).

177. Kohno, K., Sato, S. & Takano, H. The direct activation of human multidrug resistance gene (MDR1) by anticancer agents. *Biochem Biophys Res Commun*. **165(3)**, 1415-1421 (1989).

178. Ambudkar, S. V. & Kimchi-Sarfaty, C. P-glycoprotein: from genomics to mechanism. *Oncogene*. **22(47)**, 7468-7485 (2003).

179. Fletcher, J.I. & Haber M. ABC transporters in cancer: more than just drug efflux pumps. *Nat Rev Cancer*. **10(2)**, 147-156 (2010).

180. Song, J., Ren, W, Xu, T., Zhang, Y., Guo, H., Zhu, S. & Yang, L. Reversal of multidrug resistance in human lung cancer cells by delivery of 3-octadecylcarbamoylacrylic acid-cisplatin-based liposomes. *Drug Res Devel Ther*. **11**, 441-449 (2017).

181. Patel, N. R. & Rathi A. Reversal of multidrug resistance by co-delivering of taeiquidar (XR9576) and paclitaxel using long-circulating liposomes. *Int. J Pharm*. **416(1)**, 296-299 (2011).

182. Yan, Y. & Ochs, C.J. Bypassing multidrug resistance in cancer cells with biodegradable polymer capsules. *Adv Mater*. **22(47)**, 5398-5403 (2010).

183. Murakami, M., Cabral, H., Matsumoto, Y. *et al*. Improving drug potency and efficacy by nanocarrier-mediated subcellular targeting. *Sci Transl Med*. **3**, 64-78 (2011).

184. Smith, N.R., Baker, D., Farren, M. *et al.* Tumor stromal architecture can define the intrinsic tumor response to VEGF-targeted therapy. *Clin Cancer Res*. **19**, 6943-6956 (2013).

185. Albert, D. Z. After Physics. Cambridge (MA): Harvard University Press (2015).

186. Chauhan, V.P. & Jain, R.K. Strategies for advancing cancer nanomedicine. *Nat Mater*. **12**, 958-962 (2013).

187. Greish, K. Enhanced permeability and retention (EPR) effect for anticancer nanomedicine drug targeting. *Methods Mol Biol*. **624**, 25-37 (2010).

188. Lutolf, M.P. & Hubell, J.A. Synthetic biomaterials as instructive extracellular microenvironments for morphogenesis in tissue engineering. *Nat. Biotechnol*. **23**, 47-55 (2005).

189. Prichard, C.D. *et al.* An injectable thiol-acrylate poly (ethylene glycol) hydrogel for sustained release of methylprednisolone sodium succinate. *Biomaterials*. **32**, 587-597 (2011).

190. Wu, D.Q. *et al*. Fabrication of supramolecular hydrogels for drug delivery and stem cell encapsulation. *Langmuir*. **24**, 10306-10312 (2008).

191. Guvendiren, M., Lu, H.D. & Burdick, J.A. Shear-thinning injectable hydrogels. *Soft Matter*. **8**, 260-272 (2008).

192. Wang, Q. *et al*. High-water content mouldable hydrogels by mixing clay and a dentritic binder. *Nature*. **463**, 339-343 (2010).

193. Flory, P. Principles of Polymer Chemistry. Cornell University Press (1953).

194. Fisher, M.E. Statistics of long chains with repulsive interactions. *J. Phys. Soc. Japan.* **26**, 42-45 (1969)

195. de Gennes, P. G. Scaling Concepts in Polymer Physics. Cornell University Press, Ithaca, New York (1985).

196. Edwards, S.F. The statistical method of polymers with excluded volume. *Proc. Phys. Soc*. **85**, 613-624 (1965).

197. Freed, K.F. Functional Integrals and Polymer Statistics. *Ad V. Chem. Phys*. **22**, 1-9 (1972).

198. Domb, C. Excluded-Volume Effect for Two- and Three-Dimensional Lattice Models. *The Journal of Chemical Physics*. **38**, 2957-2967 (1963).

199. Fisher, M.E. Shape of a Self-Avoiding Walk or Polymer Chain. *The Journal of Chemical Physics.* **44**, 616-625 (1966).

200. de Gennes, P. G. Reptation of a Polymer Chain in the Presence of Fixed Obstacles. *The Journal of Chemical Physics. American Institute of Physics*. **55 (2)**, 572–571 (1971).

201. Pickett, S.D. & Sternberg, M.J. Empirical scale of side-chain conformational entropy in protein folding. *J Mol Biol*. **231(3)**, 825-39 (1993).

202. Doig, A.J. &Sternberg, M.J.E. Side-chain conformational entropy in protein folding. *Protein Science*. **4**, 2247-2251 (1995).

203. Doi, M. & Edwards, S. F. Dynamics of concentrated polymer systems. Part 1. Brownian motion in the equilibrium state. *Journal of the Chemical Society, Faraday Transactions 2*. **74**, 1789-1799 (1978).

204. Grosberg, A. & Khokhlov, A.R. Statistical Physics of Macromolecules. *American Institute of Physics*. **34**, 56-69 (1994).

205. de Gennes, P. G. Entangled polymers. *Physics Today. American Institute of Physics.* **36 (6)**, 33–31 (1983).

206. Lamoureux, G. & Roux, B. Absolute Hydration Free Energy Scale for Alkali and Halide Ions Established from Simulations with a Polarizable Force Field. *J. Phys. Chem. B*. **110 (7)**, 3308–3322 (2006).

207. Sugita, Y. & Okamoto, Y. Ab initio replica-exchange Monte Carlo method for cluster studies. *Chem. Phys. Lett.* **314**, 141-151 (1999).

208. Krivovichev, S.V. Hydrogen bonding and structural complexity of the $Cu_3(AsO_4)(OH)_3$ polymorphs (clinoclase, gilmarite): a theoretical study. *J. Geos*. **62**, 79-85 (2017).

209. Alder, B. J. & Wainwright, T. E. Studies in Molecular Dynamics. *General Method. J. Chem. Phys*. **31 (2)**, 459-468 (1959).

210. Tuckerman, M.E., Berne, B.J., Martyna, G.J. & Berne, M. Reversible multiple time scale molecular dynamics. *J Chem Phys*. **97 (3)**, 1990–2001 (1992).

211. Di Pierro, M., Elber, R. & Leimkuhler, B. A Stochastic Algorithm for the Isobaric-Isothermal Ensemble with Ewald Summations for all Long Range Forces. *Journal of Chemical Theory and Computation*. **45**, 56-67 (2015).

212. Barron, T. H. K. & Domb C. On the Cubic and Hexagonal Close-Packed Lattices. *Proceedings of the Royal Society of London. Series A., Mathematical and Physical Sciences*. **227(1171)**, 447–465, (1955).

213. Rapaport, C. The Art of Molecular Dynamics Simulation. Cambridge University Press (2004).

214. Lennard-Jones, J. E. On the Determination of Molecular Fields. *Proc. R. Soc. Lond*. **106** (738): 463–477 (1924).

215. Lennard-Jones, J. E. Cohesion. *Proceedings of the Physical Society*. **43 (5),** 461 (1931).

216. Frenkel, D. & Smit B. Understanding Molecular Simulation (Second ed.), San Diego: Academic Press (2002).

217. Zhen Shu & Davies G.J. Calculation of the Lennard-Jones n–m potential energy parameters for metals. *Physica Status Solidi (a).* **78 (2)**, 595–605 (1983).

218. Chandler, D. Introduction to Modern Statistical Mechanics. Oxford University Press (1987).

219. McQuarri, D. A. Statistical Mechanics. Harper Collins Publishers (1976).

220. Levine, I. N. Quantum Chemistry. Englewood Cliffs, New Jersey: Prentice Hall. 455–544, (1991).

221. Procacci, P., Darden, T. & Marchi, M. A very fast molecular dynamics method to simulate biomolecular systems with realistic electrostatic interactions. *J. Phys. Chem*. **100**, 10464–10468 (1996).

222. Widom, B. Potential distribution theory and the statistical mechanics of fluids. *J. Phys. Chem B*. **86**, 869–872 (1982).

223. Behrens, P.H., Mackay, D.H.J., White, G.M. & Wilson, K.R. Thermodynamics and quantum corrections from molecular dynamics for liquid water. *J. Chem. Phys*. **79**, 2375–2389 (1983).

224. Smith, P.E. & Van Gunsteren, W.F. Methods for the evaluation of long range electrostatic forces in computer simulations of molecular systems. *Computer Simulations of Biomolecular Systems.* **2**, 182–212 (1993).

225. Ponder, J. W., & Case, D.A. Force fields for protein simulations. *Adv. Protein Chem*. **66**, 27–85 (2003).

226. Van Gunsteren, W.F., Beutler, T.C., Fraternali, F., King, P.M., Mark, A.E. & Smith P.E. Computation of free energy in practice: Choice of approximations and accuracy limiting factors. *Computer Simulations of Biomolecular Systems.* **2**, 315–348 (1993).

227. Warshel, A., Sharma, P.K., Kato, M. & Parson, W.W. Modeling Electrostatic Effects in Proteins. *Biochim. Biophys. Acta*. **1764**, 1647-1676 (2006).

228. McCammon, J.A., Gelin, B.R. & Karplus, M. Dynamics of folded proteins. *Nature*. **267** 585–590 (1977).

229. Field, M.J., Bash, P.A. & Karplus M. A combined quantum mechanical and molecular mechanical potential for molecular dynamics simulations. *J. Comput. Chem*. **11**, 700–733 (1990).

230. Gillan, M.J. The quantum simulation of hydrogen in metals. *Philosoph. Mag*. **58,** 257–283 (1988).

231. Neumann, M. Dipole moment fluctuation formulas in computer simulations of polar systems. *Mol. Phys*. **50**, 841–858 (1983).

2.

OBJECTIVES

The main goal of the present work corresponds to the study of the influence of both, molecular architecture and composition on the final properties of the HAp nanoparticles. Attention will be also be paid to the study of physiological barriers for drug delivery from HAp nanoparticles and their capacity to direct intracellular delivery. Particular objectives are the follows:

i) Study of the mineralization of HAp with adsorbed DNA:

- Evaluation by atomistic molecular dynamics methods of the structure and stability of HAp biominerals having encapsulated DNA.
- Study of the influence of Mg^{2+} and DNA templates in the nucleation and mineralization of HAp.

ii) Study of the adsorption and crystal growth of inorganic phosphates (orthophosphate, pyrophosphate, polyphosphate and bisphosphonate) onto HAp surfaces.

iii) Study of the impact of atmosphere conditions (*i.e*. nitrogen, air or carbon dioxide), temperature and pressure in the structure, electrochemical properties and solubility of fluorine-substituted hydroxyapatites (xF-HAp).

iv) Study of HAp nanoparticles toxicity impact in living cells:

- Study of several markers (*e.g.* adhesion, proliferation, migration, p53 expression and differentiation) of cellular malignancy in epithelial, endothelial and fibroblast cells pretreated with hydroxyapatite nanoparticles.
- Development of antibiotic loaded HAp nanoparticles as effective antitumor platform. Evaluation of the effect caused by a polyphosphate coating.
- Development of polylactide electrospun scaffolds incorporating chloramphenicol encapsulated hydroxyapatite nanoparticles for drug delivery.
- Revision of self-assembly hybrid hydrogel biomaterials formed by hydroxyapatite NPs and peptides.

3.

DNA ADSORBED ON HYDROXYAPATITE SURFACES

Hydroxyapatite (HAp) particles with very different surface charge and compositions (*i.e.* different Ca/P and CO_3^{2-}/PO_4^{3-} ratios) have been obtained by varying the experimental conditions used during the chemical precipitation process. The DNA adsorption capacity and protection imparted against the attack of nucleases of HAp particles have been proved to depend on the surface charge while the buffering capacity is affected by the chemical composition. On the basis of both the surface charge and the crystallinity, the predominant planes at the surfaces of HAp particles have been identified. Atomistic molecular dynamics simulations of surfaces constructed with these planes (*i.e.* the (001) and the two terminations of the (010)) with adsorbed B-DNA double helix have been performed to get microscopic understanding of the influence of the mineral in the biomolecule structure and the interaction energies. Results indicate that the DNA secondary structure is perfectly preserved on the (001) surface, this stability being accompanied by an attractive binding energy. In contrast, the (010) surface with PO_4^{3-}, OH^- and Ca^{+2} ions in the termination induces significant local and global deformations in the double helix, repulsive $OH^-(HAp)\cdots\cdots PO_4^{3-}$ (DNA) interactions provoking the desorption of the biomolecule. Finally, although the termination of the (010) surface with PO_4^{3-} and Ca^{+2} ions also deforms the double helix, it forms very strong attractive interactions with the biomolecule. These binding characteristics are in excellent agreement with the DNA adsorption and protection abilities experimentally determined for the HAp samples. Finally, the surface charge has been found less decisive than the chemical composition in the efficacy of the transfection process.

3.1 INTRODUCTION

DNA has been successfully applied for the preparation of a variety of architectures and objects specified with nanometer precision,[1-5] which opens a new strategy for the preparation of nanostructured biomaterials. On the other hand, it has been long established that bone mineral crystals are compositionally and structurally similar to the synthetic mineral hydroxyapatite (HAp), $Ca_{10}(PO_4)_6\ (OH)_2$.[6] This similarity motivated the application of HAp as synthetic biomaterial as has been evidenced in a large number of studies.[7-15] Furthermore, the formation of HAp can be regulated by DNA, which acts as a template in the process of "biomineralization".[16-19] This phenomenon is particularly important for biomedical applications requiring the protection of such biomolecules from aggressive environmental conditions. In order to elucidate the role of DNA as template to promote mineral growth, the biomineralization mechanism has been recently revealed at the atomic level.[16-19]

In very recent studies, we examined the encapsulation of DNA into HAp using computer simulation and experimental techniques.[16,19] Classical molecular dynamics (MD) simulations of inorganic Ca^{+2}, PO_4^{3-} and OH^- aqueous solutions in presence and absence of DNA showed that the biomolecule acts as template for the nucleation and growth of HAp. Simulations in absence of DNA revealed the formation of multiple calcium phosphate clusters, which subsequently transform into nucleation centers for the formation of HAp. In contrast, simulations in presence of the biomolecule revealed that calcium phosphate clusters are formed surrounding the DNA backbone, the phosphate groups of the biomolecule acting as a very large nucleus for the growing of the HAp. In summary, MD simulations clearly indicated that DNA does not inhibit, as it was early suggested,[20] but even promotes the mineral growth. These conditions were experimentally applied in the laboratory to create nanoparticles of spherical shape (diameter ≈ 20 nm) and nanocrystals (nanorods with a width of ≈ 20 nm) with DNA inside. The encapsulation of DNA into both nanospheres and nanocrystals was unambiguously determined by different techniques after all superficially adsorbed DNA was appropriately removed (*i.e.* by digestion with deoxyribonuclease).

HAp nanoparticles are also suitable as gene delivery systems for the transfection of cells with nucleic acids.[21-24] This strategy can be used to turn on (transfection, DNA) or to turn off (gene silencing, siRNA) the production of a specific protein.[25,26] Furthermore, HAp binding ability may confer protection to DNA from chemical and enzymatic degradation.

Indeed, the shielding effect to protect nucleic acids has been proved for different mineral surfaces.[27-30] In addition, HAp columns have been used as an efficient binding method for the sequestering of DNA.[31] The influence of the binding affinity of HAp surfaces for DNA on the stability of the biomolecule has been recently assessed by Brundin *et al*.,[32] results indicating that DNA-bound HAp (DNA-HAp) is more resistant to decay by ambient environmental factor and less susceptible to degradation by serum and nucleases.

Despite of the potential interest of DNA-HAp complexes, many aspects related with the ability of HAp to bind DNA remain unknown. In this work we use an approach that combines both experimental and theoretical methodologies, which is similar to that used for the study of biominerals made of DNA embedded into HAp,[16,19] to investigate different chemical and microscopic aspects related with the capacity of the mineral to adsorb DNA. For this purpose, HAp particles with different morphologies and surface compositions have been prepared. These HAp particles have been used to investigate the influence of composition and charge surface in the buffering activity, DNA adsorption capability and efficacy to protect adsorbed DNA from nucleases. After this, MD computer simulations using atomistic models have been used to examine at the microscopic level the adsorption of double helix B-DNA at the surfaces identified for experimentally prepared HAp samples. Finally, DNA-HAp complexes have been used to transfect *E. coli* bacteria, results revealing the relative importance of HAp surface charge and composition in the efficacy of the transfection process.

3.2 EXPERIMENTAL SECTION

3.2.1 Materials

Ammonium phosphate dibasic [$(NH_4)_2HPO_4$; purity ≥ 99.0 %], ammonium hydroxide solution 30 % (NH_4OH; purity: 28-30 %), Luria-Bertani (LB) medium (purity ≥ 96 %), amphicillin ($Ca_{16}H_{18}N_3NaO_4S$; purity: 96−100%) and deoxyribonuclease from bovine pancreas (DNase I enzyme; purity: protein ≥ 85 %, ≥ 400 Kunitz units/mg protein) were purchased from Sigma-Aldrich (St. Louis, USA). Calcium nitrate [$Ca(NO_3)_2$; purity ≥ 99.0 %], hydrochloric acid solution 37% (HCl; purity: 36.5−38.0 %) and sodium chloride ($NaCl$; purity ≥ 99.0 %) were purchased from Panreac (Barcelona, Spain). Ethanol (C_2H_5OH; purity ≥ 99.5 %) was obtained from Scharlab (Barcelona, Spain). The gel loading buffer (100 bp DNA ladder, 0.1 μg/μL; purity ≥ 99.5 %) and competent *E. coli*

DH5 α bacteria were obtained from Invitrogen (Carlsbad, USA). Sal I (10 U/μL; SalI enzyme; purity ≥ 99.5 %) and Su RE/Cut buffer H for restriction enzymes (purity ≥ 99.5 %) were purchased from Roche (Indianapolis, USA). The QIAprep Spin miniprep kit was purchase from QIAGEN (Manchester, UK). Finally, ethidium bromide ($C_{21}H_{20}BrN_3$; purity ≥ 99.0%) and tris-borate-EDTA (TBE) buffer (89 mM Tris, 89 mM boric acid, 2 mM EDTA; purity ≥ 99.0 %) solutions as well as commercial hydroxyapatite [$Ca_{10}(PO_4)_6\ (OH)_2$; purity ≥ 99.0 %] were obtained from Bio-Rad (Hercules, USA). All products were used as received.

3.2.2 Synthesis

HAp particles with different morphologies, which have been labeled as HAp#, were synthesized. More specifically, sheet crystals (HAp2), amorphous nanospheres (HAp3) and fusiform rods (HAp4) were prepared, whereas commercial HAp Bio-Gel® HTP Gel from BIO-RAD (HAp1) was used as control in all assays.

Samples HAp2-HAp4 were prepared using the same procedure but applying different experimental conditions. In all cases solutions of $(NH_4)_2HPO_4$ in deionized water were added drop-wise (2 mL/min) or quickly to $Ca(NO_3)_2$ ethanol or water solutions. The reagent concentrations were adjusted to get a Ca/P ratio of 1.67. The pH of the reaction, which was different for each sample, was adjusted with ammonia 30 % w/v solution. All samples were mixed 1 h by agitation (400 rpm), the subsequent aging step being carried out at hydrothermal or non-hydrothermal conditions. The specific experimental conditions used for the preparation of each sample are detailed in **Table 3.1**. After preparation, the particles were recovered from the mother liquor by centrifugation, and all samples were washed twice with de-ionized water and a 60/40 v/v mixture of ethanol-water. A white powder was obtained after freeze-drying.

Table 3.1. Experimental conditions used for the preparation of the different HAp samples.

Label	HAp particles	Conditions
HAp1	Mixed: amorphous sheets and rods	Commercial: Bio-Gel® HTP Gel purchased from BIO-RAD
HAp2	Sheet crystals: flower-like and laminar	Reagent: Quick addition of 0.3 M $Ca(NO_3)_2$ ethanol solution. Reaction: pH = 8.0 and 40ºC. Treatments: Hydrothermal conditions and 24 h of aging at room temperature.
HAp3	Nanospheres	Reagent: Quick addition of 0.5 M $Ca(NO_3)_2$ ethanol solution. Reaction: pH > 11 and room temperature. Treatments: Non-hydrothermal conditions and 24 h of aging at 37 ºC.
HAp4	Fusiform rods	Reagent: Drop-wise addition of 0.3 M $Ca(NO_3)_2$ aqueous solution. Addition of ethanolamine as surfactant. Reaction: pH = 10.0 and 60ºC. Treatments: Hydrothermal conditions and 24 h of aging at room temperature.

3.2.3 Measurements

Morphological characterization. Transmission electron microscopy (TEM) and scanning electron microscopy (SEM) were used for the morphological characterization of the different HAp samples. TEM images were obtained using a Philips TECNAI 10 electron microscope operated at 80 kV for a bright field mode. Micrographs were taken with an SIS MegaView II digital camera. Particles were deposited on carbon-coated grids.

SEM studies were carried out using a Focused Ion Beam Zeiss Neon40 microscope operating at 5 kV, equipped with an energy dispersive X-ray (EDX) spectroscopy system. Samples were deposited on a silicon disc mounted with silver paint on pin stubs of aluminum, and sputter-coated with a thin layer of carbon to prevent sample charging problems.

Fourier transform infrared (FTIR) spectroscopy. Infrared absorption spectra were recorded from powder samples with a Fourier Transform FTIR 4100 Jasco spectrometer in the 1800-700 cm^{-1} range. A Specac model MKII Golden Gate attenuated total reflection (ATR) equipment with a heated Diamond ATR Top-Plate was used.

X-Ray diffraction. Crystallinity was studied by wide angle X-ray scattering (WAXS). Patterns were acquired using a Bruker D8 Advance model with CuK_{α} radiation ($\lambda = 0.1542$ nm) and geometry of Bragg-Bretano, theta-2 theta. A one-dimensional Lynx Eye detector was employed. Samples were run at 40 kV and 40 mA, with a 2-theta range of 10−60, measurement steps of 0.02 º, and time/step of 2−8 s. Diffraction profiles were processed using PeakFit v4 software (Jandel Scientific Software) and the graphical representation performed with OriginPro v8 software (OriginLab Corporation, USA).

The crystallite size (L) in the direction representative to the (211) planes of HAp1-HAp4 samples was derived from the X-ray diffraction line broading measurement using the Scherrer equation:[33]

$$L = \frac{0.9\lambda}{\beta \cos\theta} \quad (1)$$

where λ is the wavelength (CuK_{α}), β is the full width at half maximum height of the (211) line, θ is the diffraction angle and 0.9 is a shape factor.

The crystallinity (χ_c) was obtained using the following Eqn:[34]

$$\chi_c = 1 - \frac{V_{112/300}}{I_{300}} \quad (2)$$

where I_{300} is the intensity of the (300) reflection and $V_{112/300}$ is the intensity of the hollow between the (112) and (300) reflections, which disappears in non-crystalline samples.

Zeta potential. Measurements were performed on a Malvern Zetasizer Nano-ZS (Malvern Instruments Ltd., Worcestershire, UK). The zeta potential was obtained by determining the electrophoretic mobility of the samples at 25 ºC, using Laser Doppler Velocimetry. Each measurement was conducted in a capillary cell (DTS0012). HAp samples were re-suspended in ultrapure milli-Q water (Millipore) at 0.5 mg/mL and, subsequently, were sonicated during 5 min in water bath. Each experiment was repeated five times and the average values are presented in this work.

HAp protonation assay. The protonation ability of the different HAp samples was determined using the following procedure. HAp particles suspended in milli-Q water (1 mg/mL) were protonated by adding an aqueous solution of 100 mM HCl and 50 mM $NaCl$ up to pH ≈ 3. Samples (5 mL) were maintained in a vial with continuous stirring, the pH values being determined every minute at 20 ºC using a pH-meter. The total time for this assay was 15 minutes.

Formation of DNA-HAp complexes. Aqueous suspensions of HAp particles (5 mg/mL) were prepared and subsequently sonicated to enhance the dispersion. DNA-HAp complexes were formed by adding 2.5 μL of plasmid pMT4 (0.4 μg/mL) to the volume of HAp suspension necessary to reach the following w/w DNA:HAp ratios: 1:0 1:10, 1:50, 1:100 and 1:250. DNA:HAp mixtures were incubated 90 min at 37 ºC and 200 rpm, shaking them with vortex every 30 min. Complexes were separated from the solution by centrifugation at 10000 rpm during 10 min. Sediments were re-suspended in 10 μL of sterile water.

The formation of DNA-HAp complexes was detected using agarose gel electrophoresis. For this purpose, gel loading buffer 6 x (2μL) was added to the complex solutions (10 μL) and then loaded in an agarose gel of 1% (w/v) containing ethidium bromide (EtBr, 0.5 μg/mL of the gel) in 1 x tris-borate-EDTA buffer (TBE).

DNA adsorption quantification. For quantification of adsorbed DNA on complexes obtained from DNA:HAp mixtures with 1:100 and 1:250 ratios, particles were separated by centrifugation and subsequently re-suspended on 1 mL of deionized water. An UV-3600 (Shimadzu) UV-Vis/NIR spectrophotometer controlled by the UVProbe 2.31 software was used to record the UV-Vis spectra of DNA-HAp complexes at room temperature, in the 200−400 nm range, with a bandwidth of 0.2 nm and a scan speed of 600 nm/min. Samples were homogenized by pipetting before recording the spectra. In order to evaluate the denaturalization of DNA adsorbed on the HAp particles, spectra were also recorded for samples heated at 94 ºC.

Nucleases digestion. DNA-HAp complexes formed using 1:100 and 1:250 mixtures were prepared as described before. After separating the particles by centrifugation, 9 μL of sterile water and 1 μL of enzyme DNaseI were added to each precipitate and digested 1 h at 37 ºC (200 rpm). Then, each sample was mixed with 2 μL of gel loading buffer 6x. The resulting volume was loaded in an agarose gel of 1 % (w/v) for electrophoresis.

The same procedure was applied for digestion with SalI enzyme but using SuRE/Cut buffer H for restriction enzymes instead of water.

Bacterial transfection. DNA-HAp complexes derived from 1:250 w/w mixtures were separated by centrifugation to be re-suspended in 10 μL of sterile water. Considering the transfection of all DNA bound to HAp as well the binding efficiencies estimated for each HAp sample, aliquots from 6.8 to 7.7 μL of suspensions were added to 10 μL of competent *E. coli* DH5α bacteria. Samples were mixed by pipetting, placed on a water bath for 5 min at 42 ºC, and cooled on ice at 4 ºC for 2 min After that, 200 μL of Luria-Bertani (LB) medium were added and samples were left at 37 ºC under agitation for 1 h. 100 μL of bacterial suspension was seeded on LB agar plates containing 100 μg/mL of ampicillin. Finally, samples were incubated for 24 h at 37 ºC.

To probe the transfected plasmid integrity, transformed bacteria colonies from LB-ampicillin agar plates were picked up and left to grow in a LB broth containing ampicillin (100 μg/mL). After 24 h incubation at 37ºC, bacteria colonies were washed with sterile water and pelletized by centrifugation. Purification of DNA was carried out by using the QIAprep® Spin Miniprep kit (QIAGEN). Aliquots of 10 μL of bacterial purified DNA were mixed with 2 μL of gel loading buffer 6× and the whole volume was introduced in the well of agarose 1 % electrophoresis gel.

In order to measure the transformed efficiency, bacteria colonies were scratched and washed with 10 mL of LB media. Samples were homogenized by pipetting and spectra records at 600 nm were taken using the UV-3600 spectrophotometer mentioned above. A sample of LB media was used as blank for the analysis.

Computational methods: model of DNA molecule and HAp surfaces. The DNA molecule simulated in this work consisted of the Dickerson's dodecamer (5'-CGCGAATTCGCG-3'), which is a well-known sequence that adopts a B-DNA double helix.[35] The hexagonal HAp crystal unit cell with $P6_3/m$ geometry ($a = b = 9.421$ Å, $c = 6.881$ Å, $\alpha = \beta = 90^{o}$, and $\gamma = 120^{o}$) and the 4*e* Wyckoff position occupied by two hydroxyl ions, each with ½ occupancy,[36] was generated and, subsequently, was cleaved to obtain the (001) and (010) surfaces. Following the strategy of de Leeuw and co-workers,[37] the partial occupation of the hydroxide anions was solved by assigning 1 and 0 occupation values alternatively in the columns parallel to the *c*-direction of the unitary cell. This configuration

renders equal orientation for all OH^- in a column but alternated between columns since this has been reported as the most stable ensemble.[38] The employed unit cell (44 atoms) was expanded 6 times in the x and y directions, creating a 6 × 6 supercell. The two planes considered in this work are the (001) and (010), which are the lowest energy facets.[37,38] The thickness of the supercell in the z axis entailed a 4 layer slab, being equivalent to 3 times the interplanar distance. The (001) facet has only one possible termination, whereas it is not possible to construct a slap of the (010) surface with same the same termination at both sides. More specifically, construction of a stable (010) surface, in which the total dipole moment across the slab perpendicular to the surface is cero, leads to sides that differ in the content of OH^- and Ca^{+2} ions. One side, hereafter denoted (010; Ca^{+2}) only contains Ca^{+2} and PO_4^{3-} while the other side, denoted (010; $Ca^{+2} - OH^-$) involves Ca^{+2}, OH^- and PO_4^{3-}. Although the (010; Ca^{+2}) is more stable, the (010; $Ca^{+2} - OH^-$) termination was found to be most favorable for interacting with ionic species because of its greater variation of surface species.[37] In this work we considered both the (010; $Ca^{+2} - OH^-$) and (010; Ca^{+2}) terminations at the (010) surface. Initially, the DNA was placed parallel to the surfaces at 5 Å as the average distance between its most outer groups and the atoms in the surface. Charge neutralization was performed with the addition of Na^+ counterions. Afterwards, both surfaces were solvated in the *z* direction with 17756 and 24029 water molecules for (001) and the two (010) terminations, respectively.

All energy minimizations and MD simulations were performed using the NAMD 2.6 code.[39] The potential energy was computed using the Amber force-field.[40] All force-field parameters for DNA as well as the phosphate and hydroxyl groups were extracted from Amber ff03.[41] It should be noted that the ff03 parameters are identical to the ff99-SB[42] ones for nucleic acids, phosphate and hydroxyl groups. Force-field parameters of Ca^{+2} were extracted from the work reported by Bradbrook *et al*.[43] The ability of this set of force-field parameters to reproduce the inorganic···organic interactions found in biominerals was recently proved.[16] Water molecules were represented using the TIP3P model.[44]

Initially, water and DNA coordinates were optimized through 5000 steps of conjugated gradient algorithm minimization. The resulting coordinates of the two systems underwent 0.5 ns of NVT molecular dynamics (MD) at 373 ºK (Berendsen thermostat[45]) with frozen coordinates for the DNA and HAp. Final coordinates and velocities of the NVT run were

used as input for 0.5 ns NPT (298 ºK, 1 bar) to equilibrate water density to 1 $\mathrm{g/cm^3}$ in the volume occupied by the liquid and the DNA. The Berendsen thermobarostat[45] was employed at constant xy plane area and frozen DNA and mineral slab coordinates. Productive dynamics started from the latter output, only keeping fixed the mineral atoms. Trajectories were 15.1 ns long, the 0.1 initial ns being discarded as the equilibration. In addition, the DNA double helix and the 20 $\mathrm{Na^+}$ counterions were solvated with 30000 water molecules and the density of the resulting system was equilibrated to 1 $\mathrm{g/cm^3}$ following the same protocol used for the surface slabs. Productive control dynamics were 15.1 ns long with a 0.1 ns equilibration period.

Atom pair distance cut-offs were applied at 16.0 Å to compute the van der Waals interactions. In order to avoid discontinuities in the Lennard-Jones potential, a switch function was applied to allow a continuous decay of the energy when the atom pair distances are larger than 14.0 Å. For electrostatic interactions, we computed the non-truncated electrostatic potential throughout Ewald Summations.[45] The real space term was determined by the van der Waals cut-off (16 Å), while the reciprocal term was estimated by interpolation of the effective charge into a charge mesh with a grid thickness of 5 points per volume unit, *i.e.* Particle-Mesh Ewald (PME) method.[46] Bond lengths were constrained using the SHAKE algorithm[47] with a numerical integration step of 1 fs. Periodic boundary conditions were applied using the nearest image convention, and the non-bonded pair list was updated every 1000 steps (1 ps).

3.3 RESULTS AND DISCUSSION

3.3.1 Synthesis and characterization of HAp particles

HAp particles with different morphologies were synthesized by chemical precipitation (see Experimental section) using the experimental conditions listed in **Table 3.1**. These conditions differ in the pH and temperature of the medium, the concentration of $\mathrm{Ca(NO_3)_2}$ in organic or aqueous solvent, and the application or not hydrothermal treatments. The morphologies of commercial HAp, HAp1, and the three prepared HAp samples, HAp2-HAp4, which are displayed in **Figure 3.1**, reflect the noticeable influence of each of the different factors examined in this work: pH, temperature of the reaction, solvent used with the reagents, and both hydrothermal and aging conditions. HAp2 (**Figures 3.1 d and e**) and HAp4 (**Figures 3.1 h and i**) show crystals with very different morphologies (*i.e.* flower-like and laminar crystals and fusiform rods). HAp3 particles,

which were obtained in an extremely alkaline reaction medium (pH > 11) and without hydrothermal treatment, are the only with nanospherical morphology (**Figures 3.1 f** and **g**).

Different morphologies were consistent with Ca/P ratios that deviate from the value of 1.67 for the stoichiometric cases, which reflects the presence of different faces *(i.e.* the formula unit of the surface unit cell cannot be expressed as an integer multiple of the formula of the HAp bulk unit cell). **Table 3.2** displays the Ca/P ratio for the different HAp particles as measured by EDX spectroscopy. The Ca/P ratio for HAp1 is 1.71 ± 0.25, the large deviation of the values being attributed to the coexistence of two different morphologies in such commercial sample (**Figures 3.1 a-c**). HAp2 exhibits a value lower than the stoichiometric ratio (1.37 ± 0.07), whereas HAp4 shows a higher value (1.94 ± 0.08). Finally, the HAp3 showed a stoichiometric Ca/P ratio of 1.69 ± 0.05.

Table 3.2. Ca/P ratio, zeta potential (ZP), particle dimensions (w = width; ℓ = length; h = height; and R = radious), surface area (S), crystallite size (L) and crystallinity (χ_c) obtained for HAp1-HAp4 particles. Average ± standard deviation values were derived from 6 independent measures.

Sample	**Ca/P ratio**	***ZP* (mV)**	***Particle dimensions* (nm)**	***S* (nm^2)**	***L* (nm)**	χ_c **(%)**
HAp1	1.71 ±0.25	−2.5±0.2	Sheets: w=273±37, ℓ=693±114, h=19±2 Rods: R=17±3, ℓ =105±12	Sheets: 10968±2129 Rods: 420330±117802	12±2	50±4
HAp2	1.37±0.07	−3.6±0.2	w=262±95, ℓ=227±68, h=15±4	125950±12656	22±3	100
HAp3	1.69±0.05	−1.3±0.1	R=32±4	13050±3060	6±1	3±1
HAp4	1.94±0.08	0.6±0.1	R=42±5, ℓ =276±15	1498±189	14±3	68±5

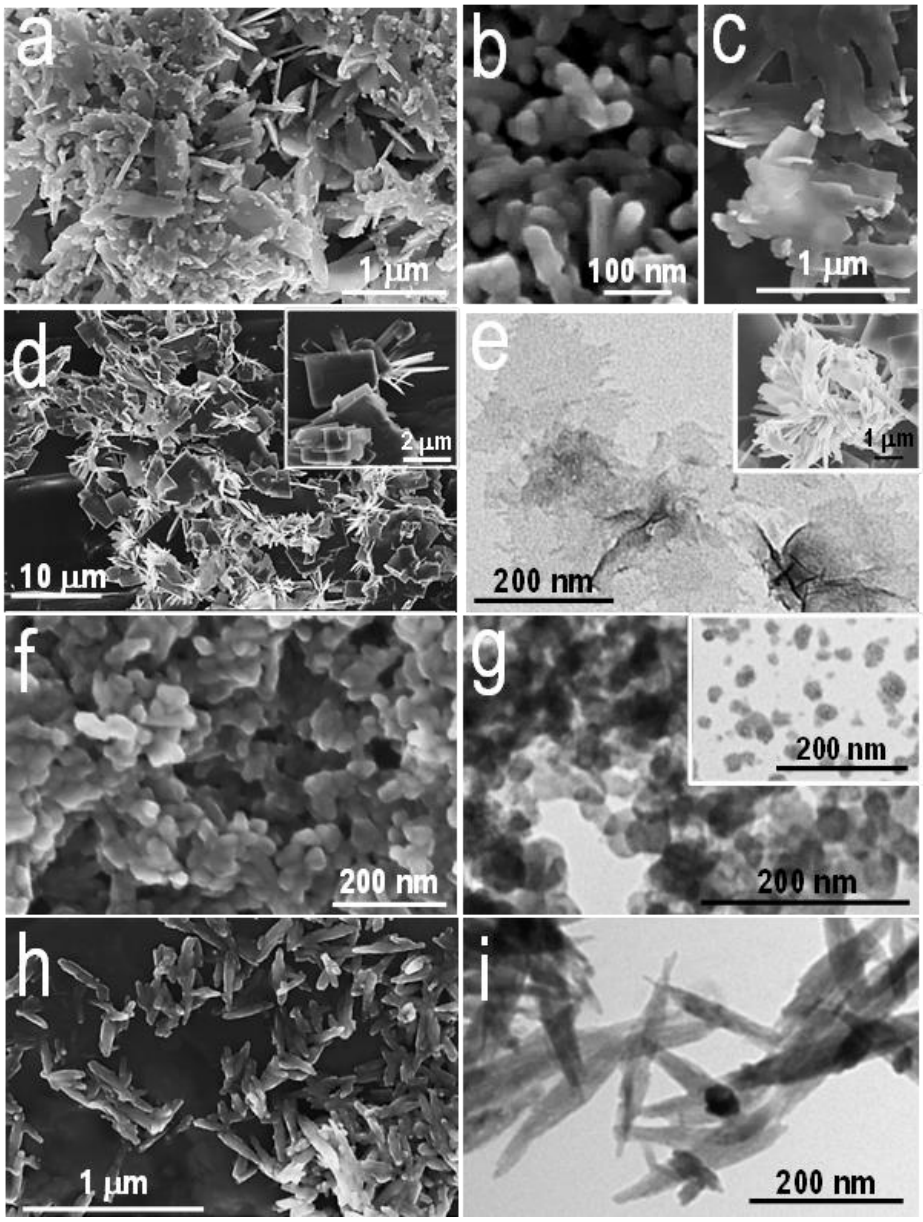

Figure 3.1. Morphology of HAp particles studied in this work: HAp1 (a-c), HAp2 (d-e), HAp3 (f-g), and HAp4 (h-i). HAp1 refers to commercial samples while HAp2-HAp4 correspond to samples prepared in this work by chemical precipitation (see Methods) using the experimental conditions displayed in **Table 3.1**. SEM images: a, b, c, d, f and h. TEM images: e, g and i.

Table 3.2 includes the main physical properties (*i.e*. zeta potential, particle dimensions, surface area, crystallite size and crystallinity) of the four HAp samples studied in this work. The zeta potential values of HAp3 and HAp4 (ZP = -1.3 ± 0.1 and $+0.6 \pm 0.1$ mV, respectively) are higher than those of commercial HAp1 (ZP = -2.5 ± 0.2 mV), which in turn is higher than that obtained for HAp2 (ZP = -3.6 ± 0.2 mV). As the zeta potentials were determined in deionized water, these values should be considered equivalent to the surface charge. These results combined with the crystallinities and $\mathrm{Ca/P}$ ratios listed in **Table 3.2** suggest that the surfaces of HAp4 and HAp2 crystallites may be dominated by the (010; $\mathrm{Ca^{2+}}$) and (010; $\mathrm{Ca^{2+}}$–$\mathrm{OH^{-}}$) terminations, respectively, of the (010) plane. Thus, the (010; $\mathrm{Ca^{2+}}$–$\mathrm{OH^{-}}$) termination, which involves $\mathrm{Ca^{2+}}$, $\mathrm{OH^{-}}$ and $\mathrm{PO_4^{3-}}$ at the top, and the (010; $\mathrm{Ca^{2+}}$) termination, with only $\mathrm{Ca^{2+}}$ and $\mathrm{PO_4^{3-}}$ at the top are consistent with the negative and positive surface charges obtained for HAp2 and HAp4, respectively. The zeta potential of HAp1, which is less negative than that of HAp2, may be attributed to the predominance of the (001) plane at the surface. The (001) plane is the most stable HAp surface[48] and was identified as the crystal growth plane during the biomineralization of teeth and hard tissues (dentine and enamel).[49-52] Furthermore, these faces also determine a morphology transformation from needles to plates.[52] All these features are consistent with the crystalline rods contained in HAp1 samples (**Figures 3.1 a and b**), which only show a crystallinity of 50 ± 4 %. Although the association of HAp1, HAp2 and HAp4 to the (001), (010; $\mathrm{Ca^{2+}}$– $\mathrm{OH^{-}}$) and (010; $\mathrm{Ca^{2+}}$) surfaces, respectively, is an assumption derived from the zeta potential values and the surface Ca/P ratios listed in **Table 3.2**, results described in the next-subsections are fully consistent with these hypotheses (see below). Finally, the moderately negative zeta potential of HAp3 samples, which are amorphous, results from the non-regular distribution of $\mathrm{Ca^{2+}}$, $\mathrm{PO_4^{3-}}$ and $\mathrm{OH^{-}}$ ions. This disordered distribution of ions is fully consistent with the stoichiometric $\mathrm{Ca/P}$ ratio measured at the surface of HAp3 samples by EDX.

The FTIR spectra of the four studied HAp samples are compared in **Figure 3.2** while **Table 3.3** quantifies the characteristic absorption bands by integrating the corresponding areas. Spectra clearly indicate a relationship between the morphology of HAp particles and the environment of phosphate groups. Spectra recorded for HAp1, HAp3 and HAp4 samples show typical $\mathrm{PO_4^{3-}}$ bands at the region comprised between 950 and 1200 $\mathrm{cm^{-1}}$, even though quantitative differences are detected, as is clearly evidenced in **Table 3.3**. Thus, the FTIR spectrum of commercial HAp1 sample shows characteristic

vibrational modes of PO_4^{3-} at $\nu_1 = 957\ cm^{-1}$ and $\nu_3 =$ 1016, 1084 cm^{-1}, the other two samples showing small (red and blue) shifts with respect to such values (*i.e.* $|\Delta\nu_1| \leq 5\ cm^{-1}$ and $|\Delta\nu_3| \leq 6\ cm^{-1}$). The spectrum of HAp2 shows a very remarkable resolution, presenting high (blue) shifts ($|\Delta\nu_1| \leq 37\ cm^{-1}$ and $|\Delta\nu_3| \leq 42{,}41\ cm^{-1}$) in comparison with the rest of the samples, which is consistent with a notorious morphological change and their Ca/P ratio.

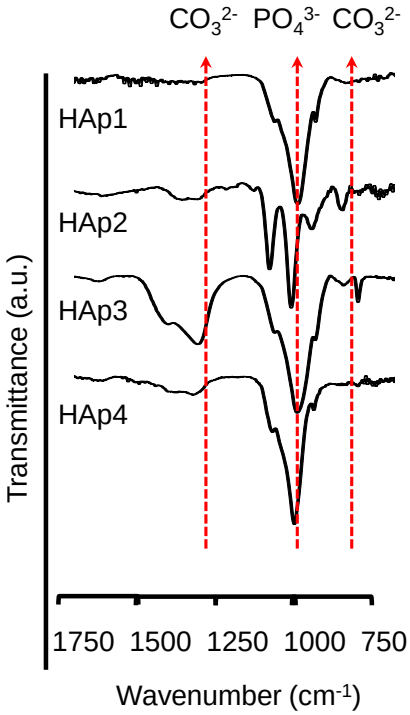

Figure 3.2. FTIR spectra of the HAp particles studied in this work.

Table 3.3. Main infrared absorption bands (cm^{-1}) for HAp particles. Integrated band relative areas are displayed in parenthesis.

	PO_4^{3-}		CO_3^{2-}	
	ν_1	ν_3	ν_2	ν_3
HAp1	957	1016, 1084	862	1419
	(5.03 %)	(57.93 %, 19.87 %)	(3.73 %)	(13.43 %)
HAp2	994	1058, 1125	900	1376
	(19.30 %)	(38.79 %, 22.97 %)	(5.15 %)	(13.78 %)
HAp3	954	1013, 1090	826, 873	1330,1424
	(2.91 %)	(44.16 %, 10.04 %)	(1.24 %, 1.21 %)	(23.18 %, 17.26 %)
HAp4	962	1022, 1059, 1089	867	1346, 1433
	(5.28 %)	(52.06 %, 4.22 %, 17.6 %)	(3.22 %)	(10.58 %, 7.03 %)

The absorption bands at ~ 870 cm^{-1} (ν_2) and the most intense ~1400 cm^{-1} (ν_3) due to CO_3^{2-} reflects that this group also plays an important role in HAp morphology. Thus, independently of the experimental conditions used for the preparation of the particles, carbonated HAp samples have been obtained in all cases. However, HAp3 sample, in which ν_2 and ν_3 occur as broad doublets at 826, 873 cm^{-1} and 1330, 1424 cm^{-1} (**Figure 3.2**), respectively, shows the highest fraction of CO_3^{2-}. The integrated area ratios of the bands due to CO_3^{2-} and PO_4^{3-} groups in HAp3 is 0.75 while in the rest of the samples this ratio is smaller than 0.3

Characterization of four investigated particles by X-ray diffraction (**Figure 3.3**) was focused on peaks at 33º–34º 2θ, which are characteristics of the (211), (112), and (300) HAp reflections. As it can be seen in **Figure 3.3 b**, the diffraction pattern of HAp2 clearly reflects the presence of other crystalline calcium phosphate forms, in addition to those characteristic of HAp. More specifically, dicalcium phosphate anhydrous ($CaHPO_4$; DCPA), and dicalcium phosphate dihydrate ($CaHPO_4 \cdot 2H_2O$; DCPD) are identified in such sample, explaining its low Ca/P ratio. The coexistence of HAp and other calcium phases in HAp2, which has been also observed in the material precipitated from aqueous calcium phosphate solutions, has been attributed to the incomplete transformation of transient phases to HAp or to the co-precipitation of HAp with the other calcium phosphate phases. The coexistence of different calcium phosphates has been observed *in vivo*, also suggesting that DCPA and DCPD are intermediate phases.[53] In fact the latter assumption is reinforced by the transformation of dicalcium phosphate into HAp upon immersion in synthetic body fluid solutions.[54]

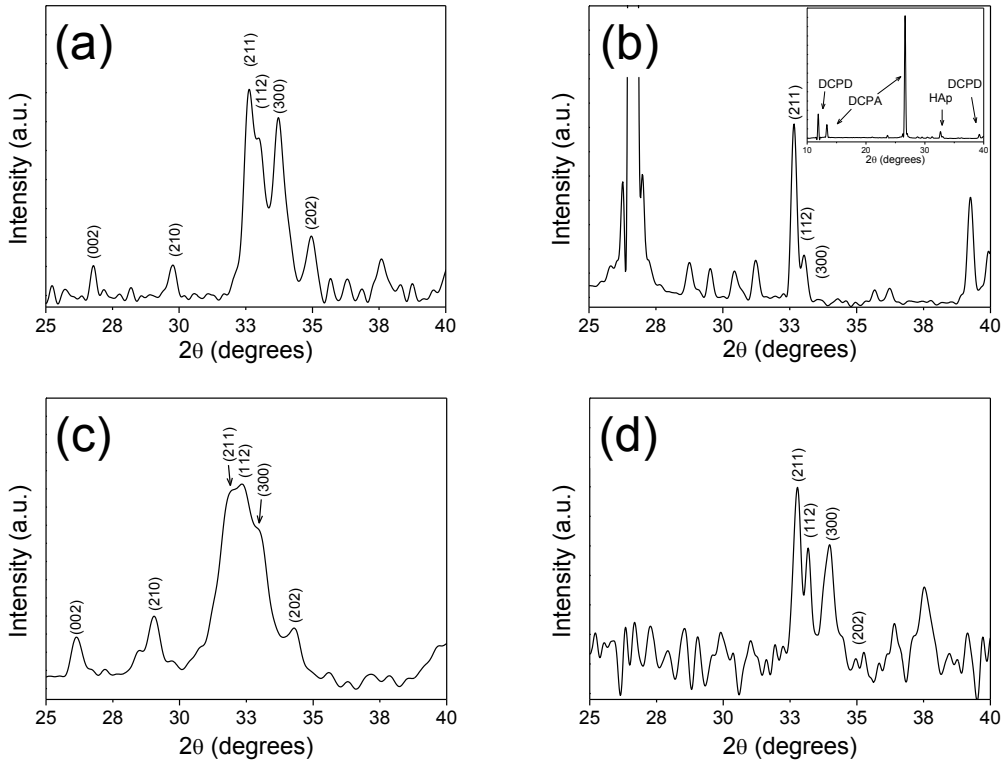

Figure 3.3. X-ray diffraction patterns of the HAp particles studied in this work. The hydroxyapatite was identified by the peaks at 33º–34º 2θ. (a) HAp1, (b) HAp2, (c) HAp3 and (d) HAp4. Inset in (b) shows the patterns at 10º–40º 2θ to demonstrate the mixture of HAp with others calcium phosphate phases (see text).

The use of HAp particles as non-viral gene carrier requires not only the adsorption of of DNA but also the dissolution of the inorganic particles once HAp-DNA complexes have penetrated into the cell. As the latter process may be determined by the compositional and physical differences (**Tables 3.2 and 3.3**), investigation of the response of the four HAp particles to acidic environments is required. Titration results (**Figure 3.4**) indicated a steep pH gradient for HAp4, whereas the slow and gradual variation of the pH evidenced a remarkable buffering effect for the rest of the samples. The exponential decay of the pH (y) against the concentration of HCl (x) for suspensions of the different particles was modeled using the following Eqn:

$$y = y_0 + A \cdot e^{\left(\frac{-x}{\tau}\right)} \qquad (3)$$

where y_0 corresponds to the pH of the acidified suspension once stabilized, *A* is a constant that represent the reduction of the pH with respect to the initial value and τ is a

constant to express the pH exponential decay. Adjustment of the experimental data led to the parameters listed in **Table 3.4**. As it can be seen, the buffering effect is very low for HAp4 that shows the highest *A* value (3.20 ± 0.10). The latter value perfectly reflects the measured pH reduction, ΔpH, from 7.08 to 3.61. HAp1 and HAp3 present the highest buffering effect with *A* values of only 1.55 ± 0.07 and 1.79 ± 0.06, respectively, while HAp2 shows an intermediate situation (*i.e.* $A = 2.16 \pm 0.07$). On the other hand, comparison of the τ values indicates that the buffering response is about two-folds faster for HAp1 than HAp3. The overall of these results evidence that chemical composition, especially the CO_3^{2-}/PO_4^{3-} ratio, plays a major role in the proton-buffering capacity in HAp particles.

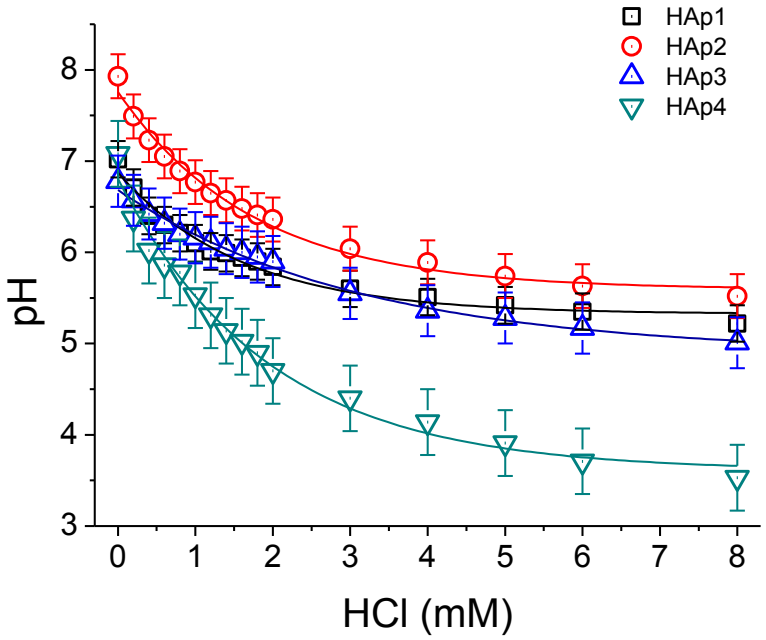

Figure 3.4. Proton-buffering capacity of the HAp particles studied in this work.

Table 3.4. Results obtained from modeling (see Eqn 3) of the protonation ability of HAp particles.

	pH (initial)	y_0	*A*	τ (mM)	r^2
HAp1	7.02	5.32 ± 0.05	1.55 ± 0.07	1.61 ± 0.17	0.9726
HAp2	7.93	5.59 ± 0.06	2.16 ± 0.07	1.75 ± 0.13	0.9866
HAp3	6.78	4.89 ± 0.07	1.79 ± 0.06	3.12 ± 0.28	0.9907
HAp4	7.08	3.61 ± 0.09	3.20 ± 0.10	1.94 ± 0.17	0.9852

3.3.2 Binding of plasmid DNA to HAp particles

In order to evaluate the capacity of HAp surfaces to adsorb biomolecules, particles obtained in the previous section were incubated with plasmid DNA. Complexes were separated by centrifugation and detected by electrophoresis. **Figure 3.5 a** indicates that DNA is adsorbed onto the surface of all prepared HAp particles. However, the concentration of biomolecule adsorbed by different HAp samples, which was quantified by measuring the relative intensity of the fluorescence bands (**Figure 3.5 b**), grows with concentration of HAp in the DNA:HAp mixture. Furthermore, DNA adsorption depends on the HAp properties, HAp3 and HAp4 samples adsorbing more DNA than HAp1 and HAp2 (**Figure 3.5 b**). This is fully consistent with the zeta potential values displayed in Table 1 and the assumption that the surfaces of HAp2 and HAp1 particles are dominated by the negatively charged (010; $Ca^{+2} - OH^{-}$) and (001) planes, respectively. Thus, the DNA polyanions are easily adsorbed onto the amorphous and positively charged surfaces associated to HAp3 and HAp4, respectively. On the other hand, HAp1 commercial particles show a linear behavior, even though the relative intensity of the fluorescence band for complexes formed using a 1:250 DNA:HAp mixture is relatively low (~ 20 %). In contrast an exponential behavior was identified for all synthesized particles, the relative intensity of the fluorescence band associated to DNA-HAp complexes derived from 1:250 mixtures reaching values of ~ 40 % (HAp2), ~ 70 % (HAp4) and ~ 80 % (HAp3).

The stability of DNA-HAp complexes was evaluated by examing the protection imparted by the HAp particles against *Sal*I restriction enzyme and *DNase*I endonuclease. Sal1 cuts off the pMT4 plasmid DNA at only one restriction site while *DNase*I is an unspecific endonuclease that attacks DNA independently of the sequence. The protecting activity was tested for complexes derived from DNA:HAp mixtures with 1:100 and 1:250 w/w ratios, which showed the highest concentration of adsorbed DNA. **Figure 3.6 a**, which displays the electrophoretograms obtained after enzymatic digestion, clearly indicates that DNA receives protection against *Sal1* restriction enzymes in DNA-HAp complexes. Moreover, quantitative analyses of the fluorescence bands (**Figure 3.6 b**) evidences that HAp3 and HAp4 particles impart a very remarkable protection since ~ 80% of the DNA contained in both 1:100 and 1:250 complexes was preserved from *Sal1*. Results related with the protection imparted against unspecific *DNase*I are even more exciting. Although this enzyme attacks all positions of DNA because of its unspecific activity, biomolecules adsorbed onto HAp3 and HAp4 resist considerably the aggressive action of this enzyme

(**Figure 3.6 a**). Thus, ~ 20 % of DNA in DNA-HAp3 and DNA-HAp4 complexes remains protected from the digestion with *DNase*I (**Figure 3.6 c**).

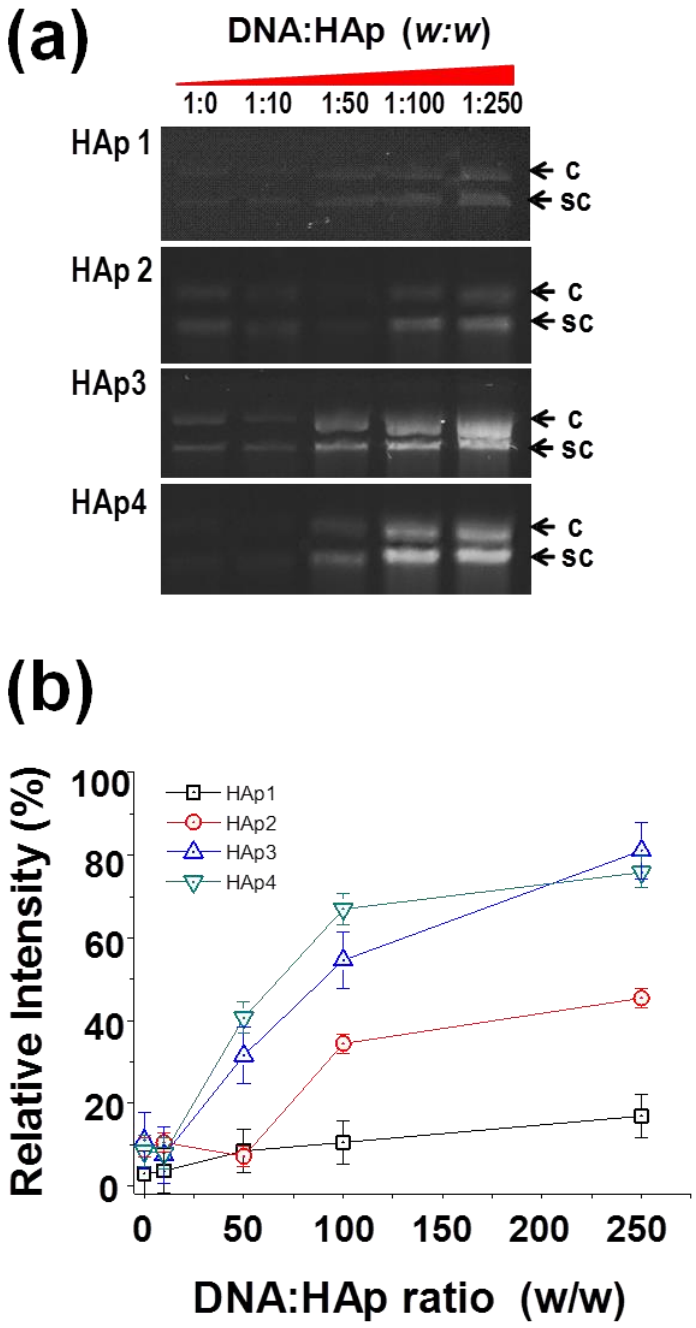

Figure 3.5. DNA:HAp complexes formed by mixing pMT4 plasmid DNA and HAp1-HAp4 particles considering 1:0, 1:10, 1:50, 1:100 and 1:250 w/w ratios: (a) agarose gel electrophoretograms in which circular and supercoiled conformations (c and sc, respectively) are observed; and (b) quantification through the relative intensity of the fluorescence band of the amount of DNA adsorbed in complexes derived from mixtures with different weight ratios.

In order to investigate the thermal stability of the biomolecules in DNA-HAp, complexes obtained using 1:100 and 1:250 mixtures were submitted to a thermal denaturalization process. **Figure 3.7 a** shows that the absorbance of DNA at 260 nm without HAp, which was used as control, increases ~ 41 % (hypochromic shift) when heated to 96 ºC for 10 min because of the higher exposure of all nitrogen bases. Analysis of the DNA response upon heating in DNA-HAp complexes reveals three different behaviors (**Figure 3.7 b**). Nitrogen bases are very exposed in DNA-HAp2 complexes, as is evidenced by the very large hypochromic effect. In contrast, the hypochromic shift is very low for DNA bases in complexes with HAp3 particles. This is consistent with a DNA compaction and, therefore, higher resistance against thermal denaturalization. Finally, the behavior of the biomolecule in DNA-HAp1 complexes is similar to that displayed by the control while the shift found for DNA-HAp4 complexes is intermediate between those of DNA-HAp1 and DNA-HAp3. The overall of these results clearly indicate that thermal denaturalization of DNA in DNA-HAp complexes is influenced by the physical properties of mineral particles, differences being fully consistent with the response of the different complexes towards the enzymatic attack.

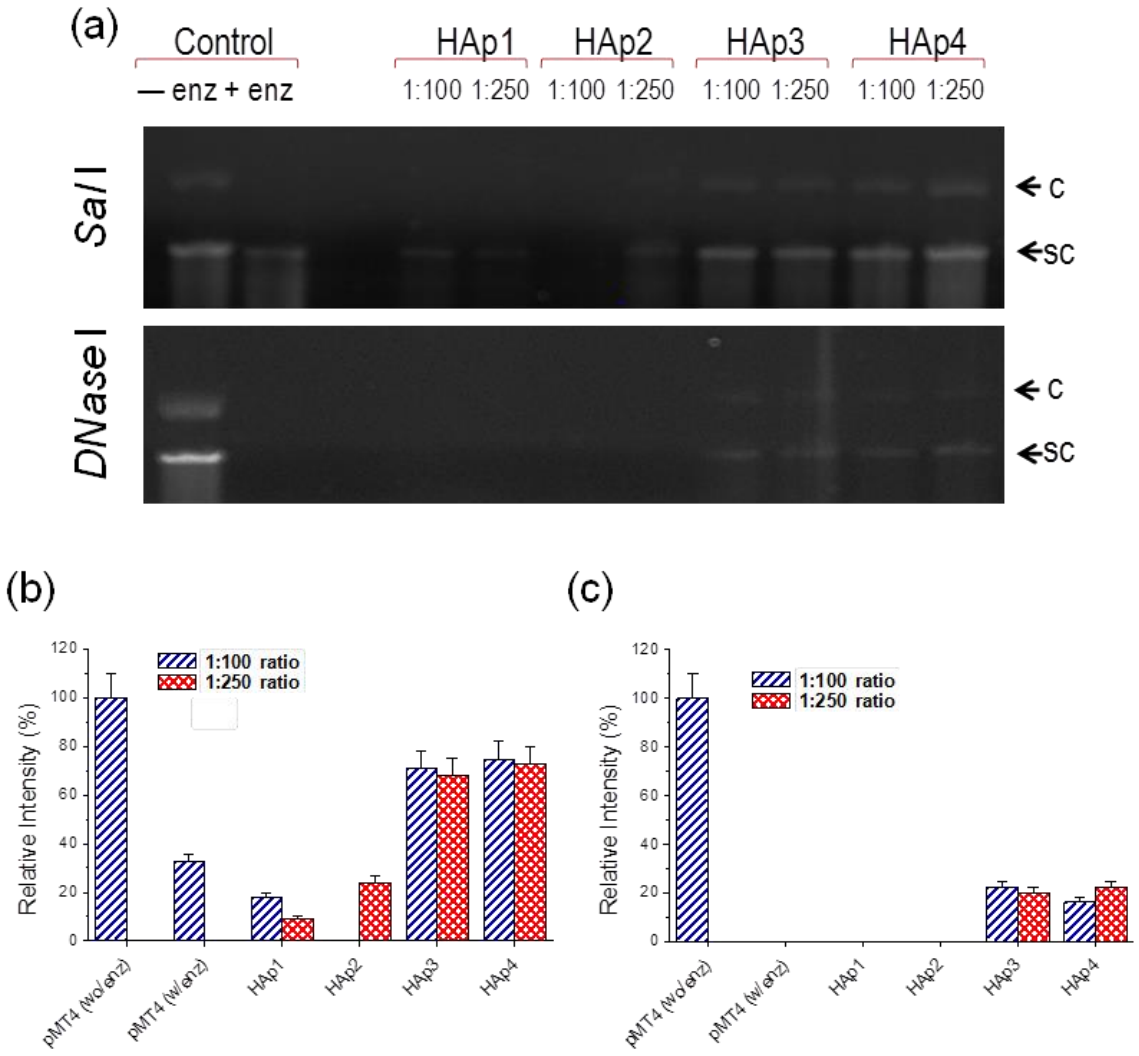

Figure 3.6. Enzymatic digestion of the DNA:HAp complexes: (a) agarose gel electrophoretograms of complexes derived from 1:100 and 1:250 mixtures after digestion with *Sal*I and *DNase*I. The pMT4 plasmid was used as control in the absence of the enzyme (– enz) and digested with the enzyme (+enz); (b) quantification of DNA that remains in the complexes after digestion with *Sal*I restriction enzyme; and (c) and quantification of DNA that remains in the complexes after digestion with *DNase*I unspecific nuclease.

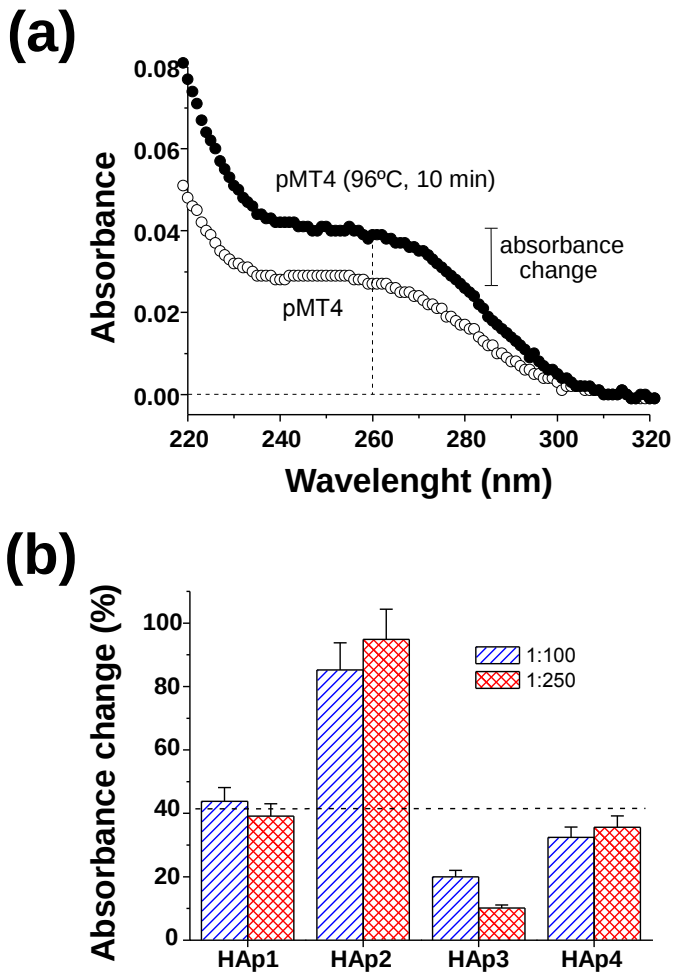

Figure 3.7. Thermal denaturation of DNA in DNA-HAp complexes: (a) hypochromic effect detected upon denaturation of pMT4 plasmid by incubating at 96 ºC during 10 min; (b) absorbance change after thermal denaturation for DNA-HAp complexes derived from mixtures with 1:100 and 1:250 w/w ratios. The dashed line represents the absorbance change in the pMT4 plasmid used as a control (see a).

3.3.3 Computer simulation of DNA adsorption onto HAp surfaces

To understand in detail the mechanisms of interaction between HAp and DNA at the molecular level, the focus should be on the microstructure of HAp. For this purpose, we have concentrated in the most significant HAp surfaces, which are the (001) and (010). More specifically, the ability to bind DNA has been modeled considering surfaces constructed using the (001) plane and both the (010; $Ca^{+2} - OH^{-}$) and (010; Ca^{+2}) terminations, which have been attributed to the HAp1, HAp2 and HAp4 samples, respectively. The (010) surface with the hydroxyl channels lying parallel to the surface has been found to interact more strongly with some negative charged species than the

(001).[37] In spite of this, the (010) is thermodynamically less stable than the (001) plane.[37,52]

The DNA double helix was placed above each constructed surface and considering different starting positions. All these systems were solvated and neutralized by adding water molecules and Na^+ ions, respectively. After several short MD runs to thermalize and equilibrate, for each surface the most stable system was selected for production NPT-MD runs. **Figure 3.8** compares the initial system with the system after 15 ns of NPT-MD for each surface. The response of the DNA double helix towards the (001), (010; $Ca^{+2} - OH^-$) and (010; Ca^{+2}) surfaces is apparently very different. Thus, the forces exerted by OH^-ions of the (010; $Ca^{+2} - OH^-$) termination seem to induce significant structural distortions in the bounded DNA double helix while such secondary structure is preserved for the biomolecule adsorbed by the (001) and (010; Ca^{+2}) surfaces.

In order to analyze this feature, representative structural parameters have been examined. **Figure 3.9** represents the temporal evolution of the end-to-end distance (d_{ee}) as the distance between the center of masses of the first and last pairs of nucleotides, the inter-strand distance (D_{cc}), which has been calculated as the average distance between the center of masses of each pair of nucleotides, and the root mean square deviation (RMSD) between the DNA structures adsorbed onto HAp surfaces and the canonical B-DNA double helix. Furthermore, an additional 15 ns NPT-MD simulation has been carried out considering the B-DNA double helix immersed in simulation box full of explicit water molecules. Results, which are included in **Figure 3.9**, have allowed us to set the upper and lower limits of variation for dee and D_{cc}. Thus, these limits have been defined using standard deviation associated to the average values obtained in for the stable B-DNA double helix in aqueous solution (*i.e*. without HAp).

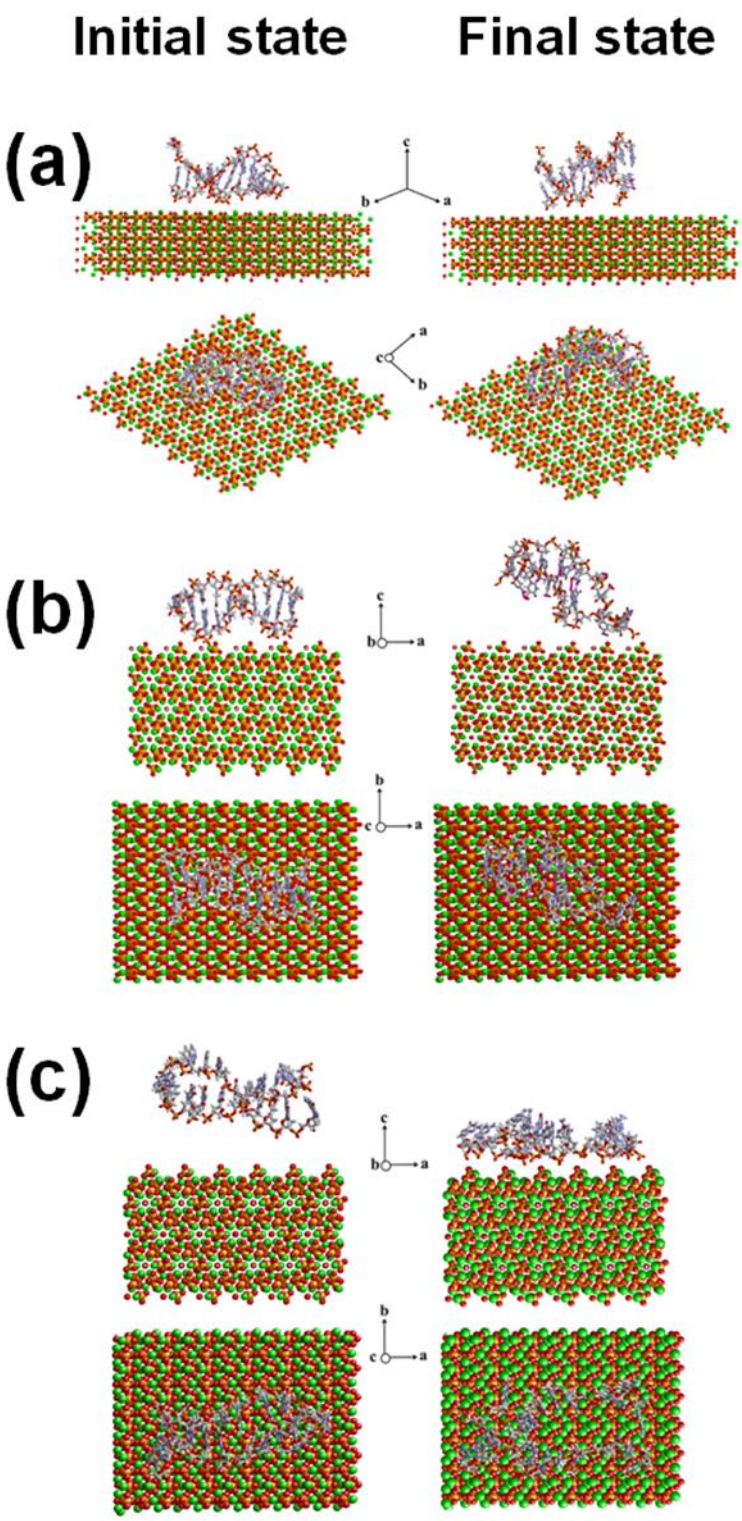

Figure 3.8. Snapshots showing the double helix DNA adsorbed at the (a) (001), (b) (010; Ca^{+2} – OH^{-}) and (c) (010; Ca^{+2}) surfaces at the beginning and end of the 15 ns NPT-MD simulations.

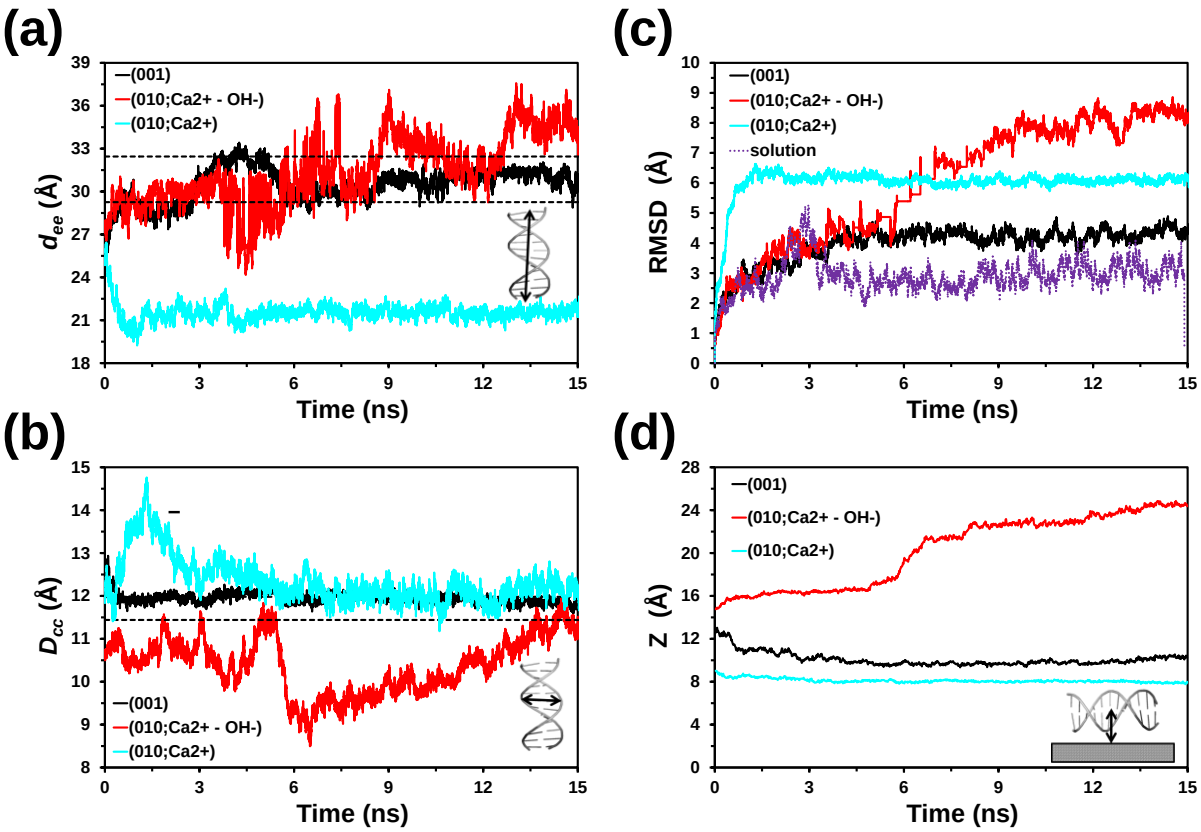

Figure 3.9. Temporal evolution of (a) the end-to-end distance, d_{ee}, the (b) inter-strand distance, D_{cc}, (c) the root mean square deviation, RMSD, with respect to the canonical B-DNA double helix, and (d) the distance between the center of mass of the double helix and the HAp, expressed as the z-coordinate of the normal vector to the surface, *Z*, for DNA adsorbed onto the (001), (010; $Ca^{+2} - OH^{-}$) and (010; Ca^{+2}) surfaces. Upper and lower limits for the dee and D_{cc}, B-DNA double helix, which were estimated from a 15 ns MD simulation in solution, are represented in (a) and (b) using dashed lines. The RMSD obtained for the DNA in solution has been included in (c).

The temporal evolution of the d_{ee} (**Figure 3.9 a**) for the DNA adsorbed onto the (001) surface remains within the lower and upper limits defined by DNA in solution during almost the whole trajectory. Thus, the average dee value for the bounded biomolecule, $\langle d_{ee} \rangle = 30.5 \pm 1.2$ Å, is practically identical to that obtained in solution, $\langle d_{ee} \rangle = 30.8 \pm 1.6$ Å. The d_{ee} of the DNA adsorbed onto the (010; $Ca^{+2} - OH^{-}$) exhibits significant fluctuations exceeding the upper and lower limits, as is evidenced by the large deviation associated to the average value, $\langle d_{ee} \rangle = 31.5 \pm 2.4$ Å. Finally, the biomolecule experiences a drastic shortening upon adsorption onto the (010; Ca^{+2}), stabilizing very rapidly, $\langle d_{ee} \rangle = 21.5 \pm 0.6$ Å. Similar conclusions are reached by examining the temporal evolution of D_{cc} (**Figure 3.9 b**). The value for the DNA adsorbed onto the (001) surface

remains practically constant and very close to the upper limit derived from simulations in solution. In contrast, the value for the biomolecule bounded to the (010; $Ca^{+2} - OH^{-}$) shows significantly fluctuations and is clearly smaller than the lower limit. The latter reduction is consisting with a loss of secondary structure. Finally, although the adsorption onto the (010; Ca^{+2}) initially provokes an expansion of the inter-strand distance, after ~ 5 ns this parameter equilibrates at a value ~ 0.4 Å higher than that reached for the (001). Thus, the average D_{cc} values for the DNA adsorbed onto the (001), (010; Ca^{+2} – OH^{-}) and (010; Ca^{+2}) surfaces is $\langle D_{cc} \rangle = 11.95 \pm 0.13$, 10.40 ± 0.67 and 12.33 ± 0.53 Å, respectively. The value reached in diluted aqueous solution, $\langle D_{cc} \rangle = 11.71 \pm 0.27$ Å, is similar to that obtained for the biomolecule onto the (001) surface. **Figure 3.9 c** shows the RMSD with respect to the canonical B-DNA. The double helix is remarkable stable when the biomolecule is in solution or bounded to the (001) surface with an average value of 2.91 ± 0.54 and 3.96 ± 0.25 Å, respectively. In opposition, the RMDS increases progressively for the DNA adsorbed onto the two terminations of the (010) surface, values higher than 8 and 6 Å being reached after 15 ns for the (010; $Ca^{+2} - OH^{-}$) and (010; Ca^{+2}), respectively.

Local distortions in adsorbed DNA have been investigated by comparing the radial distribution functions of $P \cdots P$ pairs (where P refers to the phosphor atoms contained in phosphate groups of DNA), $g_{P-P}(r)$ (**Figure 3.10 a**), and $H \cdots O$ pairs (where H and O refers to the hydrogen atoms of $R - NH_2$ groups and oxygen atoms of DNA bases located at the internal side of the double helix), $g_{H-O}(r)$ (**Figure 3.10 b**), for the biomolecules adsorbed onto the (001), (010; $Ca^{+2} - OH^{-}$) and (010; Ca^{+2}) surfaces and the biomolecule in aqueous solution. The $g_{P-P}(r)$ profile calculated for the DNA in solution show a sharp bimodal peak centered at $r = 6.4$ and 7.0 Å that is enhanced for the biomolecule adsorbed onto the (001) surface. However, the peak of the profile calculated for (010; $Ca^{+2} - OH^{-}$) becomes smaller and broader, suggesting some type of short-range deformations at the DNA backbone. The biomolecule adsorbed onto the (010; Ca^{+2}) also deviates from the in solution behavior, even though differences are considerably less pronounced than for the (010; $Ca^{+2} - OH^{-}$). These local distortions affect inter-strand hydrogen bonding interactions, which are essential to retain the secondary structure. Thus, the $g_{H-O}(r)$ calculated for the DNA in solution clearly

indicates a large number of sharp and narrow peaks, the one centered at r =1.9 Å being associated to hydrogen bonds between complementary bases. This peak is clearly identified in the profile calculated for the DNA adsorbed onto the (001) surface but it disappears when the biomolecule is deposited onto the two terminations of the (010) surface. Thus, the first peak detected for the (010; $Ca^{+2} - OH^{-}$) and (010; Ca^{+2}) is centered at r = 3.2 and 3.5 Å, respectively, indicating that the accumulation of local distortions provokes the loss of secondary structure evidenced in **Figures 3.8 and 3.9**.

Snapshots at the end of the MD trajectories (**Figure 3.11**) suggest that the DNA on the (010; $Ca^{+2} - OH^{-}$) surface is only partially adsorbed (*i.e.* one of the double helix extremes fluctuates freely) while the biomolecule is completely adsorbed onto the (001) and (010; Ca^{+2}) because of the higher number of interaction sites. **Figure 3.9 d** represents the temporal evolution of the distance between the center of mass of the DNA double helix and the HAp, expressed as the *z*-coordinate of the normal vector to the surface (*Z*), for the three simulated systems. As it can be seen, after thermalization and equilibration trajectories the parameter *Z* at the beginning of the production trajectory was 12.6, 14.7 and 9.0 Å for the (001), (010; $Ca^{+2} - OH^{-}$) and (010; Ca^{+2}), respectively. For the former surfaces *Z* decreases to ~ 10 Å in ~ 2.5 ns while for the (010; Ca^{+2}) decreases to ~ 8 Å in ~ 5 ns, stabilizing at such values. The average value considering the last 10 ns of production trajectory is $\langle Z \rangle$ = 9.85 ± 0.25 and 8.02 ± 0.09 Å for the (001) and (010; Ca^{+2}), respectively. This feature indicates that the re-arrangements in the DNA double helix (**Figure 3.8**) are accompanied by an enhancement of the binding to the surface. In opposition, for the (010; $Ca^{+2} - OH^{-}$) *Z* progressively increases from 14.7 to ~ 16.5 Å in the first 5 ns of trajectory, the latter value increasing in only 1.5 ns to ~ 21.5 Å. Finally, in the last 7 ns of trajectory, *Z* increases slowly but progressively from ~ 22.8 to 24.5 Å. This profile indicates that, actually, DNA is slowly released from the (010; $Ca^{+2} - OH^{-}$) surface undergoing a desorption process.

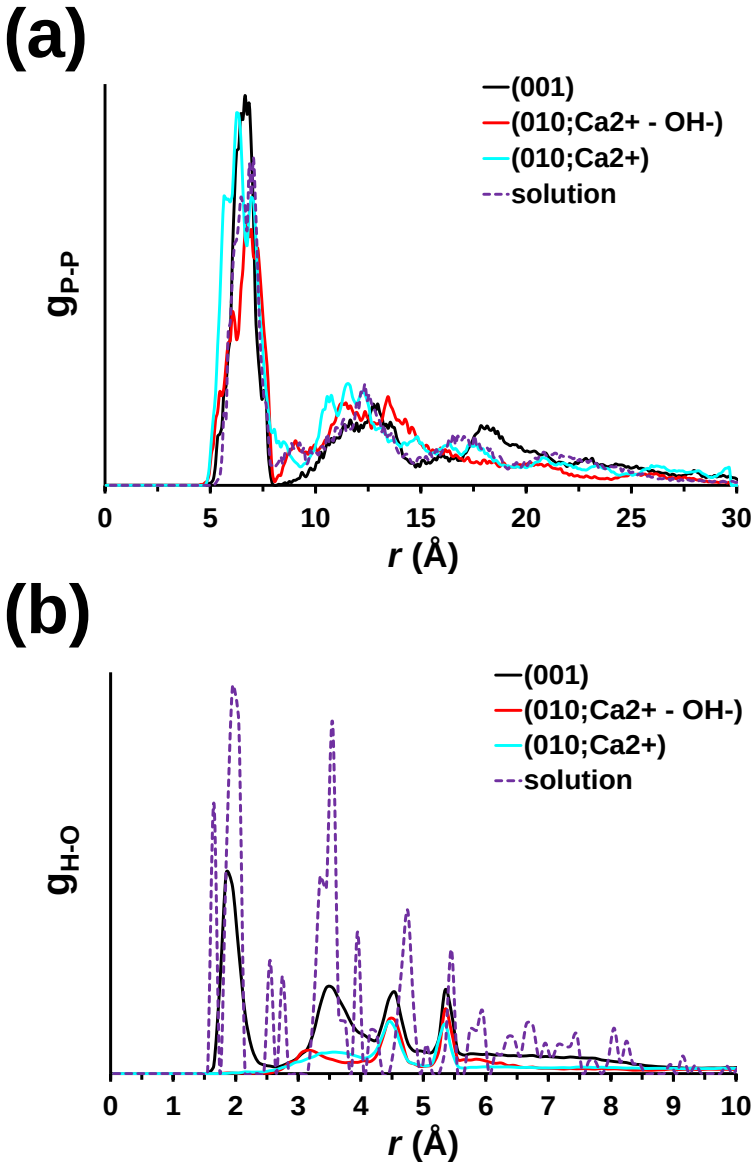

Figure 3.10. Radial distribution functions of (a) $\mathrm{P}\cdots\mathrm{P}$ and (b) $\mathrm{H}\cdots\mathrm{O}$ atom pairs for the DNA double helix adsorbed onto the (001), (010; $\mathrm{Ca}^{+2}-\mathrm{OH}^{-}$) and (010; Ca^{+2}) surfaces, and immersed in water. P refers to the phosphor atoms of the phosphate groups at the DNA backbone, whereas H and O correspond to the hydrogen atoms of $\mathrm{NH_2}$ groups and oxygen atoms of DNA bases located at the internal side of the double helix.

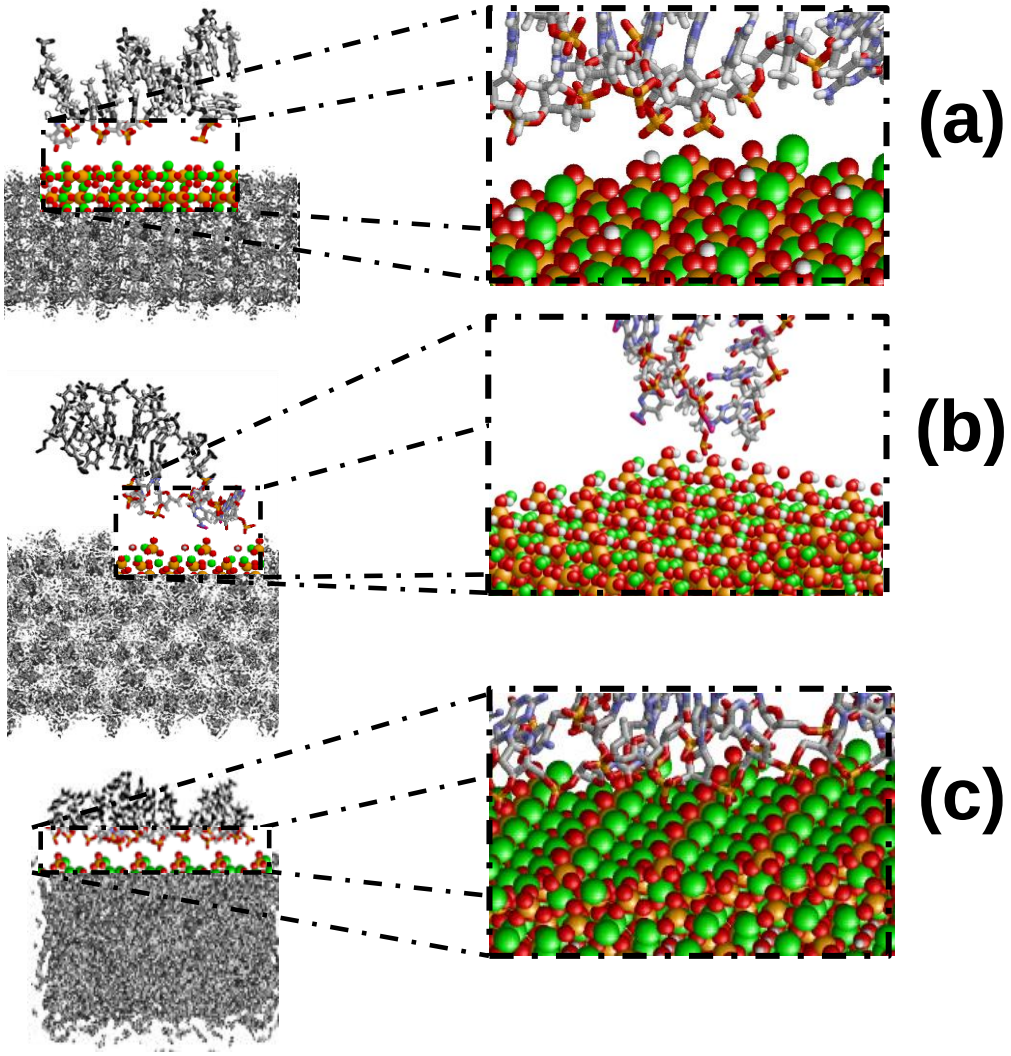

Figure 3.11. Snapshots showing details of: (a) the attractive Ca^{+2} (surface)···phosphate(DNA) interactions at the (001) surface; (b) the repulsive OH^{-} (surface)···phosphate(DNA) interactions at the (010; $Ca^{+2} - OH^{-}$) surface; and the attractive Ca^{+2} (surface)···phosphate(DNA) interactions at the (010; Ca^{+2}) surface.

The binding energy (E_{bind}) associated to the adsorption of a DNA molecule to the HAp suface was roughly estimated as the sum of the electrostatic and van der Waals contributions from DNA···surface interactions (E_{ele} and E_{vdW}, respectively). The average energy contributions obtained for the biomolecule adsorbed onto the (001) surface are $\langle E_{bind} \rangle = -8508 \pm 251$ kcal/mol, $\langle E_{ele} \rangle = -8497 \pm 252$ kcal/mol and $\langle E_{vdW} \rangle = -11 \pm 3$ kcal/mol, indicating that the adsorption of DNA at this surface is thermodynamically favorable. This process is energetically favored by the stabilizing surface···DNA electrostatic contribution, which is essentially due to the attractive Ca^{+2}

(surface)···phosphate(DNA) interactions (**Figure 3.11 a**). The strength of the interaction between the adsorbed biomolecules and the (010; Ca^{+2}) surface is almost three times more attractive: with $\langle E_{bind} \rangle = -21561 \pm 4$ 73 kcal/mol, $\langle E_{ele} \rangle = -21518 \pm 467$ kcal/mol and $\langle E_{vdW} \rangle = -43 \pm 6$ kcal/mol. This has been attributed to the disposition of the Ca^{+2} ions, which act as binding sites, is very suitable to interact with the phosphate (DNA) groups once the double helix undergoes deformation (**Figure 3.11 c**). In contrast, the average values obtained for the DNA adsorbed onto the (010; $\mathrm{Ca}^{+2} - \mathrm{OH}^{-}$) surface clearly reflect a repulsive process, which is fully consistent with the structural results and desorption process discussed above: $\langle E_{bind} \rangle = 10825 \pm 37$ kcal/mol, $\langle E_{ele} \rangle = 10868 \pm 4$ 4 kcal/mol and $\langle E_{vdW} \rangle = -43 \pm 9$ kcal/mol. The poor affinity of DNA towards the (010; $\mathrm{Ca}^{+2} - \mathrm{OH}^{-}$) is due to the disposition of the negatively charged hydroxyl group, which interact repulsively with the DNA phosphate groups. This is clearly evidenced in **Figure 3.11 b**, which displays the disposition of the surface hydroxyl groups shielding the attractive interactions Ca^{+2} (surface)···phosphate(DNA). The role of the van der Waals interactions is practically negligible for the surfaces constructed using the two terminations of (010) plane, the importance of the electrostatic contribution being noticeably higher than that reported for DNA strands deposited on other kind of surfaces, as for example gold[55] and carbon nanotubes.[56]

These results are fully consistent with experimental data discussed above, which evidenced very different sensitivities of the prepared HAp samples towards DNA adsorption. It is well-known that HAp surfaces are responsible of the crystal morphology. Synthetic HAp crystals are often facetted with the possible six equivalent faces related with the (001) surface in hexagonal symmetry.[57] All these faces have been reported to adsorb negatively charged carboxylate groups.[55] This behavior is in agreement with the affinity of HAp1 towards DNA. Thus, the surface charge and surface $\mathrm{Ca/P}$ ratio is consistent with the predominance of (001) planes in semicrystalline commercial HAp1 samples. It is possible to grow highly crystalline HAp particles with platelet morphology exposing the (010) planes as basal surfaces, and the (001) and (100) as lateral terminations.[58] Morphological and physical properties (**Figure 3.1 and Table 3.2**, respectively) suggest that the (010) is the most abundant place in of HAp2 and HAp4, difference between the two samples being attributed to the facet termination. The (010) plane was found to adsorb glycine amino acid, through both the N atom and the negatively charged COO^{-} group.[49] De Leeuw and co-workers[37] studied the interaction

of (010) HAp surfaces with glycine, proline and hydroxyproline amino acids, which are major constituents of collagen I protein. Results revealed that interactions involving the hydrogen atoms attached to the nitrogen of amine and the oxygen atoms belonging to the surface hydroxyl and phosphate groups play a decisive role in the binding of these amino acids to the (010; $Ca^{+2} - OH^{-}$) termination of this surface.[37] It is worth nothing that $N - H$ and $N - H_2$ groups belonging to the DNA bases are less accessible than the backbone phosphate groups because of the formation of inter-strand hydrogen bonds through base pairing. Accordingly, adsorption of double stranded DNA onto the (010; Ca^{+2}) is a very favorable process while it is disfavored when termination of the surface corresponds to the (010; $Ca^{+2} - OH^{-}$). These results are in excellent agreement not only with the DNA adsorption abilities determined for HAp2 and HAp4 (**Figure 3.5 b**) but also with protection imparted by these particles to adsorbed DNA (**Figures 3.6 and 3.7**). Accordingly, simulation results discussed in this section explain at the molecular level our previously discussed experimental observations, which evidenced that HAp properties affect not only to the DNA adsorption ability but also to the protection imparted to the biomolecule upon the attack of nucleases and thermal denaturalization.

3.3.4 Transfection of pMT4-HAp complexes into *E.coli*

In order to evaluate the efficacy of the different HAp particles as vectors for transfection processes, plasmid DNA was introduced and amplified into *E. coli* bacteria. pMT4 contains an ampicillin resistance gene that is commonly used as a selectable marker in routine biotechnology. A heat shock protocol was applied to transfect centrifuged DNA-HAp complexes into competent bacteria, which were subsequently seeded into ampicillin-containing LB agar plates. Growth of the seeded colonies was observed after 16-24 h indicating that the fluidity of bacteria membranes was changed by the created temperature unbalance (42 ºC × 2 min), enabling the entry of DNA-HAp complexes. Internalized complexes form endosomes, endosomal escape of DNA depending on the proton buffering capacity of the different HAp particles. Thus, the pH of the endosomes decreased to 5 with time, provoking the disintegration and release of their components. Colonies were subsequently cultured in LB plate to promote plasmid DNA amplification. **Figure 3.12** shows purified plasmid DNA extracted from these cultures, the intensity of the bands being related with the transfection efficiency. As it can be seen, DNA bands derived from complexes with HAp2 and HAp4 are weak while bands obtained using HAp1 and HAp3 complexes show intensities similar to the control.

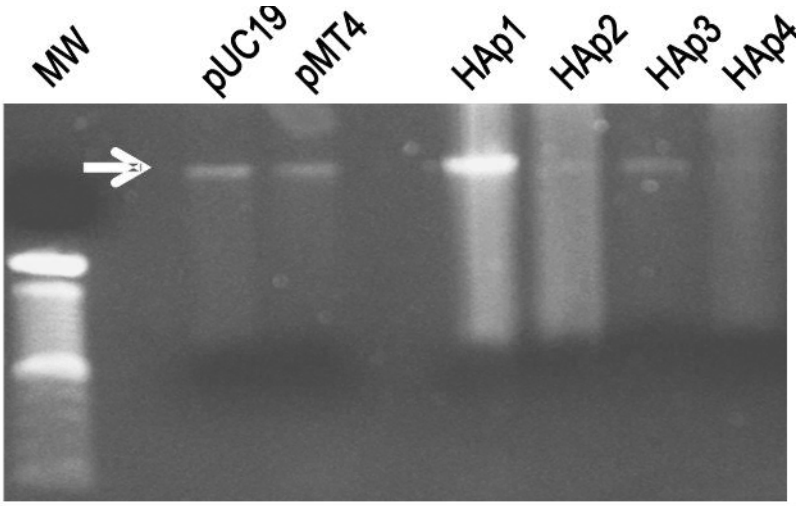

Figure 3.12. Agarose gel electrophoretograms showing the transformation of *E.coli* DH5α with the DNA:HAp complexes. The arrows indicate the pMT4 purified after of the culture of transformed bacteria**.**

Results displayed in **Figure 3.12** do not allow us to establish a direct relationship between transfection efficiency and the amount of plasmid DNA adsorbed on HAp particles (**Figure 3.5 b**) or the protection imparted by HAp particles against enzymes (**Figures 3.6 b and c**). However, comparison between results reported in **Figures 3.4 and 3.12** suggests that the response of HAp particules towards an acidic medium exerts a decisive influence in the transfection process. Thus, HAp1 and HAp3 present the highest proton-buffering capacity (**Table 3.4**).

3.4 CONCLUSIONS

HAp particles with different morphologies and composition have been prepared by modifying the experimental conditions used in the chemical precipitation process. The surfaces of these particles, which differ in the zeta potential (*i.e*. surface charge) and in the $\mathrm{Ca/P}$ ratio, show different abilities to adsorb DNA and protect the biomolecule towards nucleases. Structural changes induced in plasmid DNA during the adsorption process result in an increment of the resistance against enzymatic digestion. On the basis of their properties, the surface of HAp1, HAp2 and HAp4 crystalline particles has been assumed to be dominated by the (001), $(010; \mathrm{Ca}^{+2} - \mathrm{OH}^{-})$ and $(010; \mathrm{Ca}^{+2})$ planes, respectively. Atomistic computer simulations have been used to explain the influence of the HAp surface on the binding process and stability of DNA conformation.

The binding is favorable for the (001) surface which allows to maintain the B-DNA double helix conformation. In contrast, the binding is disfavored for the (010; $Ca^{+2} - OH^{-}$) with repulsive interactions provoking structural deformations in the DNA. The termination of the (010) surface with Ca^{+2} and PO_4^{3-} ions, (010; Ca^{+2}), adsorbs the biomolecule through very strong attractive interactions, even though the double helix undergoes structural distortions. On the other hand, the CO_3^{2-}/PO_4^{3-} ratio has been found to be responsible of different buffering capacity of HAp particles. Finally, transformation assays evidence that DNA-HAp complexes prepared in this work can be used as non-viral gene carriers. The overall of the results indicate that physical properties and composition of HAp play a crucial role in the ability to adsorb DNA while the buffering activity is essential for the transfection process.

3.5 REFERENCES

1. Dietz, H., Douglas, S.M. & Shih, W.M. Folding DNA into twisted and curved nanoscale shapes. *Science*. **325**, 725-730 (2007).
2. Stephanopoulos, N., Liu, M., Tong, G.J., Li, Z., Liu, Y., Yan, H. & Francis, M.B. Immobilization and one-dimensional arrangement of virus capsids with nanoscale precision using DNA origami. *Nano Lett*. **10**, 2714-2720 (2010).
3. Winfree, E., Liu, F., Wenzler, L.A. & Seeman, N.C. Design and self-assembly of two-dimensional DNA crystals. *Nature*. **394**, 539-544 (1998).
4. Zhang, C., Tian, C., Guo, F., Liu Z., Jiang, W. & Mao, C. DNA-Directed Three-Dimensional Protein Organization. *Angew. Chem., Int. Ed*. **51**, 3382-3385 (2012).
5. Goodman, R.P., Schaap, I.A.T., Tardin, C.F., Erben, C.M., R. M. Berry, R.M., Schmidt, C.F. & Turberfield, A.J., Rapid chiral assembly of rigid DNA building blocks for molecular nanofabrication. *Science*. **310**, 1661-1665 (2005).
6. Glimcher, M.J., in Metabolic bone disease and clinically related disorders, L. V. Avioli, S. M. Krane, Eds. (Academic Press, New York), pp. 23–50 (1998).
7. Hench, L.L., Biomaterials. *Science*. **208**, 826-831 (1980).
8. Hench, L.L & Wilson, J. Surface-active biomaterial. *Science*. **226**, 630-636 (1984).
9. Fu, Q., Saiz, E., Rahaman, M.N. & Tomsia, A.P. Toward strong and tough glass and ceramic scaffolds for bone repair. *Adv. Funct. Mater*. **23**, 5461-5476 (2013).
10. Bose, S., Fielding, G., Tarafder, S. & Bandyopadhyay, A. Understanding of dopant-induced osteogenesis and angiogenesis in calcium phosphate ceramics. *Trends Biotech.* **31**, 594-605 (2013).
11. Bohner, M. Resorbable biomaterials as bone graft substitutes. *Mater Today*, **13**, 24-30 (2010).
12. Roussiere, H., Fayon, F., Alonso, B., Rouillon, T., Schnitzler, V., Verron, E., Guicheux, J., Petit, M., Massiot, D., Janvier, P., Bouler, J.M. & Bujoli, B. Reaction of Zoledronate with beta-tricalcium phosphate, for the design of potential drug delivery systems. *Chem. Mater*. **20**, 182-191 (2008).
13. Galea, L., Bohner, M., Thuering, J., Doebelin, N., Aneziris, C.G. & Graule, T. Control of the size, shape and composition of highly uniform, non-agglomerated, sub-micrometer β-tricalcium phosphate and dicalcium phosphate platelets. *Biomaterials*. **34**, 6388-6401 (2013).
14. Zhang, J.T., Liu, W.Z., Schnitzler, V., Tancret, F. & Bouler, J.M. Calcium phosphate cements for bone substitution: chemistry, handling and mechanical properties. *Acta Biomater*. **10**, 1035-1049 (2014).
15. Schitzler, V., Fayon, F., Despas, C., Khairoun, I., Mellier, C., Rouillon, T., Massiot, D., Walcarius, A., Janvier, P., Gauthir, O., Montavon, G., Bouler, J.M. & Bujoli, B. Investigation of alendronate-doped apatitic cements as

a potential technology for the prevention of osteoporotic hip fractures: critical influence of the drug introduction mode on the in vitro cement properties. *Acta Biomater.* **7**, 759-770 (2011).

16. Revilla-López, G.**,** Casanovas, J.**,** Bertran, O.**,** Turon, P.**,** Puiggalí**,** J. & Alemán, C. Modeling biominerals formed by apatites and DNA. *Biointerphases*., **8**, 10-25 (2013).
17. Takeshita, T., Matsuura, Y., Arakawa, S. & Okamoto, M. Biomineralization of hydroxyapatite on DNA molecules in SBF: morphological features and computer simulation. *Langmuir*. **29**, 11975-11981 (2013).
18. Vasconcellos, K.B., McHugh, S.M., Dapsis, K.J., Petty, A.R., Gerdon, A.E. Biomimetic nanoparticles with polynucleotide and PEG mixed-monolayers enhance calcium phosphate mineralization. *J. Nanopart. Res.*, **15**, (1942).
19. Bertran, O., del Valle. L.J., Revilla-López, G., Chaves, G., Cardus L., Casas M.T., Casanovas J., Turon, P., Puiggalí, J. & Alemán, C. Mineralization of DNA into nanoparticles of hydroxyapatite. *Dalton Trans.* **3**, 317-327 (2014).
20. Okazaki, M., Yoshida, Y., Yamaguchi, S., Kaneno, M. & Elliot, J.C. Affinity binding phenomena of DNA onto apatite crystals. *Biomaterials*. **22**, 2459-2464 (2001).
21. Uskokovic, V. & Uskokovic, D.P. Nanosized hydroxyapatite and other calcium phosphates: chemistry of formation and application as drug and gene delivery agents. *J. Biomed. Mater. Res., Part B*. **96**, 152-191 (2011).
22. Olton, D., Li, J., Wilson, M. E., Rogers, T., Close, J., Huang, L., Kumta, N.P. & Sfeir, C. Nanostructured calcium phosphates (NanoCaPs) for non-viral gene delivery: influence of the synthesis parameters on transfection efficiency. *Biomaterials*. **28**, 1267-1279 (2007).
23. Gonzalez-McQuire, R., Green, D.W., Partridge, K.A., Oreffo, R.O.C., Mann, S. & Davis, S.A. Coating of Human Mesenchymal Cells in 3D Culture with Bioinorganic Nanoparticles Promotes Osteoblastic Differentiation and Gene Transfection. *Adv. Mater.* **19**, 2236-2240 (2007).
24. Maitra, A. Calcium phosphate nanoparticles: second-generation nonviral vectors in gene therapy. *Expert Rev. Mol. Diagn.* **5**, 893-905 (2005).
25. Epple, M., Ganesan, K., Heumann. R., Klesing. J., Kovtun, A., Neumann, S. & Sokolova, V. Application of calcium phosphate nanoparticles in biomedicine. *J. Mater. Chem.* **20**, 18-23 (2010).
26. Sokolova, V. & Epple, M., Inorganic Nanoparticles as Carriers of Nucleic Acids into Cells. *Angew.Chem. Int.Ed.* **47**, 1382-1395 (2008).
27. Keil, R.G., Montlucon D.B., Prahl, F.G. & Hedges, J.I. Sorptive preservation of labile organic matter in marine sediments. *Nature*. **370**, 549-552 (1994).
28. Ferris, J.P. Mineral catalysis and prebiotic synthesis: montmorillonite-catalyzed formation of RNA. *Elements A.* **1**, 145-149 (2005).
29. Lorenz, M.G. & Wackernagel, W. Bacterial gene transfer by natural genetic transformation in the environment. *Microbiol. Rev.* **58**, 563-602 (1994).

30. Romanowski, G., Lorenz M.G. & Wackernagel, W. Adsorption of plasmid DNA to mineral surfaces and protection against DNase I. *Appl. Environ. Microbiol.* **57**, 1057-1061 (1991).

31. Bernardi, G. Chromatography of nucleic acids on hydroxyapatite. *Nature*. **206**, 779–783 (1965).

32. Brundin, M., Figdor, D., Sundqvist, G. & Sjögren, U. DNA binding to hydroxyapatite: a potential mechanism for preservation of microbial DNA. *J. Endod.* **39**, 211-216 (2013).

33. Klug, H. & Alexander, L. in *X-Ray Diffraction Procedure for Polycrystallite and Amorphous Materials*, 2nd. Edition, John Wiley and Sons, New York (1974).

34. Landi, E., Tampieri, A., Celotti, G. & Sprio, S. Densification behaviour and mechanisms of synthetic hydroxyapatites. *J. Eur. Ceram. Soc.* **20**, 2377-2387 (2000).

35. Grzeskowiak, K., Goodsell, D.S., Kaczor-Grzeskowiak M., Cascio, D. & Dickerson, R.E. Crystallographic analysis of C-C-A-A-G-C-T-T-G-G and its implications for bending in B-DNA. *Biochemistry*. **32**, 8923-8931 (1993).

36. Stork, L., Muller, P., Dronskowski, R. & Ortlepp, J.R. A density functional theory study of the interaction of collagen peptides with hydroxyapatite surfaces. *Z. Kristallogr.* **220**, 201-205 (2005).

37. Almora-Barrios, N., Austen, K.F. & de Leeuw, N.H. Density functional theory study of the binding of glycine, proline, and hydroxyproline to the hydroxyapatite (0001) and (01$\bar{1}$0) surfaces. *Langmuir*. **25**, 5018-5025 (2009).

38. de Leeuw, N. H. Local ordering of hydroxy groups in hydroxyapatite. *Chem. Commun.* **17**, 1646-1647 (2001).

39. Phillips, J.C., Braun, R., Wang, W., Gumbart, J., Tajkhorshid, E., Villa, E., Chipot, C., Skeel, R.D., Kale, L. & Schulten, K.. Scalable molecular dynamics with NAMD. *J. Comput. Chem.* **26**, 1781-1802 (2005).

40. Cornell, W.D., Cieplak, P., Bayly, C.I., Gould, I.R., Merz, K.M., Ferguson, D.M., Spellmeyer, D.C., Fox, T., Caldwell, J.W. & Kollman, P.A. A second generation force field for the simulation of proteins, nucleic acids, and organic molecules. *J. Am. Chem. Soc.* **117**, 5179-5197 (1995).

41. Duan, Y., Chowdhury, S., Lee, M.C., Xiong, G., Zhang, W., Yang, R., Cieplak, P., Luo, R., Lee, T., Caldwell, Wang, J. & Kollman, P.A. A point-charge force field for molecular mechanics simulations of proteins based on condensed-phase quantum mechanical calculations. *J. Comput. Chem.* **24**, 1999-2012 (2003).

42. Hornak, V., Abel, R., Okur, A., Strockbine, B., Roitberg, A. & Simmerling, C. Comparison of multiple Amber force fields and development of improved protein backbone parameters. *Proteins*. **65**, 712-725 (2006).

43. Bradbrook, G.M., Gleichmann, T., Harrop, S.J., Habash, J., Raftery, J., Kalb, J., Yariv, J., Hillier, I.H. & Helliwell, J.R.. X-Ray and molecular dynamics studies of concanavalin-A glucoside and mannoside complexes Relating structure to thermodynamics of binding. *J. Chem. Soc. Faraday Trans.* **94**, 1603-1611 (1998).

44. Jorgensen, W.L., Chandrasekhar, J., Madura, J.D., Impey, R.W. & Klein, M.L.. Comparison of simple potential functions for simulating liquid water. *J. Chem. Phys.* **79**, 926-935 (1983).

45. Berendsen, H.J.C., Postma, J.P.M., van Gunsteren, W.F., DiNola, A. & Haak, J.R., Molecular dynamics with coupling to an external bath. *J. Chem. Phys.* **81**, 3684-3690 (1984).

46. Darden, T., York, D. & Pedersen, L. Particle mesh Ewald: An N -log(N) method for Ewald sums in large systems. *J. Chem. Phys.* **98**, 10089-10092 (1993).

47. Ryckaert, J.P., Ciccotti, G. & Berendsen, H.J.C. Numerical integration of the Cartesian Equations of Motion of a System with Constraints: Molecular Dynamics of n-Alkanes. *J. Comput. Phys.* **23**, 327-341 (1977).

48. Mkhonto, D. & de Leeuw, N.H., A computer modelling study of the effect of water on the surface structure and morphology of fluorapatite: introducing a $Ca_{10}(PO_4)_6F_2$ potential model. *J. Mater. Chem.* **12**, 2633-2642 (2002).

49. Kirkham, J., Brookes, S.J., Shore, R.C., Wood, S.R., Smith, D.A., Zhang, J., H. Chen, H. & Robinson, C. Physico-chemical properties of crystal surfaces in matrix–mineral interactions during mammalian biomineralisation. *Curr. Opin. Colloid Interface Sci.* **7**, 124-132 (2002).

50. Simmer, J.P. & Fincham, A.G. Molecular Mechanisms of Dental Enamel Formation. *Crit. Rev. Oral Biol. Med.* **6**, 84-108 (1995).

51. Kirkham, J., Firth, A., Vernals, D., Boden, N., Robinson, C., Shore, R.C., Brookes, S.J. & Aggeli, A. Self-assembling Peptide Scaffolds Promote Enamel Remineralization. *J Dent Res*. **86(5)** 426-430 (2007).

52. Magne, D., Pilet, P., Weiss, P. & Daculsi, G. Fourier transform infrared microspectroscopic investigation of the maturation of nonstoichiometric apatites in mineralized tissues: a horse dentin study. *Bone*. **29**, 547-552 (2001).

53. Karampas, I.A. & Kontovannis, C.G., Single molecule vibrational spectroscopy and microscopy. *Vibrational Spectroscopy*. **64**, 126-133 (2013).

54. Mandel, S. & Tas, A.C. Brushite ($CaHPO_4{\cdot}2H_2O$) to octacalcium phosphate ($Ca_8(HPO_4)_2(PO_4)_4{\cdot}5H_2O$) transformation in DMEM solutions at 36.5 °C. *Mater. Sci. Eng. C*. **30**, 245-254 (2010).

55. Liang, H., Li, Z. & Yang, J. Single-stranded DNA adsorption on chiral molecule coated Au surface: a molecular dynamics study. *Phys. Chem. Chem. Phys.* **12**, 4431-4434 (2010).

56. Karachevtsev, M.V., Gladchenko, G.O., Plokhootnichenko, A.M., Leontiev, V.S. & Karachevtsev, V.A. Adsorption of Biopolymers on SWCNT: Ordered Poly(rC) and Disordered Poly(rI). *J. Phys. Chem. B*. **117**, 2636-2644 (2013).

57. Sato, K. Inorganic-Organic Interfacial Interactions in Hydroxyapatite Mineralization Processes. *Top Curr. Chem.*, **270**, 127-153 (2007).

58. Sakhno, Y., Bertinetti, L., Iafisco, M., Tampieri, A., Roveri, N. & Martra, G. Surface Hydration and Cationic Sites of Nanohydroxyapatites with Amorphous or Crystalline Surfaces: A Comparative Study. *J. Phys. Chem. C*. **114**, 16640-16648 (2010).

4.

SYNERGISTIC APPROACH TO ELUCIDATE THE INCORPORATION OF MAGNESIUM IONS ONTO HYDROXYAPATITE

Although the content of Mg^{+2} in hard tissues is very low (*i.e*. typically $\leq$ 1.5 wt. %), their incorporation to synthetic hydroxyapatite (HAp) particles as well as their role in the mineral properties are still subject of intensive debate. In this work we use an experimental-computational approach to answer many of the open questions. Mg^{+2} –enriched HAp particles have been prepared using different synthetic approaches and considering different concentrations of Mg^{+2} in the reaction medium. The composition, morphology and structure of the resulting particles have been investigated using X-ray photoelectron spectroscopy, energy dispersive X-ray spectroscopy, scanning and transmission electron microscopies, FTIR and wide angle X-ray diffraction. After this scrutiny, the role of the Mg^{+2} in the first nucleation stages, before HAp formation, has been investigated using atomistic molecular dynamics simulations. Saturated solutions have been simulated with and without the presence of DNA, which has been recently used as a soft template in the biomineralization process. This synergistic investigation provides a complete picture of how Mg^{+2} ions affect the mineralization since the first stages.

4.1 INTRODUCTION

Bone and teeth mineral crystals are compositionally and structurally similar to the synthetic mineral calcium hydroxyapatite (HAp), $Ca_{10}(PO_4)_6(OH)_2$.[1,2] HAp allows cationic (for Ca^{+2}) and anionic (for PO_4^{3-} and/or OH^- groups) substitutions. Mg^{+2}, CO_3^{2-}, F^- and $SiO_4^{4-}$are among the most relevant ions that may be incorporated into HAp, these minor species affecting the morphology, stability and properties of the mineral.[3-6] In the case of HAp forming bone, ions are released into, or taken up from, the surrounding fluids during the normal remodeling processes. Specifically, incorporation of Mg^{+2} into the HAp lattice has been reported to be directly dependent on the Mg^{+2}/Ca^{+2} molar ratio, temperature, pH and presence of CO_3^{2-}.[7]

Mg^{+2} is widely spread in nature (*e.g*. sea and fresh water, biological fluids, and biological minerals).[8] Recent studies suggested that Mg^{+2} biologically acts as a crystallization switch by interacting with aspartate during natural biomineralization.[9] Although the content of Mg^{+2} in hard tissues is very low (Mg^{+2}. 1.23, 0.72 and 0.5–0.9 wt.% in dentine, bone and cementum, respectively),[10] it appears to play an important function in hard tissue metabolism. Mg^{+2} deficiency gives rise to decreased bone mass and increased bone fragility, owing to fewer osteoblasts and increased levels of osteoclasts.[11] Similarly, the abnormal level of Mg^{+2} in teeth is correlated with dental disease.[12] Therefore, understanding of the role played by Mg^{+2} on the regulation of calcium mineral formation is one of the important issues in the biomineralization process and biomaterials research community.

Despite a relatively large number of investigations, the influence of Mg^{+2} in HAp formation remains unclear and results generate some controversy. Some studies reported that Mg^{+2} stabilize amorphous calcium phosphate (ACP),[9,13] inhibiting the crystal growth of HAp.[14] Conversely other studies suggested that Mg^{+2} combines with PO_4^{3-} in supersaturated solutions reducing the anion activity and, therefore, inhibiting the transformation from ACP to HAp.[15] Furthermore, it has been reported that Mg^{+2} perturb the internal structure of ACP and HAp causing destabilization.[13] It has been also documented that, in opposition to the incorporated Mg^{+2}, Mg^{+2} at the surface plays a critical role in regulating the transformation from ACP to HAp.[16] There is also controversy

in the limit of substitution found for Mg^{+2}-enriched HAp, hereafter denoted Mg-HAp. In early studies, the limit of Mg^{+2} substitution found by precipitation and hydrolysis methods was reported to be 0.3 wt.%,[17] < 1 wt.%,[18,19] and 2 wt.%.[20] More recently, Suchanek *et al*.[21] managed to synthesize phase pure Mg-HAp with Mg^{+2} concentrations ranging from 0.2 to 28.4 wt.%, whereas Ren *et al.*[22] claimed that a limited amount of Ca^{2+} can be successfully substituted by Mg^{+2} in the precipitation method (*i.e*. ~ 1.2-1.9 wt.%). More recently, Yuan *et al*.[23] used step reaction and ion-exchange processes to prepare Mg-HAp. Although the Ca^{+2}/Mg^{+2} molar ratios in the feeding solution ranged from 2.5:1.5 to 15:1, the Mg^{+2} content in the final Mg-HAp particles was comprised between 1.3 and 4.2 wt.%.[23] On the other hand, Bigi *et al.*[24] used conventional hydrothermal conditions at 120 ºC to obtain Mg -HAp with up to 7.5 wt.% of Mg^{+2}.

In this work we present a combined experimental-theoretical study devoted to understand the effect of Mg^{+2} in the composition, morphology, crystallinity and nucleation of HAp. First, the influence of both the preparation conditions and the concentration of Mg^{+2} in the feeding medium on the composition and structure of the resulting minerals have been systematically investigated using scanning and transmission electron microscopy (SEM and TEM, respectively), wide angle X-ray diffraction (WAXD), energy dispersive X-ray spectroscopy (EDS) and X-ray photoelectron spectroscopy (XPS). After this, atomistic molecular dynamics (MD) simulations have been used to understand the effect of Mg^{+2} on the internal structure of HAp at the initial nucleation stages. Finally, MD simulations have been used to investigate the influence of Mg^{+2} in the process of biomineralization when the formation of HAp is regulated by DNA, which acts as a template. Also, the possible interaction between encapsulated DNA and Mg^{+2} has been examined.

4.2 EXPERIMENTAL SECTION

4.2.1 Synthesis

Diammonium hydrogen phosphate, $(NH_4)_2HPO_4$, aqueous solution (500 mM) and calcium nitrate, $Ca(NO_3)_2$, ethanol solutions (500 mM) were prepared for the synthesis of HAp particles. Part (1.5, 5 and 15 wt. %) of the $Ca(NO_3)_2$ was replaced by magnesium nitrate, $Mg(NO_3)_2$, for the synthesis of Mg-HAp. The pH of the solutions

was adjusted to 9.5 using ammonium hydroxide. The reagent concentrations were adjusted to get a $(\mathrm{Ca}+\mathrm{Mg})/\mathrm{P}$ ratio of 1.67. More specifically, 3 mL of $(\mathrm{NH_4})_2\mathrm{HPO_4}$ solution was added at once to 5 mL of the $\mathrm{Ca(NO_3)_2}$ solution. The mixture was maintained under agitation during 1 h. After this, samples were allowed to stand overnight at 37 ºC for aging, the resulting material being denoted HAp/ag and Mg-HAp/ag. In contrast, HAp/ht and Mg-HAp /ht samples were obtained by treatment on a pressure vessel at 130 ºC for 24 h. All samples were washed twice with 10 mL of MilliQ® water and with 10 mL of ethanol (analysis grade). White powders were obtained after drying by lyophilisation.

4.2.2 Measurements

Scanning electron microscopy (SEM) and energy dispersive X-ray (EDX) spectroscopy: Samples of 10 µL from 1 mg/mL suspensions in milliQ water were put on a silicon support mounted with silver paint on pin stubs of aluminium, and sputter-coated with a thin layer of carbon to prevent sample charging problems. SEM studies were carried out using a Focused Ion Beam Zeiss Neon40 microscope operating at 20 kV, equipped with an EDX spectroscopy system. The latter technique was used to estimate the composition of the HAp and Mg-HAp on samples without carbon coating.

Transmission electron microscopy (TEM). Particles suspensions of 1 mg/mL in deionized water were prepared and used to deposit samples on carbon-coated grids. TEM images were obtained using a Philips TECNAI 10 electron microscope operated at 80 kV for a bright field mode. Micrographs were taken with an SIS MegaView II digital camera.

X-Ray diffraction. Crystallinity was studied by wide angle X-ray diffraction (WAXD). Patterns were acquired using a Bruker D8 Advance model with $\mathrm{CuK_\alpha}$ radiation ($\lambda = 0.1542$ nm) and geometry of Bragg-Bretano, theta-2 theta. A one-dimensional Lynx Eye detector was employed. Samples were run at 40 kV and 40 mA, with a 2-theta range of 2−40, measurement steps of 0.02 º, and time/step of 2−8 s. Diffraction profiles were processed using PeakFit v4 software (Jandel Scientific Software) and the graphical representation performed with OriginPro v8 software (OriginLab Corporation, USA).

The average crystallite size (*L*) in the direction perpendicular to the representative (211) plane of HAp and Mg-HAp samples was derived from the X-ray diffraction line broading measurement using the Scherrer equation:[24]

$$L = \frac{0.9\lambda}{\beta \cos\theta} \quad (1)$$

where λ is the wavelength (CuK_{α}), β is the full width at half maximum height of the (211) line, θ is the diffraction angle and 0.9 is a shape factor. The crystallinity (χ_c) was obtained using the following Eqn:[25]

$$\chi_c = 1 - \frac{V_{112/300}}{I_{300}} \quad (2)$$

where I_{300} is the intensity of the (300) reflection and $V_{112/300}$ is the intensity of the hollow between the (112) and (300) reflections, which disappears in non-crystalline samples.

Fourier transform infrared (FTIR) spectroscopy. Infrared absorption spectra were recorded from powder samples with a Fourier Transform FTIR 4100 Jasco spectrometer in the 4000–500 cm^{-1} range. A Specac model MKII Golden gate attenuated total reflection (ATR) equipment with a heated Diamond ATR Top-Plate was used.

X-ray photoelectron microscopy (XPS). XPS analyses were performed in a SPECS system equipped with a high-intensity twin-anode X-ray source XR50 of $\mathrm{Mg/Al}$ (1253 eV/1487 eV) operating at 150 W, placed perpendicular to the analyzer axis, and using a Phoibos 150 MCD-9 XP detector. The X-ray spot size was 650 µm. The pass energy was set to 25 and 0.1 eV for the survey and the narrow scans, respectively. Charge compensation was achieved with a combination of electron and argon ion flood guns. The energy and emission current of the electrons were 4 eV and 0.35 mA, respectively. For the argon gun, the energy and the emission current were 0 eV and 0.1 mA, respectively. The spectra were recorded with a pass energy of 25 eV in 0.1 eV steps at a pressure below 6×10^{-9} mbar. These standard conditions of charge compensation resulted in a negative but perfectly uniform static charge. The $\mathrm{C}\ 1s$ peak was used as an internal reference with a binding energy of 284.8 eV. High-resolution XPS spectra were acquired by Gaussian–Lorentzian curve fitting after *s*–shape background subtraction. The surface composition was determined using the manufacturer's sensitivity factors.

Molecular dynamics simulations. Simulations of systems with 0.0, 0.5, 1.5, 3 and 6 wt.% Mg^{+2} involved [0,955], [19,936], [57,898], [112,843] and [214,741] [Ca^{+2},Mg^{+2}] ions, respectively, which were a solution with 567 PO_4^{3-}, anions, 189 OH^- anions and 29499 water molecules. MD simulations in NPT conditions (constant number of particles, temperature of 298 ºK and pressure of 1 atm) were performed using the NAMD 2.6[26] code. The potential energy was computed using the Amber force-field.[27] Force-field parameters for hydroxyl and PO_4^{3-}groups were extracted from Amber ff03.[28] Force-field parameters of Ca^{+2} and Mg^{+2} were extracted from the work reported by Bradbrook *et al*.[29]and Allner *et al.*[30], respectively. The density of water in the simulation box was 1.00 g/cm^3 at a temperature of 298 ºK. The water molecules were represented using the TIP3P model.[31]

The initial simulation box (92.0 × 91.5 × 108.0 Å) was equilibrated using the following strategy.[3] Before any MD trajectory, 5000 steps of energy minimization were performed to relax conformational and structural tensions. Next, different consecutive rounds of short MD runs were performed to equilibrate the density, temperature, and pressure. First, solvent and ions were relaxed by three consecutive runs: 0.5 ns of NVT-MD (volume conserved) at 500 ºK were used to homogeneously distribute the solvent and ions in the box. After this, 0.5 ns of isothermal (298 ºK) and 0.5 ns of isobaric (1 atm and 298 ºK) relaxation were run. Finally, the systems were thermalized by 0.15 ns of steady heating until the target temperature was reached (298 ºK), 0.25 ns of NVT−MD at 298 ºK (thermal equilibration) followed by 0.5 ns of density relaxation (NPT-MD).

Atom pair distance cut-offs were applied at 16.0 Å to compute the van der Waals interactions. In order to avoid discontinuities in the Lennard-Jones potential, a switch function was applied to allow a continuous decay of the energy when the atom pair distances are larger than 14.0 Å. For electrostatic interactions, we computed the non-truncated electrostatic potential throughout Ewald Summations.[32] The real space term was determined by the van der Waals cut-off (16 Å), while the reciprocal term was estimated by interpolation of the effective charge into a charge mesh with a grid thickness of 5 points per volume unit, *i.e.* Particle-Mesh Ewald (PME) method.[32] Both temperature and pressure were controlled by the weak coupling method, the Berendsen thermobarostat.[33] The relaxation times used for the coupling were 1 and 10 ps for temperature and pressure, respectively. Bond lengths were constrained using the SHAKE algorithm[34] with a numerical integration step of 1 fs. Periodic boundary conditions were applied using the nearest image convention, and the nonbonded pair list

was updated every 1000 steps (1 ps). The end of the density relaxation simulation was the starting point of the production simulations presented in this work, which were 25 ns long. The coordinates of all the production runs were saved every 1000 steps (1 ps interval).

Simulations with DNA were carried using conditions identical to those already described. For similarity with our previous simulations of Mg^{+2}-free systems [41] the DNA fragment introduced in the simulation box was the Dickerson's dodecamer (5'-CGCGAATTCGCG-3'), which is a well-known sequence that adopts a B-DNA double helix.[35]All force-field parameters for DNA were extracted from Amber ff03.[28] It should be noted that the ff03 parameters are identical to the ff99-SB[36] ones for nucleic acids, phosphate and hydroxyl groups. The ability of this set of force-field parameters to reproduce the inorganic···organic interactions found in biominerals was recently proved.[28] During thermal relaxation of solvent and ions, B-DNA was kept frozen, the whole system being relaxed during thermalization and equilibration runs before the production simulations

4.3 RESULTS AND DISCUSSION

Mg-HAp particles were prepared by chemical co-precipitation using both open system aging and hydrothermal treatment in a pressure vessel, the resulting materials being denoted Mg-HAp/ag and Mg-HAp/ht, respectively. HAp (*i.e.* Mg^{+2}-free particles) particles prepared using the same conditions, named HAp/ag and HAp/ht, were used as a control. On the other hand, the number after the label ag or ht refers to the concentration of $Mg(NO_3)_2$ in the reaction media used to prepare Mg-HAp, which can be 1.5, 5 and 15 wt.%.

Figure 4.1 displays SEM and TEM images of the HAp/ag and Mg-HAp /ag particles while micrographs of hydrothermally treated particles are provided in **Figure 4.2**. As it can be seen, HAp/ag, Mg-HAp/ag-1.5 and Mg-HAp/ag-5 adopt similar nanospherical morphologies (**Figure 4.1 a-f**). In contrast, rods with irregular morphologies are obtained when the concentration of Mg^{+2} in the reaction medium increases to 15 wt.% (**Figures 4.1 g-h**). Hydrothermal conditions led to regular rods for both HAp/ht and Mg-HAp/ht-1.5 (**Figures 4.2 a-d**), whereas regular sheet-like morphologies were obtained for Mg-HAp/ht-5 and Mg-HAp/ht-15 (**Figures 4.2 e-h**). These results indicate that both the

synthetic conditions and the presence of Mg^{+2} in the feeding medium affect significantly the morphology and, therefore, the surface area of the particles

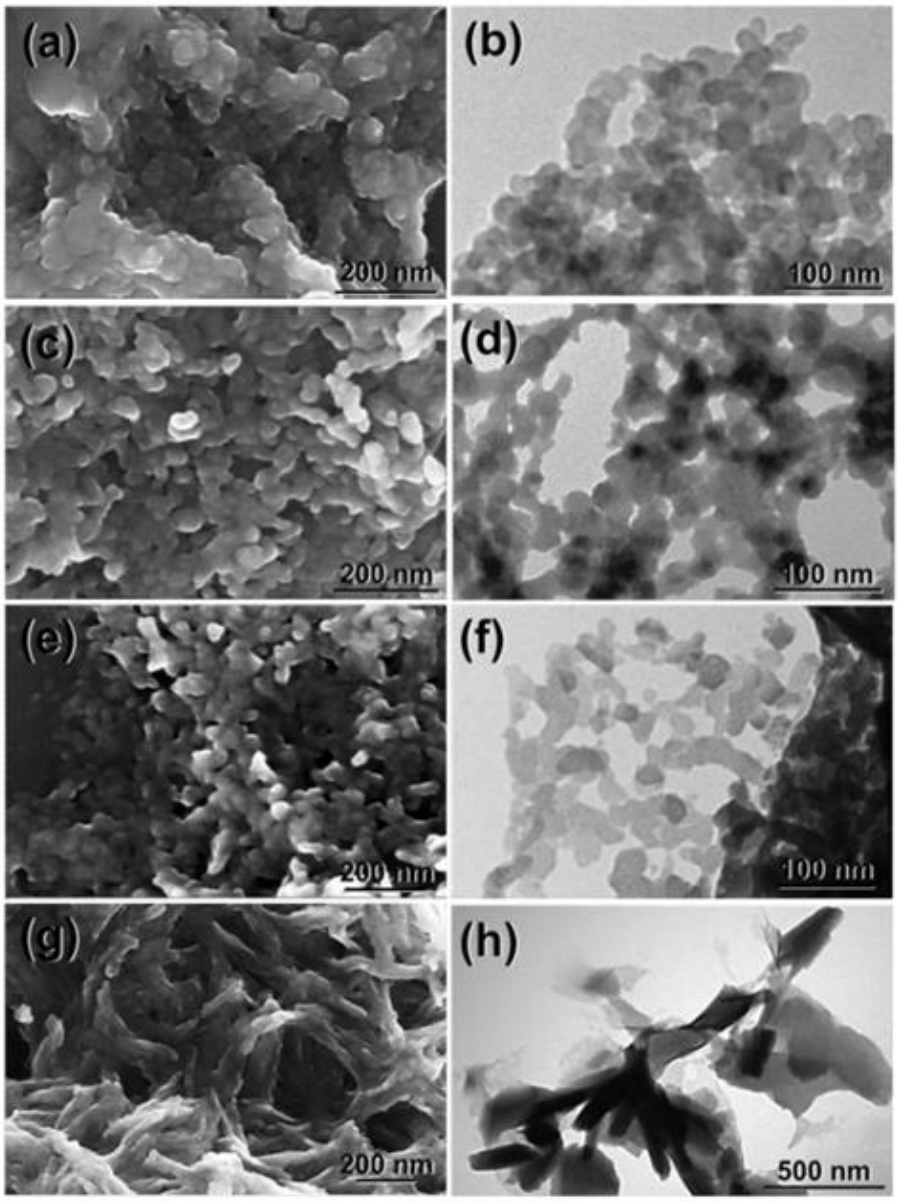

Figure 4.1. SEM (left) and TEM (right) images of: (a,b) HAp/ag; (c,d) Mg -HAp/ag-1.5; (e,f) Mg -HAp/ag-5; and (g,h) Mg -HAp/ag-15.

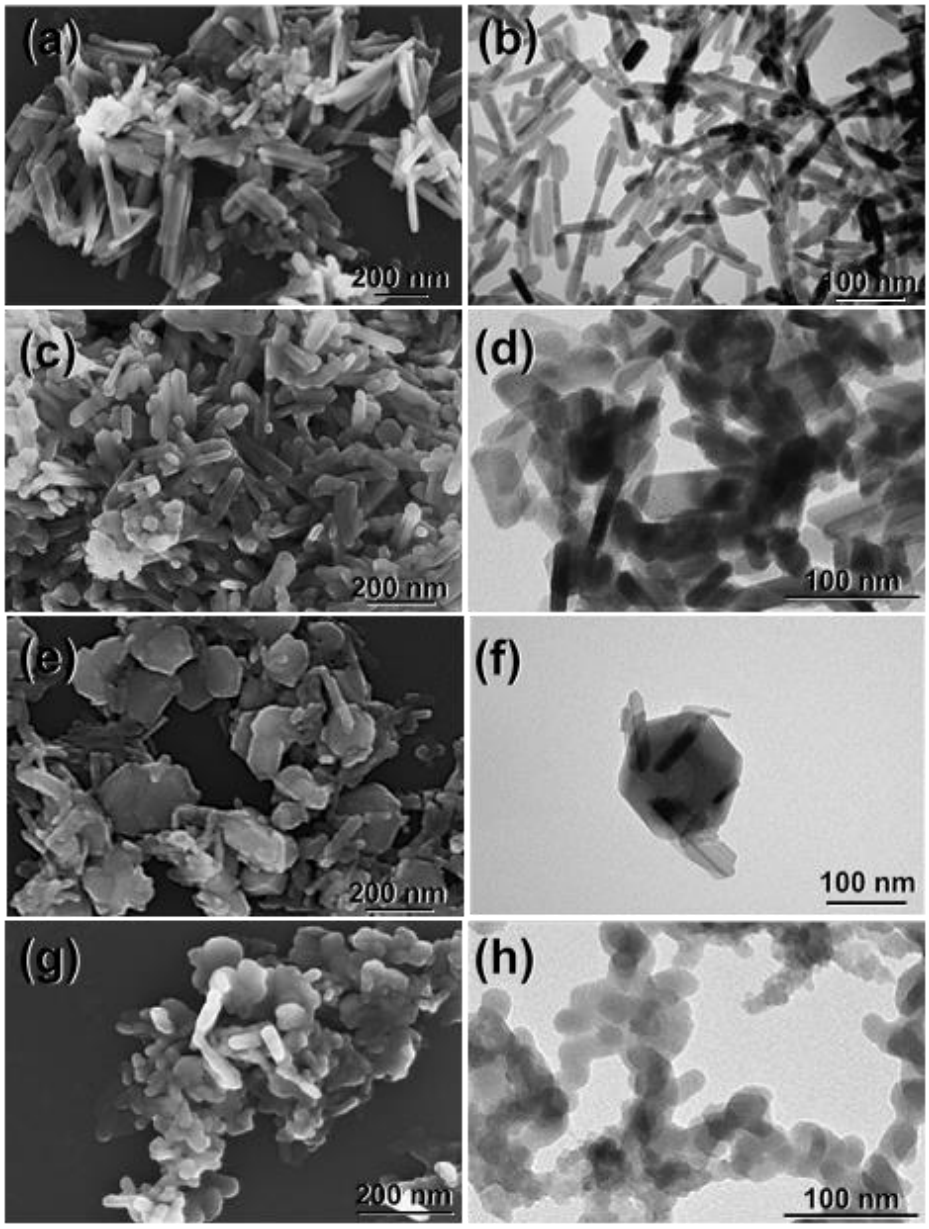

Figure 4.2. SEM (left) and TEM (right) images of: (a,b) HAp/ht; (c,d) Mg -HAp/ht-1.5; (e,f) Mg -HAp/ht-5; and (g,h) Mg -HAp/ht-15.

Structural characterization of the synthesized particles by WAXD was focused on peaks at 32 º–34 º 2θ (**Figures 4.3 and 4.4**), which are characteristics of the (211), (112) and (300) HAp reflections. These peaks were also used to determine the crystallite size (*L*) and the crystallinity (χ_c). Hydrothermal conditions favors the crystallinity and growing of the crystallites of HAp, which was determined to be $\chi_c = 0.28$ ($L = 10$ nm) and 0.50 ($L = 20$ nm) for HAp/ag and HAp/ht, respectively. However, the incorporation of Mg^{+2} affects drastically the crystallinity and crystallite dimensions. Thus, Mg-HAp/ag particles

are completely amorphous, independently of the concentration of $Mg(NO_3)_2$ in the reaction medium, while the crystallinity of Mg-HAp/ht-1.5, Mg-HAp/ht-5 and Mg-HAp/ht-15 decreases to $\chi_c =$ 0.20 (*L* = 17 nm), 0.11 (*L* = 13 nm) and < 0.05 (*L* = 11 nm), respectively.

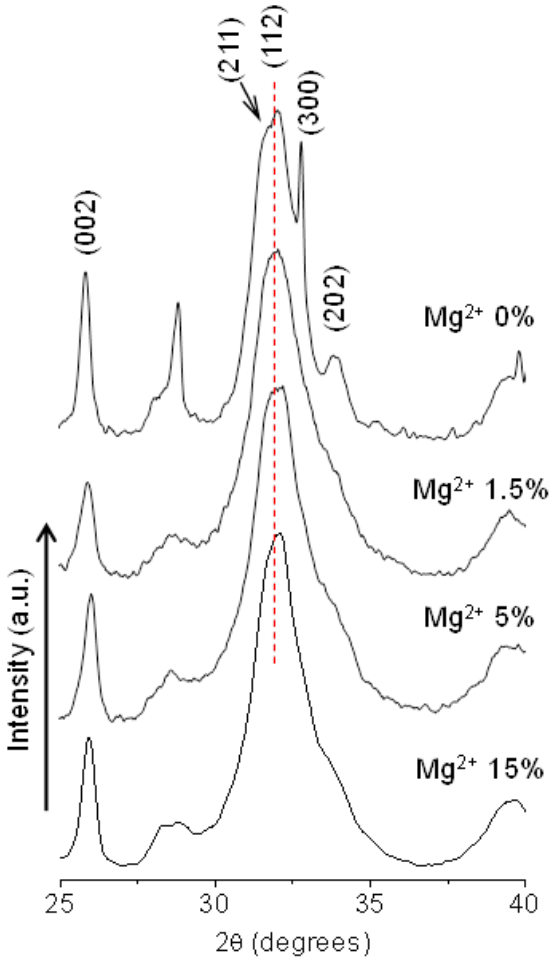

Figure 4.3. X-Ray diffraction pattern obtained for HAp/ag (i.e. 0 wt.% Mg^{+2}) and Mg-HAp/ag obtained using different concentrations of $Mg(NO_3)_2$ in the reaction medium.

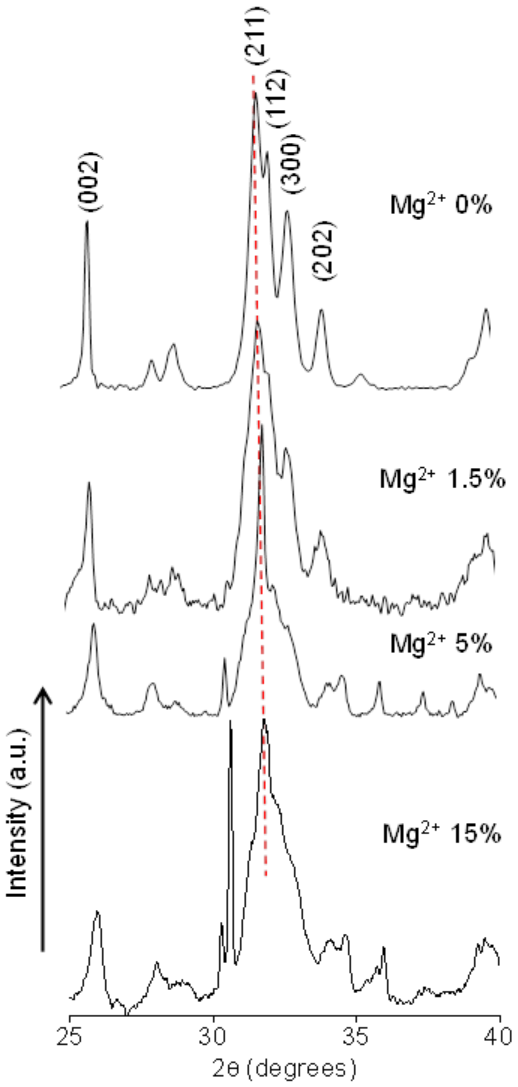

Figure 4.4. X-Ray diffraction pattern obtained for HAp/ht (*i.e.* 0 wt.% Mg^{+2}) and Mg-HAp/ht obtained using different concentrations of $Mg(NO_3)_2$ in the reaction medium.

FTIR spectra of HAp and Mg-HAp samples are compared in **Figure 4.5**. Spectra recorded for HAp/ag and HAp/ht show PO_4^{3-} bands at the region comprised between 950 and 1200 cm^{-1}, with $\nu_1 \approx 960$ cm^{-1} and $\nu_3 \approx 1020$, 1085 cm^{-1}. As it was expected, these bands are also present in all Mg-HAp samples. On the other hand, the HAp/ag spectrum shows absorption bands due to the CO_3^{2-} at ~ 862 cm^{-1} (ν_2) and the most intense, which appears as a broad doblet, at ~ 1335, 1410 cm^{-1} (ν_3). These bands decreases considerably for HAp/ht, being only shoulders. It should be noted that the source of the carbonate is not the reaction medium but the environment. Furthermore, the intensity of the CO_3^{2-} band decreases considerably in all Mg-HAp samples, being

even null for Mg-HAp/ht-1.5 and Mg-HAp/ht-5. These results show that both hydrothermal conditions and Mg^{+2} ions inhibit the formation of carbonate−containing HAp. All these observations are corroborated in **Table 4.1**, which quantifies the characteristic absorption bands by integrating the corresponding areas.

Figure 4.6 depicts the characteristic XPS spectra in the P 2p, Ca 2p and Mg 2p regions for HAp and Mg-HAp. For amorphous samples, the single P 2p peak centered at 132.7 eV, which originates from the PO_4^{3-} anions,[37,38] experiences a slight shift towards higher energies ($\Delta = 0.3$ eV) upon the incorporation of Mg^{+2} to composition. The Ca 2p spectra shows the Ca $2p_{3/2}$ and Ca $2p_{1/2}$ typically detected for Ca^{+2} in inorganic calcium–oxygen compounds with binding energies at 347.0 eV and 350.5 eV, respectively.[37] These peaks are not affected by the degree of crystallinity of the samples. The binding energy of Mg 2p at 50.2 eV,[39] which only appears in Mg-HAp samples, clearly indicates that Mg^{+2} ions of the reaction medium incorporate into HAp. Furthermore, the intensity of this Mg 2p peak reveals that such incorporation increases with the concentration of $Mg(NO_3)_2$ in the feeding medium. On the other hand, the peak at 43.4 eV corresponds to the Ca 3s , which explains its detection in all samples.

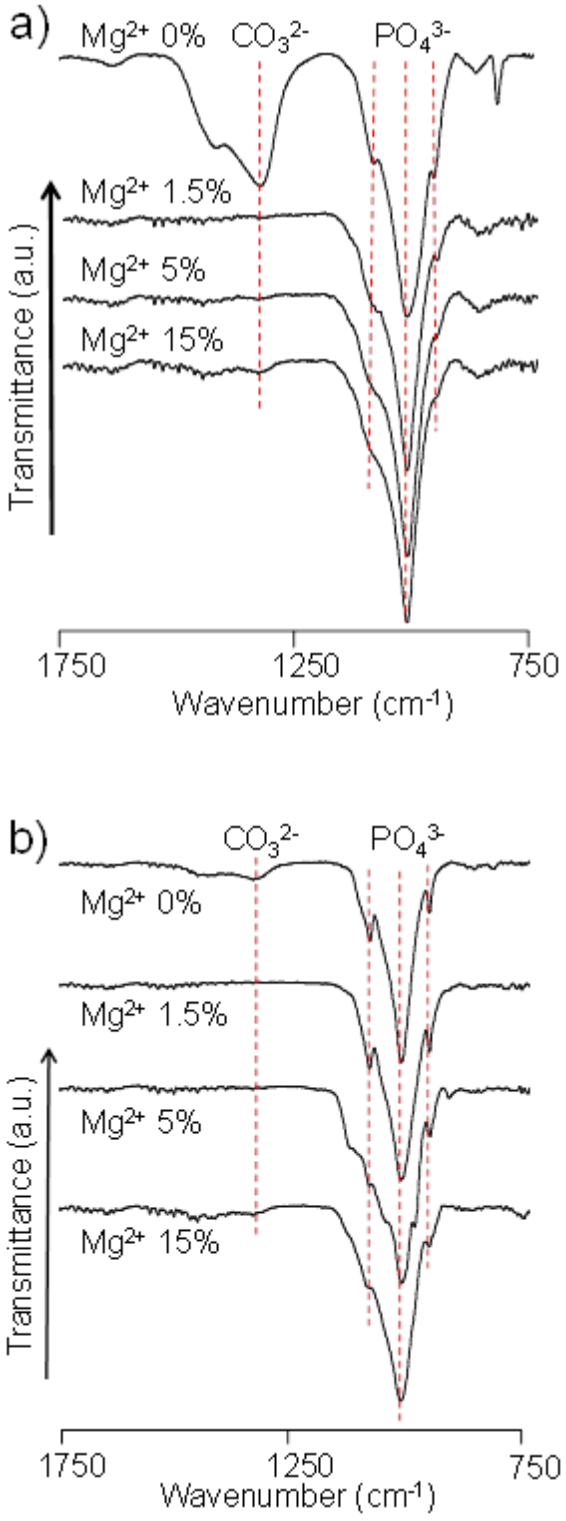

Figure 4.5. FTIR spectra of: (a) HAp/ag and Mg-HAp/ag; and (b) HAp/ht and Mg-HAp/ht.

Table 4.1. Main infrared absorption bands (cm^{-1}) for HAp and Mg-HAp particles. Integrated band relative areas are displayed in parenthesis.

	PO_4^{3-}		CO_3^{2-}	
	ν_1	ν_3	ν_2	ν_3
HAp/ag	961	1016,1082	862	1330,1413
	(8.07 %)	(31.05 %,10.60 %)		(21.10, 17.18 %)
HAp/ag-1.5	965	1022,1097	872	1328,1405
	(15.58 %)	(53.49 %, 25.37 %)		(0.57 %, 0.42 %)
HAp/ag-5	976	1026,1103	877	1356,1450
	(10.58 %)	(52.93 %, 29.87 %)		(0.71 %, 0.68 %)
HAp/ag-15	976	1026,1107	877	1356,1456
	(9.92 %)	(54.06 %, 28.37 %)		(1.12 %, 0.98 %)
HAp/ht	960	1022,1088	862	1337,1423
	(8.72 %)	(67.23 %,19.19 %)		(2.23 %, 1.65 %)
HAp/ht-1.5	964	1022,1092	863	-
	(12.72 %)	(63.49 %, 23.12 %)		
HAp/ht-5	962	1019,1079	874	-
	(10.58 %)	(58.72 %, 30.29 %)		
HAp/ht-15	966	1022,1086	-	1337,1430
	(9.73 %)	(57.87 %, 30.52 %)		(1.17 %, 0.71 %)

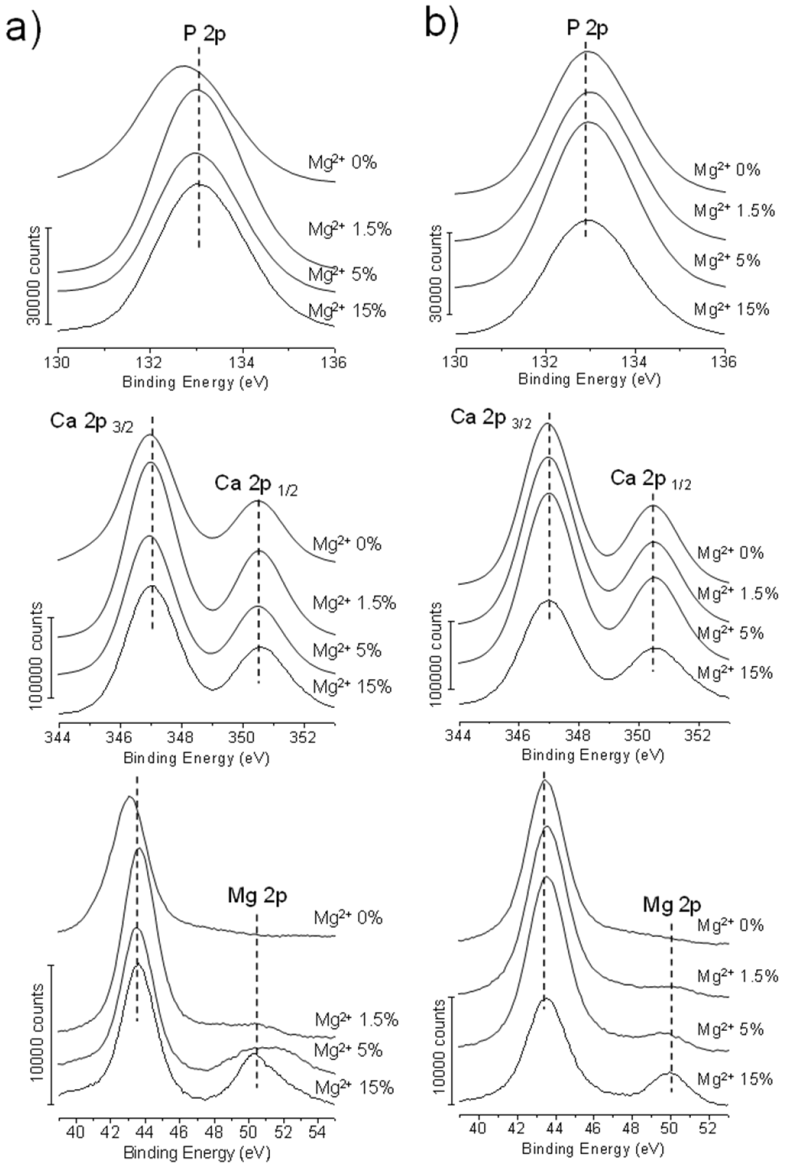

Figure 4.6. High-resolution XPS spectra for HAp and Mg -HAp samples prepared using (a) open aging conditions and (b) hydrothermal treatment: $\mathrm{P\ 2p}$, $\mathrm{Ca\ 2p}$ and $\mathrm{Mg\ 2p}$ regions.

The content of Ca, Mg and P elements, as determined by XPS, in HAp and Mg-HAp is displayed in (**Table 4.2**). The $\mathrm{Ca/P}$ molar ratio of Mg^{+2}-free samples and the $(\mathrm{Ca}+\mathrm{Mg})/\mathrm{P}$ molar ratio of Mg-HAp samples are lower than the stoichiometric value of 1.67. This has been attributed to the formation of amorphous phases, which is consistent with the WAXD results. The $\mathrm{Ca/P}$ molar ratio found in HAp is coherent with the substitution of $\mathrm{PO_4^{3-}}$ (rather than $\mathrm{OH^-}$) by $\mathrm{CO_3^{2-}}$ and the consequent apparition of vacancies.[40]

Table 4.2 also shows that the Ca/Mg molar ratio in Mg-HAp particles is considerably lower than in the feeding medium, reflecting that, in spite of the replacement of Ca^{+2} by Mg^{+2} in particles, many Mg^{+2} ions remain into the solution, independently of the conditions used for the synthesis. Thus, the Mg^{+2} content in Mg −HAp particles ranges from 0.32 wt. % in Mg-HAp/ht-1.5 to 3.82 wt. % in Mg-HAp/ag-15. On the other hand, the content of Mg^{+2} is systematically lower for Mg-HAp/ht than for Mg-HAp/ag, suggesting that the hydrothermal treatment protects the HAp lattice from the strain induced by the substitution of Ca^{+2} by Mg^{+2}.

Table 4.2. Ca, Mg and P concentration (wt.%), and $(Ca + Mg)/P$, Ca/P, Mg/P and Mg /Ca molar ratios determined by XPS of Mg-HAp/ht | Mg-HAp/ag prepared using Mg^{+2} in the reaction medium of 1.5, 5 and 15 wt.%. Composition of Mg^{+2}-free HAp obtained by applying the same treatments in the aging step are displayed for comparison.

	HAp [a]	Mg-HAp 1.5 wt.%[a]	Mg-HAp 5 wt.%[a]	Mg-HAp 15 wt.%[a]
Ca (wt.%)	33.84|32.88	33.60|31.38	32.76|30.66	30.28|28.69
Mg (wt.%)	- | -	0.32|0.43	0.65|3.03	2.71|3.82
P (wt.%)	17.64|18.56	17.53|19.64	18.03|17.75	18.50|18.94
(Ca+Mg)/P	1.49|1.37	1.50|1.26	1.45|1.55	1.45|1.43
Ca/P	1.49|1.37	1.50|1.26	1.40|1.33	1.26|1.17
Mg/P	- | -	0.02|0.03	0.05|0.22	0.19|0.26
Mg/Ca	- | -	0.02|0.02	0.03|0.16	0.15|0.22

[a] Values refer to materials aged in a pressure vessel applying a hydrothermal treatment | aging in an open system.

The overall of these results reflects not only that the crystallinity, morphology and carbonate-substitution level of HAp are drastically affected by a small amount of Mg^{+2}, but also that the substitution of Ca^{+2} by Mg^{+2} is severely limited when typical synthetic processes are used. This observation has been also corroborated by energy dispersive X-ray (EDX) spectroscopy on selected representative regions of Mg-HAp particles

(**Table 4.3**). It is worth noting that the content of Mg^{+2} found in this work is considerably smaller, and therefore closer to that found in hard tissues, than that recently described by Yuan *et al.*[23] for Mg-HAp prepared using the reactants and open aging conditions identical to those employed in this work.

Table 4.3. Ca, Mg and P concentration (wt.%), and (Ca + Mg)/P, Ca/P, Mg/P and Mg /Ca molar ratios determined by EDX spectroscopy of Mg -HAp /ht | Mg −HAp/ag prepared considering Mg^{+2} content in the reaction medium of 1.5, 5 and 15 wt.%. Spectra were recorded on representative regions of the particles from a morphological point of view, the limited incorporation of Mg^{+2} into the HAp particles being systematically reproducible. Standard deviations (six measures) are given for all the compositions. Composition of Mg^{+2} –free HAp obtained by applying the same treatments in the aging step are displayed for comparison.

	HAp[a]	Mg-HAp 1.5 wt.%[a]	Mg-HAp 5 wt.%[a]	Mg-HAp 15 wt.%[a]
Ca (wt.%)	40.68 ± 2.32|41.09 ± 2.04	39.75 ± 1.86|34.84 ± 2.41	37.12 ± 3.05|37.11 ± 2.45	36.59 ± 1.37|31.90 ± 2.71
Mg (wt.%)	- | -	0.53 ± 0.08|0.28 ± 0.03	1.13 ± 0.04|0.64 ± 0.06	2.33 ± 0.07|2.87 ± 0.11
P (wt.%)	18.90 ± 2.71|18.79 ± 1.75	18.84 ± 1.28|18.46 ± 2.01	17.77 ± 1.39|20.13 ± 2.17	17.71 ± 1.18|20.82 ± 2.18
(Ca+Mg)/P	1.66|1.69	1.67|1.48	1.70|1.47	1.76|1.36
Ca/P	1.66|1.69	1.63|1.48	1.70|1.47	1.76|1.36
Mg/P	- | -	0.04|0.02	0.08|0.04	0.17|0.18
Mg/Ca	- | -	0.02|0.01	0.05|0.03	0.11|0.15

[a] Values refer to materials aged in a pressure vessel applying a hydrothermal treatment | aging in an open system.

Although these results provide valuable systematic information about the implications of the incorporation of Mg^{+2} in HAp characteristics, they also open many questions related with microscopic aspects of the formation of Mg-HAp particles. For example, there is no information about the role of Mg^{+2} ions in the formation of initial calcium phosphate clusters before the formation of Mg-HAp particles. Aspects related to the possible formation of magnesium phosphate aggregates at the early state stages of the inorganic reaction, the position and coordination of Mg^{+2} in the initial clusters and, also, the

interaction of Mg^{+2} with DNA in the biomineralization of such biomolecule[41] remain completely unknown.

Although, employment of experimental techniques to solve these small length- and/or time-scale problems is a very complex task, atomistic computer simulations currently represent a distinctive and, probably, the only viable method, for answering some of these questions. In order to get relevant microscopic information about the role of Mg^{+2} ions in the nucleation of Mg-HAp particles, atomistic MD simulations have been carried out on aqueous solutions containing Ca^{+2}, Mg^{+2}, PO_4^{3-} and OH^-. According to our previously discussed observation on the limited incorporation of Mg^{+2} to HAp particles, force-field MD simulations were performed considering inorganic solutions with 0.5, 1.5, 3 and 6 wt. % Mg^{+2} in the composition (see Experimental section). These simulations, labeled as MD-W (where W refers to the wt. % Mg^{+2}), represent the initial states of Mg-HAp nucleation. It should be noted that the nucleation of HAp particles (*i.e.* without Mg^{+2}) was described in a very recent study as a multi-clustering process[41] and, therefore, the present work is focused on the effects associated to Mg^{+2} ions.

The shape of the radial distribution functions (RDFs) of $PO_4^{3-}\cdots PO_4^{3-}$, $Ca^{+2}\cdots Ca^{+2}$ and $Ca^{+2}\cdots PO_4^{3-}$ pairs ($g_{P-P}(r)$, $g_{Ca-Ca}(r)$ and $g_{Ca-P}(r)$, respectively) remains practically unaltered for the four investigated compositions (**Figure 4.7**) and are extremely similar to those already reported for the nucleation of HAp.[41] However, as it was expected, the height of the peaks of the $g_{Ca-Ca}(r)$ profiles decreases with increasing content of Mg^{+2} (*i.e.* decreasing content of Ca^{+2}).

On the other hand, the RDF of $Ca^{+2}\cdots Mg^{+2}$ and $Mg^{+2}\cdots OH^-$ pairs ($g_{Ca-Mg}(r)$ and $g_{Mg-OH}(r)$, respectively) essentially differ in the intensity of the peaks, which increases with the content of Mg^{+2}. The $g_{Ca-Mg}(r)$ profiles (**Figure 4.8 a**) show sharp peaks centered at 3.6, 4.1 and 5.5 Å with similar relative intensities (2.1:1.4:1, 2.2:1.2:1, 1.7:1.1:1 and 1.9:1.2:1 for MD−W with W = 0.5, 1.5, 3 and 6 wt. % Mg^{+2}, respectively). These peaks, which correspond to Mg^{+2} immersed in aggregates, are followed by some broad peaks and shoulders at associations to ions that remain in the solution.

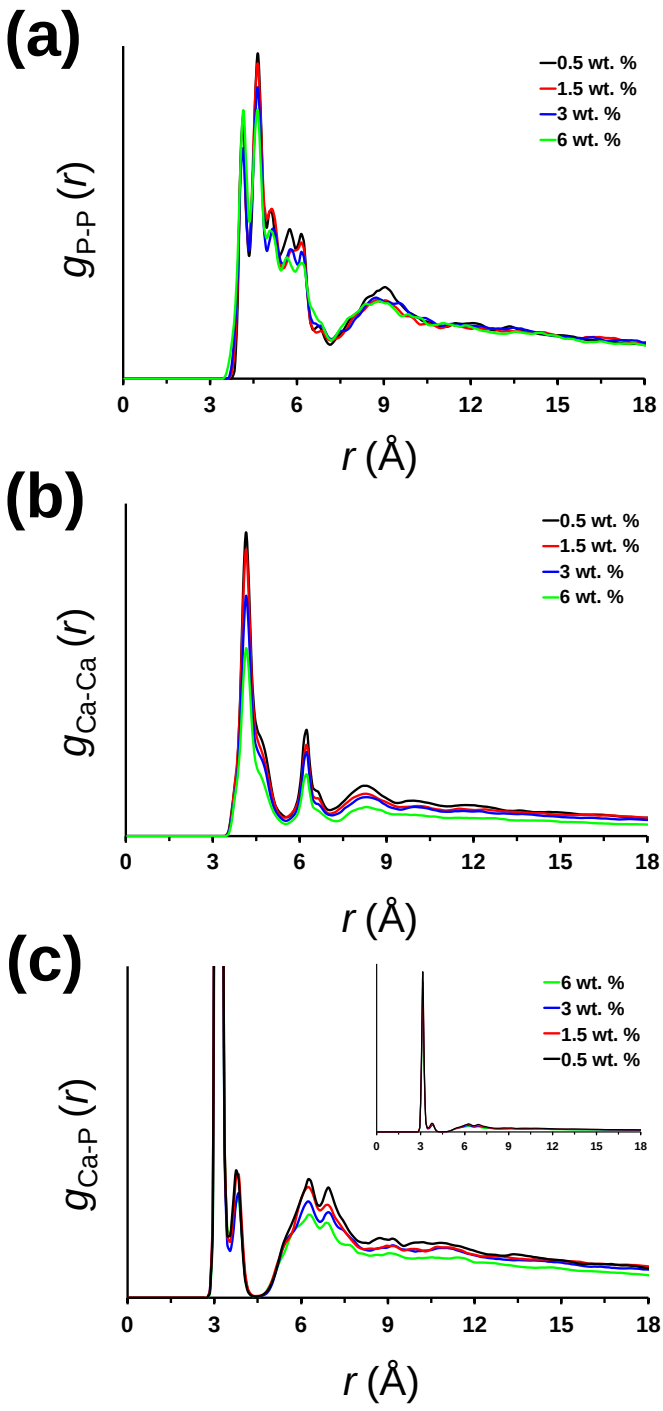

Figure 4.7. Radial distribution functions of (a) $PO_4^{3-}\cdots PO_4^{3-}$, (b) $Ca^{+2}\cdots Ca^{+2}$ and (c) $Ca^{+2}\cdots PO_4^{3-}$ pairs calculated using the snapshots recorded from MD-W simulations with W = 0.5, 1.5, 3 and 6 % wt. Mg^{+2}. Profiles were calculated using all the snapshots recorded during the whole production runs.

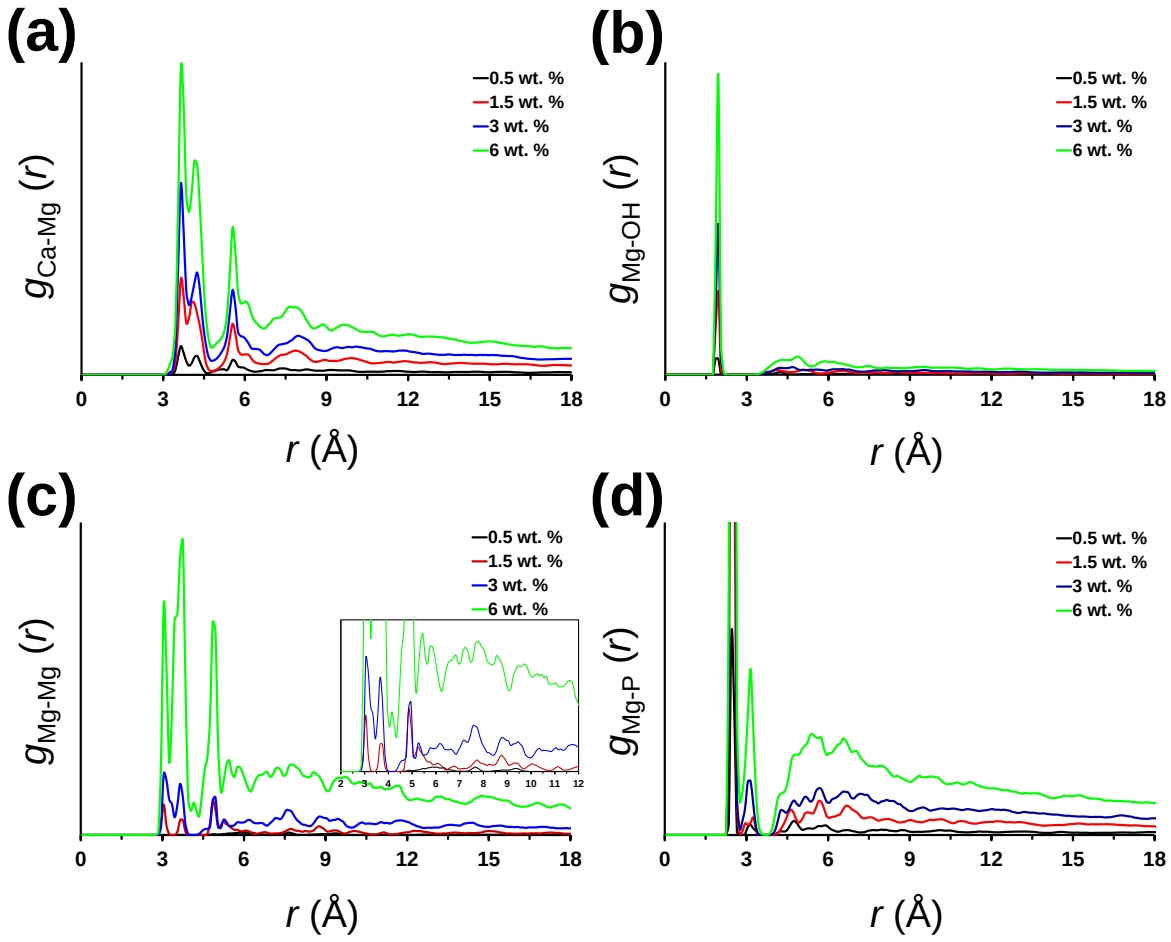

Figure 4.8. Radial distribution functions of (a) $Ca^{+2}\cdots Mg^{+2}$, (b) $Mg^{+2}\cdots OH^{-}$, (c) $Mg^{+2}\cdots Mg^{+2}$ and (d) $Mg^{+2}\cdots PO_4^{3-}$ pairs calculated using all the snapshots recorded during the whole production MD-W simulations with W = 0.5, 1.5, 3 and 6 % wt. Mg^{+2}.

The $g_{Mg-OH}(r)$ profiles of the four calculated systems (**Figure 4.8 b**) present a well-defined peak, which is very sharp and intense, centered at r = 1.9 Å. Analysis of the $g_{Mg-OH}(r)$ calculated at different times indicates that this peak already appears with high intensity after only 1 ns of simulation (**Figure 4.9**), revealing that Mg^{+2} ions tend to form complexes with one OH^{-} anion. In a previous study devoted to simulate the nucleation of Mg^{+2}-free HAp particles, we found that the diffusion of the OH^{-}anions through the inorganic solution is the limiting step for the growing of the mineral structure.[41] Thus, the coordination of Mg^{+2} and OH^{-} competes with that of Ca^{+2} with the same anion, which can be an explanation for the induced thermodynamical stability of the HAp precipitates in presence of Mg^{+2}.[42]

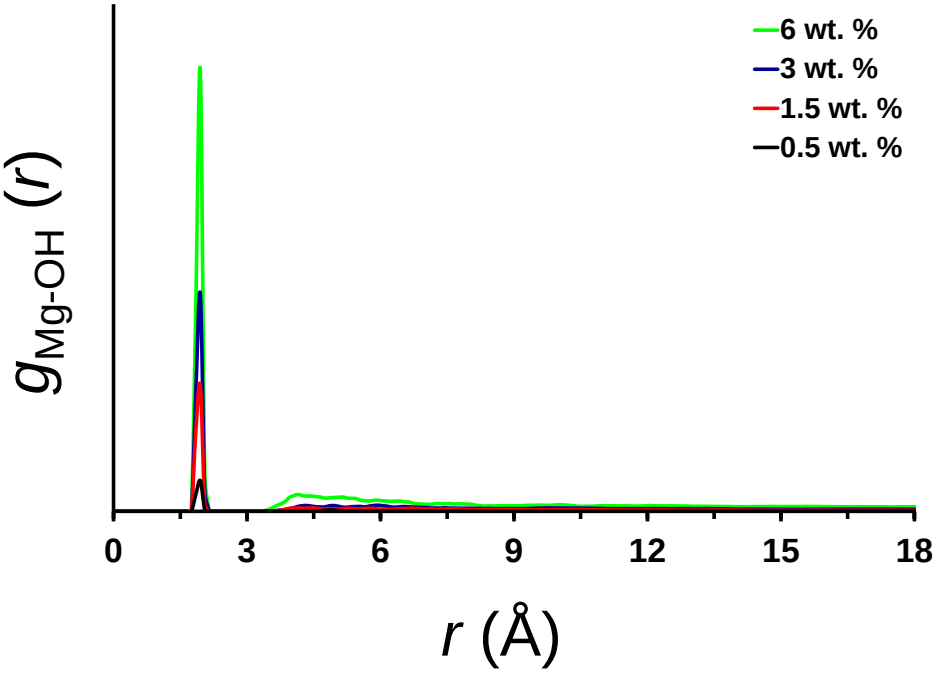

Figure 4.9. Radial distribution functions of $Mg^{+2}\cdots OH^{-}$ pairs calculated using the snapshots recorded from MD-W simulations with W = 0.5, 1.5, 3 and 6 wt. % Mg^{+2}. Profiles were calculated using the snapshots recorded during the first ns of the production runs.

The shape of the profiles obtained by calculating the RDF of $Mg^{+2}\cdots Mg^{+2}$ pairs, $g_{Mg-Mg}(r)$ (**Figure 4.8 c**), strongly depends on the concentration of Mg^{+2}. Thus, the intensity and complexity of the profiles, in terms of number and sharpness of the peaks, increase considerably with the concentration of Mg^{+2}. However, only well-defined peaks below 6–7 Å are related with Mg^{+2} incorporated to clusters, the other peaks being essentially due to ions in the bulk solution.

Analysis of the temporal evolution of the $g_{Mg-Mg}(r)$ profiles (**Figure 4.10**) provides important microscopic information. The $g_{Mg-Mg}(r)$ profile derived from the MD-0.5 simulation (**Figure 4.10 a**) does not show any clear peak at r < 6 Å after 1 ns, whereas a sharp and narrow peak centered at $r = 6.4$ Å, which corresponds to the incorporation of the first Mg^{+2} ions into the aggregates, appear after 15 ps. However, the $g_{Mg-Mg}(r)$ profile becomes much more complex at the end of the production run (25 ns), reflecting the incorporation of more Mg^{+2} ions. This feature suggests that the latter ions tend to be located close to the surface of previously formed calcium phosphate aggregates. Similar trends are observed for MD-1.5 and MD-3 (**Figures 4.10 b** and **c**, respectively),

even though in those cases some internal Mg^{+2} ions appear after the first ns of simulation. Detailed analysis of the MD-3 profiles reveals that many of these internal Mg^{+2} ions migrate towards the surface of the aggregates, as is reflected by the reduction in the intensity of some peaks detected after 1 and 15 ns at low r values. Finally, this tendency is less clear (because of the higher content of ions) but still detectable in MD-6 (**Figure 4.10 d**).

These predictions are in good agreement with the experimental findings recently reported by Ding *et al.*[16] These authors concluded that the formation of HAp from supersaturated solutions occurs through a five step process: (1) formation of ion clusters, giving place to ACP; (2) stabilization of the already formed ACP; (3) transformation from ACP to crystalline HAp via dissolution and crystallization; (4) classical crystal growth of HAp; and (5) HAp aging under a near equilibrium state. Interestingly, Mg^{+2} plays a crucial role regulating some of such steps. More specifically, the adsorbed Mg^{+2} was found to be more effective than the incorporated one in stabilizing ACP to retard the HAp formation (step 2). Accordingly, the surface Mg^{+2} rather than the incorporated Mg^{+2} is fundamental in the mineralization process of ACP-mediated HAp crystallization. The surface distribution of Mg^{+2} predicted by MD simulations is fully consistent with such observations.

Figure 4.8 d represents the RDF of $Mg^{+2}\cdots PO_4^{3-}$ pairs, $g_{Mg-P}(r)$. As it can be seen, all $g_{Mg-P}(r)$ profiles consist of two sharp and well-defined peaks centered at r = 2.3 and 3.1 Å, which are followed by multiple poorly defined peaks emerging from a broad band that extends from $r \approx$ 4 to 9 Å. The shape of these profiles is very similar to that displayed by $g_{Ca-P}(r)$ in **Figure 4.7 c**, suggesting that PO_4^{3-} anions organize similarly around Mg^{+2} and Ca^{+2}. These peaks have been associated to the formation of clusters and aggregates that are relatively ordered at a very short length scale, even though this order tends to disappear at a medium length-scale.

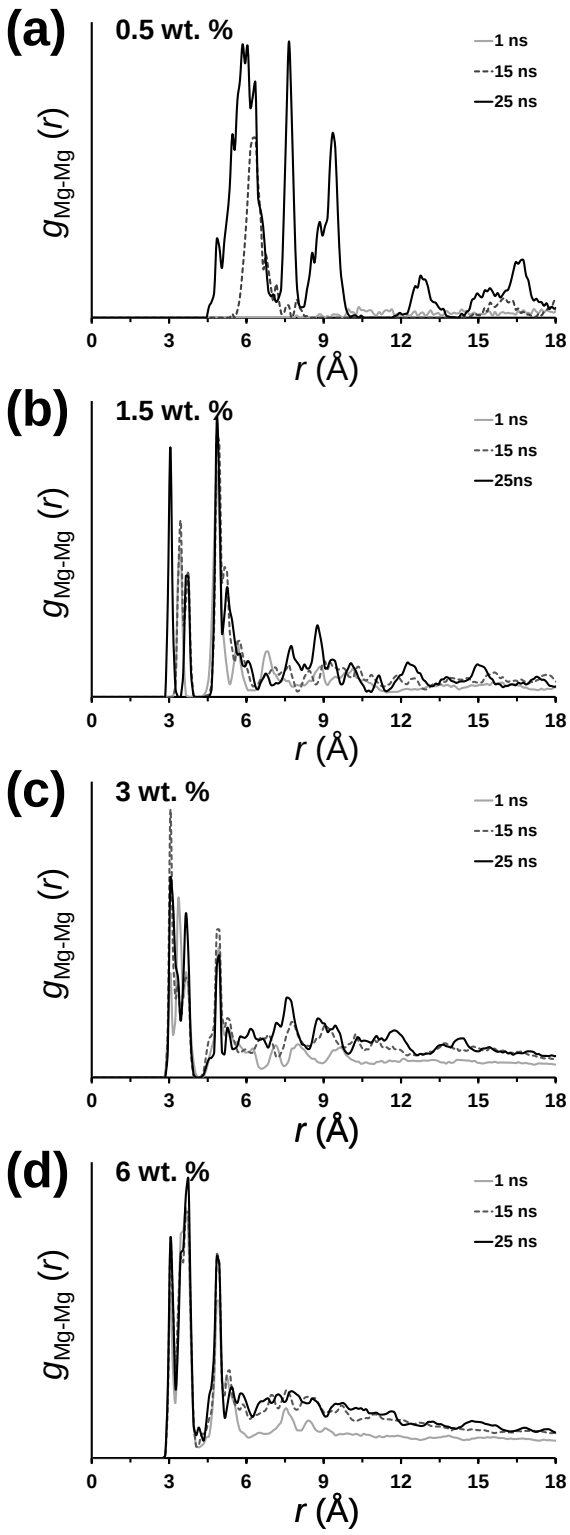

Figure 4.10. Radial distribution functions of $Mg^{+2}\cdots Mg^{+2}$ pairs calculated using the snapshots recorded from (a) MD-0.5, (b) MD-1.5, (c) MD-3 and (d) MD-6 simulations. Profiles were calculated using the snapshots recorded after 1, 15 and 25 ns of the production runs.

In order to get deeper information about the role of Mg^{+2} in the nucleation of Mg-HAp aggregates, we have evaluated the distribution of distances between the center of mass of each aggregate and the Mg^{+2} ions incorporated to it (**Figure 4.11 a**). As it can be seen, there is no Mg^{+2} in the central core of the aggregates indicating that the first step is the formation of calcium phosphate. Inspection of representative snapshots indicate that the diameter of the aggregates formed along 25 ns of simulation typically are around 6−8 Å, independently of the concentration of Mg^{+2}. This is consistent with the formation of multiple nucleation centers and suggests that systems evolve towards poly-organized Mg-HAp. This multi-nucleation behavior is coherent with previous studies devoted to investigate the growth of HAp particles.[43,44] The incorporation of Mg^{+2} to the calcium phosphate clusters is illustrated in **Figure 4.11 b**, which represents the last snapshot extracted from MD-6 (snapshots taken from the rest of simulations are depicted in **Figure 4.12**).

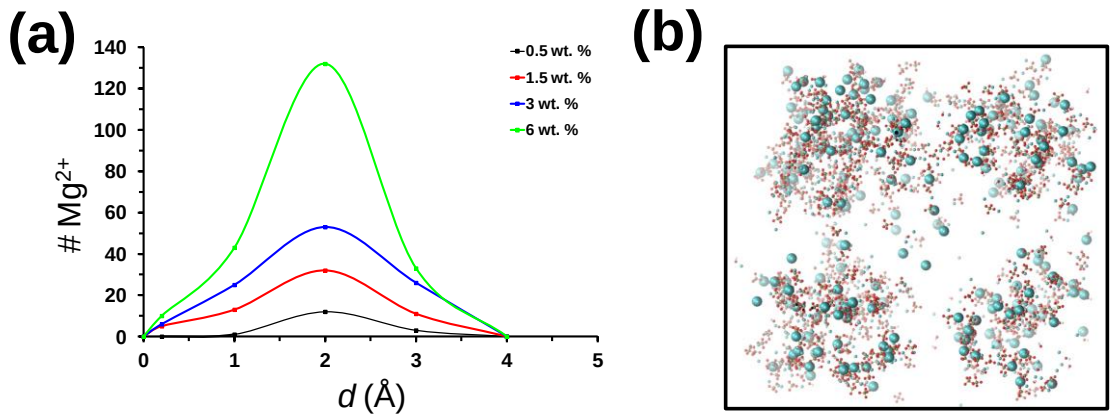

Figure 4.11. (a) Distribution of the number of Mg^{+2} incorporated to formed clusters as a function of the distance from the center of masses of the cluster. (b) Last snapshot of the MD-6 production run. Mg^{+2} ions are represented by large blue balls, Ca^{+2} by small blue balls, and the phosphorus and oxygen atoms of PO_4^{3-} by small green and red balls, respectively. Solvent molecules have been omitted for clarity.

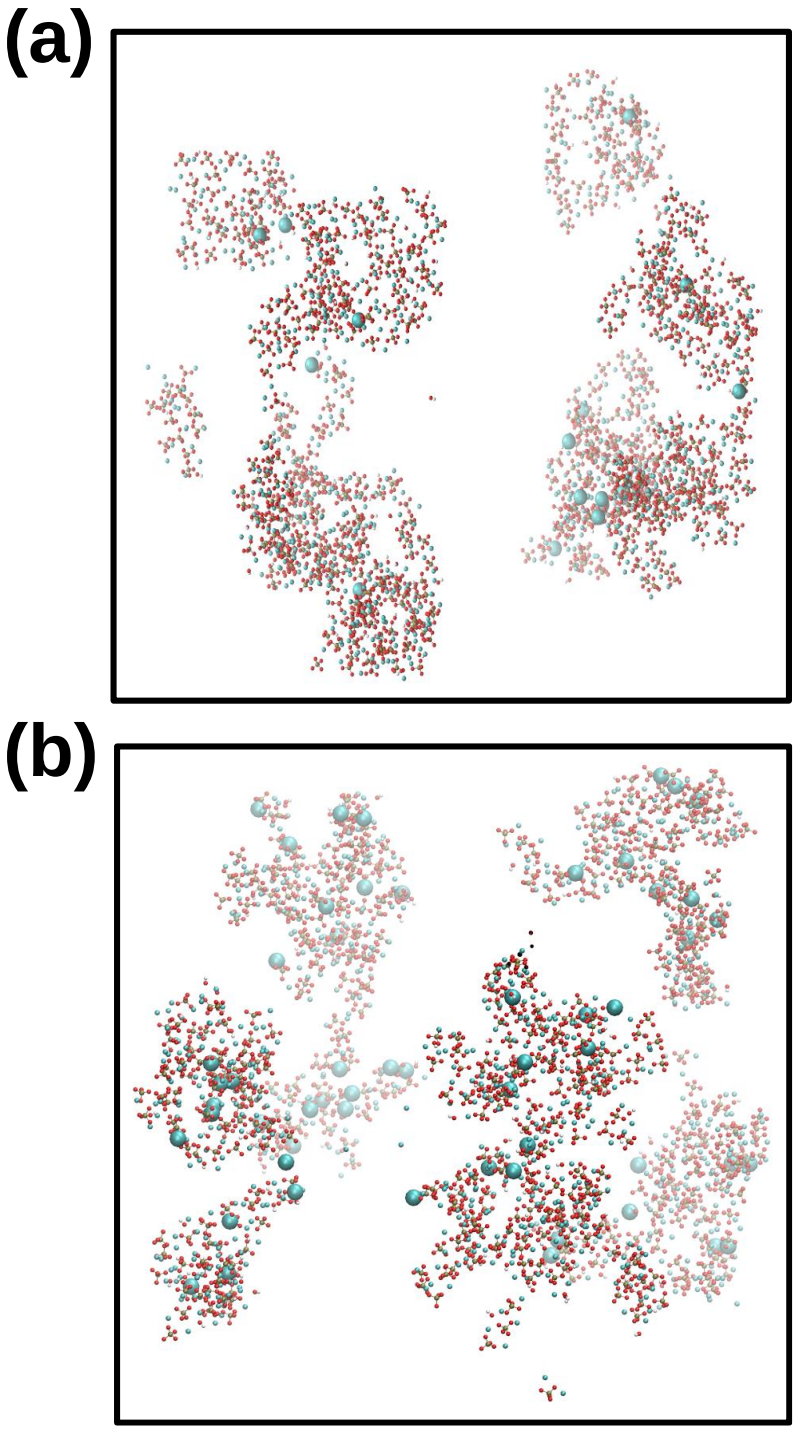

Figure 4.12. Last snapshot of the (a) MD-0.5 and (b) MD-1.5 production runs. Mg^{+2} ions are represented by large blue balls while Ca^{+2} and PO_4^{3-} are represented by small balls. Solvent molecules have been omitted for clarity.

Analysis of the radial average velocities of the different components of the inorganic solutions, which were calculated with respect to the Mg^{+2} ions in the bulk (*i.e.* negative and positive velocities indicate that molecules get close to or away from magnesium), evidences a homogeneous behavior in the solution (**Figure 4.13**). Furthermore, all components tend to approach magnesium at large distances. This feature, which is more prominent for Ca^{+2} and PO_4^{3-}, is consistent with the incorporation of Mg^{+2} to clusters and aggregates.

Both hydration and dehydration of ions is of crucial interest for the understanding of aggregation and clustering phenomena from saturated aqueous solutions. **Figure 4.14** represents the percentage of Ca^{+2}, Mg^{+2} and PO_4^{3-} ions surrounded by a number N_{H_2O} of water molecules (*i.e.* ion$\cdots H_2O$ distance lower than 3.85, 3.28 and 3.17 Å for Ca^{+2}, Mg^{+2} and PO_4^{3-}, respectively). Results derived from a new free Mg^{+2} simulation (MD-0.0) have been also included in **Figure 4.14**, since the interactions between ions and water molecules were not examined in our previous HAp study.[41] Values have been obtained by averaging the 25 ns of the production trajectories. Obviously, the number of surrounding water molecules decreases when ions group into clusters or aggregates, N_{H_2O} being minimum and maximum for ions located at the internal regions of such condensed nanostructures ($N_{H_2O} = 0$) and for ions remaining in the bulk solution ($N_{H_2O} = 8$), respectively. Low N_{H_2O} values can be attributed to either ions located at the surface of the clusters or ions in the bulk surrounded by both waters and other ions.

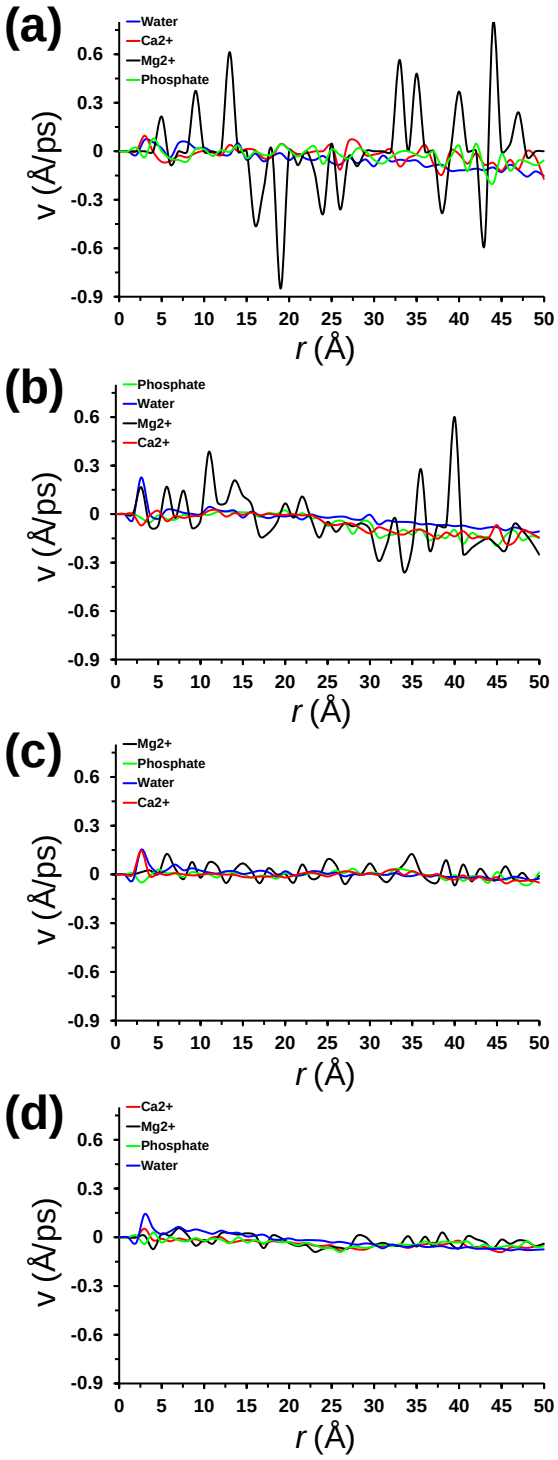

Figure 4.13. Analysis of the radial average velocities of the different components of the inorganic solutions, which were calculated with respect to the Mg^{+2} ions in the bulk (*i.e.* negative and positive velocities indicate that molecules get close to or away from magnesium for MD-W simulations with W= (a) 0.5, (b) 1,5, (c) 3 and (d) 6 % wt. Mg^{+2}.

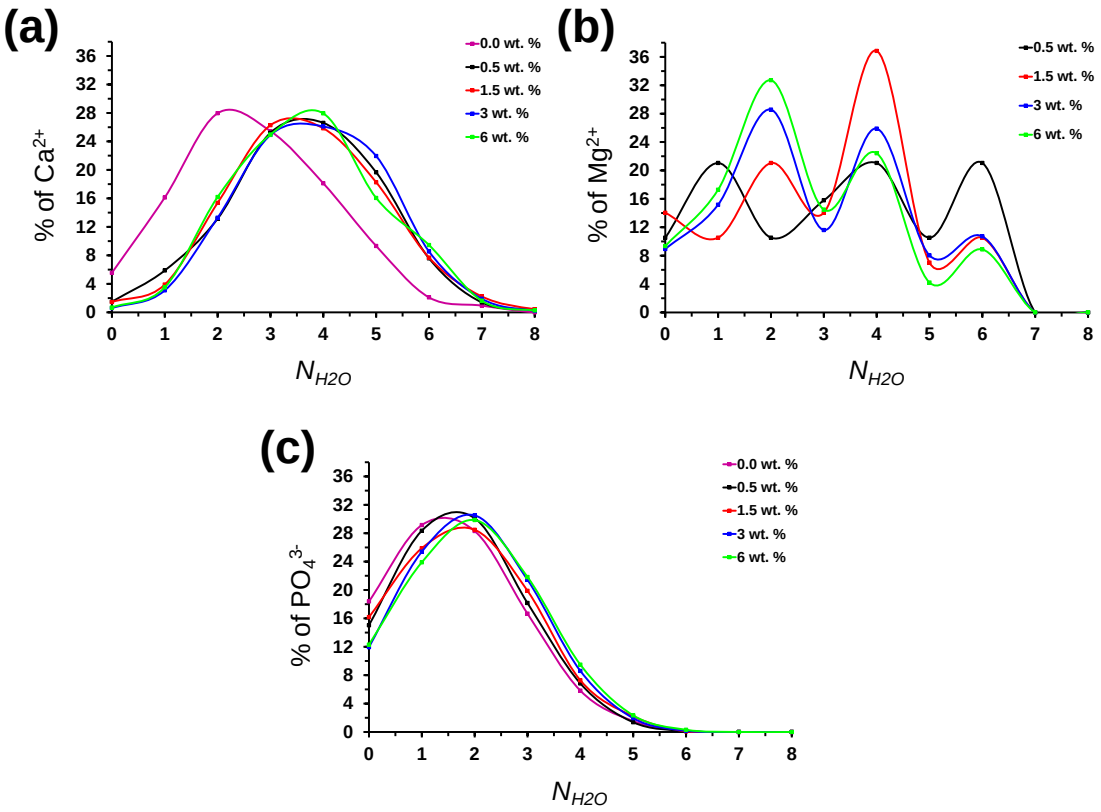

Figure 4.14. Percentage of (a) Ca^{+2}, (b) Mg^{+2} and (c) PO_4^{3-} ions surrounded by a number of water molecules (N_{H_2O}), which can range from 0 to 8, for MD-W simulations with W= 0.0, 0.5, 1,5, 3 and 6 % wt. Mg^{2+}.

Although all Ca^{+2} hydration profiles show a Gaussian-like shape, the characteristics of the curves are very different in absence or presence of Mg^{+2} (**Figure 4.14 a**). Thus, ~ 53 Ca^{+2} ions (5.5 %) are located at the internal regions of aggregates in MD-0.0, this amount decreasing to only 5−14 ions (0.7 % for MD-6, 1.5 % for MD-0.5) when Mg^{+2} ions are in the solution. Furthermore, the maximum of the peak appears at $N_{H_2O} \approx 2$ in absence of Mg^{+2} and at around $N_{H_2O} \approx 3.5$ in presence of Mg^{+2}. In contrast, Mg^{+2} hydration profiles present a multimodal distribution with several peaks (**Figure 4.14 b**). Interestingly, the average number of Mg^{+2} ions with $N_{H_2O} = 0$ is 2, 8, 10 and 20 for MD-0.5, MD-1.5, MD-3 and MD-6, respectively. Although these results evidence a partial replacement of Ca^{+2} ions by Mg^{+2} ions at the core region of the clusters, they also reflect that Mg^{+2} inhibits the nucleation process (*i.e.* the total number of cations with $N_{H_2O} = 0$ is 53, 16, 21, 15 and 25 for MD-0, MD-0.5, MD-1.5, MD-3 and MD-6,

respectively). Furthermore, the amount of Mg^{+2} with N_{H_2O} = 1-2 is higher than with N_{H_2O} = 0 suggesting that these ions tend to be located at regions close to the surface which is in nice agreement with already experimentally reported behavior.[40] Finally, the behavior of PO_4^{3-} is similar in all cases (**Figure 4.14 c**), the profiles being practically independent of the Mg^{+2} concentrations. The number of PO_4^{3-} anions with N_{H_2O} = 0 is 104, 85, 92, 68 and 70 for MD-0, MD-0.5, MD-1.5, MD-3 and MD-6, respectively, indicating that the number of negative charges at the clusters is higher than the number of positive charges.

The formation of HAp can be regulated by DNA, which acts as a template in the process of "biomineralization".[41,44-46] This phenomenon is particularly important in biomedical applications requiring the mineral protection of such biomolecules from aggressive environmental conditions. Furthermore, in order to elucidate the role of DNA as template to promote mineral growth, the biomineralization mechanism was revealed at the atomic level.[41,45,47] In order to examine the influence of Mg^{+2} in DNA-templated Mg-HAp nucleation, MD-W simulations with W = 0.5, 1.3, 3 and 6 wt. % Mg^{+2} were repeated after introduce a B-DNA double into the initial simulation box. For consistency with our previous studies, the latter consisted in the Dickerson's dodecamer (5'-CGCGAATTCGCG-3').[40,45] Visual inspection of snapshots corroborated our previous observations derived from Mg^{+2}-free simulations: the formation of mineral clusters preferentially occur around phosphate backbone of the biomolecule, which acts as a template for Mg-HAp growth. Thus, inorganic clusters are rapidly formed surrounding the DNA backbone, which represents a significant difference with respect to the multi-nucleation behavior observed in absence of DNA. The templating role of B-DNA in the nucleation of Mg-HAp is clearly evidenced by the RDF of $P_{inorg}\cdots P_{DNA}$ pairs (**Figure 4.15 a**), where P_{inorg} and P_{DNA} refer to the phosphate groups of the inorganic solution and DNA backbone, respectively. As it can be seen, in all cases a number of intense and well-defined sharp peaks appears at r < 9 Å, evidencing that many inorganic phosphate groups are close to the DNA phosphate groups at well-defined positions. These negatively charged groups are separated by metallic divalent cations, which act as a cement. In spite of this, it is worth noting that both the number and definition of these peaks decrease, especially at the shorter distances, with increasing Mg^{+2} concentration, suggesting that magnesium also inhibits the templating role of the biomolecule. This feature is fully consistent with the results derived from MD-W

simulations without DNA and can be explained by the lower radius of Mg^{+2} when compared to Ca^{+2}.

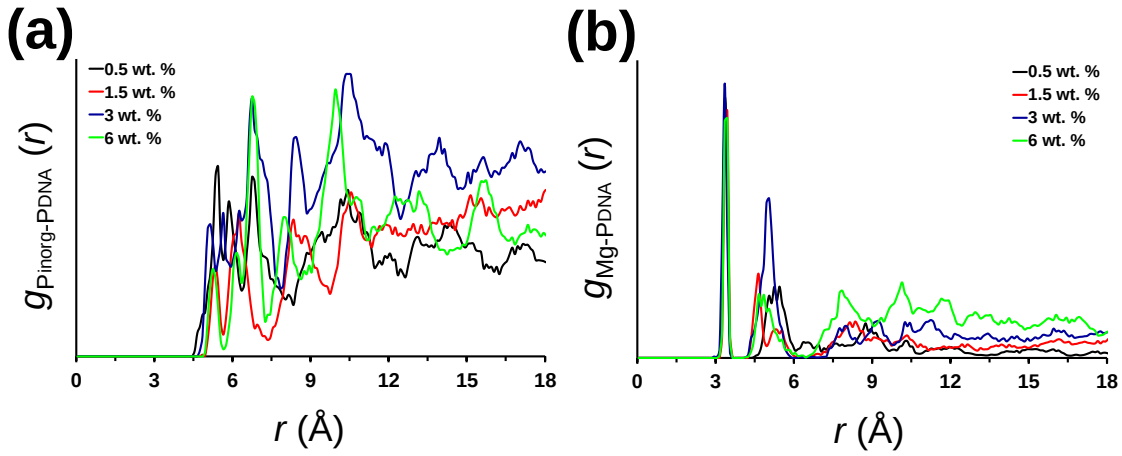

Figure 4.15. Radial distribution functions of (a) $P_{inorg}\cdots P_{DNA}$ and (b) $Mg^{+2}\cdots P_{DNA}$, pairs calculated using all the snapshots recorded during the whole production MD-W simulations in presence of B-DNA with W = 0.5, 1.5, 3 and 6 % wt. Mg^{+2}.

Finally, the RDF calculated for $Mg^{+2}\cdots P_{DNA}$ pairs (**Figure 4.15 b**) have been used to get some insights about the interaction of magnesium with DNA. The sharp and intense peak centered at $r = 3.3$ Å and the broad and less intense peaks at around ~ 5 Å clearly evidence the existence of interactions between the phosphate groups of the biomolecule and Mg^{+2}, which is fully consistent with X-ray crystallography observations.[48-50] The existence of this interaction is reinforced by the regular apparition of peaks at r ≈ 8, 10, 12 and 14 Å, which are clearly detectable for MD-3 and MD-6. Divalent magnesium can interact with both DNA bases and phosphate backbone.[50] The interaction with the latter is clearly defined by the narrow peak at $r = 3.3$ Å while the rest of the peaks should be attribute to a mixture of alternative $Mg^{+2}\cdots$phosphate coordination and $Mg^{+2}\cdots$base interactions. On the other hand, the role of Mg^{+2} in DNA structural regulation was observed to be concentration dependent.[50-52] At high concentrations there is an accumulation of Mg^{+2} binding, which induces conformational transitions from B- to Z-DNA,[50-52] while at low concentration there is a deficiency and destabilization of DNA.[50,51] The biological and clinical consequences of abnormal Mg^{+2} concentrations are DNA cleavage potentially leading to diseases and cancer.[51,52] As it is deduced from the intensity of the first peak displayed in **Figure 4.15 b**, the abundance of

$Mg^{+2}\cdots$phosphate binds is independent of the concentration of magnesium in the medium. In contrast the rest of the peaks show some dependence of the % wt. Mg^{+2}, suggesting that $Mg^{+2}\cdots$base are the only interactions affected by this variable. On the other hand, structural analysis of the double helix (not shown) indicates the bind of Mg^{+2} ions with to the phosphate groups of DNA provokes negligible changes on the B-conformation of DNA, which is in agreement with experimental evidences.[50-54]

4.4 CONCLUSIONS

The synergistic experimental-computational approach used in this work reveals how Mg^{+2} ions affect the properties of HAp and regulate the nucleation of the particles. We find that Mg^{+2} plays a crucial role in morphology and crystallinity of the particles, which in turn also depend on the synthetic procedure. Thus, a variety of morphologies (nanospheres, rods and sheets) are obtained depending on the concentration of Mg^{+2} in the reaction medium and synthetic process. Moreover, Mg^{+2} inhibits the crystallization process even when hydrothermal conditions, which promote the crystallinity of Mg^{+2}-free particles, are used. Furthermore, our results show that hydrothermal conditions and Mg^{+2} ions hinder the formation of carbonate in HAp particles. The content of Mg^{+2} in Mg-HAp particles is low (*i.e.* from 0.32 to 3.82 wt. %), independently of the synthetic method and the concentration of ions in the initial reaction medium. This is consistent with the composition of hard tissues in nature, which also exhibit very low content of Mg^{+2} in their composition.

4.5 REFERENCES

1. (a) Dorozhkin, S.V. & Epple Angew, M. Biological and medical significance of calcium phosphates. *Chem., Int. Ed*. **41**, 3130−3146 (2002); (b) Li, L., Pan, H., Tao, J., Xu, X., Mao, C., Gu, X. & Tang, R. Repair of enamel by using hydroxyapatite nanoparticles as the building blocks. *J. Mater. Chem*. **18**, 4079−4084 (2008) (c) Li, L., Mao, C., Wang, J., Xu, X., Pan, H., Deng, Y., Gu, X. & Tang, R. Bio-inspired enamel repair via Glu-directed assembly of apatite nanoparticles: an approach to biomaterials with optimal characteristics. *Adv. Mater*. **23**, 4695−4701 (2011).
2. Glimcher, M.J., in Metabolic Bone Disease and Clinically Related Disorders (Eds: L. V. Avioli, S. M. Krane), Academic Press, New York, pp. 23–50 (1998).
3. Barralet, J., Best, S. & Bonfield, W. Carbonate substitution in precipitated hydroxyapatite: an investigation into the effects of reaction temperature and bicarbonate ion concentration. *J. Biomed. Mater. Res*. **41**, 79-86 (1998).
4. Jha, L.J., Best, S.M., Knowles, J.C., Rehman, I. & Santos, J.D. Preparation and characterization of fluoride-substituted apatites. *J. Mater. Sci: Mater. Med*. **8**, 185-191 (1997).
5. Gibson, I.R., Best, S.M. & Bonfield, W. Chemical characterization of silicon-substituted hydroxyapatite. *J. Biomed. Mater. Res*. **44**, 422-428 (1999).
6. Bertinetti, L., Drouet, C., Combes, C., Rey, C., Tampieri, A., Coluccia, S. & Martra, G. Surface characteristics of nanocrystalline apatites: effect of mg surface enrichment on morphology, surface hydration species, and cationic environments. *Langmuir*. **25**, 5647-5654 (2009).
7. (a) LeGeros, R.Z., Kijkowska, R., Bautista & C., LeGeros, J.P. Synergistic effects of magnesium and carbonate on properties of biological and synthetic apatites. *Connect Tissue Res.* **33**, 203-209 (1995); (b) LeGeros, R.Z., Sakae, T., C. Bautista, Retino, M. & LeGeros, J.P. Magnesium and carbonate in enamel and synthetic apatites. *J. Dent. Res.* **10**, 225-231 (1996).
8. (a) Wang, D., Wallace, A.F., De Yoreo, J.J. & Dove, P.M. Carboxylated molecules regulate magnesium content of amorphous calcium carbonates during calcification. *Proc. Natl. Acad. Sci. U.S.A*. **106**, 21511−21516 (2009). (b) Robach, J.S., Stock, S.R. & Veis, A.Mapping of magnesium and of different protein fragments in sea urchin teeth via secondary ion mass spectroscopy. *J. Struct. Biol*. **155**, 87-95 (2006).
9. Tao, J., Zhou, D., Zhang, Z., Xu, X. & Tang, R. Magnesium-aspartate-based crystallization switch inspired from shell molt of crustacean. *Proc. Natl. Acad. Sci. U.S.A*. **106**, 22096-22101 (2009).
10. (a) Dorozhkin, S.V. Calcium ortophosphates. *J. Mater. Sci*. **42**, 1061-1095 (2007); (b) Dorozhkin, S.V. Calcium orthophosphates: occurrence, properties, biomineralization, pathological calcification and biomimetic applications. *Biomatter*. **1**, 121-164 (2011).
11. Rude, R. K., Gruber, H. E., Wei, L.Y., Frausto, A. & Mills, B. G. Magnesium deficiency: effect on bone and mineral metabolism in the mouse. *Calcif. Tissue Int*. **72**, 32-41 (2003).

12. Jälevik, B., Odelius, H., Dietz, W. & Norén, J. Secondary ion mass spectrometry and X-ray microanalysis of hypomineralized enamel in human permanent first molars. *Arch. Oral Biol.* **46**, 239−247 (2001).

13. Abbona, F. & Baronnet, A. A XRD and TEM study on the transformation of amorphous calcium phosphate in the presence of magnesium. *J. Cryst. Growth*. **165**, 98-105 (1996).

14. (a) Salimi, M.H., Heughebaert, J.C. & Nancollas, G.H. Crystal growth of calcium phosphates in the presence of magnesium ions. *Langmuir.* **1**, 119-122 (1985); (b) Kanzaki, N., Onuma, K., Treboux, G., Tsutsumi, S. & Ito, A. Inhibitory Effect of Magnesium and Zinc on Crystallization Kinetics of Hydroxyapatite (0001) Face. *Phys. Chem. B.* **104**, 4189-4194 (2000). (c) Fuierer, T.A., LoRe, M., Puckett, S.A. & Nancollas, G.H. A mineralization adsorption and mobility study of hydroxyapatite surfaces in the presence of zinc and magnesium ions. *Langmuir*. **10**, 4721-4725 (1994).

15. Yang, X., Xie, B., Wang, L., Qin, Y., Henneman, Z.J. & Nancollas, G.H. Influence of magnesium ions and amino acids on the nucleation and growth of hydroxyapatite. *CrystEngComm*. **13**, 1153-1158 (2011).

16. Ding, H., Pan, H., Xu, X. & Tang, R., Cryst. Toward a detailed understanding of magnesium ions on hydroxyapatite crystallization inhibition. *Cryst. Growth Des*. **14**, 763-769 (2014).

17. LeGeros, R.Z. in Incorporation of Magnesium in Synthetic and in Biological Apatites, Elsevier, Amsterdam, the Netherlands (1984).

18. LeGeros, R.Z. in Calcium Phosphates in Oral Biology and Medicine, Karger AG, Switzerland, Basel (1991).

19. Bertoni, E., Bigi, A., Cojazzi, G., Gandol, M., Panzavolta, S. & Roveri, N. Nanocrystals of magnesium and fluoride substituted hydroxyapatite. *J. Inorg. Biochem*. **72**, 29-35 (1998).

20. Golden, D.C. & D. W. Ming D.W. Nutrient-substituted hydroxyapatite: Synthesis and characterization. *Soil Sci. Soc. Am. J*. **63**, 657-664 (1999).

21. Suchanek, W.L., Byrappa, K., Shuk, P., Riman, R.E., Janas, V.F. & TenHuisen, K.S. Preparation of magnesium-substituted hydroxyapatite powders by the mechanochemical-hydrothermal method. *Biomaterials*. **25**, 4647-4657 (2004).

22. Ren, F., Leng, Y., Xin, R. & Ge, X. Synthesis, characterization and ab initio simulation of magnesium-substituted hydroxyapatite. *Acta Biomater*. **6**, 2787-2796 (2010).

23. Yuan, X., Zhu, B., Tong, G., Su, Y. & Zhu, X. Wet-chemical synthesis of Mg-doped hydroxyapatie nanoparticles by step reaction and ion exchange processes. *J. Mater. Chem. B.* **1**, 6551-6559 (2013).

24. Klug, H. & Alexander, L. in X-Ray Diffraction Procedure for Polycrystallite and Amorphous Materials, 2nd. Edition, John Wiley and Sons, New York (1974).

25. Landi, E., Tampieri, A., Celotti, G. & Sprio, S. Densification behaviour and mechanisms of synthetic hydroxyapatites. *J. Eur. Ceram. Soc*. **20**, 2377-2387 (2000).

26. Phillips, J.C., Braun, R., Wang, W., Gumbart, J., Tajkhorshid, E., Villa, E., Chipot, C., Skeel, R.D., Kale, L. & Schulten, K. Scalable molecular dynamics with NAMD. *J. Comput. Chem*. **26**, 1781-1802 (2005).

27. Cornell, W.D., Cieplak, P., Bayly, C.I., Gould, I.R., Merz, K.M., Ferguson, D.M., Spellmeyer, D.C., Fox, T., Caldwell, J.W. & Kollman, P.A. A Second Generation Force Field for the Simulation of Proteins, Nucleic Acids, and Organic Molecules. *J. Am. Chem. Soc*. **117**, 5179-5197 (1995).

28. Duan, Y., Chowdhury, S., Lee, M.C., Xiong, G., Zhang, W., Yang, R., Cieplak, P., Luo, R., Lee, T., Caldwell, J., Wang, J. & Kollman, P.A. A point-charge force field for molecular mechanics simulations of proteins based on condensed-phase quantum mechanical calculations. *J. Comput. Chem*. **24**, 1999-2012 (2003).

29. Bradbrook, G.M., Gleichmann, T., Harrop, S.J., Habash, J., Raftery, J., Kalb, J., Yariv, J., Hillier, I. H. & Helliwell, J.R. X-Ray and molecular dynamics studies of concanavalin-A glucoside and mannoside complexes Relating structure to thermodynamics of binding. *J. Chem. Soc. Faraday Trans*. **94**, 1603-1611 (1998)

30. Allnér, O., Nilsson, L. & Villa, A. Magnesium Ion–Water Coordination and Exchange in Biomolecular Simulations. *J. Comput. Theor. Chem*. **8**, 1493-1502 (2012).

31. Jorgensen W.L., Chandrasekhar, J., Madura, J.D., Impey, R.W.& Klein, M.L. Comparison of simple potential functions for simulating liquid water. *J. Chem. Phys*. **79**, 926-935 (1983).

32. Darden, T., York, D. & Pedersen, L. Particle mesh Ewald: An N·log(N) method for Ewald sums in large systems. *J. Chem. Phys*. **98**, 10089-10092 (1993).

33. Berendsen, H.J.C., Postma, J.P.M., van Gunsteren, W.F., DiNola, A. & Haak, J.R., Molecular dynamics with coupling to an external bath. *J. Chem. Phys.* **81**, 3684-3690 (1984).

34. Ryckaert, J.P., Ciccotti, G. & Berendsen, H.J.C. Numerical integration of the Cartesian Equations of Motion of a System with Constraints: Molecular Dynamics of n-Alkanes. J. Comput. Phys. 23, 327-341 (1977).

35. Grzeskowiak, K., Goodsell, D.S., Kaczor-Grzeskowiak, M., Cascio, D. & Dickerson, R.E. Crystallographic analysis of C-C-A-A-G-C-T-T-G-G and its implications for bending in B-DNA. Biochemistry. **32**, 8923-8931 (1993).

36. Hornak, V., Abel, R., Okur, A., Strockbine, B., Roitberg, A. & Simmerling, C. Comparison of multiple Amber force fields and development of improved protein backbone parameters. Proteins. **65**, 712-725 (2006).

37. Handbook of X-ray Photoelectron Spectroscopy, ed. J. F. Moulder, J.F., Chastain, J., Physical Electronics Division, Perkin-Elmer Corporation (1995).

38. Chang, M.C. & Tanaka, J. XPS study for the microstructure development of hydroxyapatite-collagen nanocomposites cross-linked using glutaraldehyde. *Biomaterials*. **23**, 3879-3885 (2002).

39. Cai, Y., Zhang, S., Zeng, X., Wang, Y., Qian M. & Weng, W. Improvement of bioactivity with magnesium and fluorine ionsincorporated hydroxyapatite coatings via sol–gel deposition onTi6Al4V alloys. *Thin Solid Films*. **517**, 5347-5351 (2009).

40. Silvester, L., Lamonier, J.F., Vannier, R.N., Laminoer, C., Capron, M., Mamede, A.S., Pourpoint F., Gervasini, A. & Dumeignil, F. Structural, textural and acid–base properties of carbonate-containing hydroxyapatites. *J. Mater. Chem. A.* **2**, 11073-11090 (2014).

41. Bertran, O., del Valle. L.J., Revilla-López, G., Chaves, G., Cardus L., Casas, M.T., Casanovas, J., Turon, P., Puiggalí, J. & Alemán, C. Mineralization of DNA into nanoparticles of hydroxyapatite. *Dalton Trans*. **3**, 317-327 (2014).

42. Ferguson, J.F. & McCarty, P.L. Effects of carbonate and magnesium on calcium phosphate precipitation. *Environm. Sci. Technol*. **5**, 534-540 (1971).

43. Harding, J.H., Duffy, D.M., Sushko, M.L., Rodger, P.M., Quigley, D. & Elliot, J.A. Computational techniques at the organic-inorganic interface in biomineralization. *Chem. Rev*. **108**, 4823-4854 (2008).

44. Takeshita, T., Matsuura, Y., Arakawa, S. & Okamoto, M. Biomineralization of hydroxyapatite on DNA molecules in SBF: morphological features and computer simulation. *Langmuir*. **29**, 11975-11981 (2013).

45. Revilla-López, G., Casanovas, J., Bertran, O., Turon, P., Puiggalí, J. & Alemán, C. Modeling biominerals formed by apatites and DNA. *Biointerphases*. **8**, 10-25 (2013).

46. Vasconcellos, K.B., McHugh, S.M., Dapsis, K.J., Petty, A.R. & Gerdon, A.E. Biomimetic nanoparticles with polynucleotide and PEG mixed-monolayers enhance calcium phosphate mineralization. *J. Nanopart. Res*. **15** (1942).

47. Casanovas, J., Revilla-López, G., Bertran, O., del Valle, L.J., Turón, P., Puiggalí, J. & Alemán, C. Restricted Puckering of Mineralized RNA-Like Riboses. *J. Phys. Chem. B*. **118**, 5075-5081 (2014).

48. Robinson, H., Gao, Y.G., Sanishvili, R., Joachimiak, A. & Wang, H.J. Hexahydrated magnesium ions bind in the deep major groove and at the outer mouth of A-form nucleic acid duplexes. *Nucl. Acids Res*. **28**, 1760-1766 (2000).

49. Minasov, G., Tereshko, V. & Egli, M. Atomic-resolution crystal structures of B-DNA reveal specific influences of divalent metal ions on conformation and packing. *J. Mol. Biol*. **291**, 83-99 (1999).

50. Egli, M. DNA-Cation Interactions: Quo Vadis?. *Chem. Biol*. **9**, 277-286 (2002).

51. Hanahan, D. & Weinberg, R.A. Hallmarks of cancer: the next generation. *Cell*. **144**, 646-674 (2011).

52. Colotta, F., Allavena, P., Sica, A., Garlanda, C. & Mantovani, A. Cancer-related inflammation, the seventh hallmark of cancer: links to genetic instability. *Carcinogenesis*. **30**, 1073-1081 (2009).

53. Bancroft, D., Williams, L.D., Rich, A. & Egli, M. The low-temperature crystal structure of the pure-spermine form of Z-DNA reveals binding of a spermine molecule in the minor groove. *Biochemistry*. **33**, 1073-1086 (1994).

54. Ponkumar, S., Duraisamy, P. & Iyandurai, N. Structural Analysis of DNA Interactions with Magnesium Ion Studied by Raman Spectroscopy. *Am. J. Biochem. Biotechnol*. **7**, 135–140 (2011).

5.

AN EXPERIMENTAL-COMPUTER MODELING STUDY OF INORGANIC PHOSPHATES SURFACE ADSORPTION ON HYDROXYAPATITE PARTICLES

The adsorption of orthophosphate, pyrophosphate, triphosphate and a trisphosphonate onto hydroxyapatite has been examined using experiments and quantum mechanical calculations. Adsorption studies with FTIR and X-ray photoelectron spectroscopies have been performed considering both crystalline hydroxyapatite (HAp) and amorphous calcium phosphate particles, which were specifically prepared and characterized for this purpose. Density Functional Theory (DFT) calculations have been carried out considering the (100) and (001) surfaces of HAp, which were represented using $1 \times 2 \times 2$ and $3 \times 3 \times 1$ slab models, respectively. The adsorption of phosphate onto such two crystallographic surfaces is very favored from an energetic point of view, which is fully consistent with current interpretations of HAp growing process. The structures calculated for the adsorption of pyrophosphate and triphosphate evidence that this process is easier for the latter than for the former. Thus, the adsorption of pyrophosphate is severely limited by the surface geometry while the flexibility of triphosphate allows transforming repulsive electrostatic interactions into molecular strain. On the other hand, calculations predict that the trisphosphonate only adsorps onto the (001) surface of HAp. Theoretical predictions are fully consistent with experimental data. Thus, comparison of DFT results and spectroscopic data suggest that the experimental conditions used to prepare HAp particles promote the predominance of the (100) surface. Accordingly, experimental identification of the adsorption of trisphosphonate onto such crystalline particles is unclear while the adsorption of pyrophosphate and triphosphate are clearly observed.

5.1 INTRODUCTION

Bone mineral crystals are compositionally and structurally similar to the synthetic hydroxyapatite (HAp), $Ca_{10}(PO_4)_6\ (OH)_2$.[1] Consequently, the ability of this bioceramic to interact with other with living systems, like cells, as well as with biomolecules are of key interest. In this work we focus on the capacity of HAp to interact with orthophosphate (PO_4^{3-}), pyrophosphate ($P_2O_7^{4-}$) and polyphosphate (polyP). Furthermore, the study has been extended to biophosphonates (BPs), which are stable analogues of inorganic pyrophosphates. In order to illustrate the relevance of this topic for both biomedicinal and biotechnological fields, relationships between all these compounds and HAp are briefly discussed below.

In the last years scaffolds constructed with HAp have been used for bone regeneration.[2-12] A very successful strategy was to enhance bone regeneration by adsorbing inorganic polyP onto HAp.[13-18] PolyP, which is an orthophosphate polymer found in mammalian organisms,[19] stabilizes basic cell growth and differentiation promoting bone regeneration.[20-22] Furthermore, short chains of polyP have been detected, together with, in $P_2O_7^4$ human platelets,[23] linking coagulation and inflammation.[24] PolyP has also been identified in patients with myeloma cells, a malignant transformation of plasma cells.[25] In addition, polyP plays an important role in cancer metastasis[26,27] and in virulence of different bacteria and a number of parasites.[28]

On the other hand, early studies reported that polyP and $P_2O_7^{4-}$ behave as HAp crystal growth inhibitors.[29-31] More recently, Grynpas and coworkers[32] proposed that the production of polyP, which forms strong complexes with divalent cations such as Ca^{+2},[33] can lead to a high local accumulations of total phosphate and Ca^{+2}. Accordingly, polyP was proposed to play an important role in cartilage mineralization and bone formation, this hypothesis being supported by both the adsorption of polyP onto HAp and the correlation between the hydrolytic degradation of polyP in Ca^{+2}-polyP complexes and the increment of and PO_4^{3-} and Ca^{+2} concentrations.

Despite fifteen years ago Okazaki *et al*.[34] proposed that DNA inhibits HAp growth, more recent studies proved that the formation of HAp can be regulated by DNA, which acts as a template in the process of “biomineralization”.[35-38] Thus, the role of DNA as template

to promote mineral formation and the own biomineralization mechanism has been recently examined at the atomic level.[35-38] Results showed that calcium phosphate clusters are formed surrounding the polyP backbone of DNA, which acts as a very large nucleus for the growing of the HAp. Also, HAp nanoparticles are suitable as gene delivery systems for the transfection of cells with nucleic acids.[39-41] Thus, HAp confers protection to DNA from chemical and enzymatic degradation, increasing the stability of the biomolecule.[41,42]

On the other hand, the BPs the oxygen atom that links the phosphate groups of pyrophosphates is replaced by a carbon atom. This substitution provokes resistance towards both hydrolytic and enzymatic degradations.[43] It has been observed that the affinity of BPs towards HAp can be modulated by varying the chemical nature of the groups attached to the tertiary carbon atom. In particular, the incorporation of amino functionalities increases the affinity towards HAp.[44-46] Recent studies suggested that nitrogen-containing BPs form strong hydrogen bonds with the HAp matrix.[47] Furthermore, BPs are primary agents in the current pharmacological arsenal against different bone diseases (*e.g.* osteoporosis, Paget disease of bone and malignancies metastatic to bone).[48]

In this work we examine the adsorption of PO_4^{3-}, $P_2O_7^{4-}$, polyP and amino-tris(methylenephosphonic acid), a BP hereafter denoted ATMP, on HAp using a combined experimental-theoretical approach. In order to provide a clearer picture about the influence of the phosphate size on the whole adsorption process, sodium triphosphate ($Na_5P_3O_{10}$) has been used to describe polyP in both experiments and theoretical calculations. Initially, the adsorption of $P_2O_7^{4-}$ and polyP on both amorphous calcium phosphate and crystalline synthetic HAp (hereafter named ACP and cHAp, respectively) has been investigated using FTIR spectroscopy and X-ray photoelectron spectroscopy (XPS). Once this has been proved and the influence of the compound concentration and the pH have been determined, valuable microscopic information about the adsorption of PO_4^{3-}, $P_2O_7^{4-}$, polyP and ATMP on HAp have been obtained using Density Functional Theory (DFT) calculations.

5.2 EXPERIMENTAL SECTION

5.2.1 Materials

Tetrasodium pyrophosphate ($P_2O_7^{4-}$), sodium triphosphate (polyP), ATMP, ammonium phosphate dibasic [$(NH_4)_2HPO_4$; purity ≥ 99.0 %] and ammonium hydroxide solution 30 % (NH_4OH; purity: 28-30 %) were purchased from Sigma-Aldrich. Calcium nitrate [$Ca(NO_3)_2$; purity ≥ 99.0 %] was purchased from Panreac (Barcelona, Spain). Ethanol (C_2H_5OH; purity ≥ 99.5 %) was obtained from Scharlab (Barcelona, Spain).

5.2.2 Synthesis of HAp

ACP and HAp samples were prepared using the same procedure but applying different experimental conditions to the reaction mixture. Reagent conditions were adjusted to get a Ca/P ratio of 1.67. In all cases 15 mL of 0.5 M $(NH_4)_2HPO_4$ in de-ionized water (pH adjusted to 11 with ammonia 30% w/w) were added drop-wise (2 mL·min^{-1}) and under agitation (400 rpm) to 25 mL of 0.5 M $Ca(NO_3)_2$ in ethanol. After that, the reaction mixture was stirred 1 h (400 rpm) at room temperature. In the case of ACP the resultant suspension was aged for 24 h at 37 ºC, whereas hydrothermal conditions were applied during 24 h for cHAp. In both cases, the precipitate was separated by centrifugation and sequentially washed with de-ionized water and a 60/40 v/v mixture of ethanol-water (twice). A white powder was obtained after freeze-drying.

5.2.3 Measurements

X-Ray diffraction. Crystallinity was studied by wide angle X-ray diffraction (WAXD). Patterns were acquired using a Bruker D8 Advance model with CuK_α radiation ($\lambda = 0.1542$ nm) and geometry of Bragg-Bretano, theta-2 theta. A one-dimensional Lynx Eye detector was employed. Samples were run at 40 kV and 40 mA, with a 2-theta range of 2−40, measurement steps of 0.02 º, and time/step of 2−8 s. Diffraction profiles were processed using PeakFit v4 software (Jandel Scientific Software) and the graphical representation performed with OriginPro v8 software (OriginLab Corporation, USA).

The crystallite size (*L*) in the direction perpendicular to the representative (211) planes of samples was derived from the X-ray diffraction line broadening measurement using the Scherrer equation:[49]

$$L = \frac{0.9\lambda}{\beta \cos\theta} \quad (1)$$

where λ is the wavelength (CuK_α), β is the full width at half maximum height of the (211) line, θ is the diffraction angle and 0.9 is a shape factor. The crystallinity (χ_c) was obtained using the following equation:[50]

$$\chi_c = 1 - \frac{V_{112/300}}{I_{300}} \quad (2)$$

where I_{300} is the intensity of the (300) reflection and $V_{112/300}$ is the intensity of the hollow between the (112) and (300) reflections, which disappears in non-crystalline samples.

Morphological characterization. Scanning electron microscopy (SEM) studies were carried out using a Focused Ion Beam Zeiss Neon40 microscope operating at 5 kV, equipped with an energy dispersive X-ray (EDX) spectroscopy system. Samples were deposited on a silicon disc mounted with silver paint on pin stubs of aluminum, and sputter-coated with a thin layer of carbon to prevent sample charging problems.

HAp protonation assay. The protonation ability of ACP and cHAp samples was determined using the following procedure: HAp particles suspended in milli-Q water (1 mg/mL) were protonated by adding an aqueous solution of 100 mM HCl and 50 mM $NaCl$ up to pH ≈ 3. Samples (5 mL) were maintained in a vial with continuous stirring, the pH values being determined every minute at 20 ºC using a pH-meter. The total time for this assay was 15 minutes.

Adsorption onto ACP and cHAP. The ability of ACP and cHAp to adsorb polyP, $P_2O_7^{4-}$ and ATMP was determined using FTIR spectroscopy. The effects of both the concentration of adsorbate and the pH in the adsorption process were examined by preparing different working aqueous solutions, which were subsequently used for the incubation process. More specifically, the concentration of the adsorbate in the working solutions ranged from 25 to 200 mM while the pHs considered in this study were 4, 6, 7 and 9. In the case of $P_2O_7^{4-}$ such concentrations were reduced to a half (*i.e*. from 12.5 to 100 mM) because of limitations in the solubility of this specie.

For the incubation, 500 μL of the working solution with the adsorbate were deposited onto 50 mg of ACP or cHAp. After overnight agitation at 25 ºC, adducts were separated by centrifugation at 6500 rpm during 5 minutes at 4 ºC. Sediments were re-suspended in distilled water. After this process, which was repeated two times, the obtained pellets were frozen at −80 ºC for 3 h and, subsequently, the humidity was removed using a lyophilizer.

Fourier transform infrared (FTIR) spectroscopy. Infrared absorption spectra were recorded with a Fourier Transform FTIR 4100 Jasco spectrometer in the 1800−700 cm^{-1} range. A Specac model MKII Golden Gate attenuated total reflection (ATR) equipment with a heated Diamond ATR Top-Plate was used. The characteristic bands of the compounds studied in this work (substrates and adsorbed species) are listed in **Table 5.1.**

Table 5.1. Characteristic FTIR bands of the species studied in this work.

Compound		**ν**
ACP and cHAp	PO_4^{3-} ν_1	962
	PO_4^{3-} ν_3	1022, 1059, 1089
polyP	P–O–P symmetric stretching	734
	P–O–P asymmetric stretching	890
	PO_3^{2-} vibrations	1100-1200
$P_2O_7^{4-}$	P–O–P symmetric stretching	736
	P–O–P asymmetric stretching	889
	PO_3^{2-} vibrations	1100-1200
ATMP	P–O–CH_2 stretching	1070
	asymmetric vibrations of alkylphosphonic	939
	symmetric vibrations of alkylphosphonic	1000
	P–C stretching	985

X-ray photoelectron spectroscopy (XPS). XPS analyses were performed in a SPECS system equipped with a high-intensity twin-anode X-ray source XR50 of Mg/Al (1253 eV/1487 eV) operating at 150 W, placed perpendicular to the analyzer axis, and using a

Phoibos 150 MCD-9 XP detector. The X-ray spot size was 650 µm. The pass energy was set to 25 and 0.1 eV for the survey and the narrow scans, respectively. Charge compensation was achieved with a combination of electron and argon ion flood guns. The energy and emission current of the electrons were 4 eV and 0.35 mA, respectively. For the argon gun, the energy and the emission current were 0 eV and 0.1 mA, respectively. The spectra were recorded with a pass energy of 25 eV in 0.1 eV steps at a pressure below 6×10^{-9} mbar. These standard conditions of charge compensation resulted in a negative but perfectly uniform static charge. The $\mathrm{C}\ 1s$ peak was used as an internal reference with a binding energy of 284.8 eV. High-resolution XPS spectra were acquired by Gaussian-Lorentzian curve fitting after s-shape background subtraction. The surface composition was determined using the manufacturer's sensitivity factors.

Quantum mechanical calculations. All DFT calculations were performed using the Gaussian 09[51] computer package. Both the (100) and (001) surfaces of HAp, which were represented without periodic boundary conditions but using relatively large slab models, were considered for all the examined adsorbates. More specifically, the following strategy was used to choose the dimensions of the slab models. Initially the orthophosphate adsorption onto HAp was studied considering following slab dimensions for the (100) surface: 1 × 1 × 1, 1 × 1 × 2, 2 × 1 × 2 and 1 × 2 × 2; while for the (001) surface these were: 2 × 1 × 1, 2 × 2 × 1, 2 × 2 × 2 and 3 × 3 × 1. The selection of the models was based on the following two conditions: (i) the interaction pattern between the surface and the adsorbate is not altered by the enlargement of the slab dimensions (*i.e.* the influence of the boundary effects in the mode of interaction is null); and (ii) the variation of the binding energy (BE) due to the enlargement of the slab model is ≤ 8 %. In this work, only results obtained using the two larger slab models, which were used to adsorb $\mathrm{P_2O_7^{4-}}$, polyP and ATMP, are discussed since interactions provided the smaller models are not representative. **Table 5.2** displays the molecular formulas of all systems studied in this work (both adsorbed molecules and slab models).

The hexagonal HAp crystal unit cell with $\mathrm{P6_3/m}$ geometry ($a = b =$ 9.421 Å, $c =$ 6.88 Å, $\alpha = \beta =$ 90 º, and $\gamma =$ 120 º) and the 4e Wyckoff position occupied by two hydroxyl ions, each with $\frac{1}{2}$ occupancy,[52] was generated and, subsequently, was cleaved to obtain the (100) and (001) surfaces. Initial configurations for the adsorptions complexes between the two considered surfaces and the four studied compounds

(PO_4^{3-}, $P_2O_7^{4-}$, polyP and ATMP) were prepared by considering all possible coordination modes. Geometries of the different initial adsorbate configurations for all the investigated systems were fully optimized using the B3LYP[53,54] functional combined with the 6-31G(d) basis set.

BEs were corrected with the basis set superposition error (BSSE) by mean of the standard counterpoise (CP). The BE of the complex is defined as usual by subtracting the energy of the surface and the adsorbate from the energy of the complex. It should be remarked that, due to the limitations of models described above (*i.e*. gas-phase, limited size of the surface, static description of the system, etc…), the calculated BEs cannot be interpreted as a quantitative description of the strength of the system. However, qualitative comparison of the relative BEs is expected to provide microscopic understanding of experimental observations.

Table 5.2. Molecular formula of all systems studied in this work

#	**System**	**Molecular formula**
Adsorbed compounds	Orthophosphate	PO_4^{3-}
	Pyrophosphate	$P_2O_7^{4-}$
	PolyP	$P_3O_{10}^{5-}$
	ATMP	$N(CH_2PO_3)_3^{-6}$
(100) Surface	1 ×1 × 1 slab model	$Ca_{10}(PO_4)_6\ (OH)_2$
	1 × 1 × 2 slab model	$Ca_{20}(PO_4)_{12}\ (OH)_4$
	2 × 1 × 2 slab model	$Ca_{40}(PO_4)_{24}\ (OH)_8$
	1 × 2 × 2 slab model	$Ca_{40}(PO_4)_{24}\ (OH)_8$
(001) Surface	2 × 1 × 1 slab model	$Ca_{20}(PO_4)_{12}\ (OH)_4$
	2 × 2 × 1 slab model	$Ca_{40}(PO_4)_{24}\ (OH)_8$
	2 × 2 × 2 slab model	$Ca_{80}(PO_4)_{48}\ (OH)_{16}$
	3 × 3 × 1 slab model	$Ca_{90}(PO_4)_{54}\ (OH)_{18}$

5.3 RESULTS AND DISCUSSION

5.3.1 Characterization of ACP and cHAp

The morphologies of ACP and cHAp, which are displayed in **Figure 5.1**, reflect the noticeable influence of hydrothermal and aging conditions. cHAp samples, which were prepared using hydrothermal conditions, show laminar crystals and fusiform rods, while ACP particles obtained using open aging, exhibit an pseudo-spherical morphology of nanometric dimensions. The average dimensions of ACP pseudo-spheres and cHAp rods are displayed in **Table 5.3**.

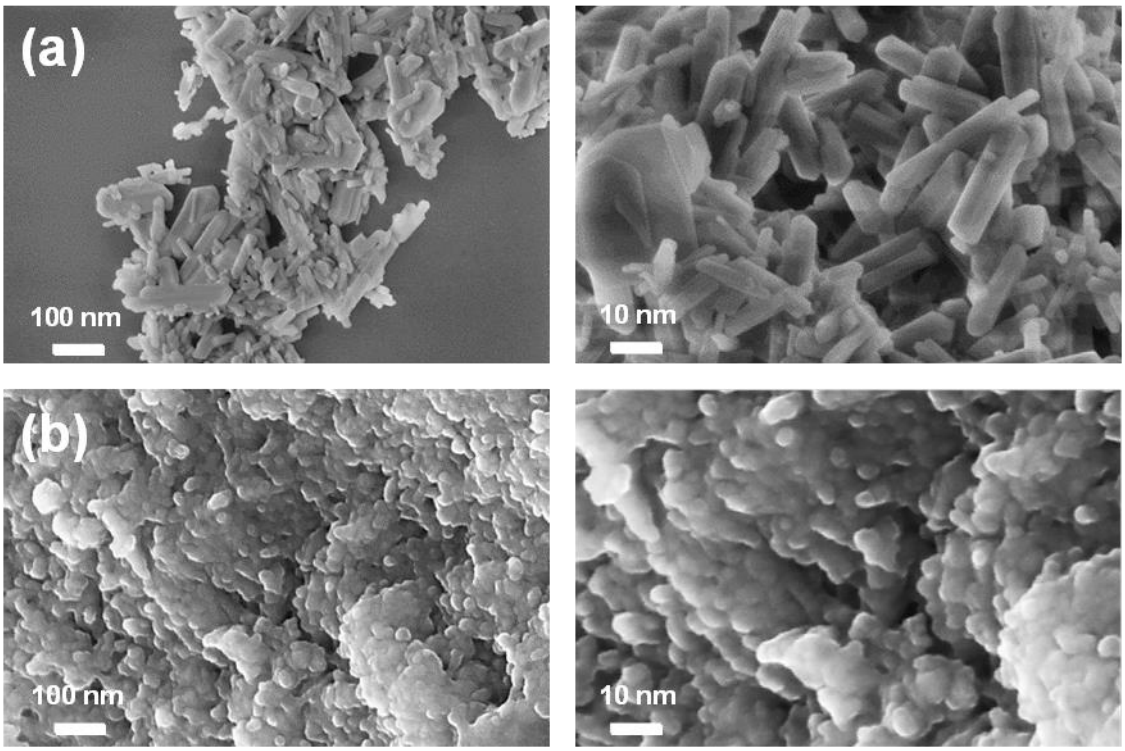

Figure 5.1. Morphology of particles synthesized for this study: (a) cHAp and (b) ACP. Left and right show low and high resolution SEM micrographs.

Table 5.3. Physical parameters as determined by SEM and X-ray diffraction for ACP and cHAp.

	ACP	**cHAp**
Average radius (R) and length (ℓ) of the observed nanostructures	R= 2.6 ± 0.2 nm	R = 2.8 ± 0.2 nm ℓ = 21 ± 3 nm
Cristallinity (see Eqn 1)	χ_c= 3 ± 1 %	χ_c= 56 ± 4 %
Crystallite size (see Eqn 2)	L = 6 ± 1 nm	L = 55 ± 8 nm

Characterization of two synthesized particles by X-ray diffraction (**Figure 5.2**) was focused on peaks at 2θ between 31.5 º and 34.5 º, which correspond to the (211), (112), and (300) HAp reflections. The crystallinity and crystallite size determined for ACP and cHAp samples are listed in **Table 5.3**. The physical differences between ACP and cHAp particles are expected to affect their properties. This is proved in **Figure 5.3**, which compares the response of the two HAp particles to acidic environments. Thus, titration results display a steep pH gradient for cHAp, whereas the slow and gradual variation of the pH evidences a remarkable buffering effect for the ACP sample. This result indicates that crystallinity plays a major role reducing the proton-buffering capacity of HAp.

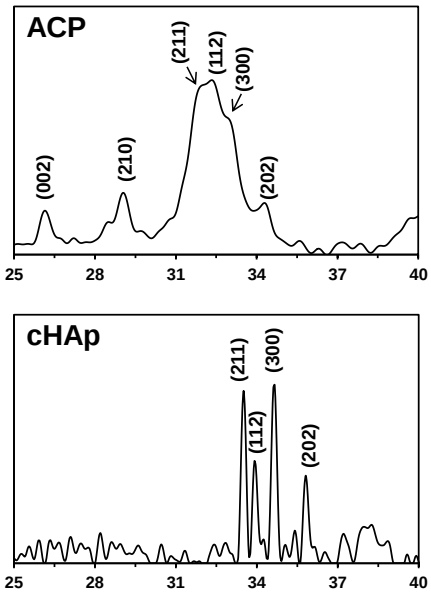

Figure 5.2. X-ray diffraction patterns of the HAp particles prepared in this work: ACP and cHAp. The hydroxyapatite was identified by the peaks at 33 º–34 º 2θ.

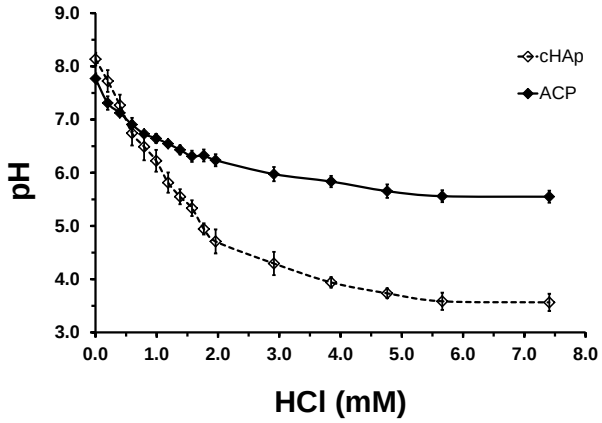

Figure 5.3. Proton-buffering capacity of the cHAp and ACP particles prepared in this work.

5.3.2 Experimental detection of adsorption onto ACP and cHAp

The FTIR spectra of the synthesized ACP and cHAP, polyP, $P_2O_7^{4-}$ and ATMP are displayed in **Figure 5.4**, while the most characteristic bands of each compound are listed in **Table 5.1**. It should be noted that the asymmetric and symmetric stretching vibration of the $P-O-P$ bridges are characteristic of polyP and $P_2O_7^{4-}$, even though they are not observed for ACP and cHAp. The PO_3^{2-}vibration modes of polyP and $P_2O_7^{4-}$ are detected in 1000−1200 cm^{-1} domain, as detailed in previous work.[55] On the other hand, the ATMP spectrum was recently described by some of us.[56]

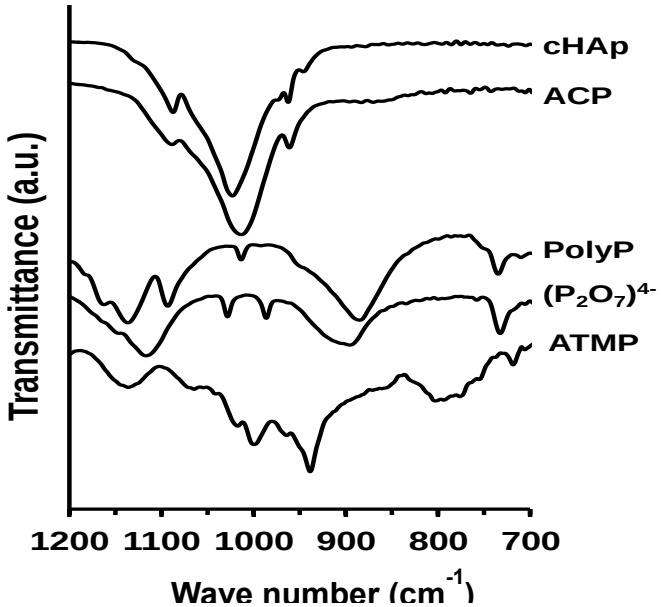

Figure 5.4. FTIR spectra of cHAp, ACP, polyP, $P_2O_7^{4-}$and ATMP.

Figure 5.5 displays the FTIR spectra of cHAp and ACP recorded after incubation in solutions with different concentrations of polyP, $P_2O_7^{4-}$ and ATMP at neutral pH. For polyP the characteristic absorption band is clearly identified at around 891–894 cm^{-1} for all concentrations ≥ 50 mM, even though it is only a weak shoulder for 25 mM. The band at 734 cm^{-1} is only detectable for the largest concentration, 200 mM. Regarding the adsorption of $P_2O_7^{4-}$, a very weak shoulder associated to the band at 889 cm^{-1} is observed for all tested concentrations while, in opposition, the band at 736 cm^{-1} remains practically undetectable. Although these results evidence the adsorption of polyP and $P_2O_7^{4-}$, difficulties in the identification of some characteristic bands suggest some limitations in such association processes. Theoretical calculations provide microscopic details about such limitations in next sub-sections. Unfortunately, identification of adsorbed ATMP molecules is a very complex task, especially in cHAp samples, in which no clear band is observed. For ACP, the shoulder detected at ~ 900 cm^{-1} for ATMP concentrations ≤ 100 mM, transforms into a broad but weak band for 200 mM.

The influence of the pH in the adsorption process is displayed in **Figure 5.6**, which shows the FTIR spectra of cHAp and ACP after incubation in 200 mM polyP, 100 mM $P_2O_7^{4-}$ and 200 mM ATMP at pH 6, 7 and 9. As it can be seen, adsorption is detected in all cases, even though changes in the spectra recorded at pH 6 point to the degradation of the nanoparticles. This is particularly evident for ACP, which presents the higher proton-buffering capacity than cHAp. Such feature suggests that the chemical protection against the acid is provoked by the delivery of anionic species during the degradation process. On the other hand, the adsorption of polyP and $P_2O_7^{4-}$ is apparently favored at pH 7 with respect to pH 9 for both ACP and cHAP, this feature being corroborated by the ratios (not shown) between the intensity of the characteristic band associated to each of these compound and the intensity of the PO_4^{3-} band for cHAP and ACP.

The ability of cHAp and ACP to bind polyP and $P_2O_7^{4-}$ has been corroborated by XPS. **Figure 5.7** represents the characteristic XPS spectra in the $O\ 1s$ region of cHAp as prepared and after incubation in presence of polyP (200 mM), $P_2O_7^{4-}$ (100 mM) and ATMP (200 mM). The sharp peak at 531.2 eV involve in all cases to the $O\ 1s$ of the PO_4^{3-} and OH^- groups of cHAP.[57] The spectra of samples incubated in presence of

polyP and $P_2O_7^{4-}$ show a shoulder at 533.3 eV, which corresponds to the oxygen atom involved in symmetric bridging $P-O-P$ groups of the adsorbed molecules.[58] This result supports the adsorption previously detected by FTIR spectroscopy. Finally, the broad peak at 536.3 eV, which is only detected in samples with adsorbed polyP and $P_2O_7^{4-}$, can be attributed to non-bridging oxygen atoms,[59] water accompanying the adsorbed compounds[60] or a combination of both.

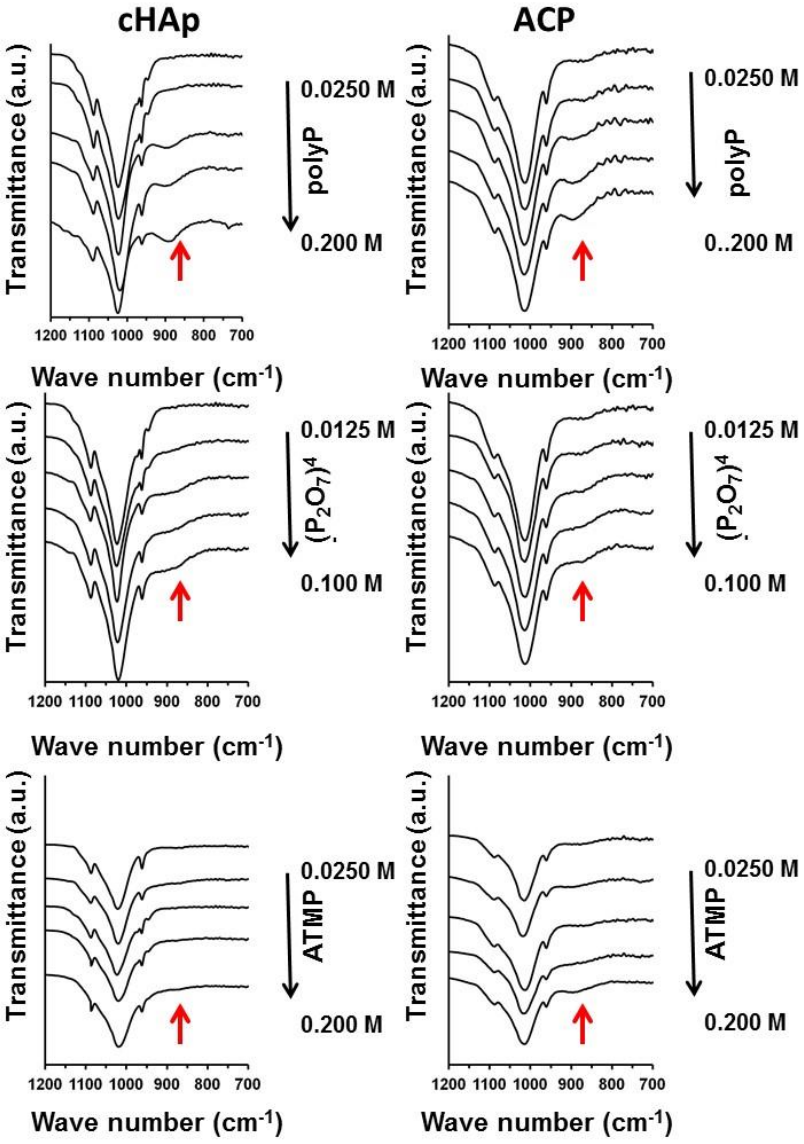

Figure 5.5. FTIR spectra of cHAp (left) and ACP (right) samples incubated in presence of different concentrations of polyP (25, 50, 100 and 200 mM; top), $P_2O_7^{4-}$ (12.5, 25, 50 and 100 mM; middle) and ATMP (25, 50, 100 and 200 mM; bottom). The concentration of adsorbate increases from top-to-down. The most important band are marked with arrows.

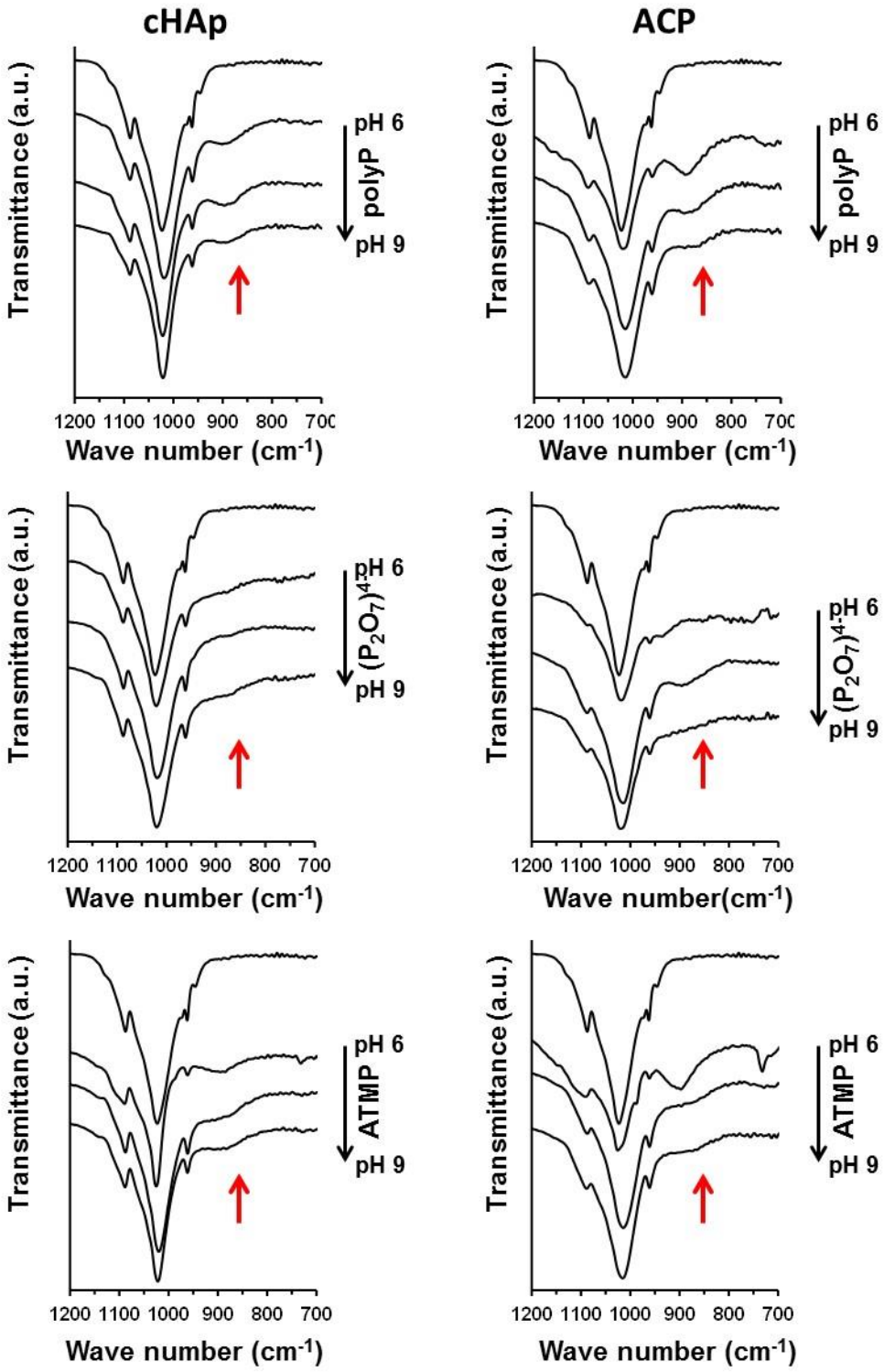

Figure 5.6. FTIR spectra of cHAp (left) and ACP (right) samples incubated in presence of polyP (200 mM; top), $P_2O_7^{4-}$ (100 mM; middle) and ATMP (200 mM; bottom) at pH 6, 7 and 9. The pH increases from top-to-down. The most important band are marked with arrows.

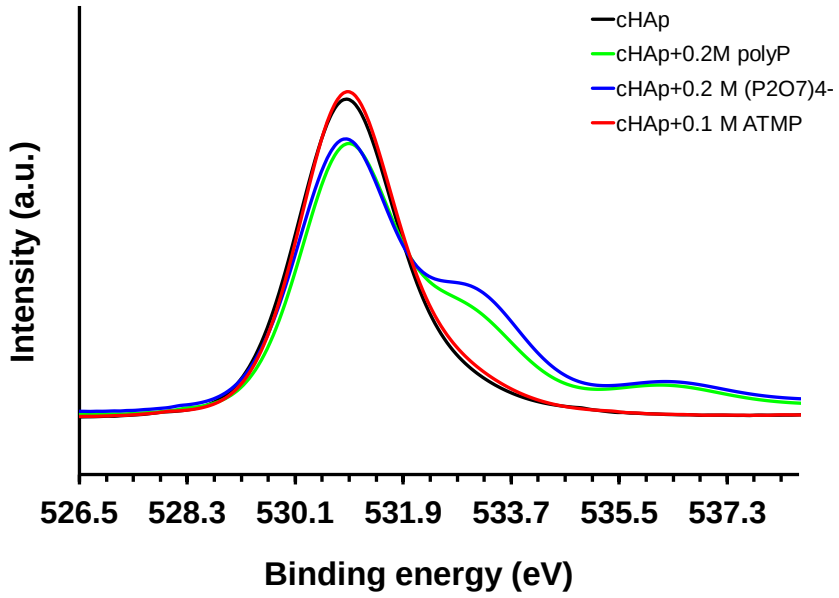

Figure 5.7. High-resolution XPS spectra in the $O\ 1s$ region for cHAp samples before and after incubation in presence of polyP (200 mM; top), $P_2O_7^{4-}$ (100 mM; middle) and ATMP (200 mM; bottom) at pH 7.

5.3.3. Theoretical characterization of orthophosphate adsorption onto HAp

The two HAp planes considered in this work are the (001) and (100), which is isostructural with the (010). The (001) is the most stable HAp surface[61-64] and was identified as the crystal growth plane during the biomineralization of teeth and hard tissues.[64-66] **Figure 5.8 a** shows the projection of the (001) plane in the unit cell as well as the 2 × 2 × 1 and 3 × 3 × 1 slab models. In order to preserve as much as possible the surface symmetry and the electroneutrality, species farthest from the center of the supercell were added in the first model, or removed in the second one. As a consequence of such changes, the boundaries of the two surfaces present some differences that involve the hydroxyl groups. However, comparison between the results obtained for these slab models (see below) indicated that such differences are located far enough from the adsorption sites and do not affect the interaction pattern. The selected 2 × 2 × 1 and 3 × 3 × 1 models contain 201 and 293 explicit atoms, respectively. On the other hand, it is not possible to construct a slap of the (100) surface with same termination at both sides. Thus, construction of a stable (100) surface, in which the total dipole moment across the slab perpendicular to the surface is zero, leads to sides that differ in the content of OH^- and Ca^{+2} ions. One side only contains Ca^{+2} and PO_4^{3-} while the other side involves Ca^{+2}, OH^- and PO_4^{3-}. In a recent study[41] we found that the binding of

DNA is disfavored for the latter termination. In this study we have only considered the termination with OH^- and Ca^{+2} ions for the (100) surface. **Figure 5.8 b** represents the projection of the (100) plane in the unit cell as well as the 1 × 2 × 2 slab model (176 explicit atoms).

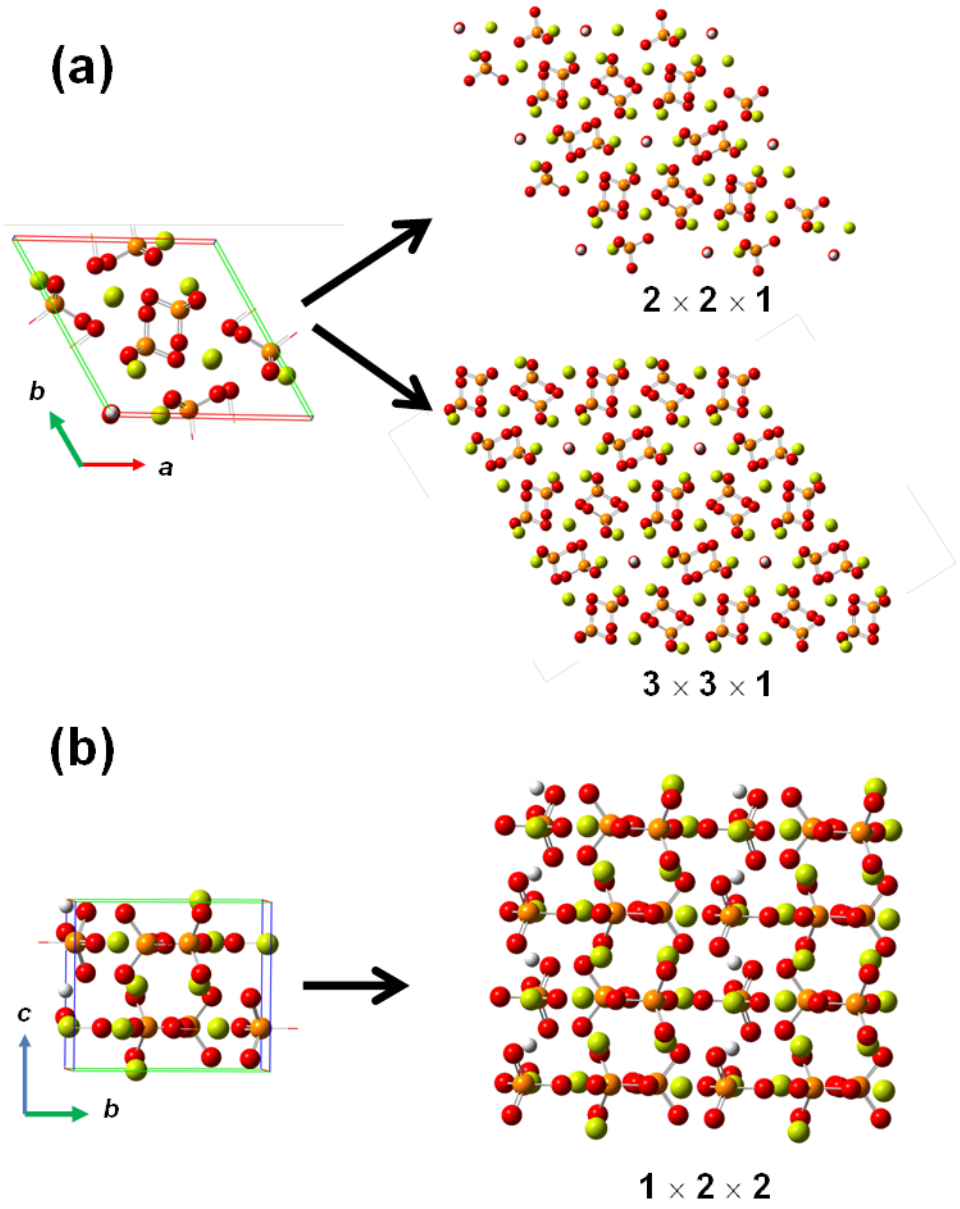

Figure 5.8. Unit cell (left) and *n* × *m* × *n* slab models (right) used to represent the (a) (001) and (b) (100) surfaces in DFT calculations

Although different initial configurations were considered for the adsorption of PO_4^{3-} onto the (001) and (100) surfaces of HAp, all them converged to the same complex (*i.e.* excluding those complexes in which the adsorbate moved towards the outer regions of the finite model used to described the surface) and those in which the slab model was

too small (*i.e.* 2 × 1 × 1 and 1 × 1 × 1 for the (001) and (100), respectively). **Figure 5.9** displays details of the geometric features of the adsorbed complex obtained for each surface while binding energies (BEs) are displayed in **Table 5.4**. As it can be seen in **Figure 5.9 a**, which represents the complex calculated using the largest slab model, the adsorption of PO_4^{3-} involves two interaction sites located at different heights. Consequently, the resulting $Ca^{+2}\cdots O$ distances differ by ~ 0.15 Å in the two calculated models. Although the BE improves by increasing the slab size of the (001) surface, the adsorption onto the (100) surface is clearly favored. The adsorption onto the (100) surface occurs through a tridentate coordination mode (**Figure 5.9 b**). The additional interaction site and the most favorable geometry, which is reflected by smaller $Ca^{+2}\cdots O$ distances, provoke a reduction in the BE with respect to that obtained the (001) surface. On the other hand, it should be mentioned that enlargement of the thickness of the simulated HAp using the slab models described in **Table 5.2** does not provide any change in terms of both interaction pattern and relative BEs for both (100) and (001) surfaces (**Table 5.4**).

Table 5.4. Geometric and binding energies of the adsorbed complex

Surface	Slab model	Adsorbate	BE (kcal/mol)
(001)	2 × 2 × 1	PO_4^{3-}	−518.8
	2 × 2 × 2	PO_4^{3-}	−526.4
	3 × 3 × 1	PO_4^{3-}	−548.1
		$P_2O_7^{4-}$	Unstable
		PolyP	−735.0
		ATMP	−1138.5
(100)	1 × 1 × 2	PO_4^{3-}	−531.5
	2 × 1 × 2	PO_4^{3-}	−545.9
	1 × 2 × 2	PO_4^{3-}	−594.9
		$P_2O_7^{4-}$	−748.8
		PolyP	−871.5
		ATMP	Unstable

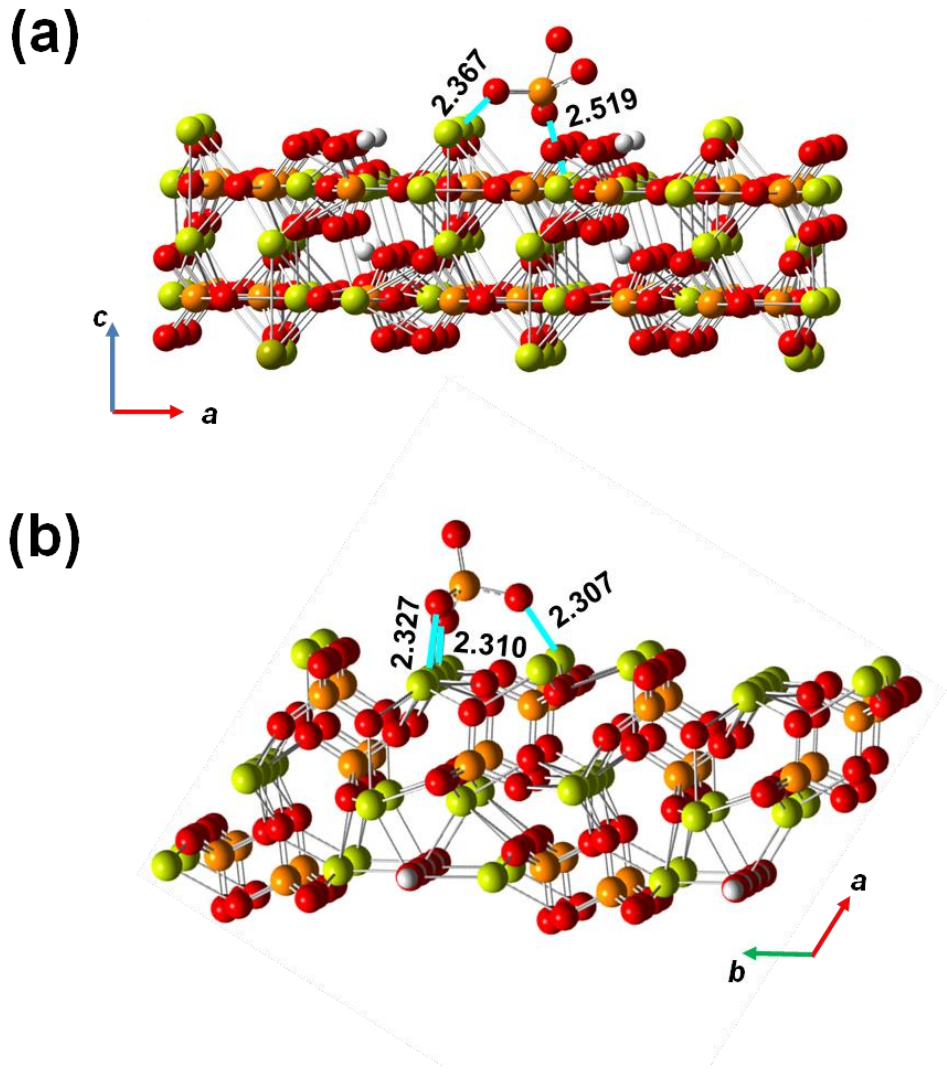

Figure 5.9. Lowest energy structure obtained for the adsorption of PO_4^{3-} onto the (a) (001) and (b) (100) surfaces of HAp. The (001) and (100) surfaces are represented by 3 × 3 × 1 and 1 × 2 × 2 slab models. $Ca^{+2}\cdots O$ interactions are indicated by blue lines, distances (in Å) between the coordination sites and the oxygen atoms of the adsorbate being also displayed.

The favorable BEs obtained for adsorption of PO_4^{3-} onto the examined surfaces (**Table 5.4**) is consistent with the different models used to explain the crystal growth of HAp. In the current interpretation of the crystal growth process, the existence of calcium phosphate clusters acting as HAp growth unit seems to be widely accepted.[67,68] Following such cluster growth model, the formation of small calcium phosphate particles has been also examined using computer simulation techniques based on classical force-fields, which evidenced that clusters play a key role in the biomineralization process.[38,69] Another model is the surface-induced crystallization, which is a common event in the mineralization of bone and dental hard tissues. The low interfacial energy between PO_4^{3-}

and the HAp surfaces[67,70] clearly suggests that adsorption of the former ions favors the crystal growth from an early forming phase. Quantum mechanical results described in this section evidence that the incorporation of new PO_4^{3-} ions onto both already formed crystals and incipient crystals formed through the aggregation of small clusters is very favored from an energetic point of view.

5.3.4 Theoretical characterization of pyrophosphate adsorption onto HAp

Different possible orientations of the $P_2O_7^{4-}$ anion onto the (100) surface of HAp were identified, all such configurations being constructed and used as starting geometries for calculations. Geometry optimizations using the 1 × 2 × 2 slab model led to different minima with favorable BEs. **Figure 5.10 a** displays the disposition of the $P_2O_7^{4-}$ molecule onto the (100) surface for the most stable complex, the BE being included in **Table 5.4**. The adsorption occurs through four monodentate sites, which provides a symmetric interaction pattern with two asymmetric bindings at each phosphate unit. Thus, the two $Ca^{+2}\cdots O{-}P$ distances associated to each phosphate unit are ~ 2.27 and 2.42 Å. Local minima with similar BEs and $Ca^{+2}\cdots O{-}P$ distances were also obtained, a representative one being shown in **Figure 5.10 b**. In this structure, which is 42 kcal/mol less stable than the global minimum, the interaction also occurs through four monodentate sites.

Calculations related to the adsorption of $P_2O_7^{4-}$ onto the (001) surface did not lead to any stable complex. Thus, the most frequent situation, which was identified from different starting configurations, corresponded to the fragmentation of the $P_2O_7^{4-}$ molecule into PO_4^{3-} and PO_3^-. Then, the PO_4^{3-}. anion was adsorbed onto the surface in a coordination mode similar to that displayed in **Figure 5.8 a** while the PO_3^- fragment, which is less stable, was repelled by the surface.

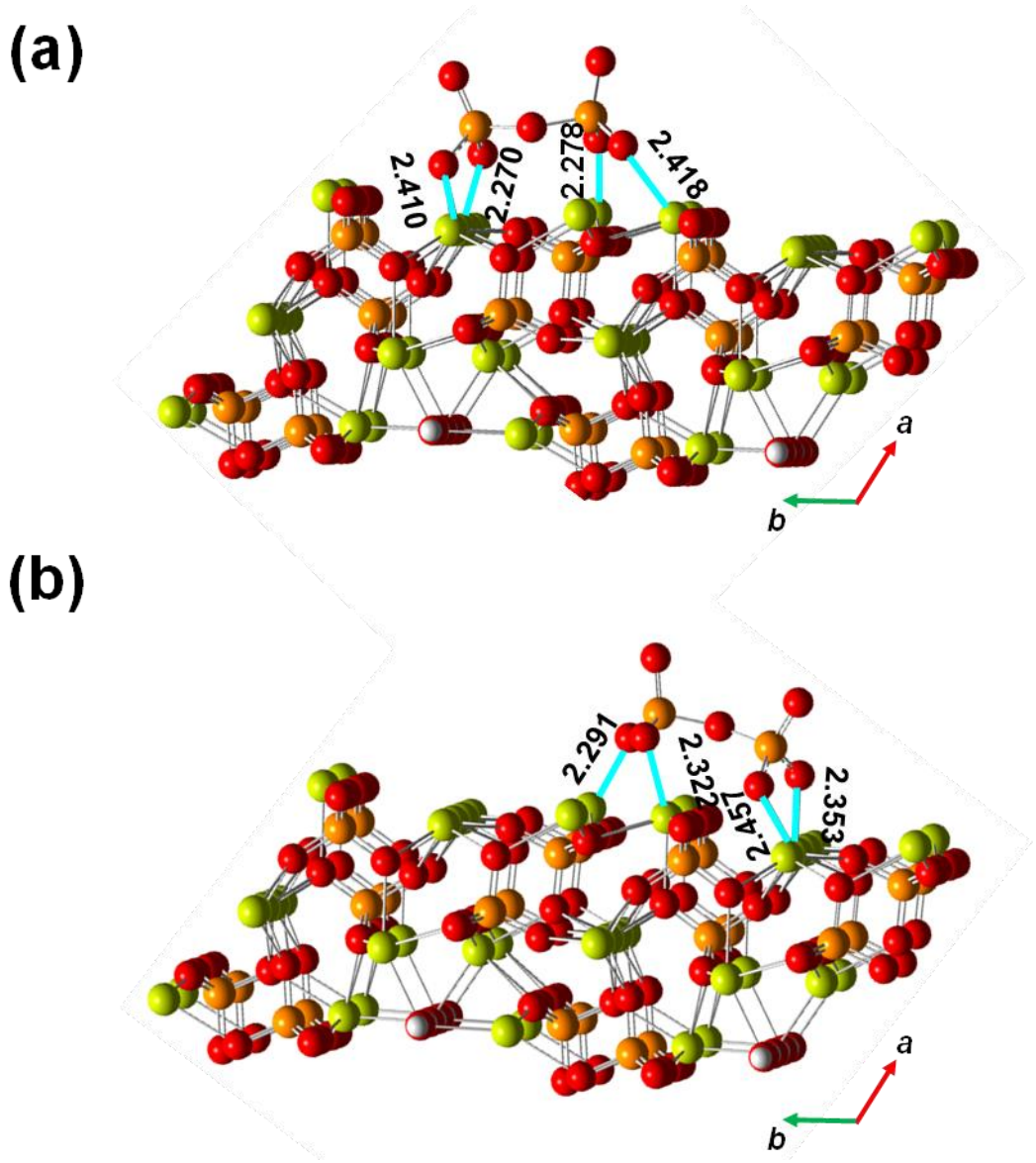

Figure 5.10. (a) Lowest energy structure and (b) representative local minimum obtained for the adsorption of $P_2O_7^{4-}$ onto the (100) surface of HAp. The (100) surface is represented by a 1 × 2 × 2 slab model. $Ca^{+2}\cdots O$ interactions are indicated by blue lines, distances (in Å) between the coordination sites and the oxygen atoms of the adsorbate being also displayed.

The overall of these results is fully consistent with experimental observations displayed in **Figure 5.5**. Thus, the very weak shoulder detected at 889 cm^{-1} indicates that the adsorption of $P_2O_7^{4-}$ onto the mineral is a restricted to surfaces in which the positions of the Ca^{+2} cations favor the process energetically. Furthermore, the disposition of adsorption sites with respect to crystallographic positions of Ca^{+2} and PO_4^{3-} in HAp suggests agree with the role attributed to $P_2O_7^{4-}$ as HAp crystal growth inhibitor.[29-31] This is supported by the systematic formation of asymmetric links in all stable complexes,

which are identified by different $Ca^{+2}\cdots O{-}P$. Thus, adsorbed $P_2O_7^{4-}$ molecules should be viewed as important structural defects appeared onto the adsorption surface. Moreover, destruction of adsorbed $P_2O_7^{4-}$ molecules by the action of tissue non-specific alkaline phosphatase has been shown to favor the mineralization by promoting the continuation of previously inhibited crystal growth.[71]

5.3.5 Theoretical characterization of polyphosphate adsorption onto HAp

Six different configurations were constructed to study the adsorption of polyP onto each examined HAp surface. In the most stable structure obtained after optimization of the configurations constructed for the (100) surface (**Figure 5.11**), the three phosphate units of the polyP molecule participate in the coordination with the surface. Specifically, six oxygen atoms interact with four Ca^{+2} cations at the surface and the $Ca^{+2}\cdots O$ distances range from 2.372 to 2.498 Å. Comparison with the previously calculated complexes indicates that such interval of variation increases with the size of the adsorbate. Thus, the $Ca^{+2}\cdots O$ distances in complexes involving $P_2O_7^{4-}$ and PO_4^{3-} ranged from 2.270 to 2.418 Å and from 2.307 to 2.327 Å, respectively. This is consistent with differences in the strength of the complexes. Analysis of the BEs obtained for the most stable complex of PO_4^{3-}, $P_2O_7^{4-}$ and polyP adsorbed onto the 1 × 2 × 2 slab model of the (100) surface (**Table 5.4**) indicates that the strength of the interaction between the adsorbate and the surface increases less than expected with the number of $Ca^{+2}\cdots O$ interactions. Thus, the BE decreases −153.9 kcal/mol when the number of interactions increases from 3 in PO_4^{3-} to 4 in $P_2O_7^{4-}$, such stabilization being of only −122.7 kcal/mol when the number of interactions enlarges from 4 to 6 in polyP. Such behavior is due to the fact that the restrictions in the complexation process increase with the number of phosphate units in the adsorbate. In order to avoid repulsive interactions with the anions located at the surface, the adsorbate adapts its geometry to the crystallographic positions of the Ca^{+2} ions, provoking strain. This effect increases with the size of the adsorbate, explaining the enlargement of the $Ca^{+2}\cdots O$ distances and the reduction in the strength of the interaction.

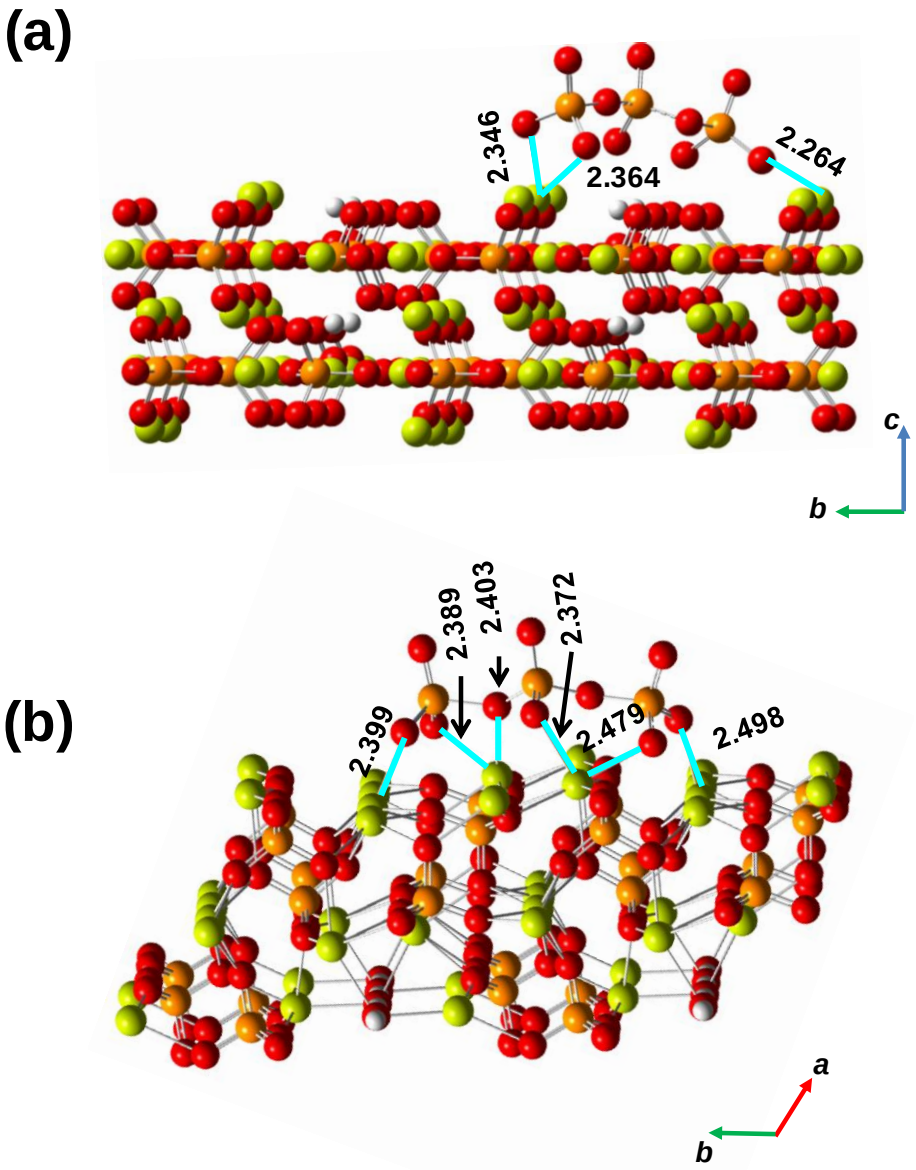

Figure 5.11. Lowest energy structure obtained for the adsorption of polyP onto the (a) (001) and (b) (100) surfaces of HAp. The (001) and (100) surfaces are represented by 3 × 3 × 1 and 1 × 2 × 2 slab models. $Ca^{+2}\cdots O$ interactions are indicated by blue lines, distances (in Å) between the coordination sites and the oxygen atoms of the adsorbate being also displayed

Most of the structures constructed to study the adsorption of polyP onto the 3 × 3 × 1 slab model of the (001) surface led to the decomposition of polyP into fragments (*i.e.* one fragment remained adsorbed onto the surface while the other was repelled, as observed above for the pyrophosphate). However, a stable complex, which is displayed in **Figure 5.11 a**, was also achieved. In this structure two Ca^{+2} cations act as coordination sites, interacting with two and one oxygen atoms located at the two end phosphate units of the

adsorbed polyP molecule. In contrast, the central phosphate unit of polyP does not interact with the surface. The most remarkable characteristic of this complex is the significant strain exhibited by the adsorbate. This is reflected by the values of the two $\angle$ P−O−P angles, which are 174.1 º and 105.8 º in the complex and 144.2 º in the free-state (*i.e*. $\angle$ P−O−P angles are 137.2 º and 140.4 º in the structure displayed in **Figure 5.11 b**). In spite of this strain and poor coordination, the $Ca^{+2}\cdots O$ distances are relatively short in comparison to those obtained for the (100) surface (**Figure 5.11 b**). The BE is similar to that obtained for the $P_2O_7^{4-}$ molecule adsorbed onto the (100) surface, which showed four $Ca^{+2}\cdots O$ interactions.

The overall of these results indicate that adsorption of polyP onto HAp is easier than of $P_2O_7^{4-}$. The BE decreases with the increasing number of phosphate units when the Ca^{+2} sites are located at favorable positions, as occurs in the (100) surface (**Table 5.4**). Furthermore, the additional phosphate unit of polyP facilitates the interaction with surfaces in which the position of the coordination sites is not adequate. Thus, although unfavorable repulsive electrostatic interactions induced by the (001) surface provokes strain in central phosphate unit of polyP, an energetically favorable adsorption process is achieved through the end phosphate units. In contrast, the repulsive electrostatic interactions exerted by the (001) surface provoked the fragmentation of $P_2O_7^{4-}$. These features are in excellent agreement with experimental observations displayed in **Figures 5.5** and **5.6**, which evidence that the adsorption of polyP onto cHAp is more clear than that of $P_2O_7^{4-}$ for all the tested concentrations.

5.3.6 Theoretical characterization of ATMP adsorption onto HAp

Five different starting configurations of ATMP adsorbed onto the (100) surface were build. After geometry optimization, none of such complexes resulted stable and the adsorbate broke into two fragments. As occurred for $P_2O_7^{4-}$, a fragment remained onto the surface while repulsive interactions repelled the other.

Six starting geometries were constructed for the adsorption of ATMP onto the 3 × 3 × 1 slab model of the (001) surface, the most stable structure derived from geometry optimization being displayed in **Figure 5.12**. In this tricoordinated structure ATMP makes one monodentate $O\cdots Ca^{+2}$ interaction and two bidentate interactions, in which two different oxygen atoms bind the same Ca^{+2}. The $Ca^{+2}\cdots O$ distances range from 2.358

to 2.541 Å, evidencing that the adsorption of ATMP onto the (001) surface is due to the balance between the number and strength of the $Ca^{+2}\cdots O$ interactions. Furthermore, comparison of the geometries displayed in **Figures 5.11 b** and **5.12**, as well as of the BEs (**Table 5.4**) clearly indicates that the adsorption of ATMP onto the (001) surface is favored with respect to the adsorption of polyP on the same surface.

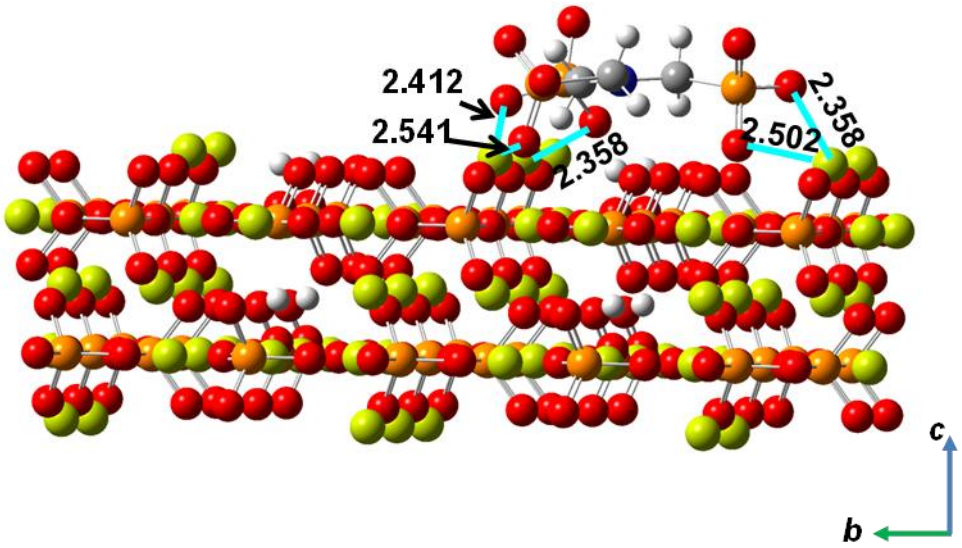

Figure 5.12. Lowest energy structure obtained for the adsorption of ATMP onto the (001) surface of HAp, which is represented by a 3 × 3 × 1 slab model. $Ca^{+2}\cdots O$ interactions are indicated by blue lines, distances (in Å) between the coordination sites and the oxygen atoms of the adsorbate being also displayed.

It is worth noting that the overall of theoretical results is fully consistent with the FTIR spectra displayed in **Figure 5.5**. Thus, calculations predict that complexes derived from the adsorption of polyP and $P_2O_7^{4-}$, onto the (100) surface of HAp are very stable from an energetic point of view, whereas the adsorptions of such species onto the (001) surface are energetically disfavored. In contrast, DFT calculations predict that ATMP only adsorbs onto the (001) surface (**Figure 5.12**). FTIR spectra clearly proved the adsorption of polyP and $P_2O_7^{4-}$ onto cHAp suggesting that such crystalline nanoparticles are dominated by the (100) surface. According to this, the adsorption of ATMP onto cHAp should not be a favored process and, consistently, no clear absorption band was identified for cHAp incubated in ATMP solutions. This excellent correlation between theoretical and experimental results provides direct understanding on the adsorption mechanism. Furthermore, it should be noted that previous studied evidenced that the dominant surface of crystalline nanoparticles depend on the experimental conditions

used for their preparation.[41] This feature suggests that the adsorption process can be modulated *a priori* during the synthesis of HAp.

5.3.7 Adsorption provokes the nucleation of crystals

As a proof of concept, the growing of polyP, $P_2O_7^{4-}$ and ATMP crystals onto the surface of cHAp and ACP particles was investigated. Thus, molecular adsorption is necessarily the initial stage of such surface-induced crystal growing process. **Figure 5.13** shows high resolution SEM micrographs of cHAp and ACP samples after incubation in concentrated solutions of polyP (2 M), $P_2O_7^{4-}$ (1 M) and ATMP (2 M). As it can be seen, in all cases crystals grew onto the surface of both cHAp and ACP particles corroborating the molecular adsorción processes described in previous sub-sections.

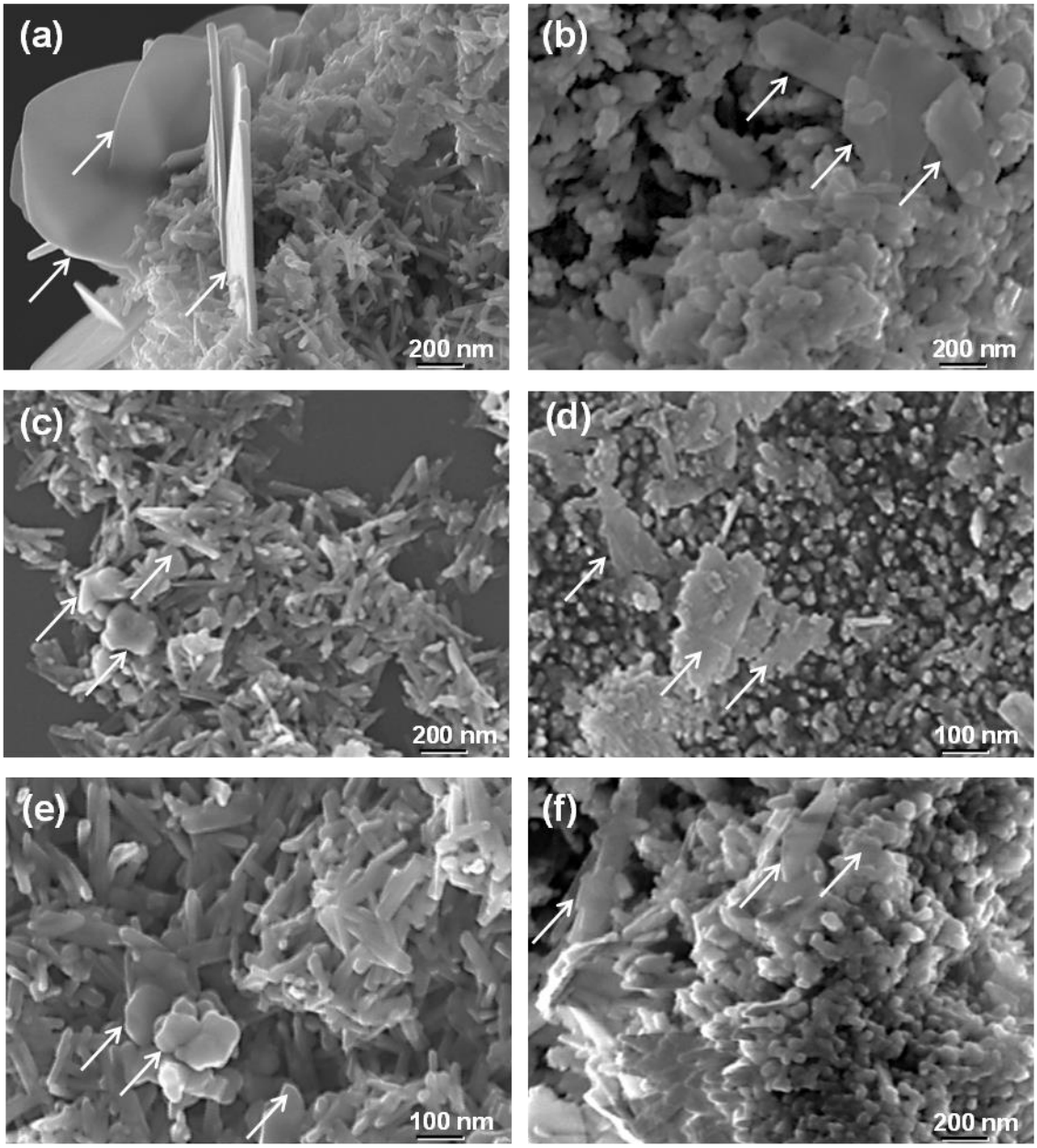

Figure 5.13. SEM micrographs of cHAp and ACP particles after incubation in presence of concentrated polyP (2 M), $P_2O_7^{4-}$ (1 M) and ATMP (2 M; bottom) solutions at pH 7: (a) cHAp + polyP; (b) ACP + polyP; (c) cHAp + $P_2O_7^{4-}$; (d) ACP + $P_2O_7^{4-}$; (e) cHAp + ATMP; and (f) ACP + ATMP. Crystals of polyP, $P_2O_7^{4-}$ and ATMP grown onto the surface of cHAp and ACP particles are indicated by arrows.

5.4 CONCLUSIONS

The combination between experimental techniques and atomistic quantum mechanical calculations have been used to prove that the interaction between PO_4^{3-}, $P_2O_7^{4-}$, polyP or ATMP and HAp occurs in very different ways. While the adsorption of PO_4^{3-} onto HAp is a very favored process that promotes the crystal growth, the interaction of $P_2O_7^{4-}$ with the mineral depends on the geometry of the crystal surface, which can induce strong repulsive surface···adsorbate interactions. An intermediate situation is observed for polyP that, due to its higher number of phosphate units, remains adsorbed onto all tested surfaces. Thus, when the geometry of the surface is not appropriated, the adsorbed polyP molecule turns repulsive interactions into molecular strain while retain enough attractive adsorbate···surface interactions. The interactions described by theoretical calculations are fully consistent with experimental data, which clearly indicate that polyP adsorbs onto cHAp more easily than $P_2O_7^{4-}$. On the other hand, DFT calculations predict the molecular architecture of ATMP is not compatible with the geometry of the (100) surface while adsorption of such BP onto the (001) surface is energetically favored. This, result is fully consistent with the conclusions reached from the comparison of theoretical and experimental results achieved for mono-, di- and triphosphates, which indicated that the behavior of the cHAp particles prepared in this work is dominated by the (100) surface.

In summary, our findings provide relevant information related not only with the abilities of crystalline HAp and ACP to interact with PO_4^{3-}, $P_2O_7^{4-}$, polyP and ATMP but also with the chemical microscopic details that are responsible of the formation or not of such interactions. The interactions between the inorganic systems described in this work are relevant for the biomedical field. Phosphates play a crucial role in bone regeneration and have been identified in platelets and carcinogenic cells. The fact that phosphates have an important role in cancer metastasis and in the virulent effects of some bacteria and parasites, make these results interesting for the design of new treatments based on the adsorption ability of HAp. On the other hand, nitrogen-containing BPs are currently used in medical therapies related with bone degradation and malignancies, as for example osteoporosis and metastasis, respectively. Also results obtained in the work contribute to understanding of biomineralization, which should be considered relevant not only as new therapeutic approximation but also as a process related with the origin of life.

5.5 REFERENCES

1. Glimcher, M.J. in Metabolic Bone Disease and Clinically Related Disorders, Academic Press, New York, 23–50 (1998).
2. Bensaid, W., Oudina, K., Viateau, V., Potier, E., Bousson, V., Blanchat, C., Sedel, L., Guillemin, G. & Petite, H. De novo reconstruction of functional bone by tissue engineering in the metatarsal sheep model. *Tissue Eng*. **11**,814–824 (2005).
3. Mastrogiacomo, M., Corsi, A., Francioso, E., Di Comite, M., Monetti, F., Scaglione, S., Favia, A., Crovace, A., Bianco, P. & Cancedda, R. Reconstruction of extensive long bone defects in sheep using resorbable bioceramics based on silicon stabilized tricalcium phosphate. *Tissue Eng*. **12**, 1261–1273 (2006).
4. Kruyt, M.C., Wilson, C.E., de Bruijn, J.D., van Blitterswijk, C.A., Oner, C.F., Verbout, A.J. & Dhert, W.J.A. The effect of cell-based bone tissue engineering in a goat transverse process model. *Biomaterials*. **29**, 5099–5106 (2006).
5. Marcacci, M., Kon, K., Moukhachev, V., Lavroukov, A., Kutepov, S., Quarto, R., Mastrogiacomo, M. & Cancedda, R. Stem cells associated with macroporous bioceramics for long bone repair: 6- to 7-year outcome of a pilot clinical study. *Tissue Eng*. **13**, 947–955 (2007).
6. Zakaria, S.M., Sharif, S.H., Othman, M.R., Yang, F. & Jansen, J.A. Nanophase hydroxyapatite as a biomaterial in advanced hard tissue engineering: a review. *Tissue Eng. Part B Reviews.* **19**, 431–441 (2013).
7. Cardoso, D.A., Jansen, J.A. & Leewenburgh, S.C.G. Synthesis and application of nanostructured calcium phosphate ceramics for bone regeneration. *J. Biomed. Mater. Res. Part B Reviews.* **100**, 2316–2326 (2012).
8. Holzwart J.M. & Ma, P.X. Biomimetic nanofibrous scaffolds for bone tissue engineering. *Biomaterials*. **32**, 9622–9629 (2011).
9. Chen, F.M., Zhang, J., Zhang, M., An, Y., Chen, F. & Wu, Z.F. A review on endogenous regenerative technology in periodontal regenerative medicine. *Biomaterials*. **31**, 7892–7927 (2010).
10. Matsumoto, T., Okazaki, M., Nakahira, A., Sasaki, J., Egusa, H. & Sohmura, T. Modification of apatite materials for bone tissue engineering and drug delivery carriers. *Curr. Med. Chem*. **14**, 2726–2733 (2007).
11. Candedda, R., Giannoni, P., & Mastrogiacomo, M. A tissue engineering approach to bone repair in large animal models and in clinical practice. *Biomaterials*. **28**, 4240–4250 (2007).
12. Dorozhkin, S.V. Bioceramics of calcium orthophosphates. *Biomaterials*. **31**, 1465–1485 (2010).
13. Doi, K., Kubi, T., Takeshita, R., Kajihara, S., Kato, S., Kawazoe, Y., Shiba, T. & Akagawa, Y. Inorganic polyphosphate adsorbed onto hydroxyapatite for guided bone regeneration: An animal study. *Dent. Mat. J*. **33**, 179–186 (2014).
14. Comeau, P.A., Frei, H., Yang, C., Fernlund, G. & Rossi, F.M. *In vivo* evaluation of calcium polyphosphate for bone regeneration. *J. Biomat. Appl.* **27**, 267–275(2012).

15. Jeon, B.J., Jeong, S.Y., Koo, A.N., Kim, B.C., Hwang, Y.S. & Lee, S.C. Fabrication of porous PLGA microspheres with BMP-2 releasing polyphosphate-functionalized nano-hydroxyapatite for enhanced bone regeneration. *Macromol. Res.* **20**, 715–724 (2012).

16. Siggers, K., Frei, H., Fernlund, G., & Rossi, F. Effect of bone graft substitute on marrow stromal cell proliferation and differentiation. *J. Biomed. Mat. Res. Part A.* **94**, 877–885 (2010).

17. Morita, K., Doi, K., Kubo, T., Takeshita, R., Kato, S. & Akagawa, Y. Enhanced initial bone regeneration with inorganic polyphosphate-adsorbed hydroxyapatite. *Acta Biomat.* **6**, 2808–2815 (2010).

18. Yuan, Q., Kubo, T., Doi, K., Morita, K., Takeshita, R., Kato, S., Shiba, T. & Akagawa, Y. Effect of combined application of bFGF and inorganic polyphosphate on bioactivities of osteoblasts and initial bone regeneration. *Acta Biomat.* **5**, 1716–1724 (2009).

19. Kumble, K.D. & Kornberg, A. Inorganic polyphosphate in mammalian cells and tissues. *J. Biol. Chem.* **270**, 5818–5822 (1996).

20. Shiba, T., Nishimura, D., Kawazoe, Y., Onodera, Y., Tsutsumi, K., Nakamura, R. & Ohshiron, M. Modulation of mitogenic activity of fibroblast growth factors by inorganic polyphosphate. *J. Biol. Chem.* **278**, 26788–26792 (2003).

21. Kawazoe, Y., Shiba, T., Nakamura, R., Mizuno, A., Tsutsumi, K., Uematsu, T., Yamaoka, M., Shindoh, M. & Kohgo, T. Induction of calcification in MC3T3-E1 cells by inorganic polyphosphate. *J. Dent. Res.* **83**, 613–618 (2004).

22. Hacchou, Y., Uematsu, T., Ueda, O., Usui, Y., Uematsu, S., Takahashi, M., Kawazoe, Y., Shiba, T., Kurihara, S., Yamaoka, M. & Furusawa, K. Inorganic polyphosphate: a possible stimulant of bone formation. *J. Dent. Res.* **86**, 893–897 (2007).

23. Ruiz, F.A., Lea, C.R., Oldfield, E. & Docampo, R. Human platelet dense granules contain polyphosphate and are similar to acidocalcisomes of bacteria and unicellular eukaryotes. *J. Biol. Chem.* **279**, 44250–44257 (2004).

24. Morrissey, J.H., Choi, S.H. & Smith, S.A. Polyphosphate: an ancient molecule that links platelets, coagulation, and inflammation. *Blood*, **119**, 5972–5979 (2012).

25. Jimenez-Nuñez, M.D., Moreno-Sanchez, D., Hernandez-Rios, L., Benítez-Rondán, A., Ramos-Amaya, A., Rodríguez-Bayona, B., Medina, F., Brieva, J.A. & Ruiz, F.A. Myeloma cells contain high levels of inorganic polyphosphate which is associated with nucleolar transcription. *Haematologica*. **97**, 1264–1271 (2012).

26. Tammenkoski, M., Koivula, K., Cusanelli, E., Zollo, M., Steegborn, C., Baykov, A.A. & Lahti, R., *Biochem.* Human metastasis regulator protein H-prune is a short-chain exopolyphosphatase. *Biochem.* **47**, 9707–9713 (2008).

27. Wang, L., Fraley, C.D., Faridi, J., Kornberg, A. & Roth, R.A. Inorganic polyphosphate stimulates mammalian TOR, a kinase involved in the proliferation of mammary cancer cells. *Proc. Natl. Acad. Sci. U S A.* **100**, 11249–11254 (2003).

28. Morena, S.N.J. & Docampo, R. Polyphosphate and its diverse functions in host cells and pathogens. *PLoS Pathog*. **9**, e1003230 (2013).

29. Fleisch, H. & Bisaz, S. Mechanism of calcification: inhibitory role of pyrophosphate. *Nature*. **195**, 911–911 (1962).

30. Fleish, H., Russel, R. & Straumann F. Effect of pyrophosphate on hydroxyapatite and its implications in calcium homeostasis. *Nature*. **212**, 901–903 (1966).

31. Fleisch, H., *Progress in Molecular and Subcellular Biology*, Springer- Verlag Press, Heidelberg, 197–215 (1999).

32. Omelon, S., Georgiou, J., Henneman, Z.J., Wise, L.M., Sukhu, B., Hunt, T., Wynnyckyj, C., Holmyard, D., Bielecki, R., & Grynpas, M.D. Control of vertebrate skeletal mineralization by polyphosphates. *PLos One*. **4**, e5634 (2009).

33. Van Wazer, J.R. & Campanella, D.A. *J. Am. Chem. Soc.* Structure and properties of the condensed phosphates. IV. Complex ion formation in polyphosphate solutions. *J. Am. Chem. Soc*.**72**, 655–663 (1950).

34. Okazaki, M., Yoshida, Y., Yamaguchi, S., Kaneno, M. & Elliot, J.C. Affinity binding phenomena of DNA onto apatite crystals. *Biomaterials*. **22**, 2459-2464 (2001).

35. Revilla-López, G., Casanovas, J., Bertran, O., Turon, P., Puiggalí, J. & Alemán, C. Modeling biominerals formed by apatites and DNA. *Biointerphases*. **8**, 10-25 (2013).

36. Takeshita, T., Matsuura, Y., Arakawa, S. & Okamoto, M. Biomineralization of hydroxyapatite on DNA molecules in SBF: morphological features and computer simulation. *Langmuir*. **29**, 11975-11981 (2013).

37. Vasconcellos, K.B., McHugh, S.M., Dapsis, K.J., Petty, A.R. & Gerdon, A.E. Biomimetic nanoparticles with polynucleotide and PEG mixed-monolayers enhance calcium phosphate mineralization. *J. Nanopart. Res.* **15**, (1942).

38. Bertran, O., del Valle. L.J., Revilla-López, G., Chaves, G., Cardus L., Casas, M.T., Casanovas, J., Turon, P., Puiggalí, J. & Alemán, C. Mineralization of DNA into nanoparticles of hydroxyapatite. *Dalton Trans*. **3**, 317-327 (2014).

39. Olton, D., Li, J., Wilson, M. E., Rogers, T., Close, J., Huang, L., Kumta, N.P. & Sfeir, C. Nanostructured calcium phosphates (NanoCaPs) for non-viral gene delivery: influence of the synthesis parameters on transfection efficiency. *Biomaterials*. **28**, 1267-1279 (2007).

40. Gonzalez-McQuire, R., Green, D.W., Partridge, K.A., Oreffo, R.O.C., Mann, S. & Davis, S.A. Coating of human mesenchymal cells in 3D culture with bioinorganic nanoparticles promotes osteoblastic differentiation and gene transfection. *Adv. Mater.* **19**, 2236–2240 (2007).

41. del Valle, L.J., Bertran, O., Chaves, G., Revilla-López, G., Rivas, M., Casas, M.T., Casanovas, J., Turon, P., Puiggalí, J. & Alemán, C. DNA adsorbed on hydroxyapatite surfaces. *J. Mater. Chem. B.* **2**, 6953-6966 (2014).

42. Brundin, M., Figdor, D., Sundqvist, G. & Sjögren, U. DNA binding to hydroxyapatite: a potential mechanism for preservation of microbial DNA. *J. Endod*. **39**, 211-216 (2013).

43. Kamat, S.S. & Raushel, F.M. The enzymatic conversion of phosphonates to phosphate by bacteria. *Curr. Opin. Chem. Bio.* **17**, 589–596 (2013).

44. Nancollas, G.H., Tang, R., Phipps, R.J., Henneman, Z., Gulde, S., Wu, W., Mangood, A., Russell, R.G.G. & Ebetino, F.H. Novel insights into actions of bisphosphonates on bone: differences in interactions with hydroxyapatite. *Bone*. **18**, 617–627 (2006).

45. Ebetino, F.H. & Dansereau, S.M., Biophosphonate antiresorptive structure-activity relationships, *Elsevier Press*, Amsterdam, 139–153 (1995).

46. Ebetino, F.H. & Francis, M.D. Mechanisms of action of etidronate and other bisphosphonates. *Rev. Contemp. Pharmacother.* **9**, 233–243 (1998).

47. Russell, R.G.G. & Ebetino, F.H. Mechanisms of action of bisphosphonates: similarities and differences and their potential influence on clinical efficacy. *Osteoporos. Int.* **19**, 733–759 (2008).

48. Gronich, N. & Rennet, G. Beyond aspirin-cancer prevention with statins, metformin and bisphosphonates. *Nat. Rev. Clin. Oncol.* **10**, 625–642 (2013).

49. Klug. H. & Alexander, L., *X-Ray Diffraction Procedure for Polycrystallite and Amorphous Materials*, 2nd. Edition, John Wiley and Sons Press, New York (1974).

50. Landi, E., Tampieri, A., Celotti, G. & Sprio, S. Densification behaviour and mechanisms of synthetic hydroxyapatites. *J. Eur. Ceram. Soc.* **20**, 2377-2387 (2000).

51. Frisch, M.J., Trucks, G.W., H. B. Schlegel, H.B., Scuseria, G.E., Robb, M.A. & Fox, D.J. *Gaussian 09, revision A.01*, Gaussian, Inc.: Wallingford, CT (2009).

52. Stork, L., Muller, P., Dronskowski, R. & Ortlepp, J.R. A density functional theory study of the interaction of collagen peptides with hydroxyapatite surfaces. *Z. Kristallogr*. **220**, 201-205 (2005).

53. Lee, C., Yang, W. & Parr, R.G. Development of the Colle-Salvetti correlation-energy formula into a functional of the electron density. *Phys. Rev. B.* **37**, 785–789 (1988).

54. Becke, A.D. Density-functional thermochemistry. III. The role of exact exchange. *J. Chem. Phys.* **98**, 5648–5652 (1993).

55. Guan, X.H., Liu, Q., Chen, G.H. & Shang, C. Surface complexation of condensed phosphate to aluminum hydroxide: An ATR-FTIR spectroscopic investigation. *J. Colloid Interface Sci.* **289**, 319–327 (2005).

56. Dalmoro, V., dos Santos, J.H.Z., Armelin, E., Alemán, C. & Azambuja, D. A synergistic combination of tetraethylorthosilicate and multiphosphonic acid offers excellent corrosion protection to AA1100 aluminum alloy. *Appl. Surf. Sci.* **273**, 758–768 (2013).

57. Zhu, X.L., Chen, J., Scheideler, L., Reichl, R. & Geis-Gerstoefer, J. Effects of topography and composition of titanium surface oxides on osteoblast responses. *Biomaterials*. **25**, 4087–4103 (2004).

58. Shih, W.Y.P.Y. & Chin, T.S. FTIR and XPS studies of P_2O_5–Na_2O–CuO glasses. *J. Non-Cryst. Solids*, **244**, 211–222 (1999).

59. Goretzki, H., Chun, H.U., Sammet, M. & Bruckner, R. XPS measurements and structural aspects of silicate and phosphate glasses. *J. Non-Cryst. Solids*. **42**, 49–60 (1980).

60. Singamsetty, C.S.K., Pittman, C.U., Booth, G.L., He, G.R. & Gardner, S.D. Surface characterization of carbon fibers using angle-resolved XPS and ISS. *Carbon.* **33**, 587–595 (1995).

61. Almora-Barrios, N., Austen, K.F. & de Leeuw, N.H. Density functional theory study of the binding of glycine, proline, and hydroxyproline to the hydroxyapatite (0001) and $(01\bar{1}0)$ surfaces. *Langmuir.* **25**, 5018-5025 (2009).

62. de Leeuw, N. H. Local ordering of hydroxy groups in hydroxyapatite. *Chem. Commun*. **17**, 1646-1647 (2001).

63. Mkhonto, D. & de Leeuw, N.H., A computer modelling study of the effect of water on the surface structure and morphology of fluorapatite: introducing a $Ca_{10}(PO_4)_6F_2$ potential model. *J. Mater. Chem*. **12**, 2633-2642 (2002).

64. Kirkham, J., Brookes, S.J., Shore, R.C., Wood, S.R., Smith, D.A., Zhang, J., H. Chen, H. & Robinson, C. Physico-chemical properties of crystal surfaces in matrix–mineral interactions during mammalian biomineralisation. *Curr. Opin. Colloid Interface Sci.* **7**, 124-132 (2002).

65. Simmer, J.P. & Fincham, A.G. Molecular Mechanisms of Dental Enamel Formation. *Crit. Rev. Oral Biol. Med*. **6**, 84-108 (1995).

66. Magne, D., Pilet, P., Weiss, P. & Daculsi, G. Fourier transform infrared microspectroscopic investigation of the maturation of nonstoichiometric apatites in mineralized tissues: a horse dentin study. *Bone*. **29**, 547-552 (2001).

67. Wang, L. & Nancollas, G.H. Calcium orthophosphates: crystallization and dissolution. *Chem. Rev.* **108**, 4628–4669 (2008).

68. Onuma, K. Recent research on pseudobiological hydroxyapatite crystal growth and phase transition mechanisms. *Prog. Cryst. Growth Charact. Mater*. **52,** 223–245 (2006).

69. Bertran, O., del Valle, L.J., Revilla-López, G., Rivas, M., Chaves, G., Casas, M.T., Casanovas, J., Turon, P. & Puiggalí, J. Synergistic approach to elucidate the incorporation of magnesium ions into hydroxyapatite. *Chem. Eur. J.* **21**, 2537–2546 (2015).

70. Liu, Y., Wu, W., Sethuraman, G. & Nancollas, G.H. Intergrowth of calcium phosphates: an interfacial energy approach. *J. Cryst. Growth*. **174**, 386–392 (1997).

71. Murshed, M., Harmey, D., Millán, J.L., McKee, M.D. & Karsenty, G. Unique coexpression in osteoblasts of broadly expressed genes accounts for the spatial restriction of ECM mineralization to bone. *Genes Dev*. **19**, 1093–1104 (2005).

6.

INFLUENCE OF THE ATMOSPHERE CONDITIONS IN THE STRUCTURE, PROPERTIES AND SOLUBILITY OF FLUORINE-SUBSTITUTED HYDROXYAPATITES

The influence of synthetic conditions in the composition and properties of chemically precipitated hydroxyapatite (HAp), fluorine-substituted HAp (*x*F-HAp) and fluorapatite (FAp) has been examined considering different atmospheres (nitrogen, air and carbon dioxide), temperatures (37 ºC and 150 ºC) and pressures (hydrothermal conditions). Results indicate that the synthetic conditions not only affect the fluorination degree but also have a pronounced effect on the carbonation degree, the crystallinity, the surface wettability and the thermal stability. Besides, the electrical polarization of HAp-based minerals mainly depends on the fluoride content, the formation of ordered channels of vacancies along the sintering and thermal polarization processes becoming more difficult with increasing fluorination degree. This limits the utilization of *x*F-HAp and FAp as electro-responsive scaffolds and electrocatalysts, as has been recently proposed for polarized HAp. Finally, the effects of the carbonation and the fluoridation degrees, the concentration fluoride anions supplied from an external source, and the pH on the solubility of HAp-based minerals has been examined. Observations indicate that, although strategies based on the substitution of HAp by *x*F-HAp or FAp have been proposed for coatings of dental implants, external fluoride anions inhibit the solubility more effectively than the fluorination of the own mineral matrix. Accordingly, HAp combined with an effective external supply of fluoride anions is more appropriated than *x*F-HAp and FAp for the fabrication of dental coatings.

6.1 INTRODUCTION

Fluoroapatite (FAp), $Ca_{10}(PO_4)_6F_2$, is the most stable, least soluble and hardest calcium orthophosphate mineral.[1-3] Compared to hydroxyapatite (HAp), $Ca_{10}(PO_4)_6(OH)_2$, FAp is prepared using similar synthetic procedures but introducing CaF_2, NaF or NH_4F to transmit fluoride (F^-) ions.[4] Moreover, previous studies have suggested that FAp a similar biocompatibility with HAp in terms of its fixation to bone and bone in-growth.[5-7] Indeed, among all human calcified tissues, the greatest concentration of FAp is found in bones, and the lowest in enamel.[8] However, even where there is the largest concentration of FAp, the amount of F^- is usually reduced related to stoichiometric quantities.

FAp has been mainly used as clinical restorative material[9,10] and catalyst.[11,12] Regarding to the former application and considering that the ionic substitution (doping) of HAp is a relatively easy process[13-17], in the last decade fluorine-substituted HAp has attracted substantial attention[18-24] because F^- ions can reduce the formation of caries in bacterially contaminated environments and promotes mineralization and crystallization of calcium phosphates in the formation of bone.[25] In spite of the physiological significance of F^- ions, the utilization of FAp and, in general, of fluorine-substituted HAp as clinical restoration materials is limited their very low solubility, since they exhibit much lower bioresorption rate than HAp.[2]

On the other hand, carbonate (CO_3^{2-}) is also present in biological apatites (enamel, dentine, bone, and pathological calcifications) by substitution at phosphate (PO_4^{3-}) and hydroxide (OH^-) sites, tending to increase its solubility in comparison with pure hydroxyapatite (HAp).[26-27] Indeed, CO_3^{2-} substitution has been recently used to enhance HAp higher solubility and promote other desired properties (*e.g*. enhance the antibacterial effect in silver-substituted HAp,[28] increase the bioresorption capacity,[29] and the ionic substitution[30]).

In this work we combine the impact of the simultaneous incorporation of F^- or/and CO_3^{2-} ions in the properties of HAp. For this purpose, fluorine-substituted minerals with different fluorination and carbonation degrees have been prepared by controlling the atmosphere and temperature during the chemical precipitation process. After this, the

influence of the composition on the spectroscopic, structural, thermal, solvent-affinity (wettability and water absorption) and electrochemical properties of the resulting minerals has been evaluated. Finally, the impact of the carbonation and fluorination degrees of the HAp matrix, the concentration externally supplied F^- anions, and the pH on the solubility of hydroxyapatite has been examined. Results are in controversy with recent recommendations for the fabrication of mineral coatings for dental implants according which it was proposed to replace HAp by fluorine-substituted HAp.

6.2 EXPERIMENTAL SECTION

6.2.1 Synthesis of HAp

Hydroxyapatite (HAp). The reagent conditions used to prepare HAp were adjusted to get a Ca/P ratio of 1.67. In all cases 15 mL of 0.5 M $(NH_4)_2HPO_4$ in de-ionized water (pH adjusted to 11 with an ammonia 30 % w/w solution) were added drop-wise (rate of 2 mL·min^{-1}) and under agitation (400 rpm) to 25 mL of 0.5 M $Ca(NO_3)_2$ in ethanol. After that, the reaction mixture was stirred (400 rpm) 1 hour at room temperature. Resultant suspension was aged for 48 h at 37 º C. The precipitate was separated by centrifugation and washed sequentially with de-ionized water and a 60/40 v/v mixture of ethanol-water (twice). A white powder was obtained after freeze-drying. Particles were filtered through a 0.22 µm filter (Millipore, Billerica, MA). Filtration was performed at a flow rate of 1 mL·min^{-1} using a 10 mL syringe and concentration of the particles was achieved using an IE C MultiRF centrifugue (Thrmo IEC, Needham Heights, MA, USA).

Fluorine substituted HAp (xF-HAp) and fluorapatite (FAp). Solid solutions with formula $Ca_{10}(PO_4)_6\ (OH)_{2-x}F_x$ were obtained by incorporating F^- instead of OH^-groups. In all cases 0.5 M NH_4F was added into a constantly stirred Ca and P containing solution, prepared as described above. Different amounts of ammonia fluoride solution ($x = 0$; 0 mL of 0.5 M NH_4F; $x = 0{,}4$; 1 mL of 0.5 M NH_4F; $x = 0{,}8$; 2 mL of 0.5 M NH_4F; $x = 1{,}2$; 3 mL of 0.5 M NH_4F; $x = 1{,}6$; 4 mL of 0.5 M NH_4F; $x = 2{,}0$; 5 mL of 0.5 M NH_4F) were added individually to control the value x in the general formula. When x was 0 and 1 the obtained powders were named HAp and FAp, respectively, while the ceramic compositions with $x = 0.4$, 0.8, 1.2 and 1.8 were denoted 0.4F-HAp, 0.8F-HAp, 1.2F-HAp and 1.6F-HAp, respectively (*x* refers to the degree of fluorination).

Three different experimental conditions were considered for the precipitation:

• *Atmospheric (ATM) conditions*. The precipitation mixture was stirred 1 hour by agitation (400 rpm) at 37 ºC or 150 ºC under atmospheric conditions, hereafter denoted ATM (37 ºC)- and ATM (150 ºC)-conditions, respectively. It is worth nothing that ATM (37 ºC)- conditions correspond to those used for the preparation of HAp (see above).

• *Hydrothermal (HT) conditions*. The reaction mixture was stirred 24 hours by agitation (400 rpm) at 150 º C under a pressure of 200 bars.

• *Nitrogen (N_2) conditions*. The precipitation occurs after stirring (400 rpm) 1 hour at 37 ºC or 150 ºC under inert N_2 atmosphere, hereafter denoted N_2 (37 ºC)- and N_2 (150 ºC)-conditions, respectively.

• *Carbon dioxide (CO_2) conditions*. The precipitation occurs after stirring (400 rpm) during an interval comprised between 1 and 3 hours, depending on the desired CO_3^{2-} content, at 37 ºC under CO_2 atmosphere. Thus, these conditions have been employed to regulate the carbonation degree of *x*F-HAp and FAp.

Discs preparation. HAp, *x*F-HAp and FAp powders were uniaxially pressed at 620 MPa for 10 min to obtain dense discs suitable for characterization. The dimensions of these specimens were 10 mm of diameter × 1.7 mm of thickness.

6.2.2 Measurements

Fourier transform infrared (FTIR) spectroscopy. Infrared absorption spectra were recorded with a Fourier Transform FTIR 4100 Jasco spectrometer in the 1800-700 cm^{-1} range. A Specac model MKII Golden Gate attenuated total reflection (ATR) equipment with a heated Diamond ATR Top-Plate was used.

X-ray photoelectron spectroscopy (XPS). XPS analyses were performed in a SPECS system equipped with a high-intensity twin-anode X-ray source XR50 of $\mathrm{Mg/Al}$ (1253 eV/1487 eV) operating at 150 W, placed perpendicular to the analyzer axis, and using a Phoibos 150 MCD-9 XP detector. The X-ray spot size was 650 µm. The pass energy was set to 25 and 0.1 eV for the survey and the narrow scans, respectively. Charge compensation was achieved with a combination of electron and argon ion flood guns.

The energy and emission current of the electrons were 4 eV and 0.35 mA, respectively. For the argon gun, the energy and the emission current were 0 eV and 0.1 mA, respectively. The spectra were recorded with pass energy of 25 eV in 0.1 eV steps at a pressure below 6×10^{-9} mbar. These standard conditions of charge compensation resulted in a negative but perfectly uniform static charge. The $\mathrm{C}\ 1s$ peak was used as an internal reference with a binding energy of 284.8 eV. High-resolution XPS spectra were acquired by Gaussian–Lorentzian curve fitting after s −shape background subtraction. The surface composition was determined using the manufacturer's sensitivity factors.

X-Ray diffraction. Crystallinity was studied by wide angle X-ray diffraction (WAXD). Patterns were acquired using a Bruker D8 Advance model with CuK_α radiation ($\lambda = 0.1542$ nm) and geometry of Bragg-Bretano, theta-2 theta. A one-dimensional Lynx Eye detector was employed. Samples were run at 40 kV and 40 mA, with a 2-theta range of 2−40, measurement steps of 0.02 º, and time/step of 2−8 s. Diffraction profiles were processed using PeakFit v4 software (Jandel Scientific Software) and the graphical representation performed with OriginPro v8 software (OriginLab Corporation, USA).

The crystallite size (*L*) in the direction perpendicular to the representative (211) planes of samples was derived from the X-ray diffraction line broadening measurement using the Scherrer equation:

$$L = \frac{0.9\lambda}{\beta\cos\theta} \quad (1)$$

where λ is the wavelength (CuK_α), β is the full width at half maximum height of the (211) line, θ is the diffraction angle and 0.9 is a shape factor. The crystallinity (χ_c) was obtained using the following equation:

$$\chi_c = 1 - \frac{\mathrm{V}_{112/300}}{\mathrm{I}_{300}} \quad (2)$$

where I_{300} is the intensity of the (300) reflection and $\mathrm{V}_{112/300}$ is the intensity of the hollow between the (112) and (300) reflections, which disappears in non-crystalline samples.

Thermal stability. Thermogravimetric analyses (TGA) for studying thermal stability a relatively low temperatures (< 600 ºC) were performed at a heating rate of 20 º C/min (sample weight *ca.* 5 mg) with a Q50 thermogravimetric analyser of TA Instruments and under a flow of dry nitrogen. Test temperatures ranged from 30 to 600 ºC.

Wettability. Contact angle measurements for water and fetal bovine serum (FBS), a growth supplement for cell culture media, were carried out using the sessile drop method. Images of milliQ water drops (0.5 µL) were recorded after stabilization with the equipment OCA 15EC (Data-Physics Instruments GmbH, Filderstadt). SCA20 software was used to analyze the images and determine the contact angle value, which was obtained as the average of at least ten independent measures for each sample.

Water absorption. The water absorption capacity (W_A) of mineral discs was determined according to:

$$W_A = \frac{w_W - w_D}{w_D} \quad (3)$$

where w_W is the weight of the discs after 60 min immersed in milli-Q water and w_D is the weight of the discs dried at room temperature.

Cyclic voltammetry (CV). The electrochemical behavior of the prepared mineral was determined by CV using an Autolab PGSTAT302N equipped with the ECD module (Ecochimie, The Netherlands) with a three-electrode cell under a nitrogen atmosphere (99.995 % in purity) at room temperature. A 0.1 M phosphate buffer saline solution (PBS; pH = 7.2 adjusted with NaOH) was used as the electrolyte in the three-electrode cell. The working compartment was filled with 30 mL of the electrolyte solution. Steel AISI 316 sheets of 1 × 1.5 cm^2 (thickness 0.1 cm) were used as both the working and the counter electrodes, and an $\mathrm{Ag|AgCl}$ electrode was used as the reference electrode which contained a KCl saturated aqueous solution (offset potential versus the standard hydrogen electrode, E_0 = 0.222 V at 25 °C). All potentials given in this work are referenced to this electrode. HAp, *x*F-HAp and FAp discs prepared as described above were fixed on the working electrode using a two-side adhesive carbon layer. The initial and final potentials were −0.40 V, whereas a reversal potential of 0.80 V was considered. The scan rate was 50 mV/s. The electroactivity, which indicates the ability to exchange charge reversibly, was evaluated by examining the similarity between the anodic and

cathodic areas of the control voltammogram (*i.e*. the ratio between the reduction and oxidation charges).

Solubility. The mass solubility of HAp, *x*F-HAp and FAp was determined by gravimetry in a solution of de-ionized water with 100 mM HCl and 50 mM $NaCl$ at room temperature and atmospheric pressure. More specifically, 500 mg of pulverized solid mineral were added to 50 mL of solution, and agitated by a magnetic stirrer overnight. After this time, the oversaturated solution was filtered and the residue was dried in a lyophilizer during 72 h. The masses were determined using a CPA26P Sartorius analytical microbalance with a precision of $2 \cdot 10^{-6}$ g.

6.3 RESULTS AND DISCUSSION

6.3.1 Spectroscopic characterization

The FTIR spectra of HAp, *x*F-HAp and FAp prepared using ATM (37 ºC) and N_2 (37 ºC) -conditions show typical PO_4^{3-} bands at the region comprised between 950 and 1200 cm^{-1} (**Figure 6.1**): $\nu_1 \approx 955\ cm^{-1}$ and $\nu_3 = 1016, 1084\ cm^{-1}$.[31] However, comparison of the spectra indicate that the atmosphere used during the precipitation process significantly affects the composition of the samples. Thus, samples prepared under ATM (37 ºC)-conditions absorption bands at 3242 and 3033 cm^{-1}, which are associated to the adsorbed water, and at 820 cm^{-1} (ν_2) and 1416,1308 cm^{-1} (ν_3) due to CO_3^{2-}. The position of these bands is consistent with the predominant B-type substitution, according to which PO_4^{3-} is replaced by CO_3^{2-} (*i.e.* the bands of A-type CO_3^{2-}, which replace OH^-, usually appear at higher wavenumbers).[32] Moreover, the intensity of the CO_3^{2-} bands increases significantly with the F^- intake, while it is negligible for HAp. This feature suggests that HAp fluoridation in non-controlled ATM-conditions promotes the substitution of PO_4^{3-} by CO_3^{2-}. In opposition, the intensity of water and CO_3^{2-} absorption bands is imperceptible for *x*F-HAp and FAp samples obtained under N_2 -conditions (**Figure 6.1 b**).

Although the FTIR spectra of samples prepared using ATM (150 ºC) - and N_2 (150 ºC)-conditions are similar to those described above (**Figure 6.2**), they exhibit some differential features. The most remarkable one is that the absorption of water in samples

prepared under ATM (150 ºC)-conditions decreases drastically with respect to those obtained using ATM (37 ºC)-conditions (**Figure 6.2 a**). Also, the CO_3^{2-} bands become less intense at the highest temperature, even though they occur at the same positions confirming the predominant B-type substitution. Moreover, the intensity of the CO_3^{2-} increases with the F^- content, which is consistent with the boosting effect of fluoridation in the PO_4^{3-} by CO_3^{2-} discussed above. On the other hand, the protective effect exerted by the N_2 atmosphere with respect to the adsorption of water and the incorporation of CO_3^{2-} is preserved at 150 ºC (**Figure 6.2 b**).

The presence of F^- in *x*F-HAp and FAp samples prepared under ATM (37ºC)-conditions is demonstrated in **Figure 6.1 c**. High resolution XPS spectra in the $F\ 1s$ region of *x*F-HAp show a peak located at 684.1 eV, which is the fingerprint that proves that F^- ions have been successfully incorporated into the lattice HAp structure.[33] Interestingly, for FAp the XPS spectrum in the $F\ 1s$ region presents two peaks. In this case, the second peak, which is centered at 686.5 eV, has been associated to the formation of CaF_2 traces when the concentration of F^- ions coming from the addition of NH_4F to the reaction solution is the maximum.[34]

Table 6.1 compares the atomic percent compositions of HAp, *x*F-HAp and FAp samples prepared under N_2 (37 ºC)-conditions. As it can be seen, the Ca/P ratio increases from 1.60 (HAp) to 1.67 with the fluorine content. This feature has been related with the influence of F^- and OH^-sizes ($F^- < OH^-$) in the reaction kinetics. Thus, the incorporation of small F^- anions is faster than that of OH^- anions producing the expected Ca/P ratio of 1.67 only when the degree of fluorination is the maximum ($x = 2$). When $x < 2$, the fluoride content is not enough to complete the reaction, inducing the deficiency of calcium (Ca/P < 1.67). The maximum deficiency is reached when the fluoride content is null (HAp). The increment of the F/Ca ratio accompanies the one of the Ca/P ratio, proving that the incorporation of F^- increases with the amount of NH_4F solution added to the reaction medium. The maximum value reached for the Ca/F ratio was 0.190, which is still below the stoichiometric limit of FAp, *i.e.* $F/Ca = 2/10 = 0.200$ for $Ca_{10}(PO_4)_6\ F_2$. Accordingly, the addition of the highest amount of 0.5 M NH_4F was

not enough to form stoichiometric FAp, part of the F^- anions participating in the formation of CaF_2 (**Figure 6.1 c**).

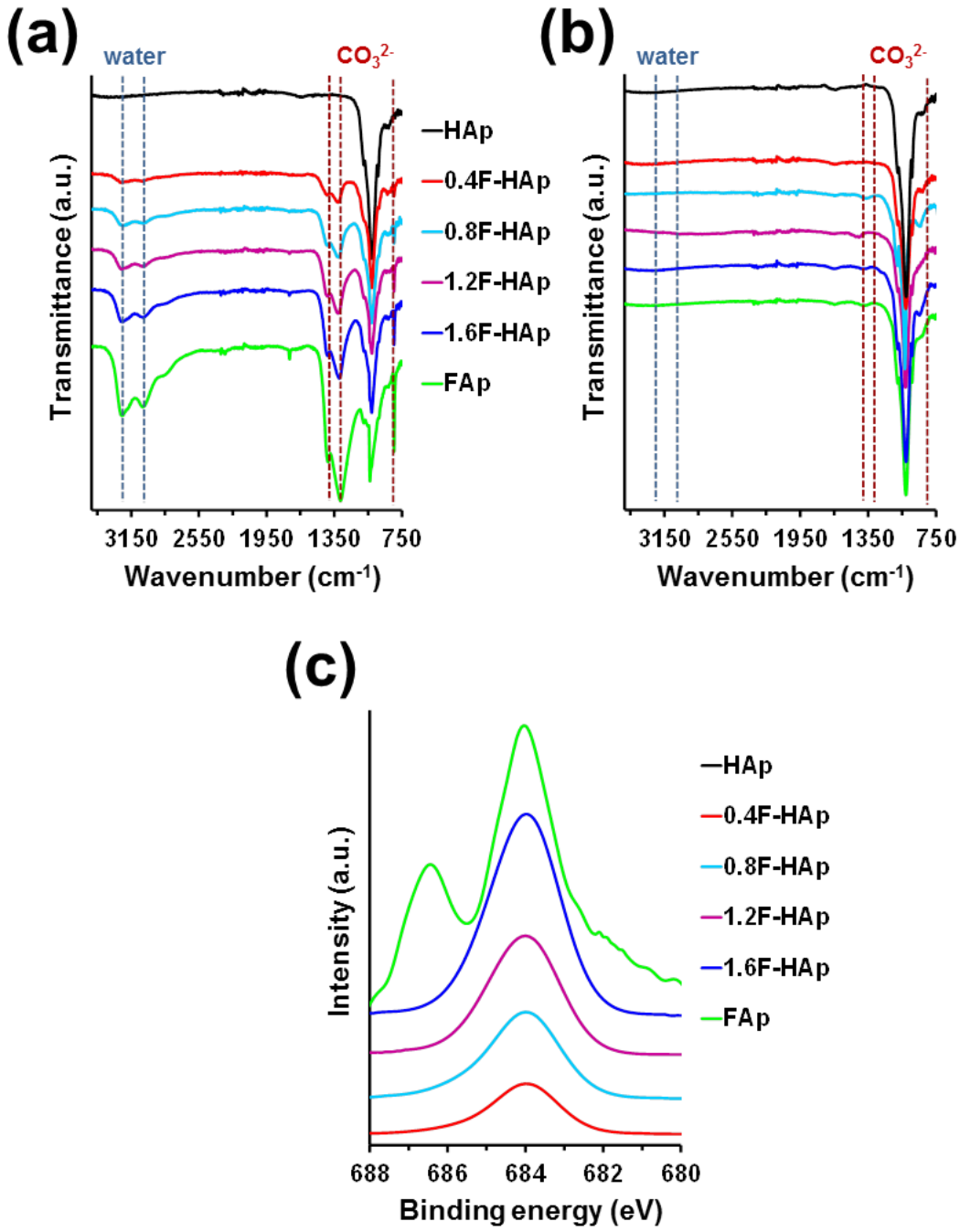

Figure 6.1. FTIR spectra of HAp, *x*F-HAp and FAp samples prepared using (a) ATM (37ºC)- and (b) N_2 (37ºC)-conditions. The position of the main bands for CO_3^{2-} and water are displayed using red and blue dashed lines, respectively. (c) High-resolution XPS spectra in the $F\ 1s$ region for HAp, *x*F-HAp and FAp samples prepared using N_2 (37ºC)-conditions.

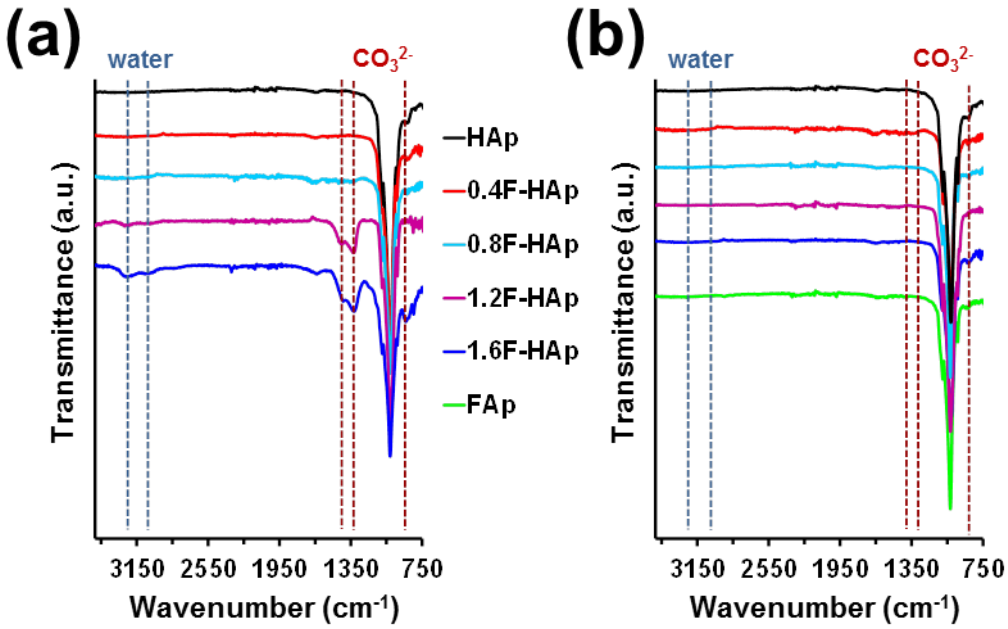

Figure 6.2. FTIR of HAp, *x*F-HAp and FAp samples prepared using (a) ATM (150 ºC)- and (b) N_2 (150 ºC)-conditions. The bands corresponding to adsorbed water and PO_4^{3-} by CO_3^{2-} substitution are displayed by dashed blue and red lines, respectively.

Inspection of the atomic percent compositions of samples prepared under ATM (37 ºC)-conditions, which are included in **Table 6.1**, reveals that the incorporation of F^- ions is also lower than the stoichiometric value. However, these samples present a remarkable composition differences with respect to the samples obtained under N_2 (37 ºC)-conditions. This is reflected by the carbon content and the O/Ca ratio that grow rapidly with x in samples prepared under ATM (37 ºC)-conditions while they maintain approximately constant in samples obtained under N_2-conditions. These variations are due to the replacement of PO_4^{3-} by CO_3^{2-} , which as observed by FTIR is a phenomenon promoted by the fluoridation in uncontrolled atmospheres.

Table 6.1. Atomic percent composition (Ca, P, O, F and C) of HAp, *x*F-HAp and FAp prepared under N_2 (37 ºC)- and ATM (37 ºC)-conditions. Ca/P, F/Ca and O/Ca ratios are displayed for each compound.

	Ca	P	O	F	C	Ca/P	F/Ca	O/Ca
				N_2 (37 ºC)-conditions				
HAp	39.69	19.18	40.94	0.0001	0.19	1.60	0.002	2.57
0.4F-HAp	39.82	19.15	40.80	0.0023	0.23	1.61	0.044	2.55
0.8F-HAp	39.81	18.91	41.11	0.0037	0.17	1.63	0.071	2.58
1.2F-HAp	39.77	18.58	41.44	0.0065	0.21	1.65	0.124	2.60
1.6F-HAp	39.72	18.47	41.65	0.0086	0.15	1.66	0.165	2.62
FAp	40.00	18.48	41.42	0.0100	0.09	1.67	0.190	2.58
				ATM (37 ºC)-conditions				
HAp	38.29	18.18	43.34	0.0001	0.19	1.63	0.002	2.83
0.4F-HAp	35.80	16.87	46.82	0.0020	0.51	1.64	0.043	3.27
0.8F-HAp	33.87	15.95	49.25	0.0035	0.93	1.64	0.079	3.63
1.2F-HAp	29.77	14.01	54.81	0.0046	1.41	1.64	0.118	4.60
1.6F-HAp	26.72	12.47	58.91	0.0055	1.89	1.66	0.157	5.51
FAp	25.42	12.01	60.49	0.0064	2.08	1.64	0.195	5.95

Figure 6.3 compares the WAXS patterns of HAp, *x*F-HAp and FAp prepared under HT- and ATM (37 ºC)-conditions. Characterization of the prepared samples by X-ray diffraction is focused on peaks at 32 º–34 º 2θ, which are characteristics of the (211), (112), and (300) HAp reflections. As it can be seen, the diffraction patterns of all minerals are similar and exhibit the peaks associated to the reflections characteristic of the $P6_3/m$ hexagonal crystal structure of HAp, independently of the F^- concentration and the experimental condition used for their preparation. However, it is worth nothing that the peaks of the samples prepared under HT conditions (*i.e*. air atmosphere with high temperature and pressure) are much better defined than those of minerals obtained at 37 ºC under ATM-conditions, indicating that the crystallinity of *x*F-HAp and FAp is largely affected by pressure and temperature. Accordingly, for each fluorination degree, the crystallinity and crystallite size are higher by more than twice for samples obtained at 150 ºC under a pressure of 200 bars than for those produced at 37 ºC under atmospheric pressure (**Table 6.2**).

On the other hand, **Table 6.2** indicates that both crystallinity and crystallite size increases with fluoride substitution. Thus, the crystallinity increases from ~ 45 % and ~10 % for HAp to ~ 61 % and ~ 27 % for FAp in samples prepared using HT- and ATM (37 ºC) -conditions, respectively. This should be attributed to the formation of $F\cdots H-O$ hydrogen bonds involving the incorporated F^- anions and the remaining OH^- groups. These interactions, which were examined in previous work[35] helps to tight these anions at their crystallographic positions.

Table 6.2. Crystallinity (χ_c) and crystallite size (L) of HAp, *x*F-HAp and FAp prepared under HT- and ATM (37ºC)-conditions.

	HT-conditions		**ATM (37 ºC)-conditions**	
	χ_c (%)	L (nm)	χ_c (%)	L (nm)
HAp	44.7 ± 1.0	49.8 ± 1.4	9.7 ± 1.7	10.3 ± 0.5
0.4F−HAp	47.2 ± 1.3	55.6 ± 1.0	13.4 ± 1.1	13.1 ± 0.8
0.8F−HAp	50.7 ± 1.4	60.6 ± 1.9	16.3 ± 0.7	17.3 ± 1.8
1.2F−HAp	53.7 ± 1.6	66.1 ± 2.1	19.4 ± 1.8	22.4 ± 1.4
1.6F−HAp	57.9 ± 1.5	70.8 ± 2.6	22.3 ± 1.9	27.0 ± 1.7
FAp	61.1 ± 1.0	76.2 ± 1.7	26.7 ± 1.2	32.5 ± 1.4

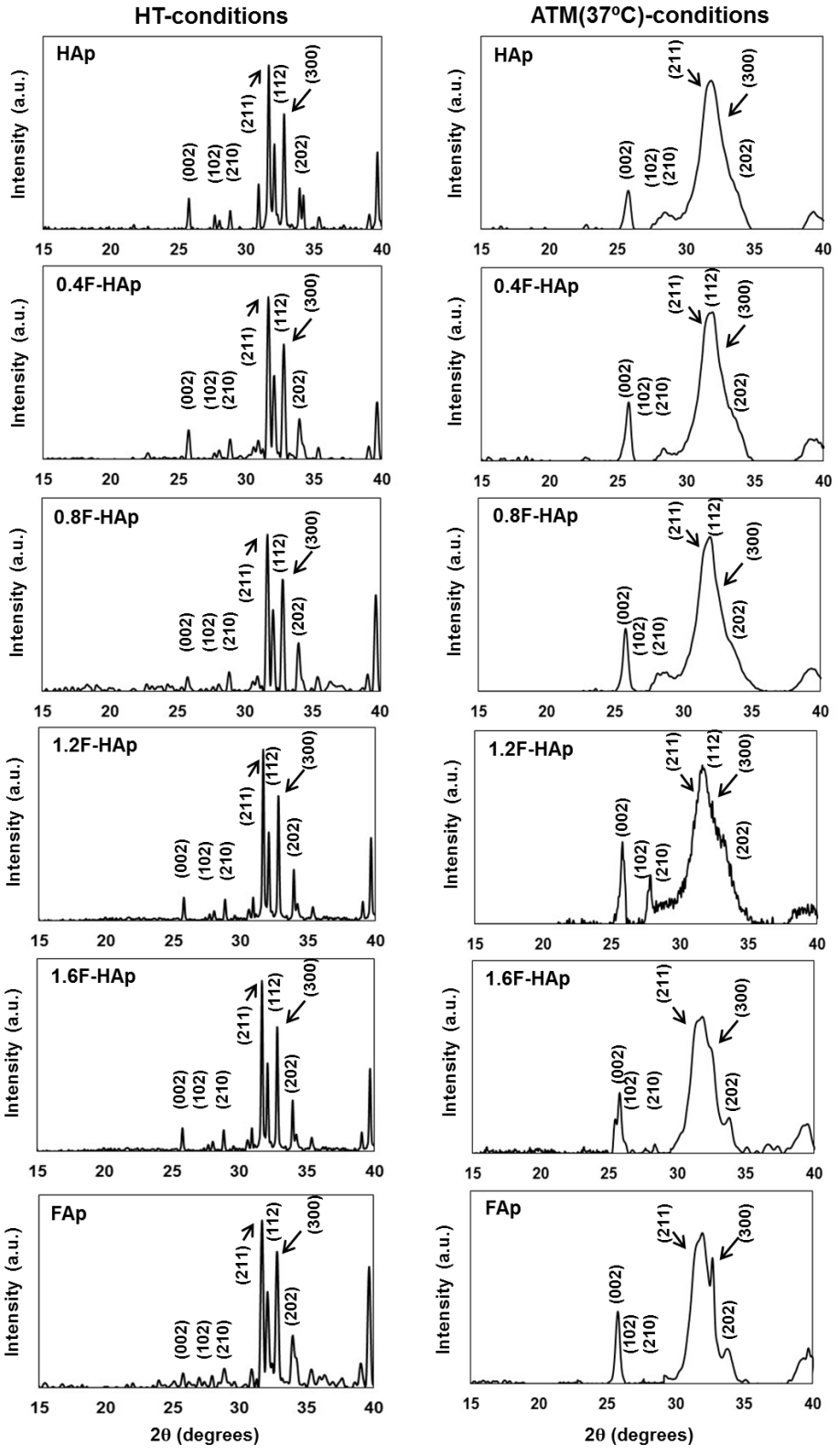

Figure 6.3. X-ray diffraction patterns of HAp, *x*F-HAp and FAp samples prepared under HT-conditions at 150 ºC and ATM (37 ºC)-conditions. The hexagonal structure typically observed for HAp was identified by the peaks associated to the (211), (112) and (300) reflections.

Figure 6.4 a displays the TGA and DGTA curves of HAp, *x*F-HAp and FAp prepared under HT-conditions. Initially, all samples display a step at around 100 ºC, which has been attributed to the evaporation of residual water (*i.e.* moisture and water superficially adsorbed). This dehydration process appears as a broad and relatively small peak in the first derivative profile. After this, samples are stable up to a temperature of 145−175 ºC, depending on the composition. At this temperature, the minerals experience a drastic weight loss, which corresponds to the highest peak of the DGTA curve. The weight loss continues progressively until 600 ºC. At the latter temperature, the weight loss increases with fluorination degree, ranging from 18 % for HAp to 22 % for FAp. The decomposition peak centered at around 200 ºC has been attributed to the dehydration of the HPO_4^{2-} groups[36] which occur according to the following reaction:

$$2HPO_4^{2-} \rightarrow P_2O_7^{4-} + H_2O \qquad (4)$$

At higher temperature, the progressive variation of the weight has been associated to the loss of CO_2.[36-38] More specifically, residual type-A CO_3^{2-} can react with HPO_4^{2-} as follows:

$$CO_3^{2-} + HPO_4^{2-} \rightarrow CO_2 + 2PO_4^{3-} + H_2O \qquad (5)$$

Above 470 ºC, the weight loss has been associated to the CO_3^{2-} from the lattice (B-type substitution), which undergoes the following reaction:[36-38]

$$CO_3^{2-} + P_2O_7^{4-} \rightarrow 2PO_4^{3-} + CO_2 \qquad (6)$$

It is worth noting that the carbonation degree increases with the F^- content, which is also consistent with the weight loss.

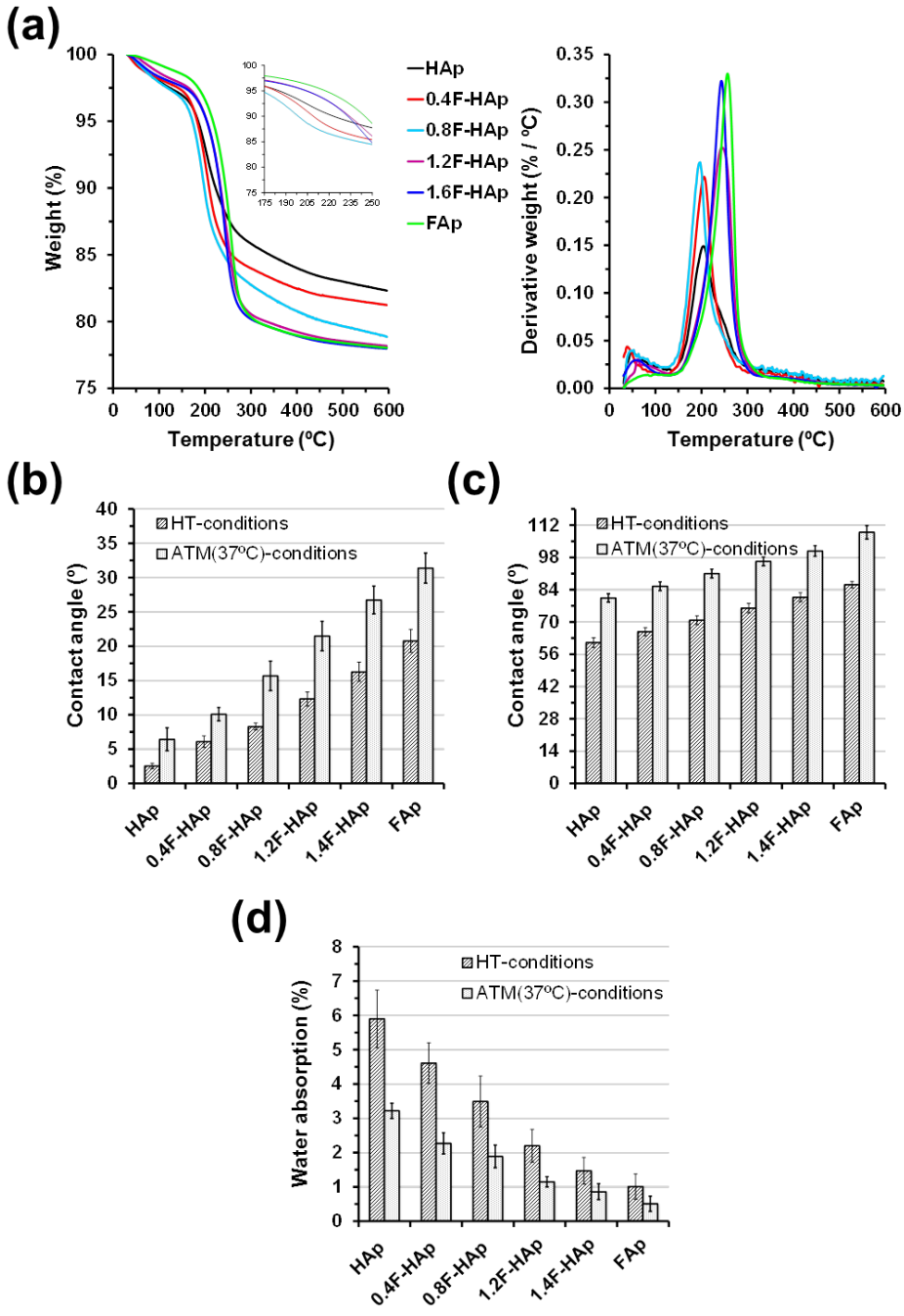

Figure 6.4. (a) TGA (left) and DTGA (right) curves for HAp, *x*F-HAp and FAp samples prepared under HT-conditions. Contact angles of (b) water and (c) FBS, and (d) water absorption capacity for HAp, *x*F-HAp and FAp samples prepared under HT-and ATM (37 ºC)-conditions.

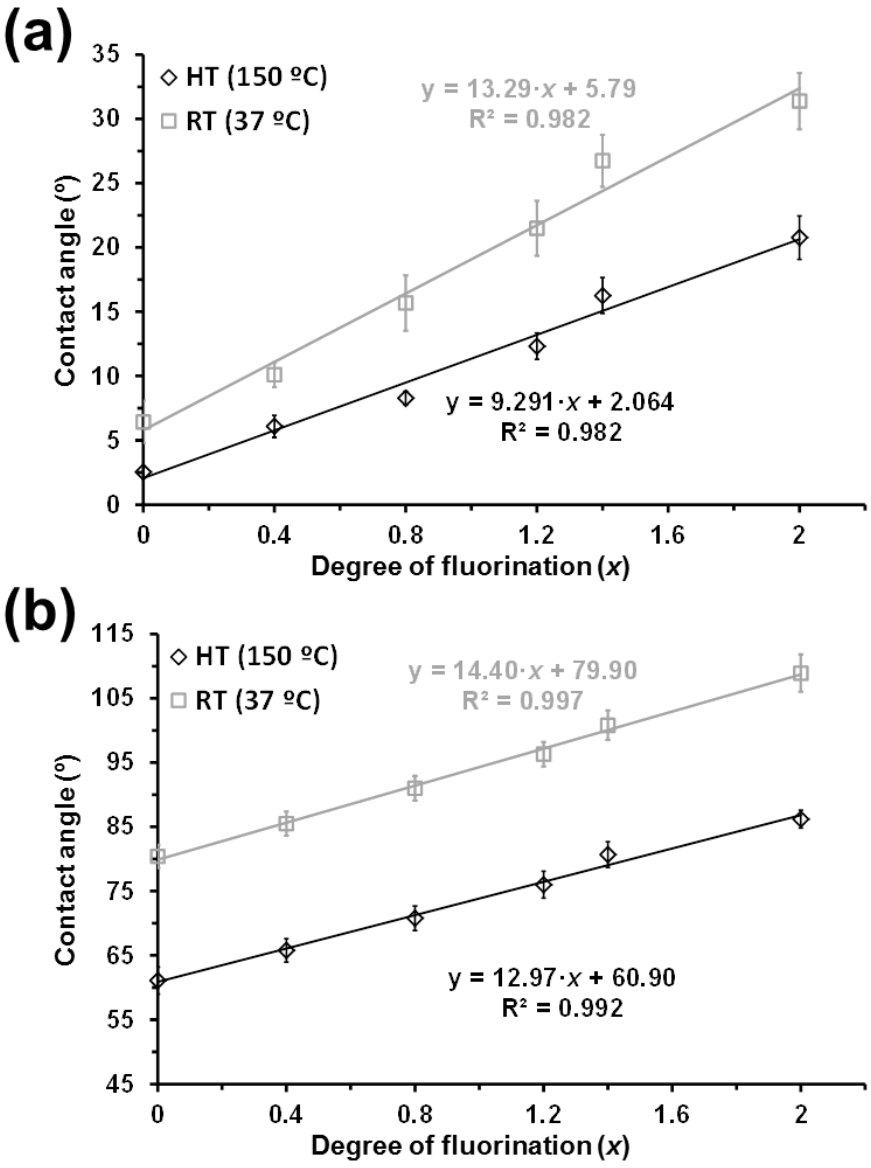

Figure 6.5. Variation of the contact angle of (a) water and (b) FBS against the fluorination degree of HAp, *x*F-HAp and FAp samples prepared under HT- and ATM-conditions at 150 and 37 ºC, respectively. The equations derived from the corresponding linear fitting (solid line) is displayed for each synthetic condition.

The wettability of HAp, *x*F-HAp and FAp prepared using prepared under HT- and ATM (37 ºC) conditions was evaluated using water and FBS, the latter mimicking a physiological environment rich in proteins. Results indicate that the contact angles determined for both solvent increases with the fluorination degree (**Figure 6.4 b-c**), evidencing that the wettability decreases with increasing fluorine content. Moreover, such increment is linear, as is illustrated in (**Figure 6.5**), which indicates the systematic pattern associated to the substitution of OH^- by F^-. Besides, the contact angle is lower

for the sample prepared under HT-conditions than for the one obtained under ATM (37 ºC)- conditions, independently of the fluorine content and the solvent. This behavior indicates that, for a given fluorination degree, the affinity of the mineral surface towards the solvent increases with the crystallinity and the size of the crystals.

As it was expected from results displayed in **Figure 6.4 b**, the water absorption capacity of the minerals decreases with increasing fluorination degree (**Figure 6.4 d**), independently of the synthetic conditions. However, it is worth noting that water absorption increases with the crystallinity and crystalline size. Minerals prepared using HT-conditions display a water absorption capacity that is around twice that of minerals prepared using ATM (37 ºC)-conditions.

6.3.2 Electrochemical behavior as a function of the fluorination degree

In recent studies the preparation and properties of polarized HAp, hereafter p-HAp, were reported. This electrochemically active material was obtained using a thermally stimulated polarization (TSP) process according to which a constant DC voltage was applied at 1000 ºC for 1 hour to already sintered HAp (s-HAp).[39-40] The most distinctive characteristic of p-HAp is the electrochemical activity, which is significantly higher than that achieved using lower polarization temperatures to samples sintered in a saturated water atmosphere.[41,42] In a very recent work, an electrophotocatalyst based on p-HAp particles was used to obtain both glycine and Alanine (D/L racemic mixture) in mild reaction conditions by fixing nitrogen from N_2 and carbon from CO_2 and CH_4.[40] Besides, the adsorption of phosphates and phosphonate was found to be significantly higher onto p-HAp than onto as prepared samples,[39] where “as prepared samples” refers to unmodified synthesized (*i.e*. non-sintered and/or non-polarized minerals).

In this work HAp, *x*F-HAp and FAp powders were sintered at 1000 ºC for 2 hours in air. After this, each sintered sample was processed into discs as described in the Methods section. Finally, a TSP process was applied to the resulting discs, which were sandwiched between stainless steel (AISI 304) plates and polarized for 1 hour under application of a constant DC voltage at 1000 ºC. After such time, samples were allowed to cool to room temperature, maintaining the DC voltage. Three DC voltages were considered for each sample: 250, 500 and 1000 V.

Polarized samples, hereafter denoted p-HAp, p-*x*F-HAp and p-FAp, were characterized by CV, results being displayed in **Figure 6.6**. Cyclic voltammograms recorded in PBS (pH 7.2) for as prepared samples, which were used as controls, reflect a very poor electrochemical behavior (**Figure 6.6 a**), even though the electrochemical activity was slightly than that bare steel (blank) in all cases. In spite of this, the electroactivity of as prepared samples decreases with increasing fluorination degree (*i.e.* the electroactivity is ~ 63 % lower for FAp than for HAp). The electroactivity enhanced considerably after the TSP process, this effect increasing with the applied DC voltage (**Figure 6.6 b-d**). Again, this increment strongly depends on the fluorination degree. Thus, the electroactivity of p-HAp obtained using 1000 V is ~73 % higher than that of as prepared HAp, while the increment is of only ~ 47 % for p-FAp. The dependence of the increment in the electroactivity of the studied minerals against the fluorination degree is represented in **Figure 6.6 e**, the electroactivity obtained for p-HAp at 1000 V being taken as the reference (100 %) for all systems.

Results displayed in **Figure 6.6** are fully consistent with previous observations on p-HAp, which showed that the electrochemically active sites are due to the de-hydroxylation of the crystals during the sintering and the subsequent re-organization of the vacancies into channels during the TSP.[39] The movement of ions through such channels during oxidation and reduction process depends on the concentration of vacancies, which in turn is related with the composition of the prepared mineral. Thus, the amount of vacancies decreases with increasing fluorination degree since the sintering-induced de-fluorination is much more difficult than the de-hydroxylation. Overall, these results indicate that *x*F-HAp and, especially, FAp are less affected by thermal and electrical treatments that HAp. This stability precludes the use of p-*x*F-HAp and p-FAp in practical applications in which electrochemical properties play a key role, while p-HAp can be used not only as electro-responsive scaffold[34] but also as electrocatalyst to fix nitrogen from N_2 and carbon from CO_2 and CH_4.[40]

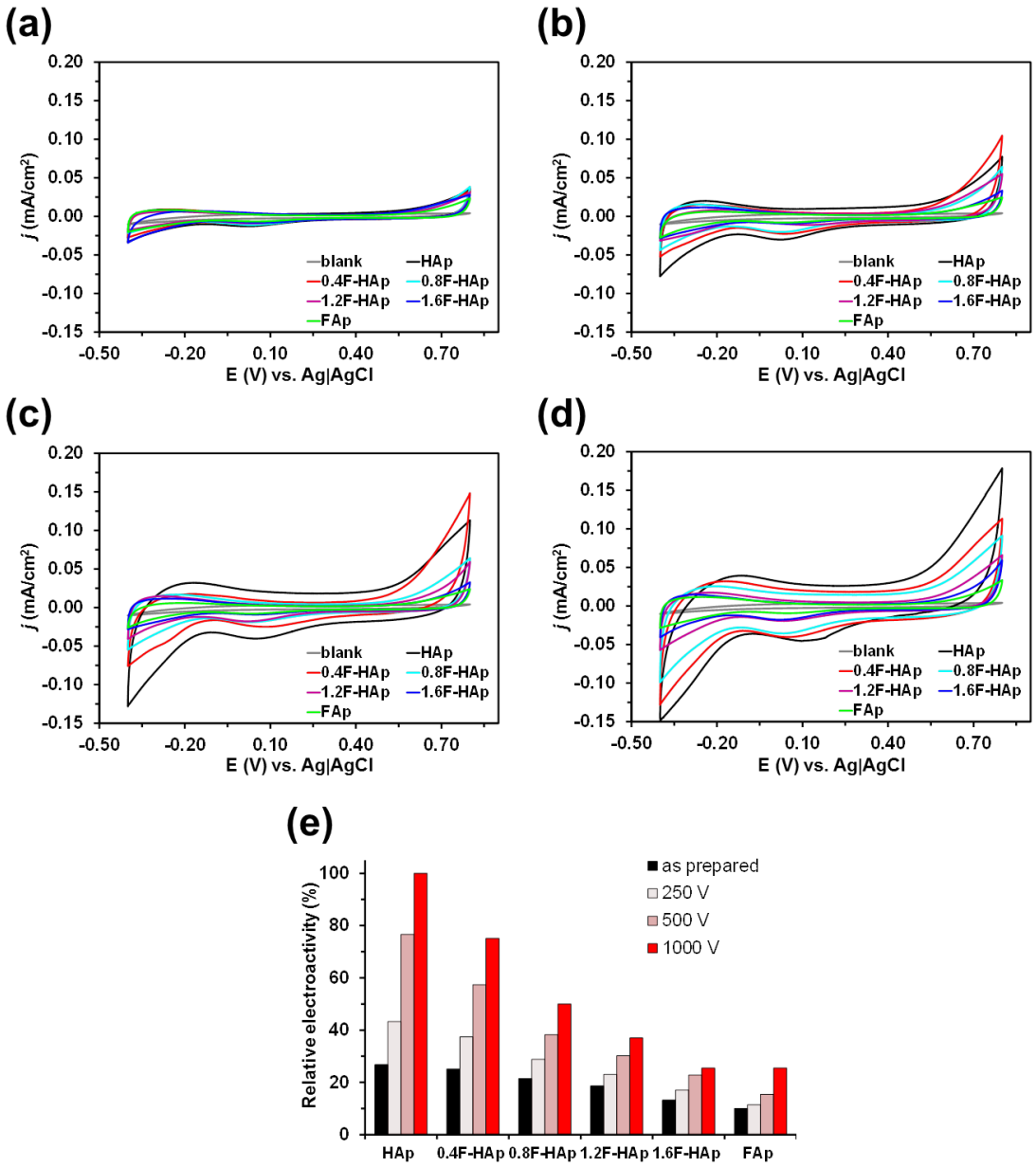

Figure 6.6. Control voltammograms of HAp, *x*F-HAp and FAp: (a) as prepared and polarized through a TSP process using a DC voltage of (b) 250 V, (c) 500 V and (d) 1000 V. Voltammograms for bare steel (blank) are included in all cases. (e) Variation of the electrochemical activity with the polarization process using different DC voltages. Values are relative to p-HAp obtained using 1000 V (taken as 100 %).

6.3.3 Effect of the fluorination degree in the solubility

The remarkable effect of CO_3^{2-} in the solubility of HAp was deeply studied by Pan and Darwell.[43] These authors attributed the increment in the HAp solubility at low pH with the substitution degree by CO_3^{2-} and the formation of complexes such as $CaH_2PO_4H_2CO_3^+$

and $CaH_2PO_4HCO_3$. In order to analyze the effect of CO_3^{2-} -substitution in the solubility of *x*F-HAp and FAp, we firstly prepared different HAp samples by varying the content of CO_3^{2-}. These carbonated HAp samples were obtained using the CO_2-conditions described in the Methods section, the CO_2 atmosphere being maintained during 1, 1.5, 2, 2.5 and 3 hours to achieve different carbonation degrees. The concentration of CO_3^{2-} (in % wt.) in the resulting samples, which was determined by considering that all atomic percent C found by XPS corresponds to such specie (**Table 6.3**), increased with the time that the CO_2 atmosphere is applied, ranging from 2.12 % (1 hour) to 16.30 % (3 hours).

The solubility of the carbonated HAp was evaluated by adding 500 mg of each sample to an aqueous solution (50 mL) with 100 mM HCl and 50 mM $NaCl$. **Figure 6.7 a** shows that, as it was expected, the solubility of HAp increases rapidly with the carbonation degree (*i.e.* from ~ 78 to ~ 763 mM when the carbonation time increased from 1 to 3 h; **Table 6.3**). In contrast, the solubility in the same medium decreases significantly with the fluorination degree, as is evidence in **Figure 6.7 b** for HAp, *x*F-HAp and FAp samples prepared under controlled N_2 (37º C)-conditions. Thus, the content of CO_3^{2-} in these samples was very low, as was discussed above (**Table 6.1**).

Table 6.3. Atomic percent composition (Ca, P, O, F and C), Ca/P ratio and content of CO_3^{2-} (in % wt.) as determined by XPS of HAp prepared using ATM- and CO_2-conditions. For the latter, the CO_2 atmosphere was during a time comprised between 1 and 3 hours (indicated in parenthesis). The % wt. of CO_3^{2-} was determined assuming that all atomic percent content of C corresponds to CO_3^{2-}. The solubility in an aqueous solution with 100 mM HCl and 50 mM $NaCl$ is also displayed.

Conditions	Ca	P	O	C	F	Ca/P	% CO_3^{2-}	Solubility (mM)
ATM	38.78	18.12	42.96	0.14	0.0003	1.65	0.27	19.5 ± 0.6
CO_2 (1 h)	36.50	16.84	46.34	0.32	0.0002	1.67	2.12	77.6 ± 2.8
CO_2 (1.5 h)	34.36	15.80	49.28	0.56	0.0002	1.68	5.10	215.0 ± 5.2
CO_2 (2 h)	30.12	14.01	54.98	0.89	0.0003	1.66	8.50	468.7 ± 6.9
CO_2 (2.5 h)	26.85	12.32	59.38	1.45	0.0002	1.68	11.67	694.1 ± 10.2
CO_2 (3.0 h)	24.12	11.15	62.95	1.78	0.0003	1.67	16.30	763.5 ± 14.3

A completely different behavior was obtained for *x*F-HAp and FAp prepared using ATM (37 ºC)-conditions (**Figure 6.7 c**). In this case, the content of CO_3^{2-} increases with the fluorination degree, ranging from 2.67 % wt. (0.4F-HAp) to 16.03 % wt. (FAp), as is explicitly labelled in **Figure 6.7 c**, and, therefore, the solubility in the acid medium increases considerably with the fluorination degree. However, such solubility is still significantly lower than that of HAp prepared under CO_2-conditions (**Figure 6.7 a**), even though the carbonation degree was similar in both cases. Thus, the inhibitory effect associated for the F^- anions and the unrestrictive effect attributed to the CO_3^{2-} anions coexist in *x*F-HAp and FAp samples prepared using ATM (37 ºC)-conditions.

In order to examine the effect of external F^- anions in the solubility of HAp prepared under N_2(37ºC)-and CO_2-conditions (CO_2 atmosphere maintained for 1 hour), very small F^- concentrations were supplied by adding NH_4F to the acid solubility medium. The variation of the solubility of these minerals as a function of the supplied F^- concentration, $[F^-]$, is compared in **Figure 6.7 d**. As it was expected, both cases, the solubility decreases with increasing external $[F^-]$. This general behavior was independent of the presence of CO_3^{2-} in the mineral matrix, even though samples prepared CO_2-conditions, which contain 2.12 % wt. CO_3^{2-}, exhibited higher solubility for all the explored $[F^-]$ concentrations. Similar observations were obtained for 0.8F-HAp prepared under N_2 (37ºC)- and CO_2 –conditions (CO_2 atmosphere maintained for 1 hour), as is reflected in **Figure 6.7 e**.

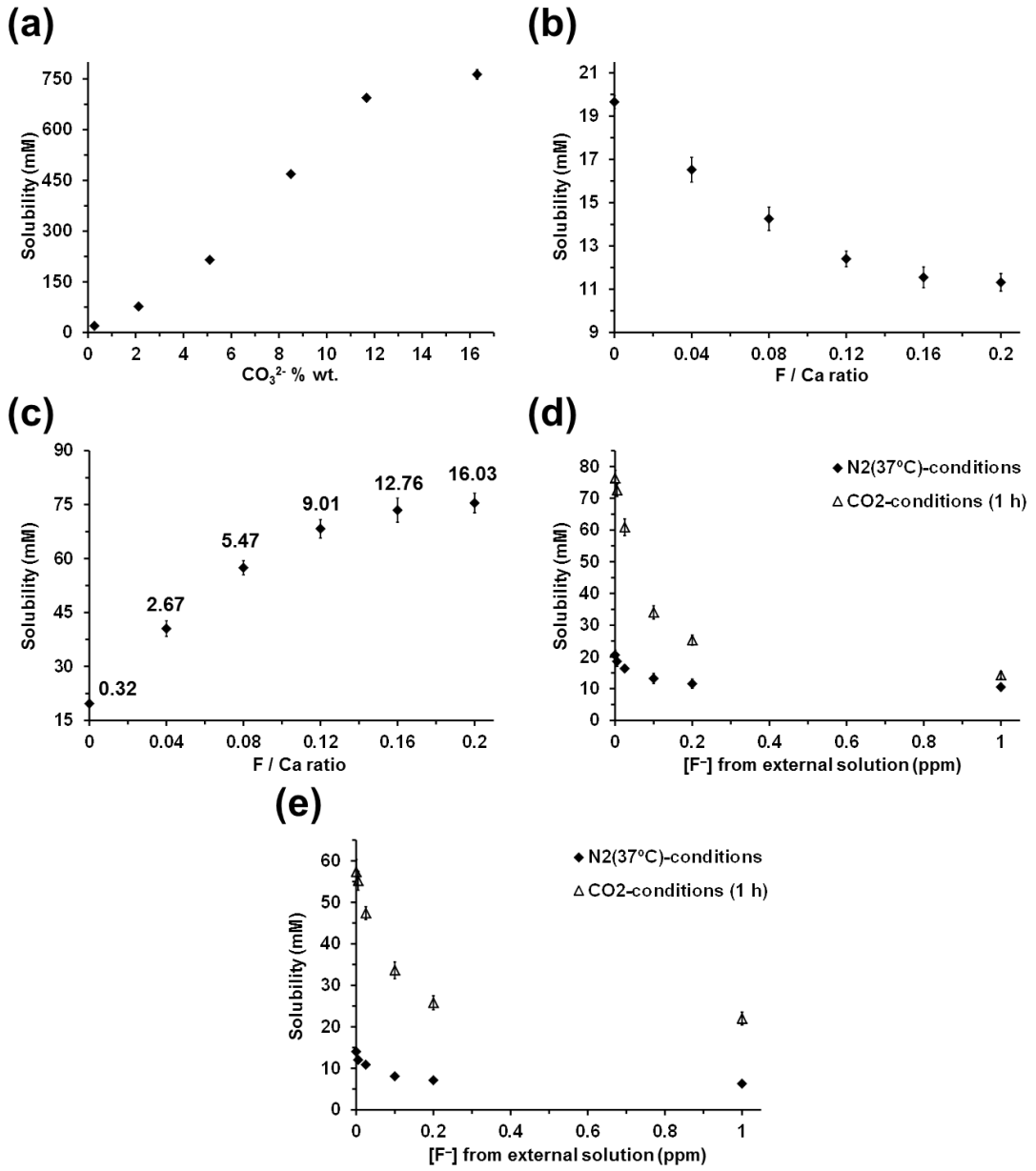

Figure 6.7. Solubility in aqueous solution with 100 mM HCl and 50 mM NaCl against: (a) the % of CO_3^{2-} (in wt.) of HAp prepared using CO_2-conditions (37 ºC), which were applied during different times to achieve different carbonation degrees; (b) the fluorination degree (expressed as F/Ca ratio) of HAp, *x*F-HAp and FAp prepared under N_2 (37 ºC)-conditions ; (c) the fluorination degree (expressed as F/Ca ratio) of HAp, *x*F-HAp and FAp prepared under ATM (37 ºC)-conditions Numerical labels indicate the % of CO_3^{2-} (in wt.) in the prepared samples as determined by XPS; (d) the $[F^-]$ supplied to the solubility medium of HAp prepared using N_2 (37 ºC) and CO_2-conditions. In the latter, the CO_2 atmosphere was applied during 1 hour; and (e) the $[F^-]$ supplied to the solubility medium of 0.8F-HAp prepared using N_2 (37 ºC)- and CO_2-conditions. In the latter, the CO_2 atmosphere was applied during 1 hour.

Overall, comparison of results displayed in **Figure 6.7** indicates that, although the incorporation of F^- into the mineral matrix reduces the solubility, external F^- anions surrounding the HAp matrix inhibit such process more effectively. Probably, the latter anions are partially adsorbed onto the mineral surface and a dynamical equilibrium with the solution, which involves re-precipitation processes, is reached. These results have remarkable implications for the use of HAp as mineral coating for dental implants. Thus, implants made from titanium, stainless steel or cobalt-chrome alloys are frequently modified at the surface by bioceramics coatings that can be applied using different technologies, even though plasma spraying is the most popular and the Food and Drug Administration (FDA)-approved method.[44] In recent years, strategies based on the substitution of HAp by *x*F-HAp or FAp coatings has been proposed as effective strategies to decrease biofilm accumulation, to inhibit the demineralization process and to combat caries-related bacteria.[45-49] However, our results clearly indicate that such fluoride-therapy is more effective by supplying F^- anions to the HAp coating from an external source (*e.g.* frequent mouthwashes with a fluoride solution) than incorporating such anions into the own mineral matrix replacing HAp by *x*F-HAp or FAp.

On the other hand, it is well known that the solubility of some minerals, as for example $NaCl$, is practically independent of the pH, while the solubility of HAp increases approximately 10 times for each unit of decrease in pH. Similar pH dependence has been reported for FAp,[43] which was reported to exhibit a solubility profile just below and nearly parallel to that of HAp. **Figure 6.7**, which represents the solubility of *x*F-HAp against the change of pH within the $2.0 \leq pH \leq 3.0$ interval, proves that such behavior is independent of the fluorination degree. These experiments, in which mimic the bacterial acid attack, support previous discussion, indicating that fabrication of HAp mineral coatings with a low or null fluorination degree is the most appropriated.

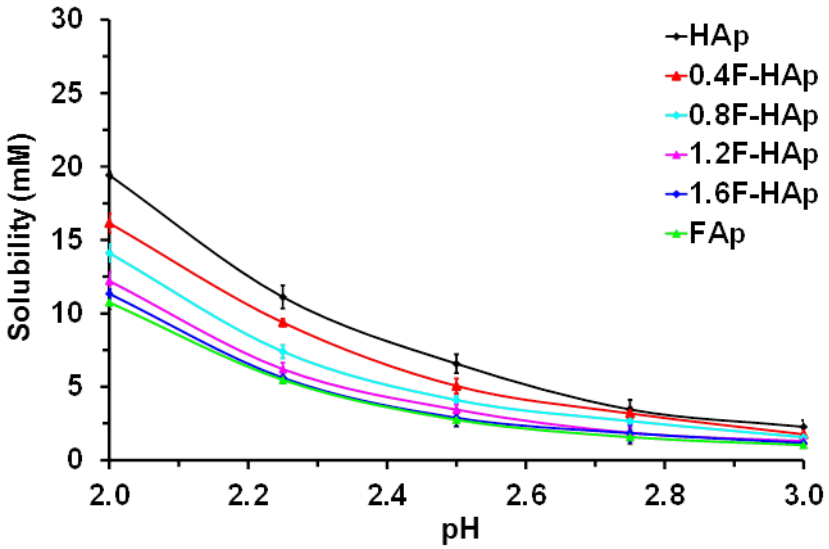

Figure 6.7. Solubility in aqueous solution with 100 mM HCl and 50 mM $NaCl$ against the pH of HAp, *x*F-HAp and FAp CO_2-conditions at 37 ºC. The CO_2 conditions were applied during 1 hour.

6.4 CONCLUSIONS

Synthetic HAp, *x*F-HAp and FAp have been prepared using experimental conditions, which differ in the environment, the temperature and/or the pressure. The synthetic conditions regulate the mineral composition in terms of CO_3^{2-} and F^- intake, the formation of vacancies, the water absorption, the crystallinity, and crystallite size. The solubility in aqueous acid media of the prepared minerals depends on their composition. More specifically, the solubility increases with the CO_3^{2-} content while it decreases with increasing fluorination degree. Moreover, the inhibitory effect associated for the F^- anions contained in the mineral matrix of *x*F-HAp and FAp enhances when F^- anions are supplied to HAp through an external solution. These results have important implications that affect the mineral coatings used to protect dental implants. Thus, non-carbonated HAp coatings enriched in F^- anions through external sources are more suitable for inhibiting demineralization than the recently proposed *x*F-HAp and FAp coatings, which contain the F^- anions within the mineral matrix.

6.5 REFERENCES

1. Kim, H.W., Kim, H.E. & Knowles, J.C. Fluor-hydroxyapatite sol-gel coating on titanium substrate for hard tissue implants. *Biomaterials*. **25**, 3351-3358 (2004).
2. Ebrahimi-kahrizsangi, R., Nasiri-Tabrizi, B. & Chami, A. Synthesis and characterization of fluorapatiteetitania (FAp-TiO_2) nanocomposite via mechanochemical process. *Solid. State. Sci.* **12**, 1645-1651 (2010).
3. Tosuaaddu, K., Gross, K.A., Pluduma, L. & Veiderma, M. A review on the thermal stability of calcium apatites. *J. Therm. Anal. Calorim*. **110**, 647-659 (2012).
4. Rintoul, L., Wentrup-Byrne, E., Suzuki, S. & Grøndahl, L. FT-IR spectroscopy of fluoro-substituded hydroxyapatite: strengths and limitations. *J. Mater. Sci- Mater. M.* **18**, 1701–1709 (2007).
5. Wang, C., Karlis, G.A., Anderson, G.I., Dunstan, C.R., Carbone, A., Berger, G., Ploska, U. & Zreidat, H. Bone growth is enhanced by novel bioceramic coatings on Ti alloy implants. *J. Biomed. Mater. Res., Part A*. **90A**, 419-428 (2009).
6. Qu, H.B. & Wei, M. The effect of fluoride contents in fluoridated hydroxyapatite on osteoblast behavior. *Acta Biomater*. **2**, 113-119 (2006).
7. Heling, I., Heindel, R. & Merin, B. Calcium-fluorapatite. A new material for bone implants. *J. Oral Implantol*. **9**, 548-555 (1981).
8. Dorozhkin, S.V. Calcium orthophosphates: occurrence, properties, biomineralization, pathological calcification and biomimetic applications. *Biomatter*. **1**, 121-164 (2011).
9. Melo, M.A.S., Guedes, S.F.F., Xu, H.H.K. & Rodrigues, L.K.A. Nanotechnology-based restorative materials for dental caries management. *Trends Biotechnol*. **31**, 459-467 (2013).
10. Moshaverinia, A., Ansari, S., Moshaverinia, M., Roohpour, N., Darr, J.A. & Rehman, I. Effect of incorporation of hydroxyapatite and fluoroapatitenanobioceramics into conventional glass ionomer cements (GIC). *Acta Biomater*. **4**, 432-440 (2008).
11. Saber, A., Smahi, A., Solhy, A., Nazih, R., Elaabar, B., Maizi, M. & Sebti, S. Heterogeneous catalysis of Friedel-Crafts alkylation by the fluorapatite alone and doped with metal halides. *J. Mol. Catal. A: Chem.* **202**, 229-237 (2003).
12. Boukha, Z., Kacimi, M., Ziyad, M., Ensuque, A. & Bozon-Verduraz, F. Comparative study of catalytic activity of Pd loaded hydroxyapatite and fluoroapatite in butan-2-ol conversion and methane oxidation. *J. Mol. Catal. A Chem.* **270**, 205-213 (2007).
13. Li, H., Mei H., Liu, H., Liu, L., Liao R. & Kumar, V. Growth mechanism of surfactant-free size-controlled luminescent hydroxyapatite nanocrystallites. *Cryst. Growth Des*. **17**, 2809-2815 (2017).

14. Yuan, Q.H., Xu, A. P., Zhang, Z.H., Chen, L., Wan, L., Shi, X., Lin, S.X., Yuan, L.B. & Deng, L.B. Bioactive silver doped hydroxyapatite composite coatings on metal substrates: synthesis and characterization. *Mat. Chem. Phys*. **218**, 130-139 (2018).

15. Popescu, A.C., Florian, P.E., Stan, G.E., Popescu-Pelin, G., Zgura, J., Enculescu, M., Oktar, F.N., Trusca, R., Sima, L.E., Roseanu, A. & Duta L. Physical-chemical characterization and biological assessment of simple and lithium-doped biological-derived hydroxyapatite thin films for a new generation of metallic implants. *Appl. Surf. Sci*. **439**, 724-735 (2018).

16. Alshemary, A.Z., Pazarceviren, A.E., Tezcaner, A. & Evis, Z. Fe^{3+}/SeO_4^{2-} dual doped nano hydroxyapatite: a novel material for biomedical applications. *J. Biomed. Mater. Res. B*. **106**, 340-352 (2018).

17. Xu, Y., An, L., Chen, L., Cao, L., Zeng, D.L. & Wang, G.H. A facile chemical route to synthesize Zn doped hydroxyapatite nanorods for protein drug delivery. *Mater. Chem. Phys*. **214**, 359-363 (2018).

18. Bhadang, K.A., Holding, C.A., Thissen, H., McLean, H.M., Forsythe, J.S. & Haynes, D.R. Biological responses of human osteoblasts and osteoclasts to flame-sprayed coatings of hydroxyapatite and fluorapatite blends. *Acta Biomater*. **6**, 1575-1583 (2010).

19. Ye, H., Liu, X.Y. & Hong, H.P. Cladding of titanium/fluorapatite composites onto Ti6Al4V substrate and the in vitro behaviour in the simulated body fluid. *Appl. Surf. Sci*. **255**, 8126-8134 (2009).

20. Müller, F., Zeith, C., Mantz, H., Ehses, K.H., Soldera, F., Schmauch, J. & Hanning, M. Elemental Depth Profiling of Fluoridated Hydroxyapatite: Saving Your Dentition by the Skin of Your Teeth?. *Langmuir*. **26**, 18750–18759 (2010).

21. Jmal, N. & Bouaziz, J. Synthesis, characterization and bioactivity of a calcium-phosphate glass-ceramics obtained by the sol-gel processing method. *Mater. Sci. Eng. C.* **71**, 279-288 (2017).

22. Li, Z.P., Huang, B.X., Mai, S., Wu, X.Y., Zhang, H.Q., Qiao, W., Luo, X. & Chen, Z.F. Effects of fluoridation of porcine hydroxyapatite on osteoblastic activity of human MG63 cells. *Sci. Technol. Adv. Mater*. **16**, 035006 (2015).

23. Stanic, V., Dimitrijevic, S., Antonovic, D.G., Jokic, B.M., Zec, S.P., Tanaskovic, S.T. & Raicevic, S. Synthesis of fluorine substituted hydroxyapatite nanopowders and application of the central composite design for determination of its antimicrobial effects. *Appl. Surf. Sci.* **290**, 346-352 (2014).

24. Kannan, S., Vieira, S.I., Olhero, S.M., Torres, P-M.C., Pina, S., Silva, O. & Ferreira J.M.F. Synthesis, mechanical and biological characterization of ionic doped carbonated hydroxyapatite/ß-tricalcium phosphate mixtures. *Acta Biomater*. **7**, 1835-1843 (2011).

25. Marie, P.J. & Hott, M. Short-term effects of fluoride and strontium on bone formation and resorption in the mouse. *Metabolism.* **35**, 547-551 (1986).

26. Wilson, R.M., Elliott, J.C., Dowker, S.E.P. & Smith, R.I. Rietveld structure refinement of precipitated carbonate apatite using neutron diffraction data. *Biomaterials*. **25**, 2205-2213 (2004).

27. Cury, J.A., Francisco, S.B., Simoes, G.S., Del Bel Cury, A.A. & Tabchoury, C.P.M. Effect of a Calcium Carbonate-Based Dentifrice on Enamel Demineralization *in situ*. *Caries Res*. **37**, 194-199 (2003).

28. Kolmas, J., Piotrowska, U., Kuras, M. & Kurek, E. Effect of carbonate substitution on physicochemical and biological properties of silver containing hydroxyapatites. *Mater. Sci. Eng. C*. **74**, 124-130 (2017).

29. Igeta, K., Kuwamura, Y., Horiuchi, N., Nozaki,,K., Shiraishi, D., Aizawa, M., Hashimoto, K., Yamashita, K. & Nagai, A. Morphological and functional changes in RAW264 macrophage-like cells in response to a hydrated layer of carbonate-substituted hydroxyapatite. *J. Biomed. Mater. Res. Part A*. **105**, 1063-1070 (2017).

30. Kumar, G.S., Thamizhavel, A., Yokogawa, Y., Kalkura, S.N. & Girija, E.K. Synthesis, characterization and in vitro studies of zinc and carbonate co-substituted nano-hydroxyapatite for biomedical applications. *Mater. Chem. Phys.* **134**, 1127-1135 (2012).

31. del Valle, L.J., Bertran, O., Chaves, G., Revilla-López, G., Rivas, M., Casas, M.T., Casanovas, J., Turon, P., Puiggalí, J. & Alemán, C. DNA adsorbed on hydroxyapatite surfaces. *J. Mater. Chem. B*. **2**, 6953-6966 (2014).

32. Zhu, Q.X., Li, Y.M. & D. Han, D. Co-substitution of carbonate and fluoride in hydroxyapatite: Effect on substitution type and content. *Front. Mater. Sci*. **9**, 192-198 (2015).

33. Wang, Y., Zhang, S., Zeng, X., Ma, L.L., Weng, W., Ya, W. & Qian, M. Osteoblastic cell response on fluoridated hydroxyapatite coatings. *Acta Biomater*. **3**, 191-197 (2007).

34. Cheng, K., Zhang, S. & Weng, W.J. The F content in sol–gel derived FHA coatings: an XPS study. *Surf. Coat. Technol*. **198**, 237-241 (2005).

35. Li, H. & Huang, W. Biomimetic synthesis of enamellike hydroxyapatite on self-assembled monolayers. *Mater. Sci. Eng. C*. **27**, 756-761 (2007).

36. Masmoudia, S., Larbot, A., El Feki, H. & Ben Amarm, R. Elaboration and properties of new ceramic microfiltration membranes from natural and synthesised apatite. *Desalination*. **190**, 89-103 (2006).

37. Chauhdry, A.A., Knowles, J.C., Rehman, I, & Darr, J.A. Rapid hydrothermal flow synthesis and characterisation of carbonate- and silicate-substituted calcium phosphates. *J. Biomater. Appl*. **28**, 448-461 (2013).

38. Barakat, N.A.M., Khalil, K.A., Sheikh, F.A., Omran, A.M., Gaihre, B., Khil, S.M. & Kim, H.Y. Physiochemical characterizations of hydroxyapatite extracted from bovine bones by three different methods: extraction of biologically desirable Hap. *Mater. Sci. Eng. C*. **28**, 1381-1387 (2008).

39. Rivas, M., del Valle, L.J., Armelin, E., Bertran, O., Turon, P., Puiggalí, J. & Alemán, C. Hydroxyapatite with permanent electrical polarization: preparation, characterization, and response against inorganic adsorbates. *Chem. Phys. Chem*. **19**, 1746-1755 (2018).

40. Rivas, M., del Valle, L.J., Turon, P., Aleman, C. & Puiggalí, J. Sustainable synthesis of amino acids by catalytic fixation of molecular dinitrogen and carbon dioxide. *Green Chem*. **20**, 685-693 (2018).

41. Nakamura, M., Sekijima, Y., Nakamura, S., Kobayashi, T., Niwa, K. & Yamashita, K. Role of blood coagulation components as intermediators of high osteoconductivity of electrically polarized hydroxyapatite. *J. Biomed. Mater. Res.* **79A**, 627-634 (2006).

42. Horiuchi, N., Nakaguki, S., Wada, N., Nakamura, M., Nagai, A., Katayama, K. & Yamashita, K. Polarization-induced surface charges in hydroxyapatite ceramics. *J. Appl. Phys.* **116**, 014902 (2014).

43. Pan, H.B. & Darwell, B.W. Hydroxyapatite solubility in simple inorganic solutions. *Arch. Oral Biol*. **52**, 801-868 (2007).

44. Campbell, A.A. Bioceramics for implant coatings. *Mater. Today*. **6**, 26-30 (2003).

45. Melo, M.A.S., Guedes, S.F.F., Xu, H.H.K. & Rodrigues, L.K.A. Nanotechnology-based restorative materials for dental caries management. *Trends Biotechnol*. **31**, 459-467 (2013).

46. Moshaverinia, A., Ansari, S., Movasaghi, Z., Billington, R.W., Darr, J.A. & Rehman, I.U. Modification of conventional glass-ionomer cements with N-vinylpyrrolidone containing polyacids, nano-hydroxy and fluoroapatite to improve mechanical properties. *Dent Mater*. **24,** 1381-1390 (2008).

47. Pepla, E., Besharat, L.K., Palaia, G., G. Tenore, G., & Migliau, G. Nano-hydroxyapatite and its applications in preventive, restorative and regenerative dentistry: a review of literature. *Ann. Stomatol*. **5**, 108-114 (2014).

48. Alhilou, A., Do, T., Mizban, L., Clarkson, B.H., Wood, D.J. & Katsikogianni, M.G. Physicochemical and antibacterial characterization of a novel fluorapatite coating. *ACS Omega*. **1**, 264-276 (2016).

49. Ge, X., Leng, Y., Bao, C., Xu, S.L., Wang, R. & Ren, F. Antibacterial coatings of fluoridated hydroxyapatite for percutaneous implants. *J. Biomed. Mater. Res. Part A*. **95**, 588-599 (2010).

7.

INTRACELLULAR CALCIUM DEREGULATION MEDIATED BY HYDROXYAPATITE NANOPARTICLES

Intracellular calcium (Ca^{2+}) is a key signaling element that is involved in a great variety of fundamental biological processes. Thus, Ca^{2+} deregulation would be involved in the cancer cell progression and damage of mitochondrial membrane and DNA, which lead to apoptosis and necrosis. In this study, we have prepared hydroxyapatite (HAp) in the form of amorphous calcium phosphate nanoparticles (ACP NPs) and we have studied their incorporation by endocytosis or electroporation to epithelial, endothelial and fibroblast cells (MCF-7, HUVEC and COS-1 cells, respectively). Our results showed that internalized ACP NPs have cytotoxic effects as a consequence of the increase of the intracellular calcium content. The endocytosis pathways showed a greater cytotoxic effect since calcium ions could easily be released from the nanoparticles and be accumulated in the lysosomes and mitochondria. In addition, the cytotoxic effect could be reversed when calcium ion was chelated with ethylene glycol-bis(2-aminoethylether)-N,N,N′,N′-tetraacetic acid (EGTA). Modification of ACP NPs by their coating with different compounds based on phosphates was also evaluated. The results indicated a reduction of the cytotoxic effect, in the order polyphosphate < phosphonic acid < orthophosphate. A differential cytotoxic effect of ACP-NPs was observed in function of the cell type; the cytotoxic effect can be ordered as *i.e.*, HUVEC> COS-1> MCF-7. The greater cytotoxic effect caused by the increase of intracellular calcium that is observed in normal cells and the greater resistance of cancer cells suggests new perspectives for cancer research.

7.1 INTRODUCTION

Calcium (Ca^{2+}) is a key signaling element that is involved in a great variety of fundamental biological processes (*e.g.* from fertilization to programmed cell death). Thus, almost every tissue and biofluid has specific functions that are controlled by Ca^{2+}.[1] Calcium is the most abundant metallic element in the body, being adequate amounts (1.0-1.2 g/day) obtained from dairy products and some green vegetables. However, calcium has recently been associated with some risk of colorectal cancer.[2-4] For example, accumulation of calcium in the peripheral zone of human prostate gland could play an important role in the prostate cancer.[5]

Calcium deregulation has extensively been studied at cellular and molecular levels due to its clear effect on cell injury, carcinogenesis and cell death.[6,7] For instance, Ca^{2+} can activate transcription factors such as nuclear factor of activated T cells (NFAT),[6] regulate cell proliferation promoting cancer cell progression,[8] and modulate poly-ADP-ribose polymerase, permeabilization of mitochondrial membrane and DNA damage leading to apoptosis and necrosis.[9]

Calcium is also a key regulator of the mitochondrial function and acts at several levels within the organelle to stimulate ATP synthesis. Deregulation of mitochondrial [Ca^{2+}] homeostasis is now recognized to play a key role in several pathologies (*e.g.* enhanced generation of reactive oxygen species (ROS), release of cytochrome C, alteration of the activity of the mitochondrial permeability transition pore),[10] which can lead to apoptosis and necrosis.[11]

It has recently been suggested that cancer cells may have a mitochondrial dysfunction, being adapted to aerobic glycolysis in order to generate ATP. The signaling role of ROS has been recognized.[12] Recent studies suggest that cancer cells, compared with normal cells, are submitted to an increased oxidative stress which can be associated with oncogenic transformation, alterations in metabolic activity, and increased generation of ROS.[13] The increased ROS in cancer cells may in turn affect certain redox-sensitive molecules and further lead to significant consequences such as stimulation of cellular proliferation, cell differentiation, alterations in sensitivity to anticancer agents, promotion of mutations and genetic instability, and contribution to carcinogenesis.[13] Perturbation of mitochondrial respiration in cancer cells leads to redox alterations and highly invasive behaviors, which seem to be mediated by elevated cytosolic calcium.[14]

Until recently, necrosis, unlike apoptosis, was considered as passive and unregulated form of cell death. However, during the last decade a number of experimental data demonstrated that, except under extreme conditions, necrosis may be a well-regulated process activated by rather specific physiological and pathological stimuli.[15] Proskuryakov *et al.* have considered mechanisms and the role of necrosis in tumor cells.[16] Mitochondrial collapse activates various proteases (*e.g.,* calpains, cathepsin) and phospholipases, and eventually leads to plasma membrane destruction, a hallmark of necrotic cell death. Necrosis, in contrast to apoptosis, usually evokes powerful inflammatory response, which may participate in tumor regression during anticancer therapy. However, excessive spontaneous necrosis during tumor development may lead to more aggressive tumors due to the stimulated growth caused by the necrosis-induced inflammation.[16]

In this study, we have addressed on the particular histological architecture of tumors. Willis defined a tumor (neoplasm) as a mass, the growth of which is uncoordinated with the surrounding normal tissues and persists in the absence of the inciting stimulus.[17] It is worthwhile considering this definition in detail. First, the mass, like any other tissue, is composed of parenchymal cells and stroma, which are the essential parts of an organ. The parenchymal cells of the mass may be well differentiated, organized as normal tissues, and had a slow proliferation, or on the contrary, they may be poorly differentiated, had little or no organization and a fast proliferation. In either situation, the host response is mediated by angiogenic factors,[18,19] which are synthesized by the parenchyma of the tumor and stimulate proliferation of all stromal cells, including fibroblasts and vascular cells.

Hydroxyapatite (HAp) nanoparticles are able to encapsulate different drugs (*e.g.* chloramphenicol)[20] and also to be internalized by endocytosis due to their small size. These nanoparticles are also a source of Ca^{2+} ions, which can be delivered inside cells due to their solubilization in acidic media. The released Ca^{2+} can be accumulated in lysosomes and mitochondria provoking a necrotic effect, which deserves also the attention of the present work. In this work, we analyse the intracellular incorporation pathway of Ca^{2+} free and released from the calcium phosphate nanoparticles (NPs), the influence of the size being also investigated in the latter case (*i.e*. NPs < 200 nm and NPs > 200 nm).

7.2 EXPERIMENTAL SECTION

7.2.1 Materials

Tetrasodium pyrophosphate ($P_2O_7^{4-}$), sodium triphosphate (polyP), aminotris(methylenephosphonic acid) (ATMP), ammonium phosphate dibasic [$(NH_4)_2HPO_4$; purity ≥ 99.0 %] and ammonium hydroxide solution 30 % (NH_4OH; purity: 28-30 %) were purchased from Sigma-Aldrich. Calcium nitrate [$Ca(NO_3)_2$; purity ≥ 99.0 %] was purchased from Panreac (Barcelona, Spain). Ethanol (C_2H_5OH; purity ≥ 99.5 %) was obtained from Scharlab (Barcelona, Spain). HEPES was purchased from Lonza.

Cell line MCF-7 (epithelial cells from human breast adenocarcinoma) and COS-1 (fibroblast cells from green monkey kidney transformed by insertion of the SV40) were obtained from ATCC (HTB-22 and CRL-1650, respectively). Dulbecco´s Modified Eagle´s Medium (DMEM) and Ca^{2+}-free DMEM, Fetal Bovine Serum (FBS), penicillin/streptomycin (pen/strep) and L-glutamine were purchased from Gibco. Cell line HUVEC (endothelial cells from normal human umbilical vein) (CC-2517) and EGM-2 Bulletkit with and without Ca^{2+} media optimized for certain HUVECs were purchased from Lonza. Poly-L-lysine was purchased from Merck Millipore (Germany).

Fura-2AM, Alamar blue reagent and ethylene glycol-bis(2-aminoethylether)-N,N,N′,N′-tetra(acetoxymethyl ester) (EGTA-AM) were purchase from Invitrogen (Invitrogen-Molecular Probes, Leiden, The Netherlands). MTT solution [3-(4,5-dimethylthiazol-2-yl)-2,5-diphenyltetrazolium bromide] was purchased from Roche. Texas red dextran (MW 10,000 g/mol); and both enzymes, trypsin-EDTA solution (0.05 % trypsin, 0.02 % EDTA) and soluble alkaline phosphatase (10 units/mL) from bovine intestinal mucosa were purchased from Sigma-Aldrich. Electroporation cuvettes were purchased from Molecular BioProducts Inc.

7.2.2 Synthesis of HAp

Amorphous calcium phosphate nanoparticles (ACP-NPs) have been considered for this study. The reagent conditions were adjusted to get a Ca/P ratio of 1.67. Specifically, 15 mL of 0.5 M $(NH_4)_2HPO_4$ in milli-Q water (pH 11 adjusted with ammonia 30 % w/v

solution) were drop-wise added (rate of 2 mL/min or less) under agitation (400 rpm) to 25 mL of a 0.5 M $Ca(NO_3)_2$ ethanol solution. The reaction mixture was stirred during 1h (400 rpm at room temperature). The reagents and the reaction were made in plastic containers to avoid the use of borosilicate glasses. Then, the resultant suspension of nanoparticles (NPs) was aged for 24 h at 37 ºC. The precipitate was separated by centrifugation and washed sequentially with milli-Q water and a 60/40 v/v mixture of ethanol-water (twice). A white powder was obtained after freeze-drying.

7.2.3 Size separation of NPs

The ACP-NPs were resuspended in milli-Q water at concentration of 15 mg/mL. The procedure was performed according to BS ISO 14887 (2000) ("Sample preparation-dispersing procedures for powders in liquids"). Thus, NPs powder (300 mg) was placed in a plastic tube of 50 mL together with 10 mL of water sterile and mixed with a spatula until all visible aggregates disappeared. The wetting step was applied in order to substitute the solid-air interface by a solid-liquid interface. 10 mL of water were then added to the tube and gently mixed using a spatula. The tube was subsequently immersed in an ice bath and the sample was sonicated to ensure a complete deagglomeration using an ultrasonic probe (Cole-Parmer® 130-Watt Ultrasonic Processors (50/60 Hz, VAC 220); product number EW-04714-51). A titanium probe of 6 mm was tuned to resonate at 20 kHz, ± 50 Hz for 20 s at 90 % amplitude.

The NPs suspension was then gently mixed with a spatula rod to ensure homogeneity, and loaded in a syringe (10 mL) to be filtered through a 0.2 µm filter. Filtration was manually performed at a flow rate approximately of 1 mL/min, particles were finally concentrated using an IEC MultiRF centrifugue (Thermo IEC, Needham Heights, MA, USA). Two fractions corresponding to the eluted (*i.e*. NPs size < 200 nm) and retained particles (*i.e.* NPs with size > 200 nm) were consequently obtained.

7.2.4 Cell cultures

MCF-7 and COS-1 cells were cultured in Dulbecco´s Modified Eagle´s medium (DMEM) supplemented with 10 % fetal bovine serum (FBS), 1 % pen/strep and 2 mM L-glutamine. HUVEC cells were cultured in EGM-2 Bulletkit medium. The cells were cultured in 25 T-flask at 37 ºC with 5 % CO_2, 95 % air and humid atmosphere. The cells of the culture that reached close to 90 % confluence were detached using 0.05 % trypsin/EDTA. Finally, cells were washed and resuspended in a Ca^{2+}-free culture

medium to be counted and treated according to the procedures described below. The growth of the cells (*e.g.* during 48 h) in these Ca^{2+}-free media was performed as a control, being cell viability always greater than 95 %.

7.2.5 Microinjection of Ca^{2+} and NPs into cells

MCF-7 and COS-1 cells were seeded onto glass cover slides of 0.8 cm diameter, which had previously been coated with 0.01 % poly-L-lysine. Coating was performed overnight at 37 °C and under agitation. Cover slides were subsequently washed twice with PBS and absolute ethanol for sterilization. Finally, they were left in a laminar flow cabinet until the ethanol in excess was evaporated.

$1.5x10^3$ cells were seeded onto each cover slide and cultured during 24 h before being microinjected. This procedure allowed that cell adhesion could resist the tensile stress that should occur during the microinjection process. This was performed according to previously described procedures.[21,22] Glass capillary (outer diameter of 2 mm) micropipettes (W-P Instruments, New Haven, CT) were prepared using a micropipette puller (PG-1, Narishige Scientific Instruments, Tokyo, Japan) that allowed getting a diameter of the tip close to 0.5-1.0 µm. After the capillary was pulled, the solution was delivered through its rear open end by means of a microloader (Eppendorf Microloader). The micropipette was then connected to the hub of the pipette holder, which was attached to the microinjector. Operations were done using a micromanipulator (Eppendorf 5171) and a microinjector (Eppendorf 5246) coupled with an inverted microscope (Olympus, Hamburg, Germany), which was equipped with phase-contrast and fluorescence optics. The temperature was maintained at 37 ºC by using a plastic housing with an incubator (i.e. having supply of hot air and CO_2).

Microinjection was controlled using a tracer based on a loading buffer (4.8 mM K_2HPO_4, 4.5 mM KH_2PO_4, 14 mM NaH_2PO_4 at pH 7.4), solution of $CaCl_2$ and Texas red dextran (final concentration, 10 mg/mL) with MW of 10,000 g/mol. The selected conjugate can remain in the microinjection place, while lower molecular weight conjugates (*e.g.* 3.000 g/mol) can move from cytoplasm to the nucleus and vice-versa.

The tracer fluorescence (410-485 nm/515 nm, Ex/Em) was followed by taking images (1-10 min after microinjection). Suspensions of both kinds of NPs (*i.e*. < 200 nm and > 200 nm) were prepared using the same loading buffer.

Ca^{2+} i*maging using Fura-2*. Ca^{2+}-free, NPs < 200 nm and NPs > 200 nm were microinjected to obtain an intracellular Ca^{2+} concentration of 400 nM. The time-course of this Ca^{2+} was followed with Fura-2 indicator. Specifically, the pippete was filled with 10 µL of the injection fluid having 1 mM Fura-2AM. Intracellular, unspecific esterases transform the acetoxymethyl ester (AM) to formaldehyde and acetic acid, which leads to the liberation of the Ca^{2+} indicator (*i.e.* Fura-2). The measurements of Fura-2 were carried out in an Olympus I×81 motorized inverted microscope (Olympus, Hamburg, Germany) controlled by Cell^M software (Olympus Soft Imaging Solution). Fura-2 was alternately excited at 340 and 380 nm every 3 min and the emitted fluorescence was detected at > 500 nm. The changes of Fura-2 fluorescence were analyzed with the Cell^M software.

Analysis of surface blebs. Microinjections were performed as described above. Ca^{2+}-free, NPs < 200 nm and NPs > 200 nm were microinjected to obtain intracellular Ca^{2+} concentrations of: 0, 100, 200, 400 and 800 nM. After 24 h of culture, images of the injected cells were taken by phase contrast microscopy and the percentage of the blebs surface was calculated on the basis of the total surface of the cells. Blebbing of the plasmic membrane is a typical feature of cells undergoing late stage of apoptosis and is usually evaluated through the visible increase of the cytoplasmic diameter. Calculations were carried out by taking micrographs after microinjection at intervals of 1 min during 24 h and then during an additional period of 90 min to determine its stability. Time-lapse and images were analyzed using the EVOS™ software.

7.2.6 Electroporation of Ca^{2+} and NPs into cells

Electroporation was carried out using a BTX T820 square wave electroporator (BTX Harvard Apparatus). The electroporation parameters for each cell line were optimized for high electro-permeabilization and low cellular death. The cells were suspended in a pH 7 HEPES buffer (10 mM HEPES, 250 mM sucrose and 1 mM $MgCl_2$ in sterile water) at concentration of 6.1x10^6 cells/mL. Then, 270 µL of cell suspension (cooled at ~ 8 °C) were electroporated in presence of different concentrations of supplemented Ca^{2+} (*i.e.* 0, 0.025, 0.05, 0.1, 0.2, 0.4, 0.6, 0.8, 1.6 and 3.2 mM). The electroporations were carried out in cuvettes of 4 mm and using 8 pulses of 99 µs with 1.4 kV/cm and 1 Hz for MCF-7 cells, 1.2 kV/cm and 1 Hz for COS-1 cells, and 1.0 kV/cm and 1 Hz for HUVEC cells. These conditions depend on the cell type. The same procedure was performed for NPs < 200 nm and NPs > 200 nm. After electroporation, the cells were washed two-

times and resuspended in a Ca^{2+}-free medium. Then, cells were incubated at 37 ºC and 5 % CO_2 during 20 min. The protocol was slightly changed when Ca^{2+} and NPs were chelated with EGTA. In these cases, cells were twice washed after electroporation and resuspended in a Ca^{2+}-free medium supplemented with 0.5 mM EGTA-AM. Finally, they were washed in culture medium and diluted to be seeded in 96-well plates at a density of 10^4 cells/200 µL in each well. Assays were performed in triplicate at 24 h and 48 h of culture, the MTT and Alamar blue assays were selected to determine cell viability.

7.2.7 Loading of Ca^{2+} and NPs into cells without electroporation

The cells after trypsinization were seeded in 96-well plates at a density of 10^4 cells/100 µL in each well. For this, a Ca^{2+}-free culture medium was used, and the plates were maintained under culture conditions for 24 h to allow cell adhesion. Then, 100 µL of the medium with 2X concentrations of Ca^{2+} were added to each well, to achieve the appropriate concentrations of Ca^{2+} (*i.e.* 0, 0.025, 0.05, 0.1, 0.2, 0.4, 0.6, 0.8, 1.6 and 3.2 mM). The same procedure was performed for NPs < 200 nm and NPs > 200 nm to obtain equivalent concentrations of Ca^{2+} despite being contained in the NPs. Each condition was tested in triplicate. At 24 h and 48 h of culture, the MTT and Alamar Blue assays were performed to determine cell viability.

For the cases of Ca^{2+} and NPs chelated with EGTA, the cells after trypsinization were electroporated in the HEPES buffer supplemented with 0.5 mM EGTA-AM in the above described conditions. Subsequently, cells were incubated at 37 ºC and 5 % CO_2 during 20 min. Then, they were washed and diluted in a Ca^{2+}-free culture medium supplemented with 0.5 mM EGTA-AM to be seeded in 96-well plates at a density of 10^4 cells/100 µL in each well. After 24 h of culture, the medium was changed with 200 µL of fresh medium supplemented with 0.5 mM EGTA-AM and Ca^{2+}-free in different concentrations (*i.e*. 0, 0.025, 0.05, 0.1, 0.2, 0.4, 0.6, 0.8, 1.6 and 3.2 mM). The similar procedure was performed for NPs < 200 nm and NPs > 200 nm having the equivalent content of Ca^{2+}. Each condition was tested in triplicate at 24 h and 48 h of culture, being MTT and Alamar Blue assays were employed to determine cell viability.

7.2.8 Adsorption of biophosphates and biophosphonate onto NPs < 200 nm

ACP nanoparticles were prepared and filtered using the above described procedure. After this, 500 µL of working aqueous solution (pH 7.4, adjusted with an ammonia 30 % -w/w solution), which contained 12.5 mM of polyP, $P_2O_7^{4-}$ or ATMP, were deposited onto 50 mg of NPs < 200 nm. After overnight agitation at 25 °C, adducts were separated by centrifugation at 6500 rpm and 4 °C during 4 minutes. Sediments were washed with milli-Q water for two-times. The obtained pellets were frozen at −80 °C for 3 h and lyophilized to remove the humidity. These NPs were named according to their coating as NPs/polyP, NPs/$P_2O_7^{4-}$ and NPs/ATMP.

NPs/coating treatment with alkaline phosphatase. This treatment is specific to hydrolyze the biophosphates in the NPs/polyP and NPs/$P_2O_7^{4-}$ samples. The uncoated NPs and NPs/ATMP were used as controls. The hydrolysis medium consisted of 10 units/mL of soluble alkaline phosphatase in 100 mM Tris-HCl buffer and 200 mM $MgCl_2$ at pH 7.4. The uncoated and coated NPs were incubated in this medium overnight at 37 ºC under orbital agitation. Then, adducts were separated by centrifugation at 6500 rpm during 5 minutes. Sediments were washed with milli-Q water for two-times. Pellets were frozen at −80 °C for 3 h and lyophilized to remove the humidity. Finally, these NPs were used in electroporation (+EP) and non-electroporation (−EP) experiments as above described.

7.2.9 MTT viability assay

Cell proliferation was evaluated using a filtered (through a 0.2 µm filter) MTT solution (1 mg/mL in phosphate buffer saline (PBS) of pH 7.4). Then, a mixture of 50 µL of MTT and 200 µL of DMEM without phenol red were added into each well of a 96-well plate (except cell-free blank wells). The plate was incubated for 4 h under culture conditions. Finally, the MTT solution was removed and replaced with 200 µL of DMSO and 25 µL of Sorensen´s glycine buffer (0.1 M glycine, 0.1 M $NaCl$, pH 10.5 after being adjusted with 0.1 M $NaOH$). The plate was maintained for 5 min at room temperature, and the optical density (OD) of each well was quantified by spectrophotometry using a plate reader (XMark™ Microplate Absorbance Spectrophotometer, Bio-Rad) at 570 nm.

7.2.10 Alamar blue viability assay

The determination of metabolic activity using this assay is based on the mitochondrial hydrolase activity. The assay was performed according to the manufacturer´s protocol. Cells were treated with 10 % Alamar blue solution and kept at 37 º C for 2 h. Red fluorescence resulting from the reduction of Alamar blue was monitored (excitation/emission: 553/590) by spectrophotometry using a plate reader (XMark™ Microplate Absorbance Spectrophotometer, Bio-Rad).

7.3 RESULTS AND DISCUSSION

The intracellular effect of calcium ion (Ca^{2+}) is still one of the most discussed aspects in the area of cellular physiology. This effect has relevant importance in the processes of cellular transfection, such as a non-viral transport of biomacromolecules. A typical intracellular level of Ca^{2+} is around 50-100 nM.[24] However, variations in cytosolic Ca^{2+}-free levels may be of great relevance in health. Transient increases in cytosolic Ca^{2+} concentration occur during the cell cycle (*i.e.* at the late G_1 prior to the initiation of the S phase and later on during G_2 before entry into M phase).[25,26]

In the case of the uptake of ACP nanoparticles, a strong disturbance in cytosolic Ca^{2+} concentration may influence the progression of the cell cycle. A sharp increase in cytosolic Ca^{2+} concentration without any recovery can be associated with cell death. On the contrary, cells survived when they were able to decrease the cytosolic Ca^{2+} concentration to the baseline level.[27] In this study, we analyzed the intracellular incorporation pathway of Ca^{2+} and calcium contained in the two amorphous calcium phosphate nanoparticle fractions (*i.e*. NPs < 200 nm and NPs >200 nm). Epithelial-type, fibroblast-type and endothelial-type cells (MCF-7, COS-1 and HUVEC cells, respectively) were considered to get more generalist conclusions.

The study was initiated with an analysis of the time-course of Ca^{2+} and NPs microinjected into the MCF-7, COS-1 and HUVEC cells to demonstrate unequivocally the direct effect of Ca^{2+} and NPs (**Figure 7.1 a**). For the microinjected Ca^{2+} (~ 400 nM), a progressive reduction of about 50 % was observed after 24 h of its microinjection. On the contrary, for the microinjected NPs (equivalent to ~ 400 nM of Ca^{2+}), a rapid release of free Ca^{2+} was observed and corresponded to 100 nM (time 0 h, at the beginning of

the experiment). These measurements were possible because the indicator Fura-2 is a ratiometric and sensitive dye for measuring intracellular Ca^{2+}. The time-course of Ca^{2+}contained in NPs showed a progressive increase in the intracellular Ca^{2+} concentration, demonstrating the occurrence of Ca^{2+} release from NPs injected into the cell cytoplasm. Thus, it was determined that after 24 h of the microinjection of NPs < 200 nm and NPs > 200 nm, the intracellular Ca^{2+} concentration was ~200 nM and ~150 nM, respectively (**Figure 7.1 a**). An observation that stands out from these pulse-chase experiments is the similar behavior of HUVEC, COS-1 and MCF-7 cells.

On the other hand, the cytotoxic effect caused by different concentrations of Ca^{2+} and NPs were also evaluated (**Figure 7.1 b**). The cytotoxicity was followed as previously indicated by the formation of cytoplasmic blebs. For the microinjected Ca^{2+}, a severe dose-dependent cytotoxic damage was observed. The highest microinjected dose (800 nM) caused a cell damage of 70-80 % for the three cell types treated (*i.e*. HUVEC, COS-1 and MCF-7 cells). However, intracellular Ca^{2+} doses in the range of 100-400 nM shown a cytotoxic damage that was dependent on the cell type. Thus, endothelial HUVEC cells were the most sensitive (*i.e.* 40 % of blebs) when the intermediate intracellular dose of 400 nM Ca^{2+} was applied. On the contrary, epithelial MCF-7 cells were less sensitive (i.e. 15 % of blebs), while COS-1 fibroblasts showed an intermediate cytotoxicity (*i.e*. 30 % of blebs). A similar behavior was observed when NPs were microinjected, but the cytotoxic damage was reduced. Thus, the intracellular doses of NPs equivalent to 800 nM Ca^{2+} only produced a cellular damage close to 30-40 % and 25-35 % of blebs for the microinjection of NPs < 200 nm and NPs > 200 nm, respectively. This cytotoxic effect of the NPs was again related to the lower availability of Ca^{2+}, since ions appear structured or bounded with the phosphate groups of the formed amorphous NPs.

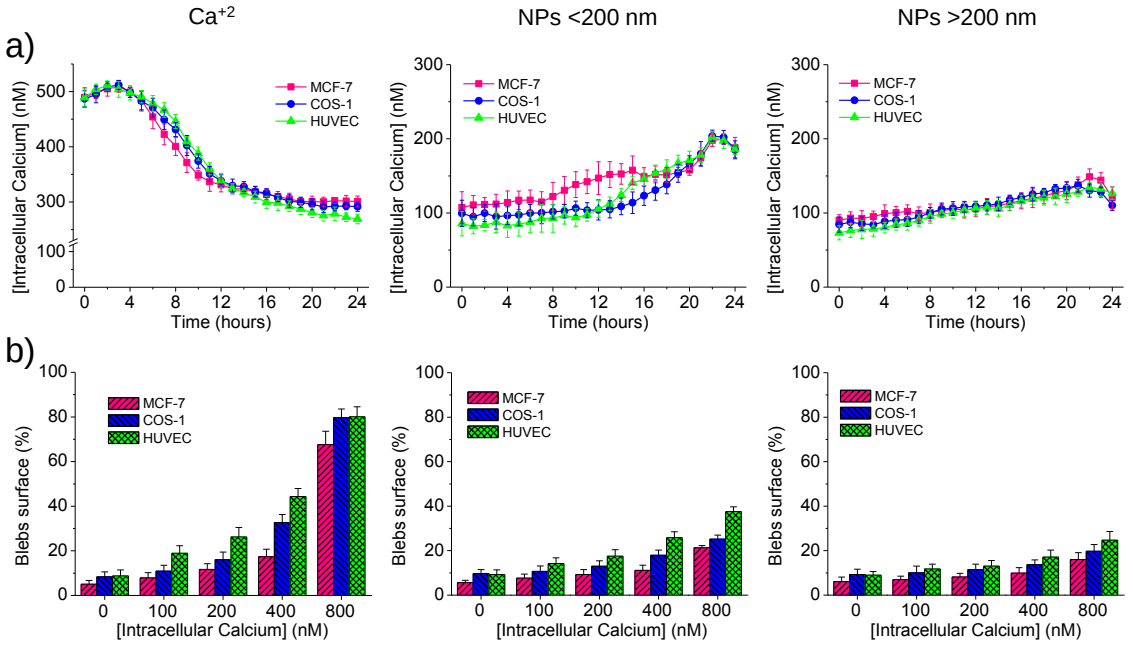

Figure 7. 1. Time-course and cytotoxic effect of the intracellular Ca^{2+}, NPs < 200 nm and NPs > 200 nm microinjected into MCF-7, COS-1 and HUVEC cells. a) Changes in cytoplasmic Ca^{2+} concentration after microinjection of 400 nM Ca^{2+} or their equivalent content in the case of NPs. Ca^{2+} concentrations are relative to the control (physiological concentration ~100 nM). b) Vesicular surface (blebs percentage) after microinjection of different concentrations of Ca^{2+} or their equivalent content in the case of NPs.

Moreover, these results demonstrated the dependence of the cytotoxicity on the cellular type but more interestingly on their origin, or genetic condition. By contrast, HUVEC endothelial cells, which are derived from primary cultures and therefore can be considered normal, were the most sensitive to cytotoxic damage. Intermediate effect was observed with COS-1 fibroblasts, which are transformed cells by genetic modification, through the incorporation of SV40 particles.

Figure 7.2 shows the viability results of cells exposed to different concentrations of Ca^{2+} and NPs. In these experiments the cellular incorporation of Ca^{2+} was performed through a non-electroporation (−EP) diffusion process (**Figure 7.2 a**) and also by electrophoretic mobilization (*i.e.* electroporation (+EP)) (**Figure 7.2 b**). The inhibition of the effect of Ca^{2+}-free and Ca^{2+} released from NPs has been produced by its chelation using EGTA in both treatments (−EP and +EP). In these experiments are highly remarkable that the MCF-7 epithelial cells derived from adenocarcinoma were the most resistant to the cytotoxic effect.

Figure 7.2 a clearly shows that during the −EP process that the different concentrations of Ca^{2+}-free and Ca^{2+} chelated with EGTA (in the range of 0-3.2 mM) have not effect on the viability of the three cell types (HUVEC, COS-1 and MCF-7). These results highlight that the entry of Ca^{2+} inside cells is an active transport through the cell membrane. Plasma membrane channels support the entry into cells of Ca^{2+} due to the gradient concentration. Various calcium channels, such as voltage-gated Ca^{2+} channels (Ca_v family), can be involved in this Ca^{2+} influx. The expression of this family of proteins is a characteristic of "excitable cells," and these channels do require depolarization of the plasma membrane for their activation.[28]

Despite Ca_v expression, Ca^{2+} entry in non-excitable cells mostly occurs through non-voltage gated channels. These include ligand-gated channels (*e.g.* P2X purinergic ionotropic receptor families); receptor-operated channels (ROC), secondary messenger-operated channels linked to GPCR activation, store-operated and stretch-operated channels. Numerous studies have shown that one or several Ca^{2+}-permeable channels in the plasma membrane are modified in expression and/or activity in different cancer cells, and play a role in most of the pathophysiological processes driving the malignant phenotype. In addition to the plasma membrane Ca^{2+} channels, changes in Ca^{2+}-transporters such as plasma membrane Ca^{2+}ATPase and Na^{+}/Ca^{2+} exchanger have also been reported to be involved in the Ca^{2+} homeostasis of cancer cells, and to tumorigenesis.[29,30] Finally, it should be considered that the entry of the Ca^{2+} ion into the cells is a biological event regulated in a highly complex manner that does not depend exclusively on its gradient as can be seen in **Figure 7.2 a** for Ca^{2+}-free experiments.

On the other hand, the forced incorporation of Ca^{2+}-free by electroporation (+EP) (**Figure 7.2 b**) caused clear cytotoxic effects. The sensitivity of cells was in the order HUVEC > COS-1 > MCF-7 with CC_{50} of 0.37, 0.51 and 0.58 mM, respectively (**Table 7.1**). In addition, this cytotoxic effect can clearly be inhibited when the $Ca^{2+}$was chelated, being logically the CC_{50} values higher (*i.e.* 0.88, 1.27 and 1.56 mM for HUVEC, COS-1 and MCF-7, respectively) (**Table 7.1**). In this study, we have introduced EGTA-AM into cells, which became active after cleaving the acetoxymethylester (AM) by intracellular esterases. The released EGTA free acid was able to chelate intracellular Ca^{2+}. Results about CC_{50} changes were relevant and demonstrated the chelating effect of EGTA and that Ca^{2+} ions were responsible or triggering the cell death. The HUVEC endothelial

cells were the most sensitive, followed by the COS-1 fibroblast cells, and finally by the MCF-7 epithelial cells.

However, both NPs < 200 nm and NPs > 200 nm showed similar dose-response effects under –EP conditions for viability of the different cell types. **Figure 7.2 a** and **Table 7.1** show that the CC_{50} for the NPs < 200 nm were 0.40, 0.53 and 0.60 mM for HUVEC, COS-1 and MCF-7 cells, respectively. In addition, these CC_{50} values were increased after Ca^{2+} chelation, being determined values of 0.88, 1.24 and 1.87 mM for HUVEC, COS-1 and MCF-7 cells, respectively. A similar situation was observed for NPs > 200 nm with CC_{50} values of 0.40, 0.65 and 0.75 mM, which after chelation increased to 0.83, 1.33 and 1.82 mM, for HUVEC, COS-1 and MCF-7 cells, respectively. These results suggest three clear features when the cells were exposed to NPs < 200 nm and NPs > 200 nm: 1) Similar cytotoxic effects were observed due to their ability to release Ca^{2+} into cells, being this effect inhibited by chelation with intracellular EGTA; 2) The occurrence of these cytotoxic effects have as a prerequisite that the NPs were internalized into the cells. The endocytosis pathway seems the most plausible via for –EP treatment; and 3) The endothelial HUVEC cells and the epithelial MCF-7 cells were the most and the least sensitive, respectively.

Table 1. CC_{50} of Ca^{2+} and NPs incorporated into cells by electroporation (+EP) and non-electroporation (-EP). Experiments were performed with and without Ca^{2+} chelation (*i.e.* +EGTA and –EGTA, respectively).

Cell line	CC_{50} (mM)					
	Ca^{2+}		NPs <200 nm		NPs >200 nm	
	-EGTA	+EGTA	-EGTA	+EGTA	-EGTA	+EGTA
-EP						
MCF-7	---	---	0.60	1.87	0.75	1.82
COS-1	---	---	0.53	1.24	0.65	1.33
HUVEC	---	---	0.40	0.88	0.40	0.83
+EP						
MCF-7	0.57	1.56	1.19	2.46	1.25	2.65
COS-1	0.51	1.27	1.07	1.51	1.15	1.60
HUVEC	0.37	0.88	0.94	1.22	1.02	1.32

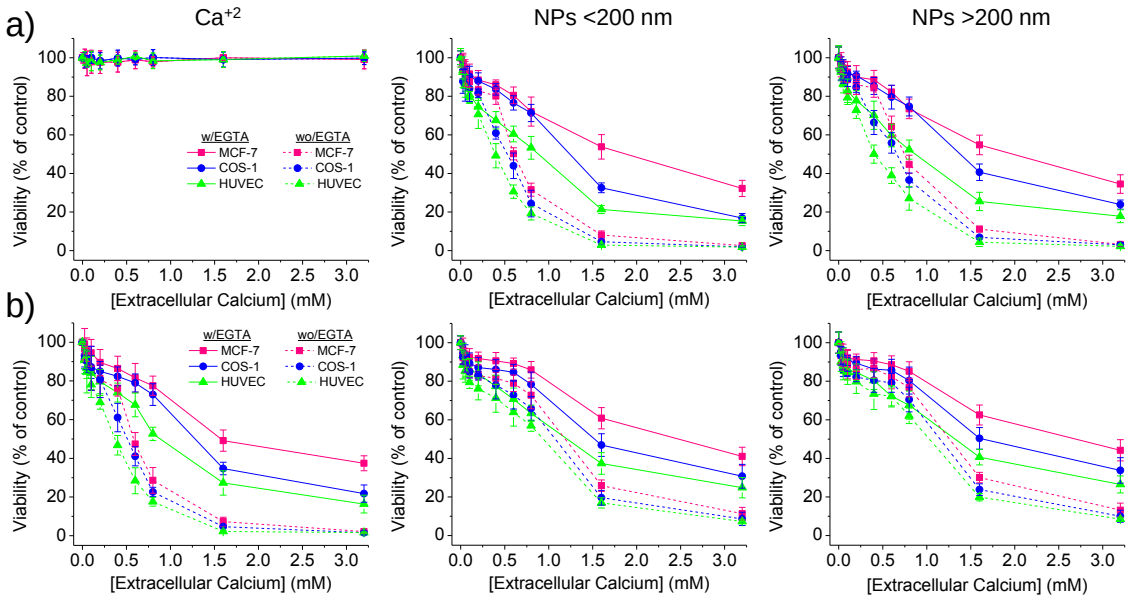

Figure 7.2. Viability of MCF-7, COS-1 and HUVEC cells treated with extracellular Ca^{2+} and NPs < 200 nm and NPs > 200 nm by non-electroporation (-EP) (a) and electroporation (+EP) (b). Ca^{2+} concentrations in the range of 0 to 3.2 mM were considered in the presence and absence of 0.5 mM EGTA as chelating agent. Cellular viability was measured with the Alamar Blue reagent after 24 h of culture.

CC_{50} values were higher under +EP conditions for both released and chelated Ca^{2+} (**Figure 7.2 b** and **Table 7.1**). Thus, CC_{50} for HUVEC, COS-1 and MCF-7 cells exposed to the NPs < 200 nm were 0.94, 1.07 and 1.19 mM for the released Ca^{2+}, and 1.22, 1.51 and 2.46 for the chelated Ca^{2+}. Highly similar values were obtained when HUVEC, COS-1 and MCF-7 cells were exposed to NPs > 200 nm. In this case, the CC_{50} values were 1.02, 1.15 and 1.25 mM for released Ca^{2+}, and 1.32, 1.60 and 2.65 mM for chelated Ca^{2+} chelated. These higher CC_{50} values can be explained taking into account that +EP fluidizes the plasma membrane and allows to increase the mobility of NPs as consequence of their electrical charge. Therefore, NPs cannot form vesicles and therefore the release of Ca^{2+} became smaller and a higher concentration of NPs was required to achieve the CC_{50} concentration. In general, the cytotoxic effect caused by +EP was lower than produced by –EP. The incorporated NPs are not vesiculated and consequently cannot reach pathways such as vesicle fusion, fusion with lysosomes or other cellular compartments when electroporation was applied.

In this study, cell viability was evaluated by its metabolic activity through the conversion of Alamar blue reagent by mitochondrial NADPH-oxidoreductase enzymes of viable cells after 24 h of culture (**Figure 7.2**). Similar results were attained after prolonging cell cultures for 48 h (**Figure 7.3** and **Table 7.2**). Additionally, cell viability was determined by the MTT reagent, which is based on the metabolic activity mediated by mitochondrial and lysosomal NADPH-dehydrogenases of the viable cells, after 24 h and 48 h of culture (**Figures 7.4, 7.5** and **Tables 7.3, 7.4**). Cell viability was found to be similar by applying both methodologies. Finally, the cytotoxic damage caused by ACP NPs could be related to their disposition to release Ca^{2+} (*e.g.* from the endocytic vesicles via fusion with lysosomes, or from the cytoplasmic aggregate via dissolution). The increase in intracellular concentration of Ca^{2+} produced cell injury through the mitochondrial damage (**Figure 7.6**).

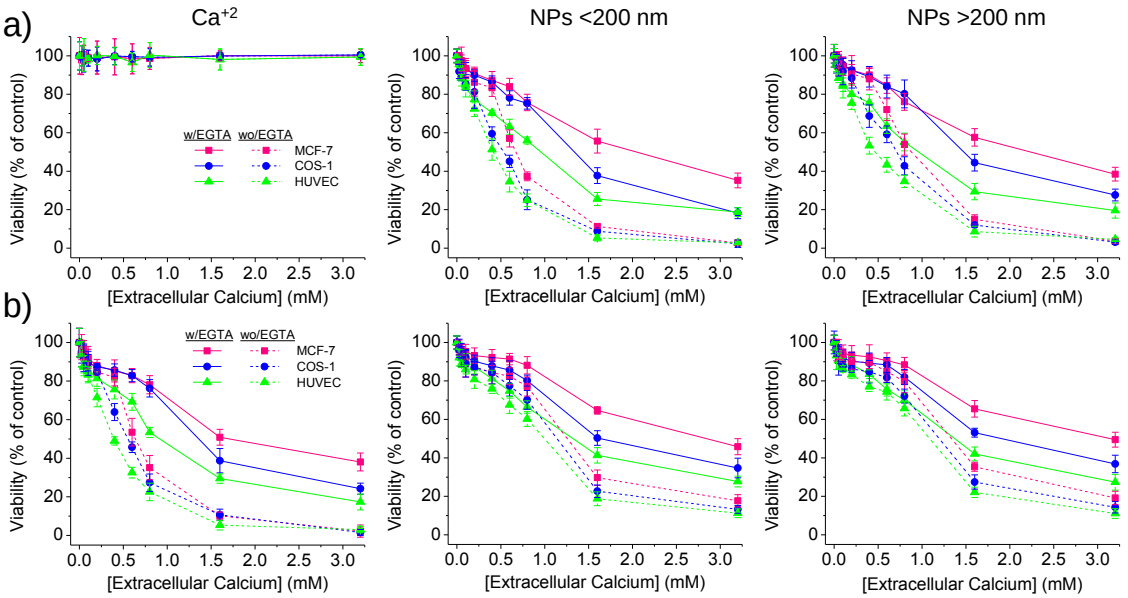

Figure 7.3. Viability of MCF-7, COS-1 and HUVEC cells treated with extracellular Ca^{2+} and the two types of loaded NPs (i.e. < 200 nm and > 200 nm) by non-electroporation (-EP) (a) and electroporation (+EP) (b). Assays were performed in presence and absence of 0.5 mM EGTA as chelating agent. The cellular viability was measured with the Alamar Blue reagent after 48 h of culture.

Table 7.2. CC_{50} of Ca^{2+} and NPs incorporated into cells by electroporation (+EP) and non-electroporation (-EP). Experiments were performed with and without Ca^{2+} chelation (*i.e.* +EGTA and –EGTA, respectively). Values were determined from curves displayed in Figure 7.3.

Cell line	CC_{50} (mM)					
	Ca^{2+}		NPs <200 nm		NPs >200 nm	
	-EGTA	+EGTA	-EGTA	+EGTA	-EGTA	+EGTA
-EP						
MCF-7	---	---	0.67	2.03	0.87	2.22
COS-1	---	---	0.53	1.33	0.71	1.47
HUVEC	---	---	0.41	0.95	0.46	0.96
+EP						
MCF-7	0.64	1.69	1.26	2.82	1.33	3.13
COS-1	0.54	1.36	1.13	1.62	1.19	1.88
HUVEC	0.39	0.92	1.00	1.32	1.08	1.37

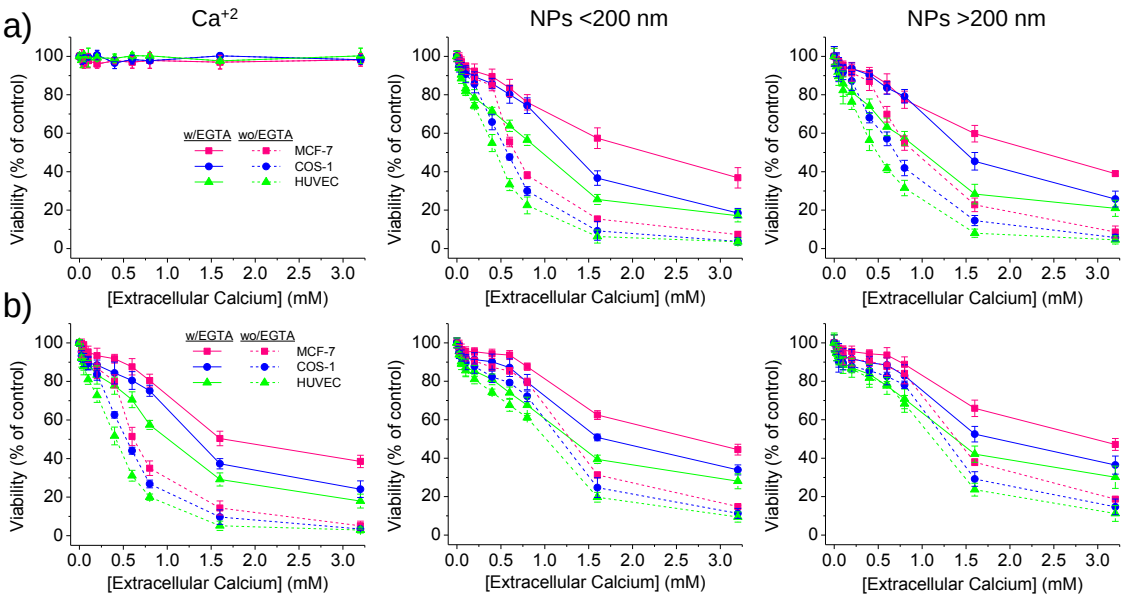

Figure 7.4. Viability of MCF-7, COS-1 and HUVEC cells treated with extracellular Ca^{2+} and the two types of loaded NPs (*i.e.* < 200 nm and > 200 nm) by non-electroporation (-EP) (a) and electroporation (+EP) (b). Assays were performed in presence and absence of 0.5 mM EGTA as chelating agent. The cellular viability was measured with the MTT reagent after 24 h of culture.

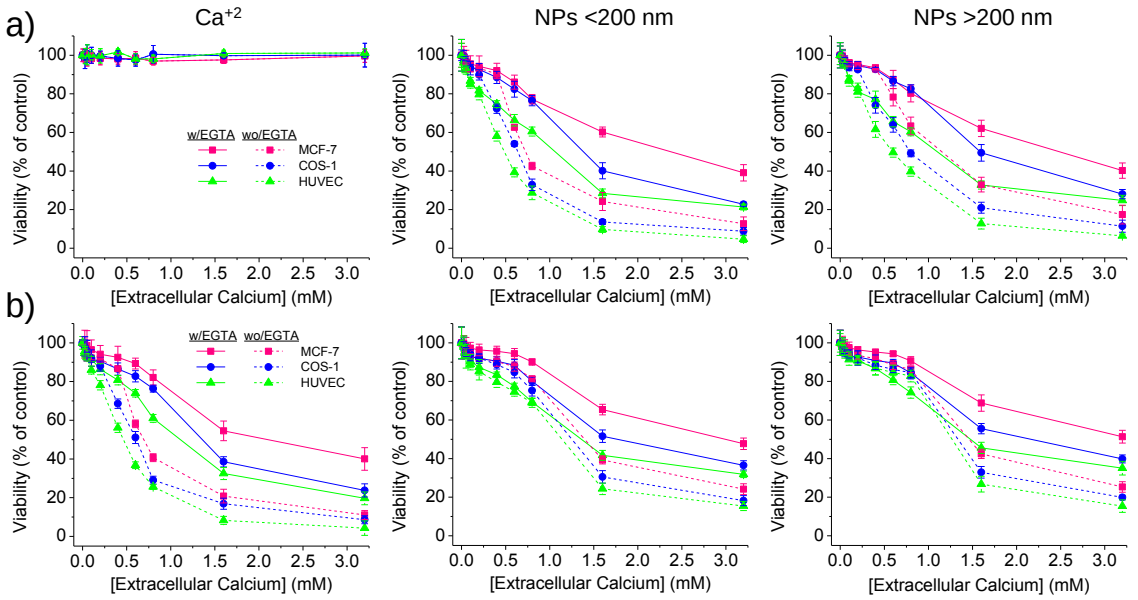

Figure 7.5. Viability of MCF-7, COS-1 and HUVEC cells treated with extracellular Ca^{2+} and the two types of loaded NPs (*i.e.* < 200 nm and > 200 nm) by non-electroporation (-EP) (a) and electroporation (+EP) (b). Assays were performed in presence and absence of 0.5 mM EGTA as chelating agent. The cellular viability was measured with the MTT reagent after 48 h of culture.

Table 7.3. CC_{50} of Ca^{2+} and NPs incorporated into cells by electroporation (+EP) and non-electroporation (-EP). Experiments were performed with and without Ca^{2+} chelation (*i.e.* +EGTA and –EGTA, respectively). Values were determined from curves displayed in **Figures 7.4** and **7.5**.

Cell line	CC_{50} (mM)					
	Ca^{2+}		NPs <200 nm		NPs >200 nm	
	-EGTA	+EGTA	-EGTA	+EGTA	-EGTA	+EGTA
-EP, 24 h						
MCF-7	---	---	0.68	2.20	0.92	2.33
COS-1	---	---	0.57	1.32	0.69	1.48
HUVEC	---	---	0.45	0.97	0.48	1.00
-EP, 48 h						
MCF-7	---	---	0.72	2.36	1.14	2.45
COS-1	---	---	0.63	1.38	0.79	1.58
HUVEC	---	---	0.49	1.06	0.59	1.09
+EP, 24 h						
MCF-7	0.62	1.68	1.29	2.69	1.39	2.94
COS-1	0.53	1.33	1.17	1.66	1.26	1.82
HUVEC	0.42	1.01	1.01	1.30	1.12	1.38
+EP, 48 h						
MCF-7	0.69	2.08	1.40	2.97	1.46	3.20
COS-1	0.60	1.36	1.24	1.75	1.33	2.15
HUVEC	0.46	1.11	1.13	1.36	1.27	1.48

Table 7.4. CC_{50} of NPs < 200 nm coated with biophosphates and phosphonates. NPs were incorporated into cells by electroporation (+EP) and non-electroporation (-EP). The effect was evaluated with and without any treatment of ALP + $MgCl_2$. Values were determined according to curves displayed in **Figure 7.9**.

Nanoparticle	CC_{50} (mM)					
	MCF-7		COS-1		HUVEC	
	-EP	+EP	-EP	+EP	-EP	+EP
No-treatment						
NP	0.72	1.24	0.54	1.14	0.41	1.00
NP/polyP	1.29	1.39	1.12	1.26	1.01	1.17
NP/ATMP	1.17	1.34	1.02	1.22	0.80	1.10
NP/$(P_2O_7)^{4-}$	0.96	1.32	0.80	1.18	0.61	1.07
Treatment: ALP+$MgCl_2$						
NP	0.67	1.25	0.54	1.15	0.41	0.99
NP/polyP	0.71	1.32	0.64	1.24	0.47	1.06
	1.20	1.34	1.02	1.22	0.86	1.17
NP/$(P_2O_7)^{4-}$	0.69	1.33	0.60	1.19	0.46	1.02

Recently, we have prepared modified ACP nanoparticles by adsorption of polyphosphates (polyP), orthophosphate ($P_2O_7^{4-}$) and phosphonate (ATMP).[31] These surface modifications of the ACP NPs had an influence on their different physical and chemical characteristics (*e.g.,* solubility). Interestingly, these surface modifications of ACP NPs can be reversed after specific treatments as it has been explored in this work. Thus, treatment with alkaline phosphatase in the presence of Mg^{2+} as cofactor can eliminate the adsorbed coating of orthophosphate and polyphosphates.[31,32]

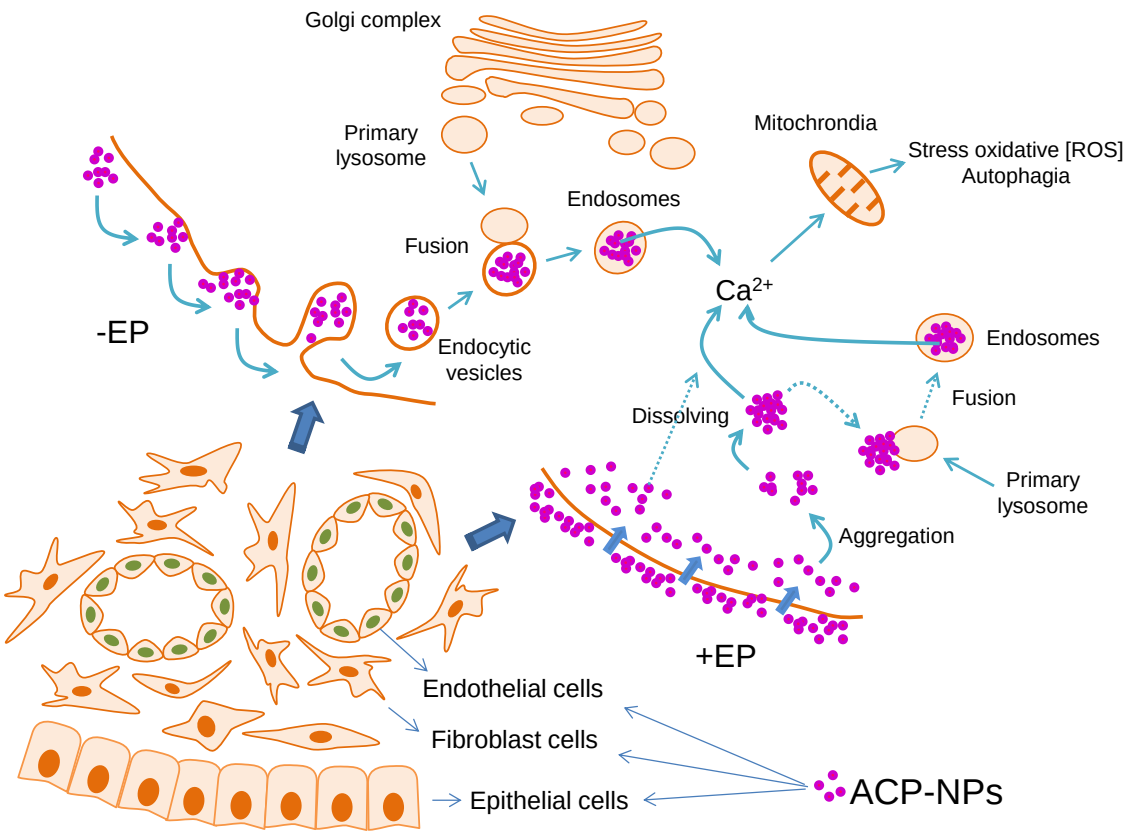

Figure 7.6. Scheme of biological events relative to the cytotoxic effect of the intracellular Ca^{2+}, NPs < 200 nm and NPs > 200 nm microinjected into MCF-7, COS-1 and HUVEC cells.

In general, NPs coated with polyP, ATMP and $P_2O_7^{4-}$ showed a similar behavior than NPs without modification when they were incorporated into the cells by –EP and +EP. Thus, HUVEC and MCF-7 cells were the most and least sensitive, respectively. In all cases, CC_{50} values were higher when the incorporation of the NPs was performed with + EP compared to –EP (**Figure 7.8 a**, **Table 7.5**). However, it is remarkable that the NPs with modified surfaces and incorporated by –EP were less cytotoxic than NPs without modification. Thus, CC_{50} values of 0.85, 0.68 and 0.52 mM were determined for HUVEC cells treated with NPs coated with polyP, ATMP and $P_2O_7^{4-}$, respectively. By contrast, the CC_{50} values of NPs without surface modification were 0.39 mM. In addition, the same order of cell damage as a function of the coating (polyP < ATMP < $P_2O_7^{4-}$) was observed for COS-1 and MCF-7 cells with the –EP treatment (**Table 7.5**). On the other hand, when the modified NPs were incorporated by +EP, the CC_{50} values were observed in the range of 1.0-1.3 mM without significant differences between the distinct NPs surface coatings (**Table 7.5**).

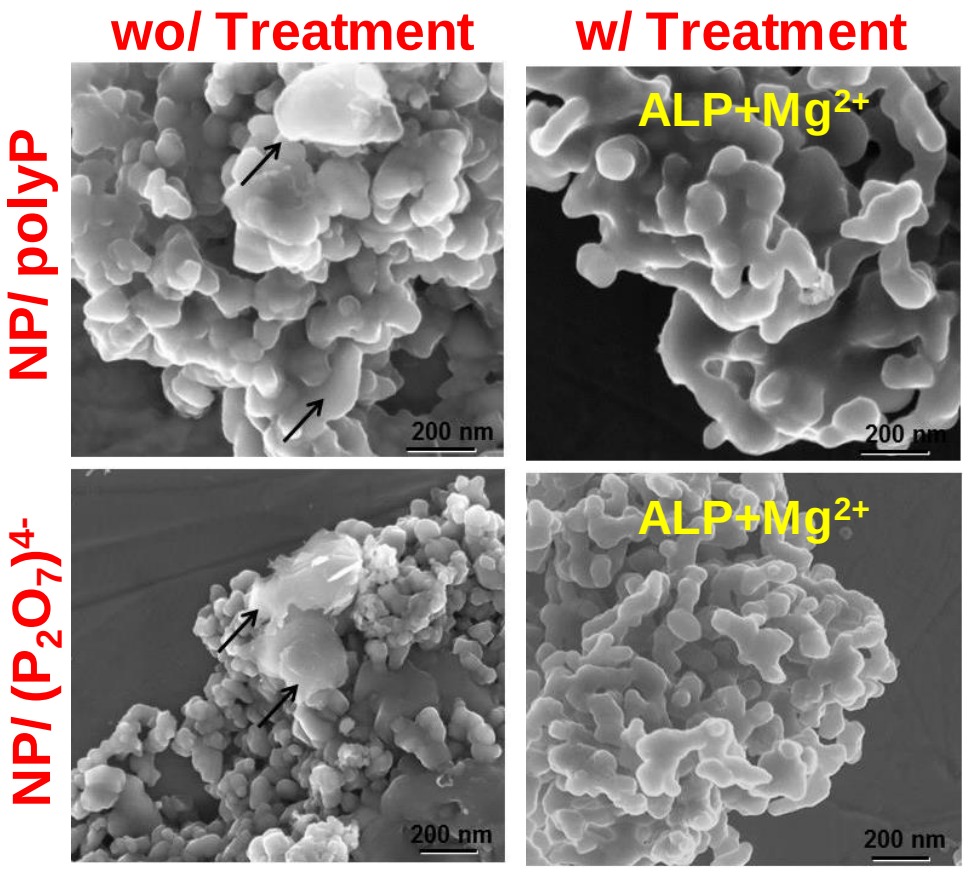

Figure 7.7. Morphology of NPs modified by adsorption of biophosphates. Specific treatments with alkaline phosphatase (ALP) and Mg^{2+} as cofactor were applied to remove biophosphate coatings.

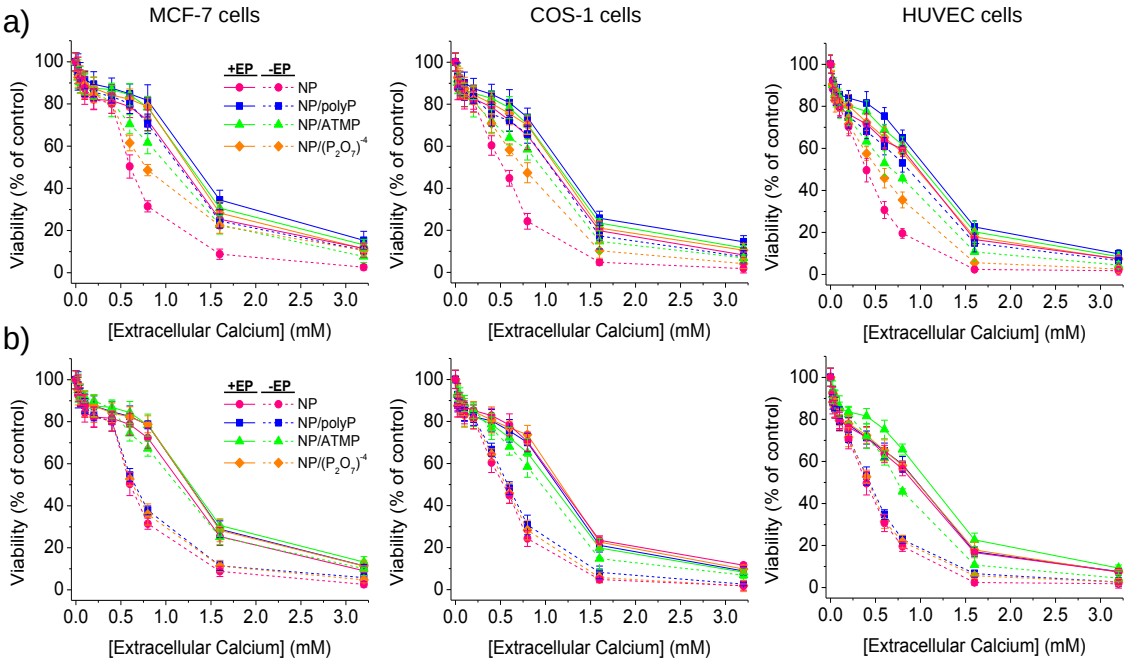

Figure 7.8. Viability of MCF-7, COS-1 and HUVEC cells treated with NPs < 200 nm coated with biophosphates and biophosphonates. NPs with Ca^{2+} equivalent concentrations in the range of 0 to 3.2 mM were incorporated by non-electroporation (-EP) and electroporation (+EP). Effect caused by coated NPs pre-treated with alkaline phosphatase alone (a) and together with Mg^{2+} as cofactor (b)The cellular viability was measured by Alamar Blue assay after 24 h of culture.

Table 7.5. CC_{50} of NPs < 200 nm coated with biophosphates and phosphonates. NPs were incorporated into cells by electroporation (+EP) and non-electroporation (-EP). The effect was evaluated with and without any treatment.

Nanoparticle	CC_{50} (mM)					
	MCF-7		COS-1		HUVEC	
	-EP	+EP	-EP	+EP	-EP	+EP
No-treatment						
NP	0.60	1.17	0.52	1.06	0.39	0.98
NP/polyP	1.15	1.34	1.06	1.20	0.85	1.08
NP/ATMP	1.03	1.28	0.95	1.15	0.68	1.02
$NP/(P_2O_7)^{4-}$	0.77	1.25	0.75	1.12	0.52	0.96
Treatment: ALP+$MgCl_2$						
NP	0.60	1.17	0.53	1.15	0.39	0.93
NP/polyP	0.66	1.26	0.58	1.13	0.43	0.96
NP/ATMP	1.13	1.28	0.95	1.06	0.74	1.10
$NP/(P_2O_7)^{4-}$	0.64	1.26	0.55	1.18	0.42	0.95

The treatment with alkaline phosphatase and the $MgCl_2$ cofactor of the superficially modified NPs resulted in a successful removal of polyP and $P_2O_7^{4-}$ modifications. Thus, the CC_{50} values of NPs incorporated by –EP were similar to the CC_{50} values of the

unmodified NPs (*e.g.* CC_{50} values for HUVEC cells incorporating NP/polyP and NP/$P_2O_7^{4-}$ were 0.43 and 0.42 mM, respectively (**Table 7.5**), which were close to the 0.39 mM value determined for NPs without surface modification). Note that these values were clearly lower than those obtained before the enzymatic treatment (*i.e.* 0.85 and 0.52 mM, respectively). In addition, this situation occurred in a similar way for MCF-7 and COS-1 cells (**Figure 7.8 b** and **Table 7.5**).

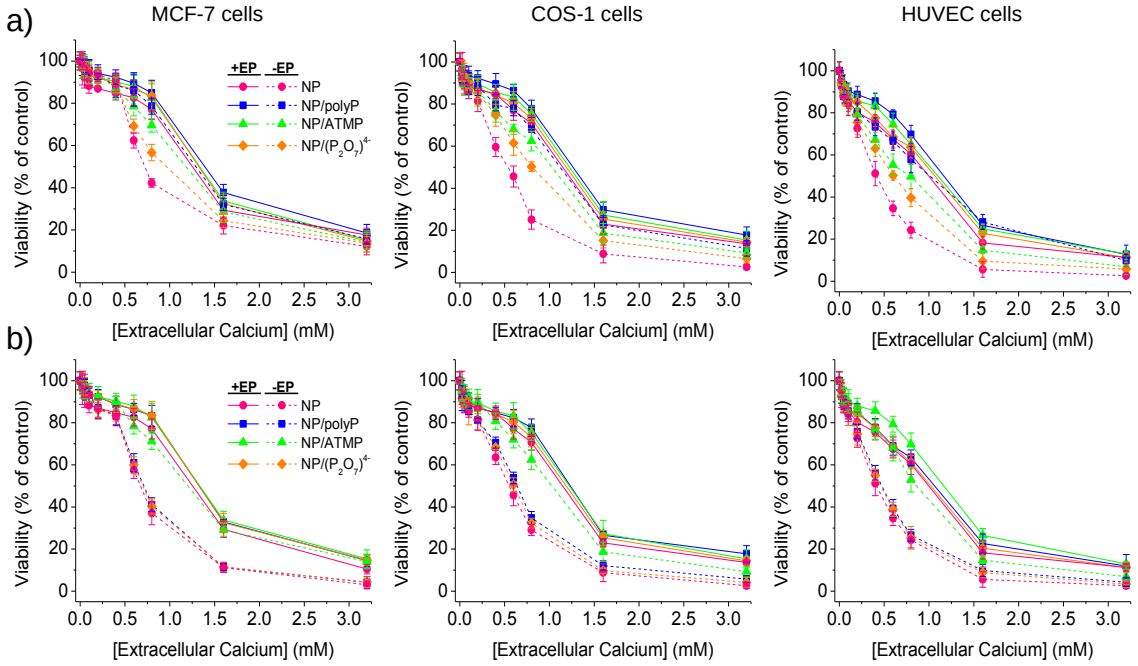

Figure 7.9. Viability of MCF-7, COS-1 and HUVEC cells after incorporation of NPs < 200 nm coated with biophosphates and biophosphonates (a). The different concentrations of Ca^{2+} were introduced by non-electroporation (-EP) and electroporation (+EP). b) Effect caused by pre-treatement with alkaline phosphatase and Mg^{2+} as cofactor. The cellular viability was measured by Alamar Blue assay after 48 h of culture.

Finally, it is remarkable that the NPs incorporated by +EP and modified with the different coatings showed CC_{50} values with slight differences (*e.g.* see **Table 7.5**) after the enzymatic attack. **Figures 7.10**, **7.11** and **Table 7.6**). In summary, a constitutive and cumulative dissolution process took place and reached similar Ca^{2+} intracellular levels for all cell types. On the other hand, the endocytic pathway (–EP) of the different cell types demonstrates greater differential sensitivity to NPs without or with surface modification. In any case, the ability to release its Ca^{2+} content and exert cell injury that ends in the death of cells is demonstrated.

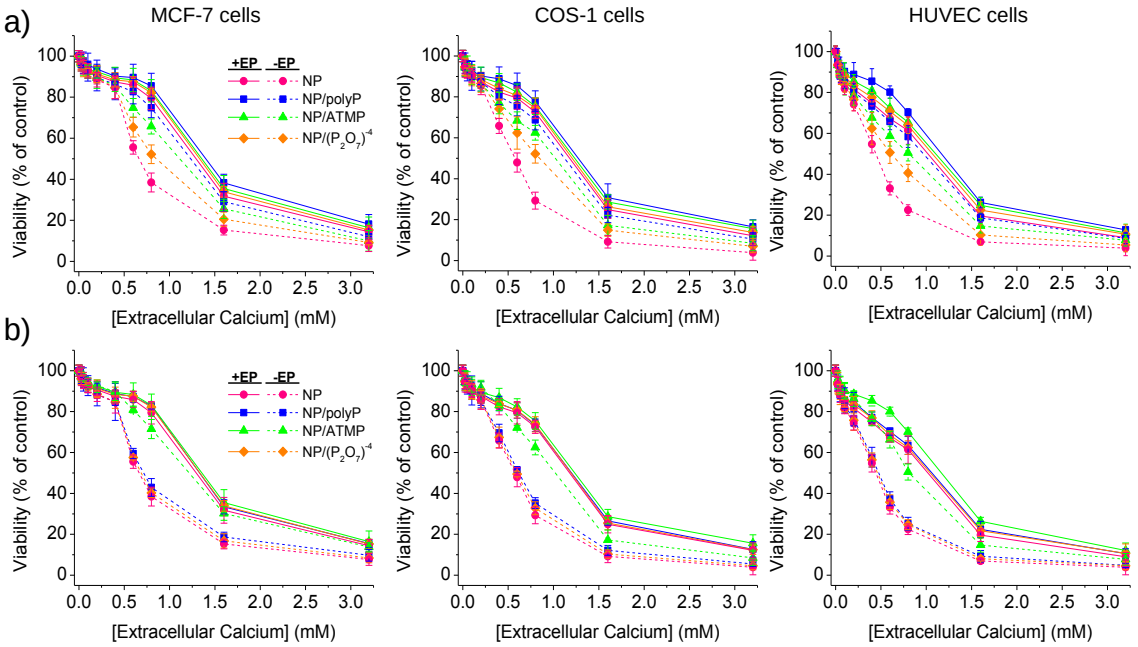

Figure 7.10. Viability of MCF-7, COS-1 and HUVEC cells after incorporation of NPs < 200 nm coated with biophosphates and biophosphonates (a). The different concentrations of Ca^{2+} were introduced by non-electroporation (-EP) and electroporation (+EP). b) Effect caused by pre-treatement with alkaline phosphatase and Mg^{2+} as cofactor. The cellular viability was measured by MTT assay after 24 h of culture.

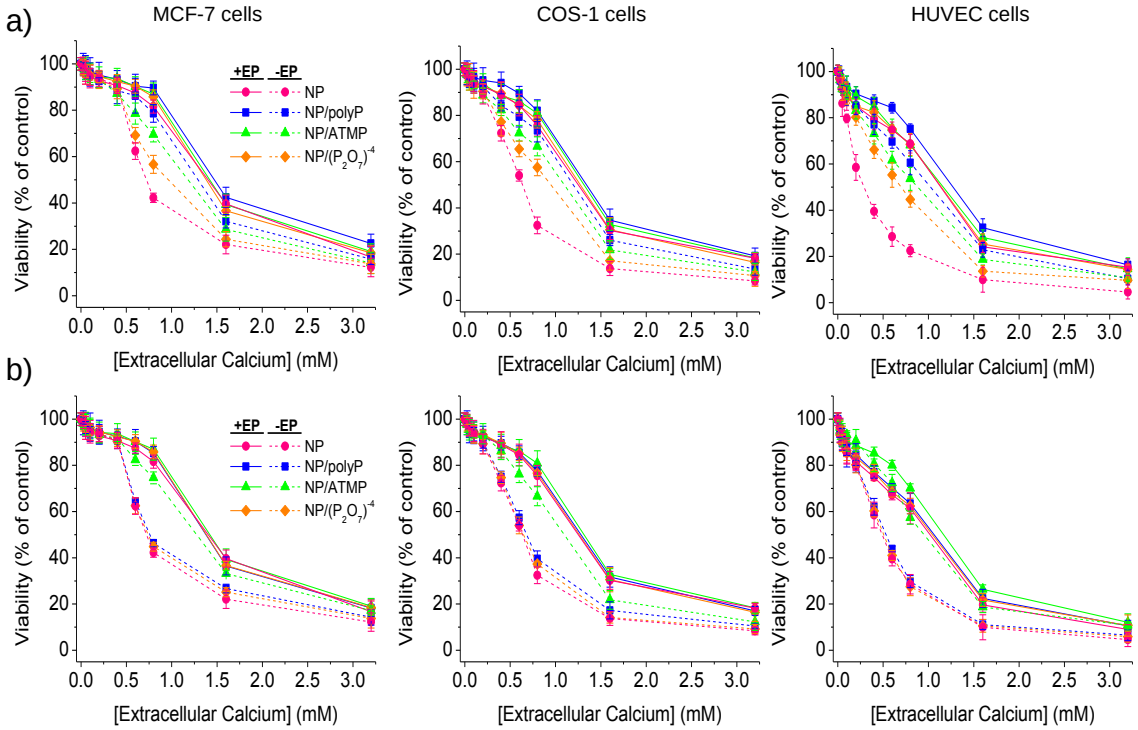

Figure 7.11. Viability of MCF-7, COS-1 and HUVEC cells after incorporation of NPs < 200 nm coated with biophosphates and biophosphonates (a). The different concentrations of Ca^{2+} were introduced by non-electroporation (-EP) and electroporation (+EP). b) Effect caused by pre-treatement with alkaline phosphatase and Mg^{2+} as cofactor. The cellular viability was measured by MTT assay after 48 h of culture.

Table 7.6. CC_{50} of NPs < 200 nm coated with biophosphates and phosphonates. NPs were incorporated into cells by electroporation (+EP) and non-electroporation (-EP). The effect was evaluated with and without any treatment of ALP + $MgCl_2$. Values were determined according to curves displayed in **Figures 7.10** and **7.11**.

Nanoparticle	CC_{50} (mM)					
	MCF-7		COS-1		HUVEC	
	-EP	+EP	-EP	+EP	-EP	+EP
No-treatment, 24 h						
NP	0.67	1.29	0.58	1.17	0.44	1.02
NP/polyP	1.23	1.40	1.13	1.28	0.97	1.16
NP/ATMP	1.12	1.35	1.02	1.24	0.81	1.10
NP/$(P_2O_7)^{4-}$	0.86	1.34	0.84	1.21	0.62	1.07
No-treatment, 48 h						
NP	0.72	1.39	0.63	1.25	0.29	1.14
NP/polyP	1.29	1.47	1.19	1.34	1.01	1.28
NP/ATMP	1.18	1.42	1.09	1.32	0.88	1.16
NP/$(P_2O_7)^{4-}$	0.97	1.38	0.94	1.27	0.70	1.14
Treatment: ALP+$MgCl_2$, 24 h						
NP	0.66	1.29	0.57	1.17	0.44	1.02
NP/polyP	0.72	1.34	0.63	1.20	0.48	1.06
NP/ATMP	1.21	1.36	1.02	1.24	0.82	1.17
NP/$(P_2O_7)^{4-}$	0.69	1.33	0.60	1.18	0.46	1.04
Treatment: ALP+$MgCl_2$, 48 h						
NP	0.72	1.40	0.64	1.24	0.48	1.02
NP/polyP	0.76	1.38	0.68	1.28	0.54	1.06
NP/ATMP	1.27	1.41	1.09	1.31	0.95	1.16
NP/$(P_2O_7)^{4-}$	0.74	1.38	0.64	1.26	0.51	1.03

7.4 CONCLUSIONS

ACP NPs have cytotoxic effects when internalized within cells. The endocytosis pathway is more harmful than the incorporation by electroporation. In this sense, the cytotoxic effect could be produced by the increase on the intracellular Ca^{2+} concentration. Ions are released from the NPs and became accumulated in the lysosomes and the mitochondria of the cells as demonstrated by both Alamar blue and MTT cell viability assays.

The surface modification of ACP NPs and consequently the physico-chemical alteration (*e.g.* solubility decrease) of the NPs in subcellular compartments such as lysosomes and mitochondria decreased the severity of their cytotoxicity in the order polyphosphates < ATMP < orthophosphate.

Our results are compatible with the following concept: In the acidic lysosomes calcium phosphate crystals of different size are dissolved, leading to significant increases of ionic calcium levels. These ions could only be slowly pumped into intracellular calcium storage sites, such as mitochondria, endoplasmic reticulum or even outside the cell. In addition, the heterogeneous calcium response may result from variable calcium sensitivities of the different cell types. The intracellular calcium concentration increased in response to the ACP NPs uptake and directly influenced the viability of cells. Repetitive high intracellular calcium concentration amplitudes and/or sharp increase reaching permanently high plateau like levels may lead to cell death.

An interesting aspect that derives from this study is the differential cytotoxicity of the ACP NPs. Thus, it has been shown that epithelial-like MCF-7 cells were the most resistant to the effect of increased intracellular Ca^{2+} derived from ACP NPs, while endothelial-like HUVEC cells were the most sensitive and COS-1 cells fibroblasts-like showed an intermediate sensitivity. This result becomes significant if we consider the cellular organization of tissues as possible targets for treatment through the metabolic imbalance of calcium.

7.5 REFERENCES

1. Berridge, M.J., Bootman M.D. & Roderick, H.L. Calcium signaling: dynamics, homeostasis and remodeling. *Nature Reviews/ Molecular Cell Biology*. **4**, 517-529 (2003).
2. Byers, T. *et al*. American Cancer Society Guidelines on Nutrition and Physical Activity for Cancer Prevention: Reducing the Risk of Cancer with Healthy Food Choices and Physical Activity. *CA*. **52**, 92-119 (2002).
3. McCullough, M.L., Robertson, A.S., Rodriguez, C., Jacobs, E.J., Chao, A., Carolyn, J., Calle E.E., Willett, W.C. & Thun, MJ. Calcium, vitamin D, dairy products, and risk of colorectal cancer in the Cancer Prevention Study II Nutrition Cohort (United States). **14(1)**:1-12 (2003).
4. Curry, M.C., Peters, A.A., Kenny, P.A., Roberts Thomson, S.J. & Monteit G.R. Mitochondrial calcium uniporter silencing potentiates caspase-independent cell death in MDA-MB-231 breast cancer cells. *Biochem Biophys Res Commun*. **434**, 695-700 (2013).
5. Zaichick, V., Zaichick, S. & Rossmann, M. Intracellular calcium excess as one of the main factors in the etiology of prostate cancer. *AIMS Molecular Science*. **3(4)**:635-647 (2016).
6. Clapham, D. Calcium signaling. *Cell*. **131**:1047-58 (2007).
7. West, A.E. Calcium regulation of neuronal gene expression. *Proc natl Acad Sci USA*.**98**:11024-31 (2001).
8. Contreras, L. Mitochondria: the calcium connection. *Biochim Biophys Acta*. **1797**:607-18 (2010).
9. Saidak, Z. The role of the calcium-sensing receptor in the development and progression of cancer. *Endocrinol Rev*. **30**:1787-95 (2009).
10. Nicholls, D.G., Budd, S.L. & Castilho, R.F. Excitotoxicity and mitochondria. *Biochem Soc Symp*. **66**; 55-67 (1999).
11. Brookes, P. S., Yoon, Y. & Sheu, S.S. Calcium, ATP, and ROS: a mitochondrial love-hate triangle. *Am J Physiol Cell Physiol*. **287**: C817-C833 (2004).
12. Storz, P. Reactive oxygen species in tumor progression. *Front Biosci*. **10**:1881-96 (2005).
13. Pelicano, H. ROS stress in cancer cells and therapeutic implications. *Cancer Res*. **7**:97-110 (2004).
14. Pelicano, H. Mitochondrial disfunction and reactive oxygen species imbalance promote breast cancer cell motility through a cxxl14-mediated mechanism. *Cancer Res*. **69**:2375-2383 (2009).
15. Vanlangenakker, N. & Vanden, T. Molecular mechanisms on pathophysiology of necrotic cells death. *Current molecular medicine*. **8[3]** (2008).
16. Proskuryakov, S.Y. & Gabai. VL. Mechanisms of tumor cells necrosis. *Curr Pharm Des*. **16(1)**:56-58 (2010).
17. Willis, R.A. Pathology of tumours 4th Edition. London. Butterworths (1967).
18. Folkman, J. & Kerbel, R. Clinical translation of angiogenesis inhibitors. *Nat Rev Cancer*. **2**, 717-739 (2002).
19. Folkman, J. Angiogenesis and apoptosis. *Semin. Cancer Biol*. **13**, 159-167 (2003).

20. Rivas, M., del Valle, L.J., Rodriguez-Rivero, A.M., Turon, P., Puiggalí, J. & Alemán, C. Loading of an antibiòtic into biocoated hydroxyapatite nanoparticles: smart antitumor platforms with regulated release. *ACS Biomater. Sci. Eng*. **26**, 3234-3245 (2018).

21. Stockem, W.,Weber, K. & Wehland, J. Influence of microinjected phalloidin on locomotion, protoplasmic streaming and cytoplasmic organization in Amoeba proteus and Physarum polycephalum. *Cytobiologie*. **70**, 2463-2470 (1978).

22. Roger, P.P., Rickaert, F., Huezt, G, Authelet, M, Hofmann, F. & Dumont, J.E. Microinjection of catalytic subunit of cyclic AMP-dependent protein kinases triggers acute morphological changes in thyroid epithelial cells. *FEBS LETTERS*. **232**, 409-414 (1988).

23. Orimo, H. The mechanism of mineralization and the role of alkaline phosphatase in health and disease. *J Nippon Med Sch*. **77**, 4-12 (2010).

24. Neuman, S. The use of size-defined DNA-functionalized calcium phosphate nanoparticles to minimize intracellular calcium disturbance during transfection. *Biomaterials*. **30**: 6794-6802 (2009).

25. Taylor, J.T., Zeng, X.B., Pottle, J.E., Lee, K. *et al*. Calcium signaling and T-type calcium channels in cancer cell cycling. *World J Gastroenterol*. **14**, 4984-4991 (2008).

26. Steinhardt, R.A. & Alderton, J. Intracellular free calcium free rise triggers nuclear envelope breakdown in the sea urchin embryo. *Nature*. **332**, 364-366 (1988).

27. Ewence, A.E., Bootman, M. *et al*. Calcium phosphate crystals induce cell death in human vascular smooth muscle cells- a potential mechanism in atherosclerotic plaque destabilization. *Circ Res*. **103**, 28-32 (2008).

28. Kaestner, L., Wang, X., Herts, L. & Bernhard, I. Voltage-activated ion channels in non-excitable cells. A viewpoint regarding their physiological justification. *Front Physiol*. **9**, 450-456 (2018).

29. Marchi, S. & Pintoni, P. Alterations of calcium homeostasis in cancer cells. *Current Opinion in Pharmacology*. **29**, 1-6 (2016).

30. Farfariello, V., Lamshanova, O., Germania, E., Fliniaux, I. & Prevarskaya, N. Calcium homeostasis in cáncer: a focus on senescence. *Biochem Biophys Acta*. **1853 (9)**, 1974-1979 (2015).

31. Rivas, M., Casanovas, J., del Valle, L.J., Bertran, O., Revilla-López, G., Turon, P., Puiggalí, J. & Alemán, C. An experimental-computer modeling study of inorganic phosphates surface adsorption on hydroxyapatite particles. *Dalton Trans*. **44**, 9980-9991 (2015).

32. Bloch-Frankenthal, L. The role of magnesium in the hydrolysis of sodium pyrophosphate by inorganic pyrophosphatase. *Biochem J*. **57(1)**: 87–92 (1954).

8.

ROLE OF THE INTRACELLULAR CALCIUM IN THE TUMOR AGGRESSIVENESS. AN INTERPLAY OF DIFFERENT CELL TYPES: EPITHELIAL, ENDOTHELIAL AND FIBROBLAST CELLS

A tumour is a cell mass where different types of cells can coexist. Recently, it has been proposed that anomalous Ca^{+2} concentrations and the subsequent redox imbalance could have an important role in the formation and progression of cancer. In this work, we have studied how extracellular Ca^{+2} can trigger characteristic responses of tumour cells in different cell types sensitized with an increase of intracellular Ca^{+2}. For this purpose, MCF-7, HUVEC and COS-1 cell clones corresponding to the epithelial, endothelial and fibroblast types were prepared. Concretely, the clones were obtained by pre-treating the cells with amorphous calcium phosphate nanoparticles, so that, cells would endocytose high amounts of Ca^{+2}.

In the cellular condition of sensitization MCF-7 epithelial cells showed high expression of the p53 pro-apoptotic factor and an increased cell migration when the intracellular Ca^{+2} concentration was raised. Alternatively, HUVEC, endothelial cells, showed a lower capacity of adhesion to matrices conditioned with collagen, vitronectin, fibrinogen or fibronectin. In addition, when stimulating factors such as VEGF and bFGF were added, cells showed synergistic and antagonistic effects for migration, respectively. This synergistic activity provided to these cells with a higher invasive capacity. Finally, COS-1 fibroblasts cells secreted factors contained in their conditioned media that can stimulate MCF-7 epithelial cells for a greater migration and invasive capacity.

These results suggest that the condition of increased intracellular Ca^{+2} in epithelial, endothelial and fibroblasts cells could support the promotion and aggressiveness of cells in tumour formation and cancer metastasis.

8.1 INTRODUCTION

Oncogenes and deregulation of tumor suppressor factors favour oncogenesis through signalling pathways that are involved in cell-death resistance, uncontrolled cell proliferation, and in the requirements needed for energy production.[1] During the last decade, alterations in intracellular Ca^{+2} signalling have emerged as an important factor in the development of tumours and their invasive and metastatic properties.[2-4] Cancer cells display alterations in the expression and regulation of different Ca^{+2} -transport systems at both the plasma membrane and the membranes of organelles, like the endoplasmic reticulum and the mitochondria. Thus, Ca^{+2}-transport systems have an impact on different hallmarks of cancer progression.[3-5]

Ca^{+2}-dependent signalling mechanism is frequently remodelled or deregulated in cancer cells. However, to date only mutations in ATP2A2 (which results in changes to SERCA2 expression) have been described in occurring or promoting cancer.[6,7] The scarcity of studies reporting mutations in genes associated with Ca^{+2} suggests that many of the changes that underpin remodelling of Ca^{+2} signalling reflect epigenetic changes in gene expression and/or post-translational changes in the properties of existing signalling components. This remodelling is a two-way process in which oncogene-dependent pathways can remodel Ca^{+2} signals while Ca^{+2} can refine oncogene-regulated signalling.

The contemporary view of cancer envisions tumors as “ecosystems”[1] that consist not only of simple cells that proliferate by alone, but also of diverse collections of recruited stromal cells that regulate cancer behaviour.[8] The endothelial cells of blood vessels are the first cells in contact with the blood-borne element and are especially prevalent in tumours.[9] This kind of cells is also critical to the biology and, therefore, the health of normal tissues.[10] For example, endothelial cells promote homeostasis in the vascular system when they are quiescent by suppressing local hyperplasia, angiogenesis and inflammation. A boost of injury, caused by the stimulation of these processes is characteristic of diseased or “dysfunctional” cells.[11] Endothelial cells present a similar role in tumors, and like other stromal cell types, regulate cancer cell behaviour. They can promote homeostasis and stimulate cancer when are dysfunctional. Endothelial cells form the structural cells of vessels and, additionally, serve as stromal regulatory active cells with privileged access to the deepest recesses of tumors. Subtle changes in

endothelial cell phenotype could be easily transmitted to the tumours with deep effects on cancer fate.

In the endothelial cells, the surface receptor stimulation may result in the activation of a variety of transmembrane signal transduction pathways. This can cause protein phosphorylation,[12] ion flux,[13] and phospholipid metabolism.[14] For example, activation of cytosolic phospholipase A2 requires the influx of Ca^{+2} in the same range that occurs in response to the activation of receptor-operated Ca^{+2} channels.[15] Ca^{+2} regulation of receptor-mediated phosphorylation events has also been described, such as downstream phosphorylation of phospholipase C-γ (PLC-γ).[16] Particularly, Ca^{+2} is a requirement for tyrosine phosphorylation of PLC-γ which regulates the production of the second messengers. This include inositol triphosphate and diacylglycerol, further interconnecting the signaling pathways. Thus, Ca^{+2} homeostasis may regulate important cellular functions. The end result of activation of these transduction pathways includes: proliferation, invasion, and differentiation.[17]

Tumors are known as wounds that do not heal. Cells that are involved in angiogenesis and in facing injury (*e.g.* endothelial cells and fibroblast) have a prominent role in the progression, growth and spread of cancers. Particularly, fibroblasts are associated with cancer cells at all stages of cancer progression, and their structural and functional contributions to this process are beginning to emerge. Their production of growth factors, chemokines and the extracellular matrix facilitates the angiogenic recruitment of endothelial cells and pericytes. Fibroblasts are therefore a key determinant in the malignant progression of cancer and represent an important target for cancer therapies.[18-22]

Although most cancers, and by definition all carcinomas are derived from epithelia; interactions between cell types in the surrounding microenvironment (stroma) are crucial for tumor cell growth, survival, and metastatic spread.[23] For example, cancer-associated fibroblasts have been shown to induce and promote the invasion of initiated but non-malignant epithelium.[24] Also cancer cells rose from human colon,[25] breast,[26] prostate[27] and other organs present the same features. It should be noted that other studies have previously examined fibroblast and epithelial interaction in tumor growth and development by co-inoculating normal fibroblasts or cancer-associated fibroblasts with tumorigenic epithelial cells. These studies showed that these fibroblasts stimulate

mammary epithelial cell growth, differentiation and tumorigenesis, or induce epithelial-mesenchymal transition via several possible pathways.[26,28]

In previous work, we showed that the increase of intracellular Ca^{+2} by endocytosis of amorphous calcium phosphate nanoparticles (ACP-NP) exerts a cytotoxic effect, promoting autophagy due to lysosomal and mitochondrial dysfunction or damage.[29] In addition, these effects were more severe in normal endothelial cells (HUVEC) in comparison to tumour epithelial cells (MCF-7), whereas the fibroblasts cells immortalized by SV40 (COS-1) showed an intermediate cytotoxic sensitivity.[29] In this new scenario, the objective of the present work responds to the need to better understand how these effects occur in different cell types (MCF-7, HUVEC and COS-1 as representative of epithelial, endothelial and fibroblast cells, respectively) when the intracellular Ca^{+2} increases. For this purpose, we have studied the proliferation, adhesion, migration and other specific markers and characteristics of tumor cells. In summary, the modifications of these cells heve been studied in cell clones obtained by subculturing four generations in the presence of ACP-NP. These pre-treated cells were sensitized by the increase of intracellular Ca^{+2}, mimicking the metabolism of cancer cells.

8.2 EXPERIMENTAL SECTION

8.2.1 Materials

Ammonium hydroxide aqueous solution (NH_4OH; purity: 28-30 %) was purchased from Sigma-Aldrich. Calcium nitrate [$Ca(NO_3)_2$; purity ≥ 99.0 %] was purchased from Panreac (Barcelona, Spain). Ethanol (C_2H_5OH; purity ≥ 99.5%) was obtained from Scharlab (Barcelona, Spain).

MCF-7 (epithelial cells from human breast adenocarcinoma) and COS-1 (fibroblast cells from green monkey kidney transformed by insertion of the SV40) cell lines were obtained from ATCC (HTB-22 and CRL-1650, respectively). Dulbecco´s Modified Eagle´s Medium (DMEM) and Ca^{+2}-free DMEM, Fetal Bovine Serum (FBS), penicillin/streptomycin (pen/strep) and L-glutamine were purchased from Gibco. HUVEC (endothelial cells from normal human umbilical vein) (CC-2517) cell line and EGM-2 Bullet-kit with and without Ca^{+2} media optimized for certain HUVECs were purchased from Lonza. Poly-L-lysine was purchased from Merck Millipore (Germany).

Alamar blue reagent was purchase from Invitrogen (Invitrogen-Molecular Probes, Leiden, The Netherlands). MTT solution [3-(4,5-dimethylthiazol-2-yl)-2,5-diphenyltetrazolium bromide] was purchased from Roche. Trypsin-EDTA solution (0.05 % trypsin, 0.02 % EDTA) was purchased from Sigma-Aldrich.

8.2.2 Synthesis of amorphous calcium phosphate

The considered ACP-NPs have been synthesized following a well-established protocol. The reagent conditions were adjusted to get atypical Ca/P ratio of 1.67. Specifically, 15 mL of 0.5 M $(NH_4)_2HPO_4$ in milli-Q water (pH 11 adjusted with the 30% w/v ammonia solution) were drop-wise added (rate of 2 mL/min or less) under agitation (400 rpm) to 25 mL of a 0.5 M $Ca(NO_3)_2$ ethanol solution. The reaction mixture was stirred during 1h (400 rpm at room temperature). Reaction was performed in plastic containers to avoid the use of borosilicate glass. Then, the resultant suspension of nanoparticles (NPs) was aged for 24 h at 37 ºC. The precipitate was separated by centrifugation and washed sequentially with milli-Q water and a 60/40 v/v mixture of ethanol-water (twice). A white powder was obtained after freeze-drying.

Size separation of NPs was performed according to BS ISO 14887 (2000) ("Sample preparation-dispersing procedures for powders in liquids"). Specifically, the ACP-NPs powder (300 mg) was placed in a plastic tube and re-suspended in 10 mL of milli-Q water. The dispersion was gently mixed with a spatula until all visible aggregates disappeared. Finally, another 10 mL of water were added while manual mixing was maintained. The tube was subsequently immersed in an ice bath and sonicated to ensure a complete sample de-agglomeration. An ultrasonic titanium probe of 6 mm (Cole-Parmer® 130-Watt Ultrasonic Processors (50/60 Hz, VAC 220); product number EW-04714-51) was employed and tuned to resonate at 20 kHz, ± 50 Hz for 20 s at 90 % amplitude.

The NPs suspension was then gently mixed again with a spatula rod to ensure homogeneity, loaded in a syringe (10 mL) and filtered through a 0.2 µm filter at a flow rate of approximately of 1 mL/min. Particles were finally concentrated using an IEC MultiRF centrifuge (Thermo IEC, Needham Heights, MA, USA). Two fractions corresponding to the eluted (*i.e.* NPs size < 200 nm) and the retained particles (*i.e.* NPs with size > 200 nm) were obtained.

8.2.3 MCF-7 epithelial cancer cells

8.2.3.1 Pre-treatment of cells to obtain sensitized clones

MCF-7 and COS-1 cells were cultured in DMEM (ATCC, Manassas, VA) supplemented with 10 %-v/v FBS, 1 % pen/strep, 2 mM L-Glutamine. HUVEC cells were cultured in EGM-2 Bullet-kit medium. The cells were cultured in 25 T-flask at 37 ºC with 5 % CO_2, 95 % air and humid atmosphere. The cells of the culture that reached ~ 90 % confluence were detached using 0.05 % trypsin/EDTA.

ACP-NPs with diameter < 200 nm were mixed with the medium until final concentrations of Ca^{+2} equivalent to 25 and 50 µM. The clones were obtained after four subcultures in the above indicated conditions and used in the subsequent assays as described in the following sections. Cultures and cell assays were performed with a cell viability greater than 90-95 %, which was determined by the MTT and alamar blue assays.

These clones were named pre-treated cells and corresponded to cells sensitized by the increase of their intracellular Ca^{+2} level. Cells without pretreatment (named as no pre-treated, parental or wild-type) were the controls and were prepared in a similar way as the clones (*i.e.* after the same number of subcultures).

The cell proliferation assay was performed by the incorporation of Bromodeoxyuridine (BrdU), using the Kit Cell Proliferation (ELISA BiotrakTM System, version 2, Amersham Biosciences). This test was performed adopting the procedure described by Lloveras *et al.*[30,31]. The MCF-7 cells, parental and clones obtained by subculturing with 50 µM Ca^{+2}, were seeded in a 96-well plate, at a concentration of $3x10^4$ cells/well in a volume of 100 µL of complete culture medium. Cells were cultured for 24 h to allow their adhesion to the plate. Then, the medium was exchanged with a serum-free medium supplemented with different doses of Ca^{+2} (extracellular Ca^{+2}) in the range of 0-3.2 mM. The plate was maintained under culture conditions for additional 24 h. Finally, 10 µL of BrdU/well were added to the serum deprived medium to obtain a final concentration of 10 µM, and then the plate was incubated for other 2 h. Following the protocol of the kit, the assay was completed by reading the plates at 450 nm in an ELISA reader (Thermo-Electro Corporation).

8.2.3.2 p53 ELISA assay of MCF-7 cells

A sandwich immunoassay was performed for quantitation of the p53 protein as described by Gannon *et al.*.[32] Mouse monoclonal antibodies were employed to recognize either human or mouse p53 protein as solid-phase reagents. Captured proteins were detected using a polyclonal rabbit antiserum of the p53 protein (CM-1). Microtiter plates of 96-wells were coated overnight at room temperature with 50 µL/well of 20 µg/mL purified mouse monoclonal antibody. These were blocked for 2 h with 3 % bovine serum albumin (BSA) in PBS and rinsed with PBS. The plates with MCF-7 clone (50 µM Ca^{+2}) and parental cells were prepared as described in the previous section. Cells were subsequently trypsinized, washed once in PBS and resuspended in 100 µL of PBS. Finally, 50 µL of the MCF-7 cell suspension were added to each well of the plate having adsorbed CM-1 and then incubated for 3 h at 4 ºC. The plates were washed once with PBS, twice with NP40 (NonidetTM P40) in PBS (0.1 %) and once again with PBS. The appropriate rabbit antiserum (diluted 1:1000 with a PBS solution containing BSA (1 %) and NP40 (0.1%)) was added and the incubation was maintained for 3 additional hours. The plates were washed as described above and peroxidase-conjugated swine antiserum of rabbit immunoglobulin (DAKO, diluted to 1:1000) was added for 2 h. Bound enzyme was detected with the tetramethylbenzidine substrate and the results were monitored with an automatic ELISA plate reader (Thermo-Electro Corporation) at 450 nm.[33]

8.2.3.3 MCF-7 cells migration assay

Migration assays were performed with some modifications according to the protocol previously described by Keely *et al*.[34] The Transwell system, which consisted on 24-well cell culture plates with inserts of light-opaque polyethylene terphthalate membrane filters having 8 µm pores, was used (Transwell HTS Fluoroblock™ Multiwell Insert System, Becton Dickinson). The upper and lower surfaces of the Transwell membranes were coated with type I Collagen (Vitrogen) using a 15 µg/mL sterile PBS solution for 2 h at 37 ºC. After coating, MCF-7 cell suspensions of wild-type (0 µM Ca^{+2}) and clones (25 and 50 µM Ca^{+2}) were resuspended with DMEM high glucose without serum and supplements. Then, $1x10^5$ cells in 100 µL of the medium were seeded onto the upper side of each Transwell membrane. Then, DMEM high glucose supplemented with 2 % FBS, was added to the lower compartment of the 24-well plates to test the capacity of cells to migrate towards the chemotactic stimulus. After 4 h at 37 ºC, cells that migrated (lower side) were stained with 5 µM Calcein-AM (Calbiochem) for 25-30 min at 37 ºC.

The quantification of the assay was performed by measuring the area filled by the cells in the lower compartment of the insert, using image ProPlus software (Media Cybernetics Inc.).

8.2.4 HUVEC endothelial cells

8.2.4.1 HUVEC cell adhesion assay

The cell adhesion assay was adapted from that described by Marshall *et al*.[35] 96-well flat bottom plates were coated by incubation overnight at 4 ºC with 10 µg/mL of fibrinogen (Sigma), 10 µg/mL f type I collagen (Vitrogen), 10 µg/mL of fibronectin (Sigma) or 1 µg/mL of vitronectin (Sigma). After incubation, plates were washed with PBS and flooded in a PBS-BSA solution (0.1 %-w/v) for 1 h at 37 ºC. HUVEC cells, wild-type (0 µM Ca^{+2}) and clones (25 and 50 µM Ca^{+2}), were harvested, re-suspended in the cell adhesion medium (EBM supplemented with 1 %-w/v BSA) at 3x10^4 cells in 50 µL/well, and added to the wells. Plates were incubated at 37 ºC for 1 h. Adherent cells were fixed with 4 % of paraformaldehyde for 20 min at room temperature. After two washes with milli-Q water, cells were stained with 50 µL of 0.1 % crystal violet for 20 min at room temperature, washed with milli-Q water and dried overnight at 37 ºC. The quantification of adhered cells was determined by adding 50 µL/well of 0.1 M HCl and reading the absorbance at 630 nm (BIO-RAD Microplate reader model 550).

8.2.4.2 HUVEC cell migration assay

Migration assays were performed with the Transwell system previously described (section **8.2.3.3**). After coating with type I collagen, cell suspensions of HUVEC cells, (1x10^5 wild-type (0 µM Ca^{+2}) or clone (25 and 50 µM Ca^{+2}) cells in 100 µL of EBM without serum and supplements were seeded onto the upper side of each Transwell system. Then, EBM supplemented with EGM and 10 % FBS was added to the lower compartment of the 24-well plates to test the capacity of the cells to migrate towards the chemotactic stimulus. After 4 h at 37 ºC, cells that had migrated (lower side) were evaluated as described above (section **8.2.3.3**).

8.2.4.3 Synergy between Ca^{+2} and VEGF/bFGF for migration in HUVEC cells

4 h after deprivation (incubation in EBM alone), the HUVEC cells (wild-type, 0 µM Ca^{+2}; and clones of 25 and 50 µM Ca^{+2}) were treated with EBM, and EBM supplemented with

1 and 10 ng/mL VEGF (vascular endothelial growth factor) or bFGF (basic fibroblast growth factor). 24 h after the addition of the stimulus, the migrated cells were quantified as described above (section **8.2.4.2**). Each point was normalized with the positive control that represents 100 % migration. This control corresponds to the cells incubated in EBM plus the EGM Bulletkit supplements and 10 % FCS (complete medium).

8.2.4.4 HUVEC cells wound healing assay

Wound healing assays were performed adapting the procedure described by Dimmeler *et al.*[36] To examine wound healing, cell suspensions (wild-type, 0 µM Ca^{+2}; and clones of 25 and 50 µM Ca^{+2}) of HUVEC (8x10^4 cells/cm^2) in EBM (Clonetics) supplemented with EGM (Bullet-kit, Clonetics) and FCS (10 %-v/v), were seeded onto 12-well plates. After 24 h at 37 ºC, cells were washed twice with PBS to remove the debris and kept in EBM without serum and supplements. Then, HUVEC cells grown in 12-well plates as confluent monolayers were mechanically scratched using a pipette tip to create the wound. Cells were washed twice with PBS before the treatment with 50 ng/mL of VEGF (24 h at 37 ºC). Phase contrast images of the wound were then taken at different time points. The quantification of the assay was performed by measuring the area re-filled by the cells in the well, using an inverted Leica DM IRBE microscope with image Quantimed software (Leica Microsystems). The data were expressed as the percentage of closed area in relation to the negative control (EBM without supplements or FCS).

8.2.4.5 HUVEC cells tube-like formation assay

This assay was performed with some modifications following the protocol previously described by Ishida *et al.*[37] HUVEC cells (wild-type, 0 µM Ca^{+2}; and clones of 25 and 50 µM Ca^{+2}) were seeded at a density of 5x10^4 cells/well in 24-well plates coated with a thin gel of 10 mg/mL of Matrigel (Becton Dickinson) as a matrix and maintained with EBM supplemented with 20 ng/mL of bFGF and 1 %-w/v od BSA. The quantification of the assay was determined by measuring the length of the structures formed using ProPlus software (Media Cybernetics Inc.).

8.2.5 COS-1 fibroblast cells

8.2.5.1 Migration assay of MCF-7 cells with fibroblast conditioned medium

Migration assays were performed with the Transwell system described previously (section **8.2.3.3**). After coating, MCF-7 cell suspensions of wild type (0 µM Ca^{+2}) and

clones (25 and 50 μM Ca^{+2}) were seeded at 1x10^5 cells in 100 μL of DMEM high glucose without serum and supplements, onto the upper side of each Transwell membrane. Then, conditioned medium from COS-1 cultures at different conditions (wild-type, 0 μM Ca^{+2}; and clones of 25 and 50 μM Ca^{+2}), was added to the lower compartment of the 24-well plates to test the capacity of the cells to migrate towards this chemotactic stimulus. After 4 h at 37 º C, cells that had migrated (lower side) were evaluated as above described (section **8.2.3.3**).

8.2.5.2 Wound healing assays with co-culture MCF-7/COS-1 cells

Wound healing assays were performed adapting the procedure previously described by Dimmeler *et al*.[36] To examine wound healing, MCF-7 and COS-1 cells (wild-type, 0 μM Ca^{+2}; and clones of 25 and 50 μM Ca^{+2} for each cell type) suspensions of each cell type were mixed (1:1 v/v) in a DMEM/F12 medium supplemented with antibiotics (100 IU/mL penicillin and 100 μg/mL streptomycin) and 2 %-v/v of FCS. MCF-7/COS-1 cells at a concentration of 8x10^4 cells/cm2 were seeded in 12-well plates. After 24 h at 37 ºC, the co-culture cells were washed twice with PBS to remove the debris, and kept in DMEM/F12 without serum and other supplements during 24 h. Then, MCF-7/COS-1 cells grown in 12-well plates as confluent monolayers were mechanically scratched using a pipette tip to create the wound. Cells were washed twice with PBS and then were maintained 12 h at 37 ºC. Phase contrast images were evaluated as above described (section **8.2.4.4**).

8.3 RESULTS AND DISCUSSION

8.3.1. Effect of Ca^{2+} in epithelial cells: Proliferation, p53 expression and migration.

Figure 8.1.A shows the proliferative capacity of MCF-7 cells with and without pre-treatment when were exposed to different extracellular Ca^{+2} concentrations. The cells were cultured with the labelling medium that contains the BrdU (5-bromo-2'-deoxyuridine) pyrimidine analogue. This was incorporated in the place of thymidine into the newly synthesized DNA of proliferating cells. Inhibition of cell proliferation (anti-proliferative effect) is often considered as an injury or cell damage. In both cases, MCF-7 cells with and without pre-treatment showed the same susceptibility to cytotoxic damage. Thus, cell proliferation was significantly reduced in function of the increase in

extracellular Ca^{+2}, producing approximately 10-95 % of cell proliferation inhibition, when the cells were exposed to doses in the range of 0.05-3.2 mM of extracellular Ca^{+2}. The dose-response analysis of these results established that the cytotoxic concentration of extracellular Ca^{+2} that produces the proliferative inhibition of 50 % of the cell population (cytotoxic concentration, CC_{50}) was 0.50 ± 0.06 mM and 0.53 ± 0.06 mM for the MCF-7 cells without and with pre-treatment, respectively.

In order to establish differences between epithelial cells sensitized with Ca^{+2} during pretreatment and non-sensitized or non-pretreated cells, we have studied the expression of the p53 tumour marker. The p53 protein is a transcription factor that is recognized as a tumour suppressor protein. It is a ubiquitous protein that is expressed in all tissues, and therefore has a great importance as a tumour marker. The protein has different functions but it is important to point out the ability to stop the cell cycle including gene transcription, the capacity to activate DNA repair enzymes, initiate the senescence process and activate apoptosis. Thus, the p53 tumour suppressor protein is involved in several central cellular processes that are critical for cellular homeostasis.[38-39] In this study, we showed that p53 protein in breast cancer (adenocarcinoma) cells such as MCF-7 was down-regulated by the cytoplasmic Ca^{+2} concentration increase when the cells were sensitized or pre-treated with Ca^{+2}(**Figure 8.1.B**).

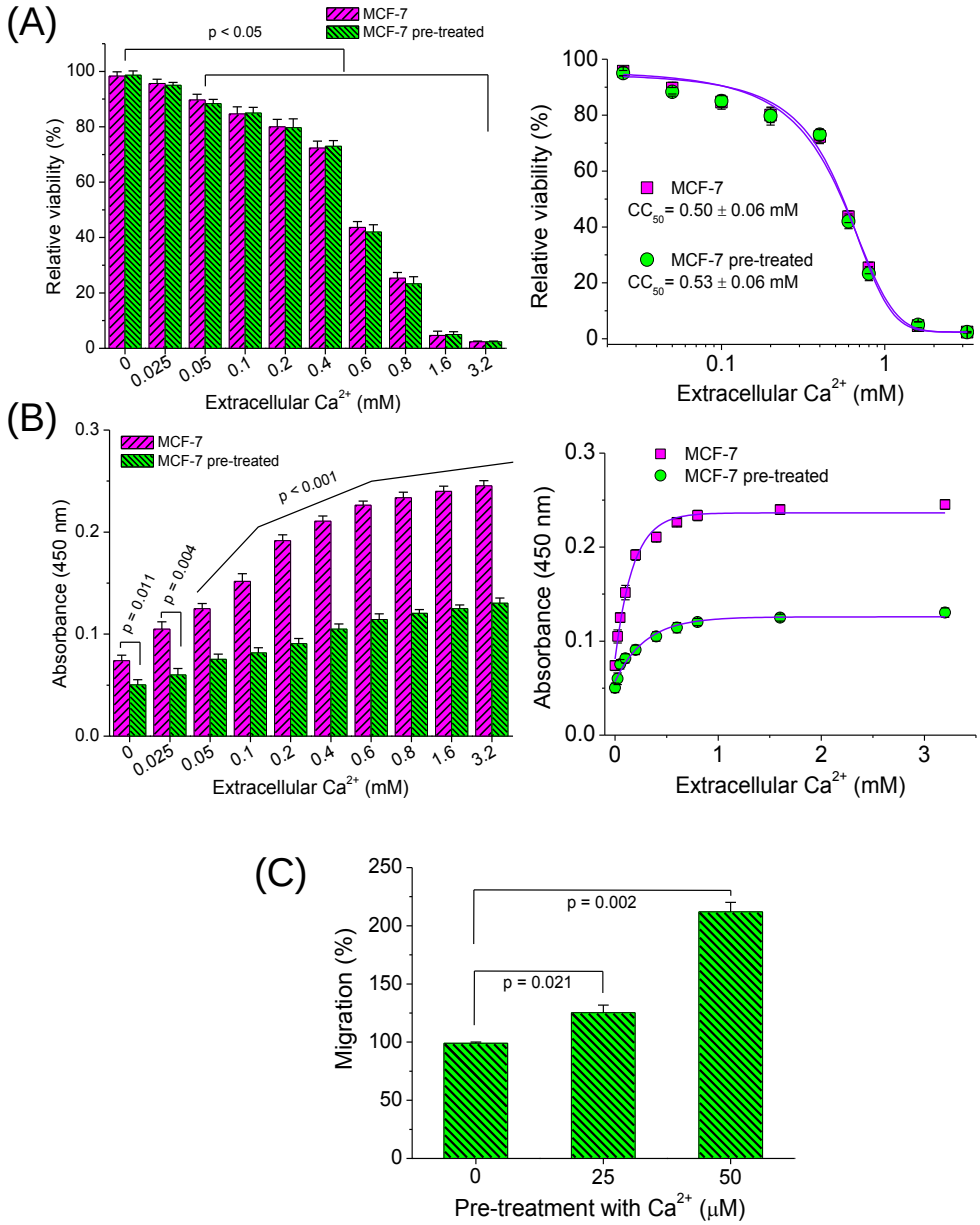

Figure 8.1. Effect in the proliferation (A), p53 protein expression (B), and cellular migration (C) caused by extracellular Ca^{+2} in MCF-7 epithelial cells and clones pre-treated with ACP-NP. The lineal representations show the dose-response (A) and the p53 expression dependence (B) to extracellular Ca^{+2}. CC_{50}, indicates the half cytotoxic concentration.

The levels of the p53 protein in the cells were increased as a function of the extracellular Ca^{+2} concentration. The effect of Ca^{+2} was the stimulation of the increase of p53 in a dose-response manner under an exponential model. Thus, in the range of low doses of Ca^{+2} (*e.g.*, 0.025-0.6 mM) the p53 level linearly increased, whereas the level was stable at a maximum value when high doses (*e.g.,* 0.8-3.2 mM) were applied. Interestingly, the p53 levels doubled the values found with pre-treated cells (**Figure 8.1.B**). Considering

the functions of p53, it could be concluded that extracellular Ca^{+2} stimulated the pro-apoptotic behaviour in MCF-7 cells without the nanoparticle pre-treatment. Thus, the obtained results suggest that the cytotoxic damage observed in **Figure 8.1**. A for non pre-treated MCF-7 cells could occur by both necrosis and apoptosis, while pre-treated MCF-7 cells mainly died by necrosis and the expression of the apoptotic factor p53 was diminished.

Cell motility is a clear stimulated feature in tumour cells and is widely related with metastasis. **Figure 8.1.C** shows a statistically significant increase in the migratory capacity of pre-treated MCF-7 cells when they were grown in 25 μM of extracellular Ca^{+2}, this increase was even close to 25 %. The migration effect of MCF-7 cells was increased being about 100% when pre-treated cells were cultured in 50 μM of extracellular Ca^{+2}. The increase of cytosolic Ca^{+2} concentration in sensitized cancer cells promoted migration and led to a more aggressive malignant behaviour and metastasis. It should be pointed out, however, that an elevated cytosolic Ca^{+2} concentration may also cause cellular damage, including senescence. Note that only those cancer cells capable of mobilizing their antioxidant systems and other regulatory mechanisms can effectively counteract the adverse effects, re-establish the redox balance and emerge as highly malignant clones.

8.3.2. Effect of Ca2+ in endothelial cells: Adhesion, migration, invasion and differentiation.

Figure 8.2.A shows that HUVEC endothelial cells pre-treated with nanoparticles and then exposed to 25 and 50 μM of extracellular Ca^{+2} significantly decreased their ability to adhere to the basement membrane and matrices formed by different extracellular matrix proteins (*e.g.,* collagen, vitronectin, fibrinogen and fibronectin). In addition, a linear dose-response was found for pre-treated HUVEC cells in the range of studied concentrations (*i.e.* 0, 25 and 50 μM of Ca^{+2}). Cell adhesion progressively decreased with the increase of the extracellular Ca^{+2} concentration. This result is very noticeable taking into account that cell invasion is a key process against the integrity of the surrounding tissue. Namely, it is the hallmark of malignancy. However, caution is necessary since the invasive process of adhesion, proteolysis, and migration is not limited to cancer. The role of Ca^{+2} in the regulation of invasion is now an emerging concept[40] because it is understood that the components of cell adhesion pathway could

be key to the proteolytic degradation of the basement membrane. This degradation would consequently allow cell migration in response to factors of motility and extracellular matrix components.[41-43]

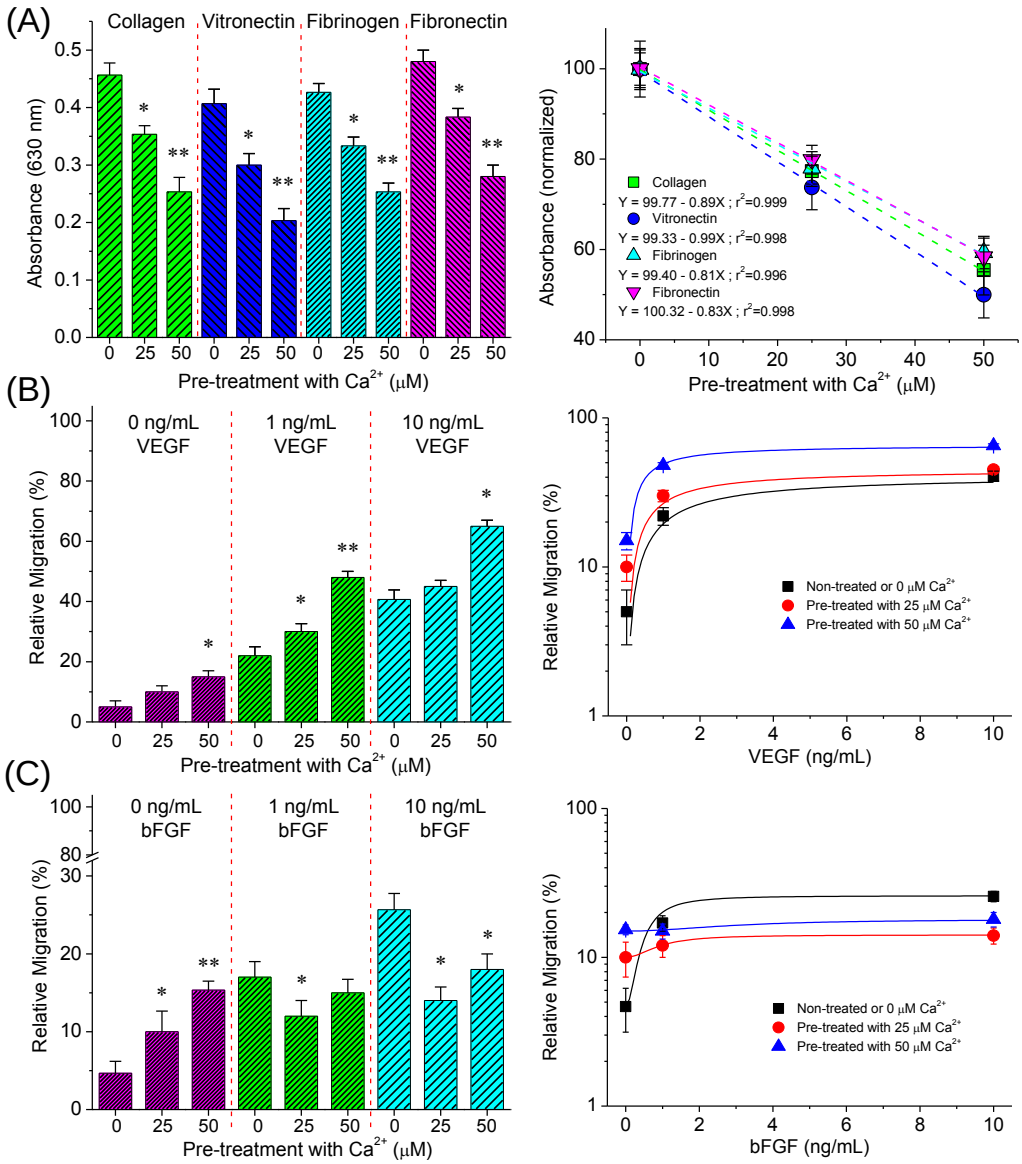

Figure 8.2 Effect of the Ca^{+2} in HUVEC endothelial cells and clones pre-treated with ACP-NP. Adhesion of the HUVEC cells to different components of the extracellular matrix (A). Migration of HUVEC cells due to the synergism between Ca^{+2} and VEGF (B), and between Ca^{+2} and bFGF (C). Lineal representation of the cellular adhesion in dependent manner of Ca^{+2} (A); and association of the migration to VEGF (B) and bFGF (C). *p < 0.05 vs control (HUVEC cells without pre-treatment of Ca^{+2}), **p < 0.05 vs clone of HUVEC cells pre-treated with 25 μM Ca^{+2}.

The growth of any solid tumour depends on angiogenesis, and among the known angiogenic factors, bFGF and VEGF are potent and representative factors involved in tumour development. It has been reported that bFGF and VEGF showed a synergistic effect in both in-vitro and *in-vivo* angiogenesis.[44] However, the interaction of these factors on tumour development and angiogenesis, including mammalian carcinoma, has not yet been elucidated. The effect of VEGF and bFGF on the sensitization of pre-treated HUVEC cells with the increase of intracellular Ca^{+2} concentration are shown in **Figure 8.2.B** and **Figure 8.2.C** respectively.

The synergistic response between extracellular Ca^{+2} and VEGF concentrations on the migration of pre-treated HUVEC cells is clearly observed. This is notorious, considering the increase of migration from 20 % and 40 % (greater than the control) for VEGF doses of 1 and 10 ng/mL, respectively, to 50 % and 60 % when an additional extracellular Ca^{+2} concentration of 50 µM was used (**Figure 8.2.B**).

The synergic effect of bFGF was also evaluated as shown in **Figure 8.2.C.** bFGF in the absence of extracellular Ca^{+2} stimulated in a dose-dependent manner the migration of pre-treated HUVEC cells in a similar than observed for VEGF (**Figure 8.2.B**). However, the combined presence of extracellular $Ca^{+2}$and bFGF had no stimulatory effect on cell migration. For example, cell migration in the presence of 10 ng/mL bFGF was around 15 % and 20 % when the extracellular Ca^{+2} concentration was 25 µM and 50 µM, respectively; but it was close to 30 % in the absence of migration in the presence of 10 ng/mL bFGF was around 15 % when the extracellular Ca^{+2} (**Figure 8.2.C**).

Extracellular Ca^{+2} has a clear inhibitory effect on the migration stimulated by bFGF. Literature data indicated that bFGF acts as a factor inducing migration, which is in agreement with the results obtained in the absence of extracellular Ca^{+2}. Finally, it is intuitively demonstrated that VEGF together with bFGF in the presence of extracellular Ca^{+2} will increase cell migration, and therefore it is sustainable that cell migration obeys a synergistic effect between extracellular Ca^{+2} and VEGF and bFGF factors. However, it is also clear that HUVEC endothelial cells showed a cellular response when without any extracellular Ca^{+2} stimulation were sensitized with the ACP-NP pre-treatment. Cell migration would therefore be related to the storage of Ca^{+2} during the sensitization step.

Figures 8.2.B and **8.2.C** show that VEGF is a more potent factor to induce migration of HUVEC endothelial cells than bFGF. Therefore, the increase of cytoplasmic Ca^{+2} induces an increase in cell migration and mobility. These effects become highly significant when VEGF is added due to the synergistic dose-dependent response. The observed crosstalk between the two cellular factors is consequence of the corresponding mechanisms of action. Thus, under VEGF serum deprived conditions, the action of bFGF is necessary to increase both the expression of its VEGFR2 (KDR) receptor in endothelial cells, and of VEGF itself, by the enhancement of mitogenic activity.[45] Once bFGF induced the KDR expression, VEGF can significantly increase the expression of its receptor. In summary, VEGF cannot stimulate the expression of KDR under basal conditions due to the low expression of the receptor, and therefore the action of other factors such as bFGF is required.[46]

The invasive capacity of the endothelial cells was determined by the "wound healing" model using HUVEC cells (**Figure 8.3.A**). These results showed that a highly significant increase in the invasiveness of the sensitized or pre-treated cells with the ACP-NP when the stimulation was induced by the combination of VEGF extracellular Ca^{+2}. This increase led to a coordinated repair of the wound. The repair or filled area of the wound was faster in the presence of VEGF and Ca^{+2} compared to the presence of VEGF or Ca^{+2} separately (**Figure 8.3.A**). Logically, these results are closely related to the above discussed migration results (**Figure 8.2.B**).

Finally, the differentiation of endothelial HUVEC cells for tube-like formation (**Figure 8.3.B**) has been evaluated. The results showed that this morphology characterized by its length was directly dependent to the stimulation of extracellular Ca^{+2} in the pre-treated cells. The length of the tube-like significantly increased as the extracellular Ca^{+2} increased. Therefore, migration, invasiveness and differentiation of HUVEC endothelial cells sensitized or pre-treated with ACP-NP appear fundamental for cells to promote a malignancy phenotype.

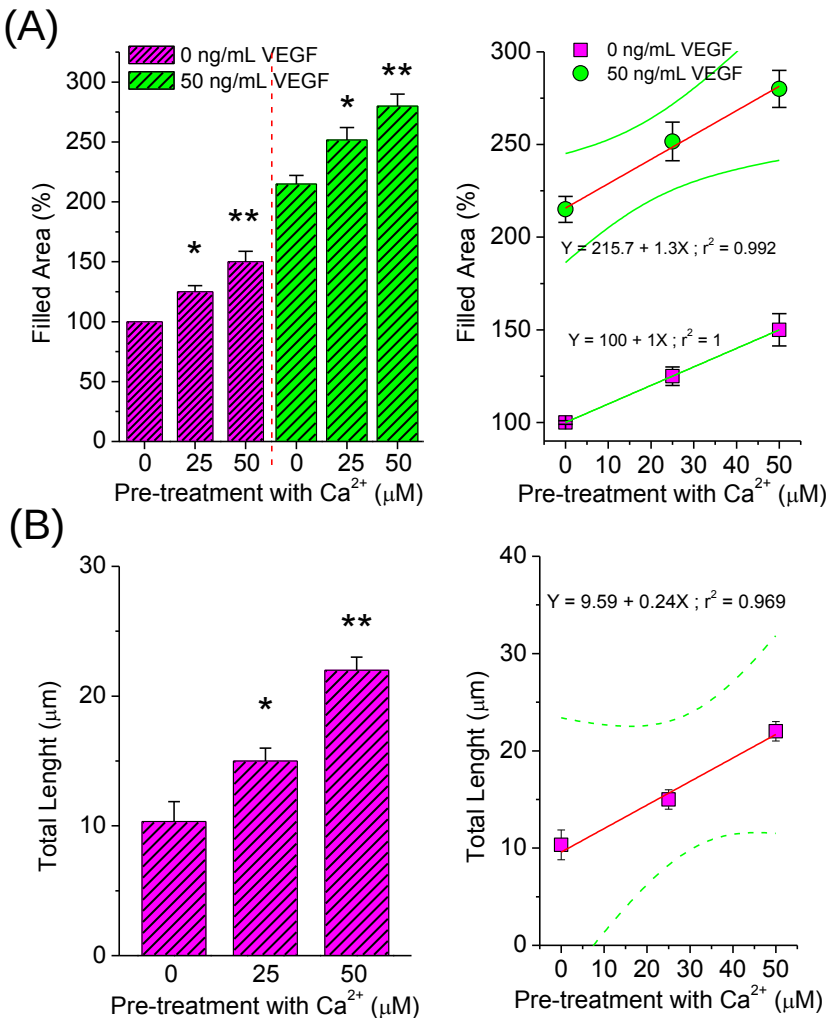

Figure 8.3. (A) In-vitro wound healing of HUVEC endothelial cells pre-treated with ACP-NP and stimulated with VEFG. (B) Effect of Ca^{+2} in the tube-like formation of HUVEC cells. The lineal representation shows the relation of clones with Ca^{+2} concentration. Green lines indicate the 95 % confidence interval. *p < 0.05 vs control (MCF-7 cells without Ca^{+2} pre-treatment), **p < 0.05 vs clone of MCF-7 cells pre-treated with 25 µM Ca^{+2}.

8.3.3. Effect of Ca^{+2} in fibroblast cells: Secreted factors for the stimulation of epithelial cells

Tumours are known as wounds that do not heal, a feature that implies that cells involved in angiogenesis and response to injury (*e.g.* endothelial and fibroblast cells) have a prominent role in the progression, growth and spread of cancer. Fibroblasts are associated with cancer cells at all stages of cancer progression, and their structural and functional contributions to this process are beginning to emerge. Fibroblast cells produce growth factors, chemokines and the extracellular matrix which facilitate the angiogenic

recruitment of endothelial cells and pericytes. Fibroblasts are therefore a key factor in the malignant progression of cancer and represent an important target for cancer therapies.[18-22]

Figure 8.4.A shows the interplay between fibroblasts and epithelial cells under the stimulation of extracellular Ca^{+2}. Specifically, conditioned media of COS-1 fibroblasts cells sensitized or pre-treated with ACP-NP (at concentration equivalent to Ca^{+2} of 0, 25 and 50 µM) were obtained after stimulation with different concentrations of extracellular Ca^{+2} (0, 25 and 50 µM Ca^{+2}). These conditioned media would represent the metabolic state of the pre-treated fibroblasts stimulated with extracellular Ca^{+2}. These media should contain the factors secreted by cells during their intracellular peak of Ca^{+2}. In this work we have evaluated the role of these factors to stimulate the migration of MCF-7 epithelial cells, which were also sensitized or pre-treated with ACP-NP (at concentration equivalent to Ca^{+2} of 0, 25 and 50 µM).

Results shown in **Figure 8.4.A** allow us to conclude that the conditioned media of COS-1 fibroblasts constitute a chemotactic stimulus for MCF-7 epithelial cells when were exposed to extracellular Ca^{+2}. Both the content of the factors secreted by the sensitized fibroblasts and the migratory activity of the sensitized MCF-7 epithelial cells were high when both cell types were exposed to 50 µM extracellular Ca^{+2} (*e.g.,* the migration of the MCF-7 cells under these conditions tripled the value of the migration in the conditions of the control, in the absence of extracellular Ca^{+2} for both types of cells). Finally, it can be indicated that the factors secreted by the fibroblasts linearly stimulate the migration of MCF-7 epithelial cells as a cellular response to extracellular Ca^{+2} exposure (**Figure 4A**). These results clearly demonstrate the interrelation between different cell types (*i.e.* fibroblast and epithelial) to establish a possible tumour tissue managed by an increase of intracellular Ca^{+2}.

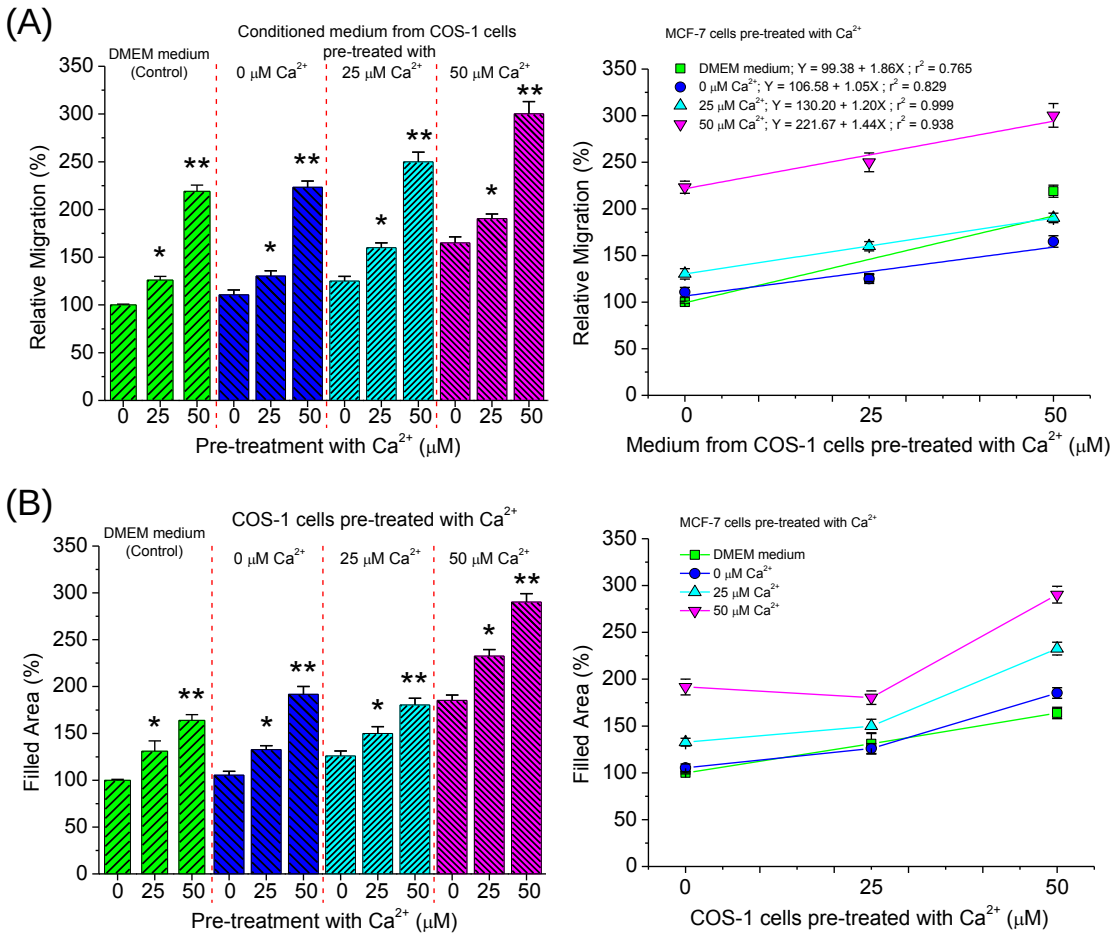

Figure 8.4. (A) Effect on the migration of the clones of MCF-7 cells caused by the conditioned medium of COS-1 fibroblast cells and their clones pre-treated with ACP-NP. (B) *In-vitro* wound healing promoted by co-cultures of clones of COS-1 fibroblasts and MCF-7 epithelial cells. Linear graphics are shown to support the indicated effects. *p < 0.05 vs control (MCF-7 cells without pre-treatment of Ca^{+2}), **p < 0.05 vs clone of MCF-7 pre-treated with 25 μM Ca^{+2}.

Interrelation between fibroblast and epithelial cells was also followed through the wound-healing assay with a co-culture of both sensitized or pre-treated fibroblast and epithelial cells to increase their intracellular Ca^{+2} levels. **Figure 8.4.B** demonstrated that the closed area of the wound caused by MCF-7 epithelial cells (control) was dependent of the extracellular stimulation of Ca^{+2}. Thus, an increase of 25 % and close to 75 % with respect to cells without extracellular stimulation of Ca^{+2} was observed for the wound healing when the extracellular Ca^{+2} stimuli was 25 and 50 μM, respectively. This result is in agreement with the increase of their migratory capacity in these same conditions (**Figure 8.1.C**).

Similar wound-healing results were obtained for the co-culture of fibroblast and epithelial cells (COS-1/MCF-7 cells) without pre-treating and stimulation with extracellular Ca^{+2}. A wound closure greater than the double of the closure observed in the absence of extracellular Ca^{+2} was reached with a concentration of 50 μM of extracellular Ca^{+2}. However, pre-treatment of fibroblasts and epithelial cells with ACP-NP (equivalent to 50 μM Ca^{+2}) before co-culturing of both cells produced a significant increase in the wound closure (*i.e.* with respect to epithelial controls and the fibroblast-epithelial co-culture without pre-treatment with Ca^{+2} nanoparticles). Interestingly, it has been observed that the highest wound-closure was achieved for the co-culture of pre-treated fibroblast and epithelial cells. Thus, COS-1/MCF-7 co-cultures of cells pre-treated with 50 μM ACP-NP, and were exposed to extracellular Ca^{+2} at concentration of 25 μM and 50 μM rendered double and triple wound-closure areas was with respect to that produced by co-culturing epithelial-fibroblasts without any pre-treatment.

Results pointed out an interrelation between fibroblast and epithelial cells with a clear stimulation of extracellular Ca^{+2} that occurs in a dose-response manner. Potential differential interactions between fibroblasts and epithelial cells (*e.g.* breast cancer cells) were highlighted in the study. As expected, fibroblasts were able to promote migration of MCF-7 cells in an indirect (**Figure 8.4.A**) or direct co-culture model (**Figure 8.4.B**).

8.4 CONCLUSIONS

The tumor is an abnormal mass formed by the alteration of the cellular balance between proliferation and cell death. A cancerous tumor becomes metastatic when the cells acquire the ability to migrate and increase their ability to invade other tissues. Additionally, as mentioned before, the tumor may involve different cell types in the malignant tissue. Many causes and risk factors have been associated with the malignancy of tumor and cancer cells. The intracellular Ca^{+2} participate in and regulate diverse cellular functions, deregulation could be a mechanism contributing to a tumor's malignancy. Therefore, understanding of the role of intracellular Ca^{+2} in various types of cancer.

In this paper, we have studied several markers of cellular malignancy in MCF-7 epithelial, HUVEC endothelial and COS-1 fibroblast cells. These cells were pre-treated with ACP-

NP that were internalized into the cells by endocytosis. Levels of intracellular Ca^{+2} were increased,[29] and as a consequence cells were sensitized by storage of cytosolic Ca^{+2}This pre-treatment was performed during 4 subcultures in order to establish sensitized clones with increasing levels of intracellular Ca^{+2}. The cellular responses were triggered by the direct exposure of the cells to extracellular Ca^{+2}. Results indicated that MCF-7 epithelial cells pre-treated or sensitized with Ca^{+2} showed lower expression of p53 pro-apoptotic protein and higher migratory activity. In the case of sensitized HUVEC endothelial cells, they showed less cellular adhesion to matrices of basal membrane proteins such as collagen, vitronectin, fibrinogen and fibronectin.

The migratory activity of HUVEC cells was stimulated in the presence of VEGF and inhibited by bFGF. The invasion capacity was also increased and additionally VEGF was able to stimulate this ability to invade. Finally, it can be remarked that cell differentiation to form tubes (like to blood vessels) was also increased. The sensitized COS-1 fibroblast cells were competent for the secretion of stimulating factors to the migration of MCF-7 epithelial cells and the co-culture of both cell types was observed to increase their invasiveness. In general, these results obtained with cells sensitized by the increase of intracellular Ca^{+2} transform the cells into clones with characteristics such as greater malignancy and tumour aggressiveness (**Figure 8.5**).

Intracellular Ca^{+2} also plays an essential role in the assembly of actin filaments and cytoskeleton reorganization. Ca^{+2} affects motility and cell migration and appears as a ubiquitous second messenger and a crucial regulator of cell migration.[2] Distribution changes in intracellular Ca^{+2} concentration have been well studied in healthy cells, but these regulatory processes are poorly understood in cancer cells. It is unclear if the increased cytosolic Ca^{+2} may play a role in up-regulation of glycolysis. However, most glycolytic enzymes bind to the cytoskeleton, and probably the increase of cytosolic Ca^{+2}might promote the assembly of cytoskeleton-bound glycolytic enzymes leading to higher glycolytic activity.

The p53 tumour suppressor protein is involved in several cellular processes that are critical for maintaining cellular homeostasis, including gene transcription, DNA repair, cell cycling, senescence, and apoptosis.[38,39] Compared with the information and knowledge available regarding the role of the p53 protein in apoptosis, the function of

p53 in cell differentiation is not well understood. Additional studies to examine the functional role of p53 in the differentiation of breast cancer cells will be needed for a better understanding of the complexity of p53 functions that are essential for maintaining cellular homeostasis.

Currently, the exploration of pro-cancer factors dependent on Ca^{+2} is needed to better understand its role in the origin, promotion and establishment of cancer. An interesting example within this new framework is the family of S100 proteins (a family of EF-hand Ca^{+2}-binding proteins). These proteins are excellent biomarkers and indicators of cancer prognosis,[47] but only in a few cases a functional significance has been proposed. For example, S100A4 expression is increased in many cancers, a feature that might be related to its ability to bind and inhibit wild-type p53.[47] S100A4 is also important in Ca^{+2}-dependent metastatic pathways.[48] S100A4 is localized to the nucleus, cytoplasm and the extracellular space, and it predominantly exists in cells as a symmetric homodimer that enables the simultaneous binding and the functional crosslinking of two target proteins in a calcium-dependent manner. Ca^{+2}-dependent regulation of S100A4 involves a conformational shift that occurs on Ca^{+2} binding and enables interactions with cytoskeletal proteins, including actin, nonmuscle myosin IIA and tropomyosin, resulting in increased cell migration.[49] S100A4 was shown to co-localize with its most common interaction partner, myosin heavy chain IIA, in lamellipodia structures in migrating breast cancer-derived cells.[50] Other molecular targets of S100A4 action involve the transmembrane protein tyrosine phosphatase and its interaction with liprin β1 protein, the leukocyte common antigen-related (LAR), and the tumor suppressor protein p53.[49] S100A4 has also been implicated in Epithelial-Mesenchymal Transition (EMT).[51]

It could be indicated that the increased intracellular Ca^{+2} concentration in cancer cells promotes migration leading to more aggressive malignant cellular behaviors and metastasis. It should be pointed out, however, that because elevated cytosolic Ca^{+2} concentrations may also cause cellular damage and induce senescence. Thus, those cancer cells that are capable of mobilizing their antioxidant systems and other regulatory mechanisms are more able to effectively counteract the adverse effects of increased intracellular Ca^{+2}, reestablish redox balance, and emerge as highly malignant clones.

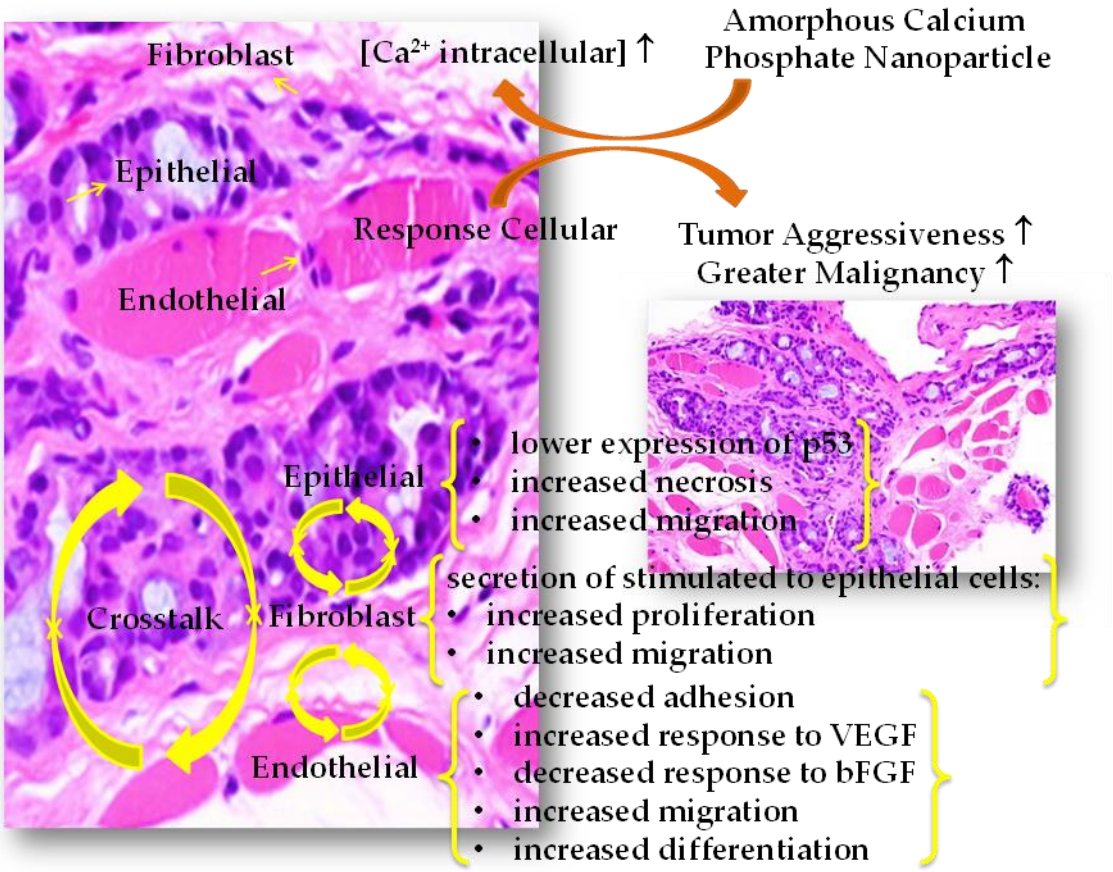

Figure 8.5. Role of the intracellular calcium (*i.e.* from ACP-NP internalized by endocytosis) is the increased malignancy and tumor aggressiveness. Crosstalk between the different cell types as epithelial, endothelial and fibroblast cells. Images of a prostate adenocarcinoma.

8.5 REFERENCES

1. Hanahan, D. & Weinberg, R. A. Hallmarks of cancer: the next generation. *Cell*. **144(5)**: 646-674 (2011).
2. Prevarskaya, N., Skryma, R. & Shuma, Y. Calcium in tumour metastasis: new roles for known actors. *Nat Rev Cancer*. **11(8)**:609-618 (2011).
3. Stewart, T. A., Yapa, K. T. & Monteith, G. R. Altered calcium signaling in cancer cells. *Biochem Biophys Acta-Biomembr* (2014).
4. Roderick, H. L. & Cook, S. J. Ca^{2+} signalling checkpoints in cancer: remodelling Ca^{2+} for cancer cell proliferation and survival. *Nat Rev Cancer*. **8(5)**, 361-375 (2008).
5. Monteith, G. R., Davis, F. M. & Roberts-Thomson, S. J. Calcium channels and pumps in cancer: changes and consequences. *J Biol Chem*. **287(38)**: 31666-31673 (2012).
6. Korosec, B., Glavac, D., Rott, T. Alterations in the ATP2A2 gene in correlation with colon and lung cancer. *Cancer Genet. Cytogenet*. **171**, 105-111 (2006).
7. Prasad, V. *et al*. Haploinsufficiency, encoding the sarco(endo)plasmic reticulum Ca^{2+}-ATPase isoform 2 Ca^{2+} pump, predisposes mice to squamous cell tumors via a novel mode of cancer susceptibility. *Cancer Res*. **65**, 8655-8661 (2005).
8. Coussens, L.M. & Werb, Z. Inflammation and cancer. *Nature*, **420**:860-867 (2002).
9. Hanahan, D. & Folkman, J. Patterns and emerging mechanisms of angiogenesis switch during tumorigenesis. *Cell*. **86**, 353-364 (1996).
10. Aird, W.C. Phenotypic heterogeneity of the endothelium: I. Structure, function, and mechanisms. *Cir Res*. **100**:158-173 (2007).
11. Carmeliet, P. Angiogenesis in health and disease. *Nat. Med*. **9**, 653-660 (2003).
12. Yardin, Y. & Ulrich, A. Growth factor receptor tyrosine kinases.*Annu. Rev. Biochem*. **56**, 443-447 (1988).
13. Meldolesi, J., Clementi, E., Fusolato, C., Zacchetti, D. & Pozzan, T. Ca^{2+} influx following receptor activation. *Trends Pharmacol. Sci*. **12**, 289-292 (1991).
14. Berridge, M. J. & Irvine, R.F. Inositol phosphates and cell signalling. Nature (London). **341**, 197-205 (1989).
15. Ling, L., Waratmann, M., Lin, A. Y., Knopf, J. L., Seth, A. & Davis, R. J. cPLA2 is phosphorylated and activated by MAP kinase. *Cell*. **72**, 269-278 (1993).
16. Gusovsky, F., Lueders, J. E., Kohn, E. C. & Felder, C. C. Muscarinic receptor-mediated tyrosine phosphorylation of phospholipase C-gamma. An alternative mechanism for cholinergic-induced phosphoinositide breakdown. *J. Biol. Chem*. **268**, 7768-7772 (1993).

17. Felder, C. C., MacArthur, L., Ma, L., Gusovsky, F. & Kohn, E C. Tumor-suppressor function of muscarinic acetylcholine receptors is associated with activation of receptor-operated calcium influx. *Proc. Natl. Acad. Sci. USA*. **90**, 1706-1710 (1993).

18. Kalluri, R. & Zeisberg, M. Fibroblasts in Cancer. *Nature Reviews Cancer*. Volume **6**, 392-406 (2006).

19. Declerck, Y A. Interactions between tumor cells and stromal cells and proteolytic modification of the extracellular matrix by metalloproteinases in cancer. *Eur J Cancer*. **36**, 1258-1268 (2000).

20. Fidler, I. J. The pathogenesis of cancer metastasis: the second 'seed and soil' hypothesis revisited. *Nat Rev Cancer*. **3**, 453-458 (2003).

21. Liotta, L. A. & Kohn, E. C. The microenvironment of the tumour-host interface. *Nature*. **411**, 375-379 (2001).

22. Radisky, D., Hagros, C. & Bissell, M. J. Tumours are unique organs defined by abnormal signaling and context. *Semin Cancer Biol*. **11**, 87-95 (2011).

23. Bhowmick, N. A. & Moses, H. L. Tumor-stroma interactions. *Curr. Opin. Genet. Dev*. **15**, 97-101 (2005).

24. Olumi, A. F. *et al.* Carcinoma-associated Fibroblasts Direct Tumor Progression of Initiated Human Prostatic Epithelium. *Cancer Res*. **59**, 5002-5011 (1999).

25. De Wever, O. *et al*. Tenascin-C and SF/HGF produced by myofibroblasts in vitro provide convergent pro-invasive signals to human colon cancer cells through Rho A and Rac. *FASEB, J*. **18**, 1026-8 (2004).

26. Orimo, A. Stromal fibroblasts present in invasive human breast carcinomas promote tumor growth and angiogenesis through elevated SDF-1/CXCL 12 secretion. *Cell*. **121**, 335-348 (2005).

27. Giannoni, E. *et al*. Reciprocal activation of prostate cells and cancer-associated fibroblasts stimulates epithelial-mesenchymal transition and cancer stemness. *Cancer Res*. **70**, 6945-56 (2010).

28. Lebret, S. C. & Newgreen, D. F. Induction of epithelial to mesenchymal transition in PMC42-LA human breast carcinoma cells by carcinoma-associated fibroblast secreted factors. *Breast Cancer Res*. **9**, R19 (2007).

29. Rivas, M., Turon, P., Alemán, C., Puiggalí, J. & del Valle, L.J. Intracellular calcium deregulation mediated by hydroxyapatite nanoparticles. *Journal of Biological Chemistry*. Submitted. Revision process (2019).

30. Gesing, A. & Karbownik, M. Influence of hemithyroidectomy on bromodeoxyuridine incorporation into DNA of rat thyroid follicular cells. *Endocr Regul*. **35,** 25-30 (2001).

31. Lloveras, B. & Edgerton, S. Evaluation of in vitro bromodeoxyuridine labeling of breast carcinomas with the use of a commercial kit. *Am J Clin Pathol*. **95**, 41-47 (1991).

32. Gannon, J. V. & Greaves, R. Activating mutations in p53 produce a common conformational effect. A monoclonal antibody specific for the mutant form. *EMBO J*. **9**, 1595-1602 (1990).

33. Harlow, E. E. & Lane, D. P. Antibodies: A Laboratory Manual. *New York: Cold Spring Harbor Laboratory Press* (1988).

34. Keely, P. J. Cdc42 and Rac1 induce integrin-mediated cell motility and invasiveness through P7(3) K. *Nature*. **390**, 632-636 (1997).

35. Marshall, J. F., Rutherford, D. C., McCartney, A. C. *et al.* Alpha v beta 1 is a receptor for vitronectin and fibrinogen, and acts with alpha 5 beta 1 to mediate spreading on fibronectin. *J Cell Sci*. **108** (Pt 3): 1227-38 (1995).

36. Dimmeler, S., Dernbach, E. & Zeiher, A. M. Phosphorylation of the endothelial nitric oxide synthase at ser-1177 is required for VEFG-induced endothelial cell migration. *FEBS Lett*. **477**, 258-262 (2000).

37. Ishida, T., Kundu, R. K., Yang, E. *et al.* Targeted disruption of endothelial cell-selective adhesion molecule inhibits angiogenic processes in vitro and in vivo. *J Biol Chem*. **278**: 34598-604 (2003).

38. Vogelstein, B. & Kinzler, K. W. p53 function and dysfunction. *Cell*. **70**:523-526 (1992).

39. Levine, A. J. p53, the cellular gatekeeper for growth and division. *Cell*. **88**:323-331 (1997).

40. Cole, K. A. & Kohn, E. C. Calcium-mediated signal transduction: biology, biochemistry, and therapy. *Cancer Metastasis Rev*. **13**, 33-41 (1994).

41. Savarase, D. M. F., Russell, J. T., Fatatis, A. & Liotta, L. A. Type IV collagen stimulates an increase in intracellular calcium. Potential role in tumor cell motility. J. *Biol. Chem.* **267**, 21928-21935 (1992).

42. Kohn, E. C., Felder, C. C., Jacobs, W., Holmes, K. A., Day, A. F., Freer, R. & Liotta, L. A. Structure-function analysis of signal and growth inhibition by carboxyamido-triazole, CAI. *Cancer Res*. **54**, 935-942 (1994).

43. Kohn, E. C. & Liotta, L. A. L651582: a novel antiproliferative and antimetastasis agent. *J. Natl. Cancer Inst*. **82**, 54-60 (1990).

44. Sagar, S. M. *et al.* Natural health products that inhibit angiogenesis: a potential source for investigational new agents to treat cancer-Part 1. *Curr Oncol*. Feb **13(1)**: 14-26 (2006).

45. Hata, Y., Rook, S. L. & Aiello, L. P. Basic fibroblast growth factor induces expression of VEGF receptor KDR through a protein kinase C and p44/p42 mitogen-activated protein kinase-dependent pathway. *Diabetes*. **48**, 1145-1155 (1999).

46. Gabler, C., Plath-Gabler, A., Killian, G. J., Berisha, B. & Schamns, D. Expression pattern of fibroblast growth factor (FGF) and vascular endothelial growth factor (VEGF) system members in bovine corpus luteum endothelial cells during treatment with FGF-2, VEGF or estradiol. *Reprod. Dormest. Anim*. **39**, 321-327 (2004).

47. Emberley, E. D., Murphy, L. C. & Watson, P. H. S100 proteins and their influence on pro-survival pathways in cancer. *Biochem. Cell Bio*. **82**, 502-515 (2004).

48. Boye, K. & Maelandsimo, G. M. S100A4 and metastasis: a small actor playing many roles. *Am. J. Pathol*. **176**, 528-535 (2010).

49. Tarabykina, S., *et al.* Metastasis-associated protein S100A4: spotlight on its role in cell migration. *Curr. Cancer Drug Targets*. **7**, 217-228 (2007).

50. Kim, E. J. & Helfman, D. M. Characterization of the metastasis-associated protein, S100A4. Roles of calcium binding and dimerization in cellular localization and interaction with myosin. *J. Biol. Chem*. **278**, 3063-3073 (2003).

9.

LOADING OF ANTIBIOTIC INTO BIOCOATED HYDROXYAPATITE NANOPARTICLES: SMART ANTITUMOR PLATFORMS WITH REGULATED RELEASE

In this research we propose a nanoplatform for anticancer therapy that is based on the combination of three components: 1) an antibiotic to target selectively the mitochondria of cancer cells, inhibiting their functions; 2) mineral nanoparticles (NPs) able to encapsulate the antibiotic and to enter into the cells across the cell membrane; and 3) a biocoating to protect the antibiotic during and/or after its regulated release, increasing its therapeutic efficacy. Chloramphenicol (CAM), a prototypical wide-spectrum antibiotic, has been used to induce mitochondrial-dysfunctions in cancer cells. Different *in situ* synthetic strategies have been tested to load such antibiotic into both crystalline hydroxyapatite (cHAp) and amorphous calcium phosphate (ACP) NPs. cHAp NPs showed higher loading capacity, in terms of encapsulation and superficial adsorption of CAM, and slower antibiotic release than ACP NPs. On the other hand, the protecting role played by biocoatings based on pyrophosphate and, especially, triphosphate was greater than biophosphonates, the anticancer therapeutic efficacy of CAM being maximized by the formers. *In vitro* studies using healthy and cancer cell lines have demonstrated that *in situ* CAM-loaded cHAp NPs coated with triphosphate selectively kill a great population of cancer cells, evidencing the potential of this nanoplatform in cancer treatment.

9.1 INTRODUCTION

Bone is a calcified tissue composed of 50 to 70 % mineral, 20 to 40 % organic matrix, 5 to 10 % water, and < 3 % lipids. The mineral content of bone is mostly hydroxyapatite (HAp) [$Ca_{10}(PO_4)_6\ (OH)_2$], with small amounts of carbonate, magnesium, and acid phosphate. Compared to geologic HAp crystals, bone HAp crystals are very small, measuring only approximately 200 nm in their longest dimension. The solubility of these small crystals is higher than that of geologic HAp crystals, allowing them to support metabolism. Currently, synthetic HAp is one of the most widely used biomaterials for reconstruction of the skeleton due to the lack of local or systemic toxicity in combination with its osteoconductive properties.[1-6]

On the other hand, antibiotics that target bacterial ribosome have a common mechanism of action: they are protein synthesis inhibitors.[7] The main target for such group of antibiotics is the peptidyl transferase center,[8] which forms peptide bonds between adjacent amino acids using tRNA during the protein biosynthesis.[9] Accordingly, the therapeutic success of ribosomal antibiotics killing bacteria is based on the discrimination between prokaryotic and eukaryotic ribosome structures, which exhibit differences in size, sequence, structure, and the ratio of protein to RNA.[10,11] Chloramphenicol (CAM) is a prototypical wide-spectrum antibiotic that obstructs protein synthesis and blocks essential ribosomal functions.[12-14] CAM consists of a *p*-nitrophenyl ring attached to a dichloroacetyl tail via a 2-amino-1,3-propanediol moiety (**Figure 9.1**). Thus, CAM incorporates itself to the C-terminus of a growing peptide chain, causing the premature release of the incomplete peptide.

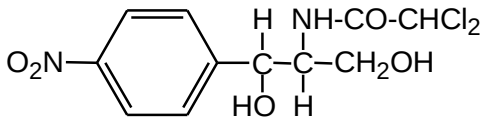

Figure 9.1. Chemical structure of CAM

On the other hand, a growing body of experimental evidences has shown that some antibiotics may inhibit mitochondrial functions of eukaryotic cells, causing changes at both molecular and physiological levels that affect the life and death of cells.[15,16] This has been attributed to the fact that mitochondrial ribosomes resemble many features of bacterial ribosomes. The metabolism of cancer cells, especially of cancer stem cells, is

fundamentally regulated by an abundance of mitochondria compared to normal cells, including normal stem cells.[17] Thus, the low energy efficiency of the mostly anaerobic metabolism of cancer cells is compensated with more mitochondria than normal cells, which exhibit an aerobic metabolism. Accordingly, clinical oncologists have recently proposed the use of antibiotics as a part of anticancer therapy and target cancer metabolisms.[18-21] Within this context, in a recent study Lisanti *et al*.[21] proved that CAM inhibits the formation of tumor stem cells, which are the responsible of metastasis by giving growth to new tumors.[22] The anticancer activity of CAM and other antibiotics reached great repercussion for its implications in clinical oncology.[18]

Synthetic HAp has an enormous capacity not only to encapsulate biomolecules (*e.g.* nucleic acids and proteins[23,24]) but also to adsorb a variety bio-organic and inorganic chemical species (*e.g.* DNA[25], amino acids,[26,27] phosphate- and biophosphonate-derivatives[28]). HAp-based platforms have been used for bone regeneration through adsorbing inorganic polyphosphates from the metabolism onto the mineral,[29-32] for the fight against different bone diseases (*e.g*. osteoporosis, Paget disease of bone and malignancies metastatic to bone) through the delivery of biophosphonates as pharmacological agents,[33,34] and for gene delivery by transfecting cells, as HAp is able to adsorb, transport and deliver nucleic acids inside the cell nucleus.[25,35,36]

The current study focuses on antitumoral nanoplatforms that combine the ability of CAM to inhibit the mitochondrial functions and the capacity of HAp to encapsulate biomolecules and enter into cells. For this purpose, CAM-loaded mineral nanoparticles (NPs) covered with an inorganic biocoating have been prepared and characterized. After this, we have demonstrated that such biocoated CAM-containing systems satisfy the most important criteria required by therapeutic nanoplatforms (*e.g.* the loaded antibiotic preserves the bioactive conformation and its release is regulated by the physical properties of both the NPs and the biocoating). Finally, different inhibitory effects of the proposed antitumoral nanoplatforms have been examined on both normal cells (HUVEC endothelial line and COS-1 fibroblast line) and cancer cells (MCF-7 breast cancer line and MIA PaCa-2 pancreas cancer line). The selectivity of biocoated HAp NPs loaded with CAM on killing cancer cells proves their potential application in cancer treatment.

9.2 EXPERIMENTAL SECTION

9.2.1 Materials

Tetrasodium pyrophosphate ($P_2O_7^{4-}$), sodium triphosphate (polyP), ATMP, ammonium phosphate dibasic [$(NH_4)_2HPO_4$; purity ≥ 99.0 %] and ammonium hydroxide solution 30 % (NH_4OH; purity: 28-30 %) were purchased from Sigma-Aldrich. Calcium nitrate [$Ca(NO_3)_2$; purity ≥ 99.0 %] was purchased from Panreac (Barcelona, Spain). CAM ($C_{11}H_{12}Cl_2N_2O_5$) was purchased from Sigma-Aldrich. Ethanol (C_2H_5OH; purity ≥ 99.5 %) was obtained from Scharlab (Barcelona, Spain).

Cell line HUVEC (human umbilical vein endothelial cells) was obtained from Lonza (Lonza CC-2517), while COS-1 (green monkey kidney fibroblast cells) and MCF-7 (epithelial cells from human breast adenocarcinoma) and MIA PaCa-2 (epithelial cells from human pancreas carcinoma) were purchased from ATCC. Dulbecco´s Modified Eagle´s medium (DMEM) was purchased from ATCC. Fetal bovine serum (FBS), penicillin/streptomycin (pen/strep) and L-glutamine were all purchased from Gibco. EGM-2 Bulletkit optimized for certain HUVECs was purchased from Lonza. 3-(4,5-dimethylthiazol-2-yl)-2,5-diphenyltetrazolium bromide (MTT, 97.5 %) and trypsin-EDTA solution (0.05 % trypsin, 0.02 % EDTA) were purchased from Sigma-Aldrich.

9.2.2 Synthesis

Synthesis of HAp. Although amorphous calcium phosphate (ACP) and crystalline HAp (cHAp) samples were prepared using a previously described procedure,[37,38] the experimental conditions of the reaction mixture were changed. The reagent conditions were adjusted to get a Ca/P ratio of 1.67. In all cases 15 mL of 0.5 M $(NH_4)_2HPO_4$; in de-ionized water (pH adjusted to 11 with an ammonia 30 % w/w solution) were added drop-wise (rate of 2 mL/min) and under agitation (400 rpm) to 25 mL of 0.5 M $Ca(NO_3)_2$ in ethanol. The reaction mixture was stirred 1 h (400 rpm) at room temperature. In the case of ACP the resultant suspension was aged for 24 h at 37 ºC, whereas hydrothermal conditions were applied during 24 h for cHAp. In both cases, the precipitate was separated by centrifugation and washed sequentially (twice) with de-ionized water and a 60/40 v/v mixture of ethanol/water. A white powder was obtained after freeze-drying. Particles were filtered through a 0.22 µm filter (Millipore, Billerica,

MA). Filtration was performed at a flow rate of 1 mL/min using a 10 mL syringe and concentration of the particles was determined using an IEC MultiRF centrifuge (Thermo IEC, Needham Heights, MA, USA).

In situ preparation of CAM–loaded HAp nanoparticles. In order to load CAM, four different strategies were tested- More specifically, these consisted in the addition of 0.517 or 4.325 mM CAM into the $(NH_4)_2HPO_4$ or $Ca(NO_3)_2$ solution (hereafter denoted Pho- or Ca^{2+}-path, respectively) combined with the conditions described above for the preparation of cHAp and ACP (*i.e.* hydrothermal conditions and aging at atmospheric pressure and 37 ºC, respectively).

Ex-situ preparation of CAM–adsorbed control nanoparticles. Control nanoparticles were prepared by incubating a 150 mM CAM working solution (pH 7) onto already synthesized mineral. More specifically, 500 μL of the working solution were deposited onto 50 mg of cHAp or ACP. After overnight agitation at 25 ºC, adducts were separated by centrifugation at 6500 rpm during 5 minutes at 4 ºC. Sediments were re-suspended in distilled water. After this process, which was repeated two times, the obtained pellets were frozen at –80 ºC for 3 h and, subsequently, the humidity was removed using a lyophilizer.

9.2.3 Measurements

Scanning electron microscopy (SEM) and energy dispersive X-ray (EDX) spectroscopy: Samples of 10 μL from 1 mg/mL suspensions in milliQ water were put on a silicon support mounted with silver paint on pin stubs of aluminium, and sputter-coated with a thin layer of carbon to prevent sample charging problems. SEM studies were carried out using a Focused Ion Beam Zeiss Neon40 microscope operating at 20 kV, equipped with an EDX spectroscopy system. The latter technique was used to estimate the composition of the HAp and Mg-HAp on samples without carbon coating.

Loading efficiency: Distribution into encapsulated and adsorbed antibiotic. The encapsulation and adsorption efficiency of cHAp and ACP samples were determined by UV-vis spectrophotometry. CAM-loaded mineral samples (20 mg) were added to a phosphate buffered saline (PBS) solution supplemented with 70 % v/v of ethanol (PBS-EtOH) for extraction. The adsorbed antibiotic was separated by centrifugation at 10,000 rpm and 4 ºC. The pellets of each Eppendorf were washed with 200 μL of PBS-EtOH, vortexed and, finally, quantified by UV–vis spectroscopy. After this, mineral samples

without adsorbed CAM were dissolved in a 100 mM HCl: 50 mM $NaCl$ mixture and the amount of antibiotic encapsulated during the loading process quantified. The amount of loaded CAM was calculated (in mg) as the difference between the total amount of antibiotic used to prepare loaded mineral and that recovered by PBS-EtOH extraction.

Spectroscopic analyses were performed using an UV-3600 (Shimadzu) UV-Vis/NIR spectrophotometer controlled using UVProbe 2.31 software. Spectra of homogenized samples were recorded in the 200–400 nm range with a bandwidth of 0.2 nm and scan speed of 600 nm/min.

FTIR spectroscopy. Infrared absorption spectra were recorded with a Fourier Transform FTIR 4100 Jasco spectrometer in the 1800-700 cm^{-1} range. A Specac model MKII Golden Gate attenuated total reflection (ATR) equipment with a heated Diamond ATR Top-Plate was used.

X-Ray diffraction. Crystallinity was studied by wide angle X-ray diffraction (WAXD). Patterns were acquired using a Bruker D8 Advance model with CuK_α radiation ($\lambda = 0.1542$ nm) and geometry of Bragg-Bretano, θ –2θ. A one-dimensional Lynx Eye detector was employed. Samples were run at 40 kV and 40 mA, with a 2θ range of 5 º– 60º, measurement steps of 0.02 º, and time/step of 2– 8 s. Diffraction profiles were processed using PeakFit v4 software (Jandel Scientific Software) and the graphical representation performed with OriginPro v8 software (OriginLab Corporation, USA).

The crystallite size (*L*) in the direction representative to the (211) planes of samples was derived from the X-ray diffraction line broadening measurement using the Scherrer equation:[39]

$$L = \frac{0.9\lambda}{\beta cos\theta} \quad (1)$$

where λ is the wavelength (CuK_α), β is the full width at half maximum height of the (211) line, θ is the diffraction angle and 0.9 is a shape factor. The crystallinity (χ_c) was obtained using the following Eqn:[40]

$$\chi_c = 1 - \frac{V_{112/300}}{I_{300}} \quad (2)$$

where I_{300} is the intensity of the (300) reflection and $V_{112/300}$ is the intensity of the hollow between the (112) and (300) reflections, which disappears in non-crystalline samples.

Morphological characterization. Transmission electron microscopy (TEM) and scanning electron microscopy (SEM) were used for the morphological characterization of the different mineral samples. TEM images were obtained using a Philips TECNAI 10 electron microscope operating at 80 kV for a bright field mode. Micrographs were taken with an SIS Mega View II digital camera. Nanoparticles were deposited on carbon coated grids.

SEM studies were carried out using a Focused Ion Beam Zeiss Neon40 microscope operating at 20 kV, equipped with an energy dispersive X-ray (EDX) spectroscopy system. Samples were deposited on a silicon disc mounted with silver paint on pin stubs of aluminum, and sputter-coated with a thin layer of carbon to prevent sample charging problems.

Adsorption of biophosphates and biophosphonate onto CAM-loaded mineral nanoparticles. CAM-loaded ACP and cHAp nanoparticles were prepared using the above described procedure. After this, 500 µL of working aqueous solution, which contained 12.5 mM of $P_2O_7^{4-}$, polyP or ATMP, were deposited onto 50 mg of the loaded sample. The pH of the three working solutions considered in this work was 7. After overnight agitation at 25 ºC, adducts were separated by centrifugation at 6500 rpm during 5 minutes at 4 ºC. Sediments were re-suspended in distilled water. After this process, which was repeated two times, the obtained pellets were frozen at −80 ºC for 3 h and, subsequently, the humidity was removed using a lyophilizer.

Bioactivity of chloramphenicol: Inhibition of bacterial growth. Assays to evaluate the bactericidal activity of the loaded antibiotic were performed with strains of *Escherichia coli* (*E. coli*). For this purpose, 10 mL of a culture grown during 16 h in the appropriated synthetic medium were transferred to a 1 L flask containing 500 mL of fresh medium. This culture was incubated in a water bath at 37 ºC and its growth was followed turbidimetrically at 420 nm until the early logarithmic phase was reached. Hopps *et al*.[41]

demonstrated that the number of cells present in an early logarithmic phase culture does not influence the minimal inhibitory concentration of CAM. Aliquots were quickly distributed to sterile cuvettes containing the desired CAM concentration, which ranged from 0.039 to 10 µg/mL. The cuvettes were then incubated at 34 ºC for 3 h period in a water bath equipped with forced circulation. Optical densities of each cuvette were read in a UV-3600 (Shimadzu) UV-Vis-NIR spectrophotometer at a wave length of 420 nm.

Release experiments. Controlled release measurements were made with weighted HAp samples. These were incubated at 37 ºC in an orbital shaker at 60 rpm in different solvents. Four release media were used in this work: 1) PBS; 2) HUVEC cells culture medium; 3) COS-1 cells culture medium; and 4) MCF-7 cells culture medium. The amount of released CAM was evaluated by UV spectroscopy using a UV-3600 (Shimadzu) UV-Vis-NIR spectrophotometer controlled by the UVProbe 2.31 software. Calibration curves were obtained by plotting the absorbance measured at 283 nm against the CAM concentration. Samples were drawn from the release medium at predetermined intervals and returned to the release vessel after measuring the absorbance. All antibiotic release tests were carried out using six replicas to control the homogeneity of the release, results being averaged. The total CAM content in the mineral samples was determined after their dissolution in a 100 mM HCl solution with 50 mM $NaCl$.

Cell culture conditions. MCF-7, COS-1 and MIA PaCa-2 cells were cultured in DMEM supplemented with 10% FBS, 1% pen/strep and 2 mmol/L L-glutamine. HUVEC cells were cultured in EGM-2 Bulletkit. MCF-7, COS-1, MIA PaCa-2 and HUVEC cells were cultured in 25 T-flask at 37 º C with 5 % CO_2 95 % air and complete humidity. Once reached ~ 90 % confluency, they were detached using 0.05 % trypsin-EDTA. Then, cells were re-suspended and added onto 96-well-plate by an 8-channel pipette.

Cytotoxic response of HUVEC, COS-1, MCF-7 and MIA PaCa-2 cell lines. Different concentrations of CAM were placed in plates of 24 wells and sterilized using UV-light for 15 min in a laminar flux cabinet. Controls were simultaneously performed by culturing cells on the surface of the tissue culture polystyrene (TCPS) plates. An aliquot of 50 µL containing 1×10^4 cells was deposited onto each sample, which was subsequently incubated under culture conditions for 30 min. Finally, 500 µL of the culture medium were added to each well. Cytotoxicity was determined after both 24 and 48 h of culture. All

viability measures were relative to TCPS used as control (*i.e*. 100 %). Viability for cytotoxicity was evaluated by the colorimetric MTT assay (see below).

Electroporation protocol and cell viability. Electroporation was performed using a BTX T820 square wave electroporator (BTX Harvard Apparatus). Electroporation parameters, which depended on the cell line, were optimized for high permeabilization and low cellular death by electroporation alone. The resulting parameters were as follows: 8 pulses of 99 µs with 1.0 kV/cm and 1 Hz for HUVEC cells, 8 pulses of 99 µs with 1.2 kV/cm and 1 Hz for COS-1 cells, and 8 pulses of 99 µs with 1.4 kV/cm and 1 Hz for MCF-7 and MIA PaCa-2 cells.

Cells were first trypsinized and then the trypsin inactivated with FBS. For harvesting, cells were centrifuging 5 min at 1000 rpm and the supernatant was removed. After this, cells were diluted in HEPES buffer (10 mM HEPES (Lonza), 250 mM sucrose and 1 mM $\mathrm{MgCl_2}$ in sterile water). The latter buffer, which does not contain phosphate, was used to prevent the precipitation of calcium phosphate. Subsequently, 270 µL of a medium with $6.1 \cdot 10^6$ cells/mL (cooled cells- approximately 8 ºC) were electroporated in presence of 8.43 mM CAM(Ca)/cHAp or CAM(Ca)/ACP NPs, which corresponds to a concentration of 100 µM CAM, using 4 mm cuvettes (Molecular BioProducts, Inc.). After electroporation, cells were incubated 20 min at 37 ºC and 5 % $\mathrm{CO_2}$. Subsequently, they were diluted in culture medium and seeded in 96-well plates (10^4 cells/200 µl). Viability of the cells following treatment with electroporation in the presence of CAM and cHAp or ACP, was measured using the MTT assay (see below). The MTT assay was performed according to the manufacturer´s protocol (Invitrogen Biosourde, USA) assay after 6, 12, 24, 48, 72, 96 and 120 h of incubation.

Evaluation of cell proliferation. Cellular proliferation was evaluated by the colorimetric MTT assay. This assay measures the ability of the mitochondrial dehydrogenase enzyme of viable cells to cleave the tetrazolium rings of the MTT and form formazan crystals, which are impermeable to cell membranes and, therefore, are accumulated in healthy cells. This process is detected by a color change: the characteristic pale yellow of MTT transforms into the dark-blue of formazan crystals.

Specifically, MTT solution (Roche 11465007001) was prepared at 1 mg/mL in PBS and was filtered using a 0.2 µm filter. Then, 50 µL of MTT and 200 µL of DMEM without phenol red were added into each well (96-well plate) with the obvious exception of the

cell-free blank wells. Cells were incubated for 4 h at 37 ºC with 5 % CO_2, 95 % air and complete humidity. After 4 h, the MTT solution was removed and replaced with 200 µL of DMSO and 25 µL of Sorenson´s glycine buffer (glycine 0.1 M, $NaCl$ 0.1 M, pH 10.5 with 0.1 M $NaOH$). The plate was further incubated for 5 min at room temperature and the absorbance at 570 nm was measured using a microplate reader (Biochrom EZ Read 400, Biochrom).

9.3 RESULTS AND DISCUSSION

9.3.1 Chloramphenicol-loaded hydroxyapatite: Preparation and characterization

Because of their different characteristics and properties, both crystalline HAp (cHAp) and amorphous calcium phosphate (ACP) NPs have been considered for this study. The experimental conditions used to prepare unloaded cHAp and ACP NPs[25,28] were adapted for the in situ loading of CAM. In both cases a 0.5 M $(NH_4)_2HPO_4$ aqueous solution was added drop-wise and under agitation to a 0.5 M $Ca(NO_3)_2$ ethanol solution, reagents being adjusted to get a Ca/P ratio of 1.67. The resultant suspension was aged for 24 h at 37 ºC to produce ACP, whereas cHAp was obtained by applying hydrothermal conditions during 24 h. Details of the experimental conditions and procedures are provided in the experimental section.

CAM-loaded NPs were prepared using four different in situ loading strategies: 2 minerals (cHAp or ACP) × 2 loading paths of the antibiotic into the corresponding $(NH_4)_2HPO_4$ or $Ca(NO_3)_2$ feeding solution (Pho- or Ca-path, respectively) = 4 strategies. The nomenclature used for the resulting NPs is indicated in **Figure 9.2.**

The loading efficiency (L_{Eff}), which is expected to be sensitive to the path because of the different strength of CAM$\cdots PO_4^{3-}$ and CAM$\cdots Ca^{2+}$ interactions, was evaluated by UV-vis spectroscopy. The *in situ* loading strategies used in this work cause both the entrapment of CAM inside the mineral matrix (*i.e.* encapsulation or mineralization) and the adsorption of CAM on the surface mineral NPs. In order to distinguish between such two situations, the L_{Eff} was determined considering: (i) the CAM extracted from the mineral surface by washing with a phosphate buffered saline (PBS) solution

supplemented with 70 % v/v ethanol (PBS−EtOH) during several hours; and (ii) the CAM encapsulated into mineral NPs that, after washing as in (i), were dissolved in a 100 mM HCl: 50 mM NaCl mixture. The UV-vis spectra of samples coming from (i) and (ii) showed the absorption band of the p-nitrophenyl chromophore (**Figure 9.1**) at around 278 nm.[42] The intensity of the peaks increased gradually with the CAM concentration enabling calibration in a linear model (**Figure 9.3**).

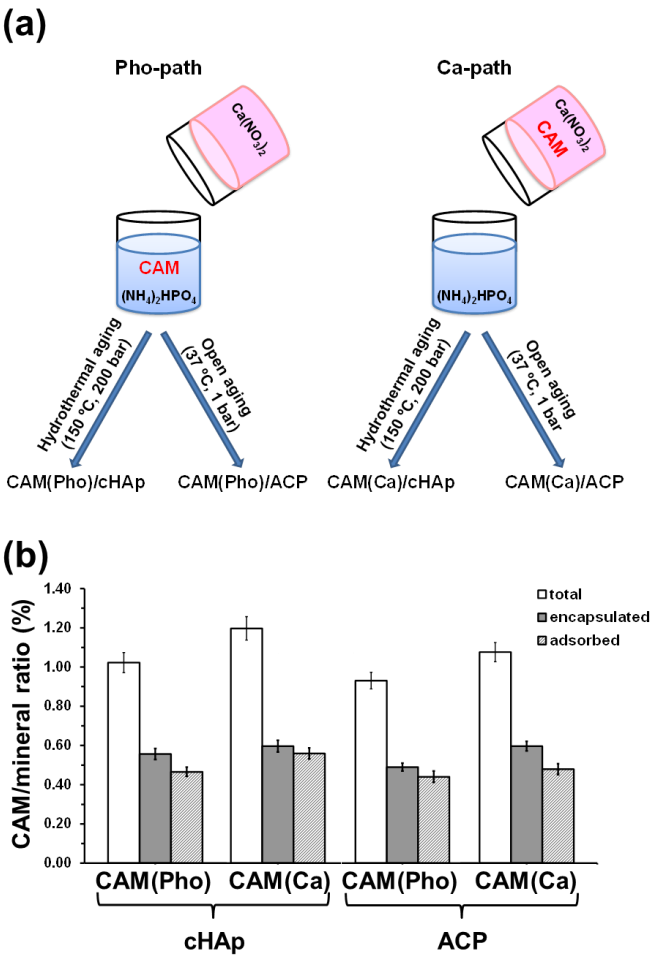

Figure 9.2. (a) Scheme to illustrate the four in situ synthetic strategies used to prepare CAM-loaded mineral NPs: CAM(Pho)/cHAp, CAM(Pho)/ACP, CAM(Ca)/cHAP and CAM(Ca)/ACP. (b) Distribution of the antibiotic loaded *in situ* during the synthesis of cHAp and ACP NPs using the Pho− and Ca −paths. The amount of antibiotic adsorbed onto the surface and encapsulated into the matrix has been evaluated separately (see text). The total amount of loaded CAM corresponds to the sum of adsorbed and encapsulated. The loading ratio is expressed with respect to the weight of dry mineral.

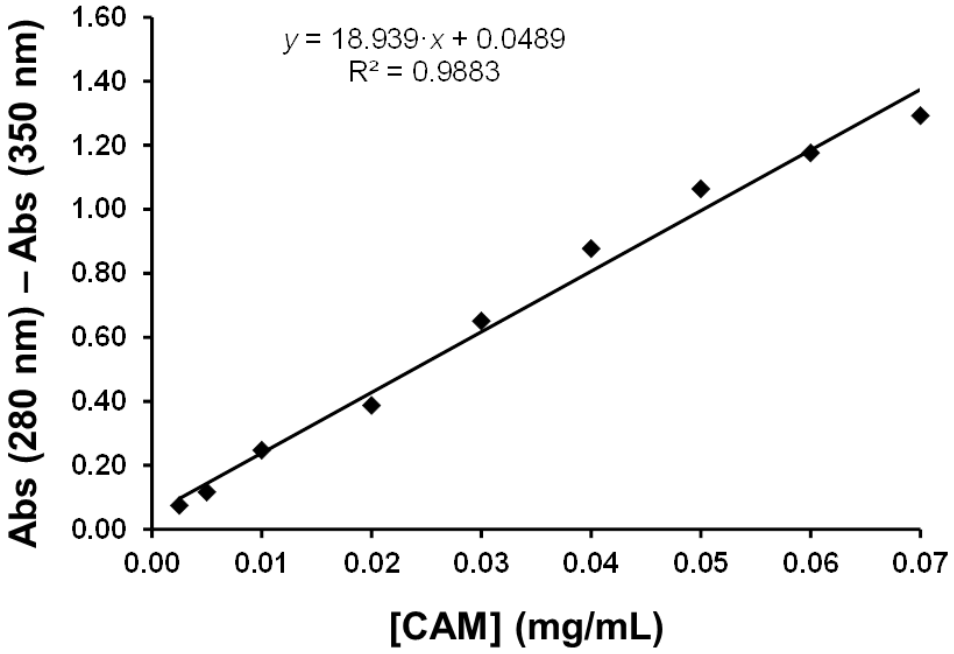

Figure 9.3. Calibration curve for the quantification of the CAM loaded during the synthesis of cHAp and ACP NPs.

The sensitivity of the CAM distribution to the path is reflected in **Figure 9.2 b**, which represents the weight ratio of adsorbed and encapsulated antibiotic with respect to the dry weight of mineral. The amount of CAM loaded through the Ca-path was greater than through the Pho-path for both cHAp and ACP. This difference mainly arises from the encapsulated antibiotic since the concentration of adsorbed CAM is similar for both ACP and cHAp NPs. This feature is consistent with the similar surface areas found for both kind of NPs.[25] Accordingly, hereafter discussion of the results have been mainly focused on CAM(Ca)-loaded cHAp and ACP NPs.

Control NPs, denoted CAM(c)/cHAp and CAM(c)/ACP, were prepared using an *ex situ* loading approach: deposition of 500 μL of 150 mM CAM solution onto 50 mg of already synthetized cHAp and ACP NPs, respectively. The distribution of the accumulated antibiotic was completely different from those found for *in situ* loaded NPs (**Figure 9.4**): the amount of CAM that penetrated into the mineral matrix for encapsulation was significantly smaller than the antibiotic adsorbed on the surface.

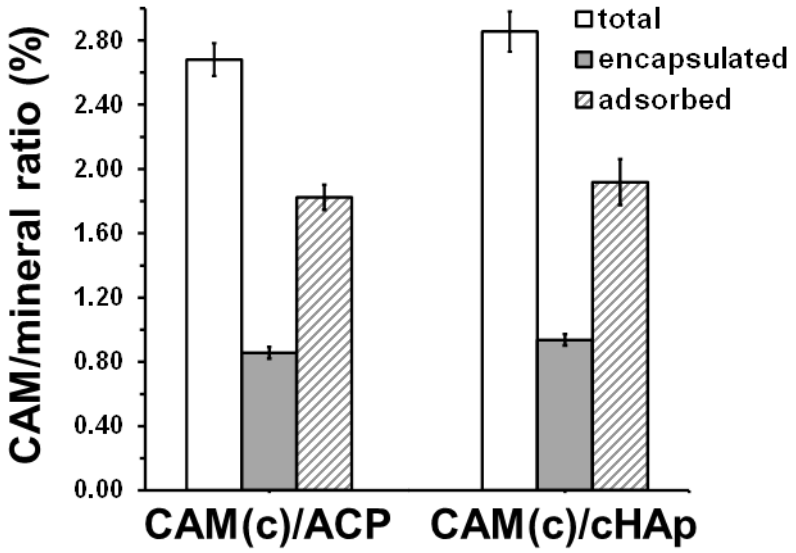

Figure 9.4. Distribution of the antibiotic loaded *ex situ* using already synthesized cHAp and ACP NPs: CAM(c)/cHAp and CAM(c)/ACP. The amounts of antibiotic adsorbed onto the surface and encapsulated into the matrix have been evaluated separately (see text). The total amount of loaded CAM corresponds to the sum of adsorbed and encapsulated.

Results, which are expressed as the weight of antibiotic with respect to the weight of dry mineral, reveal a great accumulation of antibiotic for both types of control NPs. The amount of antibiotic that remained after washing with PBS-EtOH (*i.e*. encapsulated CAM) is significantly smaller than the adsorbed one, which is similar for both CAM(c)/ACP and CAM(c)/cHAP.

Figure 9.5 a compares the FTIR spectra recorded for CAM alone, unloaded cHAp NPs, CAM(Ca)/cHAp NPs as prepared (*i.e.* with both adsorbed and encapsulated CAM), and CAM(Ca)/cHAp NPs after eliminate the antibiotic adsorbed onto the surface washing with PBS-EtOH (*i.e.* with encapsulated CAM only). The characteristic bands of cHAp (at around 1021 cm^{-1})[25] and of CAM (3350-1300 cm^{-1} interval)[43] appear in the spectra recorded for CAM(Ca)/cHAp NPs as prepared and washed with PBS-EtOH. Thus, presence of CAM is proved by the absorption peaks at 3332 ($O-H$ stret), 3248 ($N-H$ stret), 3080 ($C-H$ stret), 1683 / 1563 (amide I / amide II of the 2,2-dichlor-acetamide moiety), and 1515 / 1342 cm^{-1} (nitro / nitro-phenyl group). The absorption peaks of CAM in loaded ACP samples were detected at very similar positions (**Figure 9.6**).

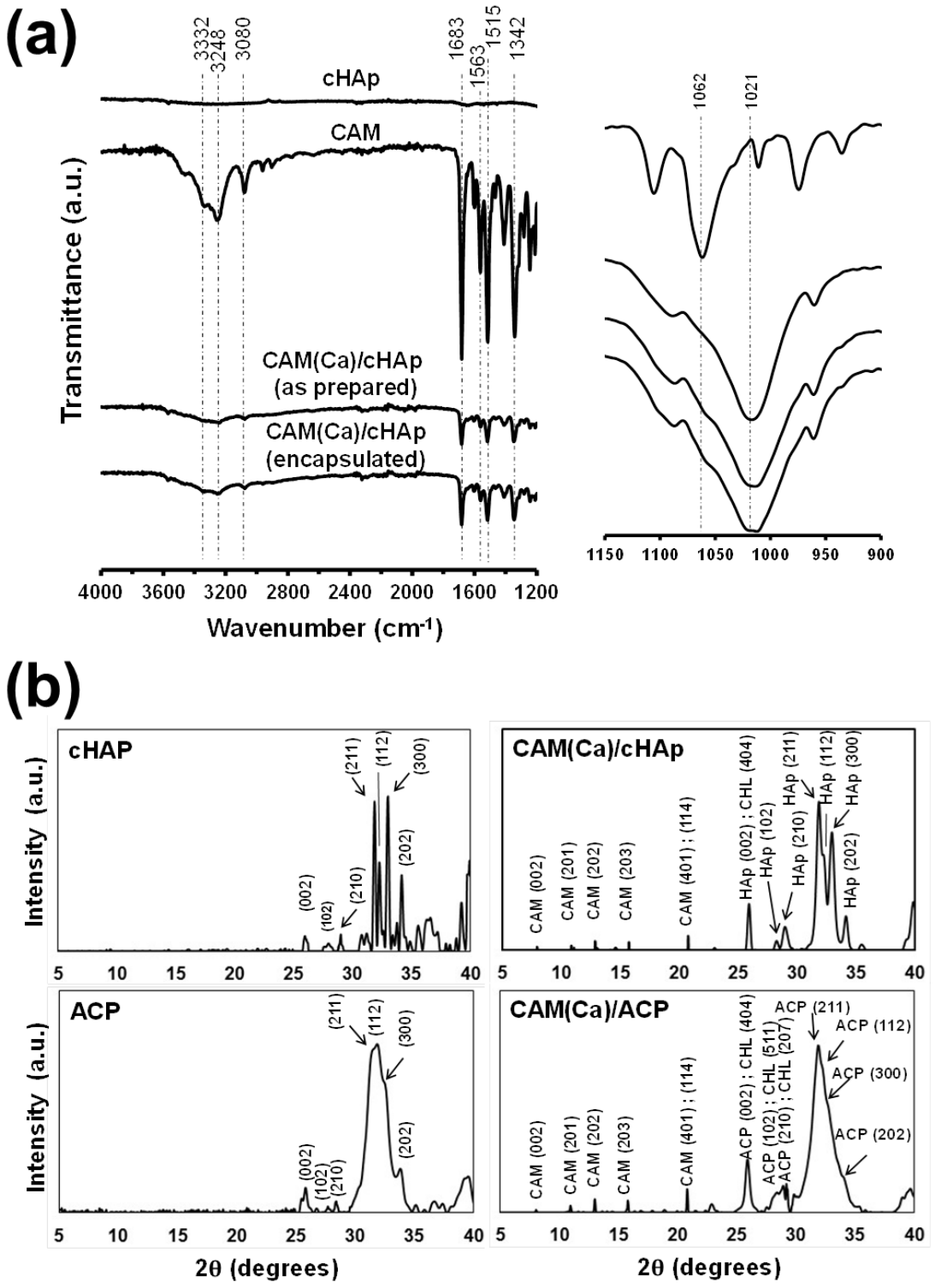

Figure 9.5. (a) Selected regions of the FTIR spectra of CAM, cHAp, CAM(Ca)/cHAp as prepared (with both adsorbed and encapsulated CAM), and CAM(Ca)/cHAp after washing with PBS-EtOH (with encapsulated CAM only). (b) X-ray diffraction patterns of unloaded and CAM(Ca)-loaded cHAp and ACP samples as prepared.

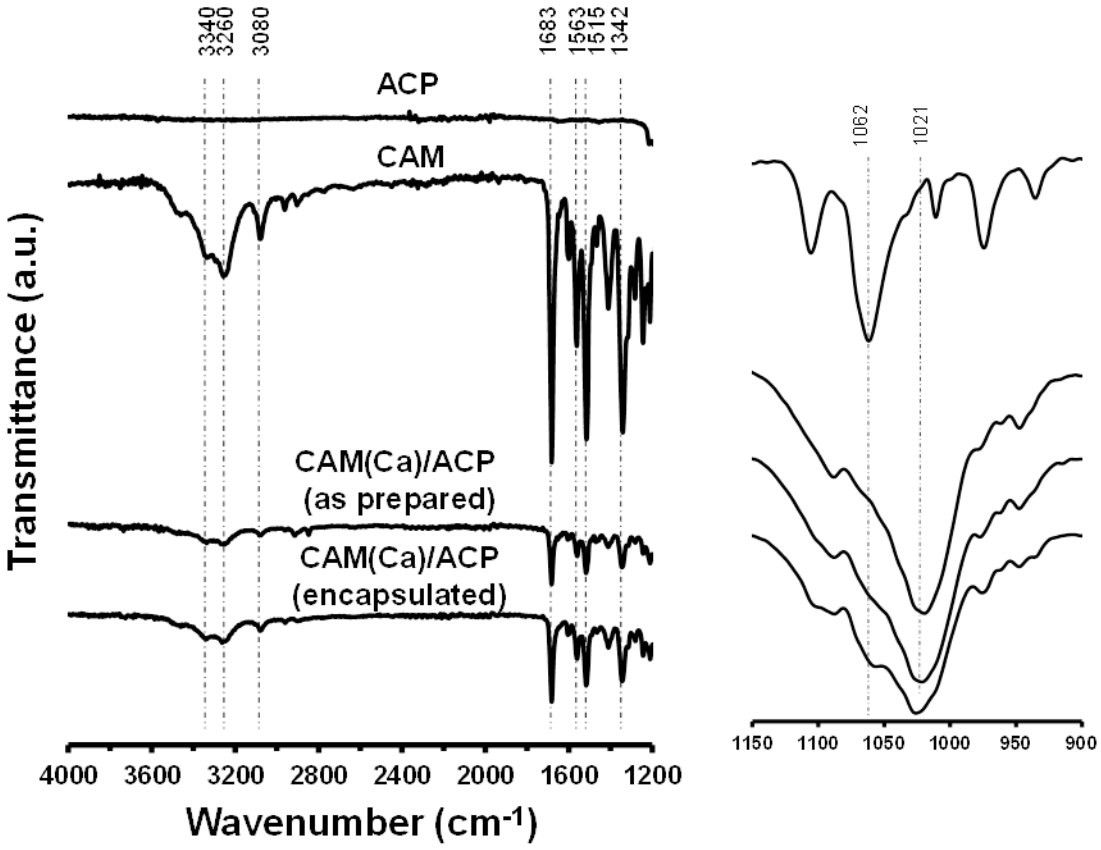

Figure 9.6. Selected regions of the FTIR spectra recorded for CAM, ACP, CAM(Ca)/ACP as prepared (with both adsorbed and encapsulated CAM) and CAM(Ca)/ACP after extraction of adsorbed antibiotic with PBS-EtOH (with encapsulated CAM only). The main absorption bands are discussed in the text.

Results from the characterization of unloaded and CAM(Ca)-loaded mineral NPs by XRD are summarized in **Figure 9.5 b** and **Table 9.1**. The reflections identified for CAM alone (**Figure 9.7**) are fully consistent with those reported in the literature for the crystal structure of most stable antibiotic form (alicyclic CAM).[44,45] The most intense reflections, which correspond to the (401) and (114) planes with d-spacing 0.428 nm, together with the (002) (d = 1.108 nm), (201) (d = 0.815 nm), (202) (d = 0.687 nm) and (203) (d = 0.564 nm), allow identification of the antibiotic in the loaded NPs, since the rest of the peaks overlap with characteristic reflections of cHAp and ACP.

Table 9.1. Crystallinity (χ_c) and crystallite size (L) of the unloaded and CAM–loaded mineral samples.

	χ_c	L (nm)
cHAp	0.66 ± 0.03	57 ± 2
CAM(Ca)/HAp	0.20 ± 0.02	36 ± 2
ACP	0.10 ± 0.02	7 ± 1
CAM(Ca)/ACP	0.06 ± 0.01	6 ± 1

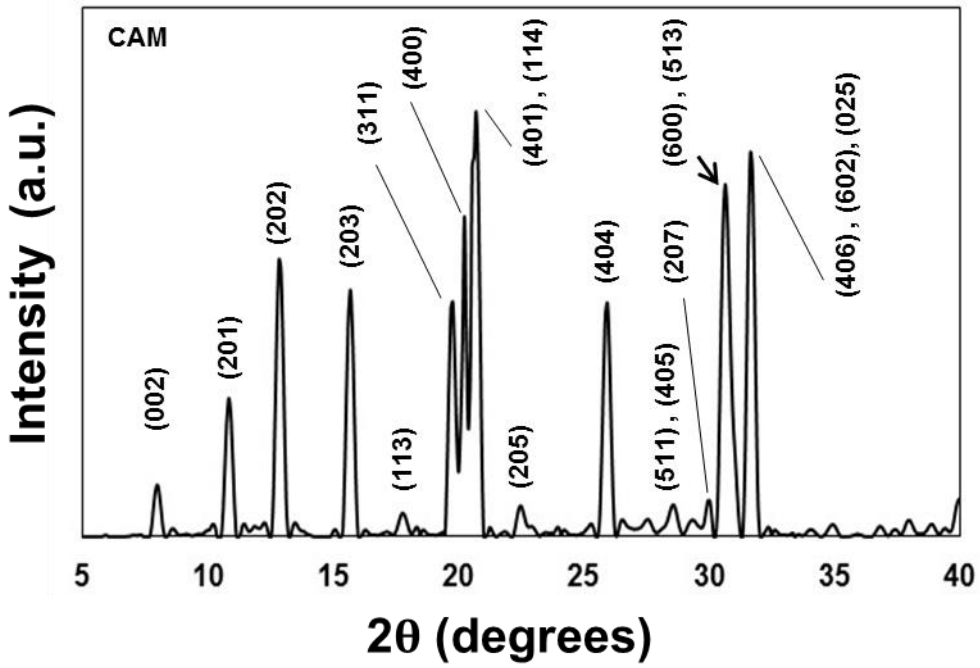

Figure 9.7. X-ray diffraction pattern recorded for CAM alone.

Both the crystallinity and the crystallite size are lower for CAM-loaded ACP and, especially, cHAp samples than for the unloaded ones (**Table 9.1**). This observation reflects that the antibiotic affects the formation of crystallization nuclei, reducing both their number and size. This phenomenon has been attributed to the competition between CAM···mineral interactions and CAM intramolecular hydrogen bonds, the latter being characteristic of the alicyclic form of the antibiotic (see next sub-section). The difficulties in the formation of CAM···mineral interactions and the stability of the alicyclic CAM

preclude the role of the antibiotic as nucleating agent. Furthermore, the incorporation of the antibiotic to the mineral matrix causes steric hindrance, inhibiting the growth of already formed crystallization nuclei.

SEM and TEM micrographs of CAM alone and CAM(Ca)-loaded mineral NPs, after elimination of the antibiotic at the surface with PBS-EtOH, are displayed in **Figure 9.8**. CAM is a crystalline antibiotic that organizes in nanoplates (**Figure 9.8 a**). The nanospherical and nanorod-like morphologies of CAM(Ca)/ACP (**Figure 9.8 b**) and CAM(Ca)/cHAp (**Figure 9.8 c**), respectively, are similar to those of unloaded minerals,[23] evidencing that the encapsulation of the antibiotic does not modify the morphology of the NPs. Accordingly, the loading strategy promotes the homogeneous integration of the antibiotic into the mineral matrix during the biomineralization process.

In previous work we described the ability of both ACP and cHAp to adsorb biophosphates (*e.g.* pyrophosphates and triphosphates, abbreviated $P_2O_7^{4-}$ and polyP, respectively) and biophosphonates (*e.g.* amino-tris(methylenephosphonic acid), abbreviated ATMP),[25] which are important for bone regeneration. Such bioadsorption capacity has been used in this study to protect the loaded antibiotic during the delivery process.

Figure 9.9 displays SEM micrographs of CAM(Ca)/ACP and CAM(Ca)/cHAp samples after incubation with $P_2O_7^{4-}$, polyP or ATMP solutions. Comparison with micrographs displayed in **Figure 9.8** reflects the formation of superficial protecting layers. The significant morphological changes have been attributed to the fact that, after the first stages of the bioadsorption process, a surface-induced crystal growing process occurred for the three biocoatings. On the other hand, quantification of the adsorbed and encapsulated amount of CAM indicates that the biocoating does not interfere with the loaded antibiotic and, therefore, does not induce its premature release during the bioadsorption process (**Figure 9.10**). FTIR and X-ray diffraction studies (**Figures 9.11-9.15**, and **Table 9.2**) confirmed the presence of the biocoating and its negligible influence in the internal structure of CAM-loaded mineral samples.

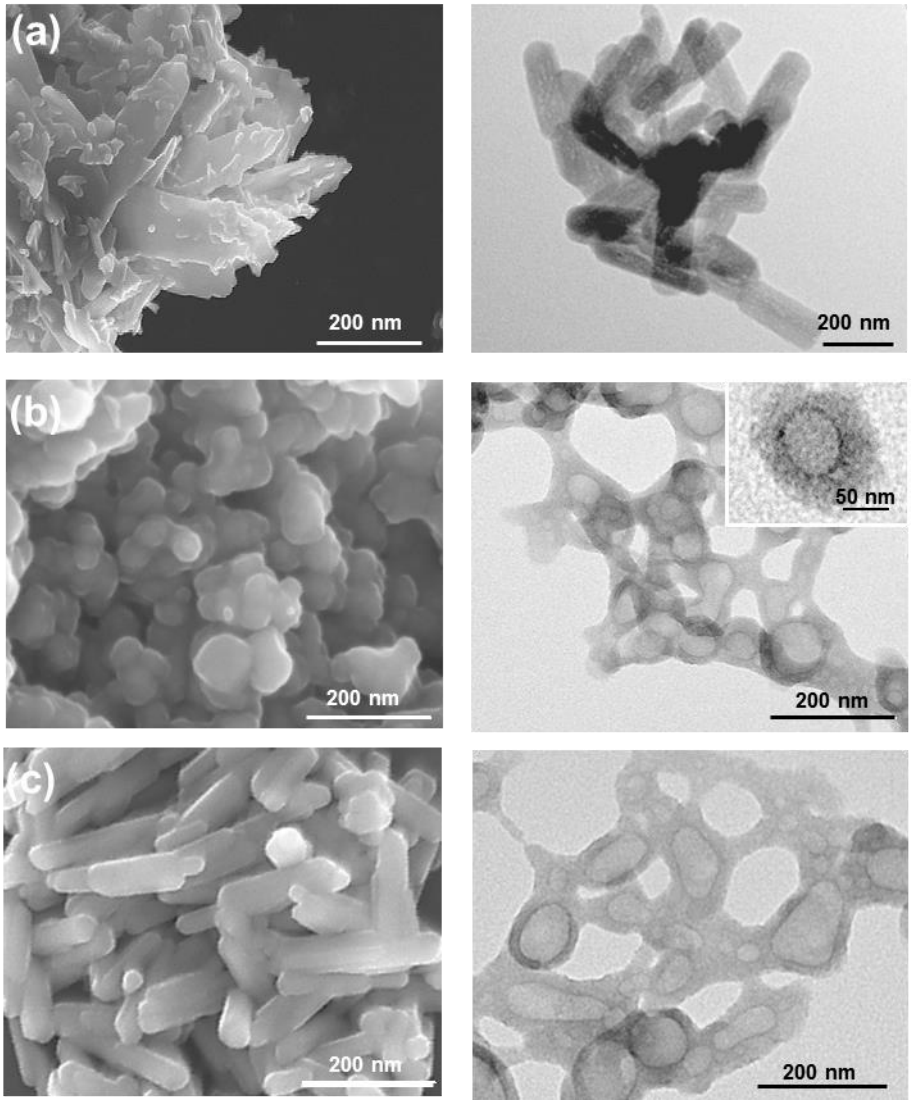

Figure 9.8. SEM (left) and TEM (right) images of (a) CAM crystals, (b) CAM(Ca)/ACP and (c) CAM(Ca)/cHAp NPs after washing with PBS-EtOH (loaded with encapsulated CAM only).

Table 9.2. Crystallinity (χc) and crystallite size (*L*) of the unloaded and CAM-loaded mineral samples before and after coating with polyP, $P_2O_7^{4-}$ and ATMP.

	χ_c	***L* (nm)**
cHAp	0.66 ± 0.03	57 ± 2
cHAp + polyP	0.61 ± 0.03	56 ± 2
CAM(Ca)/cHAp + polyP	0.24 ± 0.02	41 ± 2
cHAp + $P_2O_7^{4-}$	0.60 ± 0.02	55 ± 2
CAM(Ca)/cHAp + $P_2O_7^{4-}$	0.23 ± 0.02	41 ± 2
cHAp + ATMP	0.60 ± 0.03	55 ± 2
CAM(Ca)/cHAp + ATMP	0.23 ± 0.02	42 ± 2
ACP	0.10 ± 0.02	7 ± 1
ACP + polyP	0.11 ± 0.01	10 ± 1
CAM(Ca)/ACP + polyP	0.06 ± 0.01	7 ± 1
ACP + $P_2O_7^{4-}$	0.13 ± 0.02	11 ± 1
CAM(Ca)/ACP + $P_2O_7^{4-}$	0.07 ± 0.01	8 ± 1
ACP + ATMP	0.14 ± 0.01	10 ± 1
CAM(Ca)/ACP + ATMP	0.07 ± 0.01	8 ± 1

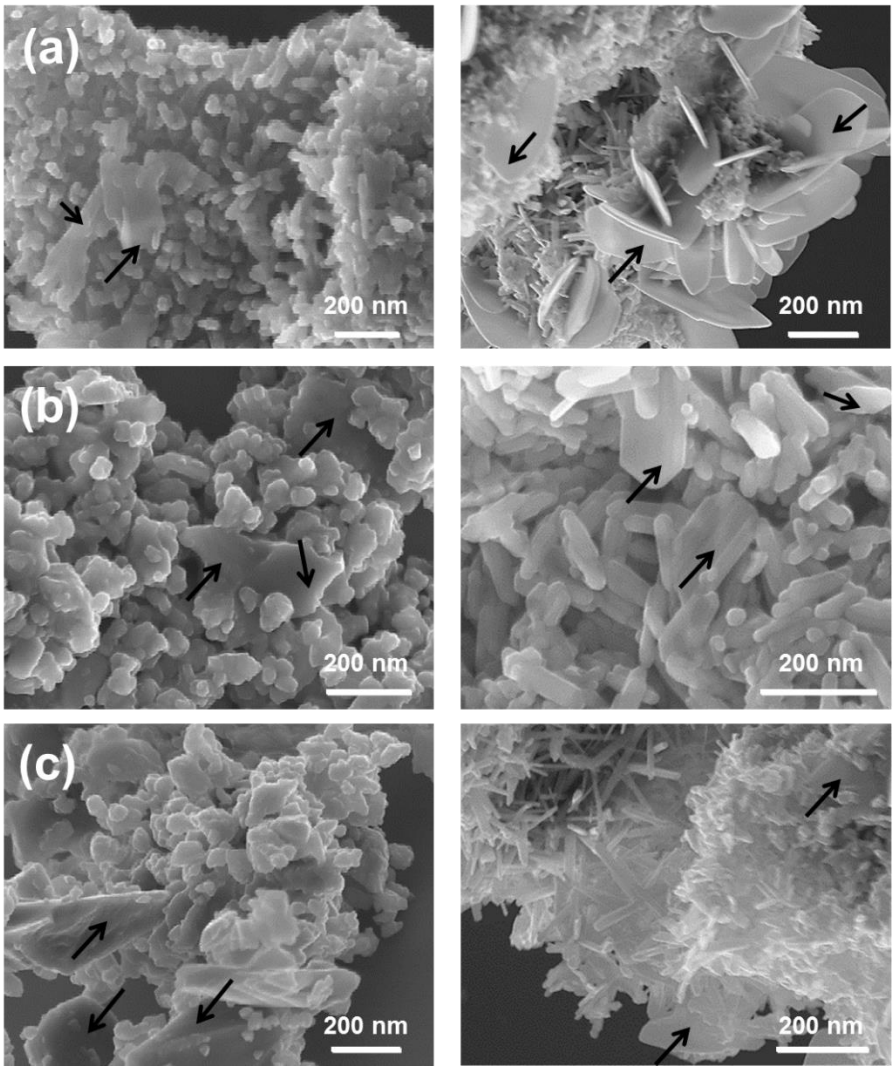

Figure 9.9. SEM images of CAM(Ca)-loaded ACP (left) and cHAp (right) NPs after incubation with (a) polyP, (b) $P_2O_7^{4-}$ and (c) ATMP aqueous solutions. The arrows indicate the presence of crystals of the bioadsorbed compounds.

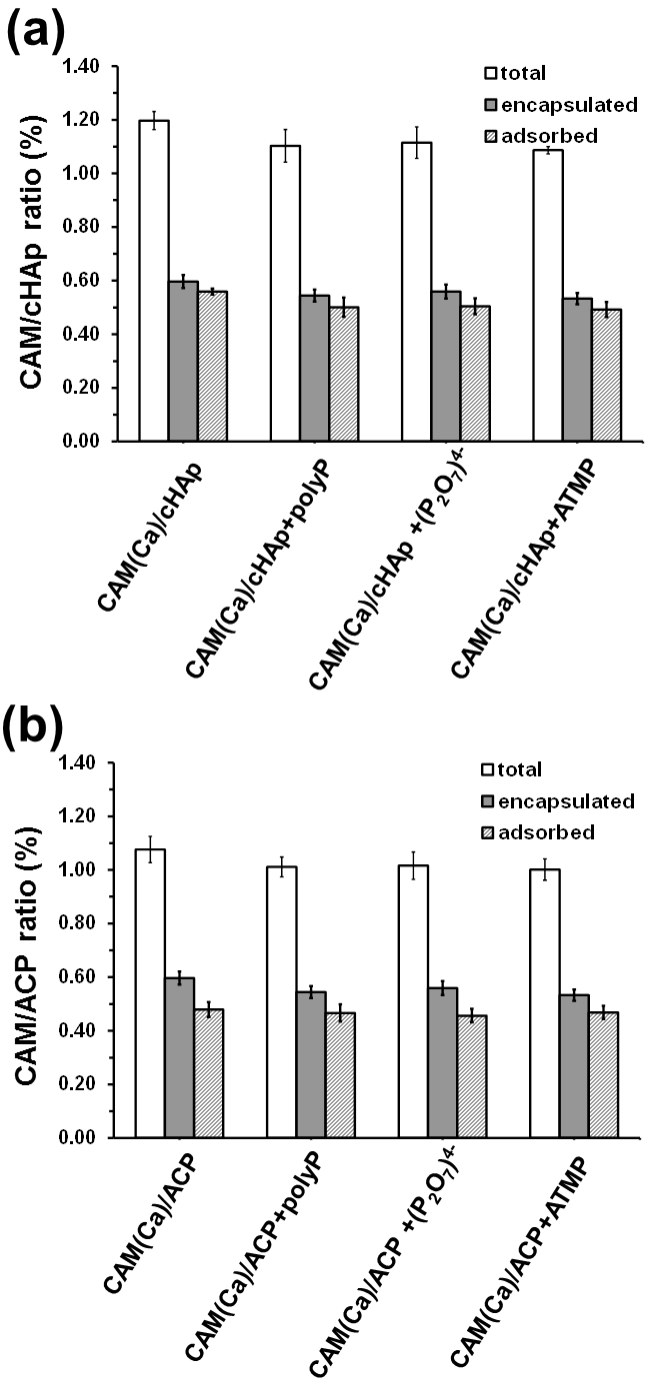

Figure 9.10. Distribution of the antibiotic loaded *in situ* during the synthesis of (a) cHAp and (b) ACP NPs using the Ca-path. The amounts of antibiotic adsorbed onto the mineral surface and encapsulated into the mineral matrix have been evaluated before and after the formation of polyP, $P_2O_7^{4-}$ and ATMP coating layers. The total amount of loaded CAM corresponds to the sum of adsorbed and encapsulated. The loading ratio is expressed with respect to the weight of dry cHAp or ACP mineral.

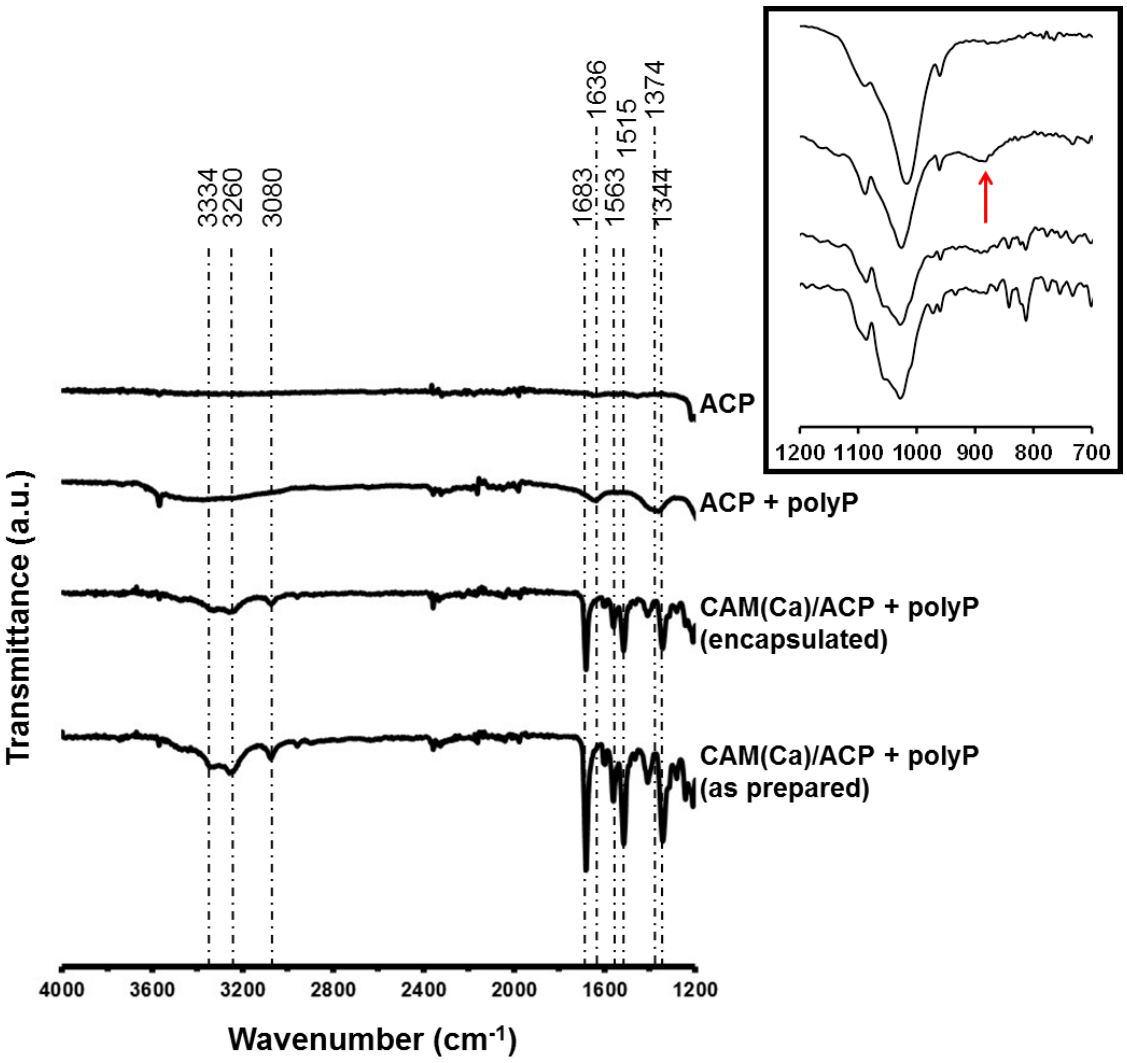

Figure 9.11. FTIR spectra of ACP alone, ACP after incubation with polyP, CAM (Ca)/ACP washed with PBS-EtOH (*i.e.* loaded with encapsulated CAM only) after incubation with polyP, and as prepared CAM(Ca)/ACP (*i.e*. loaded with both adsorbed and encapsulated CAM) after incubation with polyP. The red arrow indicates the most important band of polyP.

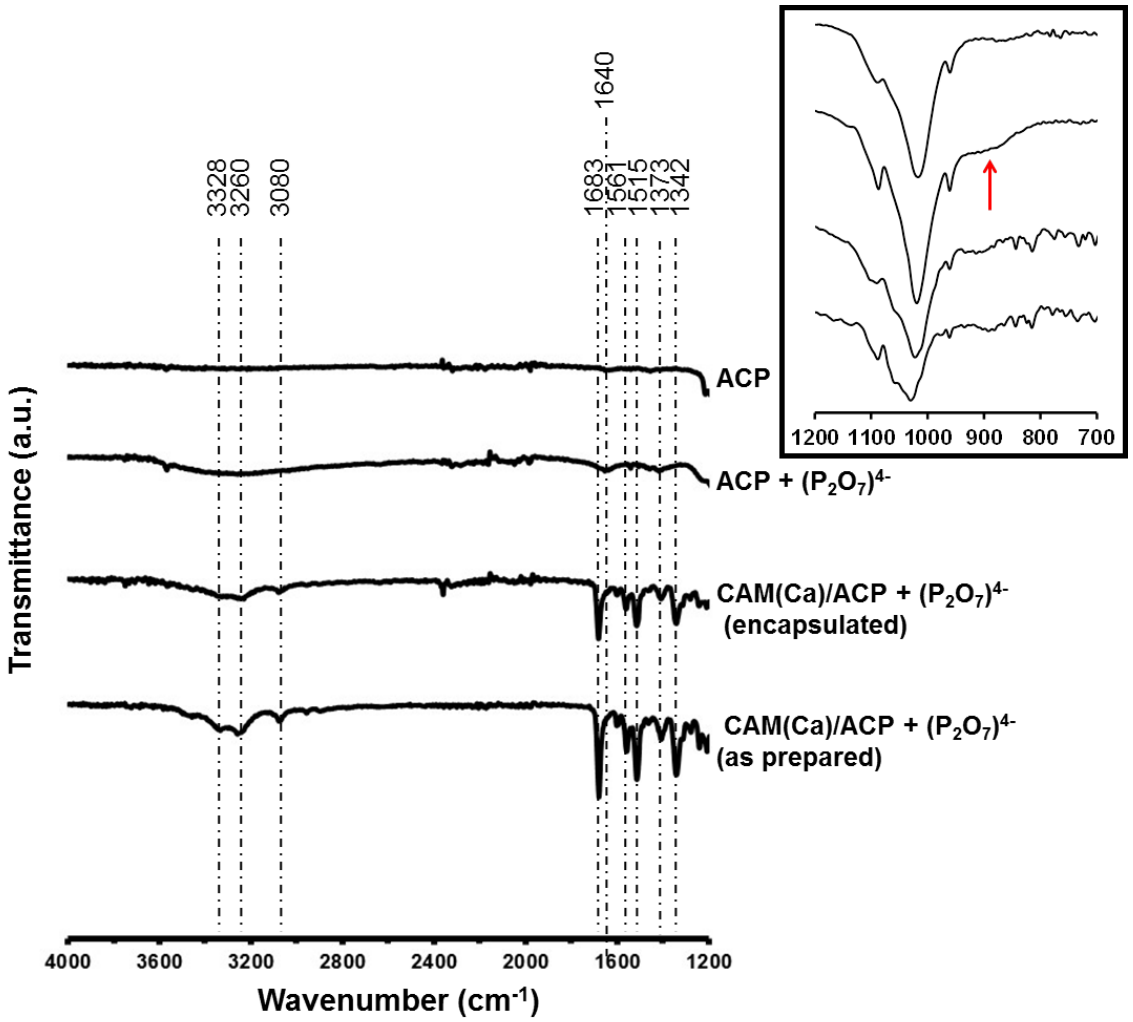

Figure 9.12. FTIR spectra of ACP alone, ACP after incubation with $P_2O_7^{4-}$, CAM(Ca)/ACP washed with PBS-EtOH *(i.e.* loaded with encapsulated CAM only) after incubation with, and $P_2O_7^{4-}$ as prepared CAM(Ca)/ACP (*i.e.* loaded with both adsorbed and encapsulated CAM) after incubation with $P_2O_7^{4-}$. The red arrow indicates the most important band of $P_2O_7^{4-}$.

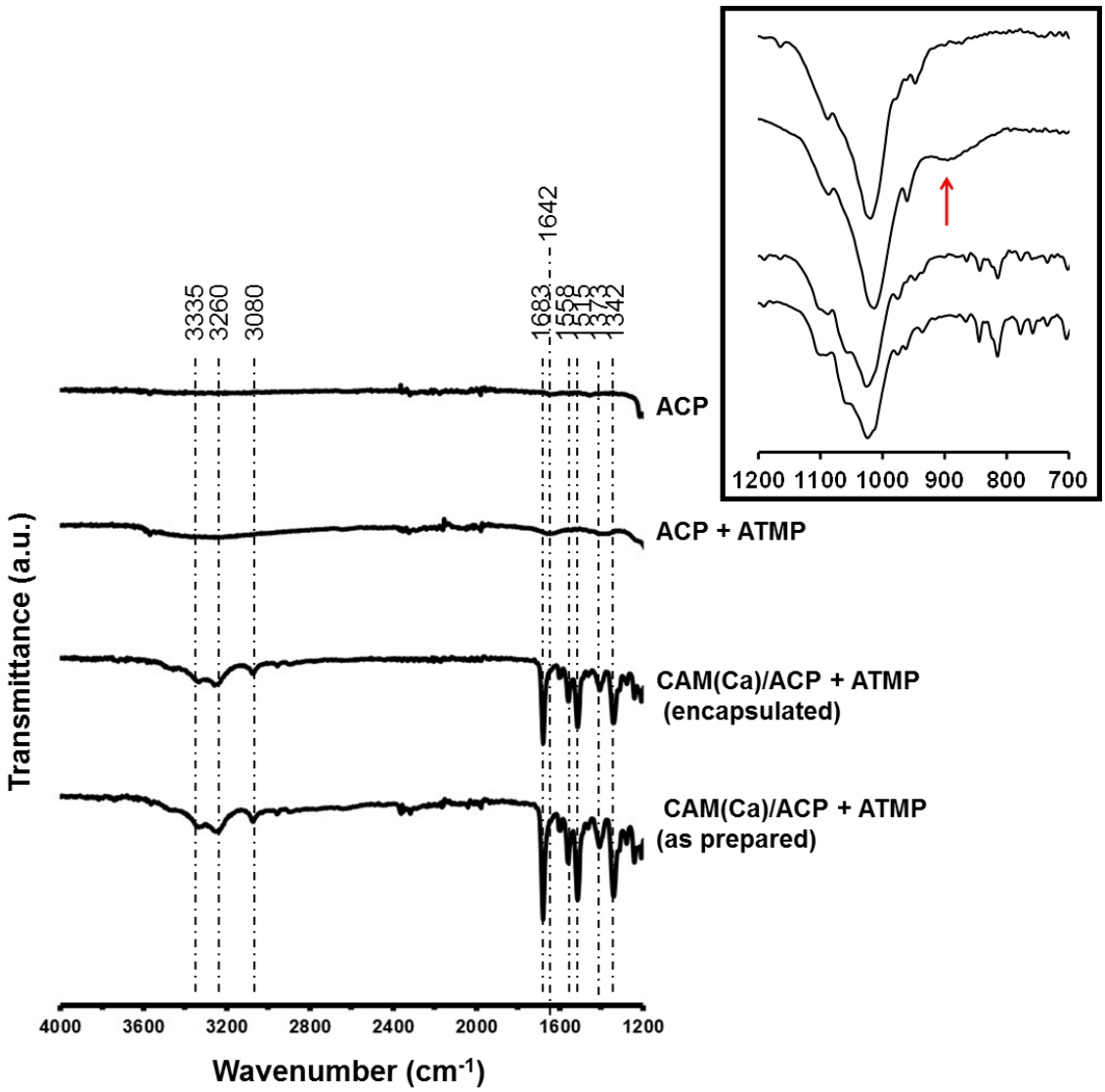

Figure 9.13. FTIR spectra of ACP alone, ACP after incubation with ATMP, CAM(Ca)/ACP washed with PBS-EtOH (*i.e*. loaded with encapsulated CAM only) after incubation with ATMP, and as prepared CAM(Ca)/ACP (*i.e.* loaded with both adsorbed and encapsulated CAM) after incubation with ATMP. The red arrow indicates the most important band of ATMP.

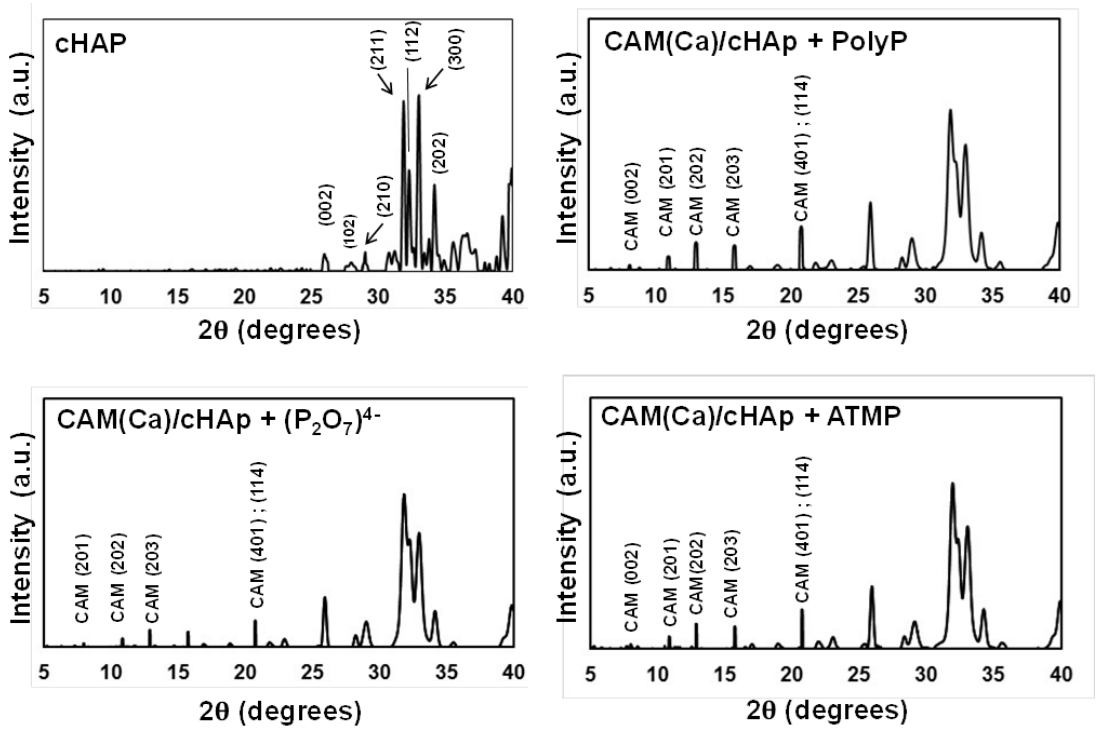

Figure 9.14. X-ray diffraction patterns of cHAp alone and CAM(Ca)/cHAp after incubation with polyP, and $P_2O_7^{4-}$ ATMP. The reflections associated to CAM are indicated**.**

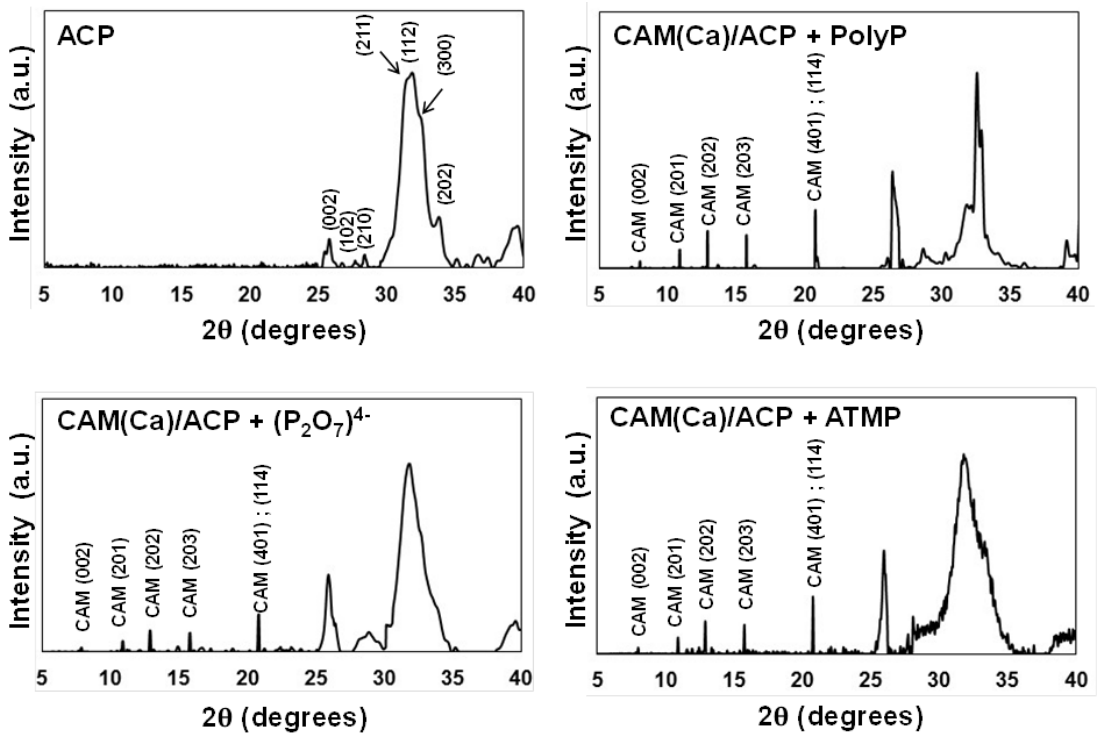

Figure 9.15. X-ray diffraction patterns of cHAp alone and CAM(Ca)/ACP after incubation with polyP, $P_2O_7^{4-}$ and ATMP. The reflections associated to CAM are indicated.

9.3.2 Effect of the loading in the bioactivity of CAM

The alicyclic form of CAM has been associated to its antimicrobial action.[46] In this bioactive conformation the hydroxyl groups of the antibiotic are engaged in closing an alicyclic ring by hydrogen bonding (**Figure 9.16**). Accordingly, the activity of CAM could be altered by structural changes that affect the functional character of such hydroxyl groups. In this sub-section, we examine the effect of CAM···mineral interactions in the bioactive response of the antibiotic.

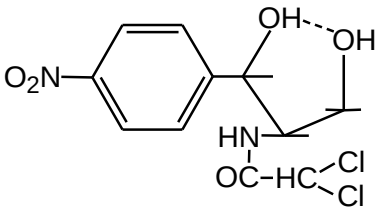

Figure 9.16. Alicyclic form of CAM

As mentioned above, the peaks identified in the diffractograms recorded for CAM(Ca)/cHAp and CAM(Ca)/ACP NPs before (**Figure 9.5 a**) and after applying biocoatings (**Figures 9.14 and 9.15**) correspond to those identified for the crystal structure of CAM (**Figure 9.7**). Accordingly, the crystalline structure of the antibiotic remains unaltered during both the loading and coating processes. In addition, the position of the O–H absorption band in the FTIR spectra is the same for the antibiotic alone and loaded (**Figures 9.5 a, 9.6 and 9.11-9.13**). Thus, the alicyclic ring is apparently unaltered by the formation of CAM···mineral, CAM···biocoating and mineral···biocoating interactions, which suggests that the antibiotic is not forming specific hydrogen bonding interactions with the mineral and/or the biocoating.

In order to confirm that the bioactive conformation of CAM was not altered by the loading and bioadsorption processes, the activity of the loaded antibiotic loaded was tested against representative Gram-positive bacteria (*E. coli*) and compared with that of free antibiotic. **Figure 9.17 a** plots the relative growth rate of the partially inhibited cultures against the logarithm of the antibiotic concentration for free CAM, CAM(Ca)/cHAp and CAM(Ca)/ACP. Symmetrical sigmoid curves similar to the dose-response curves of many biological systems were obtained in all cases. The central portion of the curve approaches linearity, allowing a graphic extrapolation of the 50 % growth inhibition levels. The half maximal inhibitory concentration (IC_{50}) of antibiotic determined for free CAM,

CAM(Ca)/cHAp and CAM(Ca)/ACP is 0.96, 0.94 and 0.94 μg/mL, respectively, reflecting that the bioactivity of CAM is preserved in loaded mineral NPs. **Figure 9.17 b and c** compares the bacterial growth inhibition of uncoated and biocoated CAM(Ca)/cHAp and CAM(Ca)/ACP NPs, respectively. It is worth noting that the bioadsorption of polyP, $P_2O_7^{4-}$ and ATMP does not alter the inhibitory characteristics of the antibiotic, evidencing that CAM preserves the bioactive conformation.

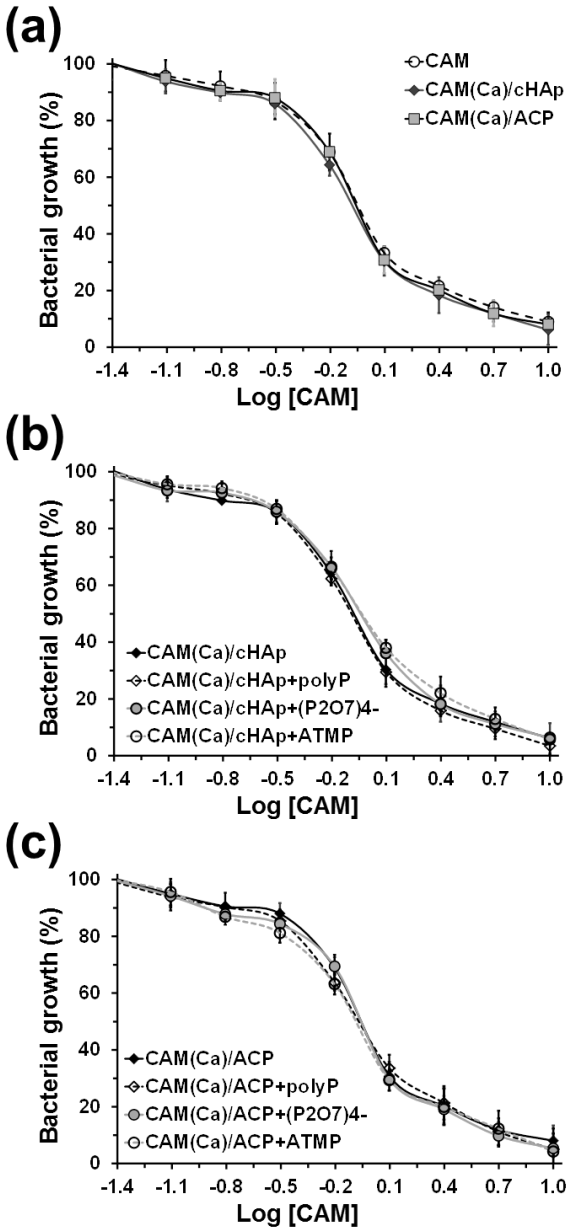

Figure 9.17. Inhibition of *E. coli* growth by CAM. Results are expressed as a percentage of the control against the logarithm concentration of antibiotic for: (a) free CAM, CAM(Ca)/cHAp and CAM(Ca)/ACP; (b) uncoated and biocoated CAM(Ca)/cHAp NPs; and (c) uncoated and biocoated CAM(Ca)/ACP NPs.

9.3.3 CAM-Release in PBS and cell culture media

Quantitative release assays in the simplest physiological medium, PBS, were performed with CAM(Ca)/cHAp and CAM(Ca)/ACP NPs, CAM(c)/cHAp and CAM(c)/ACP NPs being used as controls. Results displayed in **Figure 9.18** indicate that, although the amount of loaded antibiotic was entirely released after ~72 h in all cases, the release rate was slower for CAM(Ca)/cHAp than for CAM(Ca)/ACP. More specifically, the time necessary to release 50 % of loaded CAM (t_{50}) was ~ 23 and ~ 7 h respectively. On the other hand, the release rate was significantly faster for control NPs than for minerals loaded using the *in situ* approach (*i.e.* $t_{50} \approx$ 12 and 4 h for CAM(c)/cHAp and CAM(c)/ACP, respectively), evidencing that the encapsulation achieved by the latter procedure exerts a regulating effect. The sustained antibiotic release observed for the *in situ* loaded NPs has been attributed to the slow diffusion of the encapsulated CAM through the mineral matrix.

The behavior of CAM(Ca)–loaded mineral NPs coated with polyP, and $P_2O_7^{4-}$ ATMP (**Figures 9.18 b-d**) was similar to that described for the uncoated systems. The antibiotic release rate was faster for ACP than for cHAp, independently of the coating. Furthermore, the release rate was faster for control NPs than for those loaded using the *in situ* approach. Quantitative comparison between uncoated and coated CAM(Ca)/cHAp reflects that the release rate is the same for uncoated and polyP-coated NPs (*e.g.* $t_{50} \approx$ 23 h in both cases), whereas $P_2O_7^{4-}$ and, specially, ATMP biocoatings tend to accelerate the delivery process (*e.g.* $t_{50} \approx$ 20 and 17 h, respectively).

Antibiotic release assays from uncoated and coated CAM(Ca)/cHAp and CAM(Ca)/ACP NPs were also carried out in cell culture media using three different cell lines: human umbilical vein endothelial cells (HUVEC), green monkey kidney fibroblast cells (COS-1), and human breast cancer cells (MCF-7). The release profiles, which are displayed in **Figures 9.19** and **9.20**, were very similar to those obtained in PBS. Thus, the retardation effect increased with the crystallinity of the sample, the release from cHAp NPs being slower than from ACP NPs. These characteristic trends were also identified for biocoated NPs, the influence of the chemical specie adsorbed at the surface of the mineral NPs being practically negligible. However, the most important result is that the antibiotic release profiles obtained for uncoated and biocoated CAM(Ca)/cHAp and CAM(Ca)/ACP NPs are totally independent of cell line.

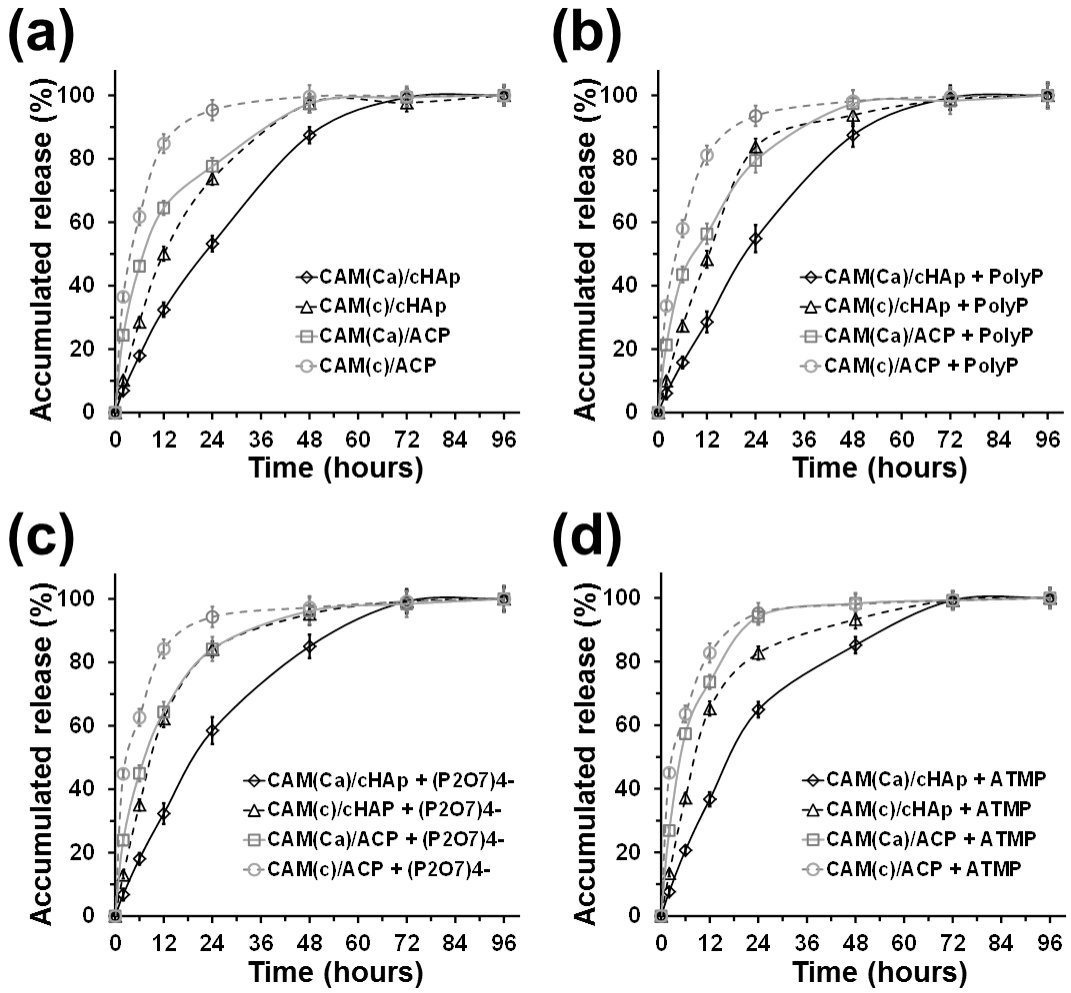

Figure 9.18. Antibiotic release profiles in PBS for (a) uncoated, (b) polyP coated, (c) $P_2O_7^{4-}$ coated and (d) ATMP coated CAM(Ca)–loaded cHAp and ACP NPs. CAM-incubated samples (uncoated and biocoated CAM(c)/cHAp and CAM(c)/ACP NPs) were used as control NPs.

The sustained release of CAM displayed *in vitro* by both cHAp and ACP, which is not affected by the biological environment, suggests that such mineral NPs could act as antitumoral nanoplatforms for in vivo treatments. More specifically, our results clearly indicate that cHAp and ACP NPs act as efficient vehicles for the CAM transport and delivery.

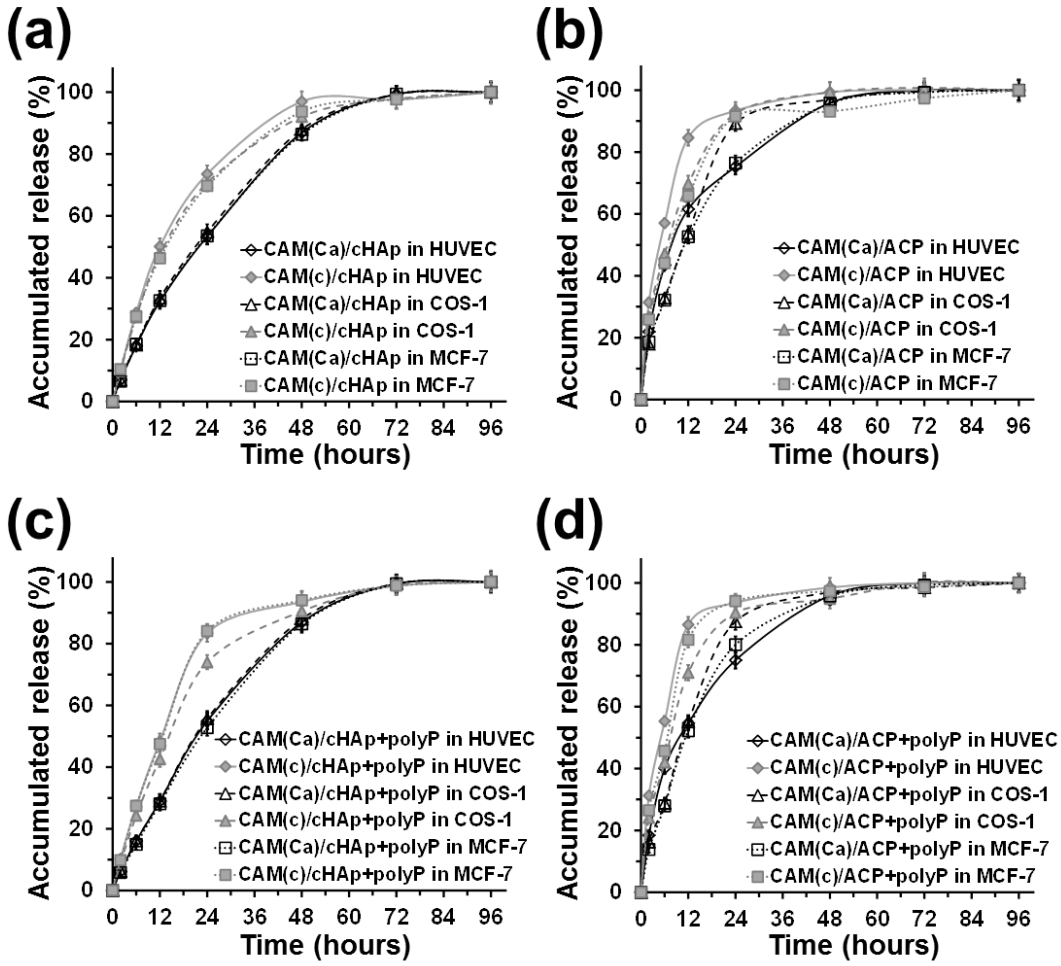

Figure 9.19. Antibiotic release profiles in different cell culture media (HUVEC, COS-1 and MCF-7 cell lines) for (a) uncoated CAM(Ca)/cHAp, (b) uncoated CAM(Ca)/ACP, (c) CAM(Ca)/cHAp coated with polyP, and (d) CAM(Ca)/ACP coated with polyP. CAM-incubated samples, CAM(c)/cHAp and CAM(c)/ACP, were used as control. Results obtained for NPs coated with $P_2O_7^{4-}$ and ATMP are displayed in **Figure 9.20.**

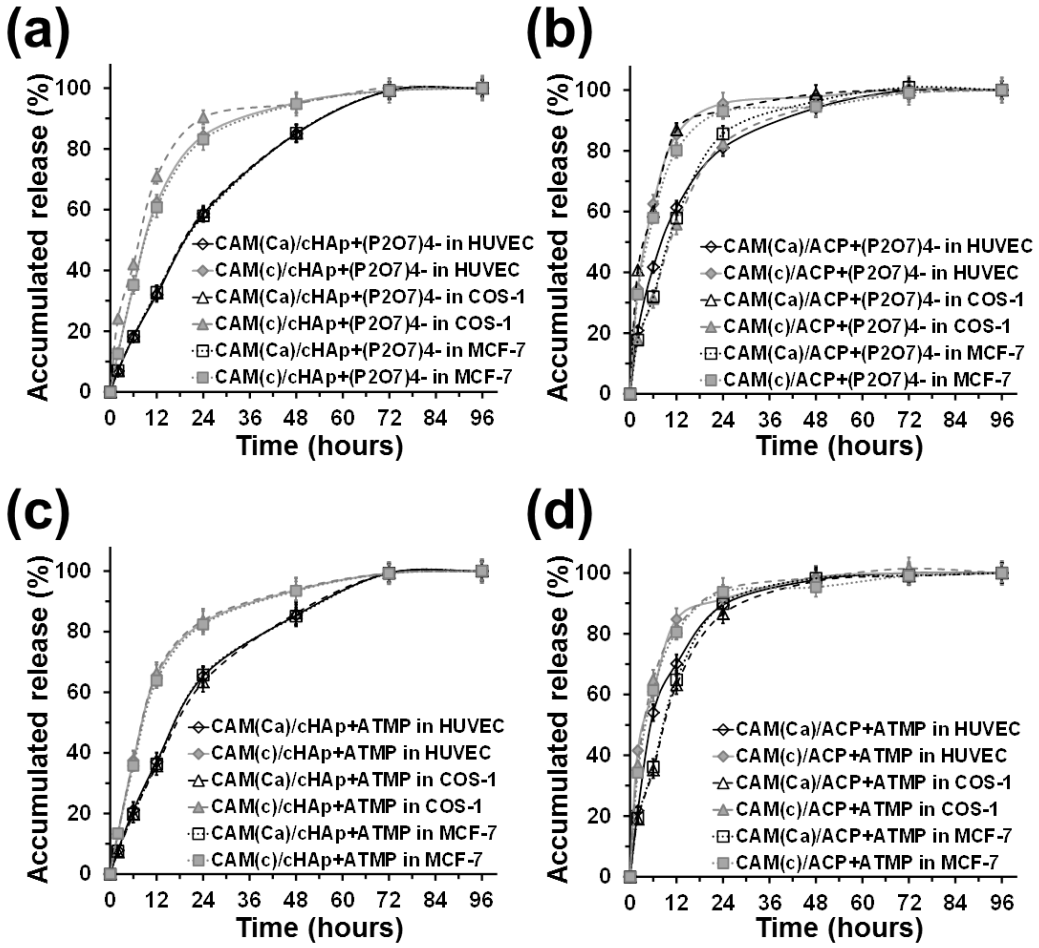

Figure 9.20. Antibiotic release profiles in different cell culture media (HUVEC, COS-1 and MCF-7 cell lines) for (a) CAM(Ca)/cHAp coated with , $P_2O_7^{4-}$ (b) CAM(Ca)/ACP coated with , $P_2O_7^{4-}$ (c) CAM(Ca)/cHAp coated with ATMP, and (d) CAM(Ca)/ACP coated with ATMP. CAM-incubated samples (CAM(c)/cHAp and CAM(c)/ACP) were used as control in all cases. Results obtained for uncoated and polyP coated NPs are displayed in **Figure 9.19**.

9.3.4 Can CAM-loaded mineral NPs be used to fight cancer cells?

In previous sub-sections, we proved that cHAp and ACP NPs prepared using the *in situ* Ca-path are efficient platforms for the loading of bioactive CAM and its delayed release with respect to platforms prepared using the usual *ex situ* incubation approach. In this section, we preliminary explore the response of cells to CAM(Ca)/cHAp and CAM(Ca)/ACP NPs. For this purpose, the electroporation technique was used to facilitate the permeation of CAM-loaded mineral NPs across cell membranes, since the anticancer therapy using antibiotics is based on the targeting of mitochondria.[15-18] Electroporation is the increment of the cell membrane permeability by exposing the cells to short electric current pulses from an external source. Such increase in permeability,

which is related with the formation of nanoscale defects or pores in the cell membrane, allows the direct physical transfer of numerous kinds of chemical species into cells. In our case, we use this effect to introduce the NPs into the cells.

Unloaded and CAM-loaded mineral NPs, without and with biocoating, were introduced in culture media with non-cancerous (HUVEC and COS-1) and cancerous (MCF-7) cells, which were electroporated to facilitate the internalization process. A sub-lethal dose of CAM was used in these assays in order to avoid generalized cytotoxicity (*i.e*. a dose that will kill less than 5 % of the test cells) and allow the population of unaffected cells to recover over time. Then, they were seeded in the culture plate and evaluated at different times. In order to investigate the effects of the antibiotic in living cells, the viability was determined through the MTT [3-(4,5-dimethylthiazol-2-yl)-2,5-diphenyltetrazolium bromide] assay. The cytotoxic response of HUVEC, COS-1 and MCF-7 cell lines exposed to the increasing concentrations of CAM is displayed in **Figure 9.21**.

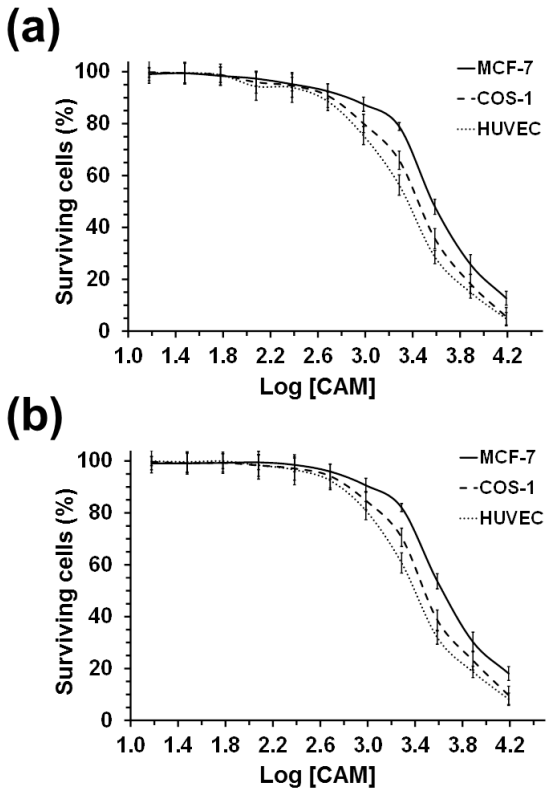

Figure 9.21. Cytotoxicity curves of CAM. Cell viability of HUVEC, COS-1 and MCF-7 cells with increasing concentration of CAM (in µM) evaluated at (a) 24 h and (b) 48 h of culture. Curves are expressed as percentage of surviving cells relative to the control against the logarithm of CAM concentration.

As it was expected due to the use of sub-lethal doses, electroporated cells remained practically unaffected after the internalization of unloaded cHAp and ACP NPs (**Figures 9.22** and **9.23**, respectively), independently of both the cell type and the biocoating. Plots representing the variation of survival cells with time indicate that, after the immediate reduction of the viability that typically brings agents extraneous to the culture medium, cells recovered in number over time until reach 100 % of the initial viability after 120 h.

Addition of uncoated and biocoated CAM(Ca)/HAp NPs into non-cancerous cell models, HUVEC and COS-1 (**Figures 9.24 a** and **b**, respectively), caused an almost identical response. Thus, the fraction of surviving non-cancerous cells after 120 h was 100 %, evidencing that CAM is not inhibiting mitochondrial functions and, therefore, preserving the cell viability. In contrast, CAM(Ca)/HAp NPs damaged MCF-7 cancerous cells (**Figure 9.24 c**), causing a high percentage of cells to die (39 % ± 5 %). The different response of normal and cancer cells against CAM(Ca)-loaded mineral NPs is due to a combination of two factors: (i) mitochondria are more abundant in cancerous cells than in non-cancerous cells;[17] and (ii) the similarity between bacterial and mitochondrial ribosomes.[15]

As CAM(Ca)- loaded cHAp NPs are very toxic for cancer cells as compared to innocuous unloaded cHAp, protection of the antibiotic using biocoatings is expected to enhance such destructive effects. Effectively, the percentage of surviving cells drops drastically for CAM(Ca)/cHAp NPs coated with polyP, $P_2O_7^{4-}$ and ATMP (**Figure 9.24 c**). More specifically, after 120 h the percentage of dead cells increased from 39 % ± 5 % for uncoated NPs to 59 % ± 3 % (polyP), 51 % ± 5 % ($P_2O_7^{4-}$) and 51 % ± 4 % (ATMP) for coated NPs. These results indicate that the protecting role exerted by the biocoating, especially by polyP, enhances the efficiency of the antibiotic as anticancer agent. According to previous discussion (**Figure 9.21**), this phenomenon cannot be attributed to a delay in the release of the antibiotic (*i.e.* release curves for uncoated and biocoated CAM(Ca)–loaded NPs were very similar). Instead, two different hypotheses can be considered two explain the protection offered by the biocoating: (1) CAM···biocoating complexes allow to protect the antibiotic molecules against enzymatic degradation, avoiding the premature reduction in the amount of effective CAM as anticancer agent; and (2) the dissolved biocoating molecules capture the antibiotic ones, transporting them to the mitochondria to enhance the antitumor activity (*i.e.* they act as targeted carriers).

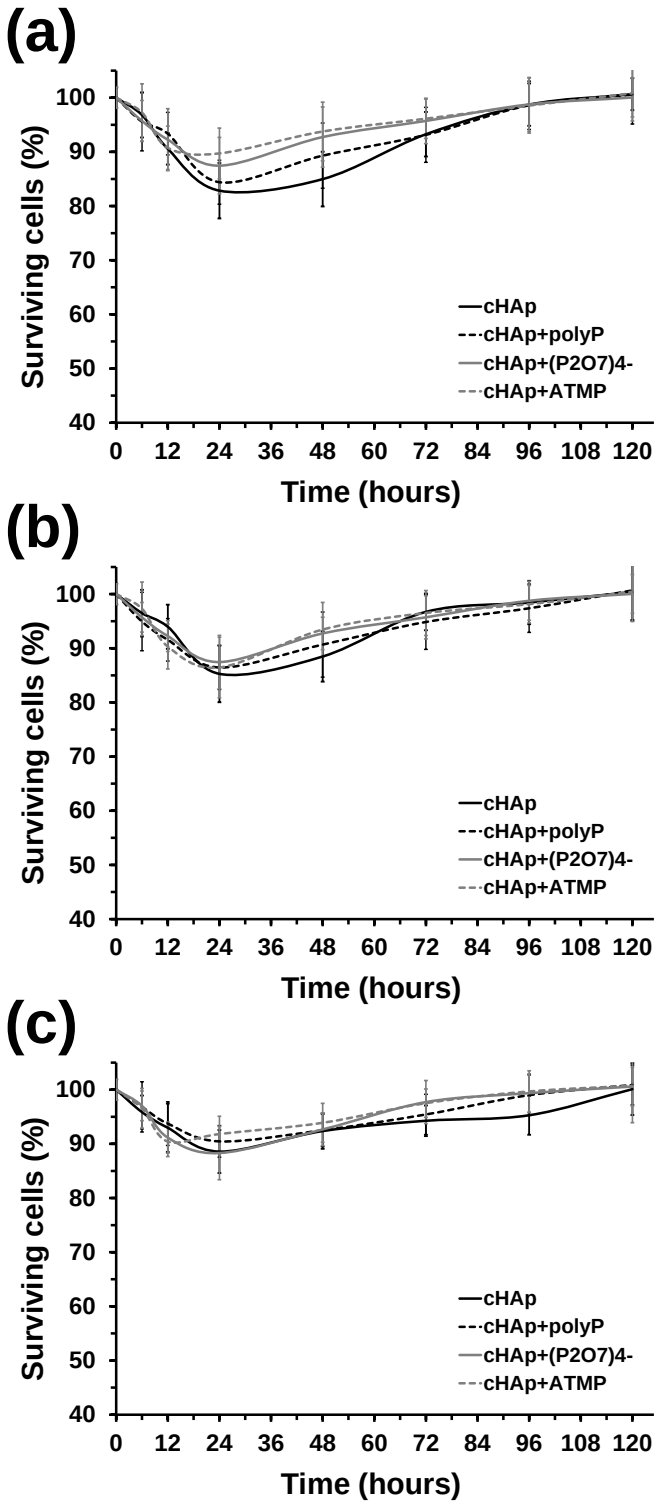

Figure 9.22. Temporal evolution of the cell viability after incorporate uncoated and biocoated cHAp nanoparticles in electroporated cell culture media: (a) HUVEC and (b) COS-1 noncancerous cells and (c) MCF-7 cancerous cells.

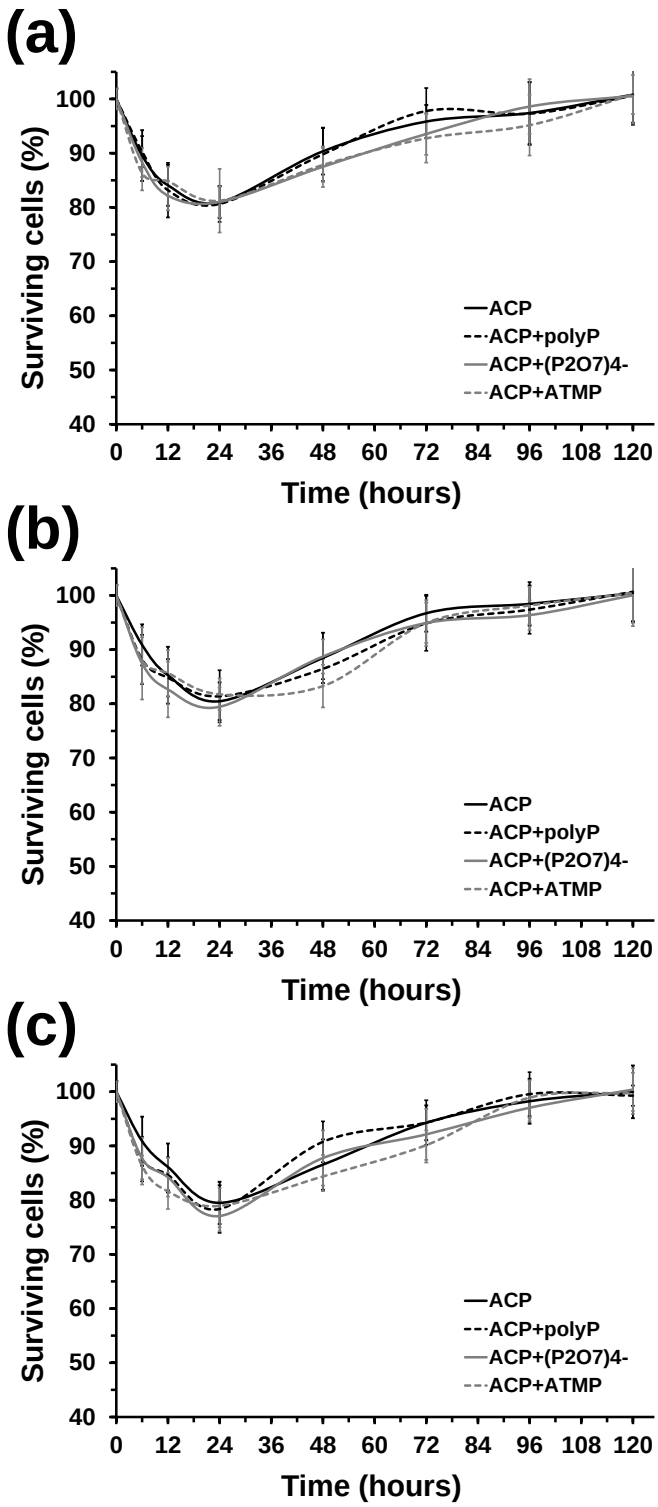

Figure 9.23. Temporal evolution of the cell viability after incorporate uncoated and biocoated ACP nanoparticles in electroporated cell culture media: (a) HUVEC and (b) COS-1 noncancerous cells and (c) MCF-7 cancerous cells.

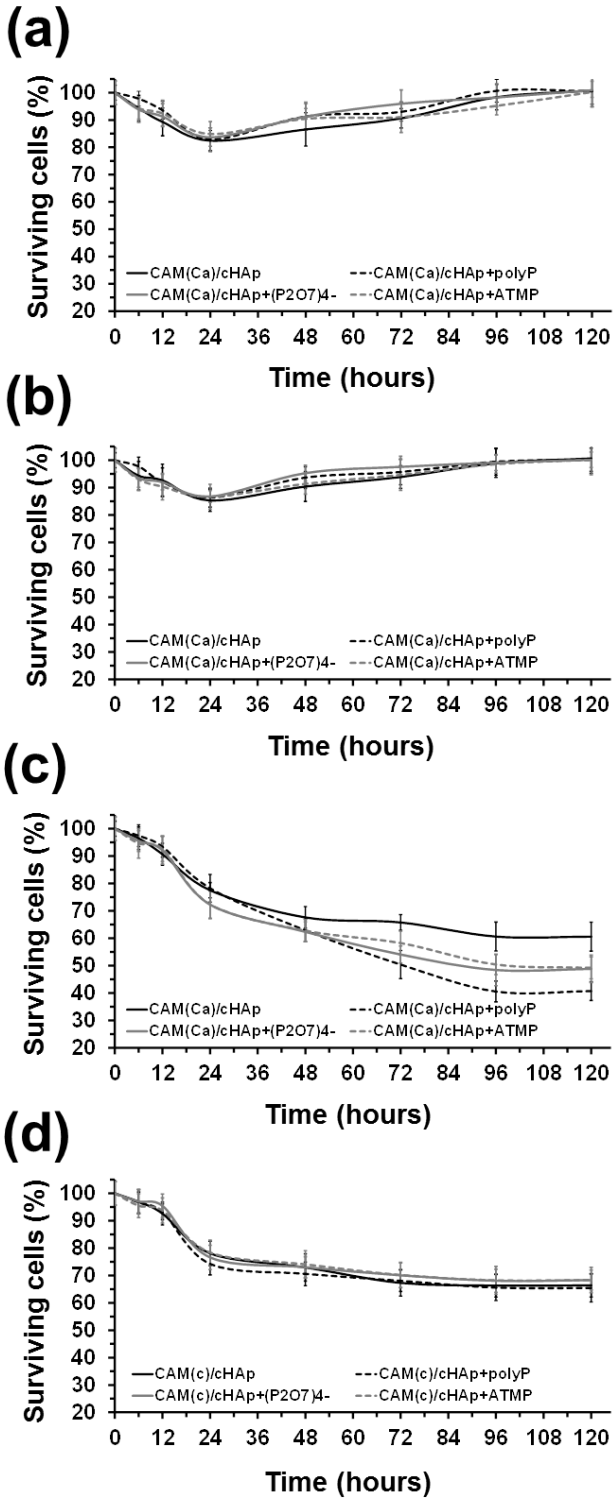

Figure 9.24. Temporal variation of the percentage of surviving cells after the incorporation of uncoated and biocoated CAM(Ca)/cHAp NPs to electroporated (a) HUVEC, (b) COS-1 and (c) MCF-7 cells, and (d) CAM(c)/cHAp NPs to electroporated MCF-7 cells.

In order to ascertain if the protecting role attributed to the biocoating affects to the CAM adsorbed onto mineral NPs only or extends to the antibiotic encapsulated into the cHAp

matrix, additional assays were performed by introducing uncoated and biocoated CAM(c)/HAp NPs into electroporated HUVEC, COS-1 and MCF-7 cells. The population of surviving HUVEC and COS-1 cells after 120 h was 100 % (**Figure 9.25**) while the amount of MCF-7 cells decreased (**Figure 9.24 d**). However, such reduction was not only smaller than that observed for CAM(Ca)/cHAp but also independent of the presence of biocoating. Thus, the percentage of dead MCF-7 cells after 120 h is 34 % $\pm$ 4 % for uncoated CAM(c)/cHAp, remaining at 35 % $\pm$ 5 % , 32 % $\pm$ 3 % and 32 % $\pm$ 5 % for NPs coated with polyP, and $P_2O_7^{4-}$ ATMP, respectively. Comparison of results displayed in **Figures 9.24 c** and **d** indicates that CAM molecules biomineralized inside the cHAp matrix through the *in situ* polymerization approach play a crucial role in the success of biocoated CAM(Ca)/cHAp NPs as antitumoral platforms. Thus, the biocoating layer probably prevents from degradation before the internalization of the NPs, increasing the therapeutic efficacy of CAM.

Qualitative analysis of the results obtained for CAM(Ca)/ACP (**Figure 9.26 a-c**) and CAM(c)/ACP (**Figures 9.26 d** and **9.27**) reflected a similar behavior. After 120 h, 100 % of non-cancerous cells survived, while the percentage of dead MCF-7 cells grew from 22 % $\pm$ 3 % for uncoated CAM(Ca)/ACP to 44 % $\pm$ 4 % (polyP), 33 % $\pm$ 4 % ($P_2O_7^{4-}$) or 33 % $\pm$ 2 % (ATMP) for coated NPs. From a quantitative point of view, the antitumor efficacy of the loaded antibiotic is around 15–20 % higher for cHAp than for ACP, independently of the biocoating. This feature has been attributed to the fact that the release from CAM(Ca)/cHAp is slower than from CAM(Ca)/ACP.

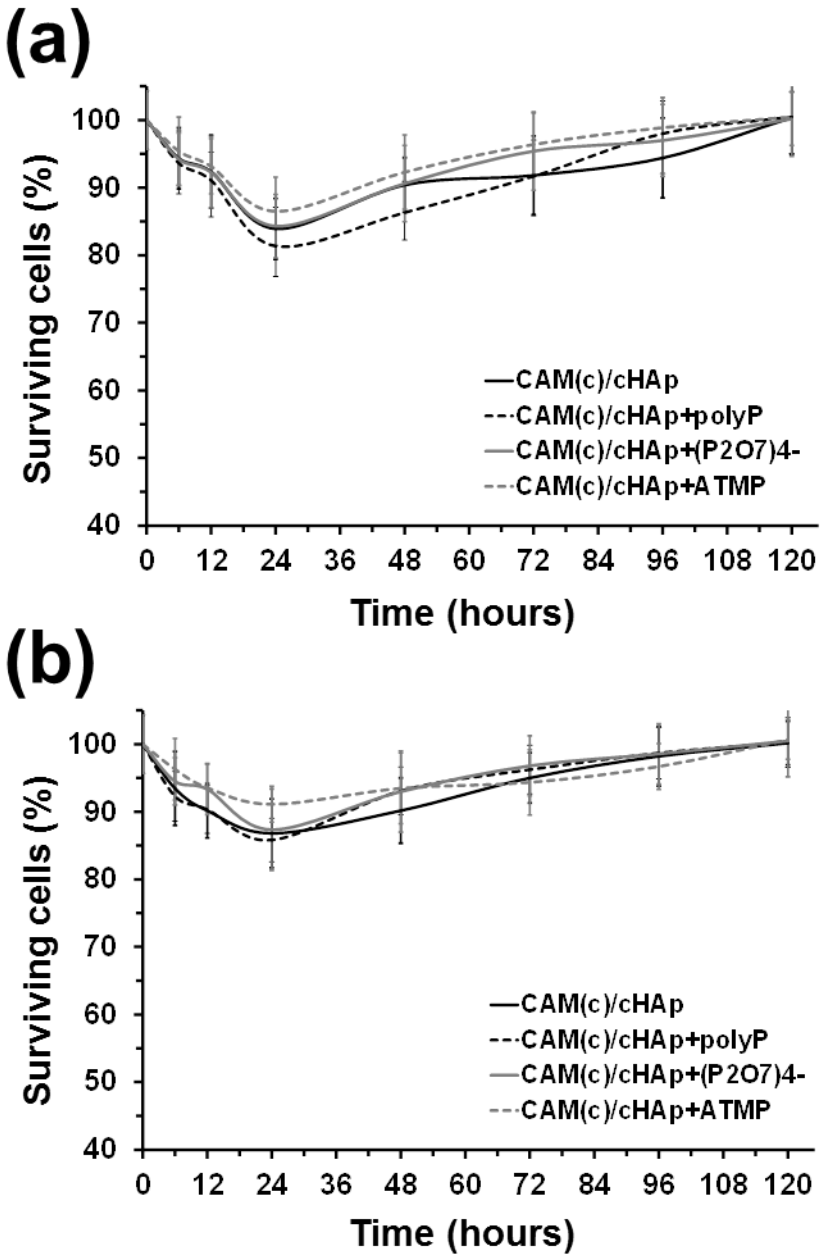

Figure 9.25. Temporal variation of the percentage of surviving cells after the incorporation of uncoated and biocoated CAM(c)/cHAp NPs to electroporated (a) HUVEC and (b) COS-1 cell culture media.

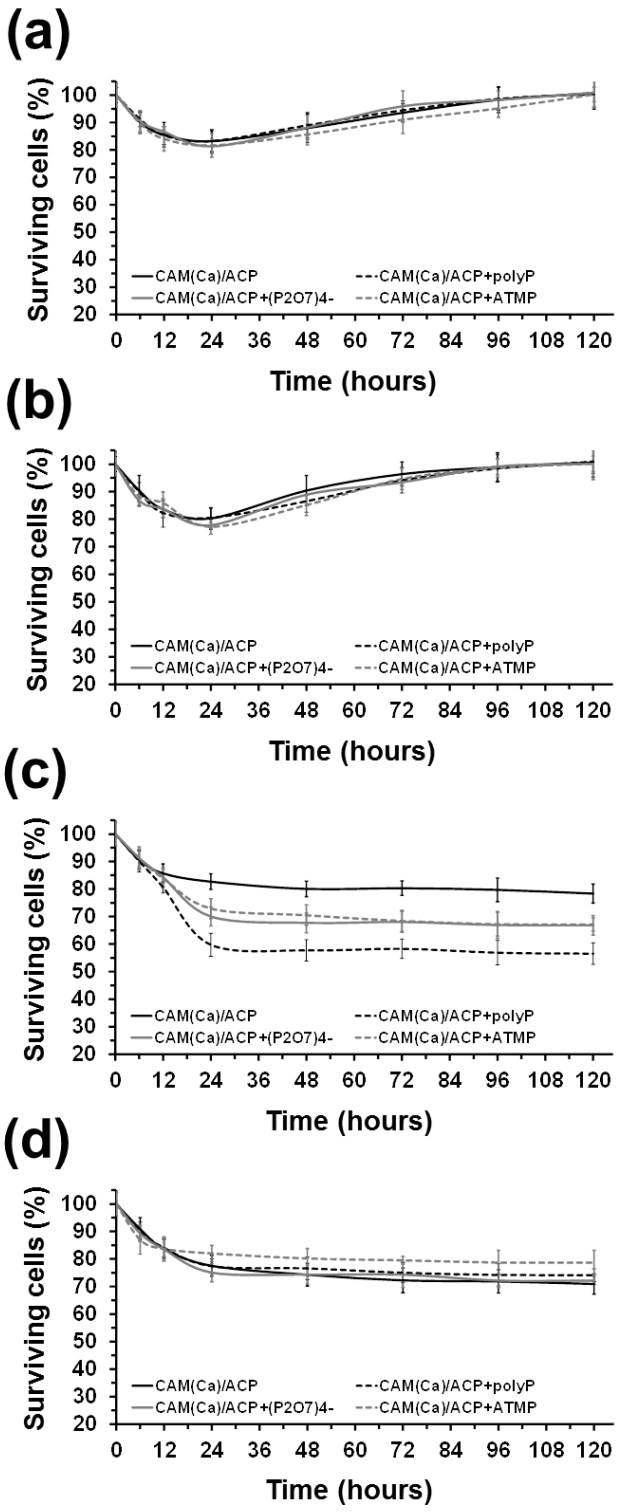

Figure 9.26. Temporal variation of the percentage of surviving cells after the incorporation of uncoated and biocoated: CAM(Ca)/ACP NPs to (a) HUVEC, (b) COS-1 and (c) MCF-7 electroporated cells; (d) CAM(Ca)/ACP nanoparticles to electroporated MCF-7 cell culture media.

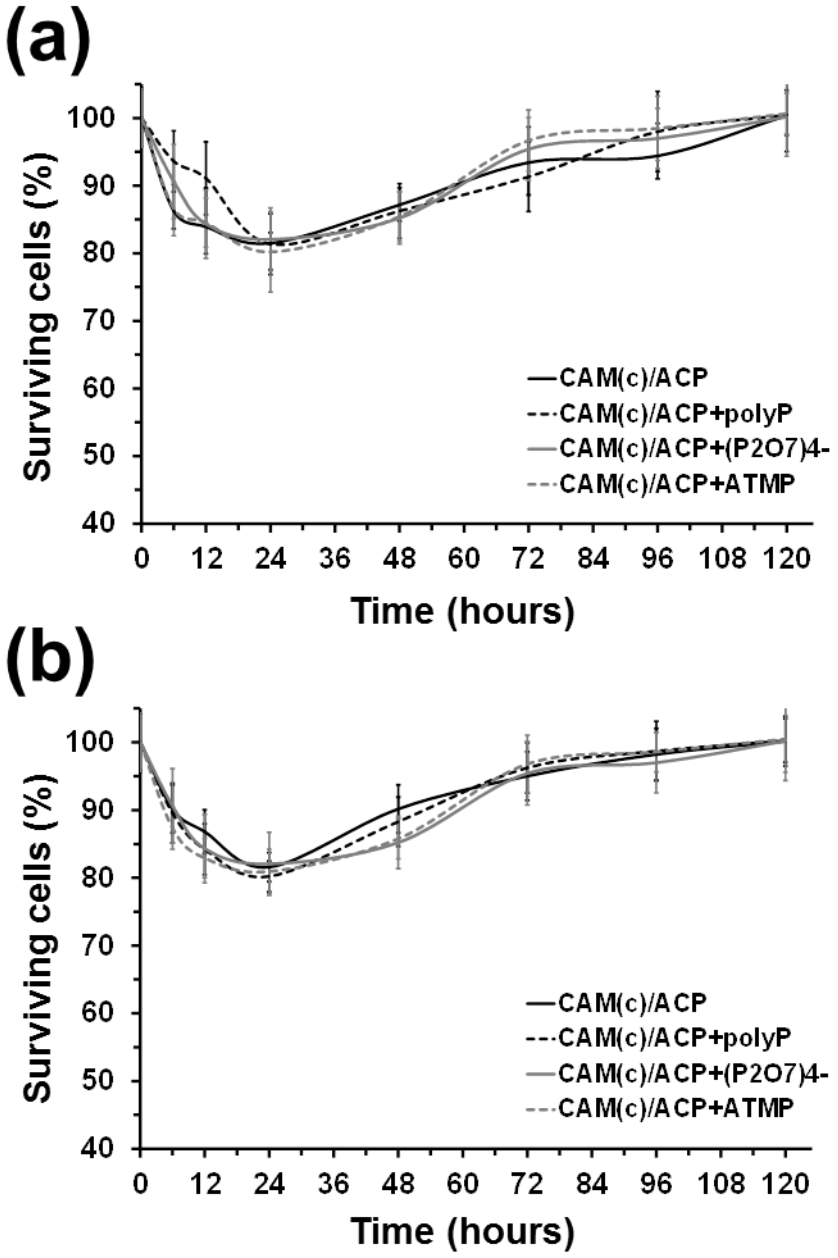

Figure 9.27. Temporal variation of the percentage of surviving cells after the incorporation of uncoated and biocoated CAM(Ca)/ACP NPs to (a) HUVEC and (b) COS-1 electroporated cells.

9.3.5 Proving the antitumor efficacy of CAM-loaded mineral nanoparticles via endocytic pathway

The last aspect to be addressed in this work refers to the cellular uptake of biocoated CAM(Ca)/cHAp NPs from the surrounding fluid without artificially created transient pores at the cell membrane (*i.e*. without apply electroporation). Endocytosis is the form of active transport used by almost all living eukaryotic cells to internalize extracellular materials that cannot pass through the membrane by simple diffusion. It is known that HAp enters

into cells through the endocytic pathway.[47-49] As the endocytosis activity of cancer cells is greater than that of normal cells[50-52] in this section we focus on the effect of both the biocoating and the loaded antibiotic in the efficiency of the endocytic process, which is expected to be closely related with the antitumor efficacy of the proposed therapeutic platforms.

The effect of the incorporation of unloaded cHAp particles into the cell culture was practically nil (**Figure 9.28**), the amount of surviving HUVEC, COS-1 and MCF-7 cells after 120 h being around 100 %, independently of the biocoating. In contrast, the incorporation of biocoated cHAp NPs loaded with a sub-lethal dose of CAM (**Figure 9.29**) inhibits selectively the viability of MCF-7 cancerous cells, while the response of HUVEC and COS-1 noncancerous cells is the same that for unloaded cHAp (*i.e*. ~100 % of surviving cells after 120 h). The inhibitory effects of CAM(Ca)/cHAp are severely affected by both presence and chemical nature of the biocoating, such dependence being considerably more pronounced than that observed in the previous sub-section for permeable electroporated cells. Thus, although for uncoated CAM(Ca)/cHAp the percentage of dead MCF-7 cells was 26 $\pm$ 5 % after 48 h, 98 % of the cell viability was recovered after 120 h (**Figure 9.29 c**). Comparison of the surviving cells profiles obtained by contacting uncoated CAM(Ca)/cHAp with electroporated and non-electroporated MCF-7 cells (**Figures 9.24 c and 9.29 c**, respectively) indicates that, in the latter case, the antibiotic release occurs mostly prior to the internalization of the NP. The apparition of temporary pores in cell membranes during the application of the electric field favors the rapid uptake of the CAM(Ca)/cHAp particles, ensuring the effectivity of the antibiotic released inside the cells once the cell membrane reseals after electroporation. In contrast, the anticancer efficacy of the antibiotic loaded in uncoated NPs is drastically limited by the rate of the endocytic process in absence of electroporation.

In opposition, biocoated CAM(Ca)/cHAp NPs improves the antitumor effectivity in absence of electroporation (**Figure 9.29 c**). More specifically, the percentage of dead cancerous cells after 120 h is 58 $\pm$ 5 %, 50 $\pm$ 5 % and 46 $\pm$ 5 % for NPs coated with polyP, $P_2O_7^{4-}$and ATMP, respectively. Accordingly, the barrier effect exerted by the biocoating with respect to the antibiotic release eliminates the rate of the endocytic as limiting step of its antitumor efficacy. The effectivity of such blocking effect varies as follows: polyP > $P_2O_7^{4-}$ > ATMP, indicating that CAM(Ca)/cHAp coated with polyP is the most effective antitumor platform.

In order to corroborate the performance of biocoated CAM(Ca)/cHAp NPs as smart antitumor platforms, additional experiments were conducted using MIA PaCa-2 pancreas cancer cells. Results, which are displayed in **Figure 9.29 d**, show that the percentage of dead cancerous cells after 120 h is 54 ± 6 %, 46 ± 5 % and 41 ± 5 % for CAM(Ca)/cHAp NPs coated with polyP, $P_2O_7^{4-}$ and ATMP, respectively. These values are fully consistent with those obtained using MCF-7 cells (**Figure 9.29 c**), confirming not only the barrier effect exerted by the biocoating but also the antitumor efficacy of antibiotic when it is appropriately released.

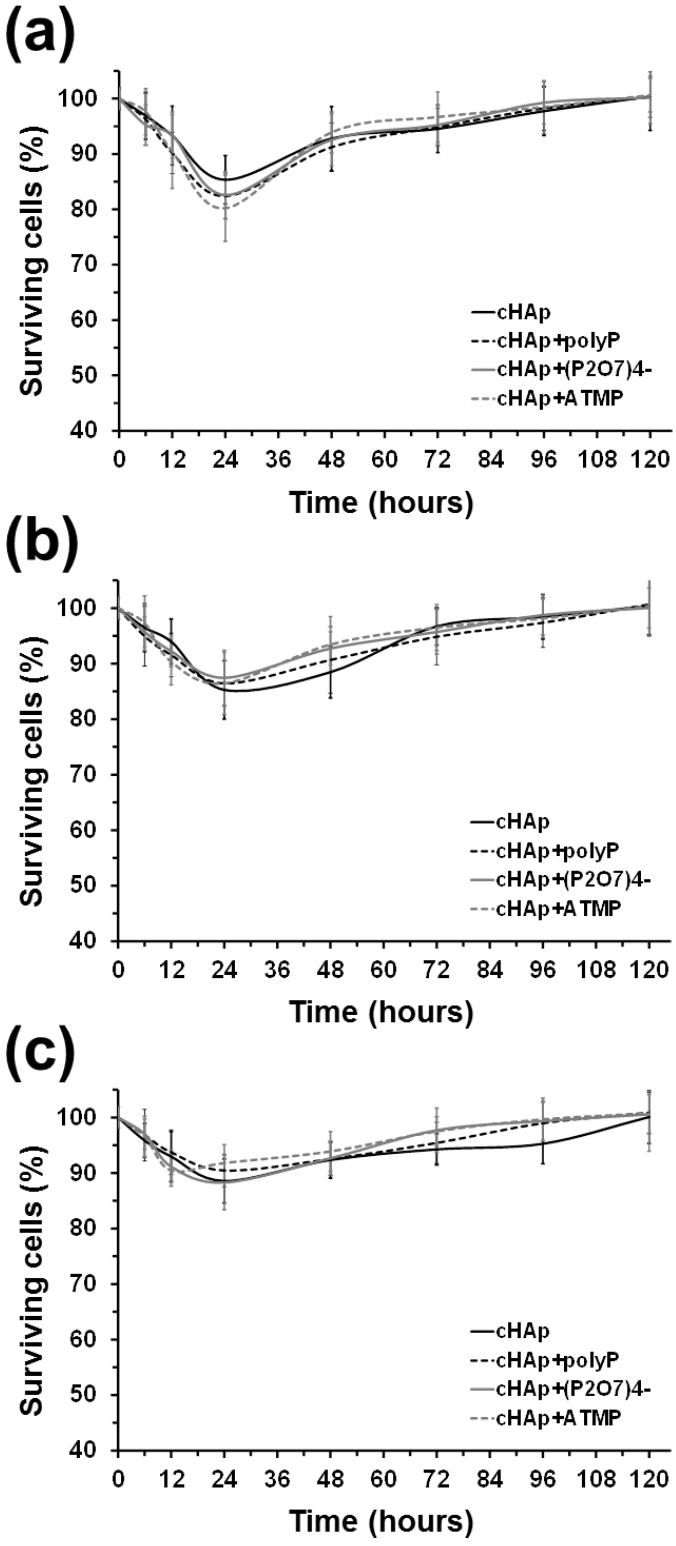

Figure 9.28. Temporal variation of the percentage of surviving cells after the incorporation of uncoated and biocoated cHAp NPs to (a) HUVEC, (b) COS-1 and (c) MCF-7 non-electroporated cells.

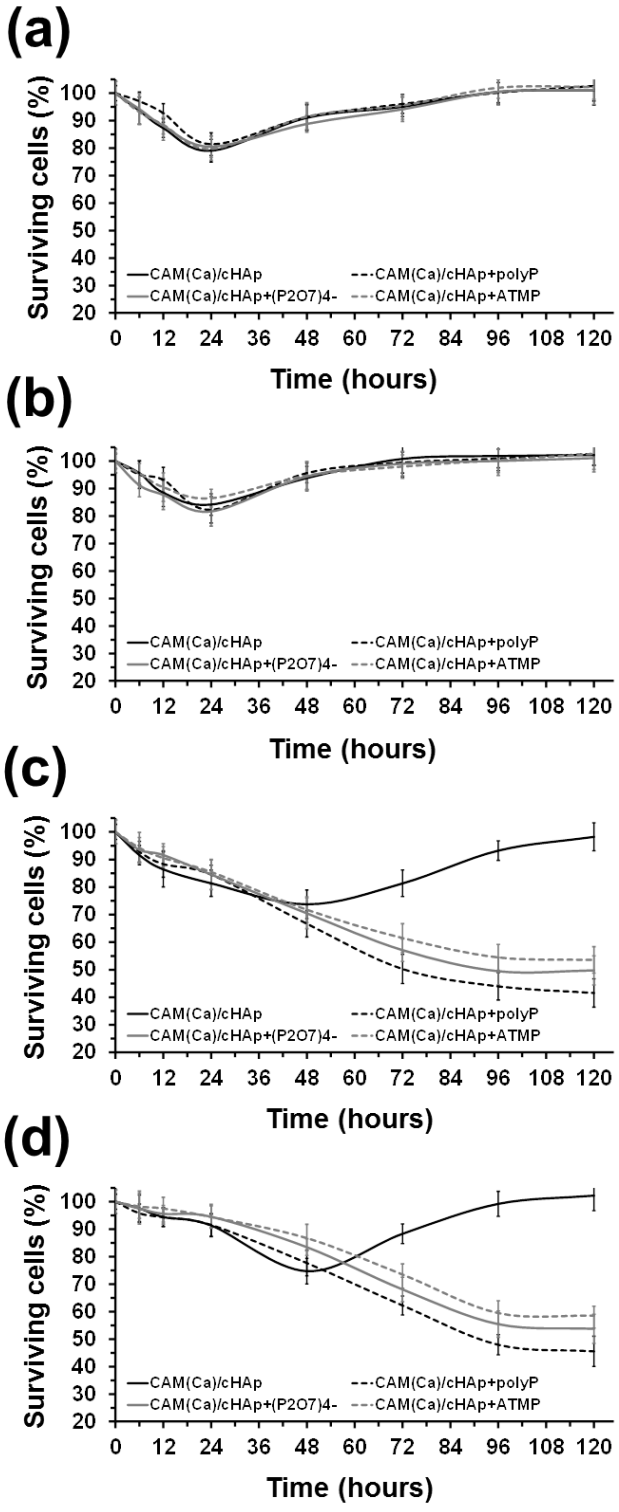

Figure 9.29. Temporal variation of the percentage of surviving cells after the incorporation of uncoated and biocoated CAM(Ca)/cHAp NPs to non-electroporated (a) HUVEC, (b) COS-1, (c) MCF-7 and (d) MIA PaCa-2 cells.

9.4 CONCLUSIONS

In the present study, we prove the very high antitumor activity of the following system: CAM loaded into cHAp NPs and, subsequently, coated with polyP. The efficiency and selectivity of CAM(Ca)/cHAp NPs coated with polyP have been demonstrated by the reduction of cancerous cells and the surviving of normal cells. The preparation strategy is essential to maximize the anticancer properties of that nanoplatform. Firstly, the *in situ* synthesis allows not only adsorbing antibiotic onto the NPs but also encapsulating CAM into the mineral matrix. Secondly, the amount of encapsulated antibiotic is higher for the Ca-path than for the Pho-path. Thirdly, hydrothermal conditions to produce cHAp are preferred with respect to aging conditions to obtain ACP. This is because the antibiotic release from cHAp is slower than from ACP, allowing a greater control of the antitumor activity. Although the biocoating is not affecting the antibiotic release process, its presence causes a drastic reduction in the amount of surviving cancer cells. Several hypotheses have been proposed to explain the role of polyP (*e.g.* as antibiotic carrier to target mitochondria or as antibiotic protector against degradation), even though more work is necessary is to provide complete understanding of the experimental observations related with the biocoating. In summary, CAM(Ca)/cHAp NPs coated with polyP in are promising bioplatforms for cancer therapy.

9.5 REFERENCES

1. Pina, S., Oliveira, J.M. & Reis, L.R. Natural-Based Nanocomposites for Bone Tissue Engineering and Regenerative Medicine: A Review. *Adv. Mater*. **27**, 1143-1152 (2015).
2. Cunniffe, S., Curtin, C.M., Thompson, E.M., Dickson, G.R. & O'Brien, F.J. Content-Dependent Osteogenic Response of Nanohydroxyapatite: An in Vitro and in Vivo Assessment within Collagen-Based Scaffolds. *ACS Appl. Mater. Interfaces*. **8**, 23477 (2016).
3. Lopa, S. & Henning, M. Bioinspired Scaffolds for Osteochondral Regeneration. *Tissue Engineering Part A*. **20**, 2052-2068 (2014).
4. Venkatesan. J. & Kim, S.K. Nano-hydroxyapatite composite biomaterials for bone tissue engineering--a review. *J. Biomed. Nanotech*. 10, 3124-3140 (2014)
5. Zakaria, S.M., Sharif, S.H., Othman, M.R., Yang, F. & Jansen, J.A. Nanophase hydroxyapatite as a biomaterial in advanced hard tissue engineering: a review. *Tissue Engineering Part B-Reviews.* **19**, 431-441 (2013).
6. Scaglione, S., Giannoni, P., Bianchini, P., Sandri, M., Marotta, R., Firpo, G., Valbusa, U., Tampieri, A., Diaspro, A., Bianco, P. & Quarto, R. Order versus Disorder: in vivo bone formation within osteoconductive scaffolds. *Sci. Rep*. **2**, 274-287 (2012).
7. Wilson, D.N. Ribosome-targeting antibiotics and mechanisms of bacterial resistance. *Nature Rev. Microbiol*. **12**, 35-48 (2014).
8. Doudna, J.A. & Rath, V.L. Structure and function of the eukaryotic ribosome: the next frontier. *Cell*. **109**, 153-156 (2002).
9. Polacek, N. & Mankin, A.S. The ribosomal peptidyl transferase center: structure, function, evolution, inhibition. *Crit Rev Biochem Mol Biol.* **40**, 285-311 (2005).
10. Sohmen, D., Harms, J.M., Schlunzen, F. & Wilson, D.N. SnapShot: Antibiotic inhibition of protein synthesis I. *Cell*. **138**, 1248-1260 (2009).
11. Poehlsgaard, J. & Douthwaite, S. The bacterial ribosome as a target for antibiotics. *Nature Rev. Microbiol*. **3**, 870-881 (2005).
12. Xaplanteri, M.A., Andreou, A., Dinos, G.P. & Kalpaxis, D.L. Effect of polyamines on the inhibition of peptidyltransferase by antibiotics: revisiting the mechanism of chloramphenicol action. *Nucleic Acids Res.* 31, 5074-5083 (2003).
13. Polacek, N., Gomez, M.J., Ito, K., Xiong, L., Nakamura, Y. & Mankin, A.S. The critical role of the universally conserved A2602 of 23S ribosomal RNA in the release of the nascent peptide during translation termination. *Mol. Cell*. **11**, 103-112 (2003).

14. Thompson, J., O'Connor, M., Mills, J.A. & Dahlberg, A.E. The protein synthesis inhibitors, oxazolidinones and chloramphenicol, cause extensive translational inaccuracy in vivo. *J. Mol. Biol.* 322, 273-279 (2002).

15. Myasnikov, A.G., Natchiar, S.K., Nebout, M., Hazemann, I., Imbert, V., Khatter, V.H., Peyron, J.F. & Klaholz, B.P. Structure–function insights reveal the human ribosome as a cancer target for antibiotics. *Nat. Commun*. **7**, 12856 (2016).

16. Kalghatgi, S., Spina, C.S., Costello, J.C., Liesa, M., Morones-Ramirez, J.R., Slomovic, S., Molina, A., Shirihai, O.S. & Collins, J.J. Bactericidal antibiotics induce mitochondrial dysfunction and oxidative damage in Mammalian cells. *Sci. Transl. Med*. **5**, 192ra85 (2013).

17. Lamb, R., Harrison, H., Hulit, J., Smith, D.L., Lisanti, M.P. & Sotgia, F. Mitochondria as new therapeutic targets for eradicating cancer stem cells: Quantitative proteomics and functional validation via MCT1/2 inhibition. *Oncotarget*. **5**, 11029-11037 (2014).

18. Killock, D. Drug therapy: Can the mitochondrial adverse effects of antibiotics be exploited to target cancer metabolism? *Nature Rev. Clin. Onc*. **12**, 190-197 (2015).

19. Brown, D. Antibiotic resistance breakers: can repurposed drugs fill the antibiotic discovery void? *Nat. Rev. Drug Discov*. **14**, 821-832 (2015).

20. Esner, M., Graifer, D., Lleonart, M.E. & Lyakhovich, A. Targeting cancer cells through antibiotics-induced mitochondrial dysfunction requires autophagy inhibition. *Cancer Lett*. **384**, 60-69 (2017).

21. Lamb, R., Ozsvari, B., Lisanti, C.L., Tanowitz, H.B., Howell, A., Martinez-Outschoorn, U.E., Sotgia, F. & Lisanti, M.P. Antibiotics that target mitochondria effectively eradicate cancer stem cells, across multiple tumor types: treating cancer like an infectious disease. *Oncotarget*. **6**, 4569-4584 (2015).

22. Nguyen, L.V., Vanner, R., Dirks, P. & Eaves, C.J. Cancer stem cells: an evolving concept. *Nat. Rev. Cancer*. **12**, 133-143 (2012).

23. Almora-Barrios, N. & De Leeuw, N.H. Molecular Dynamics Simulation of the Early Stages of Nucleation of Hydroxyapatite at a Collagen Template. *Cryst. Growth. Des*. **12**, 756-763 (2012).

24. Bertran, O., del Valle. L.J., Revilla-López, G., Chaves, G., Cardus L., Casas M.T., Casanovas J., Turon, P., Puiggalí, J. & Alemán, C. Mineralization of DNA into nanoparticles of hydroxyapatite. *Dalton Trans*. **3**, 317-327 (2014).

25. del Valle, L.J., Bertran, O., Chaves, G., Revilla-López, G., Rivas, M., Casas, M.T., Casanovas, J., Turon, P., Puiggalí, J. & Alemán, C. DNA adsorbed on hydroxyapatite surfaces. *J. Mater. Chem. B*. **2**, 6953-6966 (2014).

26. Kirkham. J, Brookes, S.J., Shore, R. C., Wood, S. R., Smith, D. A., Zhang, J., Chen, H. & Robinson, C. Physico-chemical properties of crystal surfaces in matrix–mineral interactions during mammalian biomineralisation. *Curr. Opin. Colloid Interface Sci*. **7**, 124-132 (2002).

27. Almora-Barrios, N., Austen, K.F. & de Leeuw N.H. Density functional theory study of the binding of glycine, proline, and hydroxyproline to the hydroxyapatite (0001) and (01$\bar{1}$0) surfaces. *Langmuir*. **25**, 5018-5025 (2009).

28. Rivas, M., Casanovas, J., del Valle, L.J., Bertran, O., Revilla-López, G., Turon, P., Puiggalí, J. & Alemán. C. An experimental-computer modeling study of inorganic phosphates surface adsorption on hydroxyapatite particles. *Dalton Trans*. **44**, 9980-9991 (2015).

29. Doi, K., Kubi, T., Takeshita, R., Kajihara, S., Kato, S., Kawazoe, Y., Shiba, T. & Akagawa, Y. Inorganic polyphosphate adsorbed onto hydroxyapatite for guided bone regeneration: An animal study. *Dent. Mat. J*. **33**, 179–186 (2014).

30. Comeau, P.A., Frei, H., Yang, C., Fernlund, G. & Rossi, F.M. In vivo evaluation of calcium polyphosphate for bone regeneration. *J. Biomat. Appl*. **27**, 267–275 (2012).

31. Jeon, B.J., Jeong, S.Y., Koo, A.N., Kim, B.C., Hwang, Y.S. & Lee, S.C. Fabrication of porous PLGA microspheres with BMP-2 releasing polyphosphate-functionalized nano-hydroxyapatite for enhanced bone regeneration. *Macromol. Res*. **20**, 715–724 (2012).

32. Morita, K., Doi, K., Kubo, T., Takeshita, R., Kato, S. & Akagawa, Y. Enhanced initial bone regeneration with inorganic polyphosphate-adsorbed hydroxyapatite. *Acta Biomat*. **6**, 2808–2815 (2010).

33. Kamat, S.S. & F. M. Raushel, F.M. The enzymatic conversion of phosphonates to phosphate by bacteria. *Curr. Opin. Chem. Bio*. **17**, 589–596 (2013).

34. Russell, R.G.G. & Ebetino, F.H. Mechanisms of action of bisphosphonates: similarities and differences and their potential influence on clinical efficacy. *Osteoporos. Int*. **19**, 733–759 (2008).

35. Uskokovic, V. & Uskokovic, D.P. Nanosized hydroxyapatite and other calcium phosphates: chemistry of formation and application as drug and gene delivery agents. *J. Biomed. Mater. Res., Part B*. **96**, 152-191 (2011).

36. Olton, D., Li, J., Wilson, M. E., Rogers, T., Close, J., Huang, L., Kumta, N.P. & Sfeir, C. Nanostructured calcium phosphates (NanoCaPs) for non-viral gene delivery: influence of the synthesis parameters on transfection efficiency. *Biomaterials*. **28**, 1267-1279 (2007).

37. del Valle, L.J., Bertran, O., Chaves, G., Revilla-López, G., Rivas, M., Casas, M.T., Casanovas, J., Turon, P., Puiggalí, J. & Alemán, C. DNA adsorbed on hydroxyapatite surfaces. *J. Mater. Chem. B*. **2**, 6953-6966 (2014).

38. Rivas, M, Casanovas, J., del Valle, L.J., Bertran, O., Revilla-López, G., Turon, P., Puiggalí, J. & Alemán. C. An experimental-computer modeling study of inorganic phosphates surface adsorption on hydroxyapatite particles. *Dalton Trans*. **44**, 9980-9991 (2015).

39. Klug. H. & Alexander, L. X-Ray Diffraction Procedure for Polycrystallite and Amorphous Materials, 2nd. Edition, John Wiley and Sons Press, New York (1974).

40. Landi, E., Tampieri, A., Celotti, G. & Sprio, S. Densification behaviour and mechanisms of synthetic hydroxyapatites. *J. Eur. Ceram. Soc*. **20**, 2377-2387 (2000).

41. Hopps, H.E., Wisseman Jr., C.L., Hahn, F.E., Smadel, J.E. & Ho, R. Mode of action of chloramphenicol IV. Failure of selected natural metabolites to reverse antibiotic action. *J. Bacteriol*. **4**, 561–567 (1956).

42. Waldon, J., Kubicek, M.R., Johnson, G.A. & Buhl, A.E. A HPLC-based chloramphenicol acetyltransferase assay for assessing hair growth: comparison of the sensitivity of UV and fluorescence detection. *Eur. J. Clin. Chem. Clin. Biochem*. **31**, 41-45 (1993).

43. Suzuky, M. & Shindo, M. Crystal Structure of Chloramphenicol. *Yakugaku Zasshi*. **76**, 927-939 (1956).

44. Dunitz, J.D. The Crystal Structure of Chloramphenicol and Bromamphenicol. *J. Am. Chem. Soc*. **74**, 995 (1952).

45. K. Ravindra, K., Acharya, K. & Sake Gowda, D.S. The structure of chloramphenicol. *Acta Cryst*. **B35**, 1360-1363 (1979).

46. Bulkley, D., Innis, C.A., Blaha, G. & Steitz, T.A. Revisiting the structures of several antibiotics bound to the bacterial ribosome. *Proc. Natl. Acad. Sci.* **107**, 17158-17163 (2010).

47. Motskin, M., Wright, D. M., Muller, K., Kyle, N., Gard, T. G., Porter, A. E. & Skepper, J. N. Hydroxyapatite Nano and Microparticles: Correlation of Particle Properties with Cytotoxicity and Biostability. *Biomaterials.* **30**, 3307-3317 (2009).

48. Zhang, H., Qing, F., Zhao, F., Hongsong, F., Liu, M. & Zhang, X. Cellular Internalization of Rod-Like Nano Hydroxyapatite Particles and Their Size and Dose-Dependent Effects on Pre-osteoblasts. *J. Mat. Chem. B*. **5**, 1205-1217 (2017)

49. Bauer, I. W., Li, S., Han, Y., Yuan, L. & Yin, M. Internalization of Hydroxyapatite Nanoparticles in Liver Cancer Cells. *J. Mater. Sci. Mater. Sci.* **19**, 1091-1095 (2008).

50. Sutherland, R., Delia, D., Schneider, C., Newman, R., Kemshead, J. & Greaves, M. Ubiquitous Cell-Surface Glycoprotein on Tumor Cells Is Proliferation-Associated Receptor for Transferrin. *Proc. Natl. Acad. Sci. U.S.A.* **78**, 4515-4519 (1981).

51. Daniels, T. R., Delgado, T., Rodriguez, J. A. Helguera, G. & Penichet, M. L. The Transferrin Receptor Part I: Biology and Targeting with Cytotoxic Antibodies for the Treatment of Cancer. *Clin. Immunol*. **121**, 144-158 (2006).

52. Daniels, T. R., Delgado, T., Helguera, G. & Penichet, M. L. The Transferrin Receptor Part II: Targeted Delivery of Therapeutic Agents Into Cancer. *Clin. Immunol*. **121**, 159-176 (2006).

10.

INCORPORATION OF CHLORAMPHENICOL LOADED HYDROXYAPATITE NANOPARTICLES INTO POLYLACTIDE

Chloramphenicol (CAM) has been encapsulated into hydroxyapatite nanoparticles displaying different morphologies and crystallinities. The process was based on a typical precipitation of solutions containing phosphate and calcium ions and the addition of CAM once the hydroxyapatite nuclei were formed. This procedure favoured a disposition of the drug into the outer parts of the nanoparticles and led to a fast release in aqueous media. A clear bactericide activity was derived, being slightly higher for the amorphous samples due to their higher encapsulation efficiency.

Polylactide microfibers incorporating CAM encapsulated in hydroxyapatite nanoparticles were prepared by the electrospinning technique and under optimized conditions. Drug release experiments demonstrated that only a small percentage of the loaded CAM was able to be delivered to an aqueous PBS medium. This amount was enough to render an immediate bacteriostatic effect without causing a cytotoxic effect on osteoblast-like, fibroblasts and epithelial cells. Therefore, the prepared scaffolds were able to retain CAM loaded nanoparticles, being a reservoir that should allow a prolonged release depending on the polymer degradation rate. The studied system may have promising applications for the treatment of cancer, since CAM has been proposed as a new antitumoral drug.

10.1 INTRODUCTION

Chloramphenicol (CAM) is a powerful and efficient broad-spectrum antibiotic that has been used since 1947. It was isolated from a strain of *Streptomyces venezuelae*, although it is currently obtained in a synthetic manner. CAM is considered as bactericide drug, but can act as a bacteriostatic at high concentrations or against very sensitive organisms. For example, CAM has been revealed highly effective against *Haemophilus influenzae*, *Streptococcus pneumoniae* and *Neisseria meningitidis*, which are the three main responsible bacteria of meningitis.[1] Nevertheless, several side effects (*e.g.* urotoxicity and hematologic disorders) have been reported for CAM, being somehow limited its clinical application. Therefore, different strategies to get derivatives with improved pharmacological properties have been developed.

CAM is a white crystalline material, soluble in alcohol and relatively insoluble in water. The compound has two chiral centers (**Figure 10.1**), being the D-erythro isomer the one that has the main bacteriostatic activity (98%).

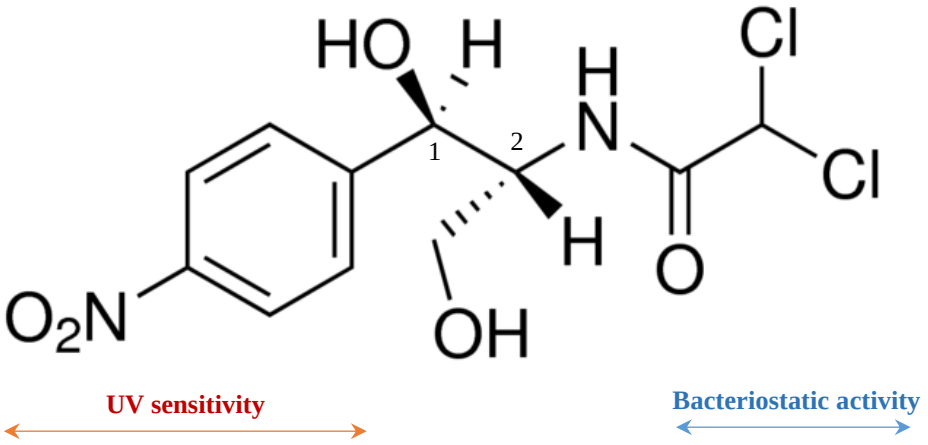

Figure 10.1. Chemical structure of CAM.

The mechanism of action of CAM consists in the interference of the bacterial protein synthesis, mainly by competitive inhibition of the peptidyl transferase activity of the bacterial ribosome. The dichloroacetyl moiety of CAM becomes essential for the antibacterial activity since it is similar to the aminoacyl-tail of tRNA.[2] Two binding sites for CAM in the 50S ribosome subunit have been determined from equilibrium studies.[3] being affinity constants equal to 2 μM and 200 μM. Non-competitive type of inhibition mechanism has also been found depending of factors such as nature of substrate, ionic

buffer or inhibitor concentration.[4-6] Clinical uses of CAM are however limited due to development of a typical antibiotic-resistance through targeted mutations[7] and specific problems related to haematological disorders such as aplastic anemia.[8]

Energy for eukaryotic cellular functions is provided by mitochondria through its capability to convert glucose into ATP. Normal human cells process glucose under aerobic conditions, firstly via a glycolysis step and subsequently via an oxidative phosphorylation step in the mitochondria that rendered pyruvate and CO_2, respectively. Glucose metabolism is reprogramed by cancer cells, being the glycolysis process enhanced with respect to oxidative phosphorylation one (as typical of anaerobic conditions for normal cells) and the final energy production consequently modified according to a named anaerobic glycolysis.[9,10]

Nowadays, it has been postulated that an efficient treatment of cancer can be performed by interfering the mitochondrial biogenesis since stem cancer cells are strongly anabolic and consequently requires a great activity for their survival and proliferative expansion. At this point, it is very interesting to note that mitochondria were originated from prokaryote organisms (*i.e.* endosymbiosis hypothesis).[11] Thus, inhibitory effects of antibiotics against bacteria would lead also to negative effects on mitochondrial protein synthesis and logically on the mitochondrial biogenesis.[12,13] The new strategy has been revealed effective for treatment of cancer and specifically different works concerned the use of CAM alone or in combination with anticancer drugs.[13-15]

Hydroxyapatite (HAp) is a bioceramic material defined by the chemical formula $Ca_{10}(PO_4)_6\,(OH)_2$. This material forms part of human bones, tendons and teeth. HAp is nowadays usually employed to prepare bionanocomposites due to its excellent biocompatibility, bioactivity and osteoconductivity.[16] A great diversity of methods have been postulated to prepare HAp, but in general those most employed are based on a simple chemical precipitation.[17-18] This could lead to amorphous (ACP) or crystalline (cHAp) particles after subsequent aging and hydrothermal processes, respectively. Moreover, morphology and size of particles can also be easily controlled by varying synthesis conditions. HAp particles have a great interest as carriers for drug delivery systems due to the facility to control texture, porosity, surface area and even to allow their surface functionalization. In fact, HAp has been employed for the release of large variety of therapeutic agents.[19-21]

Probably, one of the major limitations concerning the effectiveness of anticancer drugs is related to the capacity of cells to expel these drugs from their interior through molecular pumps such as P-glycoprotein and the multidrug resistance associated protein.[22] Chemotherapy efficiency is consequently reduced, being alternatively considered the incorporation of encapsulated drugs in order to avoid the failure of the treatment.[23,24] Calcium phosphate nanoparticles may be promising for the encapsulation of CAM, being possible to achieve the following goals: a) Effective incorporation into tumor cells via endocytosis, b) Evade to be degraded within the lysosomal, c) Capacity to release CAM in the cytoplasm due to its acidic pH and d) Capacity to display a CAM release rate sufficiently low to avoid activation of typical ejection pumps.

The present work is focused on the study of CAM encapsulation in calcium phosphate nanoparticles with different crystallinity (*i.e.* ACP and cHAp) and the evaluation of the corresponding release. Furthermore, the use of a biodegradable and biocompatible scaffold incorporating such loaded particles will also be considered. This system can serve as a reservoir for nanoparticles allowing a controlled and sustained dosage for an extended period. Specifically, PLA has been selected as the biocompatible polymer matrix due to its wide applications in the biomedical field and even for its relatively low degradation rate. Porous scaffolds have been prepared by electrospinning since it is a technique that allows an easy incorporation of nanoparticles, being also possible to minimize negative morphological changes (*e.g.* irregularities and formation of clumps) by an accurate control of the processing parameters.

10.2 EXPERIMENTAL SECTION

10.2.1 Materials

Polylactide, a product of Natureworks® (polymer 2002D), was kindly supplied by Nupik International (Polinyà, Spain). According to the manufacturer, this PLA has a D content of 4.25 wt-%, a residual monomer content of 0.3 wt-%, a relative density of 1.24 g/cc, a glass transition temperature (T_g) of 58 °C and a melting point of 153 °C.

The microbial culture was prepared with reagents and labware from Scharlau. *Escherichia coli* and *Staphylococcus aureus* bacteria strains were obtained from the Spanish Collection of Type Culture (CECT, Valencia, Spain). Human osteoblast-like cells (SAOS-2) and african green monkey fibroblasts (COS-1) and epithelial cells (VERO) were obtained from American Type Culture Collection (ATCC, USA).

10.2.2 Synthesis of ACP and HAp nanoparticles

An aqueous solution of diammonium hydrogen phosphate, ($(NH_4)_2HPO_4$; 750 mM) was dropwise added over an ethanol solution of calcium nitrate ($Ca(NO_3)_2$; 750 mM) under low stirring (100 rpm). The pH of the final mixture was continuously adjusted to 11 using an aqueous ammonium hydroxide solution (28−30 %). The reagent concentrations were consistent with the required Ca/P ratio of 1.67. The mixture was maintained under agitation (250 rpm) during 1 h.

ACP was obtained by a simple aging treatment (*i.e.* allowing samples to stand overnight at 37 ºC). Samples were washed twice with ethanol (analysis grade) and Milli-Q water, and recovered by centrifugation after each step. Finally, white powders were obtained by lyophilisation of the freezed samples (−80 ºC).

cHAp was prepared by applying a hydrothermal treatment instead of the indicated aging process. To this end, samples were loaded in a pressure vessel at 145 °C for 24 h. After this, a white powdered cHAp was recovered by applying the above indicated washing and drying protocol.

10.2.3 Encapsulation of CAM in ACP or cHAp nanoparticles

A 154 mM solution of CAM in absolute ethanol was immediately added after initiating the precipitation process of the ethanol solution of calcium nitrate with aqueous diammonium hydrogen phosphate. The added volume was calculated to get a 4.3 mM concentration of CAM in the final mixture. Aging and hydrothermal treatments to get encapsulated amorphous (ACP-CAM) and crystalline (cHAp-CAM) samples were performed according to the indicated protocols.

Encapsulation efficiency ($EE\%$) was calculated as (Equation 1):

$$EE\% = \left(\frac{W_t}{W_0}\right) \cdot 100 \qquad (1)$$

where W_t is the total amount of the incorporated CAM and W_0 is the total quantity of CAM that was initially added in the precipitation medium. W_t and W_0 were determined from UV measurements using a Shimadzu 3600 spectrometer. To this end, calibration curves were obtained by plotting the absorbance measured at 278 nm versus CAM

concentration in the initial and the nanoparticle solubilisation media. The last was a 100 mM HCl and 50 mM $NaCl$ mixture.

10.2.4 Electrospinning of PLA incorporating ACP or cHAp nanoparticles

The PLA was dissolved in a chloroform-acetone mixture (2:1 v/v) at concentration of 8 w/v-%. Electrospun fibers were collected on a target placed at different distances (10–25 cm) from the needle tip (inside diameter 0.84 mm). The voltage was varied between 10 and 30 kV and applied to the target using a high-voltage supply (Gamma High Voltage Research, ES30-5W). Polymer solutions were delivered via a single KDS100 infusion syringe pump (KD Scientific, USA) to control the flow rate (from 1 to 5 mL/h). All electrospinning experiments were carried out at room temperature. ACP or cHAp (nanoparticles with and without incorporation of CAM) loaded electrospun fibers were prepared using optimized parameters (*i.e.* collector distance, voltage and flow rate) and solvent conditions (*i.e.* polymer and drug concentrations). The nanoparticles content in the electrospinning solution was 1.6 w/v-% and 20 w/w-% for the electrospun scaffold.

10.2.5 Measurements

Fourier transform infrared (FTIR) spectroscopy. Infrared absorption spectra were recorded in the 4000–600 cm^{-1} range with a Fourier Transform FTIR 4100 Jasco spectrometer equipped with a Specac model MKII Golden Gate attenuated total reflection (ATR) cell.

Thermal stability. Thermogravimetric analyses (TGA) for studying thermal stability a relatively low temperatures (< 600 ºC) were performed at a heating rate of 20 ºC/min (sample weight *ca.* 5 mg) with a Q50 thermogravimetric analyser of TA Instruments and under a flow of dry nitrogen. Test temperatures ranged from 50 to 600 ºC.

Wettability. Contact angles (CA) were measured at room temperature with sessile drops using an OCA-15 plus Contact Angle Microscope (Dataphysics, USA) and SCA20 software. Contact angle values of the right and left sides of distilled water drops were measured and averaged. Measurements were performed 10 s after the drop (5 mL) was deposited on the sample surface. All CA data were an average of six measurements on different surface locations.

Zeta Potential. Dynamic light scattering studies were performed using NanoBrook Omni Zeta Potential Analyzer from Brookheaven Instruments. Measurement consisted of 3 runs each of 120 s duration, which were averaged to obtain the effective diameter (D_{eff}). Samples were analysed at 25 ºC using a scattering angle of 90º. In order to know the Z-potential particles were re-suspended in 1 mM KCl solution and 30 consecutive measurements were taken of each sample.

X-Ray diffraction. X-ray diffraction patterns were acquired using a Bruker D8 Advance model with CuK_{α} radiation ($\lambda = 0.1542$ nm), Bragg-Bretano, θ–2θ geometry and one-dimensional Lynx Eye detector.

Scanning electron microscopy (SEM): Detailed inspection of texture and morphology of electrospun samples was conducted by scanning electron microscopy using a Focused Ion Beam Zeiss Neon 40 instrument (Carl Zeiss, Germany). Carbon coating was accomplished by using a Mitek K950 Sputter Coater fitted with a k150×film thickness monitor. Samples were visualized at an accelerating voltage of 5 kV. The diameter of electrospun fibers was measured with SmartTiff software from Carl Zeiss SMT Ltd.

10.2.6 Release experiments

Controlled release measurements were performed with 4 mg of loaded nanoparticles of ACP and cHAp as well as with 0.5 cm × 0.5 cm square pieces of the different loaded scaffolds (*i.e.* those with CAM encapsulated in ACP or cHAp). The thickness of these scaffolds was always close to 100 μm. The corresponding samples were incubated at 37 °C in an orbital shaker at 80 rpm in tubes of 10 mL. Phosphate-buffered saline (PBS) and a 3:7 v/v mixture of PBS and ethanol were employed as release media following a two-step process. This consisted on a first release in the PBS medium during 22 h, which was the time necessary to get a constant value, and a second step for the next 40 h in the PBS-ethanol medium. Drug concentration was evaluated by UV absorbance measurements as above described but using calibration curves of the corresponding release media. All drug release tests were carried out using three replicates and the results obtained were averaged.

The combination of the Higuchi[25] and first-order[26] models were employed to describe the first (0–60 %) and last part of the release (40–100 %), respectively.

10.2.7 Antimicrobial test assays

E. coli and *S. aureus* bacteria were selected to evaluate the antimicrobial effect of CAM loaded nanoparticles and the derived electrospun scaffolds. The bacteria were previously grown aerobically to exponential phase in broth culture (5 g/L beef extract, 5 g/L $NaCl$, 10 g/L tryptone, pH 7.2).

Growth experiments were performed on a 24-well culture plate. CAM loaded ACP and cHAp nanoparticles (20 mg) and differently loaded electrospun PLA scaffolds (pieces of 1 cm x 1 cm and thickness close to 100 µm) were placed into the wells. Unloaded ACP and cHAp nanoparticles and PLA scaffolds were considered as negative controls, and PLA loaded with CAM was a positive control. Then, 2 mL of broth culture containing 103 colony forming units (CFU) was added to the samples. Cultures were incubated at 37 °C and agitated at 80 rpm. Aliquots of 100 µL were taken at 24 h and 48 h from the starting culture time for absorbance measurement at 600 nm in a microplate reader. Thus, turbidity was directly related to the relative bacterial growth by considering the maximum growth attained in the absence of any polymeric matrix (control). Experiments were performed in quadruplicate and the results averaged.

10.2.8 Cell adhesion and proliferation studies

Studies were performed with osteoblast SAOS-2 cells, fibroblast COS-1 cells and epithelial Vero cells. In all cases, cells were cultured in Dulbecco's Modified Eagle Medium (DMEM), as previously reported.[27]

Five pieces (1 cm x 1 cm and thickness close to 700 µm) of unloaded and CAM loaded scaffolds were placed and fixed in each well of a 24-well culture plate with a small drop of silicone (Silbione® MED ADH 4300 RTV, Bluestar Silicones France SAS, Lyon, France). This plate was then sterilized by UV-radiation in a laminar flux cabinet for 15 min. For cell adhesion assays, aliquots of 50–100 µL containing 2×10^5 cells, were seeded onto the samples in each well and incubated for 24 h (adhesion assay). For cell proliferation assays, the same aliquot volume but containing a lower cell concentration than for adhesion experiments (1×10^5 cells) was seeded and incubated for 96 h.

Samples were evaluated by the standard adhesion and proliferation method.[25] The procedure is based on a simple modification of the ISO10993–5:2009 standard test, which describes the appropriate methodology to assess *in vitro* cytotoxicity of medical

devices. This test is designed to determine the *in vitro* biological response of mammalian cells using appropriate biological parameters. According to this ISO standard, devices fall into one of three categories based on expected contact with the patient: (a) Limited (≤ 24 h), (b) Prolonged (> 24 h and ≤ 30 days) and (c) Permanent (> 30 days). In our case, the assay was performed according to the limited and prolonged categories and using four replicates. The results were then averaged.

10.2.9 Statistical analysis

The statistical analysis of the data was performed with OriginPro v10 software. The data were statistically analysed using one-way analysis of variance (one-way ANOVA). Multiple comparisons were carried out using Tukey test with statistical significance at $p < 0,05$.

10.3 RESULTS AND DISCUSSION

10.3.1 Encapsulation of CAM in ACP and cHAp nanoparticles

Figure 10.2 shows the morphologies of ACP and cHAp particles prepared by precipitation of an ethanol solution of $Ca(NO_3)_2$ with an aqueous solution of $(NH_4)_2HPO_4$ and after the subsequent aging or hydrothermal treatment. In order to get appropriated rounded or rod-like morphologies that could be considered appropriate for drug encapsulation, the solutions containing Ca^{2+} and PO_4^{3-} ions were quickly mixed at high pH.[28-30] The reaction mixture had a relatively high ethanol content to allow the addition of a subsequent ethanol solution of CAM without causing the precipitation/crystallization of this low water soluble drug. The applied encapsulation methodology was focused to incorporate CAM once a former hydroxyapatite nucleus was obtained. Therefore, CAM was mainly loaded in the outer shell of nanoparticles in order to facilitate its release.

Significant morphological differences were found between the nanoparticles of ACP and cHAp. The first ones were rounded with a diameter around 50−70 nm, whereas cHAp crystallized as nanorods with a length of 200 nm and a widthness around 90 nm. The degree of agglomeration of particles was also different, being higher for the amorphous ACP. **Figure 10.3** shows also that the encapsulation of CAM had not a significant influence on the derived morphologies. Furthermore, no evidences of CAM crystals,

which usually appear as platelets (inset of **Figure 10.3 b**), were detected in the different preparations as could be expected for the established washing protocol.

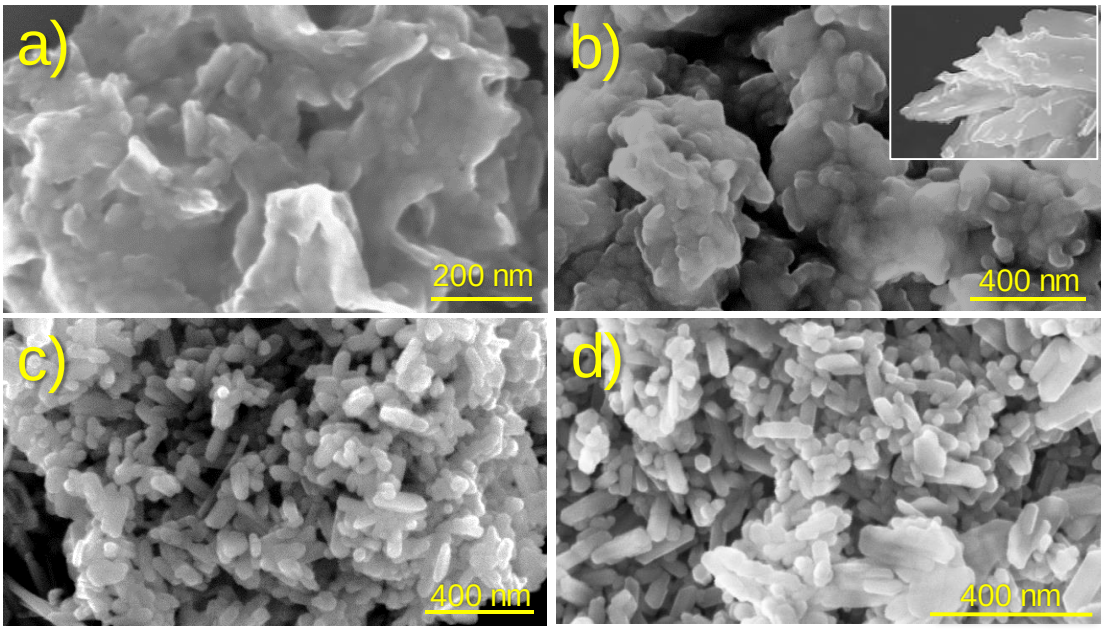

Figure 10.2. SEM images showing the morphology of nanoparticles of: a) ACP, b) ACP loaded with CAM (ACP-CAM), c) cHAp and d) cHAp loaded with CAM(HAp-CAM). Inset of (b) shows typical CAM crystals.

X-ray diffraction patterns of ACP and cHAp particles showed clear differences that mainly concern to the width of the reflections peaks, which obviously was greater for the more amorphous ACP sample (**Figure 10.3**). Degree of crystallinity was calculated considering the intensity of the (300) reflection, I_{300}, and the intensity of the hollow between the (112) and (300) reflections, $V_{112/300}$ (Equation 2):[31]

$$\chi_c = 1 - \frac{V_{112/300}}{I_{300}} \quad (2)$$

Cristallinity values of 66 % and 10 % were determined for cHAp and ACP nanoparticles, respectively, while a slight decrease up to 55 % and 9 % was observed after encapsulation of CAM. The small loaded amount of CAM made difficult for both samples the observation of distinctive peaks associated to the drug. Thus, only a small signal at 0.428 nm, which correspond to the (401) and (114) reflections of the CAM structure, could be intuited.[32]

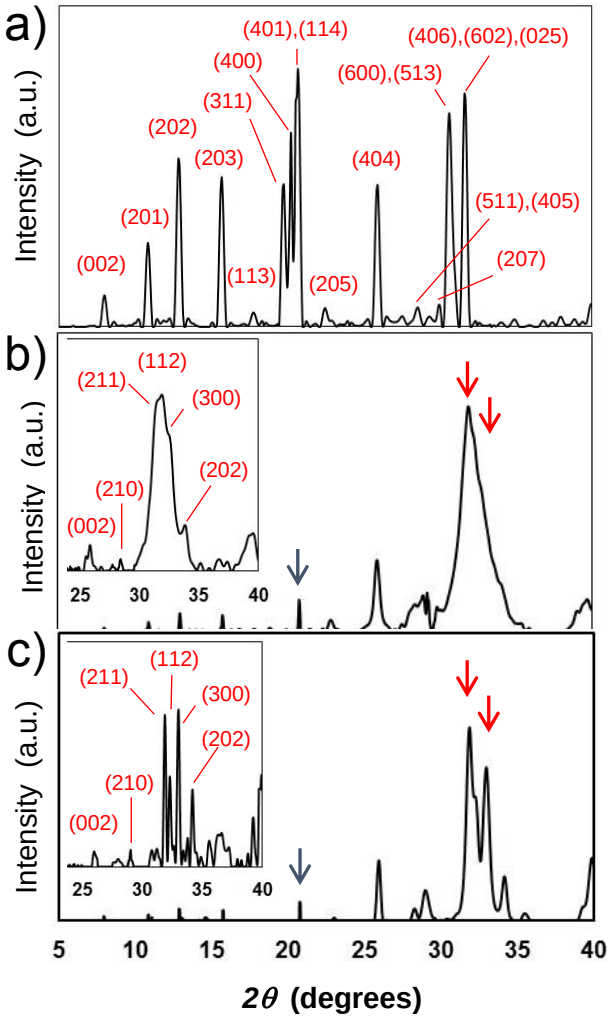

Figure 10.3. X-ray diffraction patterns of CAM (a), ACP-CAM (b) and cHAP-CAM (c) nanoparticles. Insets of b) and c) show the patterns of synthesized ACP and cHAp nanoparticles. Blue arrows point out the (401) + (114) reflections of CAM, while red arrows indicated the (211) and (300) reflections of ACP and cHAp.

UV absorbance curves of CAM were taken in the medium employed to dissolve the different kinds of nanoparticles and showed a characteristic band at 278 nm (**Figure 10.4 a**). This well-known absorption band is attributed to the *p*-nitrophenyl chromophore group and has a clear relationship with CAM concentration in the medium, as can be observed in **Figure 10.4 b**. Specifically, a calibration equation ($y = 11.77x$) with a regression coefficient (r) of 0.998 was deduced as well as a molar extinction coefficient of 1.28 $\mathrm{M}^{-1}\mathrm{cm}^{-1}$.

The amount of encapsulated drug was therefore evaluated by UV measurements, being determined encapsulation efficiencies of 23 % and 9 % for ACP and cHAp, respectively. It is clear that great differences were found depending on the applied aging and hydrothermal treatments. Thus, CAM was more easily excluded from the crystalline domains and consequently a lower encapsulating efficiency was detected for these more crystalline particles. Alternatively, a certain amount of CAM could be released from the formed nanoparticles during the prolonged hydrothermal treatment at relatively high temperature.

The amount of CAM loaded in the particles can also be referred as a weight percentage. Values of 0.63 % and 0.33 % were determined for ACP and cHAp, respectively, as shown in **Figure 10.4 c** where maximum (theoretical) percentages are also reported. Note that in this case, the maximum load is higher for cHAp due to its lower synthesis yield after the more drastic conditions of the hydrothermal treatment.

Figure 10.5 shows the hydrodynamic diameter distribution (measured in water) of the prepared nanoparticles. This distribution is narrow (*i.e.* between 10 and 100 nm) and fits to an unimodal Gaussian curve. Particles of ACP and cHAp showed very similar diameters with average values of 28 ± 8 nm and 20 ± 5 nm, respectively. The encapsulation of CAM increased the particle size and average values of 44 ± 10 nm and 26 ± 7 nm were determined. Thus, amorphous ACP had the higher increase (*i.e.* 57 % with respect to 30 % for cHAp), which is logical considering its higher CAM load.

Z potential and the electrophoretic mobility were also determined for the aqueous (pH 6.5) nanoparticle dispersions (**Figure 10.6**). It was clearly observed that the surface charge and electrophoretic mobility of the nanoparticles of ACP and cHAp with and without charge of CAM were similar and within the range of −35 to −40 mV and −2.7 to −3 (μ/s) / (V/cm), respectively. The similar potential Z values determined for the various particles supports the idea that CAM was effectively incorporated into the nanoparticles and that potentially adsorbed molecules were effectively removed by the repetitive washing performed after the encapsulation process.

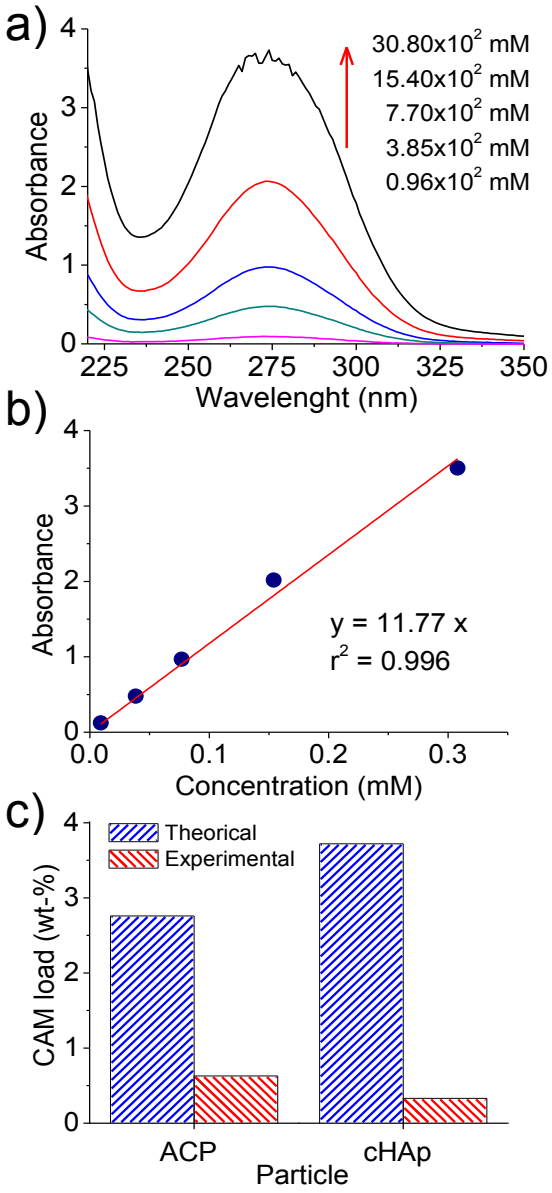

Figure 10.4. a) UV absorbance curves of CAM solutions at the indicated concentrations. b) Calibration curve for absorbance measurements at 278 nm. c) Encapsulation efficiency for ACP and cHAp nanoparticles.

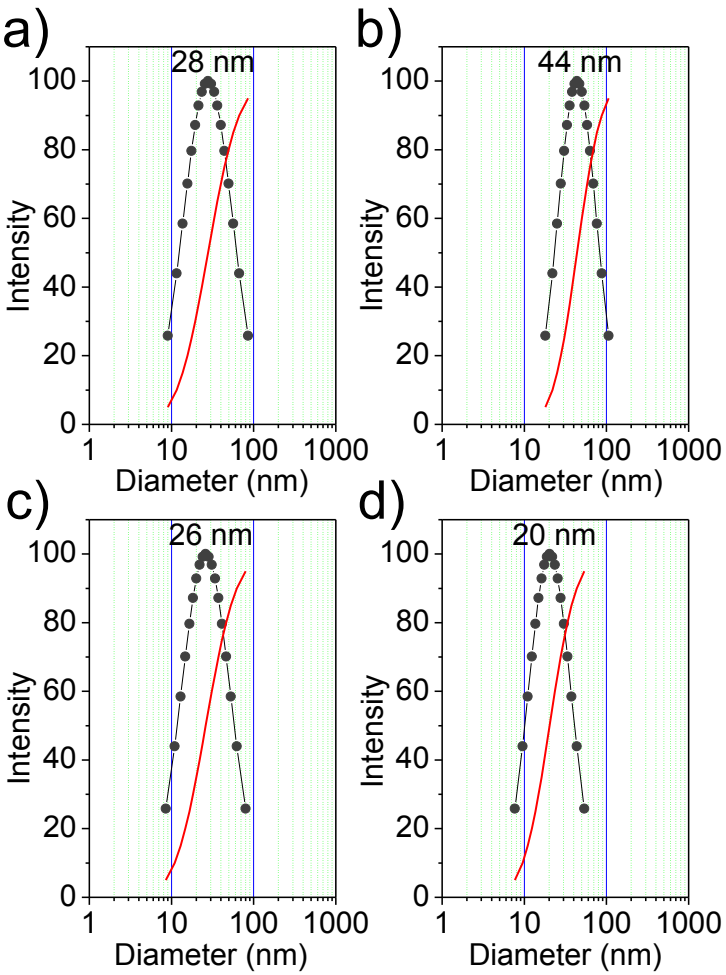

Figure 10.5. Nanoparticle diameter distribution determined by DLS for: a) ACP, b) ACP-CAM, c) cHAp, d) cHAp-CAM. Size distribution (black line) and measure correlation functions (red line).

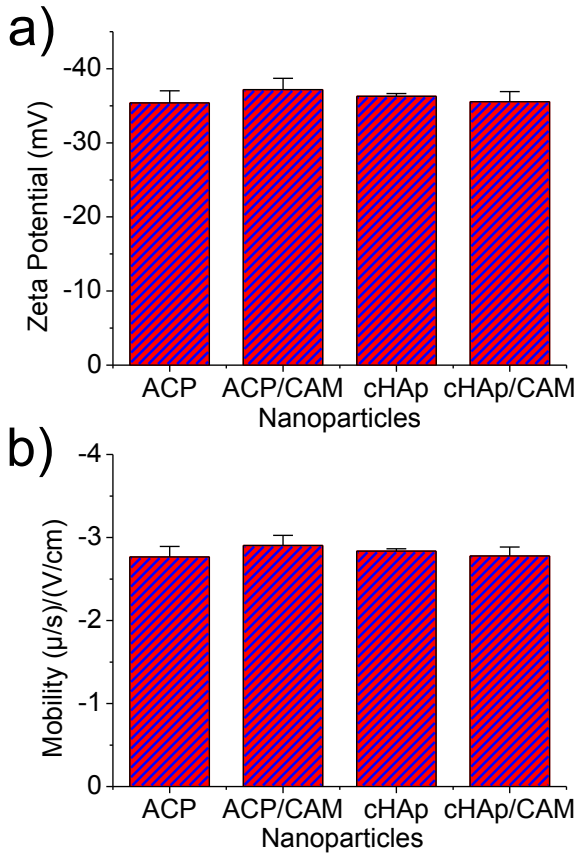

Figure 10.6. Zeta potential (a) and electrophoretic mobility (b) of the indicated unloaded and CAM loaded nanoparticles.

10.3.2 CAM release from ACP and cHAp nanoparticles

CAM was easily released from both loaded ACP and cHAp nanoparticles in the simple physiological PBS medium. **Figure 10.7** shows that CAM was released in a similar way from both types of nanoparticles despite the loading efficiency and the bactericide effect (as explained in the next section) were different. It should be pointed out that CAM was mainly incorporated in the shell of nanoparticles according to the applied loading process. Therefore, a fast delivery step that corresponded to the superficially located drug was firstly detected. The release percentages at the end of this step (up to 2 h) corresponded to about 58 % for both types of nanoparticles. After that the release mechanism changed to a first-order kinetic model that is indicative of a process where the rate depends only of the drug concentration. Kinetic constant (k_1 = 0.30 and 0.23 h^{-1} for ACP and cHAp loaded with CAM, respectively) was similar for both types of nanoparticles, although a slightly lower value was observed for the less loaded sample (*i.e*. cHAp). The released percentages achieved a constant value close to 75 % after

20 h. This stationary level was mainly consequence of the saturation of the aqueous solution with the scarcely soluble CAM drug.

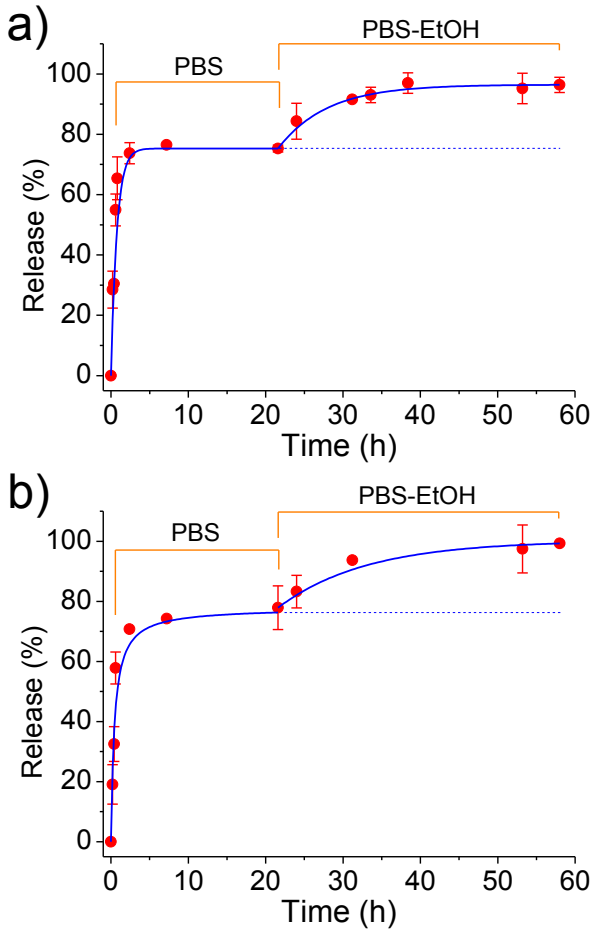

Figure 10.7. Release of CAM from ACP (a) and cHAp (b) loaded nanoparticles during exposure to the indicated media. PBS-EtOH refers to the PBS-ethanol mixture (see Methods section).

The release medium was subsequently changed by a PBS/Ethanol mixture in order to get comparative data with the subsequent experiments performed with PLA scaffolds. Basically, in the last case, ethanol had a great influence of the release behavior due to its capacity to swell nanofibers and facilitate the drug delivery. **Figure 10.7** clearly shows as the release from both types of nanoparticles was again significant due to both the renovation of the medium and the higher solubility of CAM in ethanol. Thus a complete delivery of CAM was achieved after an additional period of approximately 20 h. This release could be fitted with a first-order kinetic model with a higher constant than that previously determined. This constant decreased in a similar way as a consequence of the low CAM residual content for ACP and cHAp up to a value close to 0.12 and 0.07 h^{-1}, respectively.

10.3.3 Bactericide effect of ACP and cHAp nanoparticles with encapsulated CAM

The antimicrobial effect of CAM loaded nanoparticles was evaluated quantitatively by considering the growth curves of Gram-positive (*S. aureus*) and Gram-negative (*E. coli*) bacteria (**Figures 10.8 a** and **b**, respectively). Results clearly pointed out that a bactericide effect was preserved despite CAM was effectively encapsulated in the different nanoparticles. This bactericide effect was clearly higher for the ACP amorphous nanoparticles, being the bacterial growth completely suppressed after 24 h as a consequence of the indicated fast release. Nevertheless, bacterial growth was possible at higher exposure times due to the extinction of CAM in the culture media once it was delivered. Thus, bacterial growths of 10 % and 11 % were determined after 48 h for *S. aureus* and *E. coli*, respectively. The lower CAM load of cHAp nanoparticles led to a lower bactericide effect, being growth percentages of 25 % and 21 % found after 24 h for *S. aureus* and *E. coli*, respectively. The low release rate of CAM was demonstrated by the experiments performed with *S. aureus* since bacterial growth still decreased to 19 % after 48 h of exposure. This effect was not clear for the *E. coli* bacterium since after this period the bacterial growth still increased (*i.e*. 34 %).

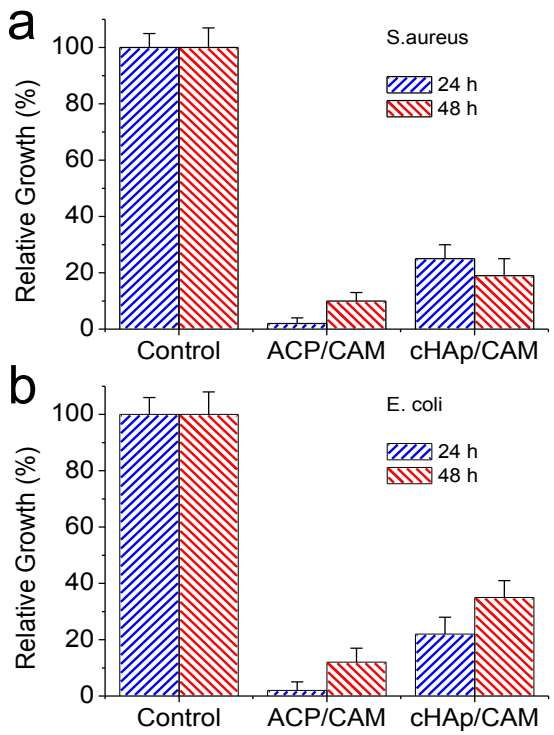

Figure 10.8. Relative growth of *S. aureus* (a) and *E. coli* (b) bacteria in the control and CAM loaded ACP and cHAp nanoparticles. *p < 0.05 vs. control.

10.3.4 Preparation of electrospun PLA microfibers incorporating ACP and cHAp nanoparticles with or without encapsulated CAM

Conditions for the electrospinning of PLA have been optimized in earlier works.[33-35] Thus, a chloroform-acetone mixture (2:1 v/v) with a polymer concentration of 8 wt-% was adequate to get fibers with diameters in the nano/micrometric range. Specifically, long continuous fibers with a narrow unimodal distribution of diameters (average size of 580 ± 10 nm) were obtained using operational parameters of 15 kV, 10 $mL \cdot h^{-1}$ and 12 cm for the applied voltage, the flow rate and the tip-collector distance, respectively. The same conditions could be successfully applied to get fibers loaded with medicated and non-medicated ACP and cHAp nanoparticles. Fibers were still continuous and relatively uniform (**Figures 10.9**), although some minor aggregates could be distinguished near their surface, especially for the thickest ones (see arrows in **Figures 10.9**). In general, the incorporation of nanoparticles led to a slight increase of the diameter without a clear effect caused by the encapsulation of CAM. Thus, fibers loaded with ACP or cHAp showed average diameters in the 660−930 nm or 600−790 nm range, respectively.

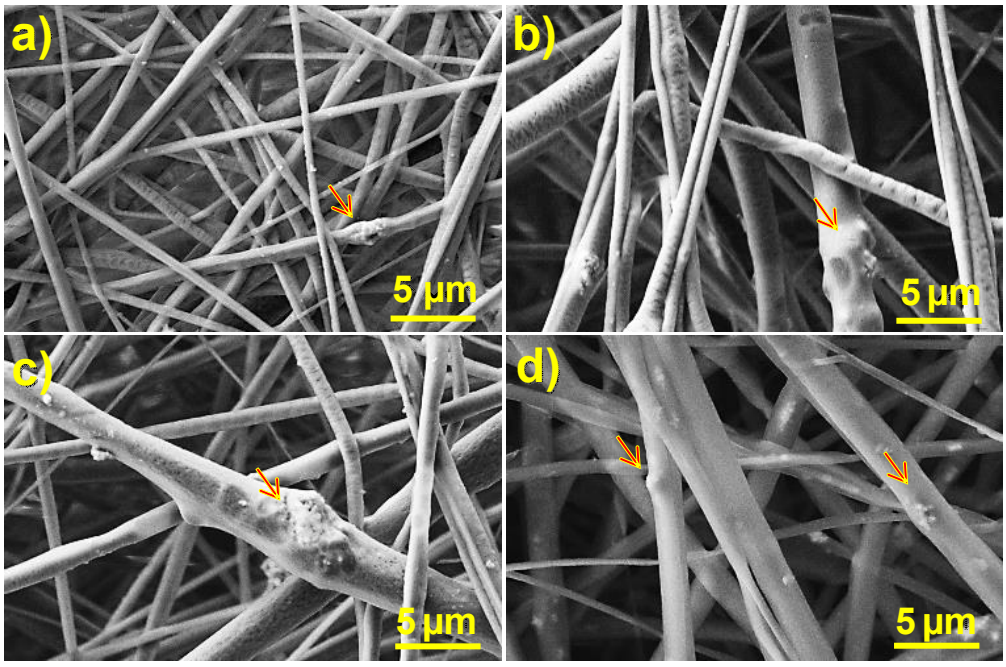

Figure 10.9. SEM images showing the morphology of PLA nanofibers loaded with: a) ACP, b) ACP-CAM, c) HAp and d) HAp-CAM. Arrows point out the presence of nanoparticle agglomerates inside nanofibres.

FTIR spectra of PLA electrospun fibers incorporating hydroxyapatite nanoparticles were practically identical to the spectrum of raw PLA even when CAM was encapsulated

(**Figure 10.10 a**). Thus, typical bands of the drug (*e.g.* vibrational peaks of carbonyl group ($C=O$), $C=C$ stretching and NO_2 stretching at 1694, 1560 and 1512 cm^{-1}, respectively) were never detected as presumable from the low CAM load. The higher content in nanoparticles gave rise to a minor change in the spectrum that logically was seen around 1026 cm^{-1} where hydroxyapatite shows the most intense signal.[36] Specifically, the low intense PLA band at 1044 cm^{-1} appeared overlapped with the indicated peak for both ACP and cHAp loaded samples. Therefore, this unequivocal trace of the calcium phosphate salt demonstrated that at least a small part of hydroxyapatite remained close to the fiber surface.

Thermogravimetric curves (**Figure 10.10 b**) showed that the thermal stability was not influenced by the incorporation of any kind of medicated hydroxyapatite. Thus, PLA always decomposed according to a single step with a maximum weight loss rate around 405 ºC. Obviously, the char yield measured at 500 ºC was in full agreement with the load amount of nanoparticles (*i.e.* 0.5 % and 10 % for PLA and PLA loaded with ACP or cHAp, respectively). Samples loaded with nanoparticles, and independently of the presence of encapsulated CAM, showed a small and continuous weight loss from 100 ºC to 300 ºC, which could be associated to the presence of volatile compounds introduced during the synthesis of nanoparticles. The onset degradation temperature of PLA was never affected, a feature that is significant since indicates that processing was not influenced by the presence of CAM molecules if they were properly encapsulated in the ACP or cHAp nanoparticles.

All prepared PLA scaffolds had an hydrophobic surface independently of incorporating unloaded and CAM loaded nanoparticles and independently of the type/crystallinity of hydroxyapatite nanoparticles. Thus, contact angle measurements (not shown) gave always values in the 125 º–128 º range.

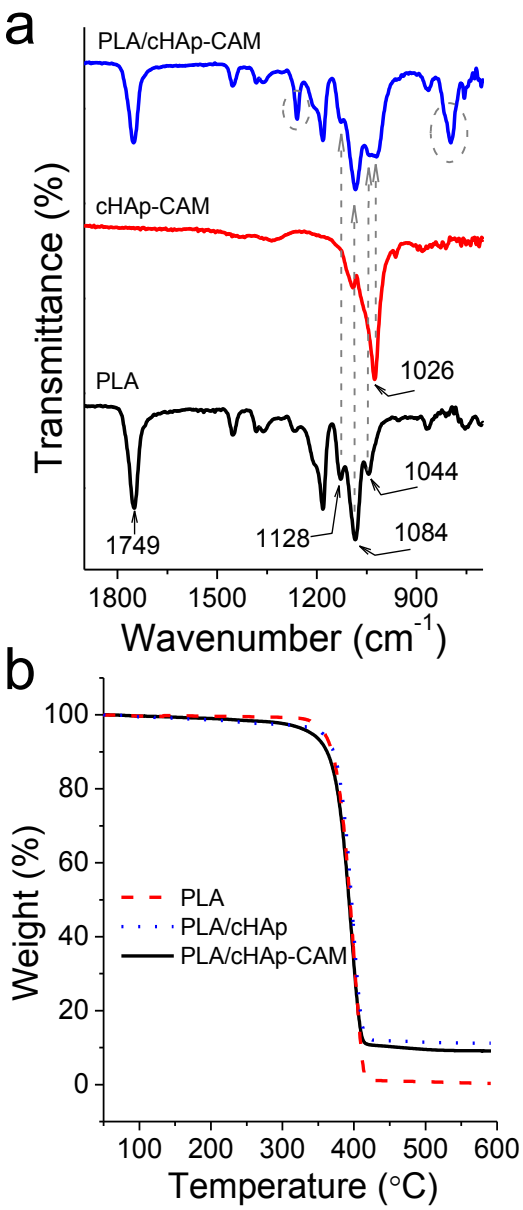

Figure 10.10. FTIR spectra for PLA (black), cHAp-CAM (red) and the PLA scaffold incorporating cHAp nanoparticles enacapsulating CAM (blue). b) Themogravimetric curves of PLA (red), PLA nanofibers incorporating cHAp (blue) and PLA nanofibers incorporating CAM loaded cHAp nanoparticles (black).

10.3.5 CAM release from PLA electrospun scaffolds incorporating ACP and cHAp nanoparticles with encapsulated CAM

Release measurements in the PBS medium indicated that CAM was effectively delivered (**Figure 10.11**) despite the loaded ACP or cHAp particles were embedded in the PLA nanofibers. Logically, the delivery was clearly delayed with respect to that observed from the nanoparticles alone since CAM had to diffuse through the polymer matrix. Specifically, first order kinetic constants of 0.17 and 0.19 h^{-1} were calculated for nanofibers incorporating ACP and cHAp particles, respectively. In any case, release percentages of 55 % and 32 % were determined after 20 h of exposure, justifying the use of this kind of scaffolds for the slow delivery of CAM. Differences on the release should be justified in this case as a consequence of the lower CAM load for PLA incorporating cHAp that reduces the driving force for the diffusion process. The influence of scaffold morphology differences can be considered negligible since a contrary behaviour could be expected for the slightly thinner fibers obtained when cHAp was incorporated. Note also that the release achieved again a stable value but at percentages clearly lower than observed for the release from the nanoparticles alone. We interpret that in this case this constant level is not a consequence of the limited solubility of CAM in PBS since the previously determined percentage should be expected. Therefore, the observed decrease on the release percentage seems to indicate the presence of encapsulated CAM in the inner particles (*i.e.* distant from the fiber surface).

Addition of ethanol in the release medium made feasible the access of solvent to these inner particles. Thus, a complete delivery was observed after a period of 40 h. Kinetics obeyed again a first-order equation, being k_1 dependent of the type of nanoparticle due to the different CAM load and even on the different facility to release the encapsulated compound. Thus, values of 0.30 and 0.21 cm^{-1} were calculated for samples containing ACP and cHAp particles, respectively. In summary, ethanol made effective the release due to its great affinity with CAM and also to its capability to swell the PLA nanofibers and facilitate the diffusion of CAM molecules through the polymer matrix.

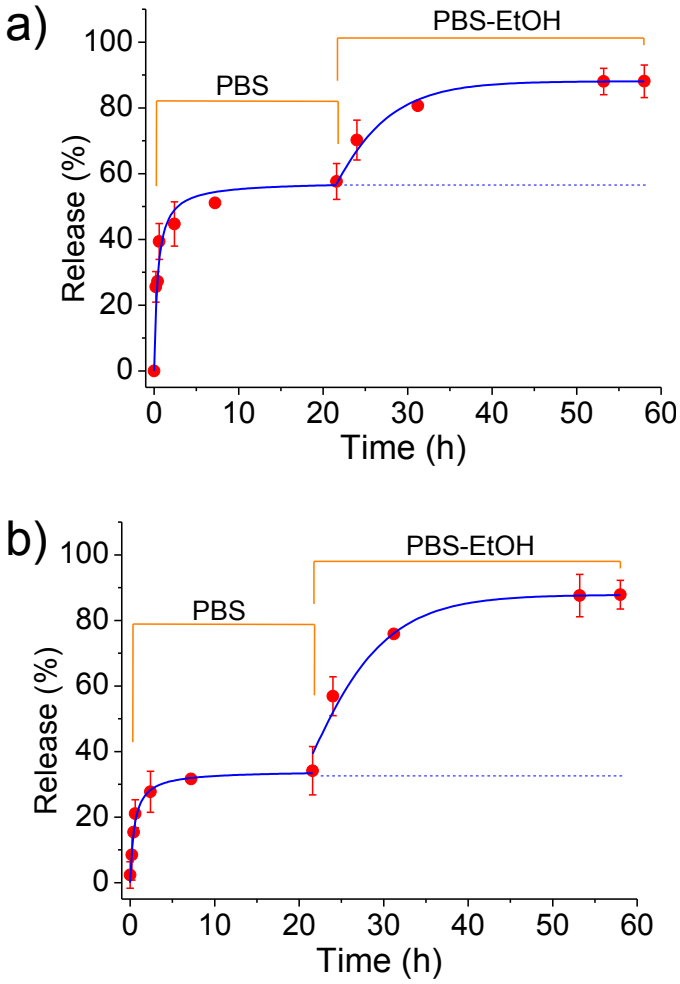

Figure 10.11. Release of CAM from PLA electrospun nanofibers loaded with ACP-CAM (a) and cHAp-CAM nanoparticles (b) during exposure to the indicated media. PBS-EtOH refers to the PBS-ethanol mixture (see Methods section).

10.3.6 Bacteriostatic effect of PLA scaffolds incorporating ACP and cHAp nanoparticles with encapsulated CAM

The antimicrobial effect of CAM loaded matrices was again evaluated quantitatively by considering the growth inhibition of Gram-negative (*E. coli*) and Gram-positive (*S. aureus*) bacteria (**Figures 10.12 a** and **b**, respectively). The control and the unloaded PLA/ACP and PLA/cHAp matrices were highly susceptible to bacterial infection. On the contrary the relative bacterial growth clearly diminished when the PLA matrix was directly loaded with the drug as well as when PLA was loaded with the drug previously encapsulated in the hydroxyapatite nanoparticles. In the three cases, the relative growth diminished to values between 60 % and 70 %, demonstrating the diffusion of CAM through the PLA nanofibers and an enough release in the culture medium to render a bacteriostatic effect.

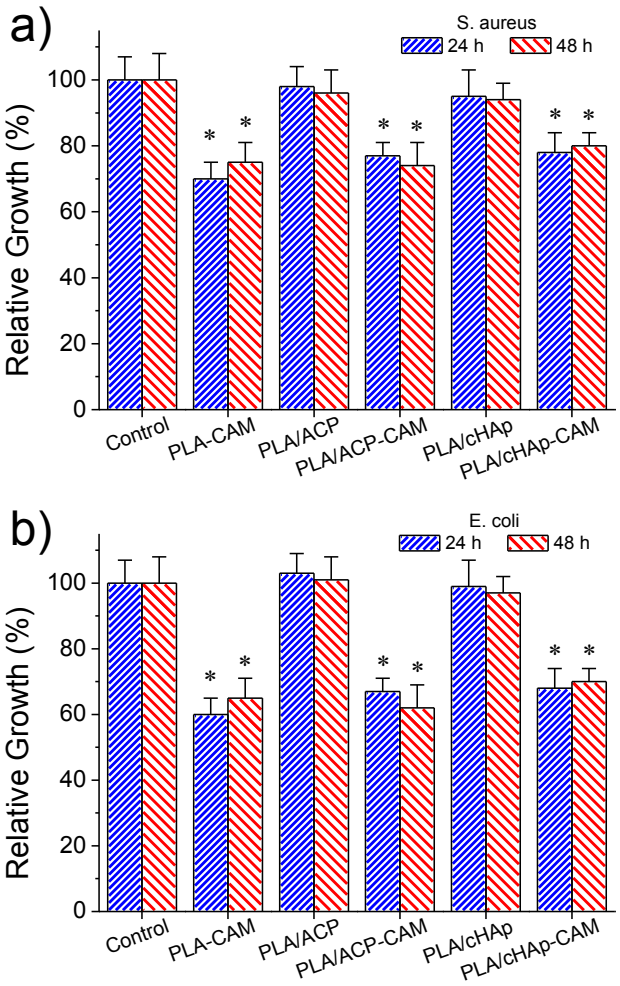

Figure 10.12. Relative growth of *E. coli* (a) and *S. aureus* (b) bacteria in the control and the indicated PLA scaffolds, *p < 0.05 vs. control.

No significant differences were found after 24 and 48 h of culture suggesting a continuous release of the drug from the matrix, a feature that is in agreement with the results given in the previous section. Differences between the three loaded matrices were not highly significant (*e.g.* the relative growth of *E. coli* bacteria diminished to 60−64 %, 66−62 % and 68−70 % for PLA/CAM, PLA/ACP-CAM and PLA/cHAp-CAM, respectively). Nevertheless, a slightly highest effectivity was detected when CAM was directly loaded in the nanofibers and a slightly lowest activity when CAM was encapsulated in cHAp. It should be pointed out that this small difference demonstrated that the activity could be well preserved despite both the significant decrease of the amount of loaded drug and the greater difficulty of releasing the encapsulated drug. In any case, the observed growth percentages from the studied PLA matrices were logically higher than observed from the loaded nanoparticles (*e.g.* 60−70 % in from of ca. 20 %) (**Figure 10.8**), demonstrating certain difficulty of the drug to diffuse through

the PLA nanofiber. Similar conclusions could be inferred when the activity of CAM loaded PLA matrices against *S. aureus* bacteria was evaluated (**Figure 10.12 b**). However, in this case the relative bacterial growth was slightly higher (*e.g.* 70−80 % with respect to 60−70 %) as consequence of the lower susceptibility of *S. aureus* bacteria towards CAM. In addition, the differences between the different PLA loaded scaffolds were even less significant than detected for the *E. coli* bacteria.

10.3.7 Cytotoxicity of PLA scaffolds incorporating ACP and cHAp nanoparticles with encapsulated CAM

Adhesion and proliferation assays (**Figure 10.13**) demonstrated that all PLA scaffolds were biocompatible and non-cytotoxic. The observed relative viabilities of the three selected cell lines (*i.e.* COS-1, VERO and SAOS-2) onto the selected scaffolds was practically identical to those determined for the control with the exception of the CAM loaded samples. In any case, the viability decreased only to a minimum value of 80 % in both adhesion and proliferation studies. This effect was slightly more noticeable for PLA samples having ACP nanoparticles due to their greater encapsulation efficiency. In any case, it is clear that the amount of released drug in the short cell exposure time of the two assays was not enough to produce a relevant toxic effect.

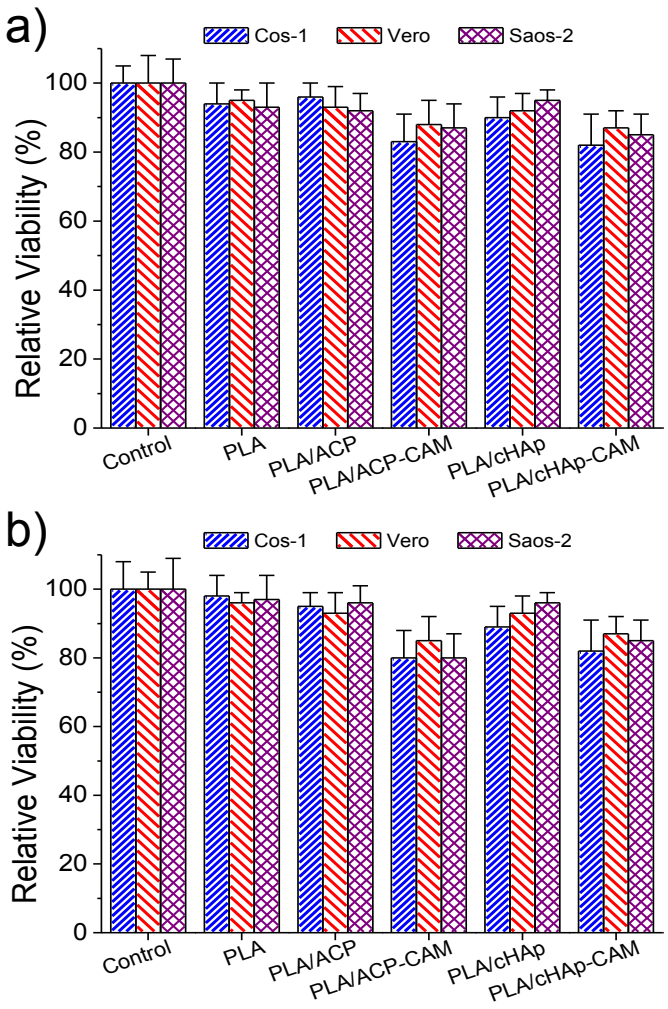

Figure 10.13. Relative viability for adhesion (a) and proliferation experiments for COS-1 (blue), VERO (red) and SAOS-2 (lilac) cells in the control and the indicated scaffolds.

10.4 CONCLUSIONS

CAM can be encapsulated within both amorphous and crystalline hydroxyapatite nanoparticles, being found differences on the encapsulation efficiency according to the crystallinity of the sample. The selected encapsulation process allows incorporating CAM once nuclei of hydroxyapatite were formed and consequently CAM should be mainly loaded in the nanoparticle shell. In this way, the drug could be easily delivered even in an aqueous medium where it was scarcely soluble. This fast release conferred a clear bactericide character to both types of nanoparticles. The aging and hydrothermal treatment performed with the precipitated nanoparticles had logically a great influence on the sample crystallinity but also on the encapsulation efficiency.

CAM encapsulated hydroxyapatite nanoparticles could be easily incorporated into polylactide microfibers by means of the electrospinning technique. The obtained fibers were continuous and relatively uniform in size but showed irregularities as a consequence of the presence of some nanoparticle agglomerates. CAM release in an aqueous PBS medium from such fibers was hindered with regard to that observed from nanoparticles. Nevertheless, a small CAM fraction could be faster released, conferring to the scaffold a bacteriostatic character. Scaffolds were biocompatible due to the low release rate of CAM. A significant drug percentage remained in the nanoparticles, being the scaffold interesting as a CAM reservoir for treatment of cancer, as recently it has been shown for this antibiotic.[12-14]

10.5 REFERENCES

1. Dinos, G.P., Athanassopoulos, C.M., Missiri, D.A., Giannopoulou, P.C., Vlachogiannis, I.A., Papadopoulos, G.E., Papaioannou, D. & Kalpaxis, D.L. Chloramphenicol derivatives as antibacterial and anticancer agents: Historic problems and current solutions. *Antibiotics.* **5(2**), 20 (2016).
2. Pongs, O. Chloramphenicol. In Mechanism of Action of Antibacterial Agents; Hann, F.E., Ed.; Springer: New York, NY, USA, **5**, 26–42 (1979).
3. Contreras, A. & Vazquez, D. Cooperative and antagonistic interactions of peptidyl-tRNA and antibiotics with bacterial ribosomes. *Eur. J. Biochem*. **74**, 539–547 (1977).
4. Fernandez-Muñoz, R. & Vazquez, D. Kinetic studies of peptide bond formation. Effect of chloramphenicol. *Mol. Biol. Rep*. **1**, 75–79 (1973).
5. Drainas, D., Kalpaxis, D.L. & Coutsogeorgopoulos, C. Inhibition of ribosomal peptidyl transferase by chloramphenicol: Kinetic studies. *Eur. J. Biochem*. **164**, 53–58 (1987).
6. Xaplanteri, M., Andreou, A. Dinos, G.P. & Kalpaxis, D.L. Effect of polyamines in the inhibition of peptidyl transferase by antibiotics: Revisiting the mechanism of chloramphenicol action. *Nucleic Acids Res*. **31**, 5074–5083 (2003).
7. Vester, B. & Garrett, R.A. The importance of highly conserved nucleotides in the binding region of chloramphenicol at the peptidyl transferase center of Escherichia coli 23S ribosomal RNA. *EMBO J*. **7**, 3577–3587 (1998).
8. Ersler, A.J. & Iossifides, I.A. In vitro action of chloramphenicol-analogues on the metabolism of human red blood cells. *Acta Haemat*. 28, 1–19 (1962).
9. Wallace, D.C. Mitochondrial genetics: A paradigm for aging and degenerative diseases? *Science*. **256**, 628-632 (1992).
10. Wallace, D.C. A mitocondrial paradigm of metabolic and degenerative diseases, aging, and cancer: A dawn for evolutionary medicine. *Annu. Rev. Genet*. **39**, 359-407 (2005).
11. Ott, M., Amunts, A. & Brown, A. Organization and regulation of mitochondrial protein synthesis. *Annu. Rev. Biochem*. **85** (2016).
12. Lamb, R., Harrison, H., Hulit, J., Smith, D.L., Lisanti, M. P. & Sotgia, F. Mitochondria as new therapeutic targets for erradicating cancer stem cells: Qualitative proteomics and functional validation via MCT1/2 inhibition. *Oncotarget*. **5**, 11029-11037 (2014).
13. Lamb, R., Ozsvari, B. Lisanti, C.L., Tanowitz, H.B., Howell, A., Martinez-Outschoorn, U.E., Sotgia, F. & Lisanti, M.P. Antibiotics that target mitochondria effectively eradicate cancer stem cells, across multiple tumor types: Treating cancer like an infectious disease. *Oncotarge*t. **6**, 4569–4584 (2015).

14. Lokhande, J., Juvekar, A.S. & Kulkarni, K.P. Chloramphenicol: Screening and review to evaluate the potential beneficial effects in leukaemia. *J. Indian Med. Assoc*. *105*, 224–228 (2007).

15. Kostopoulou, O.N., Kouvela, E.C., Magoulas, G.E., Garnelis, T., Panagoulias, I. Rodi, M., Papadopoulos, G., Mouzaki, A., Dinos, G.P., Papaioannou, D. *et al.* Conjugation with polyamines enhances the antibacterial and anticancer activity of chloramphenicol. *Nucleic Acids Res*. **42**, 8621–8634 (2014).

16. Dorozhkin, S.V. & Epple, M. Biological and Medical Significance of Calcium Phosphates. *Angew. Chem. International Edition*.**41**, 3130-3146 (2002).

17. Bakhtiari, L., Javadpour, J., Rezaie, H.R., Erfan, M., Mazinani, B. & Aminian, A. Pore size control in the synthesis of hydroxyapatite nanoparticles: The effect of pore expander content and the synthesis temperature. *Ceram. Int*. **42**, 11259–11264 (2016).

18. Turon, P., del Valle, L., Alemán, C. & Puiggalí, J. Biodegradable and biocompatible systems based on hydroxyapatite nanoparticles. *Appl. Sci*. **7**, 60 (2017).

19. Thomas, S.C., Mishra, P.K. & Talegaonkar, S. Ceramic nanoparticles: Fabrication methods and applications in drug delivery. *Curr. Pharm. Des*. **21**, 6165–6188 (2015).

20. Thomas, S.C., Sharma, H., Rawat, P., Verma, A., Leekha, A., Kumar, V., Tyagi, A., Gurjar, B.S., Iqbal, Z. & Talegaonkar, S. Synergistic anticancer efficacy of bendamustine hydrochloride loaded bioactive hydroxyapatite nanoparticles: In-vitro, ex-vivo and in-vivo evaluation. *Colloids Surf. B Biointerface*.**146**, 852–860 (2016).

21. Vallet-Regí, M., Balas, F. & Arcos, D. Mesoporous materials for drug delivery. *Angew. Chem. Int. Ed*. **46**, 7548–7558 (2007).

22. Fojo, A.T., Ueda, K., Slamon, D. J., Poplack, D .G., Gottesman, M. M. & Pastan, I. Expression of a multidrug-resistance gene in human tumors and tissue. *Proc Natl Acad Sci USA*. **84(1)**, 265-269 (1987).

23. Szakacs, G, Paterson, J. K., Ludwig, J. A., Booth-Genthe, C. & Gottesman, M. M. Targeting multidrug resistance in cancer. *Nat Rev Drug Discov*. **5(3)**: 219-234 (2006).

24. Yan, Y., Ochs, C. J., Such, G. K., Heath, J. K., Nice, E. C. & Caruso, F. Bypassing multidrug resistance in cancer cells with biodegradable polymer capsules. *Adv Mater*. **22(47)**, 5398-5403 (2010).

25. Higuchi, T. Rate of release of medicaments from ointment bases containing drugs in suspension. *J Pharm Sci*. **50**, 874-875 (1961).

26. Wagner, J. G. Interpretation of percent dissolved-time plots derived from in vitro testing of conventional tablets and capsules. *J. Pharm. Sci*. **58**, 1253-1257 (1969).

27. Llorens, E., del Valle, L. J., Díaz, A., Casas, M. C. & Puiggalí, J. Polylactide nanofibers loaded with vitamin B6 and polyphenols as bioactive platform for tissue engineering. *Macromol. Res*. **21**, 775 (2013).

28. Zhang, Y. & Lu, J. A simple method to tailor spherical nanocrystal hydroxyapatite at low temperature. *Nanopar. Res*. **9**, 589–594 (2007).

29. Wang, P., Li, C., Gong, H., Jiang, X., Wang, H. & Li, K. Effect of synthesis conditions on the morphology of hydroxyapatite nanoparticles produced by wet chemical process. *Powder Technol*. **203**, 315–321 (2010).

30. Qi, C., Zhu, Y.J., Lu, B.Q., Zhao, X.Y., Zhao, J. & Chen, F. Hydroxyapatite nanosheet-assembled porous hollow microspheres: DNA-templated hydrothermal synthesis, drug delivery and protein adsorption. *J. Mater. Chem*. **22**, 22642–22650 (2012)

31. Landi, E., Tampieri, A., Celotti, G. & Sprio, S. Densification behaviour and mechanisms of synthetic hydroxyapatites. *J. Eur. Ceram. Soc*. **20**, 2377-2387 (2000

32. Ravindra Acharya, K. & Sake Gowda, D.S. The structure of chloramphenicol. *Acta Cryst*. **B35**, 1360-1369 (1979).

33. del Valle, L.J., Camps, R., Diaz, A., Franco, L., Rodriguez-Galan, A. & Puiggali, J. Electrospinning of polylactide and polycaprolactone. *J. Polym. Res*. 18, 1903-1917 (2011).

34. Llorens, E., Calderon, S., del Valle, L.J. & Puiggalí, J. Polybiguanide (PHMB) loaded in PLA scaffolds displaying high hydrophobicity, biocompatibility and antibacterial properties. *Mater. Sci Eng*. **50**, 74-84 (2015).

35. Llorens, E., del Valle, L. J. & Puiggalí, J. Electrospun scaffolds of polylactide with a different enatiomeric content and loaded with anti-inflammatory and antibacterial drugs. *Macromol. Res*. **23**, 636-648 (2015).

36. Bertran, O., del Valle, L.J., Revilla-López, G., Chaves, G., Cardús, L., Casas, M.T., Casanovas, J., Turon, P., Puiggalí J. & Alemán, C. Mineralization of DNA into nanoparticles of hydroxyapatite. *Dalton Trans*. **43**, 317 (2014).

11.

PEPTIDE SELF-ASSEMBLY INTO HYDROGELS FOR BIOMEDICAL APPLICATIONS RELATED TO HYDROXYAPATITE

Amphiphilic peptides can be self-assembled by establishing physical cross-links involving hydrogen bonds and electrostatic interactions with divalent ions. The derived hydrogels have promising properties due to their biocompatibility, reversibility, trigger capability and tunability. Peptide hydrogels can mimic the extracellular matrix and favor the growth of hydroxyapatite (HAp) as well as its encapsulation. New designed materials offer great perspectives for applications in the regeneration of hard tissues such as bones, teeth, and cartilage. Furthermore, development of drug delivery systems based on HAp and peptide self-assembly is attracting attention.

11.1 INTRODUCTION

Peptide self-assembly of peptides allows new materials to be obtained through a bottom-up methodology.[1] Within this context, different building blocks based on peptides (*i.e.* from dipeptides to amphiphilic block copolymers) have been developed.[2] These systems have wide applications in the biomedical field (*e.g.* tissue, bone and cartilage regeneration[3-5] or controlled drug release), being inspired from nature in multiple cases. Thus, self-assembling is characteristic of actin fibrils in eukaryotic cells, of the aggregation of fibrin in blood coagulation, and amyloid fibrils, which can be employed as a component of biomembranes,[6] biosensors[7] or hydrogels,[8] in addition to being involved in well-known degenerative diseases (*e.g.* Alzheimer, Parkinson and diabetes).

Multiple studies are being performed concerning the use of short peptide sequences as coatings, gels and electroactive materials as recently been reviewed.[9-12] Self-assembled systems based on peptides offer clear advantages considering their biocompatibility, mechanical robustness, capability to be reversibly disassembled and capability to tailor their functional behavior. The potential of self-assembled peptides is continuously increasing, and it is likely that the commercialization of these kinds of materials is approaching. Self-assembling can involve short sequences such as diphenyalanine,[13,14] although single amino acids can also lead to self-aggregated fibrils.[15]

Hydrogels are hydrophilic networks with a great capacity to retain water and have a great similarity with biological tissues. Hydrogels can be classified considering the type of cross-links (*i.e.* physical or chemical) and their ability to incorporate chemical agents and cells. Furthermore, these systems can be designed to render shape memory effects, stimuli-responsive smart materials, and is situ gelling polymers. These are ideal for tissue regeneration since they can be used as injectable materials able to adapt to the form of tissue cavities. Applications of hydrogels have been extensively reviewed,[16-18] and it is clear that peptide-based hydrogelators have a great potential for biomedical applications due to the controllable self-assembling and biocompatibility, and their possibility to be formed under physiological conditions.[19]

Hydroxyapatite (HAp) is a key component of hard tissues with recognized bioactivity, biocompatibility and osteoconductivity. HAp has been extensively studied as an artificial bone substitute,[20,21] in addition to the great efforts undertaken to develop

bionanocomposites for applications in the biomedical field that varied from drug encapsulation to tissue engineering.[22,23]

The present review is focused on the recent advances in hydrogels based on peptides and utilized in biomedical applications related to HAp. To this end, we begin wuth describing the self-assembling of peptides and HAp characteristics in Sections 2 and 3, respectively. Next, HAp nanocomposites and hydrogels based on peptide self-assembly that are employed for biomedical Applications are addressed in Sections 4 and 5, respectively. Finally, specific applications related with nanoparticles/nanocapsules are discussed in Section 6 and materials employed for the regeneration of hard tissues, with the differentiation in advances concerning bones, teeth and cartilage are accounted in Section 7, followed by conclusions in Section 8.

11.2 PEPTIDE SELF-ASSEMBLY

At present, self-assembled peptides are ideal Systems for the development of new biomaterials. Various advantages that can be mentioned are as follows:[24] a) peptides with specific sequences can be easily obtained by solid-phase synthesis, b) the small size of peptides allows the design of appropriate sequences for assembly into supramolecular structures; and c) new peptides can be inspired from naturally self-assembling proteins motifs. Therefore, self-assembling peptides (SAPs) can be based on weak specific interactions (*i.e.*, hydrogen bonds and $\pi - \pi$ stacking) or strong non-specific interactions (*i.e.,* electrostatic) , and α-helices, β-sheets, coiled-coils or other naturally occurring motifs.[25-27] Peptides can also self-assemble into nanostructures through metal-ligand interactions. Metal coordination has become a powerful tool for constructing diverse molecular architectures and also for tuning the final assembly.[28]

The self assembly process in mainly driven by thermodynamics, but kinetic factors also have a critical relevance concernint estructural modulation and function Integration, as reviewed by Wang *et al.*[29] The reverse process of assembly also has a significant role in the modulation and finalization of the activity of supramolecular complexes. Self-assembly and disassembly processes are ubiquitious in nature and can be exploted for biomedical Applications sych as therapeutics and diagnostics. Recent advances in the dynamic control of small molecules' assemblies were reviewed by Feng *et al.*[30]

α-Helices comprise both hydrophilic and hydrophobic amino acid residues and are characterized by a secondary structure defined by a periodicity of 3.6 amino acids per turn. These helical motifs can be self-assembled into coiled-coil conformations due to their amphiphilic character.[31] The main problem of such assemblies is the requirement of long amino acid sequences to stabilize the helical structure. Thus, the initial attemps involved sequences of 21-28 units, as reviewed in [32].

Collagen-mimetic peptides have a great applied interest since collagen plays a fundamental structural role in both tissues and extracellular matrix (ECM).[33] Collagen is constituted by a supercoiling of three linear peptidic chains that gives rise to supramolecular fibrils. Amino acid sequences are mainly characterized by the presence of glycine, which avoids steric hindrances due to the lack of side groups, proline or hydroxyproline, and a third amino acid.

β-Sheet peptides can be self-assembled into 3D-nanofibrous structures (*e.g*. hydrogels) when ionic self-complementary peptides are involved (**Figure 11.1**).[34] Other self-assembling possibilities are based on the alternation of hydrophobic and hydrophilic residues into a β-sheet structure (*e.g*., peptides based on the Arg-Ala-Asp-Ala sequence named RADA-like SAPs), β-hairpin peptides and β-sheet tapes.[3,35,36] These self-assembled structures render a great variety of morphologies such as nanofibers, nanotubes, nanovesicles, and nanoparticles.[37]

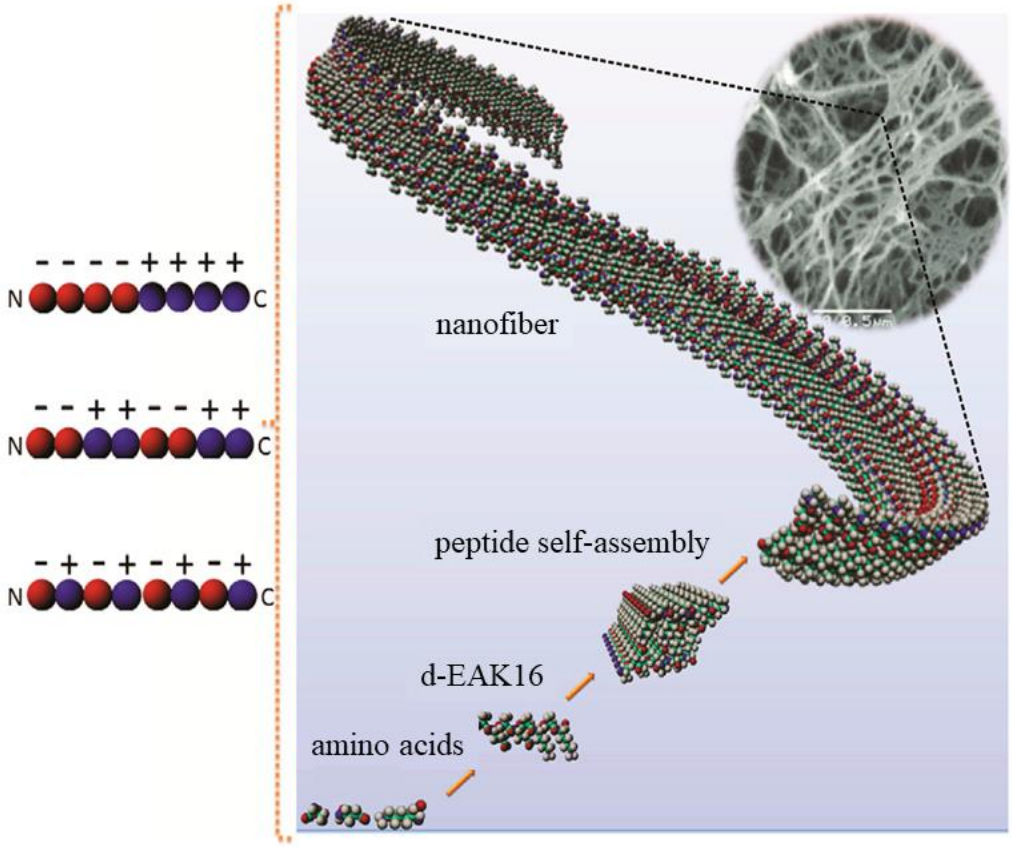

Figure 11.1. Self-assembly of a peptide consisting of alanine (A), glutamic acid (E) and lysine (K) (d-EAK) into nanofibers which were then entangled into 3D scaffolds. The self-assembling process was consequence of complementary ionic interactions between charged residues (red for negative charged glutamic acid and blue for the positive charged lysine residues), which could have different arrangements: modulus I,−−−−+ + + +; modulus II,−−++−−+ +; modulus III, − + − + − + − +). Adapted and reprinted with permission from [34,38].

Self-assembled peptides able to form β-structures can be classified according to five main architectures: (a) ionic self-complementary peptides; (b) peptides having an alternate disposition of hydrophilic and hydrophobic residues (*i.e.* RADA peptides); (c) L,D-heterochiral peptides, (d) peptide amphiphiles (Pas), and (e) N-protected peptides.

Ionic self-complementary peptides are based on the alternation of hydrophobic residues (*e.g.* alanine, isoleucine or phenylalanine) and hydrophilic residues with positive (*e.g.* lysine or arginine) or negative (*e.g.* aspartic or glutamic acids) charges.[34,39] These complementary co-assembled peptides (CAPs) are consequently based on the interactions (attractive or repulsive) between peptides having opposite electric charges.[40] Nanofibrillar structures can be formed from molecular assemblies of positive

Ac-$(LKLH)_3$-$CONH_2$ and negative (Ac-$(LDLD)_3CONH_2$ peptides. The derived β-sheets were thus constituted by double layers with hydrophobic and hydrophilic sides, the first ones being placed in inner pockets and the second ones exposed to aqueous environments.

RADA and similar sequences (*e.g.* Ac-$(RARADADA)_2$-$CONH_2$[41] and Ac-$(RADA)_4$-$CONH_2$[42]) also form self-assembled structures in aqueous media where charged side groups are oriented on one side of the sheet and hydrophobic side groups are on the other side. The characteristic RADA sequence appears interesting to promote wound healing, cell culture, and synapse growth due to its great similarity with the RGD sequence that is characterized by its well-known cell adhesion properties.

The functionalization of RADA peptides is a good strategy to control cell behaviors. Thus, scaffolds derived from RGD, DGR and PRG-modified RAD16 peptides showed a clear improvement of cell attachment, spreading, migration and osteogenic differentiation.[43,44]

Alternation of L- and D-amino acids has been proved eficient to favor self-assembled structures. A simple sequence of three hydrophobic amino acids can lead to an amphiphilic arrangement with hydrophobic side chains and hydrophilic backbone groups.[45] Cyclic peptides constituted by alternating L,D-amino acids are able to self-assemble and form nanotubes.[46] Great attention is currently being given to the effect caused by the incorporation of unnatural D-amino acids in the self-assembling peptide motifs, as recently reviewed by Melchionna *et al.*[47]

The biological potential of fiber-forming peptide amphiphile molecule was reported in 2001.[48] The molecules were constituted by a hydrophobic tail linked to a hydrophilic amino acid sequence. Effective sequences were selected trying to favor *β*-sheet arrangements, to display cell adhesive properties (*e.g*. containing epitope Arg-Gly-Asp-Ser (RGDS) ligands [49,50]) and to promote mineralization by favoring hydroxyapatite HAp growth (*e.g.* containing phosphorylated serine residues able to attract calcium ions). Furthermore, thermal annealing processes were found to make feasible the formation of liquid crystalline solutions that rendered aligned domains under shearing forces. In the presence of divalent cations, these domains could result in gels with macroscopic fiber alignment (**Figure 11.2**).[51] PA molecules are able to self-assemble in aqueous media into cylindrical nanofibers, as a result of both the establishment of hydrogen bonds between amide groups and the hydrophobic collapse of alkyl tails. Self-assembling can

be induced by low pHs and interactions with divalent ions. The latter option is more interesting for biomedical applications that require physiological pHs.

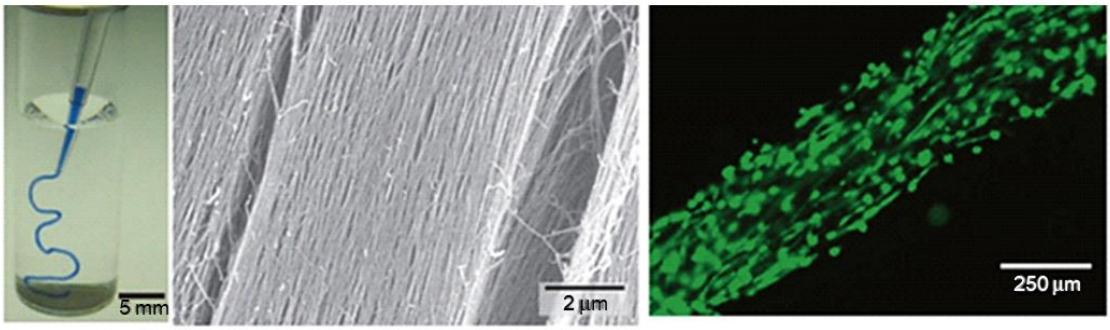

Figure 11.2. Formation of a noodle-like string from a peptide-amphiphile, coloured with tryptan blue (left). Pippeting was performed in a phosphate-buffered saline solution (middle). SEM micrograph showing the highly aligned nanofiber bundles that constitutes the gel string. Gel strings can be used to encapsulate and align cells (*e.g.,* human mesenchymal stem cells, hMSCs) along the axis of the gel (right). Adapted and reprinted with permission from [51].

Peptide self-assembly can be enhanced by the incorporation of appropriate N-terminal groups. The 9-fluorenylmethyloxycarbonil (Fmoc) group is a good exemple due to the additional driving forces that can be established (*e.g.,* hydrogen bonding from the carbonil group, aromàtic and hydrophobic interactions from the fluorenyl ring, and steric optimization from the methoxycarbonyl linker.[52] A variety of funcional aromàtic moieties (*e.g.,* spiropyrans, stylbenes, carbazoles) have also been investigated and found to give a certain degree of functionality to the derived hydrogels.[53]

Hydrogels based on fibrils based on the coassembly of Arg and Asp dipeptides (*i.e.,* Fmoc-FR-NH_2 and Fmoc-FN-OH) have been found effective to mímic the integrin-binding-RGD peptide of fibronectin. The indicated amino acid residues ha dan orientation in the formed supramolecular fibrils that facilitated the promotion of cell growth. Interestingly, covalent connections between Arg and Asp motifs were avoided.[54]

11.3 HYDROXYAPATITE

HAp is an inorganic component defined by the chemical formula $Ca_{10}(PO_4)_6(OH)_2$ that can be produced as nanocrystals by living systems under mild temperature and pressure conditions. HAp crystallizes in the monoclínic $P2_1/b$ space group (a = 0.984 nm, b = 2a, c = 0.688 nm and = 120 º), but at temperatures above 250 °C can undergo a structural

transition towards a hexagonal phase (a = b = 0.943 nm, c = 0.689 nm and γ = 120 º).[55,56] This phase can be stabilized by the presence of impurities, like those derived from a partial substitution of hydroxide (*e.g.* by fluoride or chloride ions).

Biological HAp mainly forms part of animal bones, tendons and teeth. Nowadays, HAp can be considered one of the most-employed materials in hard tissue engineering due to three basic features: biocompatibility, bioactivity and osteoconductivity.[57] Composite materials based on HAp can combine advantages of each component (inorganic or organic) in order to get similar structure and properties to those found in nature.

Considerable efforts are focused on the synthesis of nanohidroxyapatite (nHAp) particles (both in crystalline and amorphous forms). In this way, properties can be varied according to modifications in the composition and even on the morphology of nanoparticles.[58,59] The synthetic path is mainly performed according to two aqueous precipitation reactions:[60]

$$10\ Ca(OH)_2 + 6\ H_3PO_4 \rightarrow Ca_{10}(PO_4)_6(OH)_2 + 18\ H_2O \quad (1)$$

$$10\ Ca(NO_3)_2 + 6\ (NH_4)_2HPO_4 + 2\ H_2O \rightarrow Ca_{10}(PO_4)_6(OH)_2 + 12\ NH_4NO_3 + 8\ HNO_3 \quad (2)$$

Final characteristics are highly influenced by which method is used to mix the reactants and the speed at which they are mixed, pH conditions (**Figure 11.3**) and the incorporation of surfactants and chelating agents in the medium. Other processes such as hydrothermal,[61] sol-gel,[62] sonochemical[63] and emulsification[64] have been proposed in order to increase the control on the crystal morphologies.

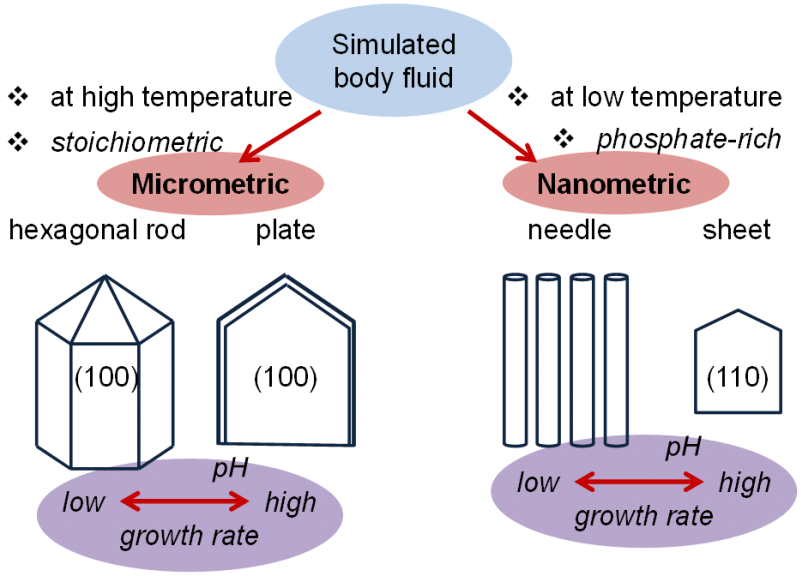

Figure 11.3. Change on the morphology of hydroxyapatite (HAp) crystals in simulated body fluid (BF) solutions according to stoichiometry, temperature, and pH. Growth rate becomes clearly enhanced by the increase of the pH of the medium. Indices indicate the Crystal growth faces. Based on Reference [65].

The low cost, biocompatibility and biodegradability of HAp justifies its use in a wide range of applications. For example, HAp has been explored as a non-viral vector taking into account the facility to prepare HAp/DNA complexes that can be incorporated into cells and release DNA after dissolution of calcium phosphate in the low-pH acidic media of cell endosomal compartiments.[66-68] Antibiotics such as chloramphenicol have also recently been encapsulated into HAp particles, giving rise to a proved selective antitumoral effect after their release inside cells.[69]

11.4 HYDROXYAPATITE NANOCOMPOSITES

It has been postulated that mineralization in natural systems is initiated by the formation of poorly crystalline calcium apatites, which subsequently undergo phase transitions towards a stable HAp with higher crystallinity.[70-71] Anionic groups (*i.e.* those from acidic proteins of the ECM or from synthetic peptide-based hydrogels) are useful for binding inorganic calcium cations and aligning them in the growing crystal lattice.[72] There is a clear correspondence between the cell dimensions of the hexagonal phase of HAp and those of the repeat unit in β-sheet structures (*i.e.,* the distances between two strands and between two residues are close to 0.48 nm and 0.69 nm, which correspond to half

of the *a* and *b* axes and the *c* axis of HAp, respectively). In nature, negatively charged surfaces of collagen fibrils nucleate the formation of the inorganic HAp phase.[73]

In a similar way, synthetic PAs can be designed in order to self-assemble into nanofibers that promote HAp mineralization. Basically, crystallographic *c* axis of the HAp hexagonal phase becomes oriented along the long axis of the peptide fiber. The ability to incorporate bioactive adhesion sequences (*e.g*. the RGD sequence) enhances the potential application of new synthetic hydrogel scaffolds for regeneration of soft and hard tissues.

nHAp particles have a high surface area and consequently a great proportion of ions become located in their surface. This feature has clear repercussions on the biological performance of the material, and specifically leads to an enhancement of cell adhesion and proliferation, osteointegration and cell differentiation. In this way, the rapid growth of new tissues can be favored.[74] nHAp appears as an ideal component to obtain nanocomposite materials for biomedical applications, which are constituted by at least two different chemical phases and the corresponding interphase. Properties of nanocomposites can be strongly modified as a function of the characteristics of: (a) the filler (*e.g.* chemical constitution, intrinsic properties, morphology, size distribution, etc); (b) the polymer matrix (*e.g.*, molecular weight, mechanical and thermal properties, etc); and (c) the polymer/filler mixture (*e.g.* ratio between components, interphase, degree of dispersion, etc). The preparation of bionanocomposites also requires biocompatibility, nontoxicity, and significant degradation rate of both filler and matrix. Basically, a simple embedding of nHAp into the polymer matrix is enough to get a suitable nanocomposite arrangement. To this end, both thermo-mechanical (*e.g.* injection and extrusion [75,76]) and physico-chemical (*e.g.,* coprecipitation and solvent casting) methods have been extensively applied.

The surface of nHAp is usually modified in order to improve the interphase characteristics with the organic matrix. In this way, surfactant molecules (*e.g*. oleic and stearic acids[77]) have been employed, and even grafting reactions (*e.g.* by ring-opening of lactide[78]) have been highly effective for both compatibilization and improvement of colloidal stability in such a way that particle aggregation is avoided.[79]

Collagen,[80] gelatin, [81,82] alginate, [83] and chitosan [84] are typical natural polymers that have been considered with the aim of obtaining scaffolds incorporating nHAp for tissue regeneration. Modified natural polymers such as cellulose acetate[85] and synthetic

polymers such as polylactide,[86] poly(lactide-co-glycolide),[87] or polycaprolactone [88] have also been employed.

HAp composites can be prepared according different methodologies, being the most applied: (a) *In situ* coprecipitation of nHAp in a co-solution with the polymer selected as a matrix. This process can avoid typical agglomeration problems of other simple mechanical mixing processes. Even the crystallization of HAp can be delayed if some chelating compounds (*e.g*. polyacrylic acid for the calcium ions [89]) are added in the solution. (b) Dispersion of nHAp particles into the monomer (*e.g.* methacrylate anhydride [90]). In this case, particles become coated by a polymer shell (*ex-situ* process) and aggregation problems are also diminished. (c) Electrospinning of polymer solutions incorporating nHAp particles. This is a promising process since it allows an easy preparation of fibrous and porous scaffolds with a biomimicking structure.[91] Finally, (d) self-assembling as a typical bioinspired process. For example, calcium and phosphate ions of the growing nHAp crystals can be assembled trough ionic interactions with peptide functional groups (*e.g.* from collagen).[92,93]

In fact, around 200 acidic proteins have been proposed for biomimetic mineralization processes, which involved different functions such as inhibition, nucleation, or more usually to act as simple templates to favor the epitaxial growth of nanocrystals.[94,95] Silk ,[96] fibrinogen [97] and SAPs can form amyloid nanofibers and 3D hydrogels [98] able to bind calcium phosphates and favor the growth of nHAp.[99]

PAs are ideal templates for the deposition of HAp crystals since can mímic, for example the phosphoserine-rich motifs of dentin proteins. Thus, an amphiphile having a polar groups based on three glutamic acid (E) units (*i.e.* Lauryl-VVAGEEE (E3-PA)) has been found highly efficient for nucleating calcium phosphate and inducing formation of HAp (**Figure 11.4**).[100]

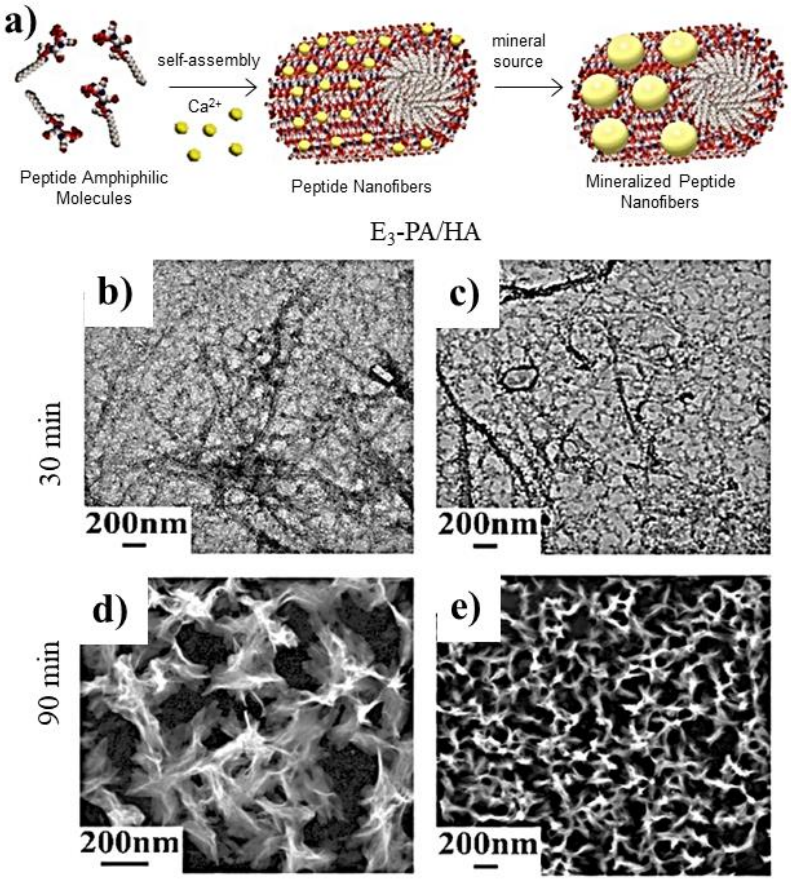

Figure 11.4. (a) Scheme showing the formation of nanofibers from peptide amphiphile molecules (Pas) and the subseqüent mineralization. Micrographs taken after (b,c) 30 and (d,e) 90 min of calcium phosphate mineralization where nanofiber (b,c) and plate-like (d,e) morphologies are visible. Reproduced from [100].

PA nanofibers containing units of serine or phosphoserine (PA-S) were able to nucleate carbonated HAp spheroidal crystals when exposed to a calcium-supplemented medium. These fibers could also be mixed (up to a 5 wt-%) with peptide amphiphiles containing the biological adhesion epitope RGDS. The mineralized nanofibers were found to promote osteogenic differentiation of human mesenchymal stem cells (hMSCs).[101]

Anderson *et al*.[102] prepared a biomimetic assembly consisting of PA nanofibers interspersed with nHAp. Specifically, a 1:1 mixture of a bioactive PA inscribed with the RGDS ligand to enhance osteoconductivity and a PA having an outer domain of inert serine with a strong gelating effect (PA-RGDS/PA-S (1:1)) was considered. The resulting scaffold was self-supporting, able to induce osteogenic differentiation, able to retain embedded HAp even at high concentration, and appeared interesting for bone tissue regeneration (**Figure 11.5**). The viscoelastic properties of the biphasic composite were

found optimal for a HAp content of 50 wt%, an increase of the ratio between storage and loss moduli (as indicator of a predominant elastic character) from 4.1 to 8.5 being detected when nanoparticles were incorporated.

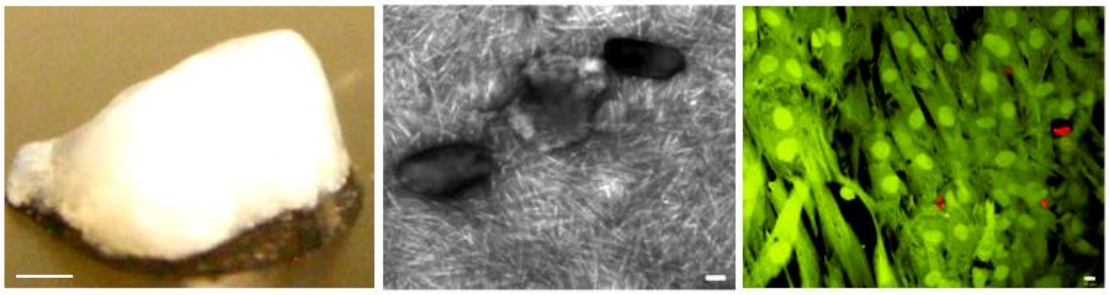

Figure 11.5. (left) Macroscopic (left), (middle) TEM and (right) confocal images of PA-RGDS/PA-S (1:1) hydrogel (left) with 50 wt% of HAp. The right image shows encapsulated hMSCs, viable and dead cells appearing in fluoresce green and red colours, respectively. Scale bars correspond to 1 mm (left), 100 nm (middle) and 10 µm (right). Reproduced from.[102]

11.5 HYDROGELS BASED ON PEPTIDE SELF-ASSEMBLY WITH INTEREST ON TISSUE REGENERATION

Different synthetic hydrogels have been developed for tissue applications, making it possible to achieve a great control on physical properties. Polymethacrylate and polyethylene glycol have been extensively considered as synthetic polymers ,[71,104,105] but they have some problems for rendering an efficient encapsulation of cells under physiological conditions via self-assembly. Furthermore, the use of polymethyl methacrylate (PMMA) is limited due to the exothermic polymerization reaction involved in the *in situ* formation of the material and also to its non-degradable nature that involves a risk for foreign body response and a delay on the healing process.

Peptide hydrogels can achieve a high water content (*i.e.,* up to 95 wt %) and thixotropic properties [106,107] since their formation is based on physical cross-links (*e.g*., hydrogen bonds, ion bonding, hydrophobic interactions). These links can be controlled according to the specific peptide sequence, peptide concentration, pH and ionic force. Applications of these hydrogels include drug delivery vehicles [108] and cell-culturing materials [109,110] due to their great safety and affinity with cells.[111,112] Hydrogels can also be easily injected, and consequently they have a great potential as bone-filling materials.

Gels based on PAs offer great advantages, such as the easy production of self-assembled three-dimensional nanofibrous networks. These appear optimum to favor cell diffusion, cell responsive degradation, and biological signaling.[113] Mechanical properties similar to the natural ECM can be obtained without employing chemical cross-linking agents. In this way, reactions that are adverse for tissues can be avoided.

The self-assembly of peptides can be initiated by screening their charged groups, which can typically take place through pH changes or addition of multivalent ions to the physiological mèdium.[3,72] Cylindrical nanostructures with peptide signals on their outer periphery are usually derived. The formation of non-covalent cross-links between fibers renders the final macroscopic hidrogel.[114,115] The peptide sequence can be modified in order to enhance specific tissue priorities (*e.g.,* osteogenic differentiation, drug delivery, or tunable gelation).[116-118]

Pro-DFDFDFDFDFD-Pro is a clear example of an amphiphilic and anionic peptide that can form hydrogels through self-assembling into β-sheets. Its capacity to induce biomineralization is an added value for bone regeneration.[119] This peptide has recently be linked to the integrin RGD motif, giving rise to Pro-DFDFDFDFDFDGGGRGDS-Pro (FD-RGD), a peptide that could be combined up to a 25 mol % with FD without disrupting the self-assembling fibril structure and increasing the density of osteoblasts cultured in the corresponding hydrogels.[118] In fact, FD-RGD was specifically designed to facilitate the juxtaposition with FD by satisfying cross-strand hydrogen bonds in the mixed fibrils (**Figure 11.6**). Thus, twelve residues were identical to those characteristic of FD, and three Gly amino acids were the linker with the integrin motif, which protrude out of the fibril to the solvent phase.

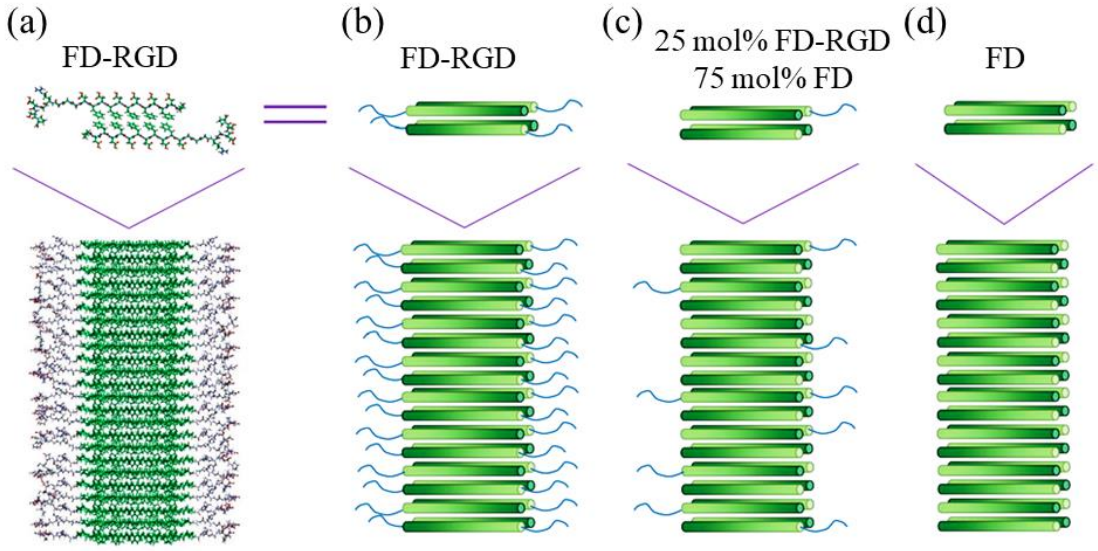

Figure 11.6. (a) Scheme showing molecular model of FD-RGD asemblies and (b-d) cylinder representation with a gradient color from the N- to C-termini (dark to bright, respectively). The β-strand conformation positions the hydrophobic, Phe side chains from both layers facing each other, while the hydrophilic side chains point to the surrounding aqueous phase. The top schemes show four peptides arranged in a bilayer that constitutes the fibril shown in the bottom scheme. Reproduced from [120].

Note that small peptides can be incorporated into a polymer matrix in order to guide the biomineralization process. Genetically engineered peptides that selectively bind to inorganic compounds (GEPIs) have been developed by exposing a pool of random amino acid sequences (placed on the surface of a bacteriophage or bacteria host organism) to a target inorganic substrate.[121,122] The more effective binding sequences have subsequently been identified[123] to produce GEPIs able to enhance the mineral formation.[124-126]

Gungormous *et al*.[121] designed a 27-residue peptide (MDG1) able to undergo triggered folding to form an unsymmetrical β-hairpin. A mechanical rigid and self-supporting hydrogel was obtained as a consequence of the self-assembly induced by the increase of the solution ionic strength. Basically, an unfolded conformation was initially expected due to the unfavorable electrostatic interactions between residue side chains, but the peptide became able to fold after charges were screened by addition of $CaCl_2$ and β-glycerolphosphate (β-GP) (**Figure 11.7**). The 20 C-terminal residues were chosen for their capability to self-assemble and consisted on two β-strands with and alternating disposition of hydrophobic and hydrophilic residues. These two sequences were

connected by an intermediate residue sequence able to render a β-turn. The *N*-terminal was constituted by a heptapeptide able to initiate the mineralization process of calcium and phosphate to produce HAp.

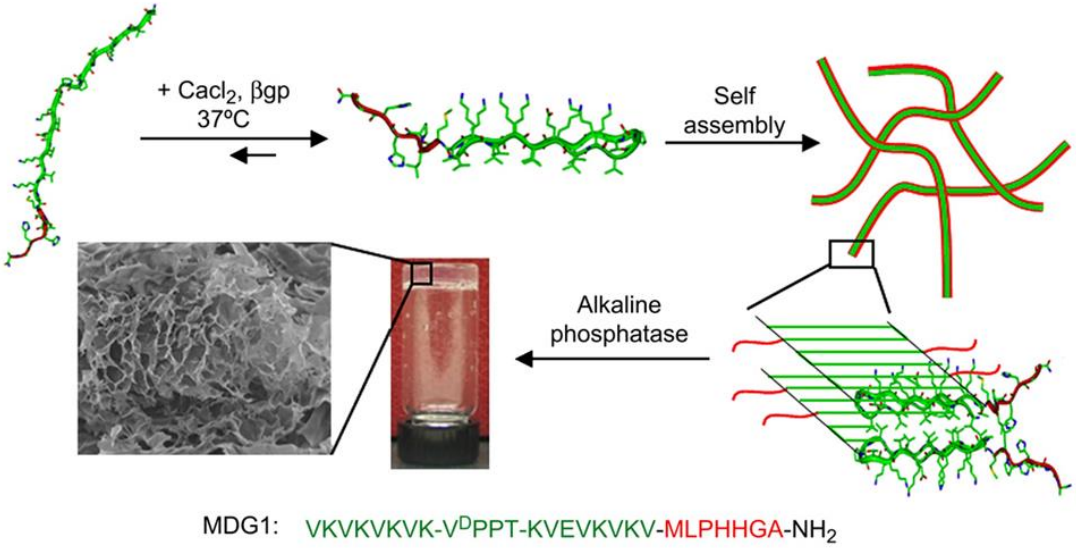

Figure 11.7. Scheme showing the self-assembling of MDG1 and the formation of three-dimensional gels after mineralization. Reproduced from [121].

11.6 NANOPARTICLES AND NANOCAPSULES BASED ON PEPTIDE SELF-ASSEMBLY

Polymer–nanoparticle (PNP) materials constitute a new class of hydrogels that are formed through nonspecific interactions between polymer chains and the surfaces of colloidal particles.[127-129] Nanoparticles can be coated with a bifunctional peptide that can establish physical cross-links with a recombinantly engineered protein. This molecular recognition allows a control over the number of physical cross-links and thereby of the mechanical (*e.g.* stiffness) performance of the material. It has been demonstrated that this approach is interesting for therapeutic delivery of cells for bone regeneration.[130] Thus, nHAp particles were embedded within a protein-engineered hydrogel (**Figure 11.8**) through physical specific interactions that could be established using a designed peptide. This hydrogel can act as a stem-cell carrier after the corresponding encapsulation and promote bone regeneration when implanted into defect sites.

Cationic nanoparticles can easily be prepared from amphiphilic peptides, and have been found highly effective as non-viral gene delivery vehicles to transport anionic nucleic acids into different cell types.[129] Nanoparticles based on peptides rich in arginine and

having the RALA sequence were proved to be non-cytotoxic and capable of crossing the plasma membrane of cancer cells. Nanoparticles with diameters lower than 100 nm and stable over a large range of temperatures for more than 6 h were prepared by incubation of RALA peptides with alendronate or other related nitrogen-containing bisphosphonates (BPs). These compounds can establish good electrostatic interactions to efficiently coat the peptidic nanocapsule. The derived particles had pH responsiveness due to conformational changes. Specifically, the peptide adopted an alpha-helical conformation that could be disrupted in the acidic medium of endosome, facilitating the release of loaded BP into the cytosol (**Figure 11.9**).[131]

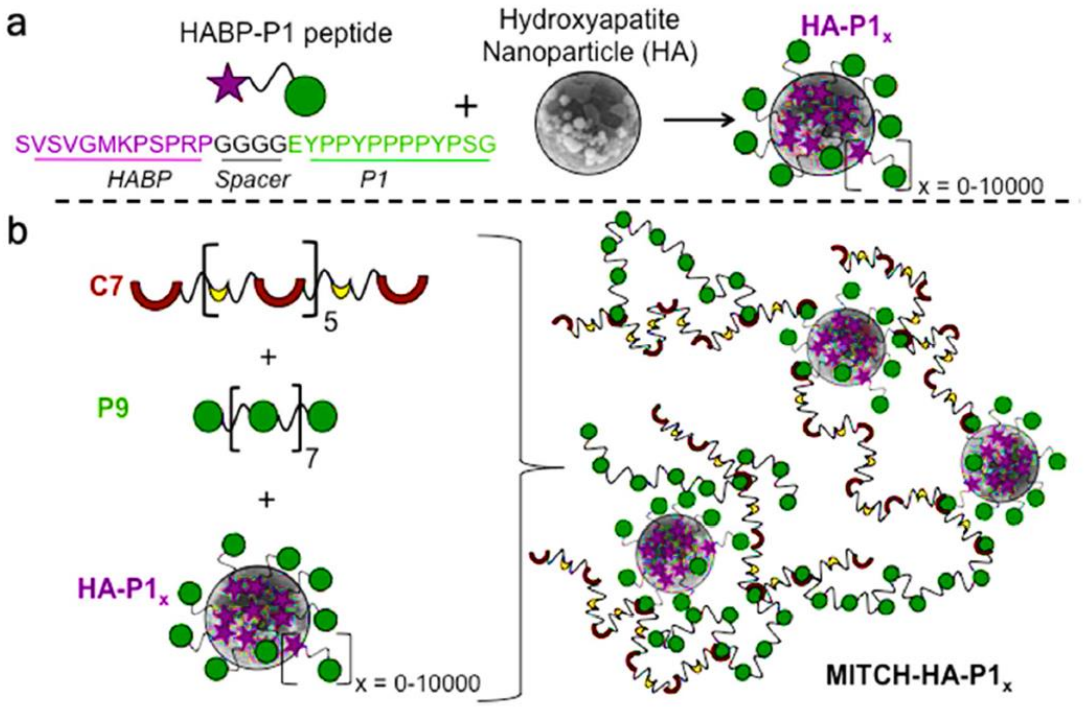

Figure 11.8. Schematic representation of a polymer–nanoparticle hydrogel with specific molecular recognition. (a) Binding of a number *x* of selected HABP-P1 peptides to the surface of hydroxyapatite nanoparticles. (b) Mixing of HA-P1*x* with recombinant proteins P9 and C7 induces the formation of a supramolecular hydrogel with direct physical linkages between the inorganic and organic phases. Adapted and reprinted with permission from [130].

Selected BPs have antitumor activity and inhibited tumor growth, migration, invasion, adhesion and angiogènesis.[132,133] BPs having hydroxyl and two phosphonate groups flanking a carbon atom showed a great affinity with HAp bone matrix, and consequently the circulating particles could be retained, avoiding a fast excretion by the kidneys.

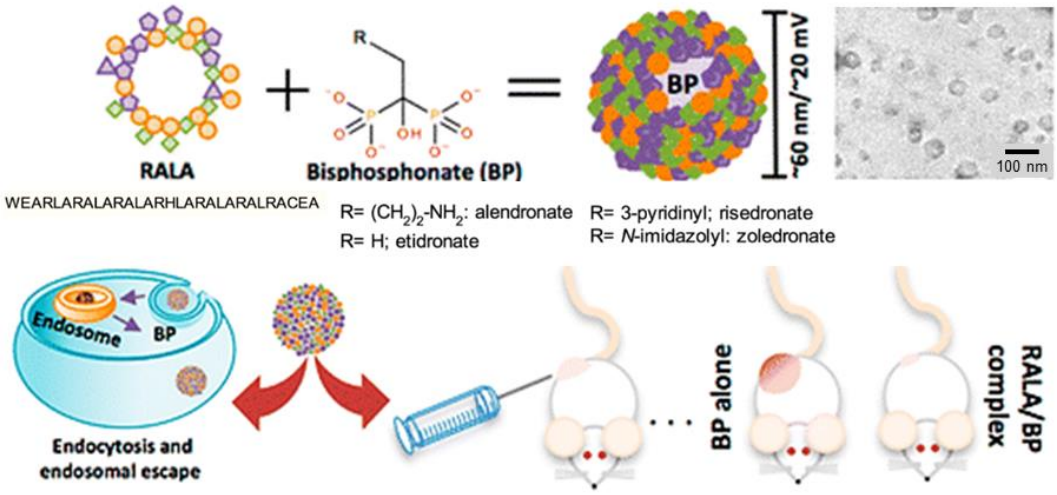

Figure 11.9. Nanoparticles with antitumoral properties based on the sef-assembled RALA peptides coated with BPs. Reproduced from [129].

11.7 HARD TISSUE REGENERATION

The aintenance of healthy bones, cartilage, and teeth is becoming one of the most relevant problems for an aging society, due also to intrinsic difficulties associated to the capability of old people to recover from fractures.

Three components (*i.e.* cells, scaffolds and signals) must be considered in regenerative medicine.[134,135] Concerning cells, bone marrow-derived hMSCs have been extensively considered due to their high capability to be differentiated into osteoblasts.[136,137] However, their proliferative activity tends to decrease with age [138] and consequently other alternatives have been considered (*e.g.* dental pulp stem cells (DPSCs).[139]

Hard tissue engineering has some inherent problems due to the limited number of cells that can be seeded effectively in the scaffold and also their uneven distribution that reduces the activity of incorporated cells in osteogenesis repair.[140] Consequently, efforts have been focused on promoting the accumulation of fibrous proteins to increase the area for the adhesion of seeded cells. In this case, problems related to the inhibition of nutrient delivery and vascularization have been reported.[141]

Basically, new formulated bionanocomposite systems try to mimic the characteristics of the extracellular matrix: (a) a hybrid structure of inorganic matter (*e.g.,* HAp) and organic

macromolecules (*e.g.,* polysaccharides and proteins); (b) a morphology based on particles with a high aspect ratio and diameter dimensions in the nanoscale range.

Effective nutrient delivery is an important factor for tissue repair due to the strong metabolic demand of osteblastic cells during tissue regeneration.[141,142] In general, cells tend to grow preferentially on the outer scaffolds regions,[143] being dynamic culture systems developed to avoid nutrient transport limitations in static culture. Bokhari *et al.*[142] used dynamic sell seeding and culturing techniques, demonstrating a higher penetration of cells (up to 3 mm) in HAp-modified scaffolds coated with RAD16-I. The peptide enhanced osteoblast differentiation and provided an appropriate environment for osteoblast growth.

Different porous scaffolds based on nHAp and chitosan (CTS) have been considered for tissue engineering applications. Nevertheless, some factors are not highly positive, the poor cell adhesion likely being the main problem limiting the material for an appropriate cell seeding. An interesting solution was the incorporation of a commercialized SAP hydrogel consisting of standard amino acids (1 % w/v) and water that could have a similar behavior to the extracellular matrix. Specifically, Zhu *et al.*[144], demonstrated that SAP/nHA/CTS scaffolds increased the adhesion of bone mesenchymal stem cells (BMSCs) and enhanced the mechanical properties of the scaffold. Assays were successfully focused on the repair of a femoral condylar bone defect in a mouse model. Experimental results indicated that healing could be achieved after 12 weeks. **Figure 11.10** compares the geometry of SAP/nHA/CTS and nHA/CTS scaffolds, with larger apertures and lesser porosity being detected for scaffolds without SAP. It was postulated that these peptides were able to fulfill the large pores and subsequently self-assembled.

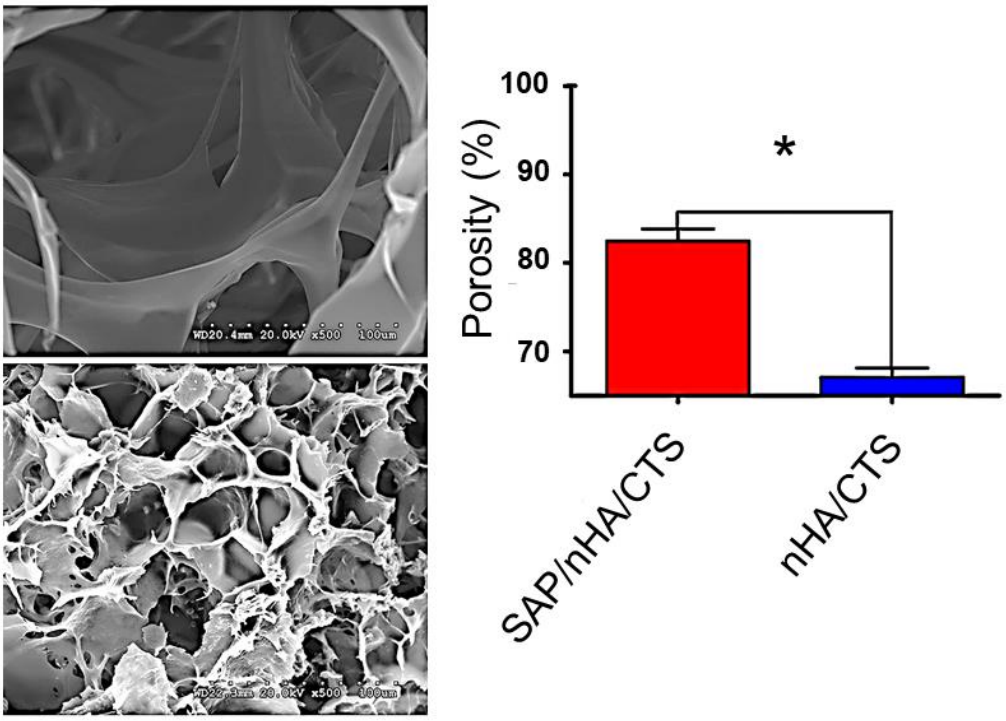

Figure 11.10. The morphology and SEM of (top-left) nHA/CTS and (bottom left) SAP/nHA/CTS. The porosity of the SAP/nHA/CTS was 84.53 %, which was significant higher than that of nHA/CTS, 67.97%, *p < 0.05. Reproduced from [144]. CTS:chitosan; SAP: self-assembled peptides.

The osteogenic differentiation of MSCs, in three-dimensional scaffolds based on RADA SAPs has been evaluated with promising results. Thus, high alkaline phosphatase activity and osteocalcin (OC) contents were determined, with the detection of a clear growth of a mineralized extracellular matrix within the hydrogel. Mesenchymal stem cells were able to undertake a 3D differentiation to form mineralized matrices within the scaffold hidrogel.[145]

Several self-assembled RADA peptides (*e.g.,* RAD16-I and RAD16-II characterized by RADARADARADARADA (modulusI) and RARADADARARADADA (modulus II) sequences, respectively) which easily form hidrogel scaffolds have been employed in tissue engineering.[107,146,147] However, the presence of carboxylic groups leads to low pH levels that are harmful for cells and host tissues. Therefore, neutralization procedures have employed.[148,149] The use of non-acidic self-assembled peptides can also solve this problem, with peptides based on arginine, alanine, leucine, and, aspartic acid (*e.g.,* SPG-178 peptide with a RLDLRLALRLDLR sequence) being interesting in this case. Specifically, SPG-18 [110,150] has an isoelectric point of 11.5 and can form a stable hydrogel at neutral pH (**Figure 11.11**). It has been demonstrated that DPSC proliferation and

osteogenic differentiation were successful using the SPG-718 hydrogel and an osteogenic induction medium containing recombinant human bone morphogenetic protein-4 (rhBMP-4). Gene expression levels of osteopontin, osteocalcin, and collagen type I were observed to increase significantly under these conditions.[135]

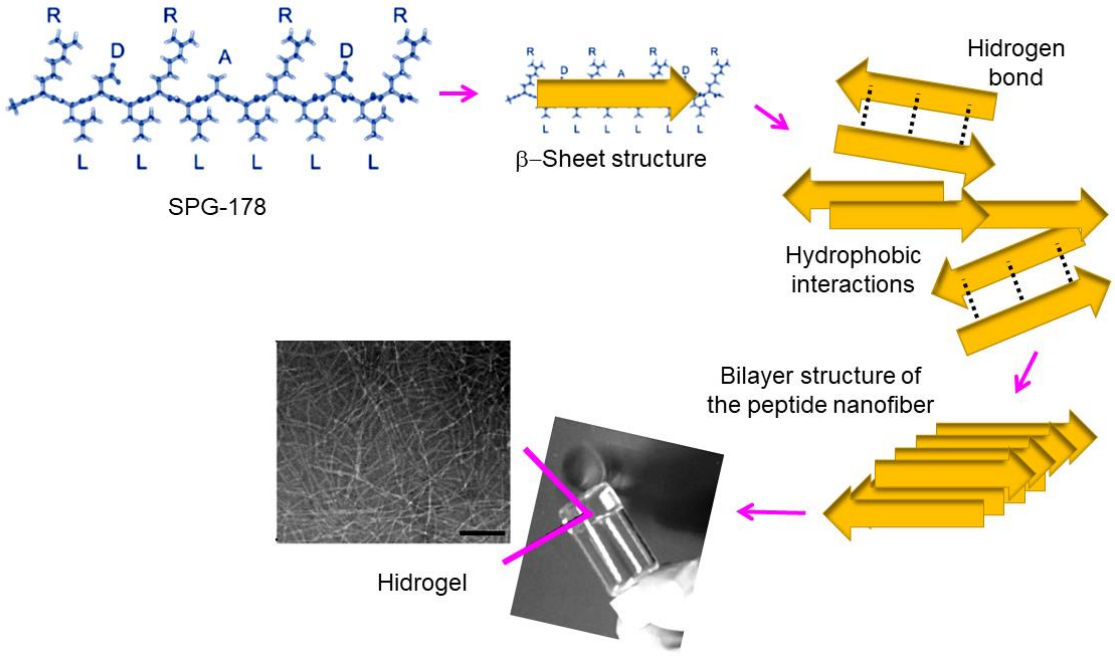

Figure 11.11. Chemical structure of the self-assembled SPG-178 peptide and scheme showing the corresponding hydrogel formation. Scale bar = 100 nm. Scheme based on [135].

Li *et al.* [95] prepared new hybrid materials based on peptide nanosheets (PNSs) derived from the self-assembly of LLVFGAKMLPHHGA and their noncovalent conjugation onto a graphene (GF) support (**Figure 11.12**). This 3D hybrid scaffold was suitable for the growth of HAp, giving rise to materials having adjustable shape, very low weight (0.017 $g \cdot cm^{-3}$), high porosity (5.17 $m^2\ g^{-1}$) that allows vascularization and transport of nutrients, excellent biocompatibility and, consequently, high potential for bone tissue and biomedical applications.

Complex systems (**Figure 11.13**) based on N-(2-hydroxypropyl)methacrylamide (HPMA) copolymers grafted with two complementary -sheet peptides (*i.e*. Beta11A (Ac–TTRFTTTFTTT–amide) and Beta11B (Ac–TTEFTTTFETT–amide) and RGD motif (*i.e*. (NH_2–GGRGDSP–amide) have also been designed for tissue regeneration.[149] Self-assembled fibrils were effective to orient the growth of HAp giving rise to a good control of mineralization. Furthermore, the system overcame some disadvantages of collagen

based scaffolds such as batch-to-batch variation, immunogenicity, complex molecular structure and poor mechanical strength.[150] Moreover, copolymers had a good solubility which appear as an advantages with respect to scaffolds based on -sheet peptides-only.

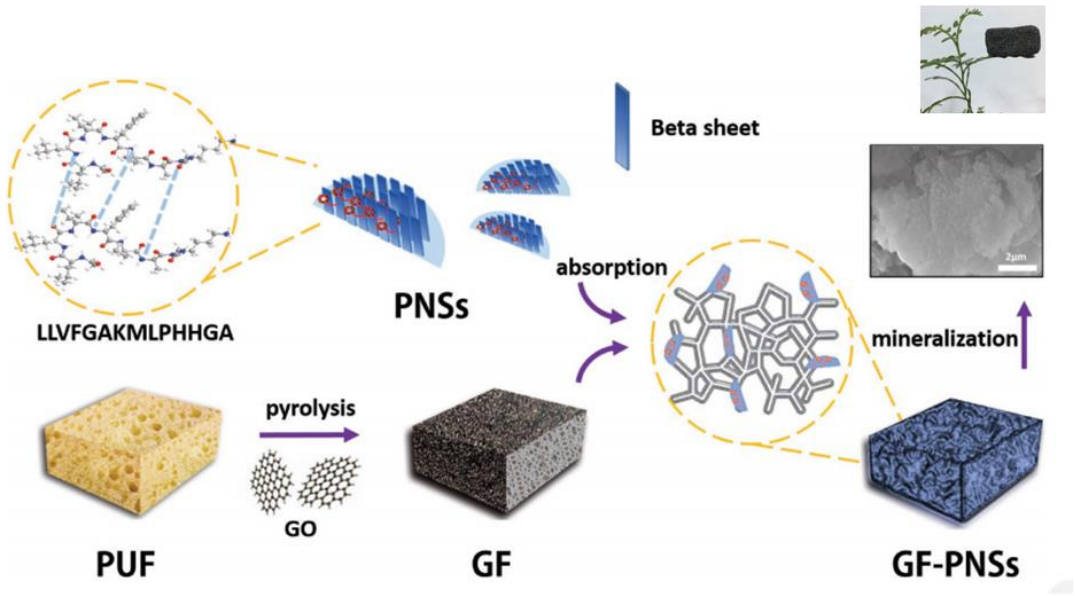

Figure 11.12. Biomimetic fabrication of 3D graphene (GF)-PNSs-HAp scaffold. PUF is a polyurethane foam used as a template for GF that can subsequently be removed from the flame, and GO is graphene oxide. Reproduced from [96]. PNS: peptide nanosheet

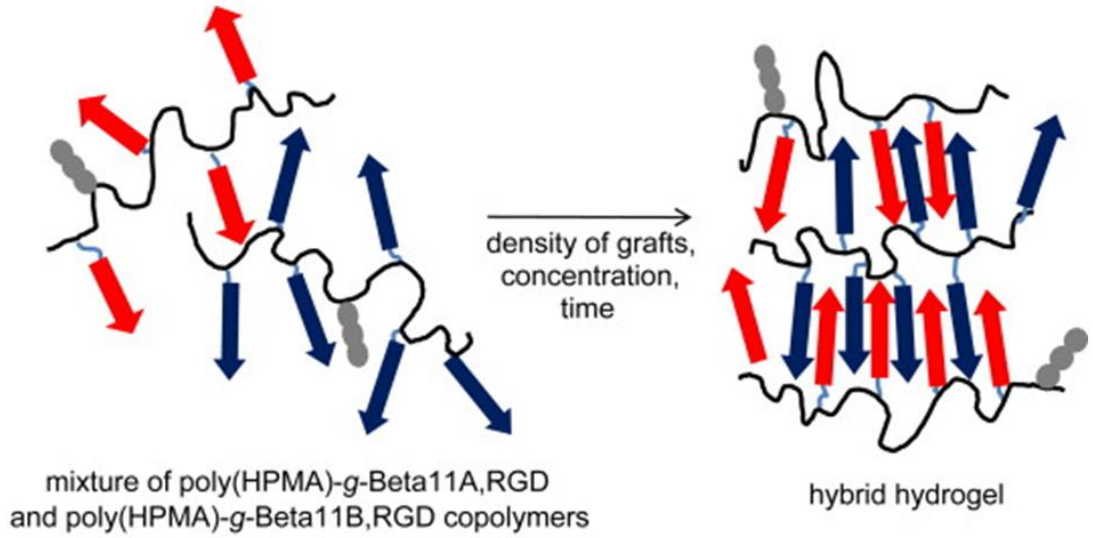

Figure 11.13. Hybrid hydrogel derived from the self-assembly of poly(HPMA)-*g*-*β*-sheet complementary copolymers (blue and red arrows). Grafted RGD motifs are indicated by gray fragments. Reproduced from [151]. HPMA: N-(2-hydroxypropyl)methacrylamide.

In vivo assays using different types of peptide amphiphiles were carried out by Mata *et al*. [152]. A strong ability to promote the nucleation of HAp crystals when phosphoserine units (S(P)) were incorporated into the peptide sequence was demonstrated. It is known from *in vitro* assays that that non-collagenous proteins rich in S(P) residues favor mineral nucleation, stimulate gene expression, and enhance osteoblast differentiation of MSCs[153]. The RGDS fibronectin epitope was also incorporated to favor adhesion of cells involved in bone regeneration (*e.g.,* mesenchymal stem cells, osteoprogenitor cells, osteoblasts, and vascular tissue cells).

Polymer-HAp nanocomposites were prepared using thermoreversibly self-assembling polymer templates (*i.e*. pentablock copolymers based on Pluronic F127 (poly(ethylene oxide)-*b*-poly(propylene oxide)-*b*-poly(ethylene oxide)) and anionic and zwitterionic blocks) with attached HAp-nucleating peptides (*i.e.,* DSKSDSSKSESDSS) at each end. These systems allowed a good control of mineralization and showded a líquid-to-solid transition at physiological temperatures. Thus, nanocomposites could be injectable, able to conform to the shape of bone or cartilage defects, and form solids at physiological conditions.[154]

11.7.1 Bone regeneration

Bone tissue engineering can overcome the problems inherent to transplantation of allogenic bone grafts (*e.g*., long-term chronic pain, nerve injury, risk of new fractures, immunogenic rejection, or even disease transmission[155,156]), providing new potential treatments for the repair of bone defects.[157] Ideal bone implants should be: (a) osteoconductive, having a capacity to favor the attachment, survival, migration and distribution of cells; (b) osteoinductive, responding to external stimuli to enhance the attachment, survival, migration, and distribution of cells; and (c) osteogenic, containing stem and osteogenic cells for regeneration.[158]

Two novel bone-filling materials were developed using $(LE)_8$ and $(VEVSVKVS)_2$ β-sheet -forming peptides.[98] These were based on the alternating disposition of hydrophobic (*i.e.* ,leucine (L) or valine (V)) and hydrophilic (*i.e.,* glutamic acid (E), serine (S) or lysine (K)) units. Both peptides were able to self-assemble giving rise to nanofibers that formed hydrogels in the presence of calcium ions (**Figure 11.14 a**). A ionic cross-linkage was established between carboxyl groups of the glutamic acid side chains of nanofibers and added calcium ions. $(VEVSVKVS)_2$ was able to retain the hydrogel structure at higher percentages of calcium ions (*i.e*. > 1.0×10^{-2} M) than $(LE)_8$ due to its lower number of

glutamic acid residues per molecule that avoid to collapse. Viscoelasticity increases with calcium ion concentration, and it was possible to obtain an appropriate strength for a bone-filling material. Amorphous calcium phosphate (ACP) and HAp were mineralized along peptide nanofibers of $(LE)_8$ and $(VEVSVKVS)_2$ under neutral and basic pHs, respectively (**Figures 11.14 b-11.14 c**).

The enhancement of the scaffold bioactivity for bone regeneration can be achieved through the encapsulation of bioactive molecules (*e.g.,* bone morphogenic proteins, BMPs). However, the release of these bio-factors is generally too fast to match the bone repair process, which requires several months to be completed.[159,160] Therefore, biomimetic peptide hydrogels based BMPs are highly interesting since they may provide a sustained release of bioactive molecules through degradation during the whole bone regeneration process. Obviously, bioactive units can also be generated inside the gel in order to promote cell differentiation and osteogènesis.[161,162]

Efforts have recently been focused on the development of peptides related to proteins having high osteoinductive properties, as it is the case of the bone morphogenic protein-2 (BMP-2). In this way, problems related to its large size, insolubility, unstability, high cost, and easy denaturation can be avoided. Thus, the morphogenetic protein-2 biomimetic peptide (BMPBP) has been proposed considering its reduced size (*i.e.,* between 20 and 30 amino acids) and the presence of typical SSPVT morphogenic sequences. Scaffolds encapsulating BMPBP were able to induce osteogenic differentiation and promote bone tissue regeneration.[163,164] However, these scaffolds could not provide sufficient bioactivity to meet the requirements of clinical application. Quan *et al*. developed new hydrogels based on BMPBP core containing 16 amino acids, phosphoserine as template to favor the deposition of calcium ions, RGDS cell adhesion peptide, and polyaspartic acid to synergistically promote osteogenesis.[165] New scaffolds were found capable to significantly accelerate the *in vivo* formation of rat cranial bone when rMSCs were also included.

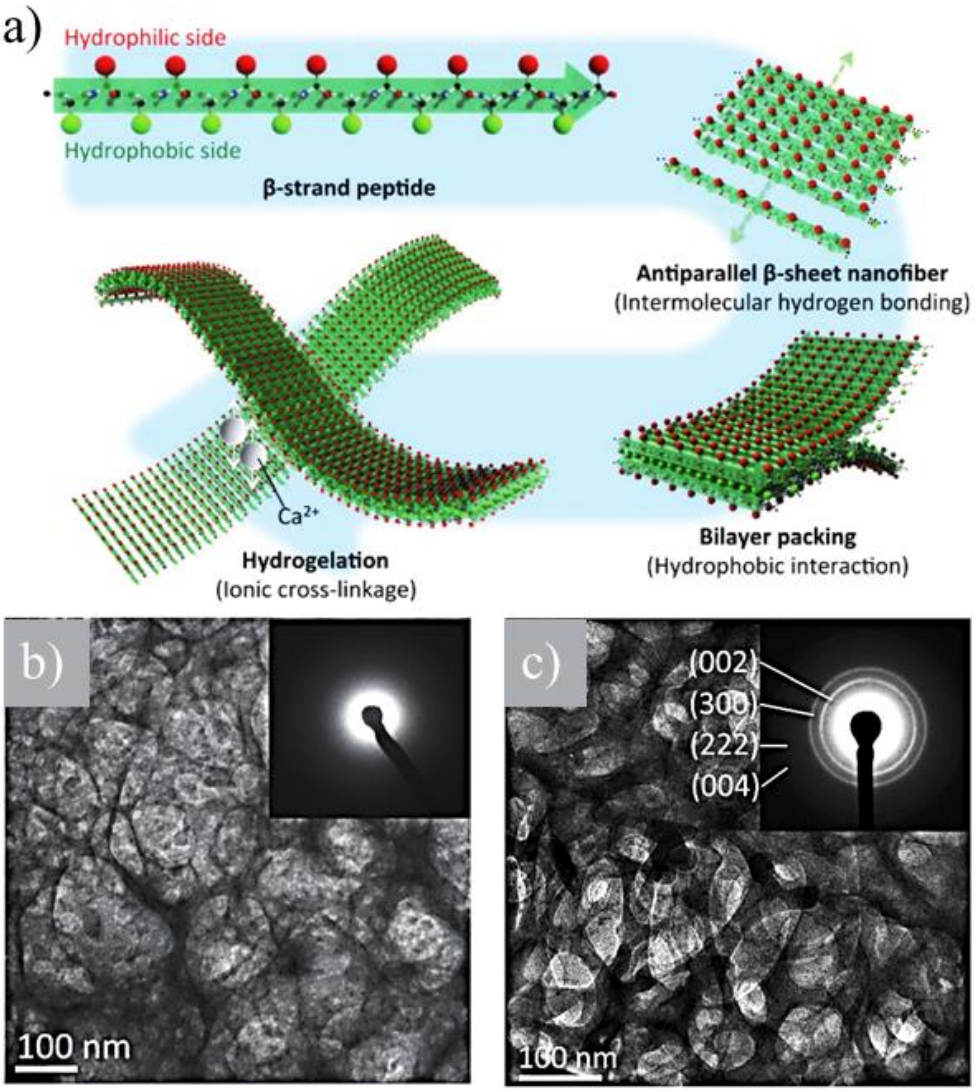

Figure 11.14. (a) β-strand $(LE)_8$ and $(VEVSVKVS)_2$ peptides formed antiparallel β -sheets, which packed face-to-face together through hydrophobic interactions between the two hydrophobic sides. The hydrophilic surfaces of bilayer nanofibers were subsequently able to cross-link by the ionic interaction between the anionic carboxyl group and the cationic calcium ion. (b) TEM image and amorphous calcium phosphate (ACP) amorphous electron diffraction pattern (inset) of the network derived from calcium phosphate and $(LE)_8$ peptide. (c) TEM image and HAp crystalline electron diffraction pattern (inset) of the network derived from calcium phosphate and $(VEVSVKVS)_2$ peptide. Reproduced from [98].

11.7.2 Tooth regeneration

Great efforts are nowadays focused on the prevention of dental. These mainly involved actions to avoid the formation of microbial films and the enhancement of effective remineralization process of the initial dental decay.[166,167]

Enamel is the hardest mineralized tissue of the human body and constitutes the external coating of teeth. This highly organized mineral is produced in the ectoderm germ layer and lacks of collagen or other precursor proteins.[168,169] The high mechanical properties are the consequence of a hierarchic organization where thousands of HAp crystals are anisotropically arranged in packed bundles or rods (*i.e*., the *c*-axis of HAp becomes aligned with the rod long axis). Ameloblast cells produce matrix proteins such as amelogenin, which self-assemble into nanospheres[170] and regulate the oriented crystal growth of HAp and ameloblastin. The latter protein facilitates the demarcation of rod boundaries and promotes cell-matrix interactions.[168] Proteins are eliminated during the last step of enamel development by the action of proteolytic enzymes.[172]

The use of liquids and pastes that contain nHAp for the repair of tooth surface is highly extended for remineralization of submicrometre-sized enamel lesions.[166] However, the treatment of larger cavities is more problematic and requires more complex solutions. Dental enamel is a hard biological tissue that cannot be repaired under the acid media derived from caries activity. The organic construction collapses, giving rise to the formation of a cavity. Self-assembled organic scaffolds are currently considered to control the crystal growth of nHAp and give rise to an ordered structure that mimics enamel. Representative advances on the development of self-assembled structures [50,173-177] appropriated for biomimetic enamel repair have been well summarized by Elkassas *et al.*[165]

Huang *et al.*[168] developed a bioactive matrix by self-assembly to induce the *in vivo* ectopic formation of enamel. A well-organized hirerarchical structure of HAp crystals was derived in close resemblance with native enamel. The matrix was based on a branched peptide amphiphile bearing high density of the epitope RGDS.

Self-assembled peptides (*i.e.,* biomimetic P11-4 having the Ac-Gln-Gln-Arg-Phe-Glu-Trp-Glu-Phe-Glu-Gln-Gln-NH_2 sequence[177]) have also been employed for caries treatment. Specifically, P11-4 is able to form a 3-D structure with Ca^{+2} binding sites, which can act as nucleation points for HAp. After application of P11-4 on the tooth

surface, the peptide self-assembles due to the low pH in the lesion and provides a scaffold similar to the enamel matrix.[178]

Romanelli *et al.* [177] used Fmoc-Val-cetylamide to form self-assembled nanofibrous gels, which had great affinity towards HAp and served as templates to bound proteins that mimicked the ECM of osteoblasts. Layer-by-layer (LBL) assembly allowed the incorporation of collagen, the sialophosphoprotein (EDPHNEVDGDK) sequence from dentin, and the osteoinductive growth factor (BMP-4). Assemblies were incubated with HAp nanocrystals, blended with varying different mass percentages of TiO_2 and finally coated with alginate to form three-dimensional scaffolds (**Figure 11.15**). These new materials were biodegradable and displayed a clear antibacterial activity. The ratio of TiO_2 nanoparticles had a great impact on antibacterial (*e.g.,* against *Staphylococcus aureus*) and biodegradability properties. Scaffolds were found to induce osteoblast differentiation and to proliferate and attach to the mouse preosteoblast MC3T3-E1 cells.

Resin-based composites are usually employed for dental restoration, but the *in vivo* degradation of the adhesive-dentin interface is a recurrent problem that limits the lifetime of the clinical restoration.[180] Viable solutions are focused on providing a minimum integrity to the indicated interphase by means of a peptide-mediated remineralization of dentin [181]. The use of specific peptides with affinity to both HAp and collagen appear ideal to promote the remineralization of dentin and seal dentine tubules.[182]

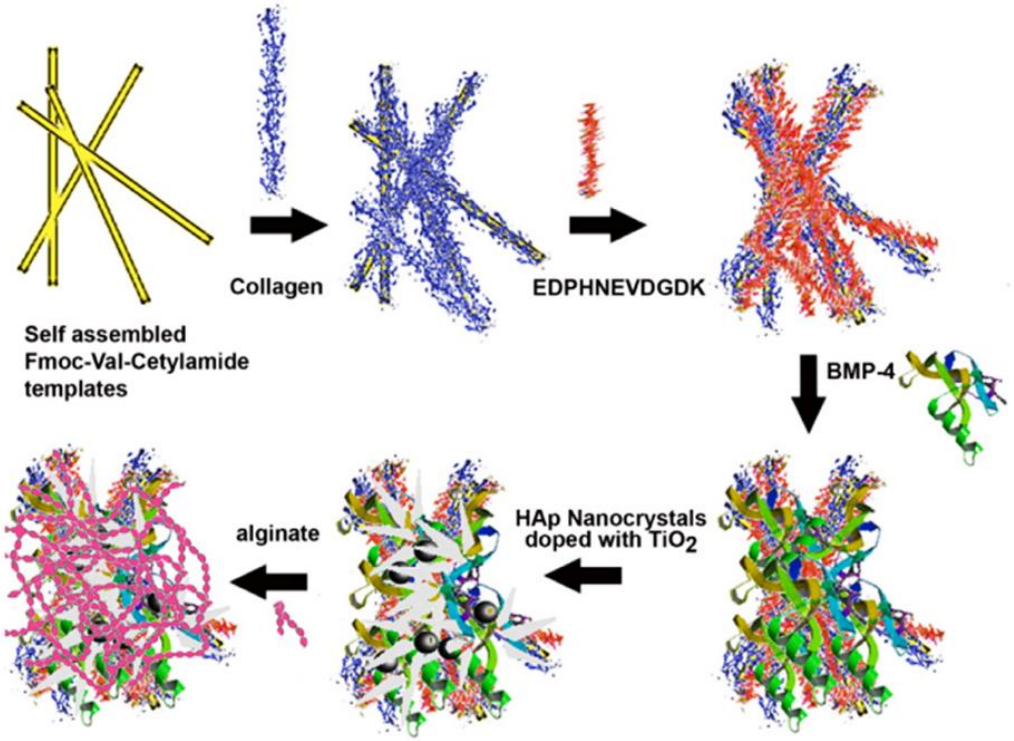

Figure 11.15. Scheme showing the preparation of 9-fluorenylmethyloxycarbonil (Fmoc)-Val-cetylamide-collagen-DT–BMP-4 biocomposites by layer-by-layer (LBL) assembly. The assemblies were finally coated with 1 % alginate to form scaffolds for bone tissue regeneration. Reproduced from [179].

11.7.3 Cartilague regeneration

Articular cartilage has a poor regenerative capacity, which is the main cause of the osteoarthritis disease typical of highly developed countries.[183] This consists on a depletion of glycosaminoglycans that causes a loss of mechanical properties and function *in vitro.*[184]

Cartilage-to-cartilage integration is more complex than typical bone-to-bone integration due to presence of stem cell and vascularity. The mechanical performance of cartilage depends on some characteristics that contribute negatively to healing and integrating with tissues.[185] Materials with suitable mechanical properties combine networks of collagen and glyycosaminoglycans, which make cell migration and adhesion difficult.[186] Furthermore, the avascular character of cartilages disrupt their accessibility to nutrients and progenitor cells.[187] All these difficulties justify the great efforts that are currently focused on the achievement of a good biomimetic cartilage graft fixation and integration.[188,189]

Chondrocytes with a well-known low metabolic activity are mainly the responsible of cartilage repair. The implantation of undifferentiated MSCs has a limited interest since, although a certain capability to promote the accumulation of cartilage-like tissue has been detected, the results are not sufficiently satisfactory to render a reliable regeneration of articular cartilage.[190] The induction of chondrogenesis is a basic point when MSCs are expected to be employed for cartilague regeneration. The *ex vivo* chondrogenic preconditioning in defined culture medium able to promote differentiation and secretion of ECM [191] is a possibility for enhancing the regeneration potential, but at the same time the use of injectable hydrogels becomes precluded[192]. Interesting works have recently been performed seeding MSCs into a self-assembling peptide (AcN-$(KLDL)_3$-CNH_2) hydrogel able to suport the chondrogenesis of the encapsulated MSCs[193,194] and facilitating the recovery of individual cell suspensions that is suited for injectable therapies.

A recent strategy consisted on the use of an osteochondral construct obtained from the interdigitation of HAp ceràmic-based material with a functionally viable neocartilage prepared by self-assembly.[189] Glycosaminoglycan and collagen were the main components of the self-assembled neocartilage.

Suitable scaffolds for cartilage repair consist of three-dimensional templates in which attached or seeded chondrocytes produce and deposit a continuous ECM network. A great variety of natural and synthetic polymers are being considered for cartilage repair (*e.g.,* collagen, alginate, polyglycolide, polylactide, polyethylene oxide [195-198]). Hydrogels derived from SAPs have also been proposed as appropriate environments for the retention of chondrocyte phenotype and the achievement of a cartilage extracellular matrix.[199]

SAPs based on tryptophan and phenylalanine residues, which are placed on the middle and on the same side of the peptide to drive ribbon formation, and charged amino acids that favor and antiparallel sheet arrangement have been proposed.[200] Specifically, $CH_3COQQRFEWEFEQQNH_2$ (P_{11}-4) $CH_3COQQRFOWOFEQQNH_2$ (P_{11}-8) and $CH_3COSSRFOWOFESSNH_2$ (P_{11}-12) sequences have been evaluated. These SAPs can be mixed with chondroitin sulphate and initially delivered as a non-viscous fluid that can be triggered to self-assemble once located in place. Hydrogels showed promising properties for biomedical applications in glycosaminoglycan-depleted tissues. The best results were achived with P_{11}-8 and P_{11}-12 samples.

11.8 CONCLUSIONS

The number of works related to the development of peptide-related hydrogels has increased exponentially since the discovery of the self-assembly capacity of molecules consisting of small peptide sequences. These hydrogelators have a wide range of applications, but the most promising ones concern the biomedical field, mainly as a consequence of the capacity of such materials to mimic the ECM. Properties like biocompatibility, establishment of physical and reversible cross-links, feasibility of cross-linking under physiological conditions, tunability, and trigger capacity justify the great interest of such materials.

The research carried out so far highlights the diversity of appropriate sequences to induce self-assembly and the possibility of changing both structure and functionality. The great potential of such materials is obviously linked to the great variability in the composition and length of peptides, which opens the possibility of a tailored design to suit a specific property.

The incorporation of charged amino acids in the peptide sequence promotes the interaction with calcium divalent ions, making it possible to use the derived hydrogels for the nucleation of HAp and even the development of nanocomposites. Promising results have been achieved in recent years concerning the development of hydrogels for the regeneration of hard tissues- mainly bones, teeth and, cartilage, as evidenced in the present review. The achievements attained in this field are very relevant, as it is expected that they will be able to reach an effective commercialization of these materials. The ability to gel under the action of suitable stimuli also allows the use of self-assembly peptides as injectable materials that can be fitted to the shape of the defect to be regenerated.

Different challenges must still be overcome in order to obtain a maximum benefit and attain an effective commercialization. Progress is needed for the development of smart materials susceptible to external stimuli (*e.g.,* electrical signals, pH changes, addition of bone morphogenetic proteins) and especially for drug delivery systems based on self-assembly peptides and HAp.

11.9 REFERENCES

1. Kim, S., Kim, J.H., Lee, J.S. & Park, C.B. Beta-sheet-forming, self-assembled peptide nanomaterials towards optical, energy, and healthcare applications. *Small*. **11**, 3623-3640 (2015).
2. Scanlon, S. & Aggeli, A. Self-assembling peptide nanotubes. *Nanotoday*. **3**, 22-30 (2008).
3. Hartgerink, J.D., Beniash, E. & Stupp, S.I. Peptide-amphiphile nanofibers: a versatile scaffold for the preparation of self-assembling materials. Proc. *Natl. Acad. Sci. U.S.A.* **99**, 5133–5138 (2002).
4. Stupp, S.I. Self-assembly and biomaterials. *Nano Lett*. **10**, 4783-4786 (2010).
5. Stupp, S.I. Biomaterials for regenerative medicine. *MRS Bull*. **30**, 546-553 (2005).
6. Andreetto, E., Malideli, E., Yan, L.M., Kracklauer, M., Farbiarz, K., Tatarek-Nossol, M., Rammes, G., Prade, E., Neumüller, T., Caporale, A., Spanopoulou, A., Bakou, M., Reif, B. & Kapurniotu A. A hot-segment-based approach for the design of cross-amyloid interaction surface mimics as inhibitors of amyloid self-assembly. Angew. *Chem. Int. Ed. Engl.* **54**, 13095-13100 (2015).
7. Li, C., Adamcik, J. & Mezzenga, R. Biodegradable nanocomposites of amyloid fibrils and graphene with shape-memory and enzyme-sensing properties. *Nat. Nanotechnol*. **7**, 421- 427 (2012).
8. Jacob, R.S., Ghosh, D., Singh, P.K., Basu, S.K., Jha, N.N., Das, S., Sukul, P.K., Patil, S., Sathaye, S., Kumar, A., Chowdhury, A., Malik, S., Sen, S. & Maji, S.K. Self healing hydrogels composed of amyloid nano fibrils for cell culture and stem cell differentiation. *Biomaterials*. **54**, 97-105 (2015).
9. Amit, M, Yuran, S., Gazit, E., Reches, M. & Ashkenasy, N. Tailor-made functional peptide self-assembling nanostructures. *Adv. Mater*. **30**, e1707083 (2018).
10. Wei, G., Su, Z., Reynolds, N.P., Arosio, P., Hamley, I.W., Gazit, E. & Mezzenga, R. Self-assembling peptide and protein amyloids: from structure to tailored function in nanotechnology. *Chem. Soc. Rev*. **46**, 4661-4708 (2017).
11. Knowles, T.P. & Mezzenga, R. Amyloid fibrils as building blocks for natural and artificial functional materials. *Adv. Mater*. 28, 6546-6561 (2016).
12. Ekiz, M.S., Cinar, G., Khalily, M.A. & Guler, M.O. Self-assembled peptide nanostructures for functional materials. *Nanotechnology*. **27**, 402002 (2016).
13. Reches, M. & Gazit, E. Casting metal nanowires within discrete self-assembled peptide nanotubes. *Science*. **300**, 625-627 (2003).
14. Adler-Abramovich, L. & Gazit, E. The physical properties of supramolecular peptides assemblies: from Building block association to technological Applications. *Chem. Soc. Rev*. 43, 6881-6893 (2014).
15. Babar, D.G. & Sarkar, S. Self-assembled nanotubes from single fluorescent amino acid. *Appl. Nanosci*. **7**, 101-107 (2017).

16. Gyles, D.A., Castro, L.D., Silva, J.O.C. & Ribeiro-Costa, R.M. A review of the designs and prominent biomedical advances of natural and synthetic hydrogel formulations. *Eur. Polym. J.* **88**, 373–392 (2017).

17. Das, N. Preparation methods and properties of hydrogel: A review. *Int. J. Pharm. Pharm. Sci.* **5**, 112–117 (2013).

18. Bae, K.H., Wang, L.S. & Kurisawa, M. Injectable biodegradable hydrogels: Progress and challenges. *J. Mater. Chem.* **1**, 5371–5388 (2013).

19. del Valle, L.J., Díaz, A. & Puiggalí, J. Hydrogels for biomedical applications: cellulose, chitosan, and protein/peptide derivatives. *Gels*. **3**, 27 (2017).

20. Wahl, D.A. & Czernuszka, J.T. Collagen-hydroxyapatite composites for hard tissue repair. *Eur. Cell. Mater*. **11**, 43–56 (2006).

21. Dorozhkin, S.V. Calcium orthophosphate bioceramics. *Ceram. Int*. **41**, 13913–13966 (2015).

22. Habraken, W., Habibovic, P., Epple, M. & Bohner, M. Calcium phosphates in biomedical applications: Materials for the future?. *Materialstoday*. **19**, 69–87 (2016).

23. Turon, P., del Valle, L.J., Alemán, C. & Puiggalí, J. Biodegradable and biocompatible systems based on hydroxyapatite nanoparticles. *Appl. Sci*. **7**, 60 (2017).

24. Rubert Pérez, C.M., Stephanopoulos, N., Sur, S., Lee, S.S., Newcomb, C. & Stupp, S.I. The powerful functions of peptide-based bioactive matrices for regenerative medicine. *Ann. Biomed. Eng*. **43**, 501-514 (2015).

25. Cui, H., Webber, M.J. & Stupp, S.I. Self-assembly of peptide amphiphiles: from molecules to nanostructures o biomaterials. *Biopolymers*. **94**, 1–18 (2010).

26. Hosseinkhani, H., Hong, P.D. & Yu, D.S. Self-assembled proteins and peptides for regenerative medicine. *Chem. Rev*. **113**, 4837–4861 (2013).

27. He, B.; Zhao, J., Ou, Y. & Jiang, D. Biofunctionalized peptide nanofiber-based composite scaffolds for bone regeneration. *Mater. Biol. Appl*. **90**, 728-738 (2018).

28. Zou, R., Wang Q., Wu, J., Schmuck, C. & Tian, H. Peptide self-assembly triggered by metal ions. *Chem. Soc. Rev*. **44**, 5200-5219 (2015).

29. Wang, J., Liu, R. & Yan, X. Peptide self-assembly: thermodynamics and kinetics. *Chem. Soc. Rev*. **45**, 5589-5604 (2016).

30. Feng, Z., Zhang, T., Wang, H., & Xu, B. Supramolecular catalysis and dynamic assemblies for medicine. *Chem. Soc. Rev*. **46**, 6470-6479 (2017).

31. Mason, J.M. & Arndt, K.M. Coiled coil domains: stability, specificity, and biological implications, *Chembiochem*. **5**, 170–176 (2004).

32. Woolfson, D.N. Building fibrous biomaterials from alpha-helical and collagen-like coiled-coil peptides. *Biopolymers*. **94**, 118-127 (2010).

33. Di Lullo, G.A., Sweeney, S.M., Korkko, J., Ala-Kokko, L. & San Antonio, J.D. Mapping the ligand-binding sites and disease-associated mutations on the most abundant protein in the human, type I collagen. *J. Biol. Chem*. **277**, 4223–4231 (2002).

34. He, B., Yuan, X. & Jiang, D. Molecular self-assembly guides the fabrication of peptide nanofiber scaffolds for nerve repair. *RSC Adv*. **4**, 23610–23621 (2014).

35. Stephanopoulos, N., Ortony, J.H. & Stupp, S.I. Self-assembly for the synthesis of functional biomaterials. *Acta Mater*. **61**, 912–930 (2013).

36. Gazit, E. Self-assembled peptide nanostructures: the design of molecular building blocks and their technological utilization. *Chem. Soc. Rev*. **36**, 1263–1269 (2007).

37. Sun, L., Zheng, C. & Webster, T.J. Self-assembled peptide nanomaterials for biomedical applications: promises and pitfalls. *Int. J. Nanomedicine*. **12**, 73–86 (2017).

35. Luo, Z., Wang, S. & Zhang, S. Fabrication of self-assembling d-form peptide nanofiber scaffold d-EAK16 for rapid hemostasis. *Biomaterials*. **32**, 2013–2020 (2011).

39. Luo, Z. & Zhang, S. Designer nanomaterials using chiral self-assembling peptide systems and their emerging benefit for society. *Chem. Soc. Rev*. **41**, 4736–4754 (2012).

40. Raspa, A., Saracino, G.A.A., Pugliese, R., Silva, D., Cigognini, D., Vescovi, A. & Gelain, F. Complementary Co-assembling peptides: from in silico studies to in vivo application. *Adv. Funct. Mater*. **24**, 6317–6328 (2014).

41. Zhang, S., Holmes, T.C., DiPersio, C.M., Hynes, R.O., Su, X. & Rich, A. Self-complementary oligopeptide matrices support mammalian cell attachment. *Biomaterials*. **16**, 1385–1393 (1995).

42. Zhang, S. & Altman, M. Peptide self-assembly in functional polymer science and engineering. *React. Funct. Polym*. **41**, 91–102 (1999).

43. Zhang, F., Shi, G.S., Ren, L.F., Hu, F.Q., Li, S.L. & Xie, Z.J. Designer self-assembling peptide scaffold stimulates pre-osteoblast attachment, spreading and proliferation. *J. Mater. Sci. Mater. Med*. **20**, 1475–1481 (2009).

44. Horii, A., Wang, X., Gelain, F. & Zhang, S. Biological designer self-assembling peptide nanofiber scaffolds significantly enhance osteoblast proliferation, differentiation and 3-D migration. *PLoS One*. **2**, e190 (2007).

45. Garcia, A., Iglesias, D., Parisi, E., Styan, K.E., Waddington, L.J., Deganutti, C., Zorzi, C. & Marchesan, S. Chirality effects on peptide self-assembly unraveled from molecules to materials. *Chem*. **4**, 2862-1876 (2018).

46. Fuertes, A., Juanes, M, Grana, J.R. & Montenegro, J. Supramolecular funcional assemblies: dynamic membrane transporters and peptide nanotubular composites. *Chem. Commun*. **53**, 7861-7871 (2017).

47. Melchioma, M., Styan, K.E. & Marchesan, S. The unexpected advantages of using D-amino acids for peptide self-assembly into nanostructured hydrogels for medicine. *Curr. Top. Med. Chem*. **16**, 2009-2018 (2016).

48. Hartgerink, J.D., Beniash, E. & Stupp, S.I. Self-assembly and mineralization of peptide-amphiphile nanofibers. *Science*. **294**, 1684-1688 (2001).

49. Castelletto, V., Moulton, C.M., Cheng, G.; Revilla, G. & Aleman C. Self-assembly of Fmoc-tetrapeptides based on RGDS cell adhesion motif. *Soft Matter*. **7**, 11405-11415 (2011).

50. López-Pérez, D.E., Revilla,G, Hamley, I.W. & Aleman, C. Molecular insights into aggregates, made of amphiphilic Fmoc-tetrapeptides. *Soft Matter*. **9**, 11021-11032 (2013).

51. Zhang, S., Greenfield, M.A., Mata, A., Palmer, L.C., Bitton, R., Mantei, J.R.; Aparicio, C., de la Cruz, M.O. & Stupp, S.I. A self-assembly pathway to aligned monodomain gels. *Nat. Mater*. **9**, 594–601 (2010).

52. Tao, K, Levin, A., Adler-Abramovivh, L. & Gazit, E. Fmoc-modified amino acids and short peptides: simple bio-inspired buikding blocs for the fabrication of funcional materials. *Chem. Soc. Rev*. **45**, 3935-3953 (2016).

53. Martin, A.D., Wojciechowski, J.P., Warren, H., Pamhuis, M., & Thordarson, P. Effect of heteocyclic capping groups on the self-assembly of a dipeptide hidrogel. *Soft Mater*. **12**, 2700-2707 (2016).

54. Lyanage, W., Vats, K., Rajbhandary, A., Benoit D.S.W. & Nilsson, B.L. Multicomponent dipeptide hydrogels as extracellular matrix-mimetic scaffolds for cell culture Applications. *Chem. Commun*. **51**, 11260-11263 (2015).

55. Elliot, J.C. Structure and Chemistry of the Apatites and Other Calcium Orthophosphates, 1st ed.; *Elsevier*: Amsterdam, Holland, 1-62 (1994).

56. Kay, M.I., Young, R.A. & Posner, A.S. Crystal structure of hydroxyapatite. *Nature.* **204**, 1050-1052 (1964).

57. Dorozhkin, S.V. & Epple, M. Biological and medical significance of calcium phosphates. *Angew. Chem. Int*. Ed. Engl. **41**: 3130–46 (2002).

58. Bigi, A., Boanini, E. & Rubini, K. Hydroxyapatite gels and nanocrystals prepared through a sol–gel process. *J. Solid State Chem*. **177**, 3092-3098 (2004).

59. Fowler, C.E., Li, M., Mann, S. & Margolis, H.C. Influence of surfactant assembly on the formation of calcium phosphate materials—A model for dental enamel formation. *J. Mater. Chem*. **15**, 3317-3325 (2005).

60. Roy, I., Mitra, S., Maitra, A. & Mozumdar, S. Calcium phosphate nanoparticles as novel non-viral vectors for targeted gene delivery. *Int. J. Pharm*. **250**, 25-33 (2003).

61. Zhang, F., Zhou, Z.H., Yang, S.P., Mao, L.H., Chen, H.M. & Yu, X.B. Hydrothermal synthesis of hydroxyapatite nanorods in the presence of anionic starburst dendrimer. *Mater. Lett*. **59**, 1422-1425 (2005).

62. Bose, S. & Saha, S.K. Synthesis of hydroxyapatite nanopowders via sucrose-templated sol–gel method. *J. Am. Ceram. Soc*. **86**, 1055-1057 (2004).

63. Jevtic, M., Mitric, M., Skapin, S., Jancar, B., Ignjatovic, N. & Uskokovic D. Crystal structure of hydroxyapatite nanorods synthesized by sonochemical homogeneous precipitation. *Cryst. Growth Des*. **8**, 2217-2222 (2008).

64. Bose, S. & Saha, S.K. Synthesis and characterization of hydroxyapatite nanopowders by emulsion technique. *Chem. Mater*. **15**, 4464-4469 (2003).

65. Kobayashi, T., Ono, S., Hirakura, S., Oaki, Y. & Imai, H. Morphological variation of hydroxyapatite grown in aqueous solution based on simulated body fluid. *Cryst. Eng. Comm*. **14**, 1143-1149 (2012).

66. Bertran, O., del Valle, L.J., Revilla-López, G., Chaves, G., Cardús, L., Casas, M.T., Casanovas, J., Turon, P., Puiggalí, J. & Alemán, C. Mineralization of DNA into nanoparticles of hydroxyapatite. *Dalton Trans***. 43**, 317-327 (2014).

67. Zuo, G., Wan, Y., Meng, X., Zhao, Q., Ren, K., Jia, S. & Wang, J. Synthesis and characterization of a lamellar hydroxyapatite/DNA nanohybrid. *Mater. Chem. Phys.* **126**, 470-475 (2011).

68. Zhu, S.H., Huang, B.Y., Zhou, K.C., Huang, S.P., Liu, F., Li, Y.M., Xue, Z.G. & Long, Z.G. Hydroxyapatite nanoparticles as a novel gene carrier. *J. Nanopart. Res.* **6**, 307-311 (2004).

69. Rivas, M.,del Valle, L.J., Rodríguez-Rivero, A.M., Turon, P., Puiggalí, J. & Alemán, C. Loading of antibiotic into biocoated hydroxyapatite nanoparticles: smart antitumor platforms with regulated release. *ACS Biomater. Sci. Eng*. **4**, 3234-3245 (2018).

70. Bonzani, I.C., George, J.H. & Stevens, M.M. Novel materials for bone and cartilage regeneration. *Curr. Opin. Chem. Biol*. **10**, 568-575 (2006).

71. Song, J., Malathong, V. & Bertozzi, C.R. Mineralization of synthetic polymer scaffolds: a bottom-up approach for the development of artificial bone. *J. Am. Chem. Soc*. **127**, 3366-3372 (2005).

72. Palmer, L.C., Newcomb, C.J., Kaltz, S.R., Spoerke, E.D. & Stupp, S.I. Biomimetic systems for hydroxyapatite mineralization inspired by bone and enamel. *Chem. Rev.* **108**, 4754-4783 (2008).

73. Zhang, W., Liao, S.S. & Cui, F.Z. Hierarchical self-assembly of nano-fibrils in mineralized collagen. *Chem. Mater*. **15**, 3221-3226 (2003).

74. Nel, A., Xia, T., Mädler, L. & Li, N. Toxic potential of materials at the nanolevel. *Science*. **311**, 622-627 (2006).

75. Mathieu, L.M., Bourban, P.E. & Manson, J.A.E. Processing of homogeneous ceramic/polymer blends for bioresorbable composites. *Compos. Sci. Technol*. **66**, 1606-1614 (2006).

76. Maiti, P., Prakash, Y. & Jaya, P. Biodegradable nanocomposites of poly(hydroxybutyrate-co-hydroxyvalerate): the effect of nanoparticles. *J. Nanosci. Nanotechnol.* **8**, 1858-1866 (2008).

77. Li, Y. & Weng, W. Surface modification of hydroxyapatite by stearic acid: characterization and in vitro behaviors. *J. Mater. Sci.: Mater. Med*. **19**, 19-25 (2008).

78. Hong, Z., Zhang, P., He, C., Qui, X., Liu, A., Chen, L., Chen, X. & Jing, X. Nano-composite of poly(L-lactide) and surface grafted hydroxyapatite: mechanical properties and biocompatibility. *Biomaterials*. **26**, 6296-6304 (2005).

79. Kato, K., Eika, Y. & Ikada, Y. In situ hydroxyapatite crystallization for the formation of hydroxyapatite/polymer composites. *J. Mater. Sci*. **32**, 5533-5554 (1997).

80. Laurencin, C.T., Kumbar, S.G. & Nukavarapu, S.P. Nanotechnology and orthopedics: a personal perspective. *WIREs. Nanomed. Nanobiotechnol*. **1**, 6-10 (2009).

81. Kim, H.W., Song, J.H. & Kim, H.E. Nanofiber generation of gelatin–hydroxyapatite biomimetics for guided tissue regeneration. *Adv. Funct. Mater*. **15**, 1988-1994 (2005).

82. Jaiswal, A.K., Chhabra, H., Soni, V.P. & Bellare, J.R. Enhanced mechanical strength and biocompatibility of electrospun polycaprolactone-gelatin scaffold with surface deposited nano-hydroxyapatite. *Mater. Sci. Eng*. **33**, 2376-2385 (2013).

83. Honghe, Z. Interaction mechanism in sol-gel transition of alginate solutions by addition of divalent cations. *Carbohydr. Res*. **302**, 97-101 (1997).

84. Thien, D.V.H., Hsiao, S.W., Ho, M.H., Li, C.H. & Shih, J.L. Electrospun chitosan/hydroxyapatite nanofibers for bone tissue engineering. *J. Mater. Sci*. **48**, 1640-1645 (2013).

85. Tóth, M., Gergely, G., Lukács, I.E., Wéber, F., Tóth, A.L., Illés, L. & Balázsi, C. Production of polymer nanofibers containing hydroxyapatite by electrospinning. *Materials Science Forum*. **659**, 257-262 (2010).

86. Wang, L., Feng, H.L., Mei, F., Hu, X.Y., Deng, X.L., Yang, X.P., Tang, J.M. & Wang, X.Z. Observation of human periodontal ligament cells cultured on electrospun PLLA/HA biomaterial. *Acta Anatomica Sinica*. **4**, 573-577 (2008).

87. Lao, L., Wang, Y., Zhu, Y., Zhang, Y. & Gao, C. Poly(lactide-co-glycolide)/hydroxyapatite nanofibrous scaffolds fabricated by electrospinning for bone tissue engineering. *J. Mater. Sci. Mater. Med*. **22**, 1873-1884 (2011).

88. Doustgani, A., Vasheghani-Farahani, E., Soleimani, M. & Hashemi-Najafabadi, S. Process optimization of electrospun polycaprolactone and nanohydroxyapatite composite nanofibers using response surface methodology. *J. Nanosci. Nanotechnol*. **13**, 4708-4714 (2013).

89. Lee, S.C., Choi, H.W., Lee, H.J., Kim, K.J., Chany, J.H., Kim, S.Y., Choi, J., Oh, K.S. & Jeong, Y.K. In-situ synthesis of reactive hydroxyapatite nano-crystals for a novel approach of surface grafting polymerization. *J. Mater. Chem*. **17**, 174-180 (2007).

90. Li, H.Y., Chen, Y.F. & Xie, Y.S. Nanocomposites of cross-linking polyanhydrides and hydroxyapatite needles: mechanical and degradable properties. *Mater. Lett*. **58**, 2819-2823 (2004).

91. Song, J.H., Kim, H.E. & Kim, H.W. Electrospun fibrous web of collagen-apatite precipitated nanocomposite for bone regeneration. *J. Mater. Sci. Mater. Med*. **19**, 2925-2932 (2008).

92. Kikuchi, M., Itoh, S., Ichinose, S., Shinomiya, K. & Tanaka, J. Self-organization mechanism in a bone-like hydroxyapatite/collagen nanocomposite synthesized in vitro and its biological reaction in vivo. *Biomaterials*. **22**, 1705-1711 (2001).

93. Kikuchi, M., Ikoma, T., Itoh, S., Matsumoto, H.N., Koyama, Y., Takakuda, K., Shinomiya, K. & Tanaka, J. Biomimetic synthesis of bone-like nanocomposites using the self-organization mechanism of hydroxyapatite and collagen. *Compos. Sci. Technol.* **64**, 819-825 (2004).

94. Prajapati, S., Tao, J., Ruan, Q., De Yoreo, J.J. & Moradian-Oldak, J. Matrix metalloproteinase-20 mediates dental enamel biomineralization by preventing protein occlusion inside apatite crystals. *Biomaterials*. **75**, 260-270 (2016).

95. Li, K., Zhang, Z., Li, D., Zhang, W., Yu, X., Liu, W., Gong, C., Wei, G. & Su, Z. Biomimetic ultralight, highly porous, shape-adjustable, and biocompatible 3D graphene minerals via incorporation of self-assembled peptide nanosheets. *Adv. Funct. Mater*. **28**, 1801056 (2018).

96. Takeuchi, A., Ohtsuki, C., Miyazaki, T., Tanaka, H., Yamazaki, M. & Tanihara, M. Deposition of bone-like apatite on silk fiber in a solution that mimics extracellular fluid. *J. Biomed. Mater. Res*. **65**, 283-289 (2003).

97. Wei, G., Reichert, J., Bossert, J. & Jandt, K.D. Novel biopolymeric template for the nucleation and growth of hydroxyapatite crystals based on self-assembled fibrinogen fibrils. *Biomacromolecules*. **9**, 3258-3267 (2008).

98. Nonoyama, T., Ogasawara, H., Tanaka, M., Higuchi, M. & Kinoshita, T. Calcium phosphate biomineralization in peptide hydrogels for injectable bone-filling materials. *Soft Matter*. **8**, 11531-11536 (2012).

99. Ceylan, H., Kocabey, H., Gulsuner, U., Balcik, O.S., Guler, M.O. & Tekinay, A.B. Bone-like mineral nucleating peptide nanofibers induce differentiation of human mesenchymal stem cells into mature osteoblasts. *Biomacromolecules*. **15**, 2407-2418 (2014).

100. Eren, E.D., Tansik, G., Tekinay, A.B. & Guler, M.O. Mineralized peptide nanofiber gels for enhanced osteogenic differentiation. *Chemnanomat*. **4**, 837-845 (2018).

101. Sargeant. T.D., Aparicio, C., Goldberger, J.E., Cui, H. & Stupp. S.I. Mineralization of peptide amphiphile nanofibers and its effect on the differentiation of human mesenchymal stem cells. *Acta Biomaterialia*. **8**, 2456-2465 (2012).

102 .Anderson, J.M., Patterson, J.L., Vines, J.B., Javed, A., Gilbert, S.R. & Jun, H.W. Biphasic peptide amphiphile nanomatrix embedded with hydroxyapatite nanoparticles for stimulated osteoinductive response. *ACS Nano*. **5**, 9463-9479 (2011).

103. Ghosh, M., Halperin-Sternfelds, M., Grigoriants, I., Lee, J., Nam, K.T. & Adler-Abramovich, L. Arginine-presenting peptide hydrogels decorated with hydroxyapatite as biomimètic scaffold for bone regeneration. *Biomacromolecules*. **18**, 3541-3550 (2017).

104. Temenoff, J.S., Park, H., Jabbari, E., Sheffield, T.L., LeBaron, R.G., Ambrose, C.G. & Mikos, A.G. In vitro osteogenic differentiation of marrow stromal cells encapsulated in biodegradable hydrogels. *J. Biomed. Mater. Res*. **70**, 235–244 (2004).

105. Benoit, D.S., Durney, A.R. & Anseth, K.S. The effect of heparin-functionalized PEG hydrogels on three-dimensional human mesenchymal stem cell osteogenic differentiation. *Biomaterials*. **28**, 66–77 (2007).

106. Yokoi, H., Kinoshita T. & Zhang, S. Dynamic reassembly of peptide RADA16 nanofiber scaffold. *Proc. Natl. Acad. Sci. U.S.A.* **102**, 8414-8419 (2005).

107. Holmes, T., de Lacalle, S., Su, X., Rich A. & Zhang, S. Extensive neurite outgrowth and active synapse formation on self-assembling peptide scaffolds. *Proc. Natl. Acad. Sci*. U.S.A. **97**, 6728-6733 (2000).

108. Bakota, E.L., Wang, Y., Danesh F.R. & Hartgerink, J.D. Injectable multidomain peptide nanofiber hydrogel as a delivery agent for stem cell secretome. *Biomacromolecules*. **12**, 1651-1657 (2011).

109. Kretsinger, J.K., Haines, L.A., Ozbas, B., Pochan, D.J. & Schneider, J.P. Cytocompatibility of self-assembled beta-hairpin peptide hydrogel surfaces. *Biomaterials*. **26**, 5177-5186 (2005).

110. Nagai, Y., Yokoi, H., Kaihara, K. & Naruse, K. The mechanical stimulation of cells in 3D culture within a self-assembling peptide hydrogel. *Biomaterials*. **3**, 1044-1051 (2012).

111. Jung, J.P., Gasiorowski, J.Z. & Collier, J.H. Fibrillar peptide gels in biotechnology and biomedicine. *Biopolymers*. **94**, 49-59 (2009).

112. Mi, K., Wang, G., Liu, Z., Feng, Z., Huang, B. & Zhao, X. Influence of self-assembling peptide, RADA16, compared with collagen I and matrigel on the malignant phenotype of human breast-cancer cells in 3D cultures and in vivo. *Macromol. Biosci*. **9**, 437-443 (2009).

113. Semino, C.E. Self-assembling peptides: from bio-inspired materials to bone regeneration. J. Dent. Res. **87**, 606–616 (2008).

114. Beniash, E., Hartgerink, J.D., Storrie, H., Stendahl, J.C. & Stupp, S.I. Self-assembling peptide amphiphile nanofiber matrices for cell entrapment. *Acta Biomater*. **1**, 387–397 (2005).

115. Anderson, J.M., Kushwaha, M., Tambralli, A., Bellis, S.L., Camata, R.P. & Jun, H.W. Osteogenic differentiation of human mesenchymal stem cells directed by extracellular matrix-mimicking ligands in a biomimetic self-assembled peptide amphiphile nanomatrix. *Biomacromolecules*. **10**, 2935–2944 (2009).

116. Andukuri, A., Minor, W.P., Kushwaha, M., Anderson, J.M. & Jun, H.W. Effect of endothelium mimicking self-assembled nanomatrices on cell adhesion and spreading of human endothelial cells and smooth muscle cells. *Nanomedicine*. **6**, 289–297 (2010).

117. Kim, J.K., Anderson, J., Jun, H.W., Repka, M.A. & Jo, S. Self-assembling peptide amphiphile-based nanofiber gel for bioresponsive cisplatin delivery. *Mol. Pharm*. **6**, 978–985 (2009).

118. Anderson, J.M., Andukuri, A., Lim, D.J. & Jun, H.W. Modulating the gelation properties of self-assembling peptide amphiphiles. *ACS Nano*. **3**, 3447–3454 (2009).

119. Amosi, N., Zarzhitsky, S., Gilsohn, E., Salnikov, O., Monsonego-Ornan, E., Shahar, R. & Rapaport, H. Acidic peptide hydrogel scaffolds enhance calcium phosphate mineral turnover into bone tissue. *Acta Biomater*. **8**, 2466-2475 (2012).

120. Green, H., Ochbaum, G., Gitelman-Povimonsky, A., Bitton, R. & Rapaport, H. RGD-presenting peptides in amphiphilic and anionic b-sheet hydrogels for improved interactions with cells. *RSC Adv*. **8**, 10072-10080 (2018).

121. Gungormus, M., Branco, M., Fong, H., Schneider, J.P., Tamerler, C. & Sarikaya, M. Self assembled bi-functional peptide hydrogels with biomineralization-directing peptides. *Biomaterials*. **31**, 7266-7274 (2010).

122. Lee, S.Y., Choi, J.H. & Xu, Z.H. Microbial cell-surface display. *Trends Biotechnol.* **21**, 45-52 (2003).

123. Sarikaya, M., Tamerler, C., Jen, A.K., Schulten, K. & Baneyx, F. Molecular biomimetics: nanotechnology through biology. *Nat. Mater*. **2**, 577-585 (2003).

124. Sarikaya, M. Biomimetics: materials fabrication through biology. Proc. *Natl. Acad. Sci. U.S.A.* **96**, 14183-14185 (1999).

125. Sarikaya, M., Tamerler, C., Schwartz, D.T. & Baneyx, F.O. Materials assembly and formation using engineered polypeptides. *Annu. Rev. Mater. Res*. 34, 373-408 (2004).

126. Tamerler, C., Khatayevich, D. Gungormus, M. Kacar, T., Oren, E.E., Hnilova, M. & Sarikaya, M. Molecular biomimetics: GEPI-based biological routes to technology. *Biopolymers*. **94**, 78-94 (2010).

127. Parisi-Amon, A., Lo, D.D., Montoro, D.T., Dewi, R.E., Longaker, M.T & Heilshorn, S.C. Protein–nanoparticle hydrogels that self-assemble in response to peptide-based molecular recognition. *ACS Biomater. Sci. Eng.* **3**, 750–756 (2017).

128. Zhang, L., Chan, J.M., Gu, F.X., Rhee, J.W., Wang, A.Z., Radovic-Moreno, A. F., Alexis, F., Langer, R. & Farokhzad, O.C. Self-assembled lipid–polymer hybrid nanoparticles: a robust drug delivery platform. *ACS Nano*. **2**, 1696– 1702 (2008).

129. Appel, E.A., Tibbitt, M.W., Greer, J.M., Fenton, O.S., Kreuels, K.; Anderson, D. G. & Langer, R. Exploiting electrostatic interactions in polymer–nanoparticle hydrogels. *ACS Macro Lett*. **4**, 848– 852 (2015).

130. McCarthy, H.O., McCaffrey, J., McCrudden, C.M., Zholobenko, A., Ali, A.A., McBride, J.W., Massey, A.S., Pentlavalli, S., Chen, K.H., Cole, G., Lougahrn, S.P., Dunne, N.J., Donnelly, R.F., Kett, V.L. & Robson, T. Development and characterization of self-assembling nanoparticles using a bio-inspired amphipathic peptide for gene delivery. *J. Control. Rel*. **189**, 141-149 (2014).

131. Massey, A.S., Pentlavalli, S., Cunningham, R., McCrudden, C.M., Mcerlean, E.M., Redpathhlam, P., Ali, A.A., Annett, S., McBride, J.W., McCaffrey, J., Robson, T., Migaud, M.E. & McCarthy, H.O. Potentiating the anticancer properties of bisphosphonates by nanocomplexation with the cationic amphipathic peptide, RALA. *Mol. Pharmaceutics.* **13**, 1217–1228 (2016).

132. Ibrahim, T., Mercatali, L., Sacanna, E., Tesei, A., Carloni, S., Ulivi, P., Liverani, C., Fabbri, F., Zanoni, M., Zoli, W. & Amadori, D. Inhibition of breast cancer cell proliferation in repeated and non-repeated treatment with zoledronic acid. *Cancer Cell Int*. **12**, 48−60 (2012).

133. Mani, J., Vallo, S., Barth, K., Makarevic, J., Juengel, E., Bartsch, G., Wiesner, C., Haferkamp, A. & Blaheta, R.A. Zoledronic acid influences growth, migration and invasive activity of prostate cancer cells in vitro. *Prostate Cancer Prostatic Dis*. **15**, 250−255 (2012).

134. Murphy, C.M., O'Brien, F.J., Little, D.G. & Schindeler, A. Cell-scaffold interactions in the bone tissue engineering triad. *Eur Cell Mater*. **26**, 120-132 (2013).

135. Tsukamoto, J., Naruse, K., Nagai, Y., Kan, S., Nakamura, N., Hata, M., Omi, M., Hayashi, T., Kawai, T. & Matsubara, T. Efficacy of a self-assembling peptide hydrogel, SPG-178-gel, for bone regeneration and three-dimensional osteogenic induction of dental pulp stem cells. *Tissue Eng*. **23**, 1394-1402 (2017).

136. Pittenger, M.F., Mackay, A.M., Beck, S.C., Jaiswal, R.K., Douglas, R., Mosca, J.D., Moorman, M.A., Simonetti, D.W., Craig, S. & Marshak, D.R. Multilineage potential of adult human mesenchymal stem cells. *Science*. **284**, 143-147 (1999).

137. Wu, G., Pan, M., Wang, X., Wen, J., Cao, S., Li, Z., Li, Y., Qian, C., Liu, Z., Wu, W., Zhu, L. & Guo, J. Osteogenesis of peripheral blood mesenchymal stem cells in self assembling peptide nanofiber for healing critical size calvarial bony defect. *Sci. Rep*. **5**, 16681 (2015).

138. Stenderup, K., Justesen, J., Clausen, C. & Kassem, M. Aging is associated with decreased maximal life span and accelerated senescence of bone marrow stromal cells. *Bone*. **33**, 919-926 (2003).

139. Gronthos, S., Brahim, J., Li, W., Fisher, L.W., Cherman, N., Boyde, A., DenBesten, P., Robey, P.G. & Shi, S. Stem cell properties of human dental pulp stem cells. *J. Dent. Res.* **81**, 531-535 (2002).

140. Mankani, M.H., Afghani, S., Franco, J., Launey, M., Marshall, S., Marshall, G.W., Nissenson, R., Lee, J., Tomsia, A.P. & Saiz, E. Lamellar spacing in cuboid hydroxyapatite scaffolds regulates bone formation by human bone marrow stromal cells. *Tissue Eng. Part A.* **17**, 1615-1623 (2011).

141. Bokhari, M.A., Akay, G., Zhang, S. & Birch, M.A. The enhancement of osteoblast growth and differentiation in vitro on a peptide hydrogel—polyHIPE polymer hybrid material. *Biomaterials*. **26**, 5198-5208 (2005).

142. Botchwey, E.A., Dupree, M.A., Pollack, S.R., Levine, E.M. & Laurencin, C.T. Tissue engineered bone: measurement of nutrient transport in three dimensional matrices. *J. Biomed. Mater. Res*. *A*. **67**, 357-367 (2003).

143. Shea, L.D., Smiley, E., Bonadio, J. & Mooney, D.J. DNA delivery from polymer matrices for tissue engineering. *Nat. Biotechnol*. **17**, 551-554 (1999).

144. Zhang, Z., Wu, G., Cao, Y., Liu, C., Jin, Y., Wang, Y., Yang, L., Guo, J. & Zhu, L. Self-assembling peptide and nHA/CTS composite scaffolds promote bone regeneration through increasing seed cell adhesion. *Mater. Sci. Eng. C.* **93**, 445-454 (2018).

145. Hamada, K., Hirose, M., Yamashita, T. & Ohgushi, H. Spatial distribution of mineralized bone matrix produced by marrow mesenchymal stem cells in self-assembling peptide hydrogel scaffold. *J. Biomed. Mater. Res*. **84**, 128–136 (2008).

146. Genové, E., Shen, C., Zhang, S. & Semino, C.E. The effect of functionalized self-assembling peptide scaffolds on human aortic endothelial cell function. *Biomaterials*. **26**, 3341-3351 (2005).

147. Semino, C.E., Merok, J.R., Crane, G.G., Panagiotakos, G. & Zhang, S. Functional differentiation of hepatocyte-like spheroid structures from putative liver progenitor cells in three-dimensional peptide scaffolds. *Differentiation*. **71**, 262-270 (2003).

148. Shivachar, A. Chapter 8: Isolation and culturing of glial, neuronal and neural stem cell types encapsulated in biodegradable peptide hydrogel. In Topics in Tissue Engineering; Ashammakhi, N., Reis, R., Chiellini, F., Eds.*; Biomaterials and Tissue Engineering Group: Oulu, Finland*. **4**, 1-22 (2008).

149. Guo, J., Su, H., Zeng, Y., Liang, Y.X., Wong, W.M., Ellis-Behnke, R.G., So, K.F. & Wu, W. Reknitting the injured spinal cord by self-assembling peptide nanofiber scaffold. *Nanomedicine*. **3**, 311-321 (2007).

150. Ando, K., Imagama, S., Kobayashi, K., Ito, K., Tsushima, M., Morozumi, M., Tanaka, S., Machino, M., Ota, K., Nishida, K., Nishida, Y. & Ishiguro, N. Effects of a self-assembling peptide as a scaffold on bone formation in a defect. *PLoS ONE*. **13**. e0190833 (2018).

151. Wu, L.C., Yang, J. & Kopecek. J. Hybrid hydrogels self-assembled from graft copolymers containing complementary β-sheets as hydroxyapatite nucleation scaffolds. *Biomaterials*. **32**, 5341-5353 (2011).

152. Mata, A., Geng, Y., Henrikson, K.J., Aparicio, C., Stock, S.R., Satcher, R.L. & Stupp, S.I. Bone regeneration mediated by biomimetic mineralization of a nanofiber matrix. *Biomaterials.* **31**, 6004-6012 (2010).

153. Jadlowiec, J., Koch, H., Zhang, X., Campbell, P.G., Seyedain, M. & Sfeir, C. Phosphophoryn regulates the gene expression and differentiation of NIH3T3, MC3T3-E1, and human mesenchymal stem cells via the integrin/MAPK signaling pathway. *J. Biol. Chem*. **279**, 53323-53330 (2004).

154. Yusufoglu, Y., Hu, Y., Kanapathipillai, M., Kramer, M., Kalay, Y.E., Thiyagarajan, P., Akinc, M., Schmidt-Rohr, K. & Mallapragada, S. Bioinspired synthesis of self-assembled calcium phosphate nanocomposites using block copolymer-peptide conjugates. *J. Mater. Res*. **23**, 3196-3212 (2008).

155. Ng, M.H., Duski, S., Tan, K.K., Yusof, M.R., Low, K.C., Rose, I.M., Mohamed, Z., Saim, A.B. & Idrus, R.B.H. Repair of segmental load-bearing bone defect by autologous mesenchymal stem cells and plasma-derived fibrin impregnated ceramic block results in early recovery of limb function. *Biomed. Res. Int*. 1–11 (2014).

156. Nkenke, E. & Neukam, F.W. Autogenous bone harvesting and grafting in advanced jaw resorption: Morbidity, resorption and implant survival. *Eur. J. Oral Implantol*. **7**, S203-S217 (2014).

157. Gu, H., Xiong, Z., Yin, X., Li, B., Mei, N., Li, G. & Wang, C. Bone regeneration in a rabbit ulna defect model: use of allogeneic adipose-derived stem cells with low immunogenicity. *Cell Tissue Res*. **358**, 453–464 (2014).

158. Laurencin, C., Khan, Y. & El-Amin, S.F. Bone graft substitutes. *Expert Rev. Med. Devices.* **3**, 49-57 (2006).

159. Huang, Q., Zou, Y., Arno, M.C., Chen, S., Wang, T., Gao, J., Dove, A.P. & Du, J. Hydrogel scaffolds for differentiation of adipose-derived stem cells. *Chem. Soc. Rev*. **46**, 6255-6275 (2017).

160. Dong, L., Wang, S.J., Zhao, X.R., Zhu, Y.F. & Yu, J.K. 3D-printed poly(ε-caprolactone) scaffold integrated with cell-laden chitosan hydrogels for bone tissue engineering. *Sci. Rep*. **7**, 13412 (2017).

161. Dehsorkhi, A., Castelletto, V. & Hamley, I.W. Self-assembling amphiphilic peptides. *J. Pept. Sci*. **20**, 453-467 (2014).

162. Liu, H., Cheng, Y., Chen, J., Chang, F., Wang, J., Ding, J. & Chen, X. Component effect of stem cell-loaded thermosensitive polypeptide hydrogels on cartilage repair. *Acta Biomater*. **73**, 103-111 (2018).

163. Mohammadi, M., Alibolandi, M., Abnous, K., Salmasi, Z., Jaafari, M.R. & Ramezani, M. Fabrication of hybrid scaffold based on hydroxyapatite-biodegradable nanofibers incorporated with liposomal formulation of BMP-2 peptide for bone tissue engineering. *Nanomedicine*. **14**, 1987-1997 (2018).

164. Babitha, S., Annamalai, M., Dykas, M.M.Saha, S., Poddar, K., Venugopal, J.R., Ramakrishna, S., Venkatesa, T. & Korrapati, P.S. Fabrication of a biomimetic Zein PDA nanofibrous scaffold impregnated with BMP-2 peptide conjugated TiO2 nanoparticle for bone tissue engineering. *J. Tissue Eng. Regen. Med*. **12**, 991-1001 (2018).

165. Quan, C., Zhang, Z., Liang, P., Zheng, J., Wang, J., Hou, Y. & Tang, Q. Bioactive gel self-assembled from phosphorylate biomimetic peptide: A potential scaffold for enhanced osteogenesis. *Inter. J. Biol. Macromol*. **121**, 1054-1060 (2019).

166. Hannig, M. & Hannig, C. Nanomaterials in preventive dentistry. *Nat. Nanotechnol*. **5**, 565-569 (2010).

167. Elkassas, D. & Arafa, A. The innovative applications of therapeutic nanostructures in dentistry. *Nanomedicine*. **13**, 1543-1562 (2017).

168. Huang, Z., Newcomb, C.J., Bringas Jr., P., Stupp, S.I., Snead, M.L. Biological synthesis of tooth enamel by an artificial matrix. *Biomaterials.* **31**, 9202-9211 (2010).

169. Paine, M.L., White, S.N., Luo, W., Fong, H., Sarikaya, M. & Snead, M.L. Regulated gene expression dictates enamel structure and tooth function. *Matrix Biol*. **20**, 273-292 (2001).

170. Fincham, A.G., Moradian-Oldak, J., Diekwisch, T.G., Lyaruu, D.M., Wright, J.T., Bringas Jr., P. & Slavkin, H.C. Evidence for amelogenin "nanospheres" as functional components of secretory-stage enamel matrix. *J. Struct. Biol*. **115**, 50-59 (1995).

171. Fukumoto, S., Kiba, T., Hall, B., Iehara, N., Nakamura, T., Longenecker, G., Krebsbach, P.H., Nanci, A., Kulkarni, A.B. & Yamada, Y. Ameloblastin is a cell adhesion molecule required for maintaining the differentiation state of ameloblasts. *J. Cell Biol*. **167**, 973-983 (2004).

172. Simmer, J.P. & Hu, J.C. Expression, structure, and function of enamel proteinases. *Connect Tissue Res*. **43**, 441-449 (2002).

173. Brunton, P.A., Davis, R.P., Burke, J.L., Smith, A., Aggeli, A., Brookes, S.J. & Kirkham, J. Treatment of early caries lesions using biomimetic self-assembling peptides – a clinical safety trial. *Br. Dent. J.* **215**, E1-E6 (2013).

174. Kirkham, J., Firth, A.,Vemals, D., Boden, N., Robinson, C., Shore, R.C., Brooke, S.J. & Aggeli, A. Self-assembling peptide scaffolds promote enamel remineralization. *J. Dent. Res*. **86**, 426-430 (2007).

175. Takahashi, F., Kurokawa, H., Shibasaki, S., Kawamoto, R., Murayama, R. & Miyazaki, M. Ultrasonic assessment of the effects of self-assembling peptide scaffolds on preventing enamel demineralization. *Acta Odontol. Scand*. **74**, 142-147 (2016).

176. Li, Q., Ning, T., Cao, Y., Zhang, W., Mei, M. & Chu, C. A novel self-assembled oligopeptide amphiphile for biomimitic mineralization of enamel. *BMC Biotechnol*. **14**, 32-43 (2014).

177. Aggeli, A., Bell, M., Boden, N., Keen, J.N., Knowles, P.F., McLeish, T.C.B., Pitkeathly, M. & Radford, S.E. Responsive gels formed by the spontaneous self-assembly of peptides into polymeric β-sheet tapes. *Nature*. **386**, 259–262 (1997).

178. Alkilzy, M., Santamaria, R.M., Schmoeckel, J. & Splieth, C.H. Treatment of carious lesions using self-assembling peptides. *Adv. Dental Res.* **29**, 42-47 (2018).

179. Romanelli, S.M., Fath, K.R., Phekoo, A.P., Knoll, G.A. & Barnejee, I.A. Layer-by-layer assembly of peptide based bioorganic–inorganic hybrid scaffolds and their interactions with osteoblastic MC3T3-E1 cells. *Mater. Sci. Eng*. **51**, 316-328 (2015).

180. Simecek, J.W., Diefenderfer, K.E. & Cohen, M.E. An evaluation of replacement rates for posterior resin-based composite and amalgam restorations in U.S. Navy and Marine Corps recruits. *J. Am. Dent. Assoc.* **140**, 200-209 (2009).

181. Ye, Q., Spencer, P., Yuca, E. & Tamerler, C. Engineered peptide repairs adhesive-dentin interface. *Macromol. Mater. Eng*. **302**, 1600487 (2017).

182. Wang, R., Wang, Q., Wang, X., Tian, L., Liu, H., Zhao, M., Peng, C., Cai, Q. & Shi, Y. Enhancement of nano-hydroxyapatite bonding to dentin through a collagen/calcium dual-affinitive peptide for dentinal tubule occlusion. *J. Biomater. Appl*. **29** , 268-277 (2014).

183. Lopez, A.D., Mathers, C.D., Ezzati, M., Jamison, D.T. & Murray, C.J. Global and regional burden of disease and risk factors, 2001: systematic analysis of population health data. *Lancet*. **367**, 1747-1757 (2006).

184. Katta, J., Stapleton, T., Ingham, E., Jin, Z. & Fisher, J. The effect of glycosaminoglycan depletion on the friction and deformation of articular cartilage. *Proc. Inst. Mech. Eng*. **222**, 1-11 (2008).

185. Khan, I.M., Gilbert, S.J., Singhrao, S.K., Duance, V.C. & Archer, C.W. Cartilage integration: evaluation of the reasons for failure of integration during cartilage repair. A review. *Eur. Cell. Mater*. **16**, 26-39 (2008).

186. Davies, L.C., Blain, E.J., Caterson, B. & Duance, V.C. Chondroitin sulphate impedes the migration of a subpopulation of articular cartilage chondrocytes. *Osteoarthritis Cartilage*. **16**, 855-864 (2008).

187. Huey, D.J., Hu, J.C. & Athanasiou, K.A. Unlike bone, cartilage regeneration remains elusive. *Science*. **338**, 917-921 (2012).

188. Nehrer, S., Spector, M. & Minas, T. Histologic analysis of tissue after failed cartilage repair procedures. *Clin. Orthop. Relat. Res*. **365**, 149–162 (1999).

189. Brown, W.E., Huey, D.J. & Hu, J.C., Athanasiou, K.A. Functional self-assembled neocartilage as part of a biphasic osteochondral construct. *PLoS ONE*. **13**, e0195261 (2018).

190. Roelofs, A.J., Rocke, J.P. & De Bari, C. Cell-based approaches to joint surface repair: a research perspective. *Osteoarthritis Cartilage*. **21**, 892–900 (2013).

191. Johnstone, B., Hering, T.M., Caplan, A.I., Goldberg, V.M. & Yoo, J.U. In vitro chondrogenesis of bone marrow-derived mesenchymal progenitor cells. *Exp. Cell Res.* **238**, 265–272 (1998).

192. Zhou, G., Liu, W., Cui, L., Wang, X., Liu, T. & Cao, Y. Repair of porcine articular osteochondral defects in non-weightbearing areas with autologous bone marrow stromal cells. *Tissue Eng*. **12**, 3209–3221 (2006).

193. Kisiday, J.D., Kopesky, P.W., Evans, C.H., Grodzinsky, A.J., McIlwraith, C.W. & Frisbie, D.D. Evaluation of adult equine bone marrow- and adipose-derived progenitor cell chondrogenesis in hydrogel cultures. *J. Orthop. Res*. **26**, 322–331 (2008).

194. Kisiday, J.D., Colbath, A.C. & Tangtrongsup, S. Effect of culture duration on chondrogenic preconditioning of equine bone marrow mesenchymal stem cells in self-assembling peptide hydrogel. *J. Orthopedic Res*.**10**, 564-578 (2018).

195. Schuman. L., Buma, P., Versleyen, D., de Man, B., van der Kraan, P.M., van den Berg, W.B. & Homminga, G.N. Chondrocyte behaviour within different types of collagen gel in vitro. *Biomaterials*. **16**, 809–814 (1995).

196. Häuselmann, H.J., Fernandes, R.J., Mok, S.S., Schmid, T.M., Block, J.A., Aydelotte, M.B., Kuettner, K.E. & Thonar, E.J. Phenotypic stability of bovine articular chondrocytes after long-term culture in alginate beads. *J. Cell Sci*. **107**, 17–27 (1994).

197. Freed, L.E., Marquis, J.C., Nohria, A., Emmanual, J., Mikos, A.G. & Langer, R. Neocartilage formation in vitro and in vivo using cells cultured on synthetic biodegradable polymers. *J. Biomed. Mater. Res*. **27**, 11–23 (1993).

198. Bryant, S.J. & Anseth, K.S. The effects of scaffold thickness on tissue engineered cartilage in photocrosslinked poly(ethylene oxide) hydrogels. *Biomaterials*. **22**, 619–626 (2001).

199. Kisiday, J., Jin, M., Kurz, B., Hung, H., Semino, C., Zhang, S. & Grodzinsky, A.J. Self-assembling peptide hydrogel fosters chondrocyte extracellular matrix production and cell division: Implications for cartilage tissue repair. *Proc. Natl. Acad. Sci*. **99**, 9996-10001 (2002).

200. Barco, A., Ingham, E., Fisher, J., Fermor, H. & Davies, R.P.W. On the design and efficacy assessment of self-assembling peptide-based hydrogel-glycosaminoglycan mixtures for potential repair of early stage cartilage degeneration. *J. Pep. Sci*. **24**, e3114 (2018).

CONCLUSIONS

The main implication of this work is the development of HAp nanoparticles coated with $P_2O_7^{4-}$, polyP or ATMP for their application as drug delivery systems with an easy internalization into cells. The main conclusions derived from this thesis can be summarized as follows.

DNA adsorbed on hydroxyapatite surfaces

- The synthesis and characterization of HAp NPs reflected that the main physical properties (*e.g.*, zeta potential, particle dimension, surface area, crystallinity and crystallite size) and morphology strongly depend on the synthesis conditions (*e.g.*, pH, temperature, solvent, and aging conditions).
- Molecular dynamic simulations indicate a specific binding affinity between HAp and DNA. The backbone of the double helix can act as an affective template for HAp growth.
- Calcium phosphate clusters are formed at the first stages of dynamic simulations, which subsequently reorganize to nucleate HAp. This effect is produced in both the absence and, the presence of DNA, indicating that DNA do not inhibit but even promote the mineral growth.
- HAp-bound DNA is more resistant to decay and less susceptible to degradation by serum and nucleases. This feature may account for the long-term persistence of DNA in bone and tooth.

Synergistic approach to elucidate the incorporation of magnesium ions into hydroxyapatite

- The synthesis and characterization of Mg-HAp nanoparticles indicated that both the synthetic conditions and the presence of Mg^{2+} in the feeding medium significantly affect the morphology and, therefore, the surface area of the particles.
- The presence of magnesium ions in the HAp host lattice did not alter the stability of the high temperature HAp phase, which is often a requeriment for ceramic processing. In both HAp and Mg-HAp samples, the calcium phosphate phase remained as a single hexagonal phase before and after the treatment.
- Computational results indicated that Mg^{2+} ions prefer to be located at the surface area of the clusters formed at the initial nucleation stage rather than at the core region. This feature is consistent with a calcium phosphate nucleation.

Furthermore, the presence of multiple clusters indicated the formation of multiply organized Mg-HAp particles, in agreement with experimental findings.

- Although the extent of magnesium elemental substitution is minimal, it is important for biological activity and the interaction between bone mineral and calcium-phosphate implant materials. Specifically crystallinity, crystallite dimensions, carbonate-substitution level, crystal growth, solubility and surface chemistry are highly influenced.

An experimental-computer modelling study of hydroxyapatite surface adsorption of inorganic phosphates

- Atomistic quantum mechanical (DFT) calculations for the adsorption of polyP and $\mathrm{P_2O_7^{4-}}$ evidenced that this process is easier for the former than for the latter. Thus, the adsorption of $\mathrm{P_2O_7^{4-}}$ is severely limited by the surface geometry while the flexibility of triphosphate allows transforming repulsive electrostatic interactions into molecular strain. On the other hand, DFT calculations predict that the molecular architecture of ATMP is not compatible with the geometry of the HAp surface
- Experimental identification of the adsorption of trisphosphonate onto HAp crystalline particles is unclear while the adsorption of pyrophosphate and triphosphate are clearly observed as predicted by theoretical calculations.
- HAp surface adsorption of inorganic phosphates rely on three factors: (i) the inherent surface properties of materials, such as degree of crystallinity, surface area, surface energy and hydrophobicity, (ii) physiological conditions including ionic strength, pH of working solutions, and (iii) specific binding at $\mathrm{Ca^{+2}}$, $\mathrm{PO_4^{3-}}$ and $\mathrm{OH^-}$ sites, non-specific binding through hydrogen bonds and electrostatic interactions.

Influence of the atmosphere conditions in the structure, properties and solubility of fluorine-substituted hydroxyapatites

- The atmosphere used during the synthesis process significantly affects the composition of xF-HAp and FAp samples. Absorption bands associated to water and $\mathrm{CO_3^{2-}}$ are typical of xF-HAp and FAp prepared under ATM (37 ºC) conditions. Moreover, the intensity of the $\mathrm{CO_3^{2-}}$ bands increases significantly with the $\mathrm{F^-}$

intake, while is negligible for HAp. In opposition, the intensity of water and CO_3^{2-}absorption bands is imperceptible for xF-HAp and FAp samples obtained under N_2-conditions.

- The biological and physicochemical properties of HAp can be altered by F^- substitution. Both crystallinity and crystallite size increase with fluoride substitution. Contact angle measurements evidenced that the wettability decreased with increasing the fluorine content. The water absorption capacity of the minerals decreased with increasing fluorination degree, independently of the synthetic conditions. However, it is worth noting that water absorption increased with crystallinity and crystallite size. Cyclic voltammograms showed that the capacity to become electroactive through a thermally stimulated polarization process decreased with increasing fluorination degree.
- Solubility in aqueous acid media of the HAp derivatives clearly depends on their composition. More specifically, the solubility increases with the CO_3^{2-} content while it decreases with increasing the fluorination degree. Moreover, the inhibitory effect associated to the F^- ions contained in the mineral matrix was enhanced when F^- ions were supplied to HAp through an external solution. Accordingly, HAp combined with an effective external supply of fluoride anions appears highly appropriate for the fabrication of dental coatings.

Intracellular calcium deregulation mediated by hydroxyapatite nanoparticles

- A small fraction of Ca^{2+} either through release from intracellular organelles (~ 10^{-5}M) or through influx from an extracellular reservoir (~ 10^{-3}M) can activate a downstream signalling cascade. Apoptotic and autophagic death in normal cells can be triggered by subtle changes in intracellular Ca^{2+} concentration.
- The sustained high cytoplasm Ca^{2+} is toxic for cells by activating cell death signalling. The low cytosolic Ca^{2+} concentration is maintained by the Ca^{2+}transport system*, i.e.* Ca^{2+}-ATPases. Particular types of cancer express an up regulation of Ca^{2+}-ATPases, so they rapidly pump cytosolic Ca^{2+} ions back into intracellular organelles, *e.g*. endoplasmic reticulum, or to exclude Ca^{2+} ions to extracellular space.

Role of the intracellular calcium in the tumor aggressiveness. An interplay of different cell types: epithelial, endothelial and fibroblast cells

- Either up or down regulation of Ca^{2+}-ATPases can facilitate that a particular type of cancer could escape from normal cellular control and to promote tumorigenesis.
- The increase in intracellular free Ca^{2+}concentration plays a major role in many cellular processes. Deregulated Ca^{2+}homeostasis may play a role more like a “driver” than a “passenger” in carcinogenesis or tumorigenesis. Disruption of normal Ca^{2+}signalling contributes to the development of malignant phenotypes. In order to proliferate at high rates, to increase cell motility and invasion, to escape death, to fool immune-attack or to have neovascularization, tumors remodel their Ca^{2+}signalling network.
- An aspect of the tumor microenvironment where signalling is likely to be particularly significant is cancer-associated fibroblasts, which are in an “activated” state and are in a dynamic signalling interplay with cancer cells. Ca^{2+}may be critical to this signalling, as reflected from COS-1 (MCF-7 cocultures assays.

Loading of antibiotic into biocoated hydroxyapatite nanoparticles: smart antitumor platforms with regulated release

- Cells remained practically unaffected after the internalization of unloaded HAp and ACP NPs, independently of both the cell type (HUVEC, COS-1, MCF-7 or Mia PaCa-2) and the biocoating. Addition of uncoated and biocoated HAp with a sub-lethal dose of CAM NPs into non-cancerous cell types (HUVEC or COS-1) caused an almost identical response.
- A sub-lethal dose of CAM damaged MCF-7 and Mia PaCa-2 cancerous cells and led to a high percentage of died cells. Moreover, CAM/HAp NPs coated with $P_2O_7^{4-}$, polyP or ATMP increased drastically the percentage of died MCF-7 and Mia PaCa-2 cells. The protecting role of the polyP biocoating enhanced the efficiency of the antibiotic as an anticancer agent.
- CAM/HAp NPs coated with $P_2O_7^{4-}$, polyP or ATMP were effective drug delivery systems that simultaneously delivered chemotherapy drugs to cancer cells and evaded the MDR proteins mechanism that pump drugs out of the cell.

Incorporation of chloramphenicol loaded hydroxyapatite nanoparticles into polylactide

- CAM encapsulated in both amorphous and crystalline hydroxyapatite nanoparticles has been successfully loaded into electrospun PLA nanofibers. CAM was delivered from the matrix according to a Fickian diffusion process.
- The release of CAM caused clear cytotoxic effects against both Gram negative and Gram positive bacteria. Cytotoxic effects were related to the diffusion of the unmodified CAM. The encapsulated CAM molecules effectively undergo a diffusion and not degradation or modification during the whole processing.
- CAM encapsulated in both amorphous and crystalline hydroxyapatite nanoparticles could be loaded into electrospun scaffolds giving rise to a potential system for a controlled and tuneable release.

Peptide self-assembly into hydrogels for biomedical applications related with hydroxyapatite

- The most interesting application of self-assembled peptides for drugs delivery is the injectable gel formulation, in which therapeutic agents can be located next to or into target tissues at high local concentrations. Due to the slow rate of release, these formulations provide more prolonged and sustained action than conventional therapeutic agents, thus enhancing therapeutic efficacy.
- A major ongoing challenge in the field of reconstructive and regenerative medicine is the successful repair or replacement of hard tissues, such as cartilage, bone and dental tissues. Self-assembled hybrid hydrogels formed by HAp NPs and peptides enable formation of scaffolds that are mechanically similar to native ECM. These materials can be formed at the site of implantation without the use of harsh chemical cross-linking agents or the presence of adverse assembling reactions that can affect the surrounding tissues.